MPP-2006-245

Technische Universität München

Max-Planck-Institut für Physik
(Werner-Heisenberg-Institut)

Measurement of very high energy gamma–ray emission from four blazars using the MAGIC telescope and a comparative blazar study

Dissertation an der Fakultät für Physik
der Technischen Universität München
vorgelegt von

Robert Marcus Wagner

Technische Universität München

Max-Planck-Institut für Physik
(Werner-Heisenberg-Institut)

Measurement of very high energy gamma–ray emission from four blazars using the MAGIC telescope and a comparative blazar study

Robert Marcus Wagner

Vollständiger Abdruck der von der Fakultät für Physik der Technischen Universität München zur Erlangung des akademischen Grades eines

Doktors der Naturwissenschaften

genehmigten Dissertation.

Vorsitzender: Univ.-Prof. Dr. A. J. Buras
Prüfer der Dissertation:
1. Hon.-Prof. Dr. S. Bethke
2. Univ.-Prof. Dr. F. von Feilitzsch

Die Dissertation wurde am 14. November 2006 bei der Technischen Universität München eingereicht und durch die Fakultät für Physik am 19. Dezember 2006 angenommen.

Measurement of very high energy gamma–ray emission from four blazars using the MAGIC telescope and a comparative blazar study

Robert Marcus Wagner

November 2006

Bibliografische Information Der Deutschen Bibliothek
Die Deutsche Bibliothek verzeichnet diese Publikation in der Deutschen Nationalbibliografie; detaillierte bibliographische Daten sind im Internet über `http://dnb.ddb.de/` abrufbar.

Frontispiece: On a rare foggy night, mysterious laser beams seem to play across the MAGIC telescope at the Roque de los Muchachos on the Canary Island of La Palma. The lasers are actually part of a system designed to automatically adjust the focusing of the innovative, seventeen meter wide, multi-mirrored instrument. The MAGIC (Major Atmospheric Gamma Imaging Cherenkov) telescope itself is intended to detect gamma rays—photons with over 100 billion times the energy of visible light. As the gamma rays impact the upper atmosphere they produce air showers of high-energy particles. The MAGIC camera records in detail the brief flashes of optical light, called Cherenkov light, created by the air shower particles that ultimately correspond to cosmic sources of extreme gamma-rays. The dramatic picture shows the telescope in May 2004.

Summary

The thesis reports on the measurement of very high energy (VHE) gamma–rays from four Active Galactic Nuclei (AGN) with the Major Atmospheric Gamma–ray Imaging Cherenkov telescope (MAGIC).

The AGN Mkn 501 was observed with the MAGIC telescope during six weeks in 2005. A baseline flux of about 25% of the Crab nebula flux as well as high flux states of up to four times the Crab nebula flux were found. Different flux states are defined and energy spectra for these states are determined in the energy range between 100 GeV and 4 TeV. The spectra show a clear spectral hardening with increasing flux level, ranging from baseline spectra of

$$\frac{\mathrm{d}F}{\mathrm{d}E} = (0.56 \pm 0.04) \times 10^{-9} \left(\frac{E}{250\ \mathrm{GeV}} \right)^{-2.39 \pm 0.06} \ \mathrm{TeV}^{-1}\ \mathrm{cm}^{-2}\ \mathrm{s}^{-1}$$

to high flux-level spectra that can be described by

$$\frac{\mathrm{d}F}{\mathrm{d}E} = (4.11 \pm 0.16) \times 10^{-9} \left(\frac{E}{250\ \mathrm{GeV}} \right)^{-2.14 \pm 0.03} \ \mathrm{TeV}^{-1}\ \mathrm{cm}^{-2}\ \mathrm{s}^{-1}.$$

When taking into account γ-ray absorption by the extragalactic background light (EBL), a hint for an inverse Compton peak is found with the peak energy moving from (0.3 ± 0.1) TeV to (1.4 ± 0.7) TeV with increasing flux level. This evidence is strengthened by the observation of a moving structure also in the measured spectra, which are free of uncertainties of the EBL model used.

Unprecedented rapid flux variability with doubling times of ≤ 5 minutes was found during some of the observation nights. These fast flares are used to infer significant limits on the size of the acceleration region of $R \cdot \delta^{-1} \leq 10^{12}$ cm for homogeneous one–zone Self–Synchrotron Compton models. Significant spectral hardening of $\Delta\alpha = 0.4$ within less than 20 minutes could be observed. The well-defined fast flares were also used to infer a lower limit on the quantum gravity energy scale of 1.5×10^{17} GeV.

For the BL Lac object 1ES 2344+514 for the first time a differential energy spectrum during a state of low γ-ray activity is inferred, which between 140 GeV and 5 TeV can be

described by a power law of the form

$$\frac{\mathrm{d}F}{\mathrm{d}E} = (1.18 \pm 0.13) \times 10^{-11} \left(\frac{E}{500\ \mathrm{GeV}} \right)^{-2.95 \pm 0.12} \ \mathrm{TeV}^{-1}\ \mathrm{cm}^{-2}\ \mathrm{s}^{-1}$$

The study of the 24-day VHE γ-ray light curve of 1ES 2344+514 yields a low flux level of $0.04 \leq F_{E>350\ \mathrm{GeV}} \leq 0.11$ times the Crab nebula flux. In combination with the all-time (1995–2005) light curve a low emission level of about $\approx$4% of the Crab nebula flux is found.

Within the thesis, predictions for the detectability of BL Lac candidate objects in VHE γ-rays with the MAGIC telescope are presented. These predictions led to the discovery of two new objects in this energy domain, PG 1553+113 and BL Lacertae. PG 1553+113 was detected at a high significance level of 8.8σ. The softest gamma ray spectrum observed so far in VHE γ-rays was found for this source. It can be described by a pure power law between 95 GeV and 500 GeV:

$$\frac{\mathrm{d}F}{\mathrm{d}E} = (0.18 \pm 0.03) \cdot 10^{-9} \times \left(\frac{E}{200\ \mathrm{GeV}} \right)^{-4.21 \pm 0.25} \ \mathrm{TeV}^{-1}\ \mathrm{cm}^{-2}\ \mathrm{s}^{-1}.$$

The spectrum is used to infer an upper limit of $z < 0.78$ on the yet undetermined redshift of PG 1553+113 by imposing a maximum hardness of the intrinsic spectrum. While the light curve does not show apparent short–term variability, simultaneously recorded optical data feature a substantial flare, which leaves room for interpretation of the non-existing correlations.

BL Lacertae, the prototype of the BL Lac objects, was detected at a significance level of 5.6σ. This object is the first low–frequency peaked BL Lac object seen in VHE γ-rays. A preliminary spectrum hints at a steep slope of ≈ -3.7 between 100 GeV and 1 TeV.

For the first time a synoptic study of all high–frequency peaked BL Lac-type objects detected as VHE gamma-ray emitters is performed. The intrinsic properties of the observed emission are compared and correlated among each other and with the individual estimated black hole masses. Key findings are (1) that all currently known VHE γ-ray blazars host supermassive black holes with masses exceeding 10^8 solar masses, (2) that in the current VHE blazar sample no obvious correlations of the VHE γ emission properties with the black hole masses of the blazars are found, (3) that a weak correlation of the intrinsic spectral hardness and the source distance is likely due to an EBL overprediction by the current EBL models, and (4) that there is a general trend of an increase of the VHE γ luminosity with the hardness of the intrinsic source spectra. The latter behavior is also found for sources that were observed in different emission states. Furthermore, the found luminosity distribution of the VHE γ blazar sample is used to constrain the distance of PG 1553+113. Depending on the strength of the assumptions taken, the limit varies between $z \leq 0.43$ and $z \leq 0.68$.

The technical part of the thesis deals with the implementation of a telescope drive system that permits the fast follow–up of gamma-ray bursts. For measuring the tracking accuracy of the telescope, a starfield monitoring system has been commissioned. Further, the implementation of the flux and light curve calculation within the framework of the MAGIC Analysis and Reconstruction Software is discussed. The application of the analysis chain is exemplified on the first large data sample taken on the Crab nebula with the MAGIC telescope. The observations were performed in 2004/5 to understand and calibrate the telescope. We find a light curve that is compatible with a constant γ-ray emission of $F_{E>200\,\mathrm{GeV}} = (2.16 \pm 0.07) \times 10^{-10}\,\mathrm{cm}^{-2}\,\mathrm{s}^{-1}$ and a differential γ-ray spectrum that can be described by a curved power law

$$\frac{\mathrm{d}F}{\mathrm{d}E} = (7.8 \pm 0.4) \cdot 10^{-10} \times \left(\frac{E}{250\,\mathrm{GeV}} \right)^{(-2.35\pm0.09)-(0.09\pm0.07)\log_{10}\left(\frac{E}{250\,\mathrm{GeV}}\right)} \mathrm{TeV}^{-1}\,\mathrm{cm}^{-2}\,\mathrm{s}^{-1}$$

in the energy range of $95\,\mathrm{GeV} - 6.5\,\mathrm{TeV}$. The results are well compatible with that of other experiments and with model predictions.

Zusammenfassung

In dieser Arbeit wird über Messungen von hochenergetischer Gammastrahlung von vier Aktiven Galaktischen Kernen (AGN) mit dem „Major Atmospheric Gamma–ray Imaging Cherenkov"–Teleskop (MAGIC) berichtet.

Mkn 501 war der zweite AGN überhaupt, von welchem hochenergetische Gammastrahlen nachgewiesen werden konnten. Diese Quelle wurde im Jahr 2005 mit MAGIC über sechs Wochen hinweg beobachtet. Neben einem Grundzustandsfluß von etwa 25% des Krebsnebelflusses traten Flüsse bis hin zum Vierfachen des Krebsnebelflusses auf. Es werden zunächst verschiedene Flußniveaus definiert, für welche dann differentielle Energiespektren zwischen 100 GeV und 4 TeV erstellt werden. Mit ansteigendem Fluß wird beobachtet, daß die Spektren härter werden. Das Grundzustandsspektrum wurde zu

$$\frac{\mathrm{d}F}{\mathrm{d}E} = (0.56 \pm 0.04) \times 10^{-9} \left(\frac{E}{250\ \mathrm{GeV}} \right)^{-2.39 \pm 0.06} \ \mathrm{TeV}^{-1}\ \mathrm{cm}^{-2}\ \mathrm{s}^{-1}$$

bestimmt, das Spektrum für die höchsten beobachteten Flüsse hingegen zu

$$\frac{\mathrm{d}F}{\mathrm{d}E} = (4.11 \pm 0.16) \times 10^{-9} \left(\frac{E}{250\ \mathrm{GeV}} \right)^{-2.14 \pm 0.03} \ \mathrm{TeV}^{-1}\ \mathrm{cm}^{-2}\ \mathrm{s}^{-1}.$$

Unter Berücksichtigung der Effekte der Gammastrahlungs-Absorption am extragalaktischen Hintergrundlicht (EHL) ergibt sich ein Hinweis auf ein Maximum in der Energiedichteverteilung der gemessenen Strahlung. Dieses wird im Rahmen von Modellen erwartet, die die Erzeugung der Gammaquanten durch leptonische Beschleunigung erklären. Mit ansteigendem Flußniveau bewegt sich dieses Maximum von (0.3 ± 0.1) TeV nach (1.4 ± 0.7) TeV. Diese Beobachtung wird unterstützt durch die Tatsache, daß auch ohne Berücksichtigung der EHL–Absorption und entsprechender Unsicherheiten eine mit dem Flußveränderliche Struktur in den Gammastrahlungsspektren gefunden werden kann.

Während einiger der Beobachtungsnächte wurde zum ersten Mal für hochenergetische Gammastrahlung ein sich auf Zeitskalen von ≤ 5 Minuten verdoppelnder oder halbierender Fluß gefunden. Unter Anwendung von Synchrotron-Self-Compton–Modellen ermöglichen diese Gammastrahlungsausbrüche eine starke Einschränkung der Größe der Beschleunigungsregion auf $R \cdot \delta^{-1} \leq 10^{12}$ cm. Eine signifikante Veränderung des

spektralen Index von $\Delta\alpha = 0.4$ konnte in weniger als 20 Minuten beobachtet werden. Klar identifizierbare Strukturen der Lichtkurven der Gammastrahlungsausbrüche in verschiedenen Energiebereichen wurden verwendet, um die Energieskala für Quanteneffekte der Gravitation auf $E_{\mathrm{qg}} \geq 1.5 \times 10^{17}$ GeV einzuschränken.

Für das BL Lac-Objekt 1ES 2344+514 wurde erstmalig ein differentielle Energiespektrum in einem Zustand niedriger Gammastrahlungsemission hergeleitet, welches zwischen 140 GeV und 5 TeV durch ein Potenzgesetz der From

$$\frac{\mathrm{d}F}{\mathrm{d}E} = (1.18 \pm 0.13) \times 10^{-11} \left(\frac{E}{500\ \mathrm{GeV}} \right)^{-2.95 \pm 0.12} \ \mathrm{TeV}^{-1}\ \mathrm{cm}^{-2}\ \mathrm{s}^{-1}$$

beschrieben werden kann. Die gefundene, sich über 24 Beobachtungsnächte erstrekkende Lichtkurve für hochenergetische Gammastrahlung zeigt eine Fluß zwischen $0.04 \leq F_{E>350\,\mathrm{GeV}} \leq 0.11$ des Krebsnebel-Flusses. Unter Hinzunahme der Beobachtungen anderer Instrumente zwischen 1995 und 2005 wird gezeigt, daß 1ES 2344+514 im Jahr 2005 in einem niedrigen Emissionszustand vorgefunden wurde.

Diese Arbeit macht Vorhersagen über die Beobachtbarkeit von BL Lac-Objekten im Licht hochenergetischer Gammastrahlung, welche zur Entdeckung von zwei bisher nicht nachgewiesenen Objekten in diesem Energiebereich führten, PG 1553+113 und BL Lacertae. PG 1553+113 wurde auf einem Signifikanzniveau von 8.8σ entdeckt. Dieses Objekt weist das bisher weichste Energiespektrum zwischen 95 GeV und 500 GeV auf:

$$\frac{\mathrm{d}F}{\mathrm{d}E} = (0.18 \pm 0.03) \cdot 10^{-9} \times \left(\frac{E}{200\ \mathrm{GeV}} \right)^{-4.21 \pm 0.25} \ \mathrm{TeV}^{-1}\ \mathrm{cm}^{-2}\ \mathrm{s}^{-1}$$

Mit Hilfe dieses Spektrums kann die bisher unbekannte Rotverschiebung von PG 1553+113 auf $z < 0.78$ eingeschränkt werden, wenn man Annahmen über die maximale intrinische Härte des Quellspektrums trifft. Die Lichtkurve für PG 1553+113 zeigt keine Hinweise auf kurzfristige Flußveränderungen, obschon gleichzeitig ein klarer Ausbruch im sichtbaren Licht festgestellt wurde.

BL Lacertae, der Prototyp der BL Lac-Objekte, wurde auf einem Signifikanzniveau von 5.6σ als Quelle hochenergetischer Gammastrahlung nachgewiesen. Dieses Objekt ist die erste in hochenergetischer Gammastrahlung beobachtete Quelle, deren Synchrotron-Energieverteilung im optischen/ultravioletten Bereich des Spektrums ihr Maximum hat. Ein vorläufiges Spektrum der vermessenen Gammastrahlungs-Emission weist zwischen 100 GeV und 1 TeV einen Spektralindex von ≈ -3.7 auf.

Erstmalig wurde eine zusammenfassende Untersuchung aller sogenannter *high–frequency peaked* BL Lac-Objekte durchgeführt, von denen hochenergetische Gammastrahlungsemission bekannt ist. Die Eigenschaften der beobachteten Strahlung werden untereinander sowie mit den abgeschätzten Massen der zentralen schwarzen Löcher verglichen und korreliert. Die wichtigsten Ergebnisse dieser Studie sind (1) alle derzeit bekannten

BL Lac-Quellen für hochenergetische Gammastrahlung beherbergen schwarze Löcher mit Massen größer der 10^8-fachen Sonnenmasse, (2) derzeit existieren keine offensichtlichen Korrelationen zwischen den Eigenschaften der hochenergetischen Gammastrahlung und den Massen der schwarzen Löcher, (3) die schwache Korrelation zwischen der Härte der quellintrinsischen Spektren und der Entfernung der Quellen ist vermutlich bedingt durch eine Überschätzung des extragalaktischen Hintergrundlichts (EHL) durch die derzeitigen EHL-Modelle, sowie (4) es existiert eine Korrelation zwischen der Luminosität der hochenergetischen Gammastahlung und der Härte des Energiespektrums der jeweiligen Quelle. Diese Beobachtung trifft insbesondere auch auf die Quellen zu, von denen verschiedene Flußzustände bekannt sind. Weiterhin können die typischerweise beobachteten Luminositäten benutzt werden, um eine Annahme über die maximale Luminosität der Quelle PG 1553+113 zu treffen. Je nach der Stärke der getroffenen Annahme läßt sich damit die maximale Entfernung dieses Objektes zu $z \leq 0.43$ bis $z \leq 0.68$ abschätzen.

Der Beitrag zur experimentellen Technik des Teleskops behandelt die Inbetriebnahme des Antriebssystem des Teleskops, welches ein schnelles Repositionieren ermöglicht, wie es zur Gammablitz–Beobachtung benötigt wird. Um die Nachführgenauigkeit des Systems zu überwachen, wurde eine Positionsbestimmung unter Zuhilfenahme des im sichtbaren Licht beobachteten, die Quelle umgebenden Sternenfeldes implementiert. Weiterhin wird der Teil der MAGIC-Analysekette besprochen, welcher der Erstellung von differentiellen Energiespektren und Lichtkurven dient. Die Anwendung der Analysekette wird anhand eines 2004 und 2005 genommenen Datensatz von Krebsnebel-Beobachtungen dargestellt, der eine Beobachtungszeit von 15 Stunden umfaßt. Diese Analyse diente dem Verständnis und der Kalibrierung des Teleskops. Die ermittelte Lichtkurve ist verträglich mit einem konstanten Gammastrahlungsfluß von $F_{E>200\,\mathrm{GeV}} = (2.16 \pm 0.07) \times 10^{-10}\,\mathrm{cm}^{-2}\,\mathrm{s}^{-1}$ und einem differentiellen Energiespektrum, welches durch ein Potenzgesetz (mit logarithmischem Abfall) der Form

$$\frac{\mathrm{d}F}{\mathrm{d}E} = (7.8 \pm 0.4) \cdot 10^{-10} \times \left(\frac{E}{250\,\mathrm{GeV}} \right)^{(-2.35\pm0.09)-(0.09\pm0.07)\log_{10}\left(\frac{E}{250\,\mathrm{GeV}}\right)} \mathrm{TeV}^{-1}\,\mathrm{cm}^{-2}\,\mathrm{s}^{-1}$$

im Energiebereich zwischen 95 GeV und 6.5 TeV beschrieben werden kann. Die gefundenen Ergebnisse stimmen im Überlappbereich mit denen anderer Experimente sowie mit Modellen der Krebsnebel-Emission gut überein.

Contents

List of Figures

List of Tables

List of Acronyms and Abbreviations

1ES	First Einstein survey	
2MASS	Two micron all sky survey	[Jar03]
AGASA	Akeno giant air shower array	sect. 1.1
AGN	Active galactic nucleus	sect. 2
AMANDA	Antarctic muon and neutrino detector array	sect. 11
AMC	Active mirror control	
ASM	All-sky monitor (detector on board RXTE)	
a.s.l.	Above sea level	
Az	Azimuth	
BATSE	Burst and transient source experiment	
BH	Black hole	
BR	Branching ratio	
BeppoSAX	Satellite per astronomia X	
CANGAROO	Collaboration of Australia and Nippon (Japan) for a gamma-ray observatory in the outback	
CAT	Cherenkov array at Themis	
CCD	Charged coupled device	
CELESTE	Cherenkov low energy sampling and timing experiment	
CGRO	Compton gamma-ray observatory	
CIB	Cosmic infrared background	
CM	Center of mass	
CMB	Cosmic microwave background	
CORSIKA	Cosmic ray simulations for KASCADE	[Hec98]
CT	Cherenkov telescope	
c.u.	Crab unit	sect. 7.4
DAQ	Data acquisition	
DKC	Drive control units used in the drive system	
EAS	Extended air shower	sect. 3.1
EBL	Extragalactic background light	sect. 1.2.2
EGRET	Energetic gamma-ray experiment telescope	
EIC	External inverse Compton	

EINSTEIN	HEAO2 mission, renamed “EINSTEIN” after launch	
EM	Electromagnetic	
EXO	EXOSAT observation log	
FADC	Flash analog to digital converter	
FK5	Fifth fundamental catalogue	[Fri88]
FSR	Fazio–Stecker relation	sect. 1.2.2
FSRQ	Flat spectrum radio quasar	sect. 2
FWHM	Full width at half maximum	
GLAST	Gamma-ray large area space telescope	
GNCT	Global network of Cherenkov telescopes	sect. 6.5
GRB	Gamma-ray burst	[Mes02]
GRH	Gamma-ray horizon	sect. 1.2.2
GZK	Greisen–Zatsepin–Kuz’min	sect. 1.1
H.E.S.S.	High energy stereoscopic system	
HBL	High–frequency peaked BL Lac	sect. 2.1
HE	High energy	tab. 1.1
HEAO2	High energy astrophysics observatory 2	
HEGRA	High energy gamma-ray astronomy	[Dau97]
HETE	High energy timing explorer	
HFSRQ	High–peaked flat spectrum radio quasar	sect. 2.1.1
HST	Hubble space telescope	
IAC	Instituto de Astrofísica de Canarias	
IACT	Imaging atmospheric Cherenkov telescope	sect. 3
IAU	International astronomical union	
IC	Inverse Compton	sect. 1.2.1
IR	Infrared	
KASCADE	Karlsruhe shower core and array detector	
KVA	Kungliga Vetenskapsakademien [telescope]	sect. 4.8
LBL	Low–frequency peaked BL Lac	sect. 2.1
LI	Lorentz invariance	
LMC	Large Magellanic cloud	
LONS	Light of the night sky	
LZA	Large zenith angle	sect. 3.4
MACS	Micro controllers used in the drive system	sect. 4.5.2
MAGIC	Major atmospheric gamma-ray imaging Cherenkov	sect. 4
MARS	MAGIC analysis and reconstruction software	sect. 5
MC	Monte Carlo [simulations]	
MHD	Magnetohydrodynamic	
MJD	Modified Julian day	
Mkn	Markarian	
NED	NASA extragalactic database	

NGC	New general catalogue of nebulae and clusters of stars	
NKG	Nishimura–Kamata–Greisen	sect. 3.1.1
NRAO	U.S. National Radio Astronomy Observatory	
NSB	Night–sky background	
ORM	Observatorio del Roque de los Muchachos	
PG	Palomar–Green catalog of UV-excess stellar objects	[Gre86]
ph.el.	photoelectrons	
PID	Proportional–integral–differential	sect. 4.5.2
PIN	Positive intrinsic negative [diode]	
PKS	Parkes catalogue of radio sources	
PMT	Photomultiplier tube	
PPM	Positions and proper motions [star catalog]	[Roe88]
PSF	Point spread function	
PWN	Pulsar wind nebula	
QE	Quantum efficiency	
RA	Right ascension	
RASS	ROSAT all-sky survey	
RF	Random forest^{TM}	
RMS	Root mean square	
ROOT	An object–oriented data analysis framework	
ROSAT	Röntgen satellite	
RXTE	Rossi X-ray timing explorer	sect. 7.6
SCUBA	Sub-millimeter common-user bolometer array	
SE	Shaft encoder	
SED	Spectral energy distribution	
SMBH	Supermassive black hole	
SNR	Supernova remnant	
SSC	Synchrotron–self Compton	sect. 2.1.1
UHE	Ultra high energy	tab. 1.1
UTC	Coordinated universal time	
UV	Ultraviolet	
UVOT	UV/optical telescope [on board Swift]	
VCSEL	Vertical cavity surface emitting laser	
VERITAS	Very energetic radiation imaging telescope array system	
VHE	Very high energy	tab. 1.1
VLA	Very large array	
WMAP	Wilkinson microwave anisotropy probe	
XBL	X-ray selected BL Lac	
XMM	XMM-Newton satellite mission	
XRT	X-ray telescope [on board Swift]	

Useful conversion units and definitions

This section provides a small collection of information on units that are commonly used in astrophysics. We also list some important conventions followed in this work.

Astrophysical units and definitions.

Electronvolt: The energy an electron acquires in vacuum from rest through a potential difference of 1 Volt: 1 eV = $1.6022 \cdot 10^{-12}$ erg = $1.6022 \cdot 10^{-19}$ Joule

MJD: The Modified Julian Date (MJD) is defined as MJD $\equiv$ JD-2400000.5, where JD is the Julian day. JD 0 is defined as January 1, -4712 (=4713 BC), 12:00 noon Greenwich mean time. MJD is used when a continuous numbering of days is more convenient than the use of the civil calendar. Fractions of the day can be added to indicate the exact time of the day.

Solar properties: Solar mass: $M_\odot$ = 1.989×10^{30} kg; Solar luminosity: $L_\odot$ = 3.90×10^{26} W; Solar radius: $R_\odot$ = 6.96×10^{8} m

Light year: 1 light year = 9.4607×10^{15} m

AU: The astronomical unit is the mean distance between the Earth and the Sun. It is commonly used to measure distances within the solar system. 1 astronomical unit (AU) = $1.49597870 \times 10^{11}$ m

Parsec: The distance at which an object would have a parallax of one arc second is defined as 1 parsec. 1 pc = 3.26 ly = 206,265 AU = 3.0857×10^{16} m

Jansky: A unit for energy flux common in radio astronomy. 1 Jansky (Jy) = 10^{-26} W m^{-2} Hz^{-1} (named after K. Jansky)

Equatorial coordinates: The equatorial coordinate system is given by the projection of the Earth's equator and its poles onto the celestial sphere. Great circles through the celestial poles are perpendicular to the celestial equator and are called hour circles. The coordinate corresponding to the latitude is called declination (Dec) and it is the angle between the position of an object and the celestial equator measured along its hour circle. The hour angle system is fixed to the Earth like the geographic coordinate system. The hour angle of a given point is defined as the angle measured westwards along the celestial equator from the local meridian to the hour circle that passes through the point. The right ascension system is in first order fixed to the stars (neglecting precession and nutation effects). RA $= 0^{\mathrm{h}}$ is the intersection point of the equatorial plane with Earth's orbital plane, the ecliptic. RA is given in time units ($0^{\mathrm{h}} - 24^{\mathrm{h}}$), while Dec takes values from $-90^\circ - 90^\circ$ (see also fig. 4.11).

Conventions.

Zenith distance, zenith angle: The distance of a given point to the local zenith along a great circle. $Zd = 90° -$ Elevation.

Spectral index, spectral slope: In the energy region to which imaging air Cherenkov telescopes are sensitive, many astrophysical γ-ray sources exhibit power law spectra. Throughout this work, *measured* power law indices are denoted by $-\alpha$, whereas *intrinsic* power law indices are given by $-\Gamma$. Intrinsic and measured spectra may differ due to γ absorption effects, cf. sect. 1.2.2.

Observation night designation: Note that within MAGIC and within this thesis, full observation nights by convention are always designated by the date or the integer MJD of the following day. This avoids ambiguities, as both the date and the integer MJD change during each observation night.

Introduction

"Never think that the poetry of Nature's moods in all their infinite variety is lost on the scientific observer, for the habit of observing refines our sense of beauty and adds a brighter hue to the richly colored background against which each particular fact is outlined."

(Marcel Minnaert)

In astronomy, the opening of each new spectral window has proven to add new, substantial, and unique information which cannot be obtained by other means. It all started with Galileo in the early years of the 17th century, when he for the first time used an optical instrument for astronomical observations. He published his discovery of the four *Galilean satellites* of Jupiter in the *Sidereus Nuncius*, the sidereal messenger: *"I should disclose and publish to the world the occasion of discovering and observing four Planets, never seen from the beginning of the world up to our own times..."*. His observations also led him to the correct physical interpretation, namely that these discovered celestial bodies were orbiting Jupiter.

From the 20th century on, astronomy witnessed many of such breakthroughs:

Radio astronomy with its foundations in the 1930s led to the discovery of new classes of objects, including pulsars, quasars and radio galaxies. The scent of extreme energetic physical processes in the universe came about by studying the underlying physical processes in these objects. Even more, radio measurements of rotation curves of galaxies prepared the postulation of dark matter, and the detection of the cosmic microwave background radiation added to the understanding of the very early universe.

Infrared astronomy, i.e. observations in the range up to submillimeter wavelengths, for the first time allowed the observation of dense interstellar dust clouds, which constitute the birthplaces of stars. Such protostars could now be observed during their contraction phase by virtue of the dust around them—long before they initiate hydrogen burning and thus enter the main sequence. The center of our own galaxy also shines brightly in the infrared: While the high concentration of dust in the galactic plane prevents visible light of the galaxy center to be observed from Earth, infrared astronomy allows the orbits of stars to be traced very close to the center of the Milky Way and thus the enclosed mass

density to be determined: Evidence for a supermassive black hole in the center of our galaxies was found.

As X-rays and gamma rays (γ-rays) coming from space are mostly absorbed by the Earth's atmosphere, γ-*ray astrophysics* dawned with the launch of the first satellite observatories. γ-ray emission was not only found to originate from within our galaxy, but from several other extragalactic sources. The term "violent universe" was coined for the observed phenomena, because the kinds of events in the universe that produce γ-rays were thought to be explosions, high-speed collisions, and other non–thermal processes. The early 1970s also revealed the currently most violent and enigmatic events observed in the universe: gamma-ray bursts (GRBs). The discipline has flourished since the 1990s when satellite missions with substantially advanced technologies were launched, namely the Compton Gamma Ray Observatory (CGRO), and other missions like BeppoSAX and Swift. They increased significantly the number of sources in this energy domain, offering information about the most energetic processes and phenomena in the universe.

γ-rays above an energy of some GeV cannot reasonably be observed by satellite detectors with their too small detection areas. In this very high energy (VHE) γ-ray domain, since the late 1980s ground-based Cherenkov telescopes have proved to be very successful in the energy range above ≈ 300 GeV, adding significant information to the understanding of and for modeling γ-ray sources and emission mechanisms.

The most recent installations like H.E.S.S., MAGIC, VERITAS, and CANGAROO–III started to become observational in 2002 and currently achieve unprecedented sensitivity and low energy thresholds of $\lessapprox 100$ GeV.

This thesis deals with recent observations of extragalactic sources of VHE γ-rays that exploit both the increased sensitivity and the unprecedented low energy threshold that the MAGIC telescope, the largest of its kind, offers. The text is organized as follows:

- A short introduction to VHE γ-ray astrophysics and to the sources of such radiation is given in chapter 1. Of particular interest for the theoretical understanding of the astrophysical objects under study are the elementary acceleration mechanisms. We also discuss the absorption of VHE γ-rays by extragalactic background light photons , which substantially attenuates the measured γ-ray spectra of sources at cosmological distances.

- Active Galactic Nuclei (AGN), the class of objects which this thesis deals with, are the subject of chapter 2. The BL Lac subclass of AGNs is characterized and acceleration models that aim to explain the non–thermal emission observed in the VHE γ-ray domain are discussed. Special emphasis is put on the description of Synchrotron Self–Compton (SSC) models, and possibilities to explain fast variability in AGNs. A source-finding strategy for MAGIC is outlined, which led to the

discovery of two new VHE γ-ray sources presented in this thesis, PG 1553+113 and BL Lacertae.

- Chapter 3 is devoted to the technique which allows so-called Imaging Air Cherenkov Telescopes (IACT) to observe γ-rays in the 30 GeV – 100 TeV energy range. We explain the development of extended air showers in the atmosphere and the subsequent emission of Cherenkov light.

- In chapter 4 the main hardware elements of the MAGIC telescope are described. Emphasis is put on the implementation of the drive system, its unique fast repositioning capabilities essential for GRB observations, and the starfield monitor that checks the tracking accuracy of the telescope.

- Chapter 5 gives an overview of the standard analysis chain used for MAGIC data and in particular in this thesis. It describes the standard MAGIC telescope analysis chain, important parts of which have been contributed by the author, namely the flux and light curve calculation.

- The *Crab nebula* with its constant high–level flux of γ-rays is the standard "candle" of VHE γ-ray astronomy. In chapter 6, the first analysis of a large set of Crab nebula data obtained with the MAGIC telescope is presented; the findings are compared with the results of other experiments and emission models for this γ-ray source.

- Chapter 7 deals with the data obtained during a 6-week observation campaign conducted in 2005 on the well–known AGN *Markarian 501*. A spectral and temporal analysis of the 24 observation nights puts special emphasis on two nights, during which high flux levels exceeding three times the Crab nebula flux were found. Thanks to the unprecedented sensitivity of MAGIC, spectral changes within a single observation night were observed and light curves with high time resolution could be produced. Studies of the variation timescales of these flares show that the interday flare states, which were found, can be accommodated by a one-zone SSC model, while the observed flares on timescales of minutes push homogeneous one-zone SSC models to their limits. The fast flares are used to infer a lower limit on the quantum gravity energy scale. In addition, the observations are put in context with previous observations of Mkn 501 in the VHE γ-ray domain.

- Another previously detected VHE γ-ray emitter, the AGN *1ES 2344+514*, was observed from August 2005 to January 2006. The analysis presented in chapter 8 shows that the object was observed at a rather low flux level with only marginal signs of variability. A differential energy spectrum derived from the observations is compared to measurements during a flare in 1995. An all-time VHE light curve is compiled, and flare and low emission energy spectra are described using a homogeneous one-zone SSC model.

- H.E.S.S. and MAGIC simultaneously discovered the VHE γ-ray source *PG 1553+113*, the redshift of which could not yet be determined. This AGN shows the steepest γ-ray spectrum observed so far in the VHE domain. The analysis of the data obtained with MAGIC is discussed in chapter 9. Assuming a maximum hardness of the intrinsic spectrum, the VHE γ-ray measurements allow an upper limit on z to be posed.

- The prototype of the class of BL Lac objects, *BL Lacertae*, has not been confirmed as a VHE γ-ray emitter. In chapter 10 we present a first analysis of MAGIC data taken on this object, which hints at VHE γ-ray emission from BL Lacertae.

- Chapter 11 compares the characteristics of the sources discussed in this thesis and all other known VHE γ-ray emitting blazars. This is the beginning of a VHE γ-ray blazar astronomy, of an assessment of common properties of this class of objects. Studies of correlations of characteristics of the observed emissions are presented. We also examine the black hole masses of VHE γ-ray BL Lac objects, compare them with the AGN black hole mass distribution and correlate them with γ-ray emission characteristics. The comparative study of BL Lac VHE γ luminosities allows a redshift limit for PG 1553+113 to be inferred. Finally, conclusions on the prospects for neutrino emission of blazars are drawn.

- The concluding remarks in chapter 12 summarize the key findings of this thesis and put them in perspective with the prospects of current and future VHE γ-ray astronomy.

Chapter 1

Very High Energy Gamma Ray Astrophysics

FIGURE 1.1: *Experiments in the early days: In 1925, Robert Millikan and his co-workers Glenn Millikan, Otto Oldenberg, Ted Cook, and C. H. Prescott, Jr. carry detectors for measuring the cosmic radiation on Mt. Whitney (picture © California Institute of Technology; taken from [Pau99]).*

1.1 Cosmic rays

In his balloon experiments in 1912, Victor Hess observed ionizing radiation permanently impinging on the Earth's atmosphere [Hes12]. These particles, coined "cosmic rays" by R. Millikan (fig. 1.1), have been found to comprise mainly electrically charged particles, namely protons, alpha particles and heavier nuclei, as well as photons and (to a small

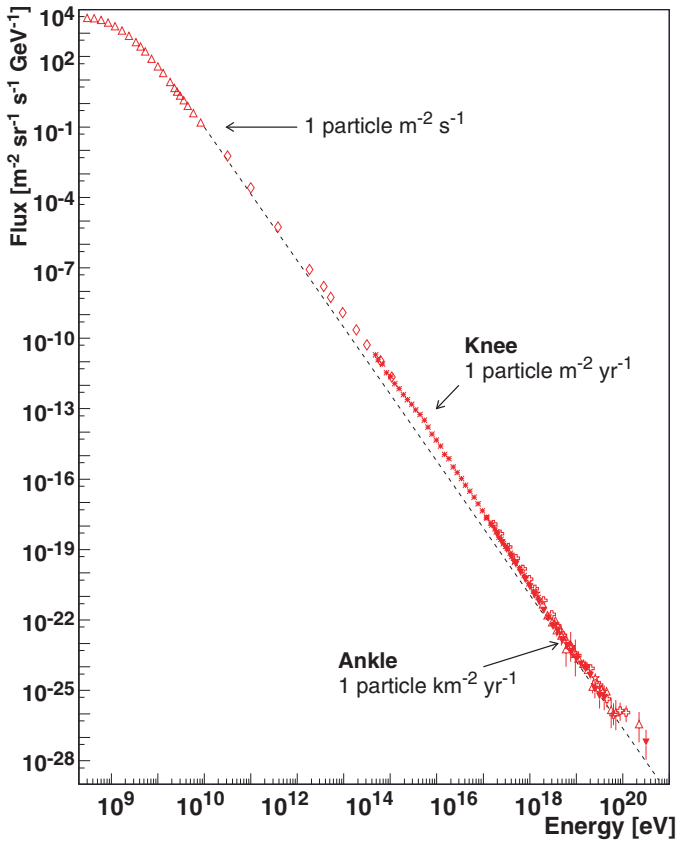

FIGURE 1.2: *All–particle cosmic ray spectrum [Bha00].*

fraction) electrons. The overall differential cosmic ray spectrum is given in fig. 1.2. It extends over an energy range of 13 orders of magnitude with the flux dropping from about 1 particle $\mathrm{cm}^{-2}\ \mathrm{s}^{-1}$ at energies of 100 MeV to 10^{-2} particles $\mathrm{km}^{-2}\ \mathrm{yr}^{-1}$ at 10^{20} eV.

Below $E = 1$ GeV, the cosmic ray flux is affected by the solar wind, which modulates the magnetic field in the solar system with a period of about 11 years. At higher energies the differential spectrum can be described by a power law with spectral index $\alpha \approx 2.7$ up to $E = 10^{15.5}$ eV and above that with $\alpha = 3$. The transition region is called *knee*. The spectrum steepens again at about $E = 10^{18}$ eV (the so-called *ankle*). It is believed that cosmic rays below the knee are produced at galactic sites like supernova remnants, pulsars, or binary systems, while cosmic rays with higher energies are not confined to our galaxy. Due to galactic and intergalactic magnetic fields, charged cosmic rays up to 10^{19} eV are isotropized. Therefore the direction of their arrival at Earth does not point back to their origin. Only at even higher energies, in the regime of the ultra high energy cosmic rays (UHECR), is the rigidity $R = E/(Ze)$ of the particles so high that they are not deflected by extragalactic or galactic magnetic fields ($r_{\mathrm{gyro}} = R/B$). Anisotropies found in the AGASA data set hint at the possibility of an astronomy of such extremely high energy particles [Tak99].

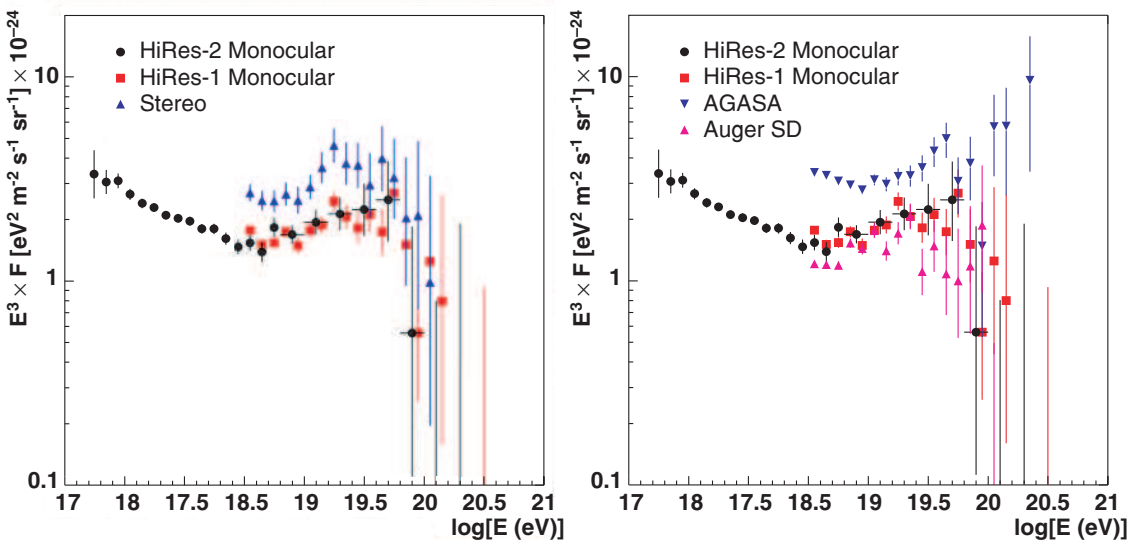

FIGURE 1.3: *Status of the UHECR field. Left figure: Monocular and stereoscopic measurements of the HiRes experiment. Taken from [Wat05]. Right figure: HiRes monocular, AGASA and preliminary AUGER surface detector spectra above* $10^{17.5}$ eV. *Note that after allowing for* $\approx$ *20% systematic errors, the HiRes and AGASA data sets are incompatible on the* 2.2σ *significance level only. Note also that the provisional stereoscopic HiRes data are not so different from the AGASA data. Taken from [PDG06].*

The GZK–cutoff. The reaction of cosmic rays with the omnipresent 2.7K microwave background radiation limits the upper edge of the cosmic ray spectrum:

$$p + \gamma_{CMB} \rightarrow n^* \rightarrow p + \pi^0, n + \pi^+.$$

The loss of energy by this process leads to the Greisen–Zatsepin–Kuz'min cutoff [Gre66, Zat66] which limits the maximum distance that cosmic rays of $E = 10^{20}$ eV and above can travel to ≈ 50 Mpc. Currently the existence of the GZK cutoff is a much debated subject. While the AGASA experiment, a 100 km^2 scintillator air shower array in Japan, observed 11 events above the GZK cutoff energy [Tak98, Hay00], the measurements performed by the HiRes collaboration, operating two fluorescence detectors in the U.S., show the expected attenuation structure both in monocular and stereoscopic observations at significance levels of 5σ and 4.8σ, respectively [Spr05]. Although the HiRes exposure exceeds that of AGASA by a factor of three [Yos05], the small number of excess events and the rather large systematic errors of the two experiments make it necessary to wait for results from the Pierre Auger Observatory,[1] a 3000 km^2 hybrid scintillator–fluorescence experiment currently becoming operational [Man05] (fig. 1.3).

Acceleration of charged particles. In astrophysics, non–thermal processes generally lead to power law spectra of the accelerated particles [Lon92]. A mechanism accounting

[1] `http://www.auger.org/`

designation	abbrev.	energy range
X-rays		$E_\gamma \leq 1$ MeV
γ-rays		$E_\gamma > 1$ MeV
low energy γ-rays	LE	1 MeV $< E_\gamma <$ 30 MeV
high energy γ-rays	HE	30 MeV $\leq E_\gamma <$ 30 GeV
very high energy γ-rays	VHE	30 GeV $\leq E_\gamma <$ 100 TeV
ultra high energy γ-rays	UHE	100 TeV $\leq E_\gamma <$ 100 PeV
extremely high energy γ-rays	EHE	100 PeV $\leq E_\gamma <$ 100 EeV

TABLE 1.1: *Definition of energy ranges in γ astronomy. The classification of high (HE), very high (VHE) and ultra high (UHE) energy particles is commonly used, even though the definition is not standard and linked in part to the threshold of instruments. In this work we will use the definitions given in the table above. Based on [Wee88, Ong98].*

for this observation was put forward by E. Fermi [Fer49]: In diffusive shock acceleration processes, particles repeatedly cross shock fronts, with an energy gain proportional to the shock velocity β at each crossing (first order Fermi acceleration). For the geometry prevalent in e.g. jets of active galactic nuclei, namely for moving plasma clouds, the energy gain is proportional to β^2 (second order Fermi acceleration). Reviews on this are given by [Bla87, Kir94]. Alternative processes discussed particularly for AGNs are associated with the magneto–rotational instability of their accretion disks via some form of magnetic reconnection [Mad06].

1.2 Gamma rays

Unlike the charged components of the cosmic radiation, cosmic ray photons are not deflected by magnetic fields and thus point back to their origins. Therefore, the knowledge of the direction of their acceleration sites allows one to use them as messenger particles that can be used to study the physical properties of their (partially still enigmatic) sources and the acceleration mechanisms at work. Usually, photons with energies above some MeV are called gamma (γ) rays. Throughout this work, we will adopt the terminology in the field as given in tab. 1.1.

1.2.1 Elementary production mechanisms of γ-rays

The thermal radiation emitted by stars is characterized by blackbody spectra that can be described by Planck's radiation formula with temperatures spanning from 3000 K to 50000 K. This translates to photons in the range of visible to ultra-violet light. The hottest objects in the universe emit radiation up to X-rays in the few-keV energy range. Higher γ-ray energies are reached in non–thermal processes either by π^0 decay from hadronic interactions with matter or the interstellar medium, or by inverse Compton scattering (IC)

of electrons on radiation fields. The most relevant elementary processes are highlighted here [Lon92]:

Hadronic production—π^0 decay. As the lightest hadrons with $m_\pi \approx 135$ MeV, neutral and charged pions are among the hadronic end products of nucleonic cascades. Charged ($\pi^\pm$) and neutral (π^0) pions are produced with the same probability; Neutral pions have a very short lifetime of $\approx 10^{-16}$ s and decay into two photons ($BR = 99\%$) or $e^+e^-\gamma$ ($BR = 1\%$). With their considerably longer lifetime of $\approx 2.6 \cdot 10^8$ s, high energy $\pi^\pm$ usually undergo further interactions before they eventually decay into electrons and neutrinos:

$$\pi^+ \rightarrow \mu^+\nu_\mu \rightarrow e^+\overline{\nu}_e\nu_\mu$$

Electromagnetic production—Inverse Compton scattering. Relativistic electrons scattering off low energy photons transfer part of their energy to these photons. For $E_e E_\gamma \ll m_e^2 c^4$ the cross–section for this process is

$$\sigma_T = \frac{8}{3}\pi r_e^2 \quad \text{(Thomson cross–section)} \tag{1.1}$$

For $E_e E_\gamma \approx m_e^2 c^4$ the exact Klein–Nishina formula has to be used, whereas in the case of ultrarelativistic electrons the expression

$$\sigma_{KN} = \pi r_e^2 \frac{1}{\varepsilon}\left(\ln 2\varepsilon + \frac{1}{2}\right) \qquad \varepsilon = \frac{E_\gamma}{m_e c^2} \tag{1.2}$$

can be used. In this regime the electrons suffer large energy losses. It can be shown that the maximum energy gain is described by

$$E_{max} \approx 4\gamma^2 E_\gamma; \tag{1.3}$$

for high Lorentz factors of $\gamma \approx 10^2 - 10^3$, keV seed photons are upscattered into the GeV–TeV domain. This mechanism is at work in SSC models (sect. 2.1).

Electromagnetic production in the presence of electromagnetic fields. When charged particles are deflected during acceleration in electric fields, they emit *bremsstrahlung*. The spectrum of the radiation emitted follows a power law with the same spectral index as the one of the particles accelerated [Ste71]. This process is one of the key processes in air shower physics (cf. sect. 3.1.1). *Synchrotron radiation* is generated by the acceleration of ultrarelativistic electrons through magnetic fields. The peak emission energy is given by $E_{peak} = 5 \cdot 10^{-9} B_{\perp,G} \gamma_e^2$ eV with the electron Lorentz factor γ_e and the transverse component of the magnetic field $B_{\perp,G}$ given in units of Gauss. This process is particularly important in astrophysical environments with high magnetic fields, like AGN jets (cf. sect. 2). The created photons, typically in the keV energy range, serve as seed photons for IC upscattering.

1.2.2 Intergalactic absorption of VHE γ-rays

The astrophysical importance of the absorption of VHE photons by low energy extragalactic background light (EBL) photons,

$$\gamma_{\mathrm{VHE}} + \gamma_{\mathrm{EBL}} \longrightarrow \mathrm{e}^- + \mathrm{e}^+ \qquad E_{\gamma_{\mathrm{VHE}}} \cdot E_{\gamma_{\mathrm{EBL}}} > 2(m_{\mathrm{e}}\mathrm{c}^2)^2 \tag{1.4}$$

was pointed out by [Gou66]. When traveling cosmological distances, the attenuation of VHE photons by virtue of $\gamma\gamma$ collision and pair production can alter observed spectra substantially and even constrain the maximum distance a particular detector can look back into the universe [Ste92] due to its energy threshold: At energies above 300 GeV, γ-rays suffer absorption for sources with redshifts $z > 0.2$. Cherenkov detectors operating with such thresholds in fact detected only few extragalactic sources with very low redshifts ($z < 0.2$), in contrast to the EGRET experiment, which detected 66 AGNs (plus 27 tentative identifications) [Har99] at $E > 100$ MeV, identifications partially yielding redshifts well above $z = 1$, e.g. [Blo97b]. This discrepancy implies that most of the EGRET sources have spectra with cutoffs between 10 GeV and 300 GeV. These turnovers are unlikely to be caused by intrinsic properties of the objects (but see [Don03]), which are expected to give rise to redshift–independent cutoffs.

The Cosmic Infrared Background (CIB) Radiation. The part of the EBL spectrum to which VHE γ-rays are sensitive is the CIB. Two of its main contributions are the (redshifted) relic emission of galaxies and star-forming systems and the light absorbed and re-emitted by dust (see [Lag05, Kas05] for reviews). The resulting spectral energy distribution (fig. 1.4) comprises two distinct peaks, one in the near infrared, $\lambda \approx 1-2\ \mu$m, and one in the far infrared, $\lambda \approx 100-200\ \mu$m. The long wavelength end of the spectrum $\lambda \gtrsim 300\ \mu$m is superseded by the 2.7K cosmic microwave background radiation. It is important to stress that the (EBL), which includes the CIB, undergoes an evolution. Owing to its origin, the evolution of the optical to ultraviolet part provides valuable information on the phase of early galaxy formation.

Direct measurements of the present EBL spectral energy distribution (see [Hau01] for a review) suffer from large uncertainties, as they are dominated by large foregrounds of galactic and zodiacal light. In turn, attempts to model the spectral energy distribution [Dwe98, Kne02] are challenged by the need for strong assumptions on cosmology, star formation rate, the distribution of matter in the universe; additionally, a good understanding of the light recycling history is required. Recently, VHE γ-ray measurements of distant AGNs were used to infer severe limits on the CIB [Aha06b], see the H.E.S.S. data points in fig. 1.4.

VHE γ-ray attenuation. To compute the attenuation of a given intrinsic VHE γ-ray spectrum, knowledge not only of the present—currently measured, $z = 0$—EBL is required, but also of its past evolution. As this cannot be measured directly, theoretical or

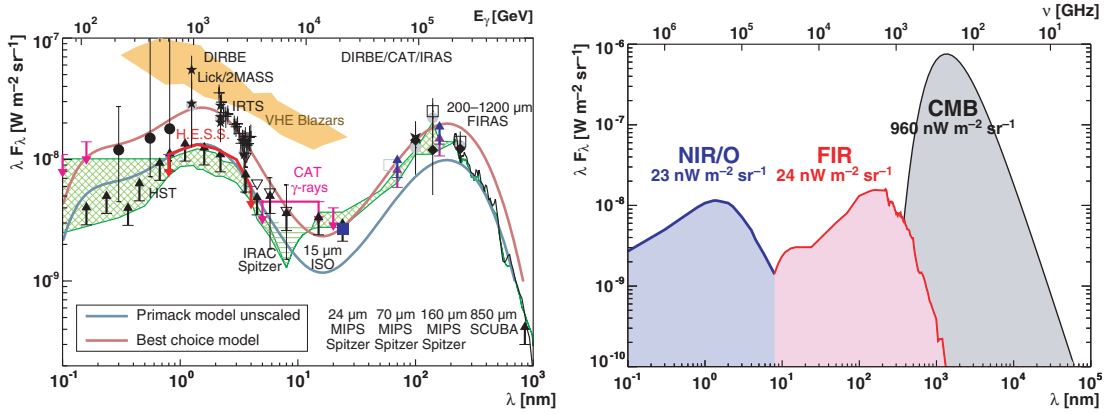

FIGURE 1.4: *Left: Measurements of the spectral energy distribution of the EBL. The limits inferred using VHE γ-ray blazar measurements comprise the H.E.S.S. data points between $(0.8-4)$ μm [Aha06b], the Whipple 98% confidence upper limit (shaded orange region) [Sch05b], and CAT upper limits [Ren01]. Lower limits are mostly given by source counts (adapted from [Dol06], see also for references). The upper horizontal axis indicates which VHE γ-ray energy is preferentially absorbed by (or probing) a given EBL photon energy. The plot also shows the allowed EBL range (green area) and two EBL models (blue and red curves) [Pri01, Aha01b]. Right: Near-IR/optical and far-IR part of the EBL spectrum along with the cosmic microwave background spectrum and the respective integrated observed brightnesses [Dol06].*

semi-empirical models have to be employed. This work makes use of a model based on stellar light produced and reprocessed in evolving galaxies developed by [Kne02, Kne04]. It yields the optical depth [Ste96]

$$\tau(E,z) = \frac{c}{H_0}\int_0^z dz'\sqrt{1+z'}\int_{-1}^{+1} d\mu\,\frac{\mu}{2}\int_{\frac{2m^2c^4}{E\mu(1+z')^2}}^{\infty} d\varepsilon\, n(\varepsilon,z')\,\sigma_{\gamma\gamma}\left[2\mu\varepsilon E(1+z')^2\right] \qquad (1.5)$$

for γ-rays of energy E produced at a distance corresponding to a redshift z. $H_0 = 71.1\ \mathrm{km\ s^{-1}\ Mpc^{-1}}$ is the Hubble constant [PDG06, sect. 21.4], $n(\varepsilon,z)$ is the EBL photon density distribution, ε the EBL photon energy, and $\sigma_{\gamma\gamma}$ the $\gamma\gamma$ cross–section. The attenuation factor as a function of VHE γ-rays is then given by

$$f(E,z) = e^{\tau(E,z)}. \qquad (1.6)$$

The energy dependence of $\tau(E_\gamma,z)$ depends on the spectrum of the background photons and may substantially modify the measured spectra due to the exponential function. Once the attenuation function f is known, the intrinsic source spectrum can be obtained by

$$F_{\mathrm{intrinsic}}(E) = f(E,z)\cdot F_{\mathrm{measured}}(E). \qquad (1.7)$$

Current EBL models result in a steepening of the intrinsic spectra in the $200\ \mathrm{GeV} \lesssim E \lesssim 2\ \mathrm{TeV}$ region (power law spectra are softened, but their form is retained), while for lower energies the effects are minimal. At $2\ \mathrm{TeV} \lesssim E \lesssim 5\ \mathrm{TeV}$, a steepening is expected ($n(\varepsilon) \propto \varepsilon^{-1} \Rightarrow \tau(E) \approx$ const.). For even higher energies a cutoff is expected (fig. 1.6).

Constraining EBL models by VHE γ-ray observations and the γ-ray horizon. The cross–section of the reaction (1.4) strongly peaks at $E_{\mathrm{CM}} = 1.8 \times (2m_{\mathrm{e}}\mathrm{c}^2)$ [Vas00], therefore a given VHE photon energy probes a narrow range of the EBL spectrum. Additionally, by virtue of the energy threshold of (1.4), for a given E only EBL photons with a minimum energy $\varepsilon > 2(m_{\mathrm{e}}\mathrm{c}^2)^2/E$ contribute to their absorption. γ-rays of energies of 1 TeV and above typically interact with IR photons re-emitted by dust ($\lambda \gtrsim 10\ \mu$m), while γ-rays below 1 TeV interact with near-IR, optical, or UV photons emitted by stars. For $z \ll 1$ the conversion reads ($\lambda_{\mathrm{e}} = \mathrm{h}/(m_{\mathrm{e}}\mathrm{c})$):

$$\lambda(E) \simeq \lambda_{\mathrm{e}} E/(2m_{\mathrm{e}}\mathrm{c}^2) = 2.4 E_{\,\mathrm{TeV}}\ \mu\mathrm{m}.$$

VHE γ-rays therefore have the potential to probe a substantial part of the EBL spectral energy distribution (fig. 1.4). By posing certain assumptions on the intrinsic spectra of the observed sources (cf. sect. 9.7) one is able to constrain EBL models ([Ste01a] and references therein). Two recently discovered blazars at distances of $z = 0.165$ and $z = 0.186$, respectively, were used to accommodate direct EBL measurements as shown in fig. 1.4 with constraints on their intrinsic source spectra [Aha06b]. Conversely, by assuming an EBL model, redshift limits for sources with unknown redshift can be inferred, as e.g. done for PG 1553+113, cf. [Aha06c, Alb06a, Maz06] and sect. 9.7.

Population studies—the γ-ray horizon. While for optical depths smaller than unity the universe is transparent, it becomes opaque for optical depths larger than 1. Correspondingly, the γ-ray horizon (GRH) is defined as a function $z_{\mathrm{GRH}}(E)$ (the Fazio–Stecker relation, FSR) with the energy–dependent distance z_{GRH} at which the optical depth exceeds 1 due to this process for a given energy E, i.e. $\tau(E,z) = 1$ (fig. 1.5). [Bla05] emphasize that any common feature observed in different γ-ray spectra from sources at the same redshift z is likely to be due to the optical depth, as the corresponding suppression factor in the γ flux (1.6) depends only on the γ energy and on the redshift.

With increasing γ-ray energy the cutoff condition $\tau(E,z) = 1$ results in a decreasing γ-ray horizon. Thus, with a decreasing IACT energy threshold, one will gain access to a larger source population. While the HEGRA telescopes were restricted by their threshold energy to observing a maximum redshift of $z \lesssim 0.2$, MAGIC should be able to see substantially further back, $z \lesssim 1.5$, into the universe (fig. 1.6). A population study of many sources should then result in a plot of the individual highest energies observed versus redshift. In such a plot one also could distinguish intrinsic source absorption from attenuation by the intergalactic background field.

Currently observed cutoffs. For several detected extragalactic objects, cutoffs in the VHE spectra have been investigated that can possibly be attributed to EBL absorption effects. For the blazar Mkn 501, a cutoff in the spectrum is observed at $E \approx 10$ TeV.

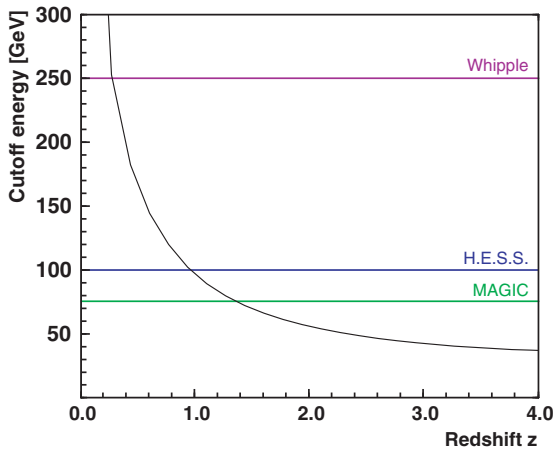

FIGURE 1.5: *Cutoff energy as a function of redshift z at an optical depth of 1. The energy threshold of the respective instrument (Whipple, H.E.S.S., MAGIC) limits the accessible population of AGNs. Adapted from [Kne02].*

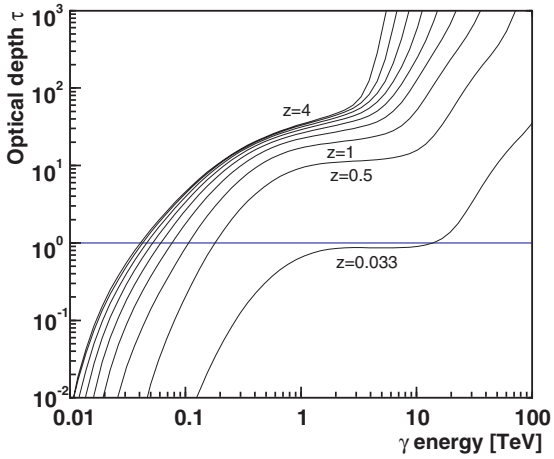

FIGURE 1.6: *Optical depth $\tau(E)$ for different redshifts z. The horizontal line at $\tau = 1$ indicates where for a given redshift a cutoff in the source spectrum is to be expected. Taken from [Kne02].*

Fig. 1.7 shows that if the measured energy spectrum [Aha01a] is corrected for EBL absorption effects, the resulting spectrum is consistent with a pure power law as expected in the SSC model (cf. sect. 2.1). For other blazars similar cutoffs have been found [Alb06g].

1.3 Astrophysical sources of γ-rays

The launch of the Energetic Gamma-Ray Experiment Telescope (EGRET) for γ-rays above 20 MeV on board the Compton Gamma Ray Observatory (CGRO) in 1990 opened up the γ-ray sky in the high energy or γ-ray domain[2] just as had happened before in the X-ray domain (fig. 1.8). EGRET discovered 271 sources [Har99], 101 of which could be associated to already known astronomical objects, while a large number of 170 newly discovered and yet unidentified sources remain.

The highest energies at which satellite experiments can detect reasonable numbers of γ-rays is determined by the steeply falling γ-ray energy spectra. Thanks to their unique detection technique (cf. sect. 3), ground–based Cherenkov telescopes with their huge detection areas are well suited to observe γ-ray emitters in the very high energy (VHE) domain of $E_\gamma \gtrapprox 10$ GeV photon energy. Until recently, before the new generation of Cherenkov telescopes became operative, these detectors had energy thresholds of $E_\gamma \gtrapprox 350$ GeV, which allowed them to detect only very few sources, the first of which was the Crab nebula [Wee89]. With the advent of IACT systems with substantially higher sensitivity and

[2]For a history of satellite γ-ray astrophysics and a review of CGRO's excellent scientific achievements, see [Sch01]

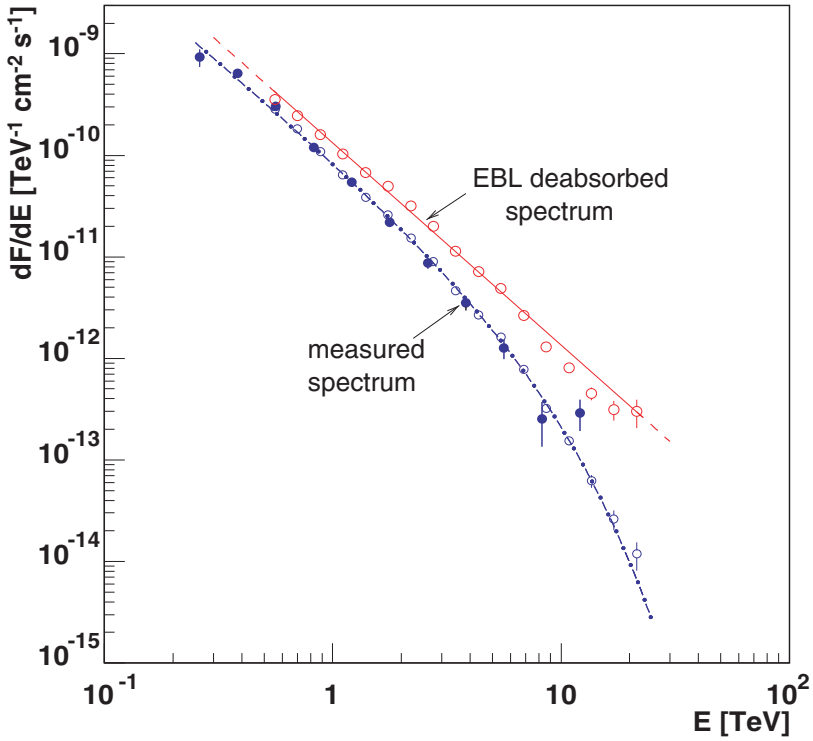

FIGURE 1.7: *The energy spectrum of Mkn 501 as measured by the HEGRA IACT array (open circles) and by the Whipple group (filled circles). A combined fit (power law plus exponential cutoff) of the data is shown by the dotted-dashed curve. The "de-absorbed" HEGRA data and a power law fit (solid line) are also shown. Taken from [Kon99b].*

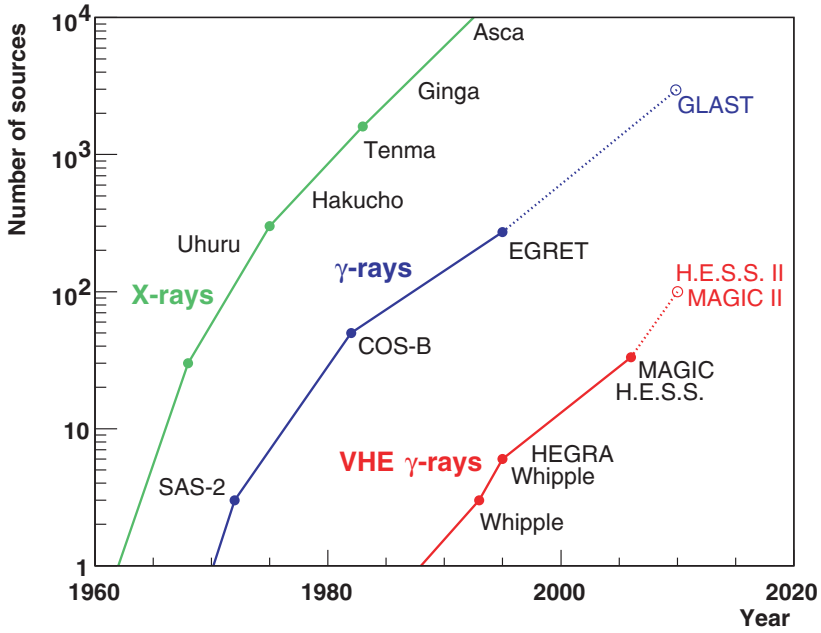

FIGURE 1.8: *Number of discovered X-ray, γ-ray and VHE γ-ray sources. Just as earlier with X-ray and HE γ-ray sources, with the advent of the new IACT installations the VHE γ-ray sky opens up. (After its inventor, Kifune–san, this plot is very often referred to as "Kifune plot").*

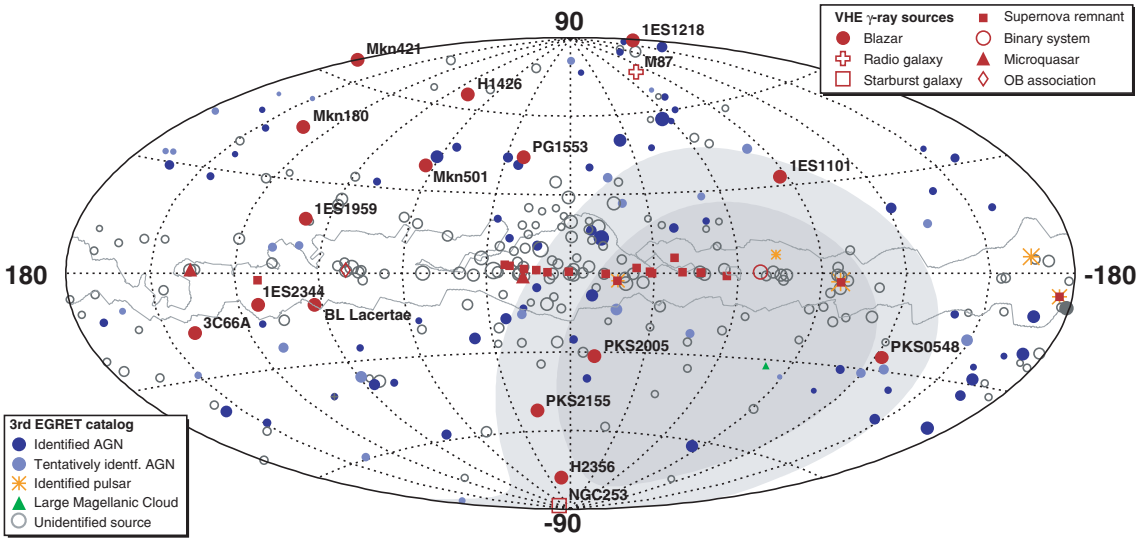

FIGURE 1.9: *The sky in γ-rays, plotted in galactic coordinates. (1) HE γ-ray sky: 3rd EGRET catalog of gamma ray sources [Har99]. The size of the symbols scales with the logarithm of their flux as measured with EGRET. (2) VHE γ-ray sky. Only the names of extragalactic VHE are given in the figure. Note the large number of (galactic) sources along the galactic plane. The source at* $(l,b) = (-5.8°, -175°)$ *is the Crab nebula. The shaded areas represent those regions in the sky that are accessible for MAGIC at minimum zenith angles of* 45° *and* 60° *only (light and dark gray, respectively). The contours show the optical extension of the galactic plane (created by J. R. Vieira [Vie00] from R. R. de Freitas Mourão, Uranografia, Descrição do Céu).*

lower energy thresholds like H.E.S.S.,[3] MAGIC, and soon also VERITAS,[4] the number of VHE γ-ray sources has dramatically increased to currently about 30, with new detections nearly every month. Fig. 1.8 also includes extrapolations to the number of discovered sources by the upgrades to MAGIC and H.E.S.S. currently under construction and the GLAST[5] satellite, which will be launched in 2007. The currently known VHE sources along with the EGRET HE sources are shown in fig. 1.9. In the following, we will briefly highlight the most prominent astronomical targets for IACT observations.

1.3.1 Extragalactic sources

Active Galactic Nuclei. Currently Active Galactic Nuclei (AGNs) are believed to be the most powerful sources of energy in the universe. The general term AGN refers to any galaxy that produces emission that cannot be attributed to its stellar content, stellar remnants and interstellar medium. A supermassive black hole with around 10^6 to 10^{10} solar masses is assumed to comprise the central region of AGNs, with an extension of often only 1 pc in diameter. The currently believed classification scheme for the many observed

[3] **H**igh **E**nergy **S**tereoscopic **S**ystem, `http://www.mpi-hd.mpg.de/HESS/`
[4] **V**ery **E**nergetic **R**adiation **I**maging **T**elescope **A**rray **S**ystem, `http://veritas.sao.arizona.edu/`
[5] **G**amma **R**ay **L**arge **A**rea **S**pace **T**elescope, `http://www-glast.stanford.edu/`

subclasses of AGNs is based on the mass of the central black hole, its evolutionary status, its accretion speed, and on the orientation of the galaxy and the emitting regions with respect to the line of sight. In order to further understand the different VHE γ-ray production mechanisms, detailed observations of different AGNs are necessary to enable constraints to be set on the different acceleration processes. Handles on such constraints can be derived from the energy spectra, the temporal variability (light curves) of the γ-ray flux and/or from multiwavelength campaigns. More details on AGNs are given in sect. 2.

Starburst galaxies. These (young) galaxies are characterized by their comparatively high star formation rate, which is associated to the density of massive, hot stars and thus a comparatively high supernova rate. The supernova remnant density is believed to be sufficiently high to fuel cosmic ray reactions with interstellar gas, resulting in VHE photon emission [Dom05b]. In 2002, the starburst galaxy NGC 253 was reported to be an extended source of VHE emission [Ito02], but alas the detection could not be confirmed by H.E.S.S. [Aha05a].

Gamma-ray bursts. Gamma-ray bursts (GRBs) are the most energetic phenomena observed in the universe. The widely accepted current understanding of these highly transient bursts is given by the fireball model [Ree92] (for other interpretations see [Dar98, Ruj02]), which assumes that a central object produces an ultrarelativistic outflow of an optically thick plasma shell, which emits the GRB as soon as it becomes optically thin. The short duration of GRBs (milliseconds to a few hundred seconds) hints at very compact progenitors. The mean distance of these progenitor objects has been measured to be $z = 2.8$ with at least 7% of the GRBs originating at $z > 5$ [Jak06]. Typically, $(10^{51} - 10^{54})$ erg s^{-1} are released within seconds up to tens of seconds (fig. 1.10). This *prompt emission* is followed by an afterglow of less energetic photons, which extends long after the initial burst and can last for days. VHE γ-rays are expected to be produced in internal shocks due to synchrotron and IC processes. To cope with the short burst durations of the isotropically distributed GRBs on the sky, the MAGIC telescope is equipped with a drive system that permits fast repositioning (cf. sect. 4.5.2) upon a GRB alert given by satellite detectors [Gar06, GCN06]. First upper limits on VHE γ-ray emission of GRBs have been published recently [Alb06d, Mor06]. Reviews on GRBs are given in [Par00b, Mes02].

1.3.2 Galactic sources

Supernova remnants and plerions. A final stage of stellar evolution is reached when a star runs out of fuel necessary for the fusion reactions that counteract the gravitational pressure. If the star is heavy enough, the collapse of the stellar core is followed by the ejection of the outer shells of the stellar material. While depending on the mass of the remaining object, a neutron star or a black hole is formed, and the ejected material forms

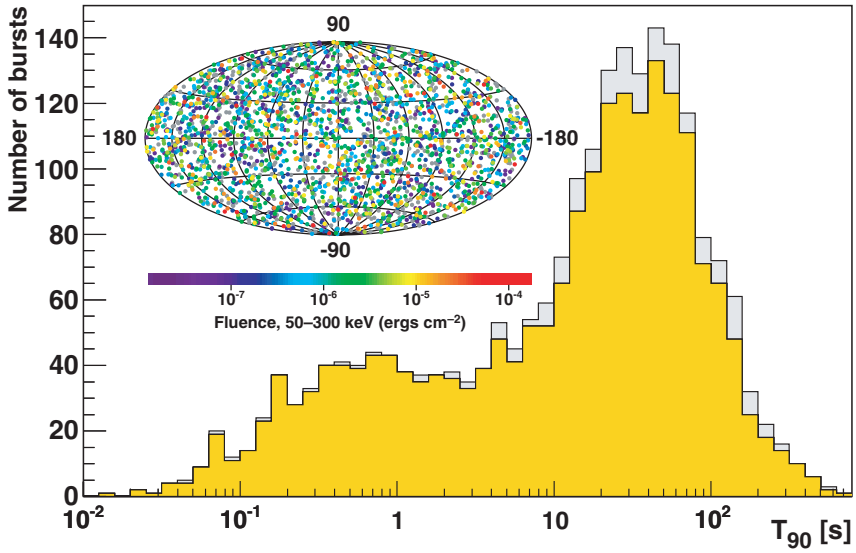

FIGURE 1.10: *The T_{90} value characterizes the time in which 90% of the intensity of a GRB is observed. The plot shows the bimodal T_{90} distribution for 2041 GRBs contained in the 3B and 4B BATSE catalog (yellow histogram, [Pac99]) and the 168 up to now registered GRBs by SWIFT (stacked gray histogram, [Mye06]). Inset: The distribution of 2704 GRBs discovered by BATSE on the sky shows the high isotropy of of these events.[Bri00].*

a nebula, sweeping up interstellar material along its way. This expanding structure is called a supernova remnant (SNR; see e.g. fig. 2.12).

After some time, the expanding material sweeps up the surrounding gas, forming shocks that can cause particle acceleration leading to steady VHE γ-ray emission. If a rotating neutron star remains in the system, it is referred to as a plerion or pulsar wind nebula (PWN). In a PWN, the generated γ-ray emission is powered by high energy electrons/positrons originating from the pulsar. The best–known example of such a system is the Crab nebula. Its VHE γ-ray emission is the subject of sect. 6.

Pulsars. Neutron stars with masses of the order of the solar mass $M_\odot$ and radii of some ten kilometers represent the densest state of stable matter known in the universe. Created in the aftermath of supernova explosions, they have been found to have very short rotational periods (down to the order of milliseconds) and intense magnetic fields ($\approx 10^{12}$ G). Pulsed VHE emission is predicted to originate either from particle acceleration and subsequent synchrotron emission near the polar caps of the pulsar [Rud75] or in the outer regions of the magnetosphere by inverse Compton scattering [Che86, Chi92].

OB associations. A source serendipitously discovered by the HEGRA collaboration, TeV J2032+4130 [Aha05d, Lan04b], without obvious counterpart was found to coincide with a region of about 2,600 OB–stars [But03]. These young, luminous stars form a dense region filled with stellar winds, which serve as seed material for SNR shocks, in

which neutral pion decay might produce VHE γ radiation [Tor04]. The search for VHE γ emission from other young open star clusters did not reveal a significant signal [Aha06a].

Microquasars. Phenomenologically, microquasars have many of the observational and morphological properties of AGNs, namely strong emission over a wide energy range, rapid flux variability and the existence of jets [Mir92]. In the standard model [Mir94a] microquasars are binary systems consisting of a black hole or a neutron star and a companion star. Matter of the companion star is stripped off and forms an accretion disk around the compact object, much like the way a miniature AGN forms jets in which the high energy emission is thought to take place. See [Mir99] for a review. Microquasars were detected by EGRET in the MeV range [Par00a] as well as recently by H.E.S.S. [Aha05b] and MAGIC [Alb06h] in the VHE range.

1.3.3 Unidentified EGRET sources

One of the biggest questions raised by the CGRO mission is the nature of the unidentified EGRET sources. Certainly, some of these sources will turn out to belong to the established classes of γ-ray sources; a few may be found to be artifacts of the galactic diffuse emission. The 3rd EGRET catalog contains 271 sources, of which only 74 have been identified either as AGNs, pulsars, the Large Magellanic Cloud (LMC) or solar flares. There are an additional 27 tentative AGN identifications. The remaining 170 objects are unidentified. 57 sources have been seen in γ-rays with energies of $E_\gamma > 1$ GeV.

How can the nature of the unidentified sources be determined? Statistical studies [Kan96, Gre95] indicate that the unidentified EGRET sources belong to two groups, namely a galactic population and an isotropic extragalactic population; at the same time—except for the LMC—AGNs constitute all identified EGRET sources at galactic latitudes $|b| > 30^\circ$. Additionally, positional correlations of EGRET sources are being sought with other object types (cf. [Nol03] and references therein). Other classification approaches comprise studying EGRET spectral shapes [Mer96] or variability of the sources [Wal00, Nol03].

1.3.4 The connection to particle physics

Dark matter. Since first observations by Zwicky [Zwi33] it became evident that the rotational velocities of galaxies do not match their observed stellar content within Newtonian dynamics. Results of the WMAP[6] mission confirmed the finding that the major fraction of the matter content $\Omega_\mathrm{m} h^2 = 0.127^{+0.007}_{-0.013}$ of the universe is non–baryonic; $\Omega_\mathrm{b} h^2 = 0.0223^{+0.0007}_{-0.0009}$ with the Hubble constant $H_0 = 100 \cdot h$ km s^{-1} Mpc^{-1} =

[6] **W**ilkinson **M**icrowave **A**nisotropy **P**robe, `http://map.gsfc.nasa.gov/`

73^{+3}_{-3} km s^{-1} Mpc^{-1} [Spe06]. The currently best candidate for this *dark matter* is the neutralino χ, the lightest supersymmetric particle. γ-ray signals of the χ self–annihilation are expected from galaxy centers and other sites of high χ concentrations, either as distinct lines from $\chi\chi \rightarrow \gamma\gamma$, $\chi\chi \rightarrow Z\gamma$ or as a spectrum from subsequent π^0 decay from $\chi\chi \rightarrow q\bar{q}$. Feasibility studies show that such signatures are accessible by IACT with a low energy threshold of 100 GeV within 250 hours of observation time at the 5σ level [Pra04].

In very recent optical and X-ray observations of the galaxy cluster merger 1E 0657–558 [Clo06] a spatial offset of the center of mass of the stellar (baryonic) component and the overall center of mass was found. This result is interpreted as direct evidence for the fact that the majority of the mass in that galaxy merger is unseen.

Lorentz invariance. Lorentz invariance (LI) was a fundamental finding in the history of physics. Repeatedly confirmed to an ever-greater precision and appealing from the mathematical simplicity of the underlying Lorentz group, it is reasonable to think that LI is a symmetry of nature [Jac06]. There are however general Lorentz–violating extensions of the standard model [Col98]. Quantum gravity theories introduce quantum fluctuations on the Planck scale $L_P \approx 10^{-33}$ cm, which result in a complex ("foamy") structure of space time at very small distances. This gives rise to deformed dispersion relations, which may result in observable energy-dependent arrival time dispersions for high energy radiation [Ame98]. More details on constraining the quantum gravity scale employing a time–structure analysis of VHE γ-ray flares are given in sect. 7.3. Lower limits on the quantum gravity energy scale have been posed using VHE γ-ray observations of extragalactic sources by [Bil99, Ell06] and in this thesis, sect. 7.8.3. Reviews on modern tests of LI are given by [Mat05, Jac06].

Chapter 2

Active Galactic Nuclei

A fraction of about 1% of all galaxies hosts central regions where non–thermal high energy processes take place, which cannot be attributed to thermal or nuclear processes which take place e.g. in stars. The observed high luminosities originate from very compact regions: These Active Galactic Nuclei (AGN, see e.g. [Rob96, Kem99]) harbor concentrations of 10^6 to 10^{10} solar masses ($M_\odot$) in a region the size of our solar system. There are several subclasses of AGN, which in the past were empirically discerned by their radio emission, the properties of their optical emission lines, morphological considerations and other properties (fig. 2.1). Today, the various AGN subclasses are believed to be connected by the unified AGN scheme (fig. 2.2): A supermassive black hole (SMBH) [Lyn69] accretes surrounding material, which forms a disk of hot plasma. Due to friction and turbulent processes in the accretion disk, gravitational energy is transformed into thermal radiation, which in turn excites or ionizes atoms in the rapidly moving gas clouds close to the SMBH. These atoms produce the observed Doppler–broadened emission lines (broad–line region; line widths of a few thousand hundred km/s). Molecular gas clouds farther away from the center move considerably slower and thus their emission lines are less broadened (narrow–line region; line widths of some hundred km/s). The system is surrounded by a dust torus, which obscures the view to the central part of the AGN along the equatorial plane. Two strongly collimated ultra–relativistic plasma outflows (jets) can be observed in some AGNs [Ree84, Urr95]. These jets are beamed by strong magnetic fields and oriented perpendicularly to the accretion disk. Actually the observation of jets supports the SMBH paradigm, in particular the idea of a central rotating body, which, acting as a stable gyroscope, is able to sustain a stable jet directionality over large periods of time.

The observed high variability in AGNs is most likely due to infalling matter at variable rate from the accretion disk to the black hole, and subsequent diffusive shock acceleration, but see sect. 2.2 for other possible explanations. Typical scales are given in tab. 2.1.

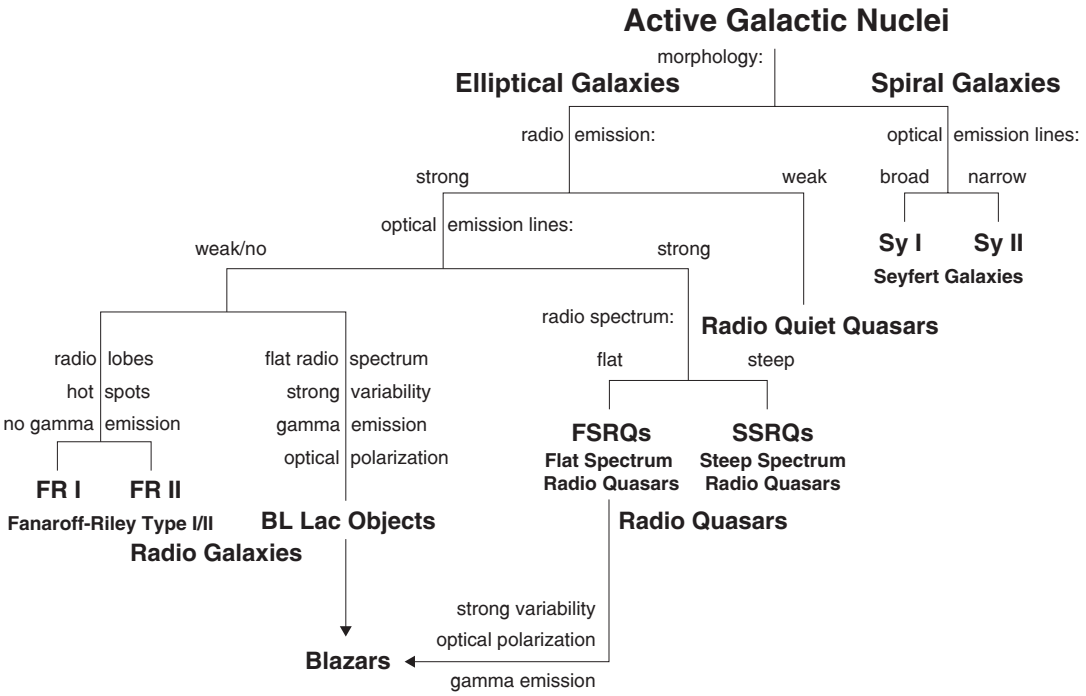

FIGURE 2.1: *Empirical classification scheme for AGNs (adapted from [Boe97a])*

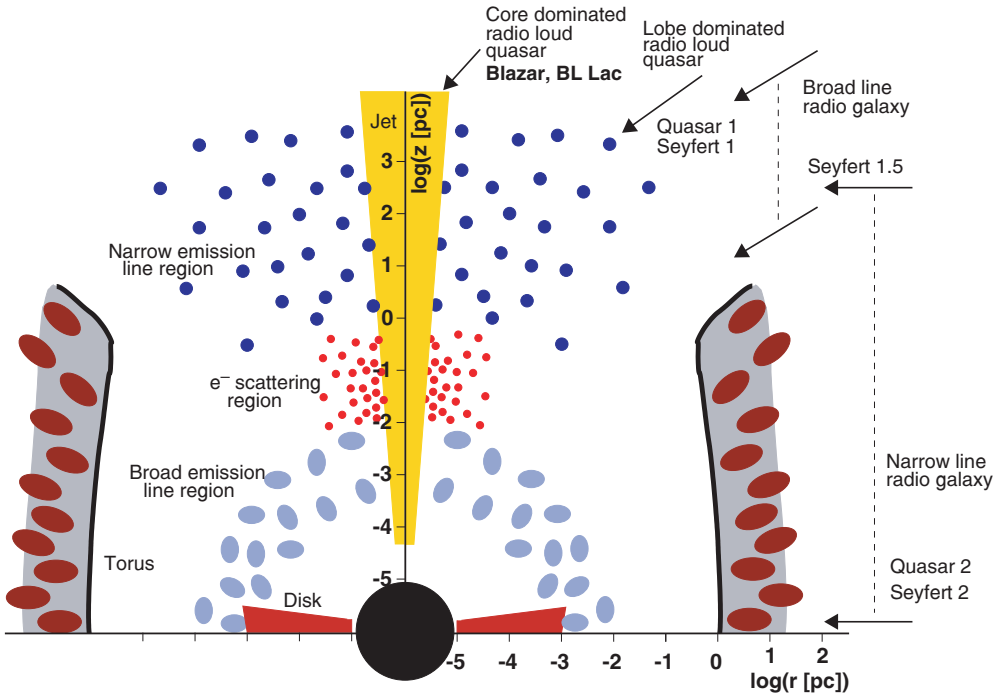

FIGURE 2.2: *Model of an AGN in the unified AGN scheme. The classification according to the viewing angle along with the different regions around the central black hole are illustrated. Note that scales are logarithmic (adapted from [Bie03]).*

Black hole radius:	$\sim 3 \cdot 10^{13}$ cm	~ 5 min
Last stable orbit (Schwarzschild BH):	$\sim 9 \cdot 10^{13}$ cm	~ 15 min
Radius of the emitting accretion disk:	$\sim (1-30) \cdot 10^{14}$ cm	~ 1 hr $-$ 1 d
Distance of the broad line clouds:	$\sim (2-20) \cdot 10^{16}$ cm	$\sim 1-10$ weeks
Inner radius of the dust torus:	$\sim 10^{17}$ cm	~ 5 weeks
The narrow line region extends from:	$\sim 10^{18} - 10^{20}$ cm	$\sim 1-10$ yr
Jet scales from:	$\sim 10^{17} - 10^{24}$ cm	30 d $-$ 30 kyr

TABLE 2.1: *Typical length scales and corresponding light travel times for a $10^8 M_\odot$ black hole (based on [Urr95])*

The different observed AGN types can largely be explained by the viewing angle under which the AGN is observed;[1] by the presence or absence of jet structures; by the mass and the rotation of the black hole, its accretion rate; by the configuration of torus, disk, and SMBH orientation; and by the evolutionary status of the system, i.e. a possible merger history. Probably after galaxy mergers events, the rotational axes of the black hole, the accretion disk, and the dust torus are not coaxial. That would explain why radio–loud AGNs have only been observed in elliptical galaxies, which are thought to result from mergers of spiral galaxies. The orientation effect stems from the geometrically and optically thick dust torus, which may obscure the view dependent on the viewing angle. Fig. 2.3 gives an account of the different AGN types and suggests that the differences are due to an orientational effect and differences in physics. In the case of jet structures, an additional orientation effect is responsible for the observation of superluminal motions or high linear polarization due to relativistic beaming effects in the jet [Dop99]. In the following we will focus our discussions on the AGN subclasses with VHE γ-ray emission. Further information on the other AGN types and extensive reading on unification schemes can be found e.g. in [Ant93, Urr95].

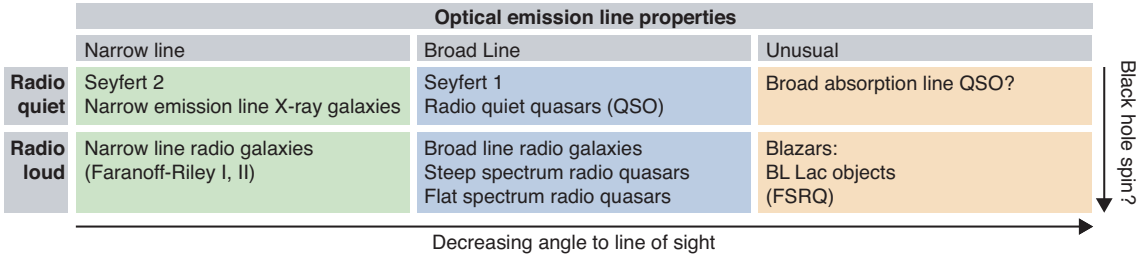

FIGURE 2.3: *AGN taxonomy suggested by [Urr95]. (Broad emission lines have a FWHM of some few thousand km/s, while narrow emission lines have widths of some hundred km/s [Kem99]). The phenomenological classification can be explained by the viewing angle and probably the black hole spin.*

Blazars. A particularly interesting AGN subclass for VHE γ-ray observation are blazars ("blazing quasars"), which are characterized by a close alignment of the jet axis with the observer's line of sight. Acceleration processes in these jets generate non–thermal, high

[1] The strong unification hypothesis, namely that all AGN classes are the same phenomenon seen at different orientations, does not hold.

energy emission over an energy range encompassing almost 20 orders of magnitude from radio to VHE emission, which almost completely masks the thermal emission from the surrounding host galaxy.

These "jets" are collimated plasma streams trapped in a magnetic field, carrying kinetic energy and angular momentum. When pointed at a large angle to the line of sight, large twin jet structures are observed to extend a few kiloparsecs to megaparsecs into the intergalactic space. If the jets are coaxial to our line of sight, the approaching jet appears Doppler brightened, while the receding one is very often too dim to be observed. While the jet production and collimation mechanism is still elusive, an accepted view is based on magnetohydrodynamic (MHD) models of the accretion disk/black hole system (see e.g. [Mei01]). Such models account for jet collimation and accelerations in the accretion framework: Jets seem to be a natural consequence of a rotating disk in presence of a magnetic field [Kud99]. The magnetic field is frozen in the outflowing plasma, which in turn can only escape along the field lines. Requirements for jet formation are a compact object to collect material to be ejected, a magnetic field anchored in it, and differential rotation to form helical magnetic field structures. Numerical simulations have shown that tightly collimated jets along the rotational axis are a general feature of rotating, gravitationally confined plasmas (fig. 2.4). Such calculations show that a very fast rotating Kerr black hole is able to accelerate material in the jets up to Lorentz factors[2] of $\Gamma = 10$. The jets are magnetically driven and collimated due to a toroidal component of the magnetic field [Sik05]. The accelerated plasma most likely originates from the outer halo of the accretion disk. There seems to be observational evidence for the presence of accretion disks in AGNs [Mar02]. Other models assume that the charged black hole acts as giant dynamo [Kir99]. Also in these models magnetic fields are naturally given.

As for the properties of the jets that lead to particle acceleration, there are *accelerating jet models* [Ghi89] which propose acceleration by an increasing bulk Lorentz factor and seed photons for VHE γ-ray productions coming from different parts of the jet as well as *shock–in–jet* models [Der94] which employ a standing shock within 0.1 pc of the central black hole that energizes the outflowing material. Accelerating jet models and shock–in–jet models can be constrained by the observation or lack of correlations of optical, X-ray, and VHE γ-ray light curves.

Blazars comprise the AGN subclasses of flat spectrum radio quasars (FSRQ), which have broad, strong emission lines, and BL Lacertae type ("BL Lac") objects, which show nearly no emission lines. Both classes are characterized by variability on all wavelength scales and timescales, by a high degree of optical polarization (up to 20%), and by γ-ray emission. FSRQs and BL Lacs are discerned by the strength of their emission lines [Lan04a].

[2]The Lorentz factor $\Gamma = \left[1 - v^2/c^2\right]^{-1/2}$ is an appropriate measure of velocities close to the speed of light c. For example $\Gamma = 10$ describes a flow at 0.995c, in with each of the particles has a mass 10 times of its rest mass.

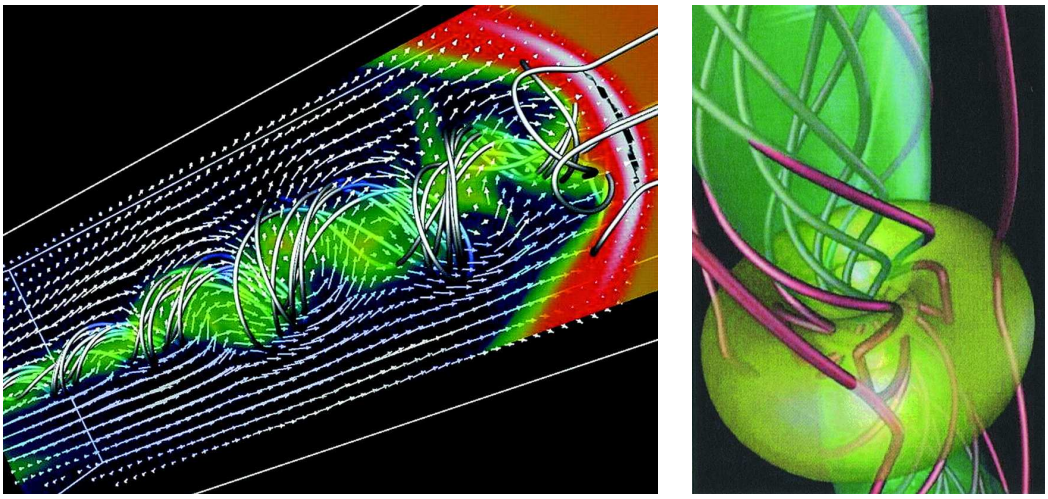

FIGURE 2.4: *Left: A 3D MHD simulation of the propagation of a magnetized jet. The arrows show the flow velocity, while the tubes mark the magnetic field lines. The rotating jet has developed a helical kink instability. Right: MHD simulation of a magnetized torus surrounding a $10^8 M_\odot$ black hole. The magnetic field lines are dragged along by the differentially rotating torus. Taken from [Mei01]. Right picture reprinted with permission from D. L. Meier et al., Science 291 (2001) 84-92. ©2001 AAAS.*

The rapid variability suggests a very compact source region. It might also imply that one in fact directly observes the source of energy in those AGNs [Lon92]. The generally more pronounced variability at higher energies, in particular in X-rays and above, hints at an origin close to the central engine. Also recent multiwavelength measurements show that X-ray production probably only takes place in the regions of the jets close to the SMBH [Jes05, Jes06, Uch06] (fig. 2.5). Therefore VHE γ-rays represent unique probes of the close vicinity of the central black hole. Indications for an unification of the two blazar subclasses are given in sect. 2.1.1.

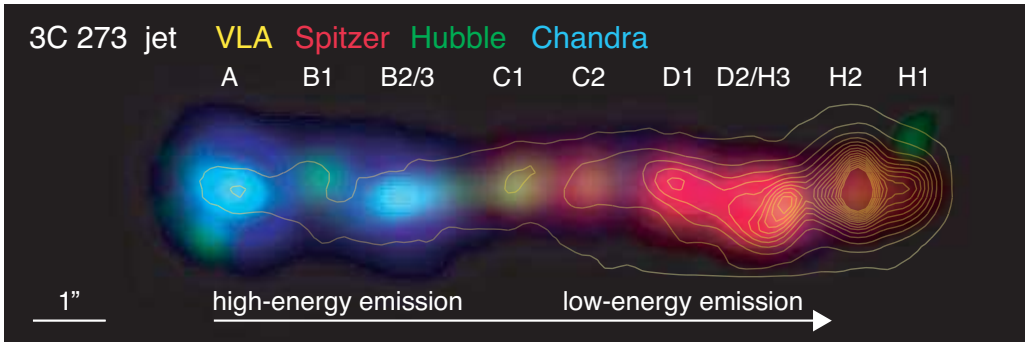

FIGURE 2.5: *Composite image of the jet of 3C 273 [Uch06]. The inner jet structures show strong X-ray emission (blue) and hard optical spectra (green), while the outer knots are seen in IR (red). Radio contours are superimposed.*

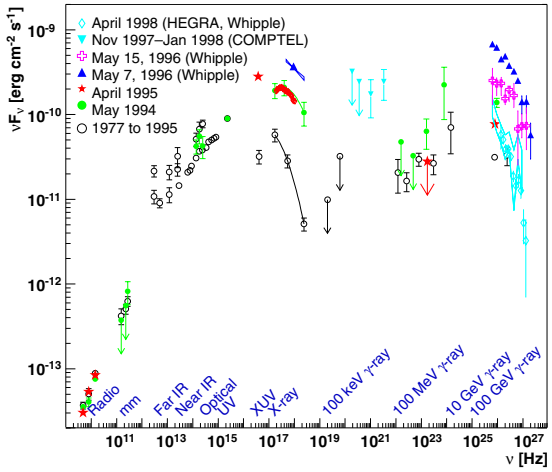

FIGURE 2.6: *Typical two–bump spectral energy distribution, here exemplarily of the HBL Mkn 421. Adapted from [Buc99], see also for references. Additional data points from [Buc06].*

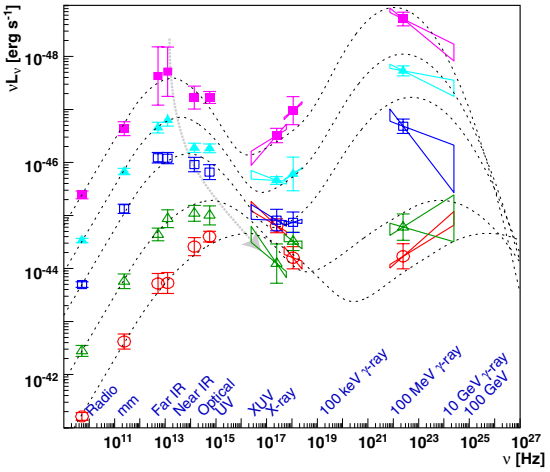

FIGURE 2.7: *Average SED for a sample of 261 blazars, showing the LBL—HBL transition. The thin lines represent model spectra within the SSC model (adapted from [Don01]).*

2.1 VHE γ-ray production mechanisms

The advent of γ-ray observations showed that blazars emit most of their power in the γ-ray frequency band, and it gave the first hints of the broad–band spectral energy distribution (SED) of such objects, which in a $\nu \times F(\nu)$ representation comprises two broad peaks (fig. 2.6). The low energy peak is found in the radio to X-ray region, while the high energy peak is located in the $\gtrapprox 1$ keV region (fig. 2.7). BL Lacs with their low energy peak in the optical—UV band are usually called *low–frequency peaked BL Lacs* (LBL), while *high–frequency peaked BL Lacs* (HBL) have their peak in the UV—X-ray band. While the commonly adopted view is that the low energy peak is due to synchrotron radiation from relativistic electrons in magnetic fields, there are competing models for the VHE γ-ray emission that is responsible for the high energy bump.

2.1.1 Leptonic models

In lepton–based models the VHE γ-ray radiation is explained by inverse Compton scattering of optical to X-ray photons off relativistic electrons and positrons in the jet (e.g. [Sik01b]). In Self–Synchrotron Compton (SSC) models [Mar92, Mar85, Blo96] the seed photons are synchrotron photons created by the electrons themselves. Experimental evidence for the SSC mechanism has been provided by the observed correlations of the X-ray and VHE γ-ray flux levels during large flares of VHE γ-ray emitting blazars [Mar99, Tak00, Kra01c]. The SSC model is widely accepted to describe VHE γ-ray emission of HBL objects.

Another source of the seed photons are ambient IR or optical photons, photons of the cosmic microwave background (IC–CMB model [Tav00]), or thermal radiation either directly from the accretion disk, or first scattered by the surrounding gas and dust clouds. Models utilizing these photons are called External Inverse Compton (EIC) models. One characteristic feature of BL Lac objects, namely the lack of strong emission lines, is commonly interpreted as evidence that ambient photon fields are not as important as the synchrotron photons. Therefore SSC models are more likely to explain the data than EIC models. Nevertheless often the predicted SSC emission is below the observed emission (e.g. in FSRQs), making EIC contributions necessary.

Indeed modern SSC models seem to be consistent with the observational data and are able to show some remarkable analogies in their interpretation of the observed blazar SED [Fos98]:

- The synchrotron peak occurs at different frequencies ranging from the radio to the X-ray regime. The higher the luminosity, the lower the synchrotron peak frequency. When arranging the blazar subclasses along their synchrotron peak frequency, they form a sequence from the powerful flat spectrum radio quasars and LBLs to HBLs and the so-called extreme BL Lac objects with their synchrotron peak in the X-ray regime of $E^{\mathrm{sy}}_{\mathrm{peak}} > 0.1\,\mathrm{keV}$ (fig. 2.7). Recent works [Nie06] promote a smooth transition from LBLs to HBLs, introducing *intermediate BL Lacs* (IBLs).
- The frequency of the high energy (γ-ray) peak is correlated with that of the low energy (synchrotron) peak, as both peaks depend primarily on the same electron spectrum. It resembles the form[3] of the synchrotron peak with a displaced maximum of the peak by the squared electron Lorentz factor, $E^{\mathrm{IC}}_{\mathrm{peak}}/E^{\mathrm{sy}}_{\mathrm{peak}} \sim \gamma^2$.
- The luminosity ratio between the high energy peak and the low energy peak increases with luminosity.
- The bulk of the emission takes place in the γ-ray range.

These trends offer the opportunity to unify the various flavors of blazars (FSRQs, LBLs, HBLs up to extreme HBLs) and call for a physical explanation. Possible interpretations are given by [Fos98, Ghi98]: From observations it was suggested that there exists a *blazar sequence* characterized by an anticorrelation between source luminosity and synchrotron peak frequency ν_{peak} (fig. 2.8). The latter is thought to be determined by the balance of electron acceleration and cooling processes. The higher energy density in the more luminous sources then implies increased cooling efficiency and thus a lower peak energy.

[3] Strictly speaking, this is only true in the Thomson regime, where even the spectral index of the photon distribution is reproduced; the transition to the Klein–Nishina regime occurs at VHE energies however and exhibits a rather complicated form.

Therefore according to the blazar sequence prediction, FSRQs with high $\nu_{\rm peak}$ should not exist. All currently detected VHE blazars are of HBL type, and thus support the predictions.

There are works [Cac04] that claim this sequence is just a selection effect caused by an undersampling of low luminosity low–frequency peaked and high luminosity high–frequency peaked sources. Tests of the blazar sequence therefore aim at checking the claimed correlation and at detecting the "forbidden" objects. In fact recent surveys [Pad03, Ant05] did not confirm the correlation (fig. 2.9). Novel blazar selection criteria, such as a radio compactness criterion, reveal objects that do not fit into the proposed sequence. Recently it was shown that there exist high–peaked flat spectrum radio quasars (HFSRQs) with SEDs similar to that of HBLs [Per01, Pad03], although with $\nu_{\rm peak} \lessapprox 10$ times smaller than that of typical HBLs. Previously FSRQs were thought not to exhibit such high synchrotron peak frequencies. Typical features expected in the blazar sequence scenarios were not found for these objects. Therefore, there is a possibility for "X-ray–strong" FSRQs, which might also emit in the VHE range. It might however be that there are physical limits for the synchrotron peak frequency of these strong–lined blazars.

It seems as if the blazar sequence in its simplest form is not valid once all selection effects are identified and eliminated, in particular as HFSRQs have been detected. Still, they do not exhibit synchrotron peak energies comparable to that of HBLs. The detection of γ-ray emission from HFSRQs could possibly shed more light on the classification of these objects within a novel blazar-ordering scheme.

2.1.2 Hadronic models

These models assume that in the jet there is a high energy protonic component ($E \gtrapprox 10^{18}$ eV) which is accelerated together with the electrons. This happens more efficiently because protons suffer less synchrotron losses than electrons. At the same time, protons have a higher gyro radius $r_{\rm gy} \propto E/B$, which is proportional to the mean scattering time [Rie05]. The low energy hump is explained by synchrotron radiation of co–accelerated electrons. VHE γ-rays are produced by the interactions of the relativistic protons with matter [Bed93, Dar97, Poh00], ambient soft photons [Man92, Man93, Man98, Mue03], both of these [Mue01], or with magnetic fields [Aha00a]. In proton-induced cascade (PIC) models [Man92] the subsequent decay of π^0 mesons generates γ-rays that enter into further collisions with low energy synchrotron photons and thus form electromagnetic cascades, which produce HE/VHE γ-rays. The expected correlated neutrino emission from charged pion decay would be a clear indicator for hadronic models. It is also conceivable that most of the VHE γ-rays are due to proton synchrotron radiation; such models are called synchrotron proton blazar (SPB) models [Mue01, Mue03].

Hadronic models are attractive, as they are characterized by particle acceleration up to

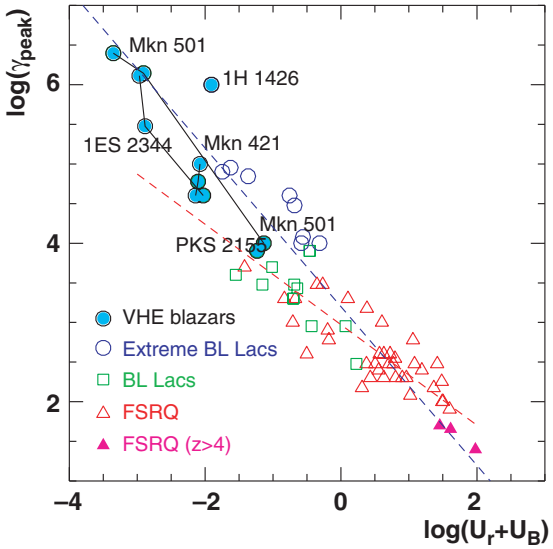

FIGURE 2.8: *Blazar sequence in SSC models: The Lorentz factor of the electrons emitting at the peak of the SED as a function of the co-moving energy density (radiative plus magnetic energy density). VHE-emitting blazars detected at multiple emission states are represented by data points connected by lines. The dashed lines represent correlations found by [Ghi98] and [Ghi02]. Taken from [Ghi02].*

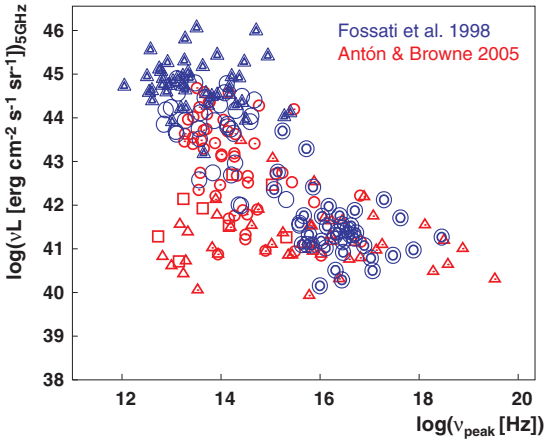

FIGURE 2.9: *Blazars in the 5 GHz-radio—synchrotron peak frequency plane. We plot the data as given by [Fos98] along with more recent data from [Ant05]. The blazar sequence seems to result from an undersampling of low–power BL Lacs. The different symbols indicate the various surveys, from which the data were collected, see [Fos98, Ant05] for references.*

extreme energies of 10^{19} eV and above, which is possible if the acceleration time is close to $r_{\rm gy}/c$. Thus they explain cosmic ray acceleration to the highest energies. This corresponds to the maximum possible acceleration rates [Aha02b]. Leptonic models generally lack this virtue. However hadronic models require extreme parameters of the acceleration region, particularly high plasma densities and high magnetic fields $B \gg 10\,\mathrm{G}$. Additionally, they have difficulties explaining the observed correlations of X-ray and VHE γ-ray emission of blazars during flares due to the longer p cooling times. Therefore it is commonly believed that the dominant emission mechanism at work in blazars is the leptonic IC mechanism. Hadronic processes admixed to IC processes are not ruled out, and could well be responsible for a fraction of the detected VHE γ-rays. The measurement of VHE ν fluxes would constitute a handle on the quantification of hadronic admixtures (see sect. 11.5 for a discussion on the VHE γ—ν connection). Orphan VHE γ-ray flares, i.e. unaccompanied by outbursts in other wavelengths—like those observed for the BL Lac object 1ES 1959+650 in the year 2002 [Dan05] in connection with a clustering of neutrino events from the direction of 1ES 1959+650 [Ber05]—can be interpreted as an indication of hadronic acceleration at work.

Note that hadronic and leptonic acceleration may very well be is present in blazar jets at the same time, e.g. hadronic acceleration (or a leptonic/hadronic admixture) might account for a baseline flux, and fast flares could be governed by additional electron ac-

celeration. Thus the corresponding models would just be extreme cases of blazar jets. In this context attempts to study the matter content of blazars [Sik00, Geo05] are of interest as well as the detection and quantification of neutrino fluxes.

2.1.3 More on SSC models: Parameters and observables

SSC models have been very successful in describing the observed HBL multi-frequency spectra with synchrotron emission for the low energy component and with inverse Compton scattering of high energy electrons for the high energy component [Tak00, Tav01].

Parameters. Homogeneous one–zone SSC models, the most simple models, assume that the γ radiation is produced in a single zone in the jet. The acceleration region is approximated by a spherical "blob" with radius R and bulk Lorentz factor $\Gamma = E_\mathrm{e}/(m_\mathrm{e}\mathrm{c}^2)$ that is moving along the jet under a small angle θ to the line of sight.

The blob contains relativistic electrons of density ρ accelerated by shock acceleration processes. Assuming that a diffusive shock acceleration mechanism is responsible for the initial electron acceleration, the electron injection spectrum can be described by a power law $\mathrm{d}N/\mathrm{d}E \propto E^{-n_1}$ with $n_1 \simeq 2$ (left panel of fig. 2.10). To take into account synchrotron cooling effects, the spectrum is modeled to show a break point where radiative cooling becomes dominant. At this energy it steepens by one unit ($n_2 \simeq 3$) and can thus be described by three parameters, E_min, E_max, and E_break. It can be shown that in the presence of a randomly oriented magnetic field with an approximately constant strength B an isotropic electron population with such a spectrum is able to produce a synchrotron photon population [Kin02] as observed in BL Lacs.

In SSC models, the seed photons needed for the inverse Compton (IC) scattering and the photons produced in the synchrotron process are identical. When upscattered to VHE by the same electron population that created the synchrotron radiation, the typical two–peaks structure in the γ-ray SED is produced (right panel of fig. 2.10). As the inverse Compton (IC) peak occurs in the Klein–Nishina regime, its energy is mainly determined by the value of E_break, as the peak synchrotron power is emitted by those electrons with the break energy. Within the SSC model, a rough mapping of the synchrotron photons and IC photons produced by electrons of a given energy is given by [Kra04]

$$E_\mathrm{IC}/\,\mathrm{TeV} \approx \left(\frac{\delta/10}{B/0.05\,\mathrm{G}}\right)^{0.5} (E_\mathrm{sy}/\,\mathrm{keV})^{0.5}$$

The maximum value of the observed energy in the Klein–Nishina regime can be computed as [Kin02]

$$E_\mathrm{SSC,max} \propto \gamma_\mathrm{max} m_\mathrm{e}\mathrm{c}^2 \frac{\delta}{1+z}. \tag{2.1}$$

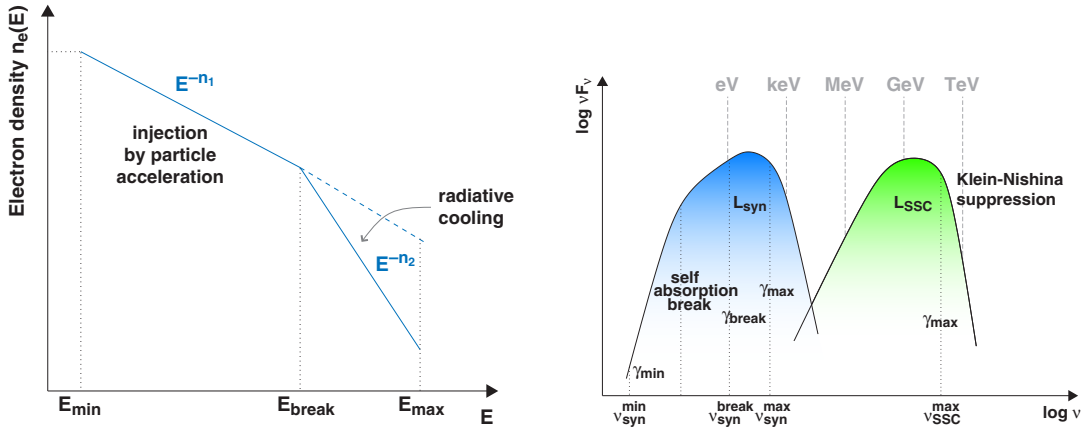

FIGURE 2.10: *Left: Schematic picture of the relativistic electron energy spectrum. For high Lorentz factors, radiative cooling decreases the number density of electrons and leads to a break in the spectrum. Right: Schematic picture of the SED produced by electron injection as shown in the left panel. The breaks stem from radio self-absorption of the created synchrotron photons, radiative electron cooling, and the cutoff in the electron injection spectrum. Klein–Nishina suppression comes about by the decrease of the IC cross–section due to quantum-electrodynamical effects (adapted from [Kin02]).*

The observed radiation will be strongly affected by relativistic effects. An additional parameter therefore is the Doppler boosting factor $\delta = [\Gamma(1-\beta\cos\theta)]^{-1}$ with the bulk velocity of the plasma βc. It describes the effects of time dilatation, boosting and jet focusing: A given emitted frequency ν by a jet looking towards the observer jet appears as $\nu \cdot \delta$, while the emission solid angle Ω is reduced by a factor δ^2, adding to an increase in brightness of $\sim \delta^3$. For jets moving away from the observer one has $\delta < 1$, often making these jets invisible to us.

In summary, the model is completely described by seven parameters, namely those which characterize the emission region: magnetic field strength B, the size of the blob characterized by R, δ, those which characterize the electron injection spectrum: $E_{\rm min}$, $E_{\rm max}$, and $E_{\rm break}$ and the electron density plus the variability timescale.

Observables. The observed SED is characterized by two broad peaks (fig. 2.10), below and above which the spectrum is quite smooth and can be approximated by power law distributions. Within the present uncertainties, the "left" side of both peaks can be described by the same spectral index [Tav98]. The observables comprise the peak frequencies $\nu_{\rm sy}$, $\nu_{\rm SSC}$ of the two peaks, their luminosities $L_{\rm sy}$ and $L_{\rm SSC}$, the spectral indices right and left of each of the two peaks and the timescale $t_{\rm var}$ of emission variability, which constrains the dimension of the source by $R \leq ct_{\rm var}\delta$. An additional constraint to the model is given by the requirement of source transparency [Mat93], which can be translated into a limit on the optical depth of the source and thus on the energy density of the soft radiation. This can be translated into a lower limit on the Doppler factor δ [Don95]. It should be noted that small dimensions imply high Doppler factors if the transparency condition is

taken into account. The verification of any such independent constraints (see [Tav98] for a more detailed discussion) can be interpreted as support for the model.

It should be noted that homogeneous one–zone models underpredict the radio to optical fluxes [Pia98, Kra04], thus suggesting that radiation in this regime is dominated by other processes than those that emit the bulk of the X-rays and γ-rays. In accordance with this, it could be shown that the variability found in the radio and optical bands is less pronounced than that in the X-rays and γ-rays.

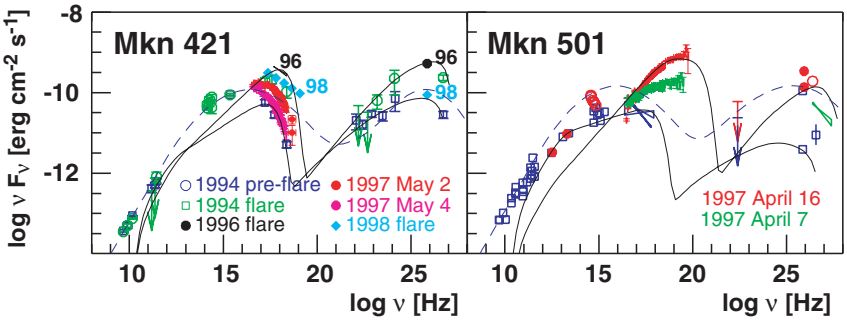

FIGURE 2.11: *SED distributions of the BL Lac objects Mkn 421 and Mkn 501. The lines represent SSC model fits by [Fos98] (dashed lines) and [Ghi02, Cos02] (solid lines).*

Source	R [cm]	$L'_{\rm inj}$ [erg s^{-1}]	$\gamma_{\rm min}$	$\gamma_{\rm br}$	$\gamma_{\rm max}$	n_1	B [G]	δ
Mkn 421 (1996 high state)	$5\cdot10^{15}$	$3.3\cdot10^{41}$	$1.0\cdot10^{5}$	$1.0\cdot10^{5}$	$1.0\cdot10^{6}$	2.5	0.34	15
Mkn 421 (1994 pre–flare)	$5\cdot10^{15}$	$2.2\cdot10^{41}$	$4.0\cdot10^{4}$	$4.0\cdot10^{4}$	$4.0\cdot10^{5}$	2.3	0.27	11
Mkn 501 (16/4/97 flare)	$5\cdot10^{15}$	$1.7\cdot10^{41}$	$1.0\cdot10^{6}$	$2.5\cdot10^{6}$	$9.0\cdot10^{6}$	1.4	0.10	20
Mkn 501 (quiescent)	$5\cdot10^{15}$	$3.7\cdot10^{41}$	$1.0\cdot10^{4}$	$1.0\cdot10^{4}$	$8.0\cdot10^{5}$	2.8	1.11	10

TABLE 2.2: *SSC model parameters for the fits given in fig. 2.11 [Ghi02]. R is the radius of the spherically assumed acceleration region, L'_{inj} the injected power measured in the co-moving frame; γ_{min}, γ_{max} are the minimum and maximum injected electron Lorentz factors, γ_{break} is the break Lorentz factor of the electrons, n_1 the power law index of the injection spectrum, B the strength of the magnetic field, and δ the Doppler factor.*

Fig. 2.11 shows SSC model fits to observational data of the well–established sources Mkn 421 and Mkn 501 as done by [Cos02]. The fit parameters are given in tab. 2.2. With these parameters the properties of AGNs in both quiescent and flaring state can be described. To discern these states, the electron Lorentz factor is the most useful parameter. The fit results indicate that the flare state is mainly caused by the increased energy of the injected electrons.

Multiple–zone SSC models. To fit the data consistently from several Mkn 501 flares, time–dependent modeling and the introduction of a second emission zone was necessary [Kra02]. Two–zone models assume e.g. a fast jet spine and a slower sheath surrounding it [Cel01] or regions of different magnetic field strength in the jet. Additional photon fields

can originate from a quasi–stationary X-ray component coming from near the black hole, from regions along the jet that emit X-rays, from synchrotron processes without high IC luminosity [Sik01a], and from the cosmic microwave background (beamed IC-CMB process [Tav00]).

2.2 Flux variability

The emission level of blazars is highly variable on all timescales, with changes of the emission level of the electromagnetic radiation by more than one order of magnitude. Flares with emission levels as high as 10 times the Crab nebula flux have been observed for the AGN Mkn 501 in 1997, while its baseline emission level can be very low—in the order of a few percent of the Crab nebula flux. The detection of the first three VHE γ-ray blazars in fact took place at rather low emission levels of about 30% (Mkn 421 [Pun92]) and $\lessapprox$ 10% that of the Crab nebula (Mkn 501 [Qui96] and 1ES 2344+514 [Cat98]). Also in follow-up observations, very low emission levels were found over extended periods of time (e.g. Mkn 501 [Gli06], 1ES 2344+514 [Tlu03] and this thesis). The presence of a low steady-state emission was also found for Mkn 501 [Xue05], although with intermittent flare activity. The flux of Mkn 421 was found to vanish, although this is likely to be an instrumental effect.

All the flaring states detected in the VHE γ-ray range are usually correlated with a flux increase in X-rays and sometimes also in the optical energy range [Cat97a]. Changes of the spectral shape with the flux level have been measured for Mkn 421 [Kre02, Aha02c], Mkn 501 [Dja99, Aha01c] and 1ES 1959+650 [Aha03b]. The minimum timescale for VHE γ-ray flux level variability was reported to be days [Aha99b] (for Mkn 501) down to 15 minutes [Gai96, Sch02b] (for Mkn 421). This work reports on the first observation of even shorter (minute–scale) flux variability in sect. 7.8.2. Such very short variability timescales can be translated into very small emission regions by employing causality: $R \lesssim c t_{\mathrm{flare}} \delta/(1+z)$. In addition, the moving shocks expected to harbor the VHE γ-ray acceleration regions are not observed in very–long baseline interferometry (VLBI) images of VHE blazars [Pin03, Pin04], pointing to a fast dissipation of the shocks from the VHE γ-ray emission scale (≈ 0.01 parsec away from the black hole) to the parsec scale and to an only initially large ($\Gamma > 10$) bulk Lorentz factor.

While many of the models given in sect. 2.1.1 and 2.1.2 are able to describe the observed SED to a certain degree, the observation of rapid, large scale flares should enable discerning constraints to be put on the different models, as the models respond differently to changes in the source conditions or the injection parameters. The flare duration itself serves as an observable for the particle cooling time, which is expected to be of the order of the flare duration. Clearly, full time-dependent calculations are superior to a series of

static models applied to snapshot data sets. [Kra02] compares selected SSC blazar models in their efforts to explain variable X-ray and VHE γ-ray emission.

The specific difficulties in comparing the performance of time–dependent models are twofold: (1) Until recently, the instrumental sensitivity and time resolution were not sufficient to track γ-ray flux variations down to the sub–hour scale. (2) For several blazars, SSC models have not proven to explain sufficiently well the observed radiation, which made it necessary to consider additional external components. The identification and observation of such external photon fields is often complicated by the fact that the beamed emission from the jet is dominating.

Several mechanisms have been put forward to explain the observed flares, particularly the fast flaring:

- **Additional population of more energetic electrons or altering the electron injection spectra:** Increasing $\gamma_{\max}$ by a factor of ≈ 5 results in large variations at X-ray and VHE γ-ray energy, while not noticeably changing flux levels at other energies. In such scenarios Doppler factors of $\delta \gtrapprox 15$ are required to account for time variations of about one day [Mas02]. Alternatively, increasing the luminosity of the injected electrons can produce a flare, however this only badly fits observational data [Mas97]. Hour–scale variability in such models require $\delta \approx 50$, which is a Doppler factor higher than indicated by the observations of superluminal motion [Ver94].

- **Modulation of the seed photon field for the IC process.** A conceivable scenario is that a small X-ray hot spot rotates on the surface of the accretion disk. This emission may also be intrinsically collimated by the hot spot geometry or by an ordered magnetic field [Bed97]. Although strong absorption does not allow VHE γ-ray generation in the hot spot itself, the energy release of such a region can explain fast flaring as observed e.g. in Mkn 421. The X-ray photons serve as external seed photons for IC acceleration in the jet.

- **Sub-shocks inside the jet.** An alternative approach to explain a flaring behavior on short timescales is to assume unsteady jets, fed by discrete ejecta. M87, often interpreted as a misaligned blazar [Tsv98], shows bright knots in the optical in its jet, which can be interpreted as internal shocks that develop from velocity irregularities in the beam [Ree78]. In other models thin shock waves comprising plasma shells with different mass, energy, and velocity move down the cylindrical symmetric jet [Spa01]. Diffusive shock acceleration may then take place whenever two shock fronts encounter each other. This concept of acceleration zones differs fundamentally from homogenous models, as it does not assume a homogeneous acceleration region, but internal shock sheets advancing down the jet. The travel distance of

FIGURE 2.12: *Filament structure in the supernova remnant SN 1006. In this Chandra false-color image, thermal radiation of hot gas is represented by red and green colors. Diffusive shock acceleration is thought to be at work in the filament structure traced by the bright X-ray emission (blue color). Additional reading: [Lon03]. Picture credit: NASA/CXC/Rutgers/J. Hughes et al.*

such sheets during a flare is given by $d \approx c t_{\rm flare} \Gamma^2$. Particle acceleration at shocks is beautifully seen in X-ray pictures of galactic supernova remnants (fig. 2.12).

- **Changes in the acceleration environment.** Not only the electron population or the seed photon population may undergo changes, but also the acceleration environment. In the context of homogeneous IC models, changes in B have been discussed in [Mas97, Cop99]. Fast flaring, however, implies small acceleration regions or high Doppler factors. Thus, a conceivable scenario for fast flares is to allow for an inhomogeneity of the acceleration region, e.g. by small regions with enhanced magnetic field strength or "B field blobs" inside the acceleration region.

Probably the correlation of X-ray and VHE γ-ray flux can help to discern the different models. If the soft photons to be upscattered by the IC process originate from the accretion disk (EIC scenario) and no correlations with X-rays are expected, modulation models are favored; conversely correlations would rather point to a SSC origin of the flares, hence to sub-shock scenarios.

More detailed discussion on flux variability is given in sect. 7.2, in particular about observations and interpretations in connection with Mkn 501.

Source	Redshift z	Discovery	Confirmation
Mkn 421	0.030	Whipple [Pun92]	[Pet96]
Mkn 501	0.034	Whipple [Qui96]	[Bra97]
1ES 2344+514	0.044	Whipple [Cat98]	[Aha04b], sect. 8
1ES 1959+650	0.047	Seven telescope array [Nis99]	[Hol03, Aha03b, Alb06f]
PKS 2155–304	0.116	Durham Mark 6 telescope [Cha99]	[Aha05f]
H 1426+428	0.129	Whipple [Hor02]	[Aha02a, Dja02]
M87	0.0044	HEGRA [Aha04b]	[Bei05]
PKS 2005-489	0.071	H.E.S.S. [Aha05e]	
1ES 1218+30.4	0.182	MAGIC [Alb06b]	
1H 2356–309	0.165	H.E.S.S. [Aha06b]	
1ES 1101–232	0.186	H.E.S.S. [Aha06b]	
PG 1553+113	0.36*	H.E.S.S. & MAGIC [Aha06c, Alb06a], sect. 9	
Mkn 180	0.045	MAGIC [Alb06c]	
PKS 0548–322	0.069	H.E.S.S. [Gie06]	

TABLE 2.3: *Discovered and confirmed extragalactic VHE γ-ray sources. A source is assumed as confirmed or established once significant ($\geq 5\sigma$) detections by at least two instruments are reported. The upper part of the table shows the confirmed sources prior to the advent of new generation installations like MAGIC and H.E.S.S., while the lower panel summarizes the newly found sources after 2002. For the location of the objects in the sky, see fig. 1.9. *) The redshift of PG 1553+113 is currently under discussion. It seems to be limited by a HST survey and VHE γ-ray measurements to $0.25 \lesssim z < 0.74$, cf. sect. 9 for details.*

2.3 Current sample of VHE-emitting AGNs

To date, all confirmed extragalactic VHE γ-ray sources belong to the class of HBL objects and the giant radio galaxy M87.[4] The initial searches for blazars in the VHE regime were stimulated by the successful detection of 3C 279 by EGRET [Har92]. The criteria for selecting AGN candidate objects changed with time as more information on γ-ray emitting AGN became available. One of the first source lists required the detection of the candidate objects by EGRET, their identification as a blazar and a low redshift [Ker95]. As expected, the first detected blazars Mkn 421 and Mkn 501 were close objects with comparatively hard γ-ray spectra. 1ES 2344+514 and 1ES 1959+650 in many aspects were very similar to these pioneering VHE γ-ray sources. The first comparatively distant object discovered was 1H 1426+428. The advent of more sensitive detectors like H.E.S.S. and MAGIC with substantially lower threshold energies than previous instruments made it possible to extend the VHE γ-ray blazar sample in the following ways: By discovering objects with (1) much weaker emission, like PKS 2005–489 (2) much softer spectra, like Mkn 180, PKS 2005–489, and PG 1553+113, and (3) much higher redshift, like 1ES 1218+304, 1H 2356–309, 1ES 1101–232, and presumably PG 1553+113. The VHE γ-ray BL Lac objects discovered so far are given in tab. 2.3. We will return to the currently known sample of VHE γ-ray emitting BL Lac objects in sec. 11.

[4] M87 can be interpreted as a misaligned BL Lac object [Tsv98]

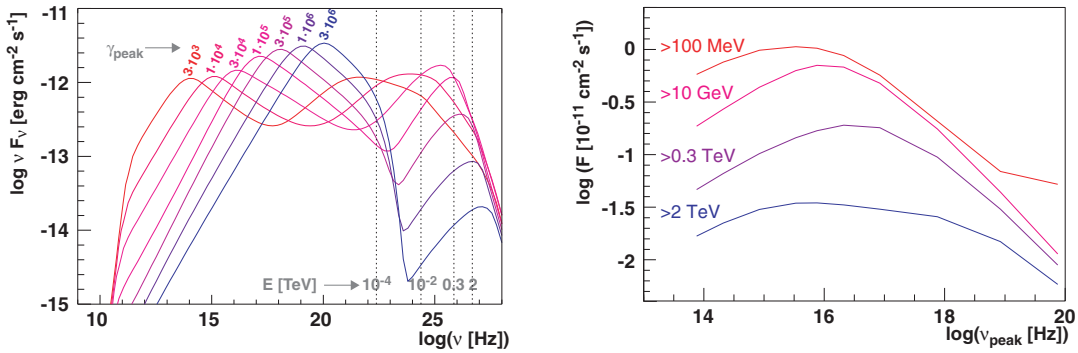

FIGURE 2.13: *Left panel: Calculated SEDs with different Lorentz factors γ_{peak} of the emitting electrons at the peak as given in the plot; all other model parameters are kept constant. Right panel: Integrated VHE γ-ray flux for different synchrotron peak energies. Figures taken from [Cos02].*

2.4 Search for new VHE-emitting BL Lac objects

2.4.1 SSC model predictions

In this section we outline our selection criteria for the search for new VHE γ-ray emitting BL Lac objects with the MAGIC telescope. They are based on a TeV candidate BL Lac object list compiled in [Cos02]. The main selection criterion was to require both high energy electrons and a sufficient amount of seed photons for the IC process. The authors show (fig. 2.13) that in a one–zone SSC model the IC luminosity is decreasing from corresponding synchrotron peak frequencies of $\approx 10^{16}$ Hz on, and with it also the integrated flux in the VHE γ-ray regime. This can be understood by the decreasing Klein–Nishina cross–section for increasing energies, or in other words, only those synchrotron photons in the Thomson regime ($h\nu' < m_e c/\gamma_{peak}$, in the co-moving frame) can efficiently contribute to the IC emission. The maximum emission of VHE photons is reached for

$$\nu_{peak} \approx 3.8 \times 10^{15} B_{Gauss}^{1/3} \frac{\delta}{1+z} \text{ Hz}.$$

Phenomenologically speaking, "good candidates" therefore are required not only to show high synchrotron peak frequencies, but also a sufficiently strong seed photon emission. As an indicator for the synchrotron peak energy the 1 keV radio flux is used by [Cos02]. They further assume that the 1.4 GHz radio flux level is an indicator for the seed photon level prevalent in the source region. Therefore, in the radio flux—X-ray flux plane, objects with both high X-ray and high radio flux are selected as candidate objects (fig. 2.14). In fact these objects also show a high optical flux (at 5500 Å) in the energy region that contains the photons to be upscattered to VHE. The optical flux, however, is in general heavily contaminated by host galaxy contributions; therefore the radio flux is an indicative measure.

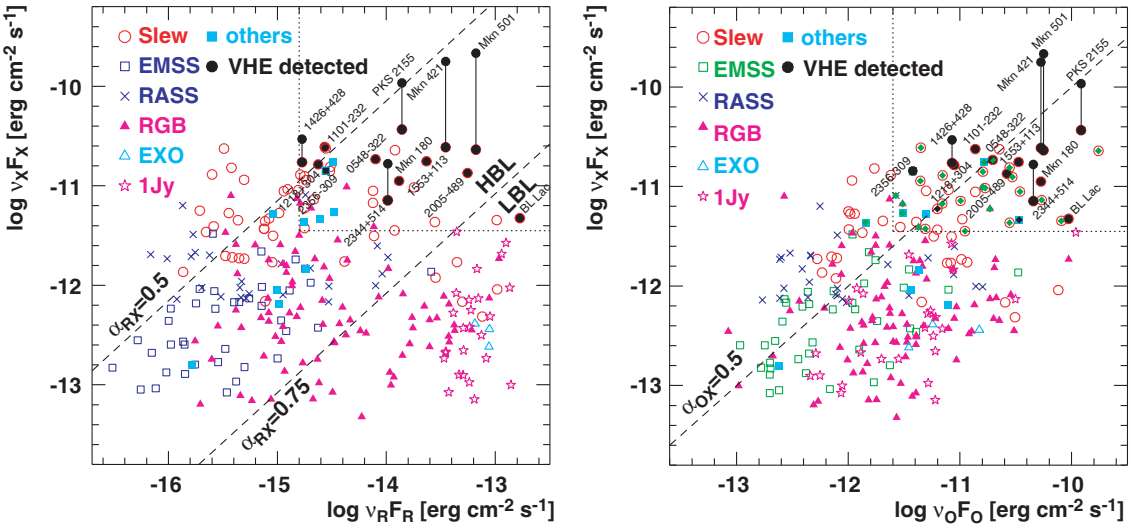

FIGURE 2.14: *BL Lac candidate selection criteria. Left figure: Radio (5 GHz)/X-ray (1 keV) plane. The discovered γ-ray emitting BL Lac objects are labeled. Where applicable, different flux levels are shown. Right figure: Optical/X-ray plane. Almost all of the selected candidates (marked by green diamonds) also show a high optical flux. The legends state the catalogs from which the sources were collected (adapted from [Cos02], see also for references on the source catalogs).*

From 246 BL Lac objects for which radio, optical and X-ray fluxes existed in catalogs or archival data, 33 passed the selection criteria. Favoring an SSC origin of the VHE γ-rays, VHE γ-ray flux predictions were derived from a homogeneous one–zone model [Ghi02] assuming reasonable parameter values inspired by well–monitored VHE γ-ray emitters like Mkn 501 and PKS 2155. In fact all 13 currently known VHE γ-ray emitting blazars fulfill the given selection criteria; only 6 of them had been discovered at the time these predictions were made.

2.4.2 Target selection for MAGIC telescope observations

The complete candidate sample put forward by [Cos02] is given in tab. 2.4, together with the VHE γ-ray flux predictions at 40 GeV by the model mentioned in sect. 2.4.1 and a phenomenological SSC model by [Fos98] for these objects. To obtain a flux prediction for observations with the MAGIC telescope, the 40 GeV flux estimate has been scaled to 80 GeV for the strongest sources in the candidate list and compared with the sensitivity of the MAGIC telescope (cf. sect. 4.6). EBL absorption effects are still small in this energy region: for $z = 0.4$, the attenuation is $\exp(-\tau) \approx 0.8$ (fig. 2.15).

For the sources under study, the predicted integrated flux above 40 GeV and above 80 GeV and the resulting maximum value of the predicted SSC energy are given in tab. 2.5.

Object	Redshift z	$F_{5\ \mathrm{GHz}}$ Jy	$F_{5500\text{Å}}$ mJy	$F_{1\mathrm{keV}}$ μJy	$F_{(>40\ \mathrm{GeV})}$ Fos / CG	$F_{(>0.3\ \mathrm{TeV})}$ Fos / CG	$F_{(>1\ \mathrm{TeV})}$ Fos / CG
0033+595	0.086[a]	0.066	2.95	5.66	15.0 / 2.93	2.04 / 0.25	0.48 / 0.04
0120+340	0.272	0.045	1.23	4.73	3.17 / 4.90	0.28 / 0.30	0.06 / —
0136+391	—[b]	0.049	3.41	2.39	5.22 / 4.00	0.56 / 0.14	0.12 / 0.0027
0214+517	0.049	0.161	0.39	1.60	43.4 / 1.59	5.93 / 0.07	1.43 / 0.0062
0219+428⋆	0.444	0.806	5.12	1.57	7.01 / **9.62**	0.14 / —	0.01 / —
0229+200	0.139	0.049	9.93	2.88	7.67 / 3.81	0.96 / 0.31	0.21 / 0.004
0323+022	0.147	0.042	0.81	4.49	6.65 / 1.18	0.84 / 0.01	0.18 / —
0414+009	0.287	0.070	0.82	9.29	2.91 / 3.42	0.23 / 0.07	0.04 / —
0548−322•	0.069	0.170	3.61	7.47	31.9 / 1.56	4.14 / 0.10	0.91 / 0.015
0556−384	0.034	0.068	0.56	2.2	37.8 / 5.51	5.84 / 0.42	1.56 / —
0647+250	—[b]	0.073	5.12	6.01	6.16 / 8.74	0.59 / 0.24	0.12 / —
0806+524	0.138	0.172	6.33	3.51	14.7 / 10.7	1.36 / —	0.27 / —
0809+024	—[b]	0.071	6.23	1.85	6.08 / 2.20	0.58 / 0.04	0.12 / —
0851+203	0.306	1.740	14.9	1.70	23.7 / —	0.42 / —	0.03 / —
1011+496	0.200	0.286	2.04	1.38	1.67 / 3.31	0.12 / 0.14	0.02 / —
1028+511	0.361	0.044	1.29	4.80	7.15 / 3.89	0.43 / —	0.06 / —
1101−232•	0.186	0.066	2.52	9.25	6.67 / 10.2	0.67 / 0.93	0.15 / 0.18
1114+202	0.139	0.074	3.03	7.31	10.1 / 8.51	1.17 / 0.10	0.28 / —
1133+704•	0.045	0.274	9.75	4.56	62.8 / 2.15	8.50 / 0.03	1.93 / —
1136.5+6737	0.135	0.040	0.49	3.40	7.30 / 5.40	0.92 / 0.10	0.21 / —
1215+303	0.237	0.445	3.08	3.7	4.06 / 0.07	0.16 / —	0.02 / —
1218+304•	0.182	0.056	1.63	6.39	6.36 / 5.82	0.67 / 0.16	0.15 / —
1417+257	0.237	0.040	0.56	2.65	3.76 / 6.88	0.38 / 0.21	0.08 / —
1440+122	0.162	0.041	0.90	1.47	6.11 / 1.89	0.78 / 0.09	0.20 / 0.01
1544+820	—[b]	0.043	1.15	2.31	4.89 / 5.37	0.54 / 0.22	0.12 / —
1553+113•	0.360[c]	0.636	6.15	6.54	8.92 / **22.3**	0.20 / 0.42	0.02 / —
1722+119	0.018	0.088	2.95	4.02	76.6 / 1.06	12.8 / 0.015	3.52 / 0.001
1727+502	0.055	0.159	1.27	2.73	38.7 / 2.64	5.19 / 0.07	1.23 / —
1741+196	0.084	0.223	1.86	2.88	31.6 / 4.31	3.59 / 0.29	0.84 / 0.01
1959+650•	0.047	0.252	1.35	9.29	56.7 / 2.08	7.46 / 0.03	1.74 / —
2005−489•	0.071	1.192	4.84	5.42	67.1 / **62.5**	5.14 / 2.67	0.90 / 0.17
2200+420⋆⋆	0.069	3.593	17.27	1.91	67.7 / **42.8**	3.32 / 0.17	0.43 / —
2356−309•	0.165	0.065	0.67	5.78	7.64 / 3.30	0.84 / 0.19	0.12 / 0.03

TABLE 2.4: *Candidate BL Lac objects for VHE γ emission put forward by [Cos02] with their observed fluxes at 5 GHz, 5500 Å and 1 keV. Integral flux predictions above 40 GeV, 0.3 TeV and 1 TeV, according to the parameterization of the SED adapted from [Fos98] (first number) and according to the SSC model discussed by [Cos02] (second number) given in units of* 10^{-11} *photons cm*$^{-2}$ *s*$^{-1}$*. The objects marked with* • *have been detected by VHE γ-ray telescopes.* ⋆ *3C 66A has been observed by MAGIC, but no signal could be detected.* ⋆⋆ *BL Lacertae shows a γ excess in recent MAGIC observations, cf. sect. 10.* [a] *tentative redshift.* [b] $z = 0.2$ *assumed.* [c] *but see discussion in sect. 9.1. Adapted from [Cos02]. The objects printed in* ***bold*** *are discussed further in this section.*

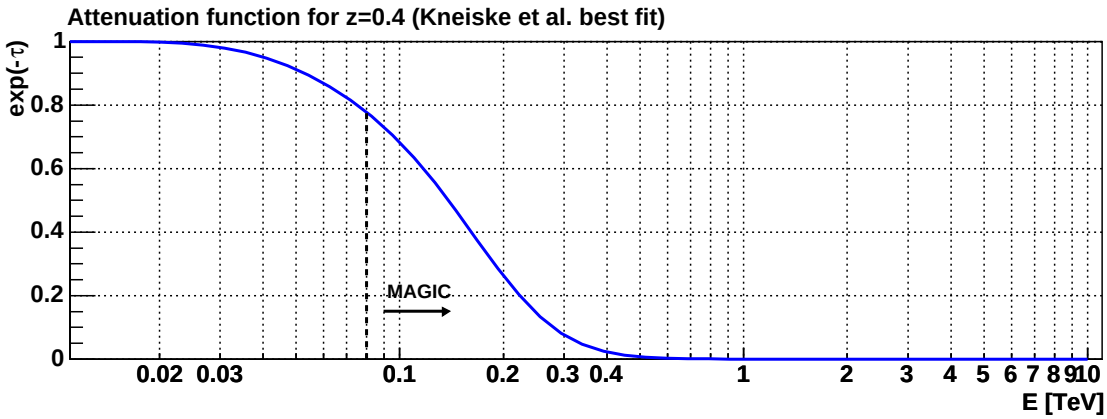

FIGURE 2.15: *Attenuation function* (1.6) *due to the EBL absorption for a redshift of* $z = 0.4$. *When dividing the measured spectrum by this function, the intrinsic source spectrum is obtained. Calculated using the best-fit model given in [Kne04].*

To estimate the flux of the chosen candidate objects we calculate the integrated flux for 80 GeV and above:

$$F_{E\geq 80\,\mathrm{GeV}} = F_{E\geq 40\,\mathrm{GeV}} \times \left(\frac{80\,\mathrm{GeV}}{40\,\mathrm{GeV}}\right)^{(-\alpha+1)} \tag{2.2}$$

assuming that the differential spectrum is similar to that of the Crab nebula ($\alpha = 2.6$) because the maximum IC intensity (tab. 2.5) is predicted to occur at energies sufficiently higher than 80 GeV.

For a threshold energy of 80 GeV the MAGIC sensitivity for a 5σ detection in 15 hours is $F_{E\geq 80\,\mathrm{GeV}} = 5.8 \times 10^{-11}\mathrm{cm}^{-2}\mathrm{s}^{-1}$ (cf. fig. 4.27). For three objects of the candidate list given in tab. 2.4 the predicted VHE γ-ray fluxes are high enough to be detected by MAGIC: PKS 2005–489 (not observable from the MAGIC telescope site), PG 1553+113, and 2200+428 (BL Lacertae). We conclude that these objects are the most probable sources among the candidate objects to be detected with the MAGIC telescope. Therefore, the observation of PG 1553+113 and BL Lacertae was proposed for the MAGIC cycle-I observations in 2005.

- The object with the highest flux prediction among the selected objects in this list, 2005–489, was successfully detected by H.E.S.S. [Aha05e]. It is however not observable by MAGIC at zenith angles lower than 75° (cf. fig. 1.9).
- PG 1553+113 was observed at low zenith angles with MAGIC in 2005 and 2006. The analysis of these data yielded a highly significant signal (on the 8.8σ level) and is presented in this thesis (sect. 9).
- BL Lacertae had been observed by the HEGRA CT–system for about 300 hours [Aha04b]. These observations resulted in upper limits of $4\% - 40\%$ of the Crab

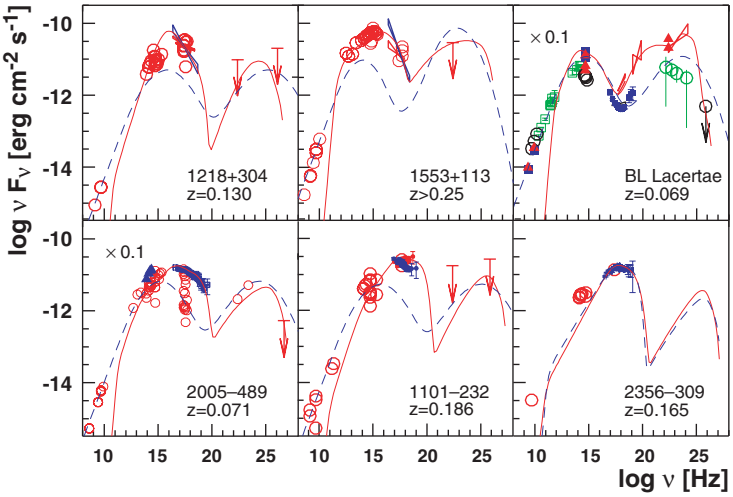

FIGURE 2.16: *Predicted SEDs for selected BL Lac candidate objects. All these objects have recently been discovered as VHE emitters. The lines represent the SED model fits by [Fos98] (blue dashed lines) and [Cos02] (solid red lines). Taken from [Cos02].*

Source	$F_{1\,\mathrm{keV}}$ [μJy]	$F_{\geq 40\,\mathrm{GeV}}$	$F_{\geq 80\,\mathrm{GeV}}$	$E_{\mathrm{SSC,\,max}}$ [GeV]
PKS 2005–489	5.42	62.5	20.6	1260
BL Lacertae	1.91	42.8	14.1	442
PG 1553+113	6.54	22.3	7.4	186

TABLE 2.5: *Measured X-ray flux $F_{1\,\mathrm{keV}}$, predicted integral fluxes at energies above 40 GeV and 80 GeV, the intensity maximum of the IC emission according to eq.* (2.1) *and the model parameters given in [Cos02]. VHE γ-ray fluxes are given in units of* 10^{-11} cm^{-2} s^{-1}.

nebula flux depending on the time of the observation. This is however compatible with the SSC model prediction at 1 TeV (cf. tab. 2.4). Even at 300 GeV, the predicted flux for BL Lacertae is only 1.7 % of the Crab nebula flux. The object was observed with MAGIC for 20 hours; the analysis shows a small, but significant excess (cf. sect. 10).

- MAGIC so far did not detect the fourth–best candidate for high energy γ-ray emission, 3C 66A (0219+428). Assuming a 110 GeV analysis threshold of the MAGIC telescope for the 3C 66A data set, from the predictions shown here we expect $\gtrapprox 40$ hours of necessary observation time as opposed to the 20 hours of available data.

It is noteworthy that quite a few more of the predicted sources have been discovered by MAGIC and H.E.S.S. recently: 1ES 1218+304 [Alb06b], 1ES 1101–232 and 1H 2356–309 [Aha06b] as well as most recently 1ES 1133+704 (Mkn 180) (triggered by an optical outburst [Alb06c]), and PKS 0548–322 [Gie06].

Chapter 3

Imaging Air Cherenkov Telescopes

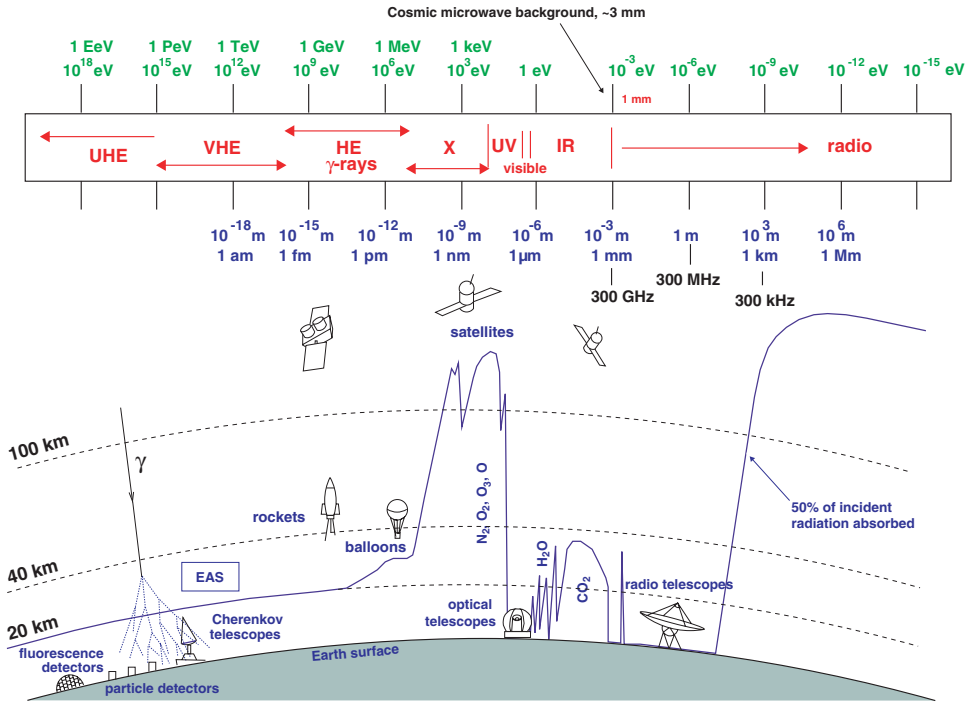

FIGURE 3.1: *Atmospheric windows for the observation of the Universe [Lon92]. The continuous line indicates the height at which a detector can receive half of the total incoming radiation for every wavelength.*

Electromagnetic (EM) waves, the main messengers from outer space, can only be detected in small energy bands in the optical and radio range directly from the ground (fig. 3.1). Observations in nearly all other energy ranges require detectors to be placed outside the Earth's atmosphere. VHE γ-rays cannot be detected directly by ground-based instruments, because they cannot traverse the Earth's atmosphere. They rather interact with nuclei of the upper part of the atmosphere, initiating a cascade of secondaries, a so-called

"extended air shower" (EAS). This chapter briefly summarizes the physics of EAS and describes the subsequent production of Cherenkov light, which is recorded by ground-based detectors like the MAGIC telescope.

3.1 Extended air showers

An air shower is initiated by a high energy particle interacting with a nucleus in the upper layers of the atmosphere. The produced secondary particles are strongly collimated along the direction of the incoming particle because of their relativistic energies. They, in turn, interact on average after one interaction length. This iterative process results in an avalanche of secondaries that traverse the atmosphere with nearly the vacuum speed of light. Since the physical length between interactions decreases with (air) density, it is useful to express it in terms of the product of density and distance, called atmospheric depth X. For vertical incidence, the atmospheric depth at sea level is $X_{\text{air}} \approx 1013$ g cm^{-2}.

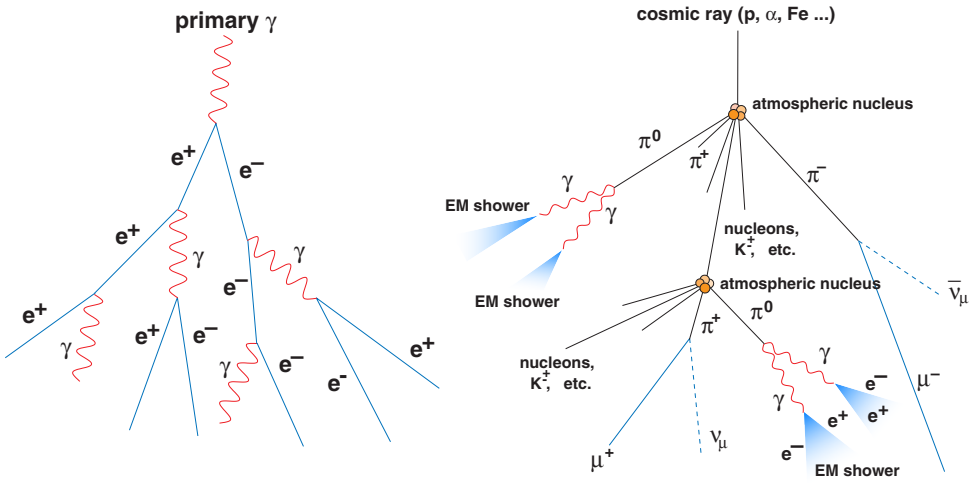

FIGURE 3.2: *Schematic description of extended air showers. Left: EM shower. Right: Hadronic shower.*

3.1.1 Electromagnetic showers

γ-rays above a critical energy of about 20 MeV lose energy in air primarily by e^-e^+ pair creation in the presence of an air nucleus[1] (fig. 3.2). The electrons and positrons in turn produce high energy photons via bremsstrahlung (above $E_C \approx 83$ MeV; below the primary process is ionization). A cascade is formed with an exponentially increasing number of created particles. The shower maximum is reached when the average energy of

[1]The photoproduction cross–section is ≈ 300 times smaller than that for pair production. If however the first interaction is due to photoproduction, the shower is indistinguishable from a hadron induced shower.

the cascade particles is decreased towards the critical energy at which ionization losses start to prevail losses due to bremsstrahlung (at the shower maximum the $e^{\pm}$ energy is ≈ 300 MeV). Once that point is reached the shower slowly dies out [PDG06].

The energy loss of an electron due to bremsstrahlung is proportional to its energy:

$$-\frac{dE_e}{dx} = \frac{E_e}{X_0^e} \quad \text{with} \quad X_0^e = 37.2\ \text{g/cm}^2 \quad \text{in air} \tag{3.1}$$

For pair creation, the relevant mean free path for γs is given by $X_0^\gamma = \frac{9}{7} X_0^e$.

The total number of electrons above the critical energy E_C in the shower can be approximated by [Ros41]:

$$N_e(t, E_0) = \frac{0.31}{\sqrt{\ln(E_0/E_C)}} \cdot \exp(t - 1.5t \ln s) \tag{3.2}$$

$$s = \frac{3t}{t + 2\ln(E_0/E_c)} \tag{3.3}$$

$$t = X/X_0 \approx \frac{X_{\text{air}}}{X_0 \cdot \cos\theta} \cdot \exp\left(-\frac{H}{H_0}\right) \tag{3.4}$$

with E_0 the energy of the primary photon, $X_{\text{air}} = 1013\ \text{g cm}^{-2}$ the column height of air at ground level and $H_0 = 8$ km the scale height of the atmospheric pressure. θ is the incident angle of the air shower. The slant depth t determines the thickness of the atmosphere in units of X_0. The parameter s is called shower age, where $s = 0$ describes the onset of the shower, $s = 1$ the shower maximum found at $t_{\max} = \ln(E_0/E_C)$ and $s = 2$ the point at which the shower dies, as can be seen from

$$\frac{dN_e(t,E)}{ds} = N_e(t,E) \cdot \frac{3\ln(E/E_C)(s - 3\ln s - 1)}{(3-s)^2} \tag{3.5}$$

The longitudinal electron distribution given by (3.2) is shown in fig. 3.3. The higher the energy of the primary, the further the air shower penetrates into the atmosphere. γ-ray induced air showers in the MAGIC energy range from 30 GeV to 30 TeV develop their maxima well above the telescope level. Showers of low energies die out completely before reaching the observatory level.

The shower fluctuations (not including fluctuations of the point of the first interaction) are described by

$$\Delta N_e(s) \simeq \frac{9}{14}(s - 1 - 3\ln s) \cdot N_e(s) \tag{3.6}$$

It is worthwhile to note that due to their statistical nature the fluctuations from shower to shower are rather large. This has important consequences e.g. for the energy estimation of the primaries.

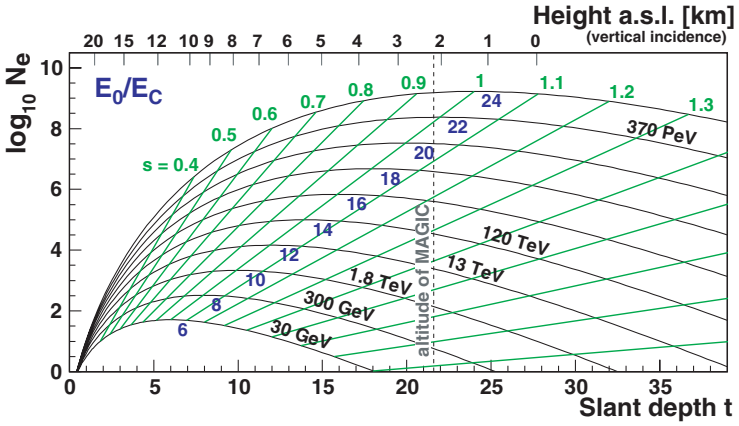

FIGURE 3.3: *Longitudinal development of an electromagnetic air shower. The shower size, characterized by the number of secondary electrons in the shower N_e, is plotted vs. the radiation length t (in air, $t \approx 37\,\mathrm{g\,cm^{-2}}$). The green lines characterize the shower development by the shower age s. For vertical incidence, the altitude of MAGIC (2200 m a.s.l.) is indicated.*

Lateral shower development. Due to multiple scattering of the shower electrons and positrons, the shower particles are deflected from the shower axis as defined by the direction of the incident cosmic ray. The lateral distribution of electrons can be parameterized by the Nishimura–Kamata–Greisen (NKG) formula [Nis52, Gre60], which is valid strictly only for $1 \leq s \leq 1.4$:

$$\rho_e(r,t,E) = \frac{\Gamma(4.5-s)}{2\pi\Gamma(s)\Gamma(4.5-2s)} \cdot \frac{N_e(t,E)}{r_M^2} \cdot \left(\frac{r}{r_M}\right)^{s-2} \left(1+\frac{r}{r_M}\right)^{s-4.5} \tag{3.7}$$

with the Moliére radius $r_M = 21.2\,\mathrm{MeV} \cdot (X_0/E_c) \approx 79\,\mathrm{m}$ in air at sea level [PDG06] and the Gamma function Γ. About 99% of the shower energy is contained within $3.5 r_M$, whereas only 10% are "lost" outside $1 r_M$.

Air showers initiated by $e^{\pm}$ primaries, which are ≈ 1000 times less numerous than γ-rays, pose irreducible background for γ-ray showers, as they develop in the same way γ-ray showers do. Due to the steep electron spectrum ($\alpha = 3.3$), these showers can normally be ignored above energies of $\gtrapprox 500\,\mathrm{GeV}$ [Wie94]. Low energy showers can only be suppressed as $e^{\pm}$ primaries arrive isotropically, while γ-ray showers point back to their astrophysical sources (see below and sect. 5.5).

3.1.2 Hadronic showers

A hadronic shower is produced by a reaction of a charged cosmic ray particle with an atmospheric nucleus governed by the strong interaction (fig. 3.2). The critical length for hadrons is the hadronic absorption length. (Elastic scattering does not produce secondaries and does not reduce energy). Mainly pions (90%), kaons (10%) and light baryons

(p, $\overline{\text{p}}$, n, $\overline{\text{n}}$) are created. The creation of other particles is possible but negligible below energies of a few 100 GeV. The produced nuclei and fragments of the incoming nucleus form part of the hadronic core of the shower, which continues to undergo hadronic interactions up to the point where the energy per nucleon is smaller than the pion production threshold ($E_{\text{pr}} \simeq 1$ GeV). Hadrons are able to transfer significant transverse momenta to their decay products. Charged pions sometimes decay into muons and neutrinos before interacting again. The muons interact almost exclusively by ionization; they only rarely decay before reaching the ground due to their high initial energy. Isolated muons with large transversal momenta can travel far away from their parent shower.

Due to the EM decay $\pi^0 \rightarrow \gamma\gamma$ an hadronic shower produces EM subshowers. As the probabilities for the production of π^+, π^-, and π^0 are about equal, about one third of the energy in inelastic interactions is transferred to EM subshowers. As hadronic reactions are strongly suppressed in EM showers, this is an irreversible process, which makes most of the initial energy of the hadronic shower end up in its EM component. An additional component is formed by muons and neutrinos, both of which due to their small cross-sections are likely to reach the ground without further interactions (in the case of the muon also supported by its long lifetime of $\tau \approx 2.2 \cdot 10^{-6}$ s).

Heavier nuclei. Cosmic ray nuclei with mass A and energy E are usually modeled by the superposition [Gai90] of A nucleons of energy E/A each. An Fe nucleus-induced shower can quite reasonably be described by the superposition of 56 proton showers of a 1/56 energy each. Heavier nuclei create showers with a larger number of secondaries and develop higher in the atmosphere than proton–initiated showers.

3.1.3 Differences between γ-ray-initiated and hadronic showers

The main challenge for Imaging Air Cherenkov Telescope (IACT) experiments that observe γ-rays is the suppression of the background created by hadronic cosmic rays, which is usually many orders of magnitude more numerous. Therefore background rejection methods have to be based on the differences between the two shower types described above. Simulations are shown in fig. 3.4. Characteristic differences are:

- The longitudinal development of hadronic air showers is governed by the hadronic absorption length in air, which e.g. for protons is $X_0^{\text{p}} = 83$ g cm^{-2} is more than double that of the EM interaction length, as hadronic cross–sections are comparatively small. Therefore hadronic showers are more extended and develop their shower maxima deeper in the atmosphere as compared to electromagnetic showers of the same primary energy.

- On the other hand the multiplicity in hadronic interactions is much higher than in EM processes.

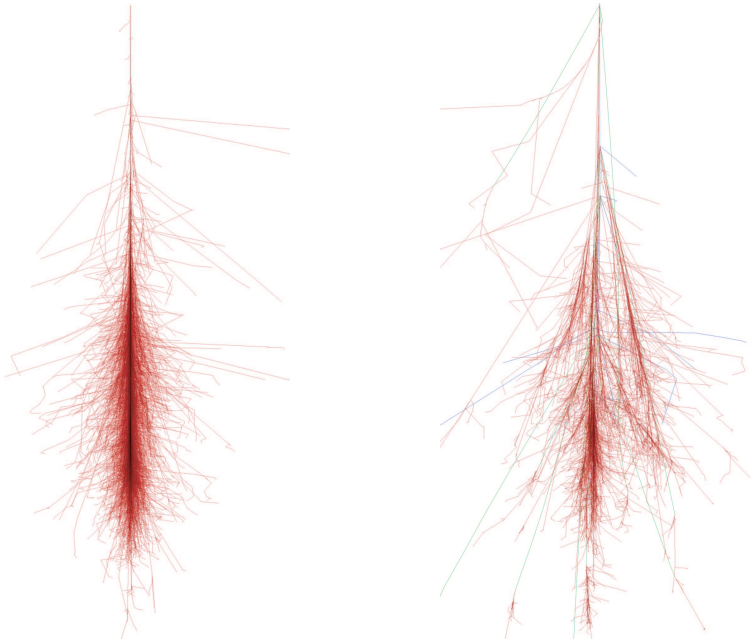

FIGURE 3.4: *Simulated extended air showers. Left: Electromagnetic shower, primary: 100 GeV γ Right: Hadronic shower, primary: 100 GeV proton. The respective particle type of the secondaries is encoded in the track color—red: $e^{\pm}$, γ; green: $\mu^{\pm}$; blue: hadrons. The pictures were created using CORSIKA (cf. sect. 4.6). Courtesy F. Schmidt, University of Leeds [Sch05a].*

Due to the exponential change in the air density this is unfortunately not so influential for gamma/hadron separation.

- The mean transverse momentum transfer in hadronic interactions is substantially larger than that of EM interactions. In addition, there are larger fluctuations in the shower development than observed in EM showers. Therefore, hadronic showers are comparatively broader and more irregular than EM showers.
- EM subshowers initiated by π^0 decay add to the less compact structure of hadronic showers.
- The main processes contributing to the widening of EM showers are multiple scattering and, at low primary energies, geomagnetic effects.

Note that generally hadron-induced showers create less Cherenkov light than gamma-induced showers (cf. fig. 3.8).

Apart from these intrinsic differences, the most striking background suppression comes about by the fact that γ-ray showers point back to the source of their γ primary, while (due to galactic and extragalactic magnetic fields) the arrival direction of cosmic ray initiated air showers is isotropized. How these differences are exploited technically for background rejection is presented in sect. 5.4.

3.2 Cherenkov light

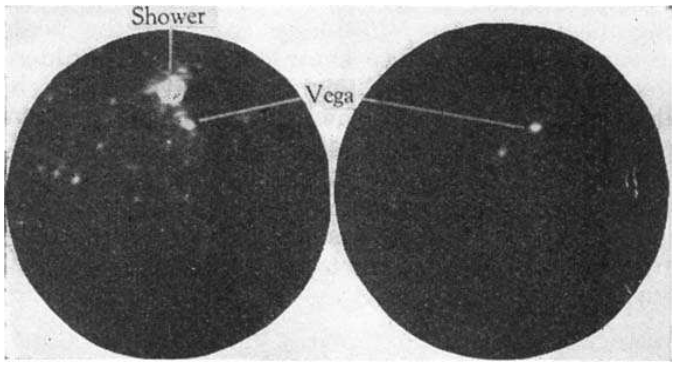

FIGURE 3.5: *First photograph taken of a Cherenkov light flash associated with an EAS in the atmosphere (left) as seen by a mirror and an image intensifier camera and a randomly triggered background picture of the same sky region around Vega (right) [Hil61].*

Air showers contain a large number of relativistic charged particles with a speed close to the speed of light in vacuum and exceeding the local speed of light of the traversed medium. Such particles produce Cherenkov light [Che34] in the atmosphere, as was first pointed out by Blackett [Bla48]. A few years later Galbraith and Jelley measured the first Cherenkov light pulses [Jel63]. Hill and Porter succeeded in photographing Cherenkov flashes associated with EAS (fig. 3.5).

3.2.1 Cherenkov light production

Cherenkov light is produced whenever a particle travels through a (transparent) medium with refractive index n with a velocity βc exceeding the local phase velocity of light (c/n). While a particle with $\beta c < c/n$ produces a symmetric polarization of the surrounding medium, particles with velocities larger than c/n are faster than the EM information that induces the polarization (fig. 3.6). Therefore a photonic shock wave is produced whose radiation is called Cherenkov light [Che34]. Cherenkov light is emitted in a narrow cone (for gases; $n \approx 1$) with a maximum emission angle given by

$$\cos\theta_C = \frac{1}{\beta n}. \tag{3.8}$$

For a given medium, this equation poses a minimum particle velocity $\beta_{min} = n^{-1}$ which is required to produce Cherenkov light. Conversely, the maximum Cherenkov angle θ_{max} is attained for $\beta = 1$. The Cherenkov condition can be converted in a kinetic energy threshold for particles with rest mass m_0:

$$E > m_0 c^2 \cdot \frac{1}{\sqrt{1-\beta_{min}^2}} = m_0 c^2 \cdot \frac{1}{\sqrt{1-1/n^2}}. \tag{3.9}$$

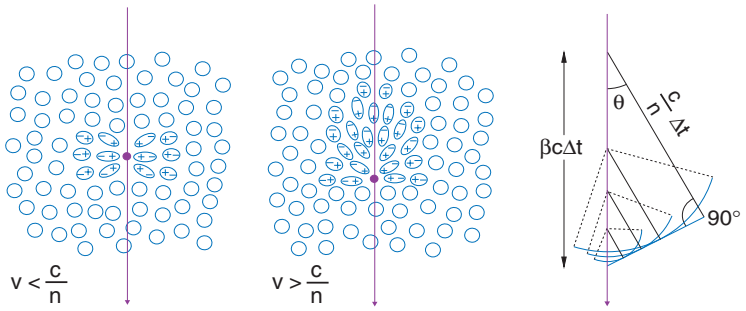

FIGURE 3.6: *A charged particle traveling with a speed higher than the local phase velocity polarizes the medium around it and produces Cherenkov light. Right panel: Huygens' construction of Cherenkov waves. Adapted from [Pau99].*

Note that in air $n \approx 1$ can be expressed as $n = 1 + \eta$ [Rao88] and thus the threshold scales with the mass of the particles. Since the lightest particles involved in EAS are electrons and positrons, they have by far the lowest Cherenkov threshold (at sea level: $E^{\mu}_{\mathrm{min}} = 4.6\,\mathrm{GeV}$, $E^{\mathrm{p}}_{\mathrm{min}} = 40\,\mathrm{GeV}$, and $E^{\mathrm{e}}_{\mathrm{min}} = 22\,\mathrm{MeV}$, respectively [Rao88]). The interplay of the electron Cherenkov threshold and the number of electrons in the shower (cf. fig. 3.3) determines the most relevant region for Cherenkov light production in an EAS, which is in the range of the shower maximum.

3.2.2 Production and attenuation of Cherenkov light in the atmosphere

The number of photons produced along the track of a charged particle is given by [PDG06]:

$$\frac{\mathrm{d}^2 N}{\mathrm{d}x\mathrm{d}\lambda} = \frac{2\pi\alpha}{\lambda^2} \cdot \left(1 - \frac{1}{\beta^2 n^2(\lambda)}\right) \tag{3.10}$$

$$\frac{\mathrm{d}^2 N}{\mathrm{d}E\mathrm{d}\lambda} \approx 370 \sin^2\theta_{\mathrm{C}}(E)\left[\,\mathrm{eV}^{-1}\,\mathrm{cm}^{-1}\right] \tag{3.11}$$

with the wavelength λ and the fine–structure constant $\alpha \approx 1/137$. In an EM air shower about 500 Cherenkov photons are created per GeV of primary γ-ray energy between 300 nm and 600 nm for $\beta \approx 1$.

Cherenkov light is composed of photons in the UV to infrared range with the intensity increasing towards smaller wavelengths: $I(\lambda) \propto \lambda^{-2}$. In the case of relativistic particles, the energy loss due to Cherenkov radiation is about 0.1% of that of the ionization loss.

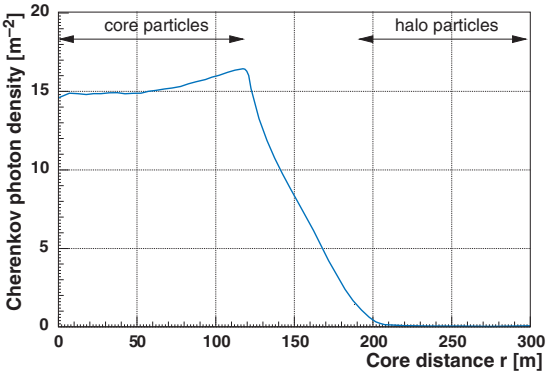

FIGURE 3.7: *Lateral Cherenkov photon density distribution of a 100 GeV γ-ray-initiated shower at an altitude of 2200 m a.s.l. for vertical incidence (Cherenkov light pool). Up to 120 m core distance predominantly the shower core is sampled, while light produced by shower halo particles contributes to the region $r > 120$ m. Adapted from [Bar98b].*

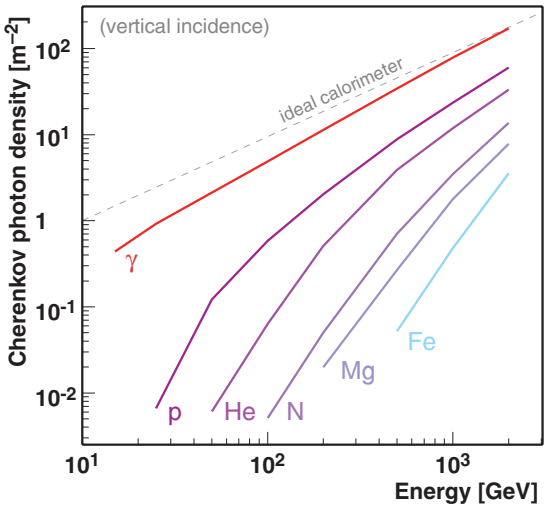

FIGURE 3.8: *Cherenkov photon yields for different particle species. The plot shows the mean Cherenkov photon density within 125 m of the shower core for vertically incident showers [Ose01]. Note that for γ-ray-initiated air showers the atmosphere behaves almost like an ideal calorimeter.*

Cherenkov radiation of air showers. The intensity of the Cherenkov light is a function of atmospheric depth ρ,

$$I \propto \left(1 - \frac{c^2}{n^2 v^2}\right) \propto \rho \tag{3.12}$$

and increases with ρ. As eventually the shower dies out, a maximum of Cherenkov light emission is formed. Much like the air shower particles itself, the Cherenkov photons form a thin disk traversing the atmosphere along the shower axis. For Cherenkov light produced by $e^{\pm}$, the Cherenkov emission angle at 2200 m a.s.l. is $\theta_C = 1.2°$. Thus, each element of a particle track produces a Cherenkov light cone that illuminates a "donut ring" on ground and these rings overlap to form the so-called Cherenkov light pool (fig. 3.7). Its area typically has a size of around 50000 m^2. The resulting lateral Cherenkov photon distribution at 2200 m a.s.l. is shown in fig. 3.7. Up to distances of ≈ 120 m from the shower axis, a flat distribution is formed, within which the Cherenkov photon density is proportional to the energy of the primary. After crossing the so-called Cherenkov hump, the distribution levels off at larger distances, because light produced in the shower halo is predominantly sampled there. The hump itself is a geometrical feature that comes about by the changing refractive index of the atmosphere and the changing Cherenkov light emission angle [Rao88], leading to a focusing effect. The photon density inside the Cherenkov light pool as a function of the energy of the primary particle is given for different particle types in fig. 3.8. For γ-rays, an almost constant fraction of the primary energy is converted into Cherenkov photons. Therefore a measurement of the Cherenkov light intensity is a good measure of the primary γ-ray energy.

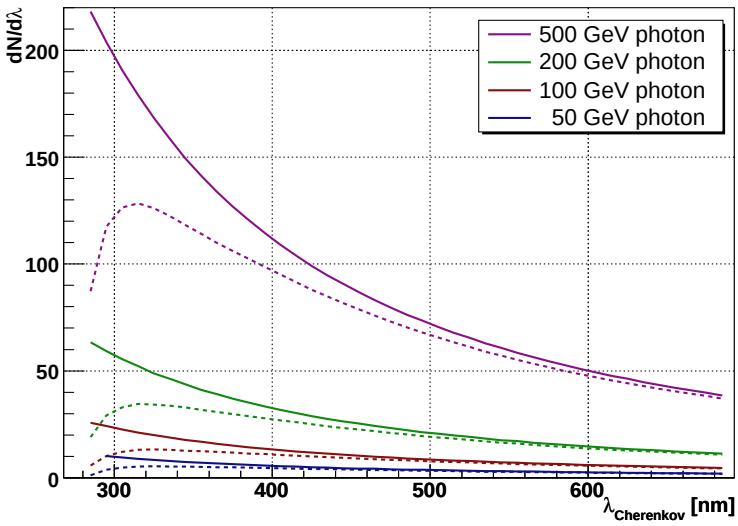

FIGURE 3.9: *Spectra of Cherenkov light emitted by vertical γ-ray showers of different primary energy at 10 km height (solid curves) and the corresponding spectra as detected at 2200 m a.s.l. (dashed curves) affected by absorption, Rayleigh- and Mie-scattering, as discussed in the text.*

Atmospheric attenuation. Due to the composition of the atmosphere, the Cherenkov spectrum observed from air showers is modified: Rayleigh-scattering off air molecules ($d < \lambda$), proportional to λ^{-4}, mainly has effects on the UV/blue part of the spectrum and is the dominant contribution during good atmospheric conditions. Mie-scattering off aerosols (also water droplets, dust) occurs without strong dependence on the photon wavelength ($\propto \lambda^{-(1-1.5)}$). Light with $\lambda < 280$ nm is strongly attenuated due to UV absorption by ozone molecules. Since ozone is present at altitudes above 10 km, this introduces a zenith angle dependence on the lower wavelength cutoff of the spectrum. Infrared absorption occurs for wavelengths above 800 nm caused by H_2O and CO_2 molecules. Fig. 3.9 summarizes these effects by comparing the Cherenkov spectrum at shower maximum with that arriving at 2200 m a.s.l. for different γ-ray primary energies.

Background light contributions. The light of the night sky (LONS, see [Roa73] for a thorough description) comprises light of bright stars, diffuse light of the galactic plane, zodiacal light, airglow, Cherenkov light ($\approx 10^{-4}$ [Bla48]), polar light and artificial light. The LONS is obviously not isotropically distributed, but shows increased levels e.g. at low galactic latitudes (in the galactic plane). Moreover it increases with increasing zenith distance.

The typical duration of the Cherenkov flash produced by a gamma ray initiated air shower is ≈ 3 ns at impact parameters below ≈ 120 m; for a hadron-initiated shower the time spread (≈ 10 ns) is slightly wider. The typical night sky photon flux has been measured to be $(1.75 \pm 0.4) \times 10^{12}$ photons m^{-2} sr^{-1} s^{-1} in La Palma [Mir94b], which translates to ≈ 0.15 ph.el. ns^{-1} for a 0.1° diameter photomultiplier tube (PMT) pixel in MAGIC

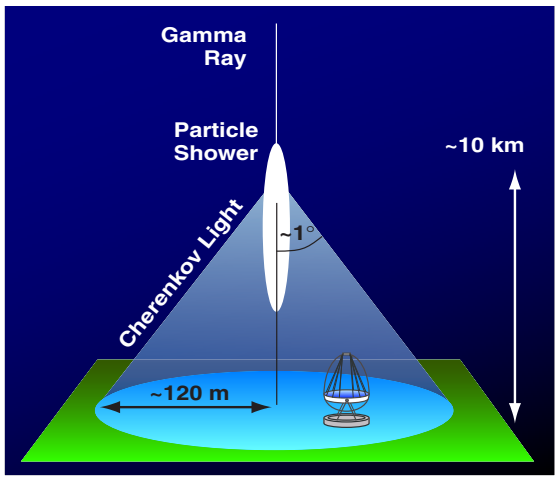

FIGURE 3.10: *Imaging technique I: A VHE γ-ray interacts with the top of the atmosphere, giving rise to an EAS that radiates Cherenkov light. An IACT is placed in the Cherenkov light pool.*

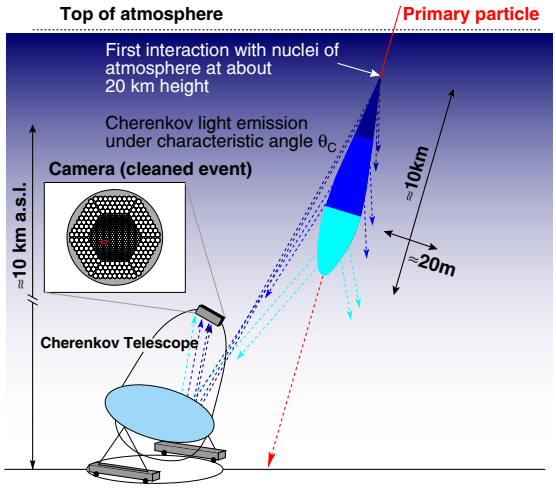

FIGURE 3.11: *Imaging technique II: The short light flash of the EAS is projected onto an (imaging) array that consists of sensitive photodetectors.*

[Pan04a]. The key element of the IACT technique therefore is to discriminate light originating from EAS from LONS. The given number is valid for dark areas of the sky outside the Milky Way with no bright stars present and for clear, moonless nights. Depending on the moon phase and the angular distance between the moon and the telescope pointing position, observations during moonshine have also been successfully carried out (e.g. [Kra99]). It has been estimated that the LONS photon flux during moonshine does not increase by more than a factor of 10 [Bar98b] so that e.g. for a quarter moon and an observation $\approx 25^\circ$ away from the moon, one expects an increase of the LONS fluctuations by a factor of 3. Note that the LONS moon spectrum is peaking around 500 nm, while the dark night LONS has its maximum in the red/IR range.

3.3 The imaging technique

Basic principle. A VHE γ-ray or cosmic ray particle initiates an air shower upon entering the atmosphere. Such an extended air shower, developing at a speed close to the speed of light, produces a short pulse of Cherenkov light of 3 ns FWHM (10 ns for hadron-initiated showers). A part of the shower is sampled by a telescope placed inside the Cherenkov light pool (fig. 3.10) and projected onto a pixelized (imaging) camera that consists of sensitive photodetectors (fig. 3.11).

The imaging of air showers. Short exposure times ($\lesssim 10$ ns) and a trigger concept that exploits spatial and temporal coincidences allow for the discrimination between EAS events and statistical fluctuations of the steady LONS flux. Fig. 3.12 shows typical EAS

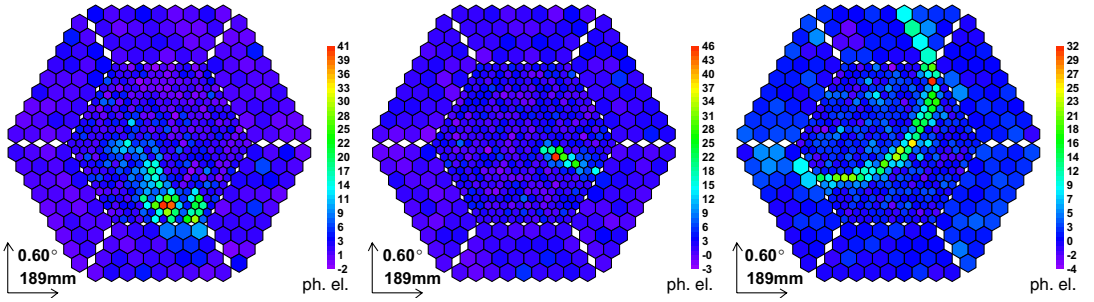

FIGURE 3.12: *Air showers as imaged with an IACT (the examples are taken from real MAGIC data). Left: Hadronic candidate event, Middle: γ candidate event, Right: Muon ring caused by an isolated muon.*

images as recorded with the MAGIC PMT camera along with the image of an isolated muon close to the telescope. Air shower images can be related to the properties of the primary particle, as

- the recorded light intensity is proportional to the number of secondaries in the shower and thus in first order to the energy of the primary particle (for an impact parameter $b < 120$ m), cf. fig. 3.8.
- for higher energies ($E \gtrsim 1$ TeV) the lateral distribution is steeply falling with b, therefore a good knowledge of r is needed for a good energy reconstruction. The same argument holds for air showers with $b > 120$ m.
- differences in the shower development of EM and hadronic showers are reflected in the image properties and allow for an efficient rejection of the hadronic background events. In addition, the Cherenkov emission properties of hadronic and EM showers differs, because only particles with velocities above the Cherenkov threshold (3.9) emit Cherenkov light.
- conclusions on the arrival direction can be drawn from the geometry of the recorded image. Therefore the arrival direction of the primaries can be reconstructed from the recorded shower image.

The low energy threshold attainable by an IACT depends on its capability to record the small and dim images of low energy showers. Additionally the fact that γ-ray showers and hadronic background showers look more and more alike at low energies poses a low energy limit. The high energy end of the accessible energy range is usually given by statistics. The expectable sensitivity of modern IACT is given in sect. 4.6.

Methods for extracting information from the shower images, rejecting hadronic background and for the reconstruction of the properties of the primary particles are discussed in sect. 5. Muon ring images are useful for telescope calibration, cf. sect. 5.3.

3.4 Large zenith angle observations

For observations at large zenith angles (LZA; $\theta \gtrsim 45^\circ$) the EAS development changes, as it increasingly takes place in the upper layers of the atmosphere. This implies a higher Cherenkov threshold (3.9) and a lower production yield (3.12). Additionally, the lower Cherenkov photon density at observation level and the atmospheric attenuation effects increase the energy threshold of the observation, which scales empirically as $E_{\mathrm{thr}} \propto \cos^{-2.7}\theta$ (from geometry only $E_{\mathrm{thr}} \propto \cos^{-2}\theta$ is expected).

A positive effect of LZA observations is the much increased collection area (fig. 3.13). Thus, the sensitivity of IACT telescopes is increased when performing LZA observations.

LZA observations may also extend the time coverage for a given source: e.g. the AGN Mkn 501, subject of the analysis discussed in sect. 7, is observable at low zenith angles for about six months a year (not necessarily however the whole night through) whereas observations under LZA would allow for an almost continuous monitoring for many Northern sources. Furthermore, the accessible source sample is extended: e.g. for MAGIC the galactic center is visible only at zenith angles larger than 58° [Alb06e]. In the context of this thesis we will show in sect. 6.5 how simultaneous observations from telescope sites at largely different latitudes, employing LZA observations, can readily produce both technical and scientific output.

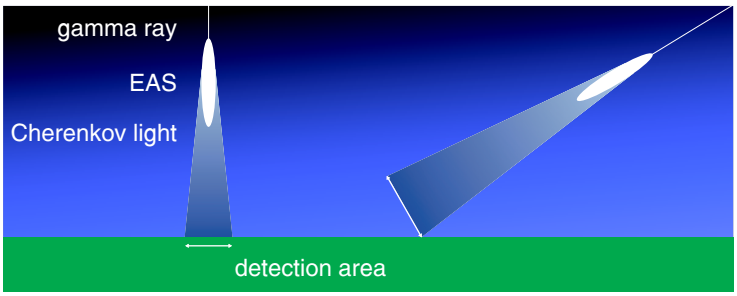

FIGURE 3.13: *Small and large zenith angle observations. When observing at large zenith angles, the shower development takes place further away from the telescope; Due to the atmospheric attenuation of the Cherenkov light emitted, showers are dimmer as compared to small zenith angles and thus the energy threshold of the observation increases. At the same time, however, the collection area increases, resulting in an increased sensitivity.*

Chapter 4

The MAGIC Telescope

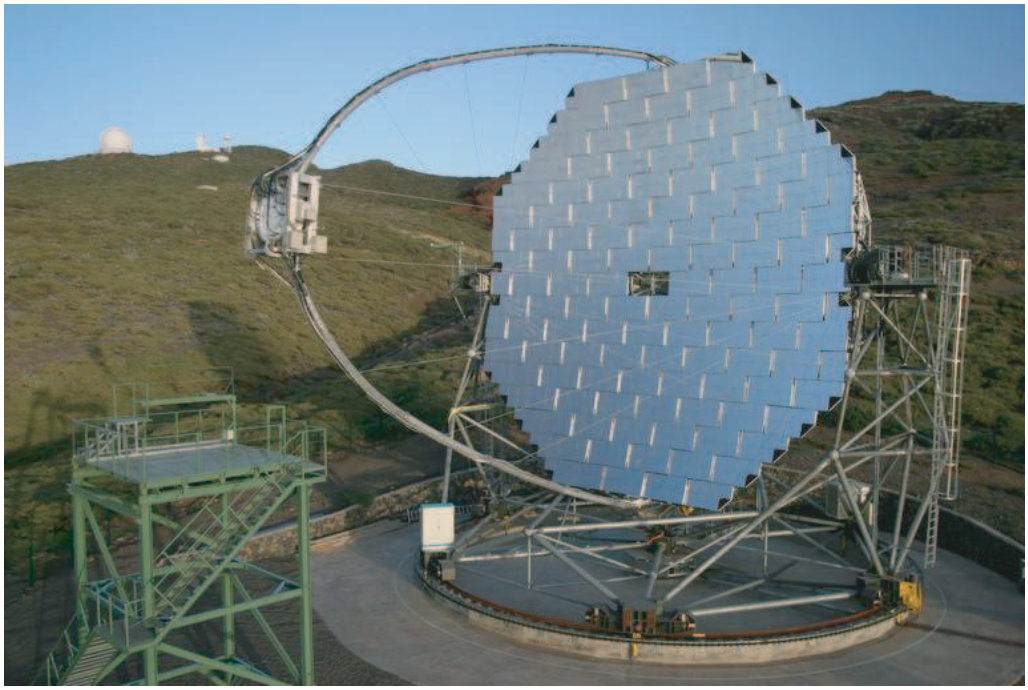

FIGURE 4.1: *Aerial view of the MAGIC telescope*

The MAGIC telescope[1] ([Bai04, Cor05], fig. 4.1) with its 17 m diameter tessellated mirror is currently the largest IACT worldwide. Its main design goal was to cover the unexplored energy region between 30 and 300 GeV in the electromagnetic γ-ray spectrum with high sensitivity, and thus to elucidate the yet only partially understood astrophysical processes in astronomical objects. Up to 2003, this part of the γ-ray spectrum was neither accessible by satellite experiments nor by the preceding generation of IACTs.

[1] **M**ajor **A**tmospheric **G**amma–ray **I**maging **C**herenkov telescope, `http://wwwmagic.mppmu.mpg.de/`

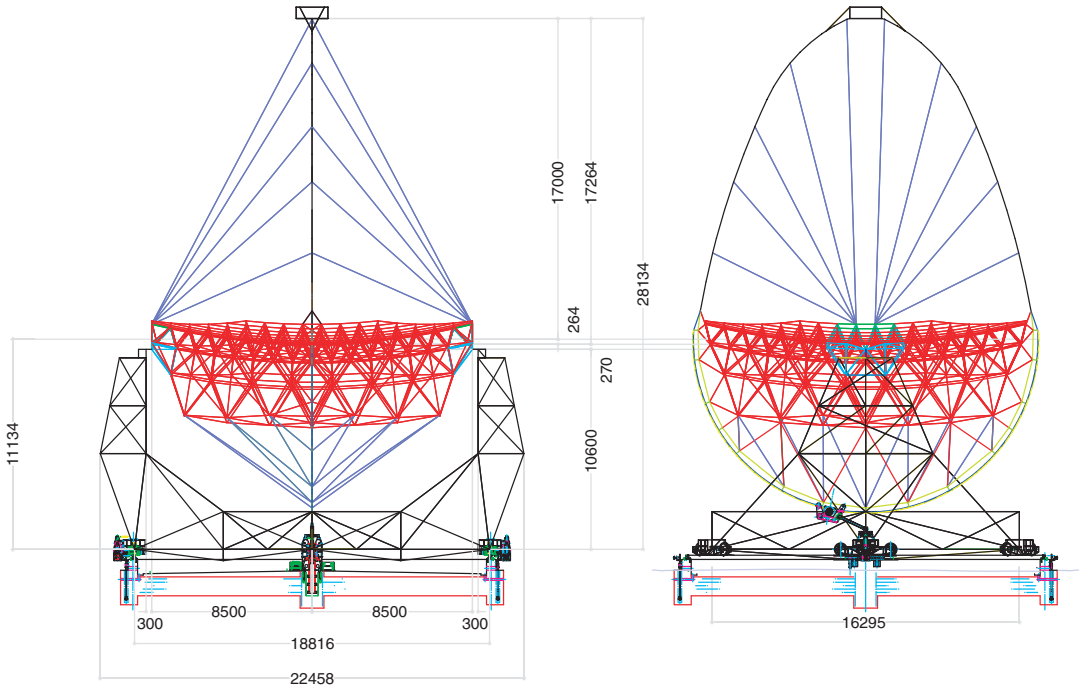

FIGURE 4.2: *Layout of the telescope and mirror support structure. Color coding—black: tubular stainless steel dish support; red: carbon fiber reinforced mirror dish support; green: stainless steel support in the central area of the mirror; blue: steel support cables. Numbers given are in millimeters. Courtesy of Max Planck Institute for Physics, construction department.*

Following the design study in 1998 [Bar98b], the production of the telescope components and civil work started in 2001. Fig. 4.2 shows the layout of the telescope structure. After a commissioning phase, which commenced in mid 2003, regular scientific observations have been carried out since fall 2004.

The telescope is located at 28°45′ N, 17°53′ W and is hosted by the Instituto de Astrofísica de Canarias[2] (IAC) at the Observatorio del Roque de los Muchachos (ORM) on the Canary Island of La Palma at an elevation of 2200 m above sea level. The ORM is considered to be one of the best observatory sites in the Northern hemisphere [McI74, Lom06] and was chosen because of its excellent astronomical conditions, specifically its high transparency, the number of expectable clear nights per year, and only minimal temperature changes during the night. Moreover, due to its high altitude and therefore its proximity to the air shower maxima, it is favorable for Cherenkov detectors. The ORM site had also been chosen for MAGIC's predecessor experiment HEGRA and its system of IACTs [Dau97].

The key components of the instrument are discussed in the following sections. The commissioning of the telescope drive system and the development of the starfield monitoring system are discussed in more detail.

[2] `http://www.iac.es/`

4.1 The mechanical structure, the reflector and the mirror control system

The MAGIC telescope has a 17 m diameter tessellated reflector [Big04] with a focal length of 17 m ($f/1$). The overall parabolic shape conserves the timing information of the reflected photons and is achieved by an arrangement of a total number of 956 spherical mirror segments of 50 cm $\times$ 50 cm area each. Their radius of curvature ranges from 36.6 m to 34.1 m at the center of the dish, with their radius of curvature selected according to their position on the parabolic surface. These lightweight, diamond-turned, all aluminum mirrors have a reflectivity of $\approx 85\%$ in the wavelength range of $350-650$ nm, which is comparable to conventional glass mirrors. Using a large dynamic range CCD, the effective reflector area (taking into account shadowing effects) was measured to be 230 m^2 [Gar06]. The mirrors are equipped with internal heating wires for de-icing and the removal of dew.

The reflecting surface of the telescope is supported by a lightweight carbon fiber space frame. In order to compensate for the small deformations of the mirror dish under gravitational load when varying the elevation angle during tracking, the individual mirror panels, on each of which four mirrors are attached, can automatically be adjusted so as to guarantee optimal focusing of the mirror system [Mir03]. The system follows very much the modern design of actively controlled mirrors of optical telescopes. The mirror supports are equipped with two motors and one laser pointer each. The latter is used to produce a spot on the closed PMT camera lid, which can be used to calibrate the focusing system.

The camera allows the optical system to be focused to (1) infinity, (2) a height of 10 km, at which the shower maxima of typical extended air showers is expected, and (3) a distance of $\approx$ 1000 m for the initial calibration of the telescope focusing using an artificial light source. During normal operations, the mirror is focused to a distance of 10 km.

It was possible to restrict the total weight of the mechanical structure including mirrors and the PMT camera to 64 tons (with about half the mass concentrated in the undercarriage structure). This was an important prerequisite for the fast repositioning of the telescope.

4.2 The imaging photomultiplier tube camera

For imaging Cherenkov air showers, MAGIC is equipped with a 1.5 m diameter, 3.5° field of view pixelized photomultiplier tube (PMT) camera [Cor03] (fig. 4.3). The hemispherical bialkali photocathode PMTs were coated with a special lacquer that enhances the quantum efficiency up to $25-27\%$ between $350-470$ nm [Pan04b]. Each PMT

FIGURE 4.3: *The imaging photomultiplier camera of the MAGIC telescope is installed at a 17 m distance from the reflector, making MAGIC an f/1 telescope. During daytime, the sensitive PMTs are shielded by two lids. The inner (1" PMTs) and outer (1.5" PMTs) parts of the camera are well visible.*

is equipped with a dedicated hexagonal light collector, which maximizes the double-crossing probability of photon trajectories at large incidence angles. The inner part of the camera is equipped with 396 1" ET 9116A PMTs. It is surrounded by 180 1.5" ET 9117A PMTs in the outer part of the camera. While a fine (0.1°) pixelization in the camera center is mandatory for observing low energy and thus small showers, the outer part of the camera generally records parts of large energy showers or shower tails, in which larger statistical fluctuations in the shower development are expected. In addition, in the outer part of the camera pointlike light spots are spread over an area of $\approx 0.2^\circ$ diameter by coma aberrations of the reflector. Therefore, the use of larger diameter (0.2°) pixels is justified and in addition saves cost and camera weight.

4.3 The readout chain

The purpose of the readout chain is to record events that were triggered by air showers. Fig. 4.4 illustrates the readout chain, which is briefly described in the following.

The Cherenkov light produced by an EAS falling onto the telescope mirror is focused on the focal plane of the pixelized PMT camera. The photons arriving at any one PMT release photoelectrons. The created pulse is pre–amplified, converted into an optical pulse by vertical cavity surface emitting lasers (VCSELs) and transmitted via 162 m long multi–mode optical fibers to the counting house. In contrast to conventional coaxial cables, this concept has various advantages, namely the negligible dispersion and attenuation of the signals, the absence of crosstalk and noise pick–up and a much–reduced weight.

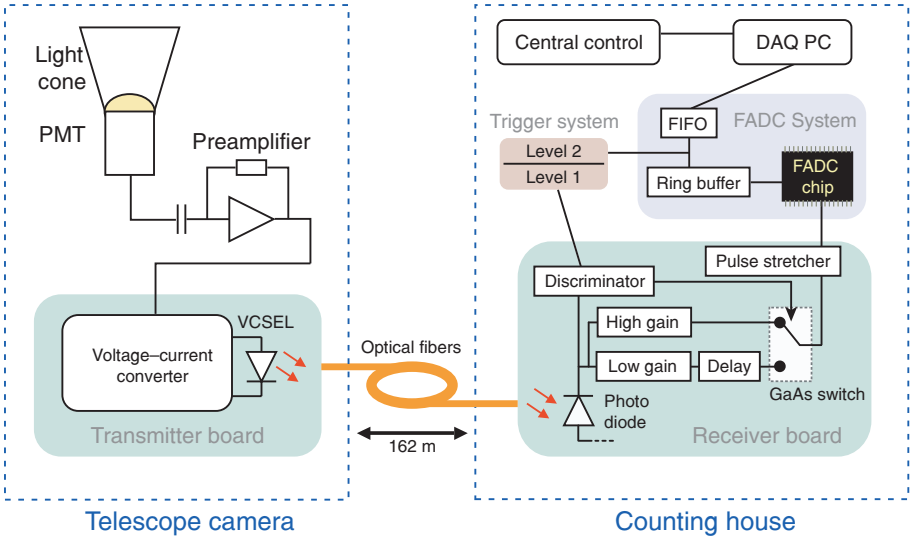

FIGURE 4.4: *MAGIC hardware readout chain. The PMT signals are reconverted into optical pulses, transferred to the counting house, and fed into the trigger and DAQ systems.*

Receiver boards in the counting house reconvert the signal back into an electrical pulse, which is split and fed into the trigger system and the flash ADC (FADC) system, respectively.

Trigger system. The MAGIC trigger system currently consists of two levels: Level 0 consists of fast discriminators, which are adjustable and mainly reject signals from the light of the night sky (LONS) fluctuations. An individual pixel rate monitor system can be used to prevent high trigger rates e.g. caused by bright stars in individual pixels. Level 1 determines the topology of the pixels above discriminator threshold and decides whether or not a given event will be recorded. Decisions are made by looking for fast coincidences of neighboring pixels. Typically coincidences of 4 or 5 double next neighbor pixels are required. The system is adjusted such that data are typically taken at a rate of 200 Hz.

The FADC system. Upon arrival of a trigger, the continuously digitizing FADC system writes out 30 time slices to a FIFO (first in, first out) buffer. The resulting dead time is $\approx 2\%$. Apart from the charge information, also time and trigger information are available in the data stream. Under normal conditions, events are recorded at a rate of ≈ 250 Hz; the maximum tolerable rate however is about 600 Hz and can be used e.g. for pulsar studies.

The camera and optical transmission system is able to transmit the very fast signals well faster than the FADC sampling rate of 300 MSamples/s. For measuring the structures of the Cherenkov light pulses with the FADC system, the typically 2.2 ns FWHM signals are artificially stretched to ≈ 6 ns.[3] To provide a dynamical range of $\gtrapprox 1000$, a two–gain

[3]The signals are between 3 ns and 10 ns wide (cf. sect. 3.3). According to the Nyquist-Shannon sampling theorem [Nyq28, Sha49], the minimum signal width for a 300 MHz FADC system should be 8 ns.

charge extraction is implemented: the signal is amplified by a factor 10 and digitized. Should this *high–gain* signal exceed 250 FADC counts, the non–amplified signal is delayed and also digitized. The recorded signal then either consists of 30 samples or of 15 high–gain samples followed by 15 low–gain samples. One sample is taken every 3.3 ns. With a typical length of the digitized signal of $4-6$ samples, in any case the full pulse is recorded. If the FADC does not record the low–gain signal, the late high–gain ought not to contain a signal and can be used for obtaining pedestals.

4.4 Calibration system

In order to obtain calibration constants for converting FADC charge into the physical quantity of photoelectrons and FADC timing into an absolute signal timing, an optical calibration system providing independent calibration methods has been installed [Sch02c]. It consists of differently colored ultra–fast LEDs (370 nm, 460 nm and 520 nm) that allow for a uniform illumination of the PMT camera with light pulses of different intensities (4 to 700 photoelectrons per inner camera pixel). In this way, the whole dynamic range of the camera is accessible. By triggering the MAGIC data acquisition (DAQ) system, calibration events are recorded in dedicated calibration runs as well as as interleaved calibration events during regular data taking (cf. sect. 4.7) so as to trace gain variations of the PMTs and the VCSELs.

4.5 The drive system

The drive system of the MAGIC telescope has to meet two basic demands: During normal observations, the 64-ton telescope has to be repositioned accurately, and has to track a given sky position with high precision. For catching GRB prompt emission and afterglows, it has to be powerful enough to reposition the telescope to an arbitrary point in the sky within a very short time ($\lesssim 30$ seconds) [Wag03b].

4.5.1 Mechanical setup and hardware components

Implications of the telescope mount. There are different options for designing the mount of astronomical telescopes. While the so-called equatorial mount needs tracking with constant speed only along one axis (the other axis is aligned towards the celestial pole), a clear disadvantage of that design is the need for heavy counterweights to guarantee the balance of the system as well as limitations on observing the entire sky. A different approach is the so-called Alt-Az-mount: the telescope dish can be moved in

FIGURE 4.5: *Left: One of the two azimuth drive units mounted on one of the six bogeys. Right: The elevation drive unit with the elevation brake visible in front.*

altitude and azimuth, and a balance of the azimuthal axis can be achieved without additional counterweights—the mirror dish is basically balanced by the camera at a distance of 17 m. Tracking celestial objects, however, requires simultaneous movements with variable speed along both axes.

One of the design goals of the drive system was to allow the continuous observation of a given source without reaching one of the end positions in azimuth. Therefore the allowed range for movements in azimuth spans from $\varphi = -90^\circ$ to $\varphi = +418^\circ$, where $\varphi = 0^\circ$ denotes geographical North (cf. fig. 4.11). To optimize slewing distances, the range for zenithal movements spans from $\theta = +105^\circ$ to $\theta = -70^\circ$, where the change of sign implies a movement "over the zenith". This so-called *reverse mode* is currently not used, as it implies possible hysteresis effects of the active mirror control system, which are difficult to handle. The accessible range in both directions is limited by software. Additional hardware end switches are installed, which are directly connected to the drive controller units and, when activated, initiate a fast, controlled deceleration of the system. To achieve an azimuthal movement range exceeding 360°, at any time one of the two azimuth end switches needs to be deactivated. Therefore, an additional "directional switch" is located at $\varphi = 164^\circ$.

Servo motors. The drive system design is based on digitally controlled industrial drive units with 11 kW servo motors. Two such motors are mounted on two of the six bogeys of the telescope structure (figs. 4.5, 4.6), which move on a circular rail with 9.5 m radius. The motors are coupled by torque control in a master–slave setup, which efficiently adds the power of the two units while preventing oscillations in the system. The number of coupled units can be increased [Wag05a]. The elevation drive is equipped with only one motor due to the mass of mirror dish, mirrors, camera and camera mast of only 24 tons. The motors exert their power via planetary gears on a drive chain, which guarantees minimum slip.

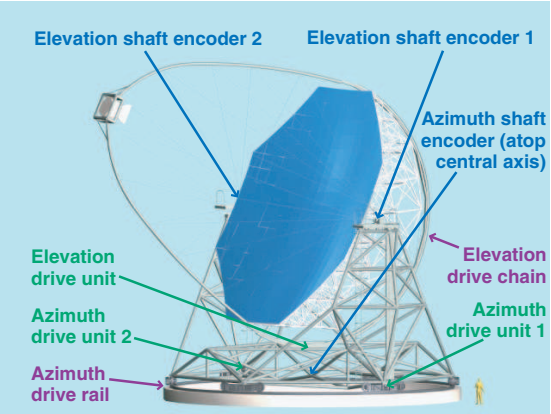

FIGURE 4.6: *Location of the shaft encoders on the telescope. Two shaft encoders for the elevation axis are arranged outside the bearings of the elevation axis. The azimuth shaft encoder is located atop the central telescope axis.*

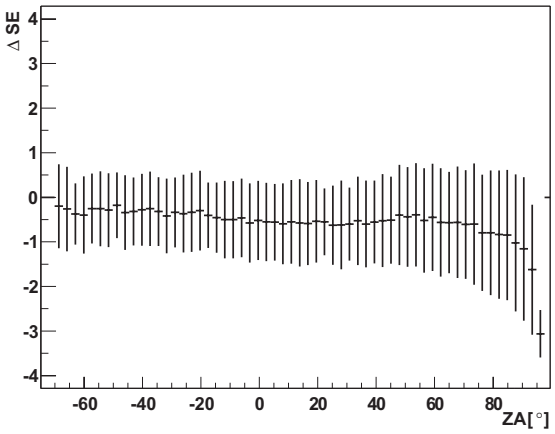

FIGURE 4.7: *Torsion between the two elevation shaft encoders in units of shaft encoder steps (*1SE = 0.022°*). Nearly no distortions are visible, except in the zenith angle range of* 60° − 90°*. This region however will not be used for measurements but only for maintenance.*

Encoders. The angular positions of the telescope are controlled by three 14-bit gray code absolute shaft encoders (two on the elevation axis, one on the azimuthal axis, fig. 4.6), which guarantee an intrinsic resolution of $< 0.022°$. The two azimuth encoders are coupled so as to increase resolution and allow measurements of the twisting of the dish (fig. 4.7). The motor positions are read at a frequency of 1 kHz by rotary encoders on the motor axes and are cross-calibrated by using the shaft encoder readout. The CAN-bus protocol is used for the communication with the motor control units and the shaft encoders.

4.5.2 The control loop

The servo motors are connected to three separate drive controller units (Bosch Rexroth DKC), which serve as intelligent power supplies that incorporate a series of control loops. These loops are mainly used to protect the motors, e.g. from too high currents, and manage the emergency rampdown of the motors. The two azimuth motors are coupled on the level of the drive controllers, i.e. the second azimuth controller acts as slave to the primary one. The drive control is managed by dedicated microcontrollers (Z&B MACS type) which have a hybrid open–loop feed forward / closed-loop PID control implemented. Separate microcontrollers regulate the elevation and azimuth motors, respectively. The control schematics are given in fig. 4.8. The requested position p_R is multiplied with a proportional factor KPROP, which governs the reaction of the system on positional deviation. The derivative factor KDER is multiplied with the derivative of the positional deviation. Choosing a large value causes a damping in the system. KINT is multiplied

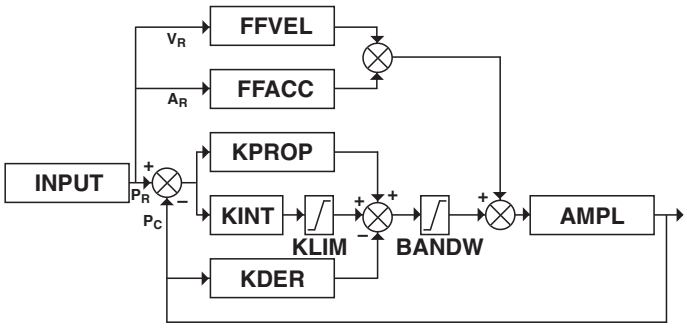

FIGURE 4.8: *Control loop implemented in the drive microcontrollers*

with the integral of the positional deviations, and therefore controls how the system acts to accumulating deviations. The (bandwidth–limited) sum of these control inputs is added to the scaled requested velocity and acceleration to form the control output. The loop iterates every microsecond.

It turned out that in particular the azimuth motor system seems to be limited by the large moment of inertia of the telescope. At the same time the requirements on the elevation drive are much less demanding. For the azimuth control loop, the currently best parameter values have been found to be KPROP=950, KDER=2000, and KINT=0, in order to damp possible oscillations in the system and to prevent accumulating deviations from becoming dominant in the control output.

Fast repositioning. The observation of gamma-ray bursts (GRB) and their afterglows in VHE γ-rays is one of the main physics goals of MAGIC. Given that alerts from satellite monitors [GCN06] provide GRB positions after a few seconds, typical burst durations of 10 s to 100 s [Par00b] (cf. fig. 1.10) demand a fast repositioning of the telescope.

Studies of the interplay of MACS and the drive controllers showed that there exists an upper limit of the acceleration to which the azimuth drive motors can be subjected. If this limit is exceeded, the system overreacts, which leads to emergency stops issued by the drive controllers (fig. 4.9). The cause for this overreaction is most likely that for short periods the motors cannot provide enough torque and that the controller subsequently increases the power demand beyond the given limit. This deficiency, however, can probably be circumvented by installing additional capacitors, which would provide additional power during acceleration. The current best value for the acceleration has been set to 11.7 mrad s^{-2}, corresponding to 0.11 m s^{-2} on the 9.5 m radius azimuth rail.

More constraining than control loop breakdowns, however, are the forces that act on the telescope when hitting an end switch and the respective resulting emergency stopping distances. Fig. 4.10 shows the distances the telescope needs for a complete stop when moving at given travel velocity. For this test, the telescope was accelerated to a given velocity

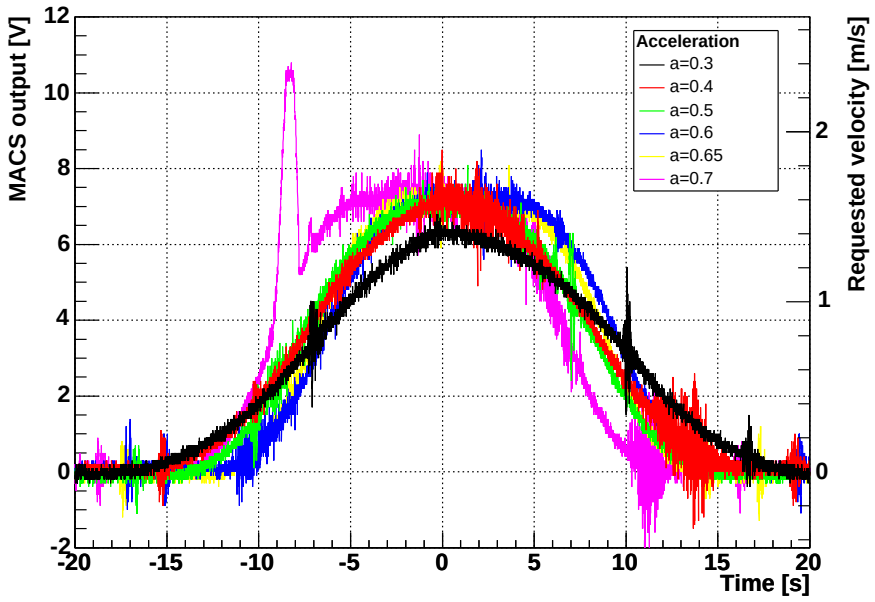

FIGURE 4.9: *Movement tests for different accelerations. The telescope was driven a distance of* $\Delta\varphi = 150°$ *in azimuth, requesting accelerations in the range of* $a = 0.3 - 0.7$ *(*$a = 1.0$ *means an acceleration to 100% of the target velocity within 8 seconds). The plot shows the command output of the MACS microcontroller to the drive controller (i.e. the requested velocity). For* $a = 0.7$ *the control loops are unable to react properly, as can be seen from the spike at* $t = -8.5$ s.

and then stopped by an artificial end switch, which leads to the best deceleration attainable without damage to the motors. The emergency stop is fully performed by the drive controllers without software intervention. For a given maximum deceleration, the maximum allowed velocity is then fully determined by the maximum allowable emergency stop distance. From these constraints, the current maximum velocity of 70.4 mrad s^{-1} was determined, corresponding to 0.67 m s^{-1} on the 9.5 m radius azimuth rail. Note that, as the emergency stopping distance evolves quadratically with the travel velocity, a possible increase of the maximum velocity would drastically increase the necessary braking distance. Even if technical changes allowed for an increase in the braking distance, as short as possible a stopping distance is desirable for security reasons.

Currently, repositioning in azimuth by $\Delta\varphi = 150°$ is achieved within 30 seconds (fig. 4.9). The repositioning time in elevation is not critical in the sense that it will never take longer than 20 seconds (due to the low weight of the mirror dish). When allowing the telescope drive to make use of the reverse mode (i.e. moving over the zenith), the requirement of reaching any position in the sky within 30 seconds with 70% of the maximum allowed power is well met, as distances in azimuth are substantially shortened.

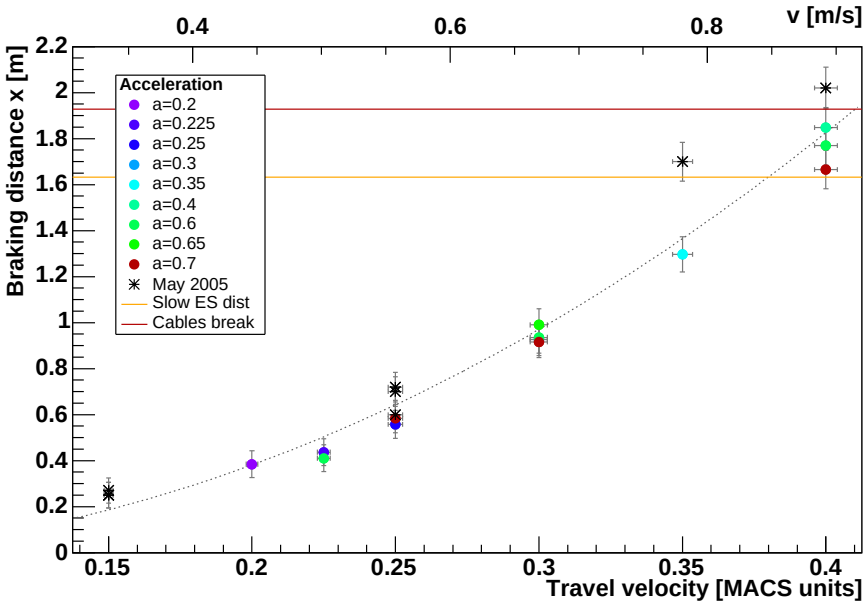

FIGURE 4.10: *Azimuthal distance needed for a complete emergency stop of the telescope for different velocities and accelerations (color coding; see fig. 4.9 for the definition; for the May 2005 measurements no accelerations are known). The telescope was accelerated to the travel velocity and then stopped by an artificial end switch. The yellow and red lines indicate the "critical distances" at which damage occurs (signal transmission fibers and cables break).*

4.5.3 The positioning & tracking algorithm

The pointing and tracking algorithms are based on a stable library for positional astrometric calculations, *Slalib* [Sla03]. The coordinate transformations performed include astrometric corrections, as explained below. The basic operation modes provided by the positioning and tracking algorithm are:

Slewing: Whenever the telescope has to be repositioned, the relative distance to the new position is calculated in telescope coordinates. Then the microcontrollers are instructed to move to this new position. If the desired position is not reached with a given precision, the procedure is repeated up to ten times, after which the system would go into error state. In almost all cases the requested position is reached after two or three trials.

Tracking: The basic algorithm of the tracking loop transforms the given celestial target position (RA, dec) into the ideal telescope pointing position (Zd, Az) at $t' = t_{\mathrm{now}} + \delta t$. This transformation includes astrometric corrections discussed below. By applying a misalignment correction, they are further transformed into the local telescope pointing position (Zd', Az'). As (Zd', Az') is given in a

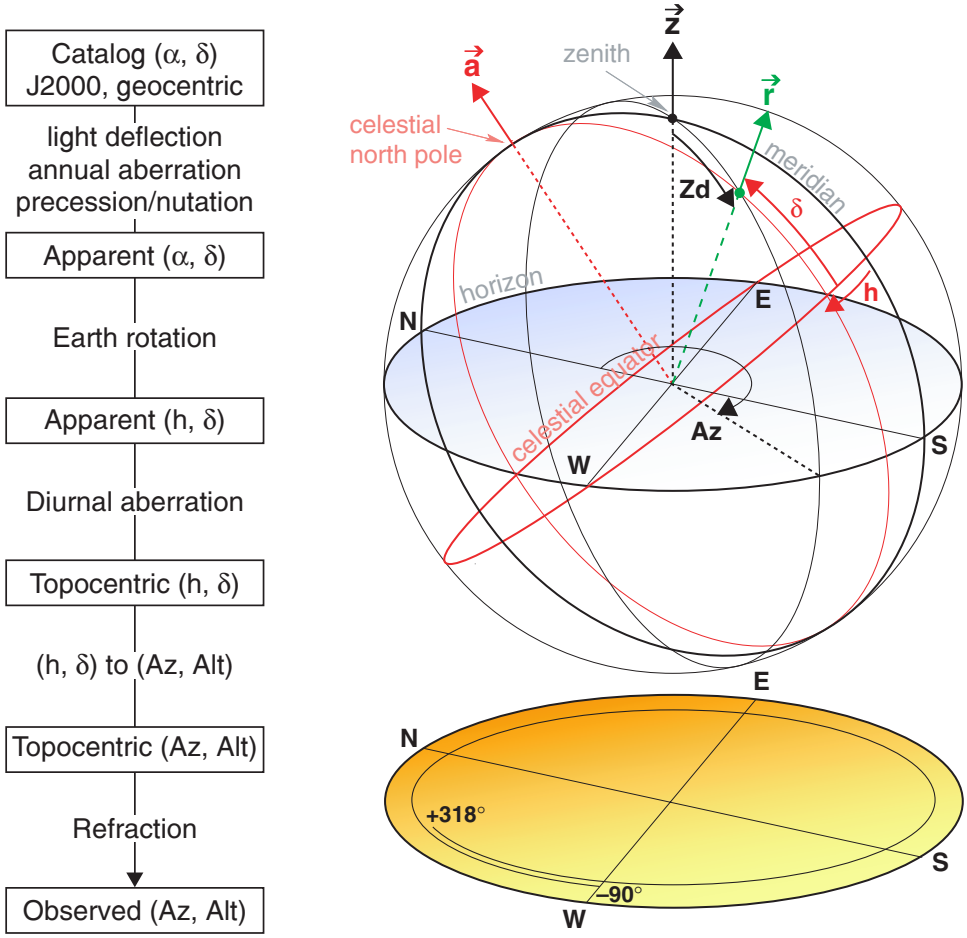

FIGURE 4.11: *Left: Relationship between celestial coordinates. The figure relates a celestial position to the actual line of sight to that position. Taken from [Sla03]. Right: Celestial sphere with the definition of the zenith angle* $Zd = 90° - Az$*, the azimuthal angle Az, the declination* δ *and the hour angle h. The vectors* $\vec{a}$*,* $\vec{z}$*, and* $\vec{r}$ *denote the Earth's rotation axis, the zenith direction, and the position of a point on the sky, respectively. Adapted from [Wit00]. Bottom: Azimuthal range of the telescope. The maximum positions are secured by hardware end switches.*

range $((0-90)°, (0-360)°)$, the position has to be further transformed into the $((-70-90)°, (-90-318)°)$ system.

Finally the required velocities to reach the new position are calculated. This is done by comparing the requested position in shaft encoder values with the current shaft encoder readings. These velocities are sent to the microcontrollers (MACS).

As a crosscheck, the calculated velocities for the two telescope axes are independently estimated using astrometric routines. For security reasons, the requested velocities are limited using the velocity estimations.

Astrometric corrections. The necessary transformations from celestial coordinates into the local telescope coordinates include astrometric corrections for a variety of effects.

The transformation chain is outlined in fig. 4.11. These transformations are performed by *Slalib* [Sla03], a library of routines intended to make accurate and reliable positional-astronomy calculations. Key features of the library are its well–tested numerical implementations and its mathematical stability. The astrometric corrections—performed when converting a catalog position to the apparent position (as seen from Earth's center)—take into account annual aberration (apparent displacements of positions caused by the finite speed of light combined with the motion of the observer around the Sun during the year) and precession/nutation effects. Further, while transforming the apparent position to the observer's position, the Earth's rotation, diurnal aberration (a small correction to the total aberration by the motion of the observer around the Earth's rotation axis) and atmospheric refraction effects are included. Some of these effects are so small that they are only relevant for nearby stars. As such stars are used for "training" the pointing model (see below), even such small effects are taken into account.

4.5.4 Pointing model

Imperfections and deformations of the mechanical construction lead to deviations from an ideal telescope. These deviations include the non–exact alignment of axes and deformations of the telescope structure. To assure reliable pointing and tracking accuracy, such effects have to be taken into account. Therefore the tracking software employs a state-of-the-art analytical pointing model based on the *TPoint*^{TM} telescope modeling software [Wal97, Wal01], which is also used for optical telescopes. This model parameterizes deviations from the "ideal" telescope. Such models often are called "bending models", as they describe the bending of telescope axes. A standard procedure is to collect data for the pointing model that allow to calculate the necessary corrections, and to apply them online. Since an analytical model is used, the source of most of the bendings can be identified and traced back to components of the telescope mount.

Corrections are parameterized by equatorial, alt-azimuthal, polynomial and harmonic terms. The most relevant pointing terms for the MAGIC telescope include:

1. Geometrical Terms:

   - Zero point corrections/offsets ("index errors", 1 term per axis): Trivial offsets between the zero positions of the axes and the zero positions of the shaft encoders.
   - Azimuth axis misalignment (2 terms): Two terms describe the misalignment of the azimuth axis in north–south and east–west direction, respectively.
   - Nonperpendicularity of axes (2 terms): These terms describe deviations from the right angles between any two axes in the system, namely (1) nonperpen-

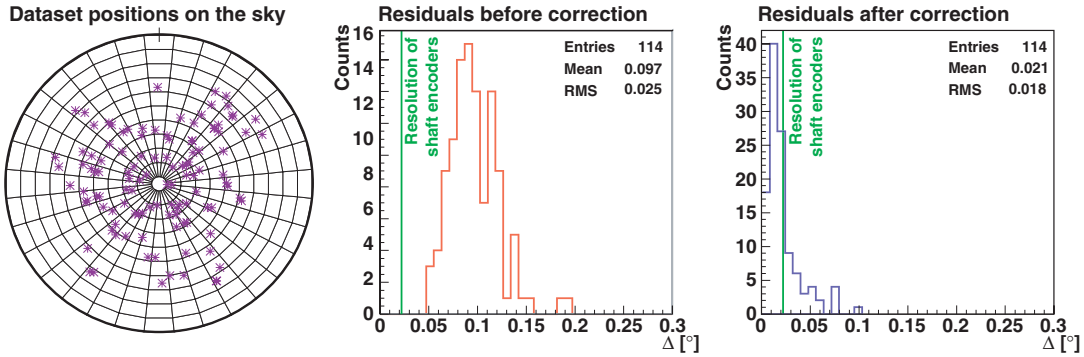

FIGURE 4.12: *Left panel: A set of data points used to calculate a bending model. Middle and right panel: Residuals before and after applying the bending model. When using a bending model, the residuals stay well within the shaft encoder resolution, as shown by the green line.*

dicularity of elevation and pointing axes (2) nonperpendicularity of azimuth and elevation axes. For MAGIC, only (1) has a non–zero value.

- Noncentricity of axes (4 terms): These terms parameterize the once–per–revolution cyclic errors produced by decentered axes. For each axis a sine and a cosine component are foreseen.

2. Bending of the telescope structure (bending of the telescope dish or flexure of support tubes):

   - MAGIC uses a single thin mast camera support strengthened by steel cables. Therefore the camera support structure is bending. This mast bending can be represented by two terms, either describing a change in the zenith angle by a sine law (the classical tube flexure model), or more empirically by a tangent law. The latter accounts for the fact that in practice for large zenith angles the observed displacement is better described by a tangent term.
   - A possible constant offset of the mast bending.

In practice, the coefficients of the bending model are determined from the positional information of $\gtrapprox 50$ bright stars. Fig. 4.12 shows a data set of star positions and the pointing residuals before and after application of a pointing model.

There exists another class of deformations of the telescope support frame and the mirrors caused by temperature changes and wind loads which are difficult to control for telescopes without dome and which cannot be modeled. They ultimately limit the tracking precision. It should be noted that the azimuth structure can change its diameter by up to 3 cm due to day–night temperature differences, indicating that thermal effects have a non-negligible and non–controllable influence.

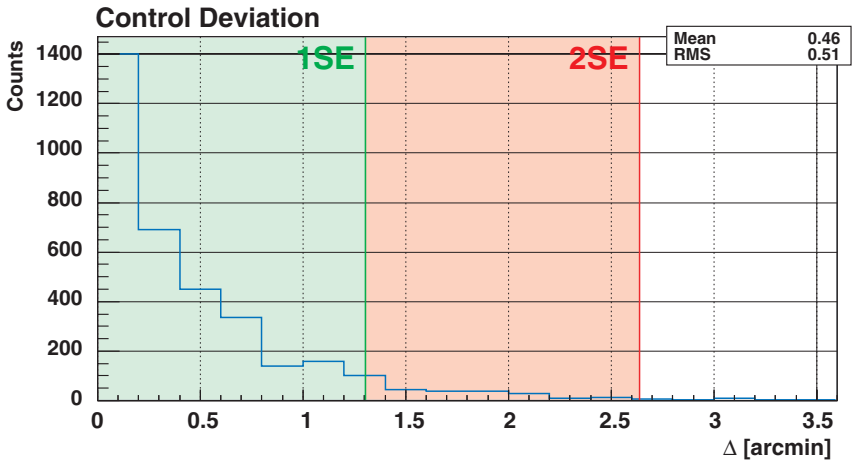

FIGURE 4.13: *The deviation of the telescope position as read by the shaft encoders from the expected position as provided by the rotary encoders. The control deviation rarely exceeds 1 shaft encoder step (1 SE), which is the intrinsic resolution of the system.*

4.5.5 Tracking accuracy

When observing astronomical objects, the drive system needs to counteract the apparent rotation of the celestial sphere. Therefore tracking velocities of much less than one revolution per day need (and can) be achieved without an indexing gear.

The intrinsic accuracy of the tracking algorithm is determined by comparing the expected position to the position found by the shaft encoders. This so called control deviation can be shown to be well below the shaft encoder resolution in almost all cases (fig. 4.13). The tracking precision is better than 1.5 arcminutes, which corresponds to half the pixel diameter of the MAGIC PMT camera.

Ultimate limits of the tracking precision are given by the mechanical setup of the telescope: The azimuth support consists of a railway rail with some small deformations in height due to the load, which result in a wavy movement not parameterized in the bending model. Also the rail is not exactly round. The six bogeys are equipped with simple, not precisely machined crane wheels. The bogeys may amplify horizontal deformations. The elevation drive exerts its power on a drive chain (cf. fig. 4.6) that is not a perfect circle, but deviates from that form by up to 30 cm. Additionally, there is a certain play between the chain and the teeth of the sprocket wheel.

4.5.6 The starfield monitor

A concept well known in optical astronomy is the use of a bright star in the field of view as a “guide star”. Potential deviations of the observed position of this star from its expected

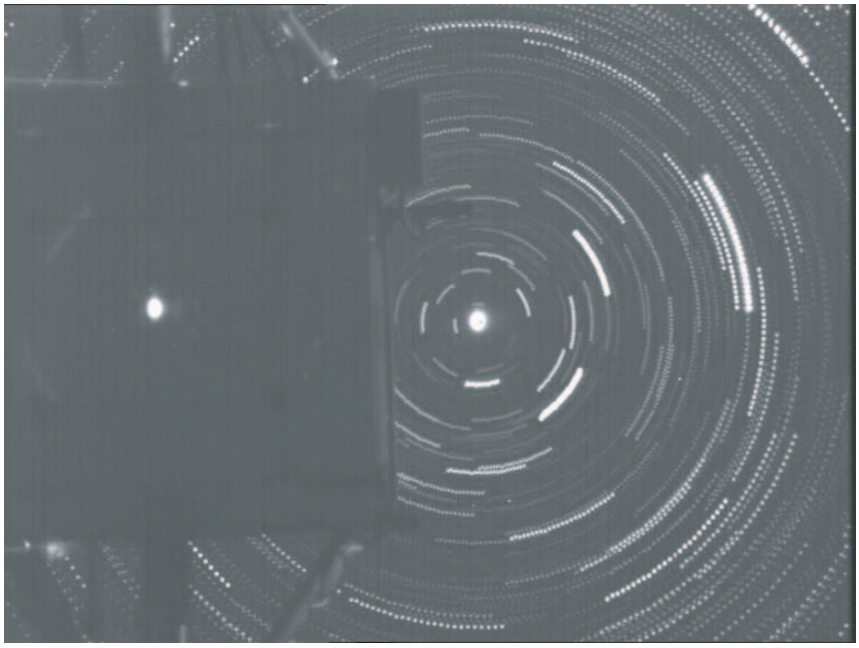

FIGURE 4.14: *A stack of images taken with the starfield monitor CCD camera while tracking the bright star Vega ($0\overset{m}{.}0$). Note the image of the Vega on the closed MAGIC PMT camera lid (left part of the picture) as well as the dim tracks of two nearby 5^m stars.*

position are counteracted by an opposing movement of the telescope, or more generally, by a feedback to the tracking system.

γ-ray sources typically are too dim in the optical for direct use for guiding. Therefore we determine a possible positional offset by comparing the observed starfield around the target position with the expected star positions from the PPM star catalog [Roe88]. This catalog provides accurate positions of astrometric reference stars and is based on the well–known FK5 system [Fri88]. The algorithm takes into account the astrometric corrections discussed in sect. 4.5.3. Fig. 4.14 shows a stacked image taken with the prototype starfield monitor while tracking the bright star Vega, illustrating the celestial movement.

The starfield monitor concept offers interesting "spin–offs" like the possibility to monitor the sky brightness and thus infer information on the atmospheric conditions, or to measure the point spread function (PSF) of the optical system (reflector and active mirror control system), using images of stars on an optional dedicated screen installed in front of the PMT camera.

Hardware and installations. A 0.0003 lux, 1/2" high sensitivity standard PAL CCD camera (type Watec WAT–902H) equipped with a multicoated, high transmission Schneider–Kreuznach Xenoplan 1.9/35mm wide–field lens is used (fig. 4.15). The high planarity of the field of view (fig. 4.16) is important for minimizing biases in the star-finding algorithm. The camera is read out at a rate of 25 frames per second using a frame

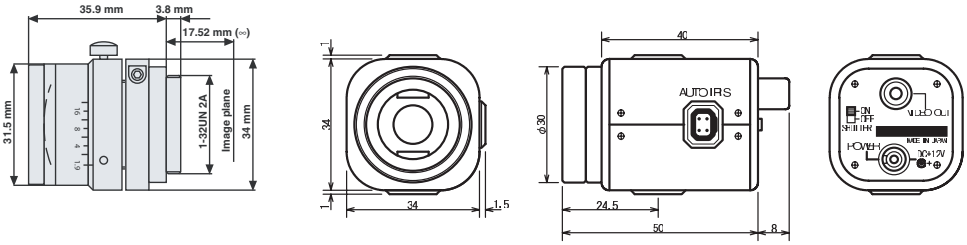

FIGURE 4.15: *Watec WAT–902H starfield monitor CCD camera with wide field Xenoplan 1.9/35mm lens (taken from the technical specifications).*

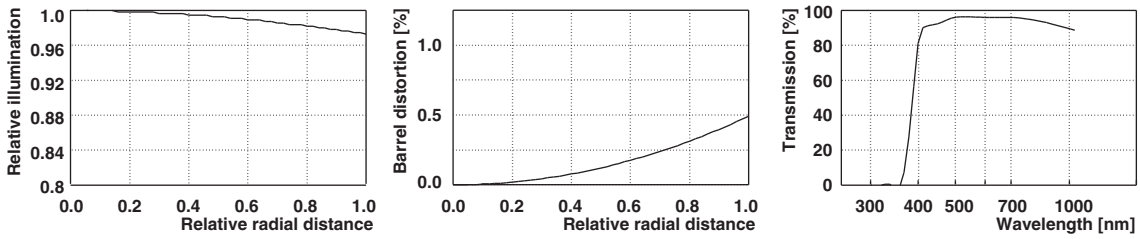

FIGURE 4.16: *Technical specifications for the Xenoplan 1.9/35mm lens (adapted from the technical specifications). Left: Relative illumination as a function of relative radial distance Middle: Distortion as a function of relative radial distance. Positive values indicate barrel distortion, negative values pincushion distortion. Right: Relative spectral transmittance.*

grabber connected to a standard PC. The trade–off for the high sensitivity of the camera is a high noise level given in each single frame recorded. By averaging typically 125 or 250 frames, a high picture quality can be achieved (fig. 4.17).

The starfield monitor camera has been installed in the central area of the reflector dish (fig. 4.18). It simultaneously observes a part of the MAGIC PMT camera and the sky position to which MAGIC telescope is pointing to (fig. 4.19). The starfield around the pointing position is observed in a $6.2^\circ \times 6.2^\circ$ area, corresponding to 460×460 CCD pixels. A set of dim reference LEDs mounted on the MAGIC PMT camera provides the

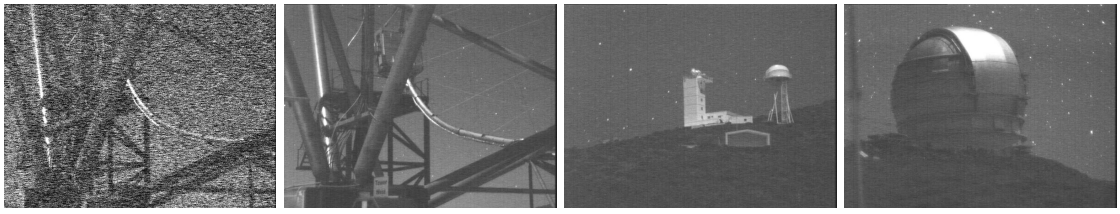

FIGURE 4.17: *Some pictures taken with the high–sensitivity CCD camera. From left to right: (1) A single shot shows the high noise of the camera (2) the high sensitivity is achieved by adding up many single shots. Landscape around MAGIC at moderate moonshine: (3) Swedish Solar Telescope, (4) Gran Telescopio Canarias. Note the many stars visible on the latter two pictures. All pictures were taken before the camera was mounted on the MAGIC telescope dish.*

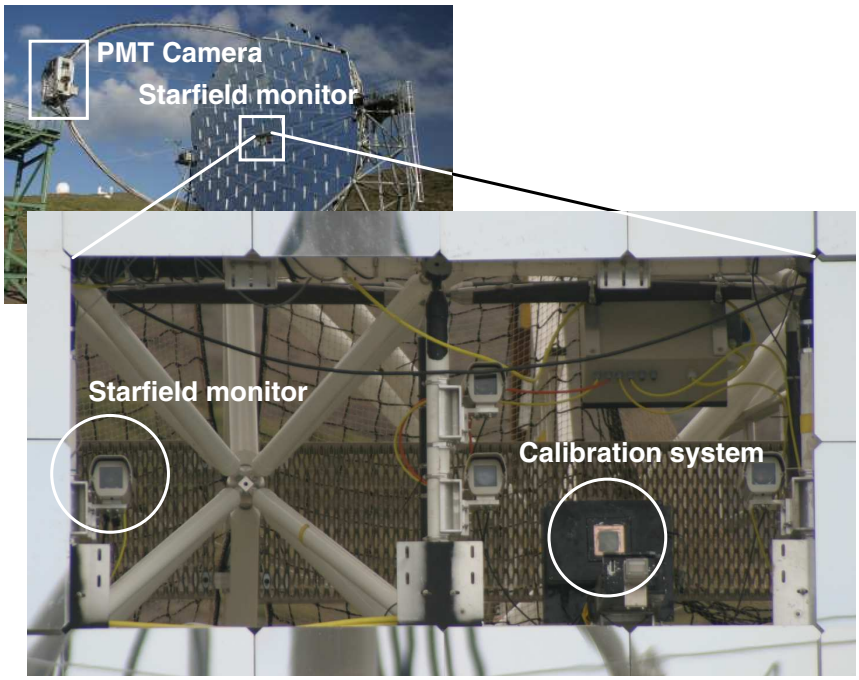

FIGURE 4.18: *Location of the starfield monitor on the MAGIC telescope: The CCD camera is installed in the central area of the mirror dish. Its optical axis is parallel to that of the telescope; in order to observe the area of the sky to which MAGIC is pointing, the camera is mounted 1 m off the mirror dish center. Fig. 4.19 details the view of the camera.*

reference frame for the mispointing determination. This compensates for potential small systematic movements of the PMT camera due to bending effects.[4] Such the starfield monitor system is independent of the absolute position of the PMT camera and becomes very robust. Typically 40 to 50 stars are visible (limiting magnitude $8\overset{\text{m}}{.}6$) of which at any given time 10 or more stars are recognized by the software.

Mispointing determination. To determine the current telescope pointing position, the vectorial differences $\overrightarrow{d_{ij}} = (\delta x_{ij}; \delta y_{ij})$ of all combinations of expected stars (i) as given in the star catalog and recognized spots (j) in the starfield CCD camera are filled in a histogram (In the following, "star" refers to the expected catalog position and "spot" to bright spots found in the CCD picture). One expects an accumulation of the "matching" star–spot pairs at small $|d_{ij}|$. The average of the positional differences of the star–spot pairs contained in the histogram bin with the highest number of entries is the mispointing. Fig. 4.20 illustrates the algorithm and shows its limitations, which are given when bad atmospherical conditions, clouds in the field of view, high noise or a bright background in the picture prevent the identification of a high enough number of spots.

The number of found spots vs. the number of expected stars or the overall picture bright-

[4]Note that also the CCD camera position could be subject to bending effects, though it is located in the center of the reflector dish where only negligible effects are expected

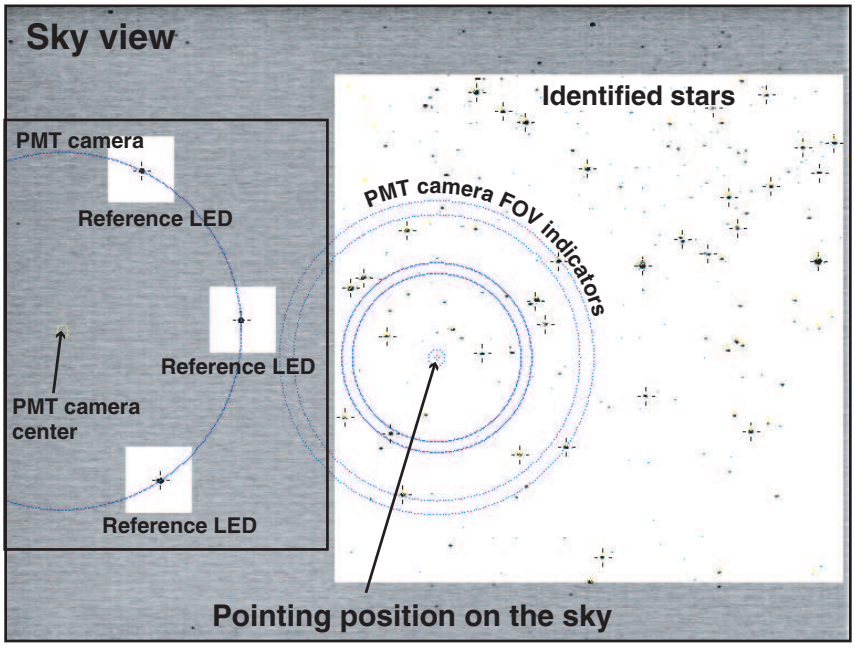

FIGURE 4.19: *Starfield monitor camera view. The picture has been inverted for clarity. In the right area, identified stars are marked with a cross. In the left area, the three LEDs mounted on the PMT camera are seen, providing the starfield monitor reference frame.*

ness are used to estimate the reconstruction quality. Mispointing values determined under adverse conditions are flagged accordingly in the data stream.

The location of the center of the PMT camera is done by fitting a circle to the three reference LED positions. Deviations from the expected position are transformed into a displacement of the location of the expected starfield. Fig. 4.21 illustrates how the PMT camera displacement is taken into account: The nominal location of the starfield in the coordinate system of the CCD picture is corrected for displacements of the PMT camera location.

The mispointing is determined every 5 or 10 seconds. Together with the CCD picture these values are available for online inspection by the telescope operator. The mispointing values are also available offline for possible pointing corrections. Since the observed mispointing is small, no active (online) corrections are performed, although technically the drive system is ready for online corrections.

Starfield monitor performance. Fig. 4.22 shows a measurement of the starfield monitor resolution conducted with a prototype installation. It was produced by running the starfield recognition algorithm while the telescope was stopped. In this way, the expected mispointing could be calculated precisely and compared with the found one. The plot shows the vectorial difference of both values. Measurements conducted with the currently installed starfield monitor are shown in fig. 4.23. It should be noted that the installed mon-

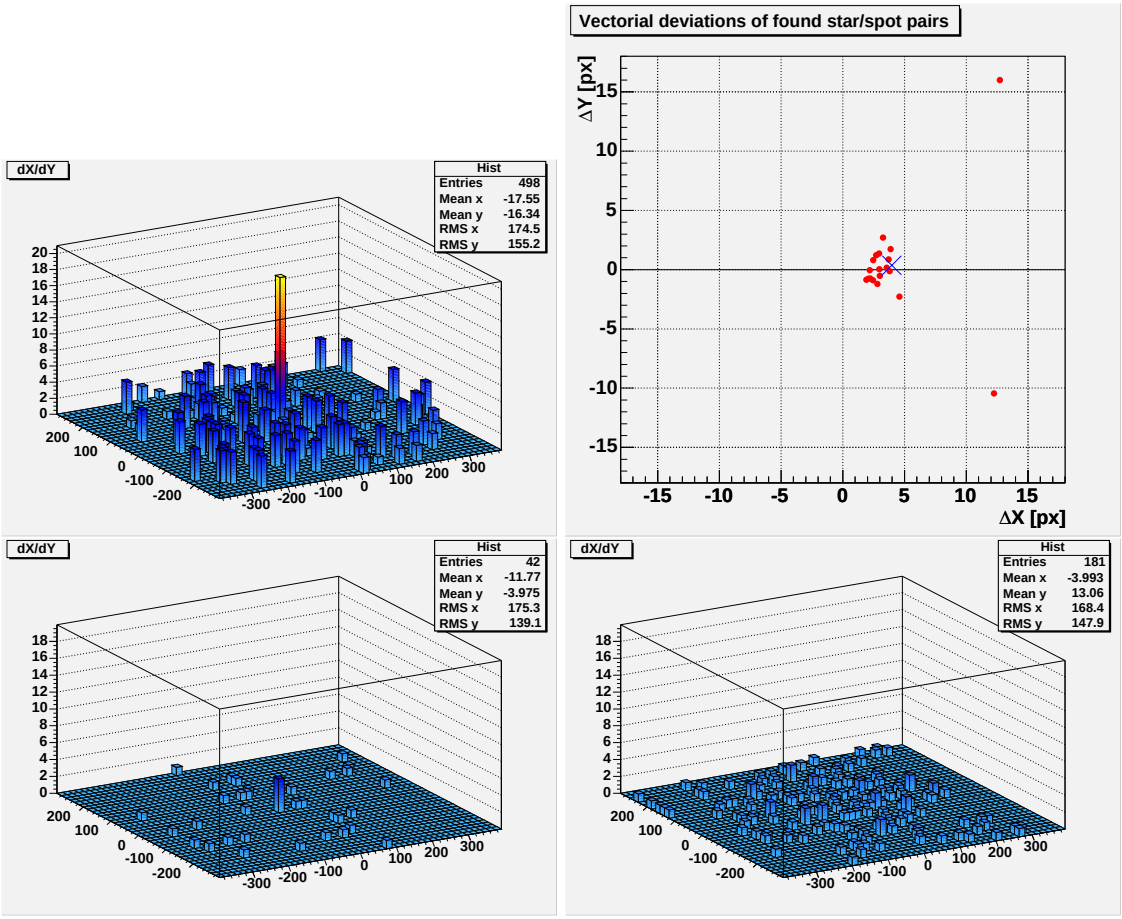

FIGURE 4.20: *Upper left panel: The vectorial differences* $\overrightarrow{d_{ij}} = (\delta x_{ij}; \delta y_{ij})$ *of all combinations of expected stars (i) and recognized spots (j) in the starfield CCD camera are filled in a histogram. One expects an accumulation of the "matching" star–spot pairs at small* $\overrightarrow{d}_{ij}$*. Units on the x and y axes—CCD pixels, on the vertical axis—number of star–spot pairs. Upper right panel: Star–spot pairs contributing to the bin with the highest number of entries in the histogram in the upper left panel. The mispointing is determined by averaging their positions. Lower left panel: A much smaller number of spots are recognized. Such conditions prevail under high background light conditions, e.g. during intense moonshine or bad atmospherical conditions. Lower right panel: In case of very adverse conditions, noise on the lines, or when the telescope is too far off the expected position, the algorithm will fail.*

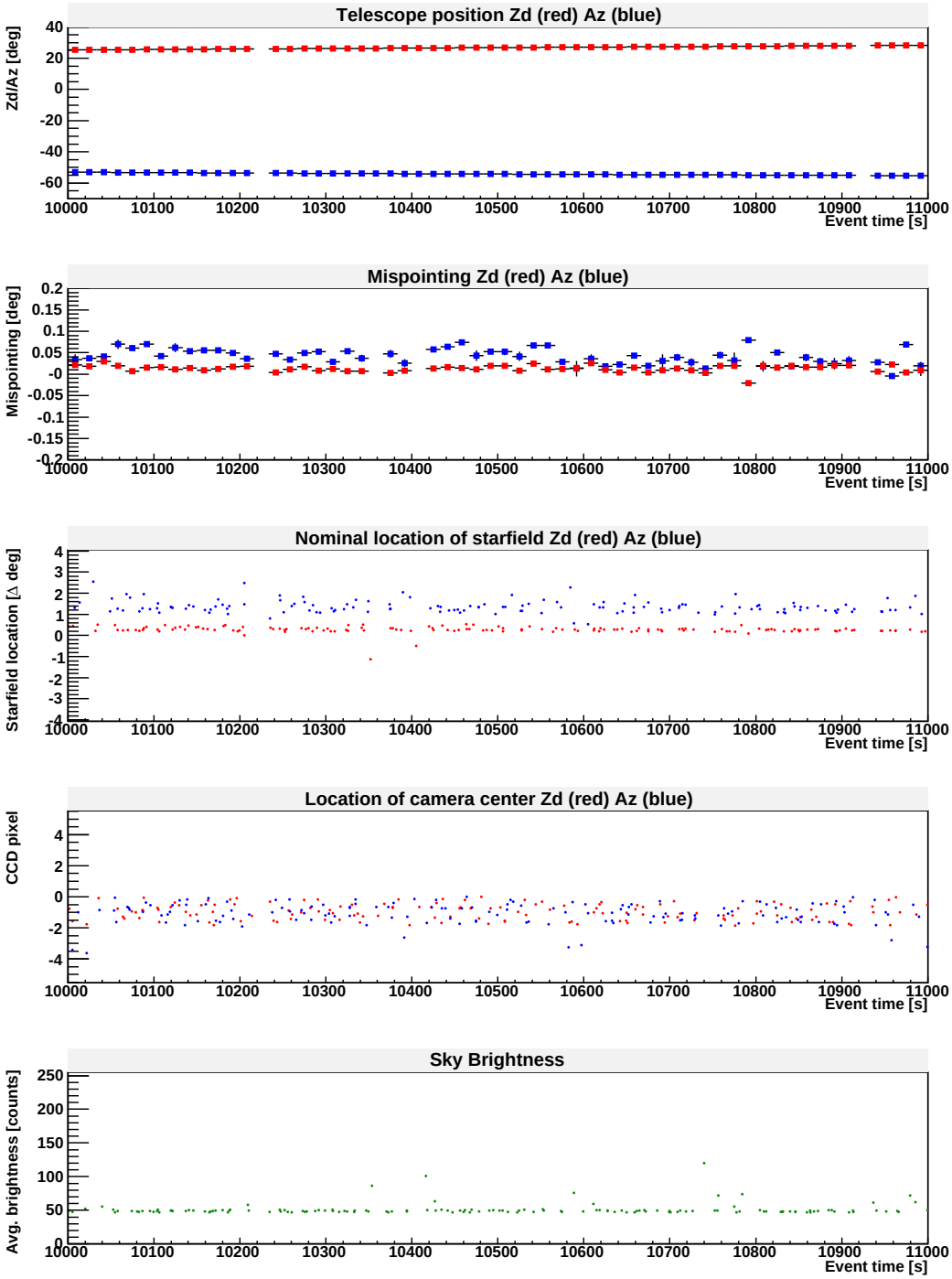

FIGURE 4.21: *Starfield monitor operation. The plots were recorded while continuously tracking a source position. (1) Nominal telescope pointing position (2) Mispointing as determined by the starfield monitor. (3) Nominal location of the starfield in the CCD camera picture (4) Location of the PMT camera in the CCD camera picture as given by the LEDs (provides reference frame). (5) Sky brightness. The few outliers are caused by induced noise on the video transmission cable, and are flagged out in data analysis.*

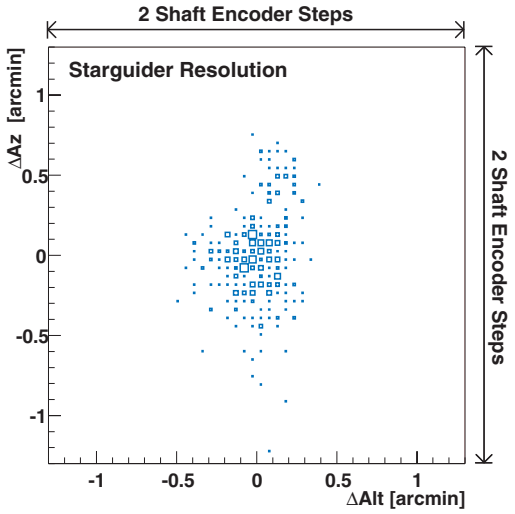

FIGURE 4.22: *The resolution of the starfield monitor can be inferred by stopping the telescope and plotting expected vs. observed mispointing.*

itoring system has a different field of view and a different magnification (pixel size in sky coordinates) as compared to the prototype system. Mispointings determined during regular tracking in a period of 2200 s have been filled into histograms. The resulting RMS values, $RMS_\theta = 0.48'$ and $RMS_\phi = 0.74'$ for zenith angle and azimuth, respectively, compare quite well with the previously found resolution of the prototype system. They allow monitoring and offline corrections of the drive system, which has an accuracy of $1.5'$ as stated before.

Another means of assessing the starfield monitor performance is to compare the "mispointing velocity" when deliberately stopping the tracking. The velocity with which a tracked position is moving away from the camera center can be compared to the increase of the reported mispointing. For the measurements shown in fig. 4.24, the telescope was stopped. When not moving, the nominal pointing position is left with a velocity of $v_\theta = (10.52 \pm 0.35)'' \text{ s}^{-1}$ and $v_\phi = (-9.35 \pm 0.16)'' \text{ s}^{-1}$ as compared to the increase of the mispointing of $v_{\delta\theta} = (11.35 \pm 0.32)'' \text{ s}^{-1}$ and $v_{\delta\phi} = (-9.46 \pm 0.09)'' \text{ s}^{-1}$ due to the Earth's rotation.

"Culmination problem". By construction the elevation axis of the telescope is nearly balanced. As a consequence, the elevation drive changes the edge of the elevation drive chain once the culmination (viz. θ' vanishes) of a given pointing position is reached while tracking it. The play in the gears and the chain as well as hysteresis effects in the telescope structure are difficult to program and therefore are not modeled in the bending model. Thus a mispointing will be present from the culmination point on (fig. 4.25) until the drive system realizes that offset. By construction, the earliest this can happen will be when one of the elevation shaft encoders reports a positional change. It could be

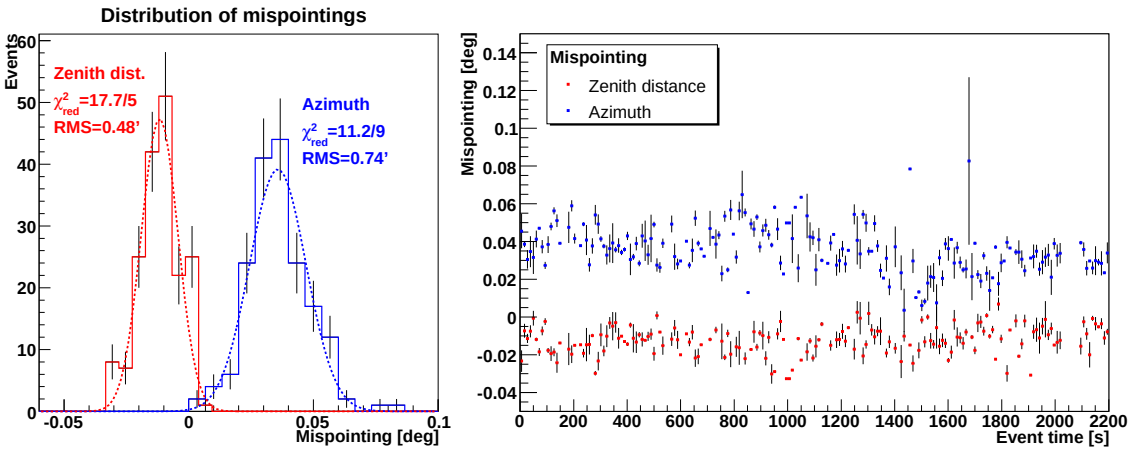

FIGURE 4.23: *Left: Distributions of measured mispointings. The RMS values indicate the resolution of the star recognition algorithm. Right: Mispointings used in the distributions. Values with large error bars are caused by noise on the RG58 video cable. They are detected by an unusually high "sky brightness" and thus are flagged as unsuitable data in the data stream.*

shown that the time the "culmination problem" lasts is proportional to the zenith angle at culmination.

The starfield monitor offers the possibility of an offline correction of the positional offset encountered at culmination. The offset is small in the sense that possible changes in camera efficiency are not to be expected.

Fig. 4.25 shows the occurrence of the "culmination problem". By measuring the mispointing velocity at culmination one obtains values very much compatible with a stop of the telescope, hinting at the scenario outlined above.

Quality monitoring—Sky Brightness. The sky brightness as shown in the lowest panel of fig. 4.21 is obtained by averaging the recorded brightness of all CCD pixels belonging to the $6.2^\circ \times 6.2^\circ$ field of view. For simplicity, currently no special measures to exclude stars are taken ($\approx 0.2\%$ of the pixels are illuminated by stars). Also, the sky brightness currently is given as an 8-bit number corresponding to the 8-bit digitization depth of the frame grabber card. In spite of this simplistic approach the sky brightness is a very useful number to judge the quality of the sky. In particular, clouds in the field of view are recognized by an increase in sky brightness as they scatter surface light. Another useful item of information is the ratio of expected to recognized stars.

PSF from stars. The starfield monitor offers the possibility to determine the PSF of the MAGIC reflector. A dedicated reflecting surface needs to be installed at the focal plane for objects at infinite distance. The width of pictures of not too bright stars (so as not to saturate the moderate 8-bit dynamical range of the CCD camera) can then be used to infer the PSF. A first technical proof of principle is shown in fig. 4.26. For MAGIC, currently

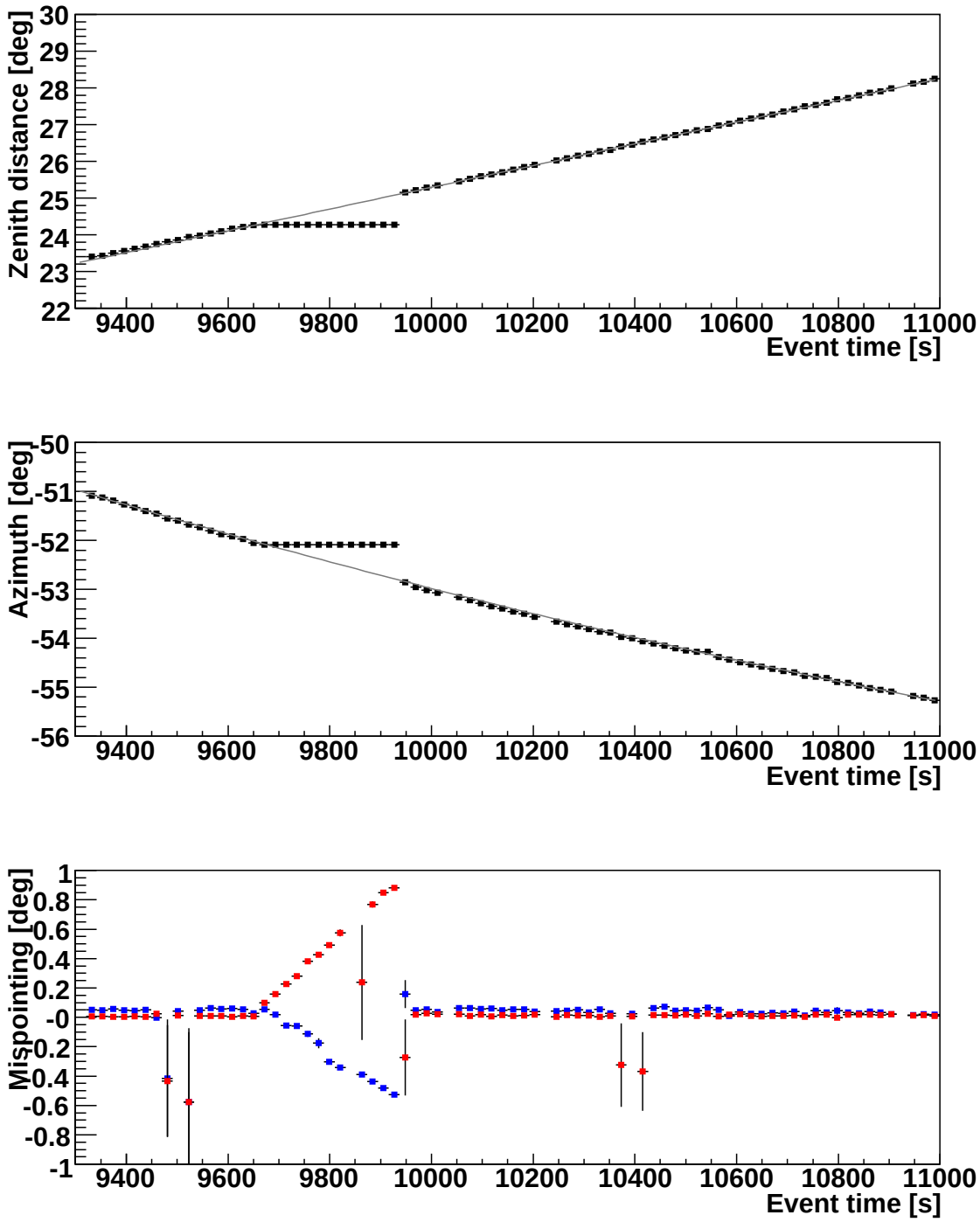

FIGURE 4.24: *Deliberate stop of the drive system as seen by the starfield monitor. Measuring the speed at which the tracking position leaves the current telescope position can be used to infer the starfield monitor performance (see text).*

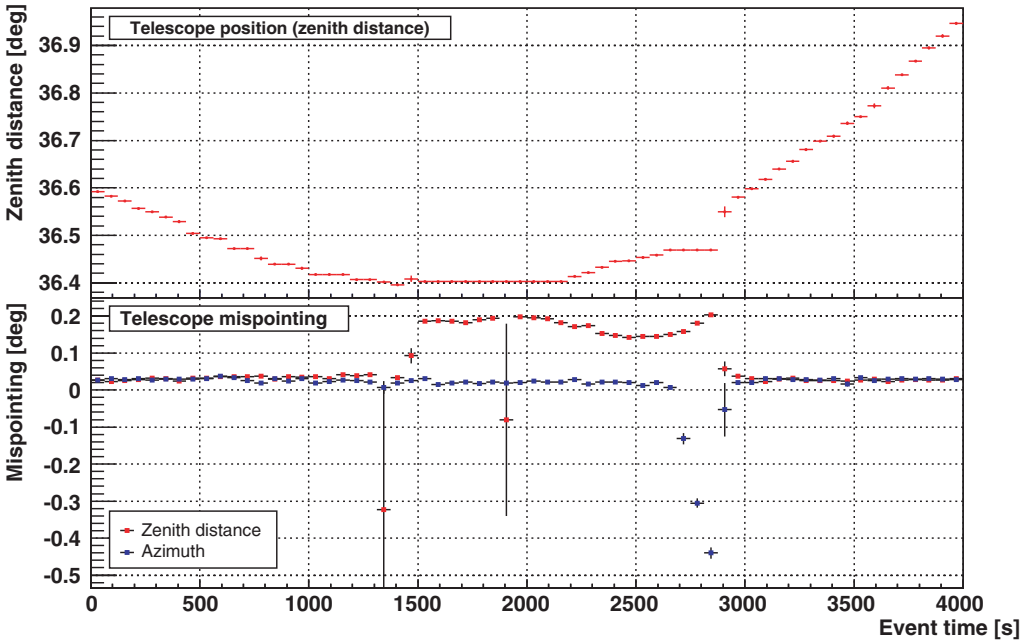

FIGURE 4.25: *When reaching the point at which a tracked source culminates (i.e. reaches its highest or lowest zenith angle, $\theta' = 0$), the drive unit's cogwheel switches the edge of the drive chain. This effect can be seen at event time 1400 s. Normally the drive system needs time to react to the subsequent mispointing. Here the shift crew stopped telescope movements at event time 2650 s and restarted the tracking.*

PSF measurements are carried out with a dedicated high dynamical range camera, which however does not provide the sensitivity the starfield monitoring requires.

4.6 Monte Carlo simulations of air showers

The simulation of extended air showers is challenged by the enormous number (exceeding 10^{10}) of secondary particles participating in an air shower and by the limited knowledge of the particle cross-sections at high energies. Still, the reconstruction of γ-ray initiated air showers and the required separation of such showers from the much more abundant showers of hadronic origin require detailed Monte Carlo (MC) simulations of the shower development and of the telescope response. In particular, when using the atmosphere as a calorimeter in the way IACT experiments do, there is no means of a "direct calibration" of the system as for calorimeters in high energy physics.[5] Sect. 5 will detail the usage of MC data in the MAGIC analysis chain.

The development of γ and hadron–initiated air showers is simulated with CORSIKA[6]

[5] Only when γ-ray satellite experiments with an overlapping energy range like GLAST come online, such possibilities will emerge [Bas05].

[6] **Co**smic **R**ay **Si**mulations for **KA**SCADE, `http://www-ik.fzk.de/corsika/`

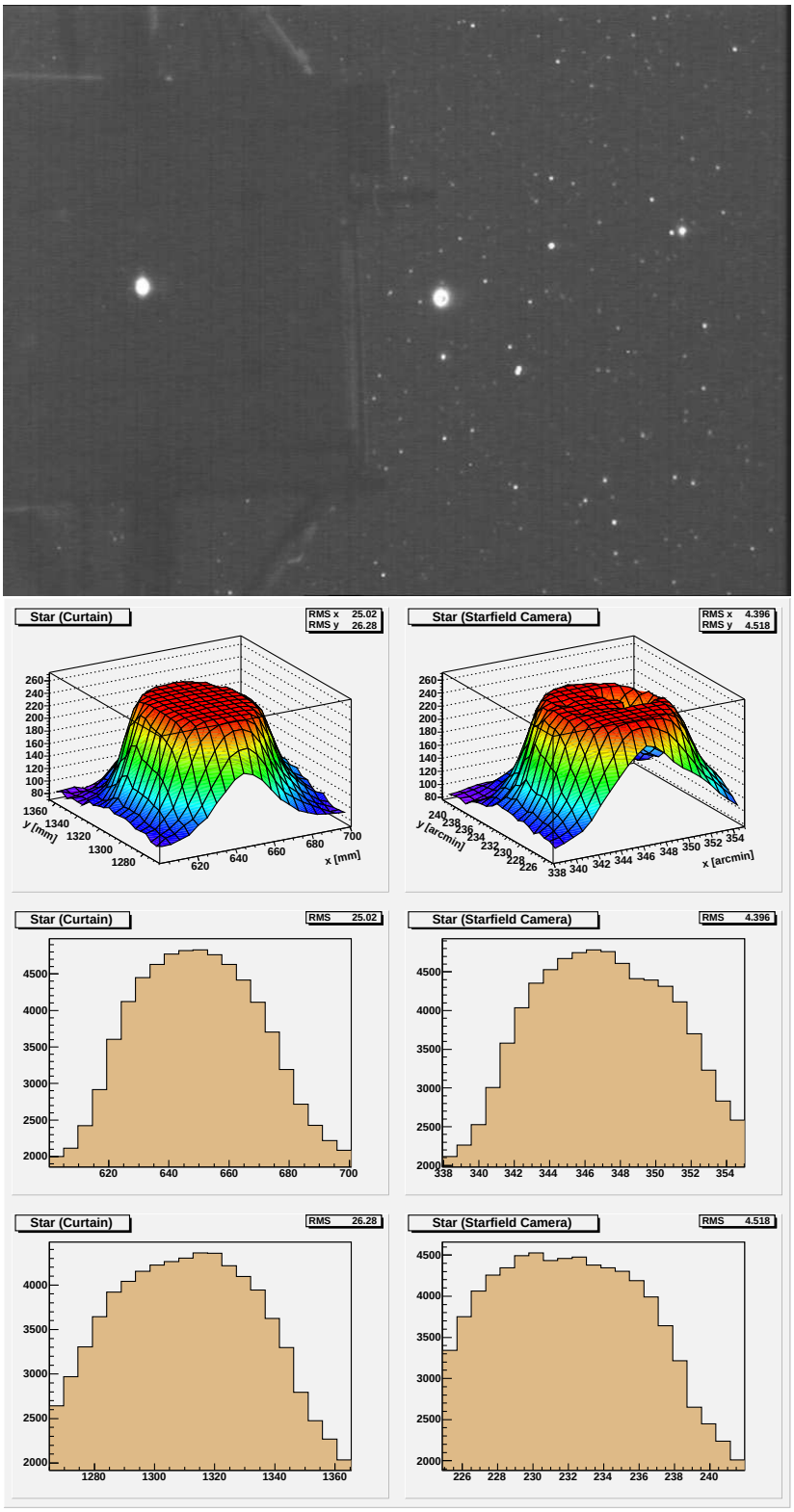

FIGURE 4.26: *The bright star Vega (α Lyrae) as seen on the closed lid of the MAGIC PMT camera (left) and on the sky (right). The light distributions are shown below the CCD picture. Due to Vega's high brightness, both pictures saturate. The histograms show projections of the picture of the star (upper histogram: along the horizontal direction, lower histograms: along the vertical direction). Units of the histograms: horizontal axes—position in millimeters/arcminutes, vertical axes—counts.*

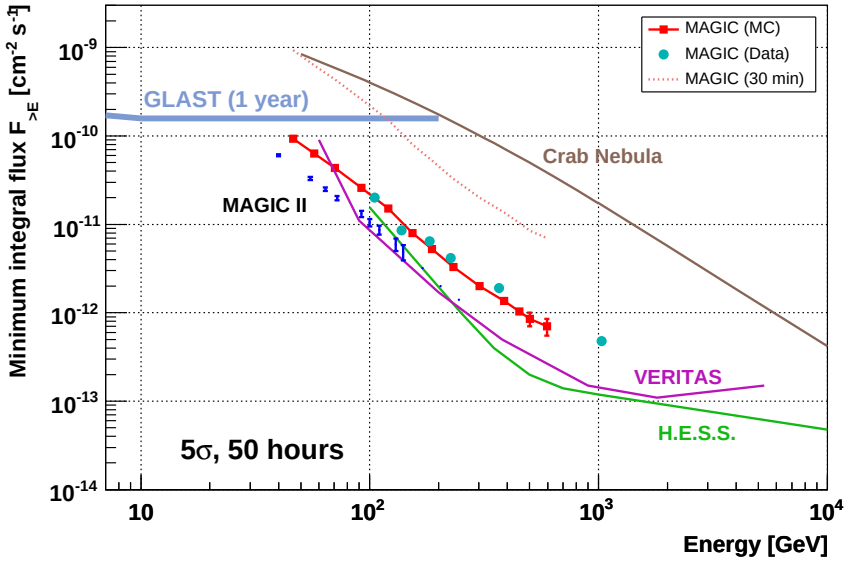

FIGURE 4.27: *Calculated (by MC simulations) sensitivity of the MAGIC telescope and other operating and future instruments for a point–like source with a Crab nebula–like (power law index $\alpha = 2.6$) spectrum for low zenith angle ($\theta \leq 30°$) observations. The plot shows the flux of the Crab nebula and the flux sensitivity for a detection on the 5σ level in 50 hours. The dotted orange line indicates the MAGIC sensitivity for a 5σ signal in 30 minutes. Also given is the inferred sensitivity from Crab nebula observations (blue dots).*

6.019 and 6.023 [Hec98], using the VENUS package [Wer93] for hadronic interactions, the U.S. standard atmosphere, and some MAGIC specific modifications. After accounting for the Cherenkov light absorption and scattering in the atmosphere [Elt64, Elt66], the reflection of the surviving photons on the MAGIC camera plane is simulated. In a further step, the response of the photomultiplier camera, the trigger and the full data acquisition system including electronic noise are simulated. The overall light collection efficiency of the telescope has been tuned at the camera simulation level using low impact parameter muons. A comparison of MC events and real MAGIC data [Maj05] shows that the experimental data are well reproduced by the simulations; the inferred sensitivity (cf. fig. 4.27) for point–like sources could likewise be confirmed with Crab nebula observations down to 100 GeV.

Simulations have been conducted in bins of $\cos\theta$ down to $\theta = 70°$ and with impact parameters up to 300 m and 400 m for gammas and nuclei, respectively. Primary γ-rays from 10 GeV to 30 TeV were simulated according to a pure power law with a spectral index of $\alpha = 2.6$ (for energies well above 1 TeV with $\alpha = 1.0$; both tunable to the spectral slope of the observed source at the level of flux determination) and as if coming from a point source. Charged primaries were simulated to follow their measured spectra [Alc00a, Alc00b] with the direction of protons and Helium nuclei originating from within a 5° cone around the telescope axis.

4.7 Observation modes and file types

Data and file types. The raw data files as provided from the DAQ system contain event-wise information of the recorded shower events as well as run-wise housekeeping data. The data are organized in "runs" of typically five minutes duration. Unique run numbers are assigned by the DAQ system. There are three different types of data files. In general, an observation sequence consists of a pedestal run, a calibration run and a number of data runs, the maximum length of which is given by file size limits.

- Pedestal runs contain 1000 randomly triggered events while tracking a given sky position. These events contain the signal baseline and its fluctuations that are given by the LONS as well as the noise of the readout chain. It is unlikely that an air shower is recorded accidentally; in any case, during offline pedestal analysis, such events would be rejected. Normally one pedestal run is taken before an observation sequence starts to obtain an initial set of pedestals.
- Calibration runs contain events triggered by the calibration system while synchronously uniformly illuminating the PMT camera by a light pulser or a DC light source. These events are used offline for calculating an initial set of calibration constants.
- Data runs contain events that triggered the telescope while tracking a given sky position. These runs contain interleaved calibration events at a rate of 60 Hz, which are used to provide a continuous recalibration. The parts of the events which do not contain parts of the recorded shower images are used to update the pedestals (cf. sect. 5.3).

Apart from the event data, a number of subsystem data files are produced by the major telescope subsystems, like the camera control system, the tracking system, the starfield monitor, and the central control system. This additional information is merged with the event data offline. At a certain point of the analysis chain, they are then synchronized to the individual events.

Observation modes. Data taking is basically done in the so-called tracking mode, i.e. the telescope follows a given position in the sky while recording shower images. There are three different modes of observing sources (fig. 4.28):

- **ON observations.** The desired source position is tracked in such a way that the center of the PMT camera points to source. When taking data only in ON mode, the estimation of the irreducible background is based on assumptions of the behavior of the background; therefore ON–only observations require a very accurate knowledge

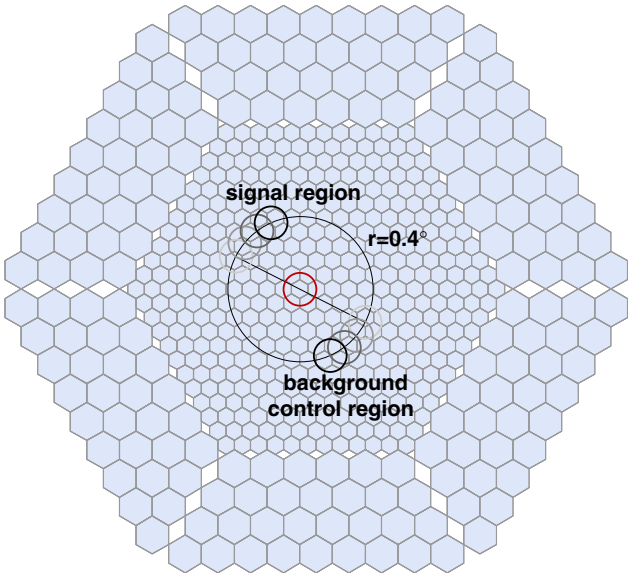

FIGURE 4.28: *Observation modes. During* ON *observations, the source is positioned in the center of the camera (red circle).* OFF *observations are conducted following the same zenith angle path as* ON *observations for accumulating background control events. During wobble observations, the source region and a background control region are displaced* 0.4° *from the camera center and observed simultaneously. More control regions can be defined along the circle on which these two regions lie. As a consequence of the telescope mount these regions move during the observation, which reduces systematic errors introduced by camera inhomogeneities.*

of the background. Note that the background conditions may vary slightly with zenith angle or more generally with the sky position.

- **ON/OFF observations.** Generally, ON observations are complemented by (ideally) an equal amount of OFF observations. In the latter mode, the telescope tracks a position in the sky in which no gamma ray is presumed to be present. The OFF position ideally has the same background light and atmospheric conditions as the corresponding ON position and follows the same track in zenith angle. The obtained data serve as background control sample for the corresponding ON data (cf. sect. 5.5).

As the efficiency of the camera is highest for a source positioned in the camera center, ON/OFF observations lend themselves to measuring very weak sources. A problem of this observation mode is that some care has to be taken to take OFF runs that exactly suit the corresponding ON runs. Also, ON/OFF observations obviously do not guarantee optimal time coverage, as observation time is lost for recording OFF–events.

- **Wobble mode observations.** This mode allows for simultaneous recording of ON and OFF data at different places in the camera [Fom94]. Therefore, the source

position is displaced a fixed distance off the camera center (fig. 4.28). The position opposite of the source position is called "anti–source position" and is used to determine the observational background while observing the source. In practice, two more background regions are very often defined at the same distance from the camera center, but $\pm 90^\circ$ displaced from the source position.

In general, wobble observations guarantee a good match of ON and OFF data. To avoid systematic errors due to the chosen source position in the camera, source and background positions are regularly swapped (normally two positions; hence the name "wobble mode"). An additional decrease of possible systematic errors is given by the fact that source and anti–source position continuously rotate around the camera center. An additional benefit of this observation mode is the best possible coverage in time. The wobble mode has the disadvantage that off–center regions in the camera possibly have somewhat lower efficiency then the central position.

4.8 Optical support observations

In particular for AGN observations, which comprise the main part of this thesis, contemporaneous measurements in different wavelength bands are essential. To this end, within the MAGIC collaboration, the Tuorla group operates an optical telescope close to the MAGIC telescope site. The KVA telescope[7] consists of a 60 cm $f/15$ Cassegrain instrument used for polarimetry and a 35 cm $f/11$ Schmidt Cassegrain telescope for multicolor photometry [Cip06]. Additional monitoring observations are conducted with the 1.03 m Dall-Kirkham-type $f/8.45$ telescope at Tuorla Observatory, Finland. The telescopes mainly serve for MAGIC blazar support observations, long–term blazar monitoring campaigns and polarimetric surveys [Sil88, Sil91]. The monitoring measurements are conducted in the Johnson *R*–band at 6400Å.

[7] **K**ungliga **V**etenskaps**a**kademien, Royal Swedish Academy of Sciences, `http://tur3.tur.iac.es/`

Chapter 5

The Analysis Chain for the MAGIC Telescope

As discussed in sect. 3.1, Imaging Air Cherenkov Telescopes (IACT) do not observe γ-rays directly, but rather record Cherenkov photons produced in the extended air showers which are induced by the γ-rays. These photons are registered by a PMT camera. Thus the very quantities measured are photoelectron pulses registered by the PMTs of a pixelized camera.

This chapter describes the reconstruction of the physical parameters of the primary γ-rays from the recorded shower images. The data analysis performed in this thesis uses the standard MAGIC Analysis and Reconstruction Software ("MARS" [Wag03a], a ROOT[1]–based C++ code) and its analysis chain. The main contribution of this thesis concerns the "high level" parts of the analysis chain, in particular the flux and light curve determination implementation for MARS (sect. 5.6).

The basic steps of the offline data analysis pipeline are:

1. Data selection and data quality checks
2. Reconstruction of charge (in FADC counts) and arrival time (in FADC clock ticks) of the Cherenkov light pulses registered for each photomultiplier tube in the camera
3. Pedestal subtraction and calibration of the extracted pixel information, i.e. conversion from FADC counts to reconstructed total number of photoelectrons released by the Cherenkov light and determination of the relative pulse arrival time in the individual pixels.
4. Event reconstruction, i.e. image cleaning and parameterization of the shower image

[1] an object–oriented data analysis framework, `http://root.cern.ch/`

5. Classification of the individual events as signal (γ-ray) or background events (hadrons, muons)

6. Energy reconstruction of the primary γ-ray using a regression tree method

7. Determination of the γ-ray excess employing statistical methods

8. Optionally: Creation of a sky map, which indicates the arrival directions of the incoming γ-rays and allows to determine the excess position or to study extended sources

9. Calculation of a differential or integral γ flux spectrum and/or of a light curve.

5.1 Data selection and quality checks

The data runs to be included in the analysis have to pass a couple of data quality checks. A very good indicator for possible problems is the event rate. The discriminator thresholds (cf. sect. 4.3) are adjusted so as to provide a trigger rate of approx. 250 Hz (at zenith; the trigger rate is zenith angle dependent). Lower rates generally indicate bad atmospheric conditions, while rate fluctuations that exceed the statistical level of fluctuations point to technical problems during data taking.

The general weather conditions as provided by the MAGIC weather station can be used to further reject data taken during nights with e.g. high humidity and adverse atmospheric conditions; additionally, the Mercator meridian telescope[2] provides atmospheric extinction coefficients that correlate with the presence of humidity or dust in the atmosphere.

Additionally, the online run books, which are part of the MAGIC database, form the shift crew's log and contain information on possible problems or shortcomings during the observations (e.g. light from bypassing cars). The database also contains certain "exclusions" (i.e. error states) on a run basis and it keeps track of observation parameters such as discriminator thresholds or trigger conditions.

5.2 Charge and arrival time reconstruction

After the data quality checks, as a next step the charge and arrival time of the Cherenkov signal pulse have to be determined for each PMT pixel of the MAGIC camera. The Cherenkov signal around the trigger signal (in units of FADC counts) is reconstructed

[2] a 1.2 m diameter semi–robotic telescope located at the Roque de los Muchachos Observatory, `http://www.mercator.iac.es/`

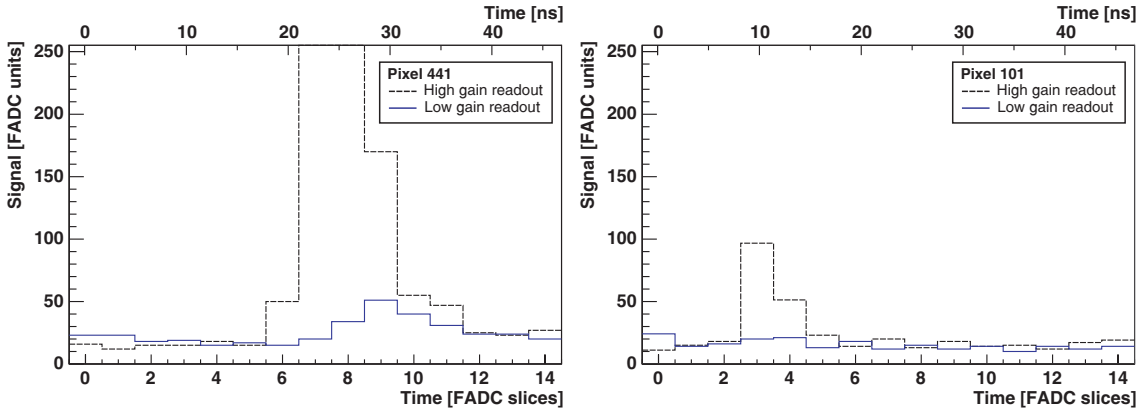

FIGURE 5.1: *FADC readout. Right figure: High–gain (black) and low–gain (blue) FADC readout. Left figure: No low–gain signal was read out, so these FADC slices (blue) can be used to evaluate the pedestal.*

from the thirty baseline–corrected FADC time slices by a dedicated signal extraction algorithm. Then it is converted to units of photoelectrons ($\propto$ photons) by using calibration constants obtained from the analysis of dedicated calibration events.

Pedestal subtraction. The charged FADC slices that are recorded comprise not only Cherenkov photons, but also fluctuations of the LONS (cf. sect. 3.2.2) and photons from sources of light close to the telescope (artificial light from bypassing cars, stray light, etc.). The pedestals comprise fluctuations induced by this background and noise induced by the readout chain. Whenever a signal is not big enough to enable the low–gain recording (cf. sect. 4.3), no Cherenkov signal is contained in the second half of the FADC readout window (fig. 5.1). Therefore, these FADC samples are evaluated and, if found not to contain an accidental signal, a charge extraction yields a pedestal reading, as discussed in sect. 4.3. In this way no dedicated pedestal runs are necessary (except for initial pedestal runs to accumulate a startup set of pedestals). The mean pedestal for each pixel and event is determined by averaging over the 500 closest pedestal values.

Charge extraction. To attribute a certain charge to a given air shower signal, different algorithms can be used. The extractors should both minimize the influence of night sky background (NSB) on the signal and have bias as small as possible. Details on the different extraction algorithms implemented for MAGIC are given in [Bar05].

- A *fixed window* extractor adds up the charges in a given number n of FADC slices. n and the window position have to be chosen such that the signal is neither truncated nor missed. While the reconstructed signals do not have any bias, provided a window has been chosen which contains the whole signal, the noise contributions are intrinsically higher than when using other extraction methods.
- The *sliding window algorithm* searches for the maximum integral charge content of n consecutive pedestal-subtracted FADC samples. This is done on a pixel-to-pixel

basis, so that the changing arrival time of the Cherenkov light of a large shower on the PMT camera is automatically taken into account. Without timing information, however, also light not caused by the shower itself (with an atypical pulse shape) might be extracted or can influence the signal extraction. To minimize the NSB pickup, n would be chosen as small as possible. The extractor determines an event arrival time as the average of the individual FADC slice times, weighted with the FADC slice charges.

- The *digital filter* calculates the extracted charge and the pulse timing as the weighted sum of n consecutive pedestal-subtracted FADC samples. The weights are determined by the expected pulse shape of the signal. The method relies on knowledge of the normalized signal shape, which is obtained from Monte Carlo generated events. This method is not appropriate if the signal arrives very early in the FADC digitization window.

- A cubic *spline* extractor interpolates the pedestal–subtracted charges in the FADC slices. As a reconstructed signal, either the amplitude of the spline maximum or the integral of the spline centered on the spline maximum can be used. Either the position of the spline maximum or the pulse half maximum on the rising edge of the position of the pulse is used as the signal arrival time.

As both the digital filter and the spline extractor are based on the selection of the highest FADC sample(s), they will be biased by construction towards mistaking LONS fluctuations with small signals. Still, they are regarded to be preferable to unbiased extraction strategies, which would have to sum up a higher number of FADC samples and thus pick up unnecessarily much more LONS.

In the analyses presented in this thesis, the digital filter has been used for signal extraction. Whenever the signal arrived very early in the FADC digitization windows, the spline extractor was used instead.

5.3 Calibration

To convert the extracted charge in FADC counts and the signal time in FADC clock ticks to a charge in photoelectrons and an absolute signal time, respectively, conversion constants have to be obtained and applied to the data [Gau05].

The excess noise factor method. From calibration events triggered by the calibration system (cf. sect. 4.4), these constants are determined by the excess noise factor method (F factor method). Assuming a Poissonian variance of the number of incoming photons, a uniform photon detection efficiency and a constant excess noise introduced by the

gain fluctuations, the mean number of photoelectrons $\langle n \rangle_{\text{ph.el.}}$ reaching the first dynode is given by [Mir97]:

$$\langle n \rangle_{\text{ph.el.}} = F^2 \frac{(\langle Q \rangle - \langle P \rangle)^2}{\sigma_Q^2 - \sigma_P^2} \tag{5.1}$$

with the mean charge of the distribution $\langle Q \rangle$, its standard deviation σ_Q, the pedestal $\langle P \rangle$ and the error σ_P introduced by LONS fluctuations, electronic noise and extractor uncertainties (all in FADC units). The excess noise factor F is defined as

$$F = \sqrt{1 + \frac{\sigma_G^2}{\langle G \rangle^2}} \tag{5.2}$$

and originates in the statistical fluctuations in the amplification of the electrons in the PMT dynode system. $\langle G \rangle$ and σ_G can be measured in the laboratory by using the single photoelectron response of PMTs. This method does however only provide the relation between FADC counts and the number of photoelectrons released in the PMT. Hence it does not cover the photon to photoelectron conversion efficiency and losses due to the plexiglass entry window of the PMT camera and the light collectors. The net conversion factor between photoelectrons and photons (the overall quantum efficiency) used is 0.18 ± 0.02.

The absolute light calibration. For a full calibration of the pixel chain, the light input to the PMT camera has to be known. Therefore, a calibrated 1 cm^2 PIN diode is illuminated simultaneously with the PMT camera.

Muon ring analysis. By reconstructing ring images of isolated muons hitting the telescope, the energy of the muons can be determined and compared with Monte Carlo predictions. This allows an alternative global absolute light collection efficiency calibration [Ros95, Goe05b]. In addition, muon images can be used to derive the optical point spread function (PSF) of the telescope, i.e. the image expected from point-like sources. Full muon ring images are recorded during data taking at a rate of about 2 Hz.

Calibration system operation. Prior to observing a particular source, the PMT camera is uniformly flashed by a UV LED system. These calibration pulses are used to calculate the relative calibration constants. Additionally, interleaved calibration events are taken during normal data taking at a frequency of 50 Hz. These events are used to recalibrate on a shorter timescale than that on which fluctuations in the optical signal transmission system occur.

5.4 Event reconstruction and background rejection

The majority of the recorded events comprise LONS fluctuations, events triggered by hadronic showers, and to a lesser extent isolated muon events. Hadronic showers are

more abundant by some orders of magnitude than electromagnetic showers.

5.4.1 Image cleaning and reconstruction

Most of the pixels in the camera do not contain information of the air shower candidate that triggered the readout of the event, but only fluctuations of the LONS. Those pixels have to be rejected in order to reconstruct an image of the air shower. This is vital as the subsequent parameterization of the image employs only the signal content of the pixels, without its corresponding errors. The image cleaning consists of four steps:

- Bad pixel treatment: About 4% of the pixels cannot be correctly calibrated because of hardware problems or because they contain a bright star. They are mostly flagged as *bad pixels* by the calibration, but can also be flagged manually. If a bad pixel has at least three correctly calibrated neighboring pixels, its signal is set to the average signal of these neighbors. Otherwise, the signal is set to zero.

- Shower core determination: All pixels i which fulfill the condition $S_i > S'_{\mathrm{Core}}/N_i$ and have at least n_{min} neighboring other pixels fulfilling this condition are tagged as *core pixels*. S_i is the charge content in pixel i and N_i the noise in that pixel. n_{min} usually is set to 2. More than one core is allowed; for hadronic showers such shower substructures are even expected frequently while γ-ray showers only rarely have substructures.

- Shower boundary determination: All pixels which are not tagged as core pixels, but fulfill the condition $S_i > S'_{\mathrm{Boundary}}/N_i$, and have at least one neighboring core pixel are tagged as *boundary pixels*.

- Cleaning. The charge of all non–tagged pixels is set to zero.

S_i denotes the calibrated signal in a given pixel in units of ph.el. There are different cleaning approaches. For *scaled cleaning*, the present noise N_i is estimated by the respective pedestal RMS of the pixel and S'_{Core} and S'_{Boundary} become thresholds for the signal to noise ratio in the pixels. A more robust cleaning requires an absolute number of photoelectrons (N_i is then set to 1). In this thesis, such an *absolute cleaning* with $S'_{\mathrm{Core}} = 7$ ph.el. and $S'_{\mathrm{Boundary}} = 5$ ph.el. has been used. Fig. 5.2 shows an event before and after the cleaning procedure.

There are additional options for the cleaning procedure, like allowing more than one ring of boundary pixels or imposing requirements on the arrival time differences in the surviving pixels.

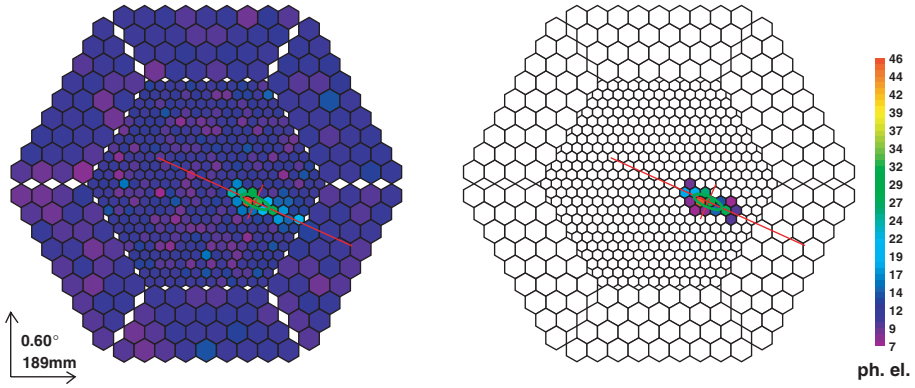

FIGURE 5.2: *An air shower event before and after image cleaning. The Hillas ellipse with its major axis and minor axis is also shown.*

5.4.2 Image parameters

The gamma–hadron separation is based on *image parameters* obtained from the moments of the light distribution in the pixels that survived the image cleaning. This method was first put forward in [Hil85]. The imaging technique in connection with the image parameterization led to the first detection of a VHE γ-ray source with Cherenkov telescopes [Wee89].

The *Hillas parameters* (fig. 5.3) include:

SIZE: The overall light content of the image is parameterized by the total number of photoelectrons contained in it. This parameter is in first approximation proportional to the energy of the primary particle. The size–energy relation also depends on the impact parameter b of the shower; this dependence is weak below $b \approx 120$ m and below energies of a few TeV.

LENGTH: A measure of the length of the air shower image, given by the RMS value

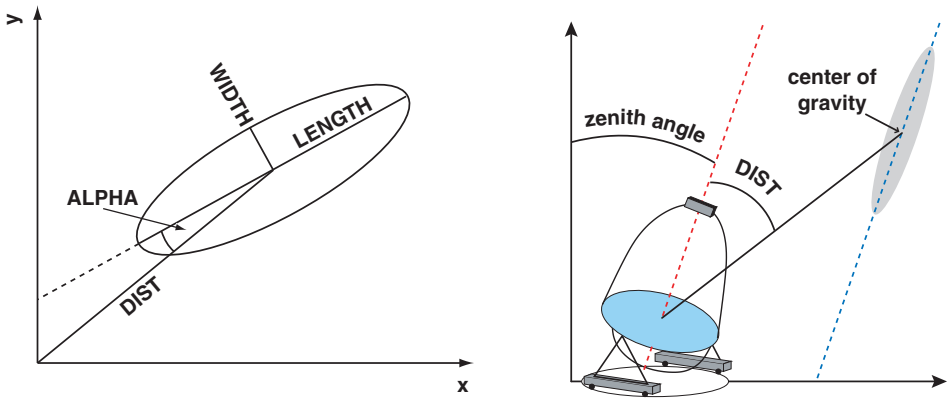

FIGURE 5.3: *The Hillas parameters* LENGTH, WIDTH, DIST, *and* ALPHA.

of the charge distribution along the major axis of the shower image. Note that LENGTH generally is larger for hadron-induced showers than for γ-induced showers.

WIDTH: A measure of the width of the air shower image, given by the RMS value of the charge distribution along the minor axis of the shower image. Due to the larger transversal momentum in hadron–induced air showers, their comparatively larger width is one of the key characteristics that the gamma–hadron separation exploits.

CONC*n*: The ratio of the light content of the *n* pixels with the highest light yield to the total light content. These parameters describe the compactness of the shower maximum region. For γ-ray induced air showers this region ought to be very compact, such that CONC can be helpful for the gamma–hadron separation.

M3LONG: The third moment of the image along its major axis. M3LONG > 0 means that the shower head is closer to the camera center than the shower tail. For low SIZEes < 200 ph.el. this parameter is not very meaningful because of its rather large statistical fluctuations.

LEAKAGE: Very large events might not be fully contained in the camera. The LEAKAGE parameter is given by the ratio of light content of the pixels belonging to the respective event in the outermost pixel ring and the total light content of the shower. This parameter is important for the energy estimation of larger (high energy) showers. At low zenith angles LEAKAGE can take values exceeding 0.5 at a few TeV, making energy estimations rather unreliable in the multi-TeV region. Thus the high energy end up to which showers can reliably be reconstructed is given by the size of the PMT camera. To extend observations to higher energies, LZA observations can be employed (cf. sect. 3.4).

The parameters LENGTH, WIDTH, CONC and SIZE describe the shape and light content of the shower, while two additional parameters, ALPHA and DIST, relate to the orientation and position of the shower in the camera. Thus, the latter parameters depend on the expected source position in the camera. In case of ON/OFF data taking, usually the source position coincides with the camera center, whereas for Wobble data taking the source position is displaced from the camera center.

ALPHA: The angle between the main shower axis and the connection line from the source position to the center of gravity of the image. The orientational parameter ALPHA becomes very small if the shower axis and the line connecting the reflector center and the source position in the camera lie within one plane. As events with small ALPHA point towards the source position, it is one of the most powerful parameters for the gamma–hadron separation. The uncertainty on ALPHA is mainly governed by the finite size of the pixels and by signal fluctuations ($\propto 1/\sqrt{\text{SIZE}}$).

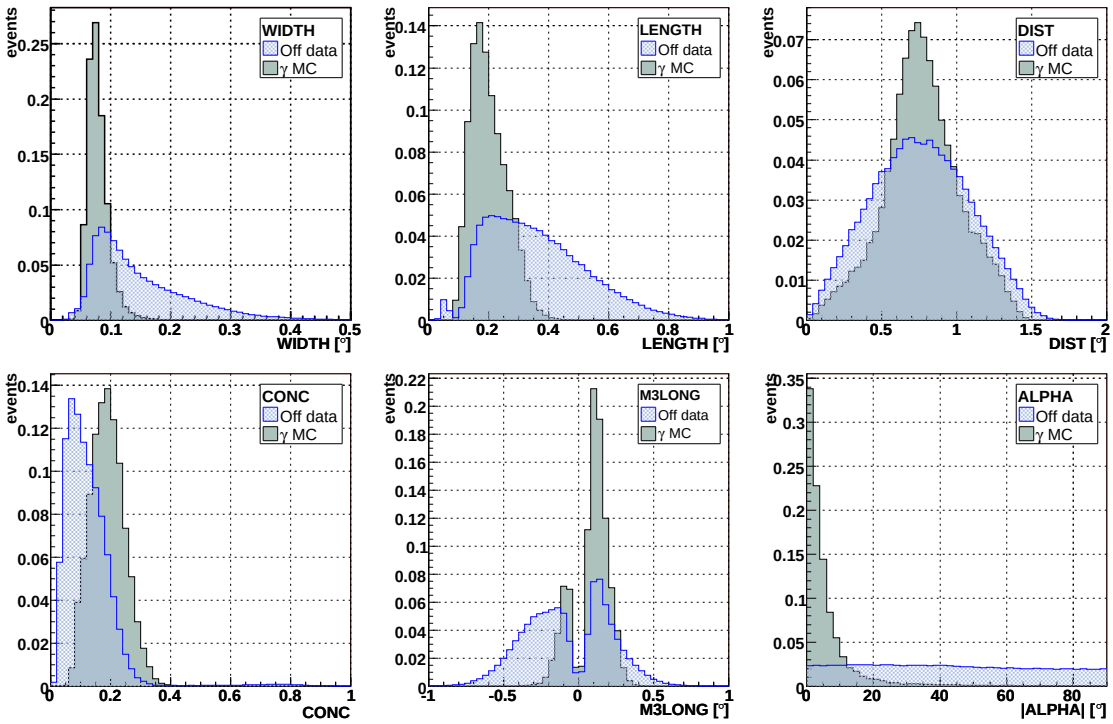

FIGURE 5.4: *Comparison of Hillas parameter distributions in* LENGTH, WIDTH, DIST, CONC, M3LONG, *and* ALPHA *of MC* γ *and hadronic background data (taken from the PG 1553+113 analysis presented in sect. 9). The parameters are given for* SIZE > 200 ph.el. *The discussed background rejection method is not only based on finding differences in the distributions of the single image parameters, but also takes into account correlations between the parameters.*

DIST: The distance between the source position and the center of gravity of the image. It describes the angle between the source position and the shower maximum. Thus for parallel showers with identical energy, it is correlated with the impact parameter of these showers. The parameter is important for the energy estimation in case of single telescope installations.

5.4.3 Rejection of the hadronic background

For the separation of the γ-ray induced shower events from the much more abundant background given by events induced by cosmic ray showers, isolated muons and LONS fluctuations, the differences between these two classes of images have to be determined and appropriately used to classify the events. Fig. 5.4 compares selected image parameter distributions of MC (γ) and background events. The apparent differences have to be used to discriminate them against the hadronic background.

Statistical learning methods are powerful tools to reject background while retaining high signal efficiencies [Zim05]. The most commonly used method for background separation

in IACT experiments [Feg97] is based on static, dynamical, or scaled cuts in the image parameters. The latter two methods are quite similar and assume parameterized dependencies on other image parameters. The cuts are trained either on strong γ-ray sources or on MC γ data samples.

In this thesis, a technique based on the Random Forest^{TM} (RF) method [Bre01, Bre04, Boc04, Hen06] is used. Its conceptual difference compared to dynamical or scaled cuts is that the cuts are not parameterized. Instead of applying an independent cut to each image parameter, a forest of decision trees is used to classify each event. Thus the RF method uses all the parameters simultaneously, automatically taking into account correlations.

MC γ-ray events and real hadronic background data samples (subjected to a lower size cut of 200 ph.el.) are used to create the decision trees. The individual trees are grown by successively choosing random image parameters and finding a cut in each of these parameters that minimizes the Gini index [Gin21]

$$Q_{\text{Gini}} = 2\left(\frac{N_{\text{signal}}^{\text{survived}} N_{\text{background}}^{\text{survived}}}{N^{\text{survived}}} + \frac{N_{\text{signal}}^{\text{rejected}} N_{\text{background}}^{\text{rejected}}}{N^{\text{rejected}}}\right)$$

where N^{survived} denotes the number of events that survived the given cut and N^{rejected} denotes the number of rejected events. A random forest typically comprises 100 uncorrelated trees.

In the presented analyses, each of the trees grown uses three image parameters randomly chosen among the included image parameters SIZE, WIDTH, LENGTH, CONC5, M3LONG and DIST. It should be noted that prior to the training, the SIZE distributions of the two training data sets are made equal, such that the RF training does not train on possible differences in the SIZE distribution, but only exploits correlations of SIZE with other parameters. The directional parameter ALPHA is not used in the RF training, as correlations with other parameters are assumed to be small and the parameter is later on used to remove irreducible background.

The discrimination power of the individual parameters can be characterized by the decrease of the Gini index (fig. 5.5). As expected from the properties of electromagnetic and hadronic air showers, WIDTH and LENGTH are the key parameters for discrimination. The high discrimination strength of SIZE can be explained as it serves as scaling parameter for WIDTH and LENGTH, i.e. scaled width and length are the effective image parameters.

MC–data comparison. For the training of the background rejector it is essential that the γ sample offered to the RFs resembles real γ events as closely as possible. Fig. 5.6 shows the comparison of image parameter distributions of a MC γ sample and γ candidate events from real data (Crab nebula data of 2005 September 29). As comprehensive studies

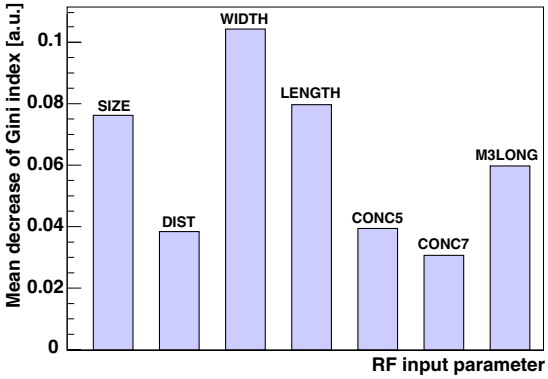

FIGURE 5.5: *Importance of RF input parameters measured by the mean decrease of the Gini index.*

show [Maj05], there is reasonable agreement between the observed γ-ray excess and the simulated γ-ray events.

Event classification. The decisions of all (i) trees are combined to classify an event, yielding one parameter $h \in [0;1]$ called hadronness. h is related to the event's probability of not being a γ-ray event and is given by

$$h = \frac{\sum_{i=0}^{N^{\text{trees}}} l_i}{N^{\text{trees}}}$$

where $l_i \in \{0;1\}$ represents the decision of tree i ($l = 1$: hadron, $l = 0$: γ). A cut in hadronness is then equivalent to a cut in the multidimensional parameter space of the image parameters included in the RF training.

The application of the decision trees to an independent MC sample can be used to study the efficiency of the gamma–hadron separation. Fig. 5.7 shows the typical h distributions for MC gammas and OFF (background) data samples. The integrated hadronness for γ and OFF events as given in fig. 5.8 represents the acceptance for signal-like and background-like events. The cut efficiency for a given hadronness can be computed from that plot.

In fig. 5.9 we show an ALPHA distribution of a γ-ray source subjected to different cuts: A set of quality cuts which only removes non-genuine shower events and three cuts of different hadronness values. The plot also contains the resulting γ survival probability or γ efficiency ε_γ, the hadron rejection factor R_h and the quality factor, which is defined as $Q = \varepsilon_\gamma \cdot \sqrt{R_\text{h}}$.

As the γ efficiency depends on the hadron rejection power, comparisons are usually made at a γ efficiency of $h = 0.5$. The chosen cut in hadronness is usually dependent on the gamma energy and is determined by optimization on either a MC gamma sample or on data of a strong source like the Crab nebula. The parameter to be optimized can be chosen among the signal significance, the gamma efficiency or combinations thereof. For

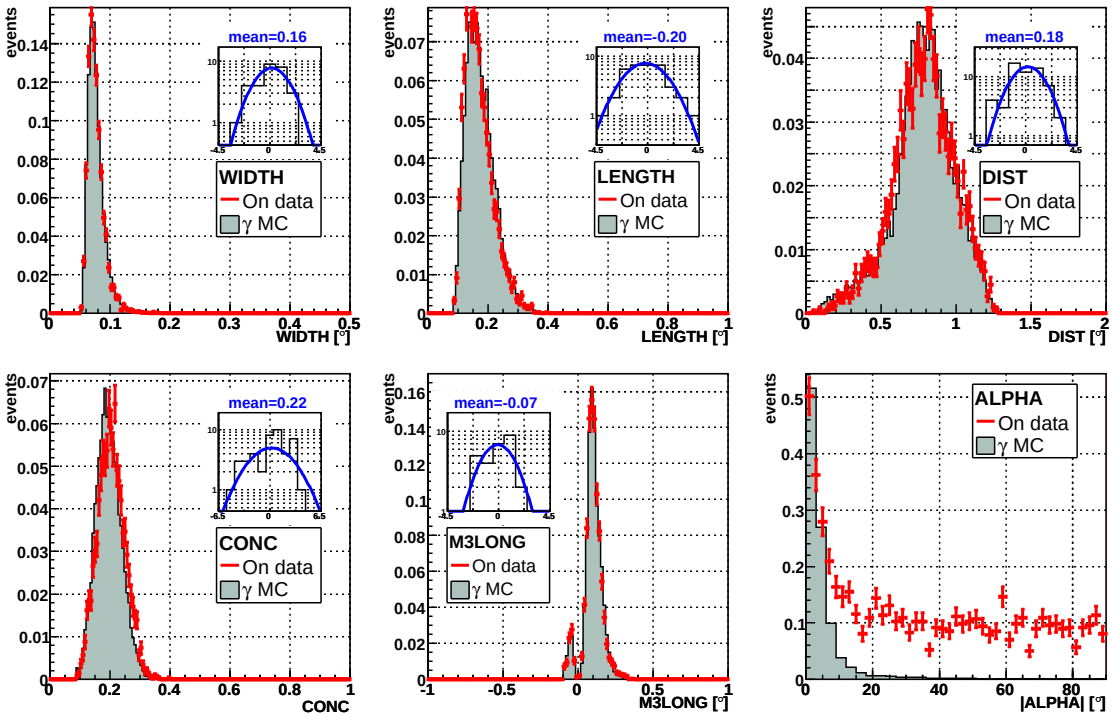

FIGURE 5.6: *Comparison of distributions for MC γ-rays (shaded histograms) and for observed γ-ray excess events (red histograms) for* SIZE $>$ 350 ph.el. *in terms of distributions of the image parameters* WIDTH, LENGTH, DIST, CONC2, M3LONG, *and* ALPHA. *The inset histograms show Gaussian fits to the error–weighted differences of the respective MC and data distributions. The* ALPHA *parameter (lower right plot) plays a special role, as it is used for discriminating against irreducible background, which is not simulated. The two samples show reasonable agreement in the image parameters.*

the discovery of new sources, significance-optimized (hard) cuts are usually selected, whereas loose cuts are usually preferable for the determination of spectra and light curves because they allow for a high gamma efficiency and thus higher γ-ray statistics.

For the production of sky maps, source–dependent image parameters like ALPHA and DIST are not included in the training parameters. This is done in order not to bias the training towards a certain sky position. DISP, a function of SIZE, WIDTH, and LENGTH is used instead (see sect. 5.4.5 for the definition of DISP).

An appropriate cut in h yields a sample retaining most of the γ-candidates while suppressing a large fraction of the hadronic background. Finally, a cut in ALPHA, the angle between the shower major axis and the line connecting the shower center-of-gravity with the source location in the field of view, further suppresses background (overall cut efficiency, i.e. γ survival efficiency: $\approx 60\%$).

At lower energies the discrimination power between γs and hadrons becomes weaker, because γ and hadron images look more and more similar. In addition, the ALPHA distributions broaden, since the shower images contain fewer PMT pixels and thus the re-

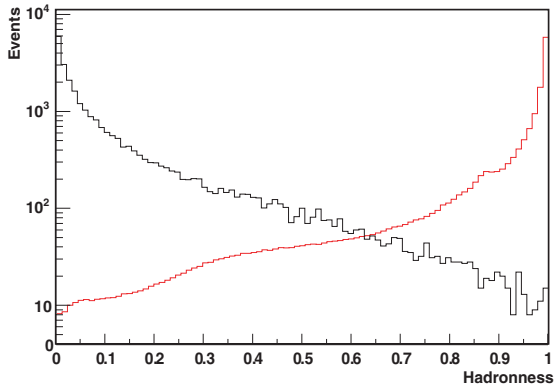

FIGURE 5.7: *Hadronness distributions for MC gammas (black) and* OFF *data (red)*

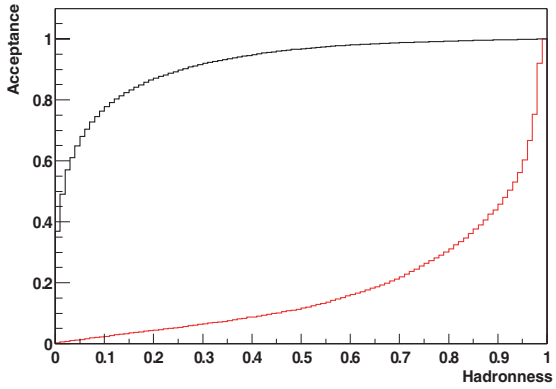

FIGURE 5.8: *The integrated hadronness yields the acceptance for signal-like and background-like events when cutting at a fixed hadronness for background rejection.*

construction of the shower direction deteriorates. The cuts in h and ALPHA are therefore chosen to depend on the reconstructed energy.

Below 100 GeV, γ/background separation becomes more difficult for several reasons: The Earth's magnetic field gradually distorts the shower images, the fluctuations of the shower structure increase, more compact and smaller images occur and, furthermore, contributions from cosmic electrons and single energetic π^0 induced showers from hadronic interactions increase where all other secondary particles are below the Cherenkov threshold.

All these effects require further studies for a good γ/background rejection below 100 GeV. It should also be mentioned that the majority of low-altitude muon-induced images could easily be rejected, but quantitative numbers are not yet available. High-altitude muons are however difficult to discriminate.

5.4.4 Energy reconstruction

The recorded light content of γ-ray-initiated air showers with an impact parameter $b <$ 120 m is in first order proportional to the initial energy. Additional dependencies exist on the zenith angle under which the event is observed, on the impact parameter and on the atmospheric extinction.

For the energy estimation, a set of random forests is used [Hen06]. A MC γ-ray data set with known simulated energy of the primary γ events is filled in fine bins of logarithmic energy. For each of those bins, respectively, a classifier is trained to discern events that belong into that particular energy bin from those which do not. The parameters given to the RFs for training are log(SIZE), DIST, WIDTH, LENGTH, log(SIZE/(LENGTH $\times$

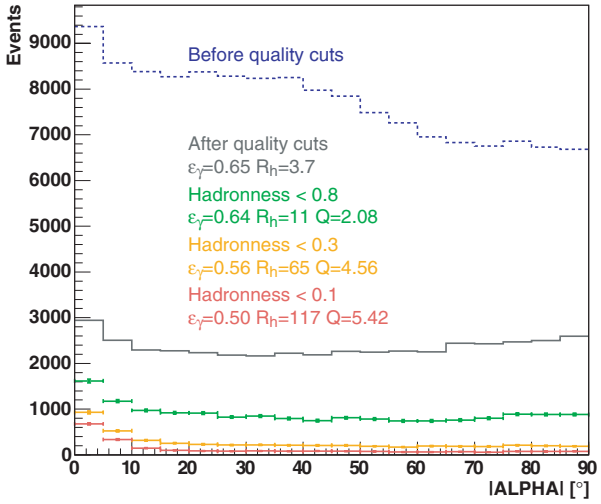

FIGURE 5.9: ALPHA *distributions (of a strong* γ*-ray source) before any cuts, with "quality cuts" applied and for different hadronness cuts of* $h \leq 0.8$*,* $h \leq 0.3$*, and* $h \leq 0.1$*.* ε_γ *denotes the* γ *survival ratio (*γ *efficiency),* R_h *the hadron suppression factor, and* $Q = \varepsilon_\gamma \cdot \sqrt{R_h}$ *the quality factor.*

WIDTH)), CONC, LEAKAGE, and the zenith angle.

After training, each classifier i should recognize a specific energy range and yield a parameter h_i analogous to the hadronness discussed in sect. 5.4.3. By applying the classifiers to observational data, the event-based estimated energy is given by

$$E_{\text{est}} = \frac{\sum_i E_i h_i}{\sum_i h_i}$$

Fig. 5.10 shows the estimated energy as a function of true (simulated MC) energy. The observed finite energy resolution and bias (fig. 5.11) require corrections of energy–dependent distributions (unfolding) when analyzing real data. Fig. 5.12 shows the resolution of the energy estimation, which for $E_{\text{true}} \gtrsim 100$ GeV does not exceed 25%.

5.4.5 Arrival direction reconstruction

The "directional" image parameter ALPHA can be used to determine the deviation of the direction of the shower axis from the reference point in the camera for which it has been calculated. While this method is useful for point–like γ-ray sources, the determination of the source direction or the analysis of extended (non point-like) sources is more complicated, because ALPHA, and other "source–dependent" parameters, like DIST, have to be recalculated to probe other reference points. Therefore, a method first put forward by [Fom94] has been developed in which no assumption about the source position is made. The method exploits the fact that the ellipticity (described by the ratio WIDTH/ LENGTH)

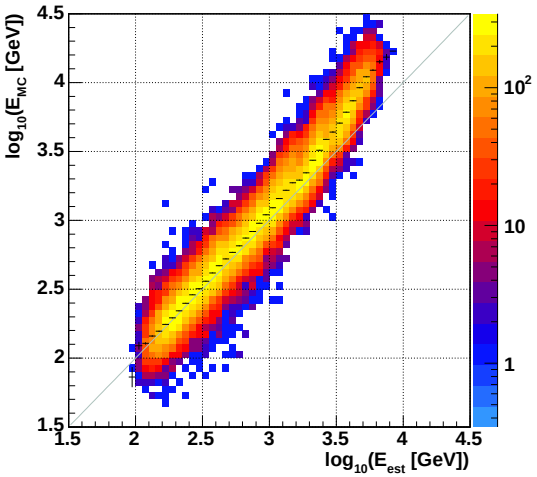

FIGURE 5.10: *Estimated (reconstructed) energy versus simulated ("MC") energy for a MC gamma sample.*

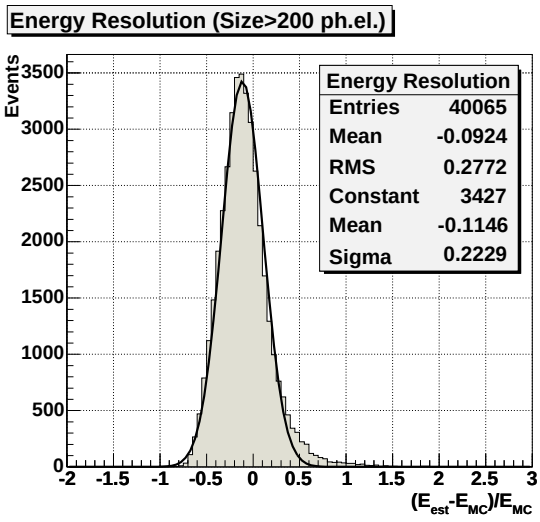

FIGURE 5.11: *Determination of the overall energy resolution of the energy estimator for* SIZE > 200 ph.el.

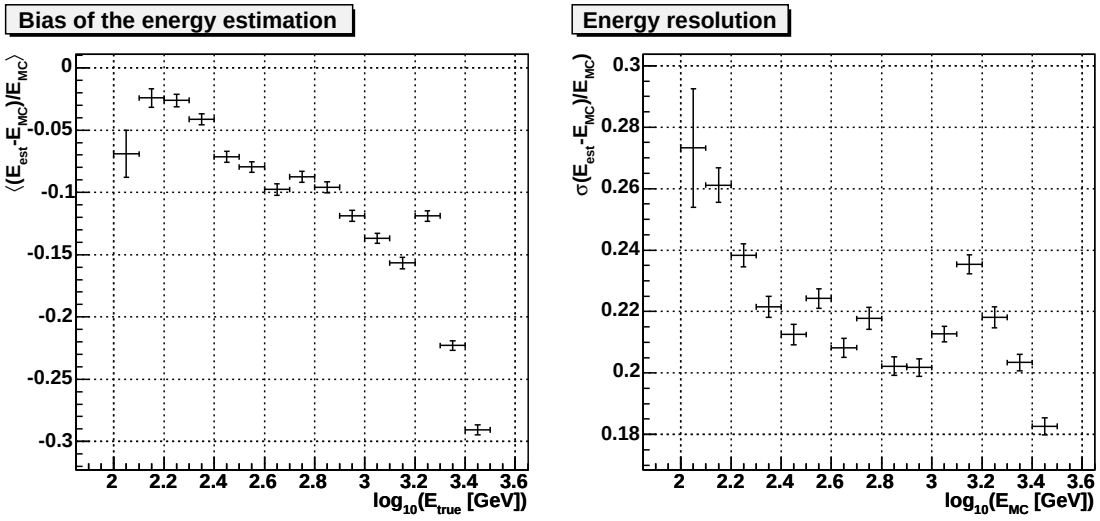

FIGURE 5.12: *Bias and resolution of the energy estimator as a function of energy.*

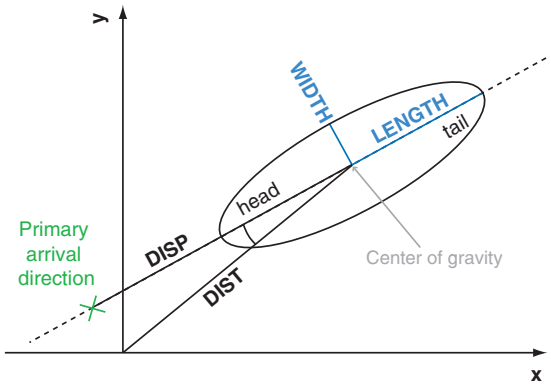

FIGURE 5.13: *The* DISP *parameter for arrival direction reconstruction is defined as the distance between the shower center of gravity and the estimated source position.*

of a given shower image depends on its distance from the source position: The DISP parameter (fig. 5.13) is defined as the angular distance between the source direction and the center of gravity of the shower image along the major axis of the shower image. The larger the DISP parameter, the more elongated is the projected image of the shower in the camera. As the arrival direction of an air shower lies on the major axis of the Hillas ellipse, an adequate parameterization of the DISP parameter (e.g. as given by [Les01] below), can be used to estimate DISP on an event by event basis:

$$\text{DISP} = \left(a + b \cdot \log_{10} \text{SIZE} + c \cdot (\log_{10} \text{SIZE})^2\right) \cdot \left(1 - \frac{\text{WIDTH}}{\text{LENGTH}}\right), \qquad (5.3)$$

The coefficients are obtained from MC γ events, for which DISP $\equiv$ DIST. While the implementation used here is not yet part of the standard MARS analysis, an implementation for MARS is discussed in [Dom05a].

Head–tail information. DISP as defined in (5.3) does not yield information on which side of the shower image the arrival direction lies. Therefore asymmetries in the images have to be exploited to identify the head of the shower, which points to the arrival direction. This is accomplished by using the M3LONG parameter.

Sky maps. Using the DISP method and a proper camera acceptance model, a sky map of the arrival directions of the γ events can be produced (fig. 5.14). For a given event in the ON data sample, the sky position can be inferred by transformation from its arrival position in camera coordinates and its arrival time information. The background model is computed by processing an OFF data sample (assuming a flat distribution in arrival direction before camera acceptance) and computing a camera acceptance distribution from it. To achieve smoother sky maps, they are folded with the γ-ray PSF (angular resolution) of the MAGIC telescope, represented by a bell–shaped (two–dimensional) Gaussian with a radial $\sigma = 0.1^\circ$. This obviously produces an artificial widening of the signal, thought to represent the PSF.

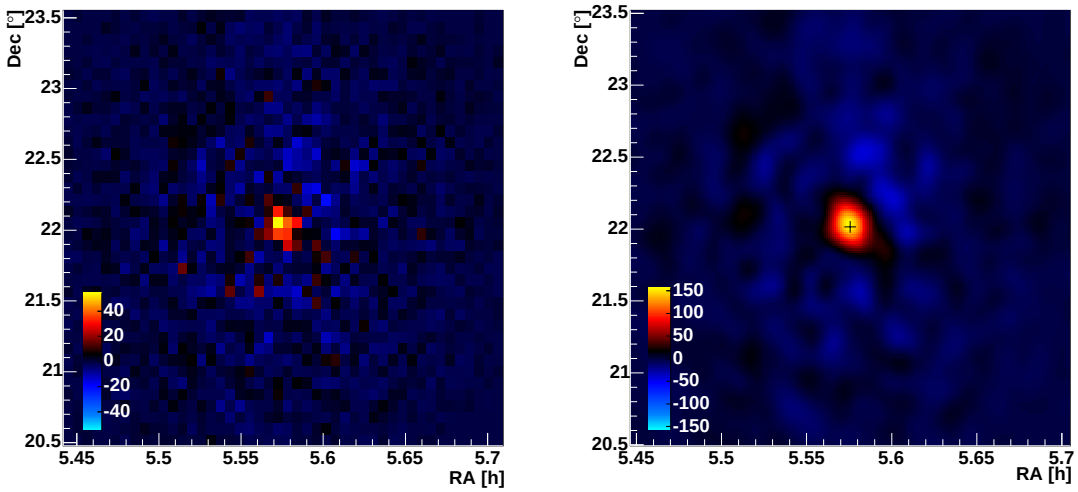

FIGURE 5.14: *Sky maps produced with the* DISP *method. Left panel: A two-dimensional histogram (here of the region around the Crab nebula) of the arrival directions of the* γ *candidate in celestial coordinates is called a sky map. The transformation from local camera coordinates is possible because the current pointing position and the respective event time are known. The color code represents the number of excess events per bin of* $0.^{\circ}056 \times 0.^{\circ}056$ *area. Right panel: Smoothed sky map. The smoothing is done by folding the sky map with a Gaussian with the width of the MAGIC* γ*-ray point spread function. The color code represents the number of excess events per* 10^{-5} sr*, i.e. in a circular area with* $r = 0.1^{\circ}$*. The black cross marks the nominal source position.*

5.5 Signal extraction

After for each event the properties of its primary cosmic ray particle (hadronness, estimated energy, orientational parameter ALPHA and/or arrival direction) have been reconstructed, the gamma excess N_γ in the data set is determined. After gamma/hadron separation cuts, N_{ON} γ-ray candidate events remain, which comprise the excess events as well as a number of irreducible background events. The background events with γ-like image parameters are estimated using a control sample (OFF data set) obtained from the observation of a region in the sky that presumably contains no γ-ray source under the same conditions (same LONS, zenith angle, telescope conditions) as during the observation. After an appropriate normalization of the two data sets by their observation times or the number of events in a normalization region (see below), the γ-ray excess can be determined:

$$N_{\mathrm{Excess}} = N_{\mathrm{ON}} - \eta N_{\mathrm{OFF}} \tag{5.4}$$

with a normalization factor η. The found excess may however have been caused by statistical fluctuations of the irreducible background. Therefore the hypothesis that all observed excess events are compatible with background fluctuations, $H : N_{\mathrm{excess}} = 0$, is tested by a method given by [Li83]. The significance level on which H can be rejected is

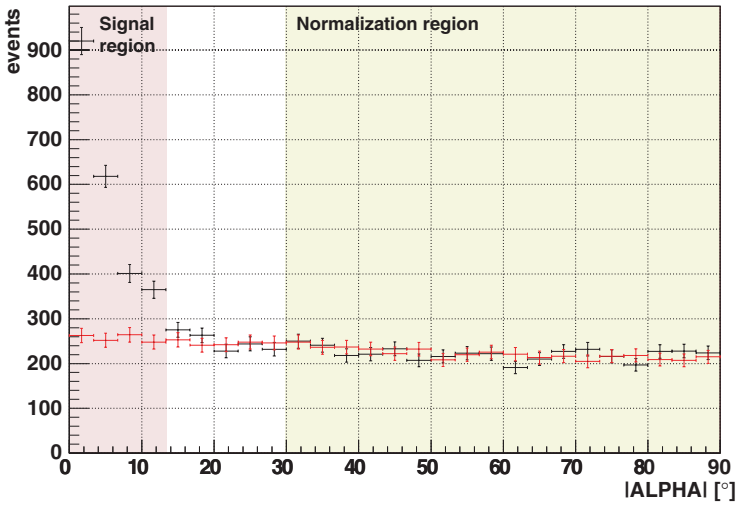

FIGURE 5.15: *Determination of the γ-ray excess by means of the image parameter* ALPHA. *A background control sample (*OFF *data; red data points) is normalized to the data sample containing the gamma candidates (*ON *data; black data points). The γ excess events originating from the pointing direction are expected in the signal region and are determined by subtracting the background contribution from the gamma candidate sample in that region.*

given by:

$$S = \sqrt{2} \cdot \sqrt{N_{\mathrm{ON}} \ln\left(\frac{(1+\eta)N_{\mathrm{ON}}}{\eta(N_{\mathrm{ON}}+N_{\mathrm{OFF}})}\right) + N_{\mathrm{OFF}} \ln\left(\frac{(1+\eta)N_{\mathrm{OFF}}}{N_{\mathrm{ON}}+N_{\mathrm{OFF}}}\right)} \tag{5.5}$$

Specific methods to normalize data and control samples and to determine the number of excess events are discussed in the following.

ALPHA method. The image orientation parameter ALPHA is expected to be small for showers coming from the source direction, while a nearly flat ALPHA distribution is expected for an isotropic background. The width of the excess distribution in ALPHA from events arriving from the source direction is given by the reconstruction accuracy of ALPHA; for SIZE < 200 ph.el., ALPHA cannot be determined very precisely. From MC studies, no showers coming from the source direction are expected with ALPHA $> 30°$. Therefore, the normalization of data and control sample is determined from the region $30° <$ | ALPHA| $< 90°$, see fig. 5.15. After normalization of the samples, a SIZE-dependent cut in ALPHA is chosen to define a γ signal region, in which the normalized control sample is used to calculate the excess events according to formula (5.4).

θ^2 method. Using the image parameter DISP, which is defined as the angular distance between the estimated shower arrival direction and the center of gravity of the shower image in sect. 5.4.5, the quadratic angular distance θ^2 between the estimated shower direction and the source direction can be determined. Normalized θ^2 distributions for a data and a background control sample can then be used to determine the number of events

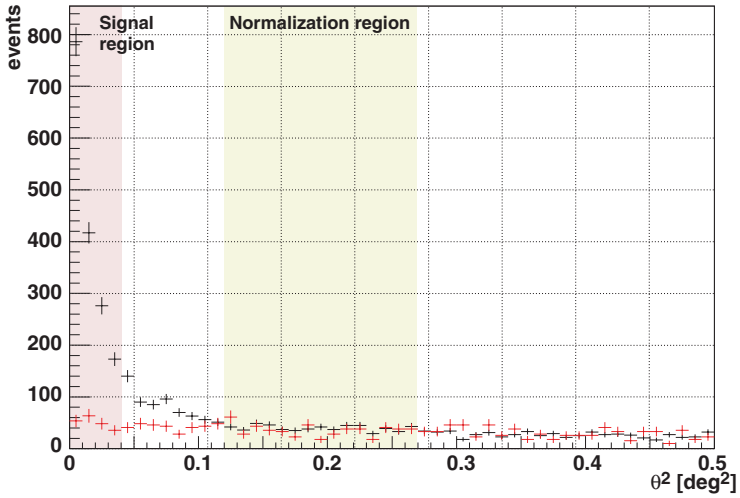

FIGURE 5.16: *Determination of the γ-ray excess by means of the quadratic angular distance θ^2. A background control sample (OFF data; red data points) is normalized to the data sample containing the gamma candidates (ON data; black data points). The γ excess events originating from the pointing direction are expected in the signal region and are determined by subtracting the background contribution from the gamma candidate sample in that region.*

that originated from the direction of the observed source (fig. 5.16). The width of the excess distribution in θ^2 can be used to study the extension of the source by comparing it to the γ-ray PSF of the telescope.

5.6 Spectrum and light curve determination

The differential photon spectrum is defined by the differential γ-ray flux

$$\frac{\mathrm{d}F}{\mathrm{d}E}(E) = \frac{\mathrm{d}N_\gamma}{\mathrm{d}E\mathrm{d}A_{\mathrm{eff}}\mathrm{d}t_{\mathrm{eff}}} \tag{5.6}$$

with the effective collection area A_{eff} (cf. sect. 5.6.1) and the effective observation time t_{eff} (cf. sect. 5.6.2).

Light curve. When the flux is determined in bins of time, the so-called light curve is created. If statistics allow, this can be done fully differentially:

$$\frac{\mathrm{d}F}{\mathrm{d}E}(E,t) = \frac{\mathrm{d}N_\gamma}{\mathrm{d}E\mathrm{d}A_{\mathrm{eff}}(t)\mathrm{d}t_{\mathrm{eff}}(t)} \tag{5.7}$$

As the effective collection area depends on the zenith angle $\theta(t)$ during the observations, it implicitly depends on the time.

Integral flux. Should the statistics not allow the measurement of a fully differential spectrum, integral fluxes can be given:

$$F_{E>E_0}(t) = \frac{\mathrm{d}N_\gamma(t)}{\mathrm{d}A_{\mathrm{eff}}\mathrm{d}t_{\mathrm{eff}}}. \tag{5.8}$$

In the following we describe the computation of A_{eff} and t_{eff}. We then discuss the technical implementation of the flux and light curve calculation. Finally, we explain why an energy unfolding of the differential energy spectra is necessary.

5.6.1 Effective collection area

The effective collection area is the area in which air showers can be observed by the telescope folded with the detection efficiency $\varepsilon(E,\theta,\phi,b)$ after all cuts:

$$A_{\mathrm{eff}}(E,\theta) = \int_0^{2\pi}\int_0^{\infty} \varepsilon(E,\theta,\phi,b)\, b\, \mathrm{d}b\mathrm{d}\phi \tag{5.9}$$

with the energy of the primary γ-ray E, the impact parameter b, the azimuth angle ϕ, and the zenith angle θ. Typical effective collection areas (for $\theta < 30^\circ$) are shown in fig. 5.17. Note that the collection area increases with the zenith angle θ (cf. sect. 3.4). While for small zenith angles the effect is negligible, large zenith angle observations ($\theta \gtrsim 45^\circ$) make it necessary to split the analysis into appropriate zenith angle ranges.

The detection efficiency $\varepsilon(E,\theta,\phi,b)$ is obtained from MC simulations by dividing the total number of simulated events by the number of showers surviving a given set of cuts $\mathbb{C}$:

$$\varepsilon(E,\theta,\phi,b) = \varepsilon(E,\theta,\phi,b)_{\mathrm{trigger}} \cdot \varepsilon(E,\theta,\phi,b)_{\mathbb{C}} = \frac{\mathrm{d}N_{\mathrm{survived}}(E,\theta,\phi,b)}{\mathrm{d}N_{\mathrm{simulated}}(E,\theta,\phi,b)} \tag{5.10}$$

In practice the correct determination of the effective collection area relies on the simulation of air showers up to impact parameters b at which the efficiency is expected to drop to zero.

It should be stressed that the efficiency and thus the effective collection area depend on the precise set of cuts used. Therefore, throughout the analysis chain, no events are discarded due to cuts before the flux determination. The application of cuts only at the flux determination stage ensures that exactly the same cuts are used for MC, data, and background control sample.

5.6.2 Effective observation time

For a given number of events n during an observation time t_0, the effective observation time t_{eff} is defined as the time in which the same number of events would be recorded by

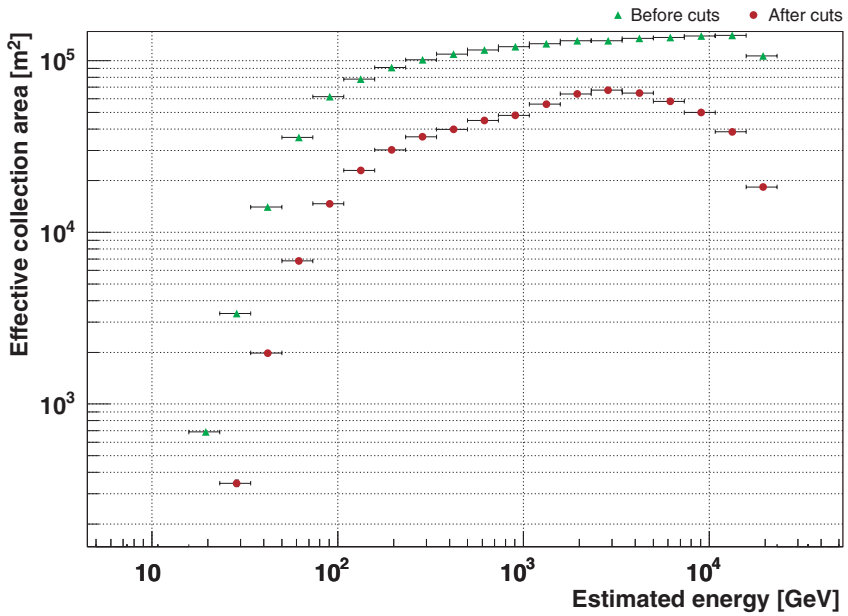

FIGURE 5.17: *Typical effective collection areas before and after cuts.*

an ideal detector:

$$t_{\text{eff}} = \frac{n}{\lambda} \tag{5.11}$$

In the MAGIC standard analysis, the event rate λ is determined by fitting the distribution of time differences of consecutive events by an exponential function

$$\frac{\mathrm{d}n}{\mathrm{d}t} = n_0 \cdot \lambda \cdot \mathrm{e}^{-\lambda t} \tag{5.12}$$

in a region of time differences t where the distribution is exponential. This method allows for non–constant dead times. The exponential fit, however, requires a constant event rate; therefore it is performed for small periods in which no rate change is expected. The determined observation times are then added up. Fig. 5.18 shows a typical distribution of time differences Δt (taken from 519.9 s of 1ES 2344+514 data, cf. sect. 8) along with the exponential fit. The effective observation time was determined to be $t_{\text{eff}} = 513.6$ s.

5.6.3 Flux and light curve determination

Required inputs for the flux determination are:

1. A sample of observational data, either ON data or wobble data
2. Optionally a background control sample (OFF–data)
3. An independent sample of MC γ data in order to compute effective collection areas

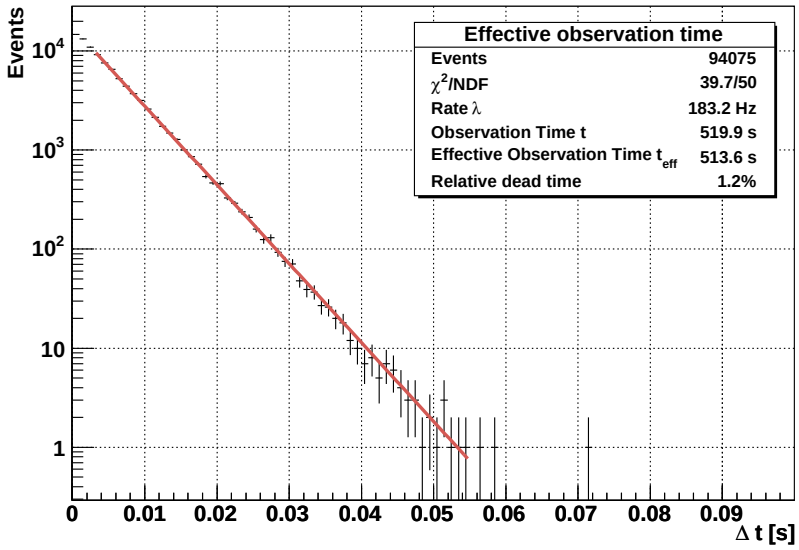

FIGURE 5.18: *Determination of the effective observation time by a fit to the distribution of the event time differences. The resulting inverse event rate, when multiplied with the number of events, yields the effective observation time.*

4. A set of cuts, including gamma/hadron separation cuts and excess determination cuts. To make sure identical cuts have been applied to data and MC, the analysis chain prior to the flux calculation only tags the events with hadronness information, but does not apply any cut in the corresponding variable h. The same goes for the directional parameters ALPHA and θ^2, respectively.

For the signal extraction, the angular variable to be used can be chosen among ALPHA and θ^2. To determine the background events in the signal region, techniques such as those presented in sect. 5.5 can be chosen and excesses and their errors will be calculated from pure event statistics.

Gamma selection cuts. For determining the number of γ events, cuts in the ALPHA variable (or θ^2, respectively) and in h are applied. These cuts are SIZE dependent and are either determined by requesting a given minimum γ efficiency ($\varepsilon_{\text{ALPHA,min}} = 0.8$, $\varepsilon_{h,\text{min}} = 0.6$) or manually. It should be noted that absolute h cuts do not mean much, because they depend on the statistics of the training sample. Typical overall cut efficiencies are shown in fig. 5.19.

Quality cuts. The SIZE-dependent upper DIST cut is also determined by requesting a minimum gamma efficiency. Generally a stringent DIST cut is not required. However, in the absence of OFF data the application of a DIST cut is advisable as it flattens the ALPHA distribution, which facilitates the extrapolation of the background level into the signal region. An absolute upper DIST cut, however, is useful to remove very distant

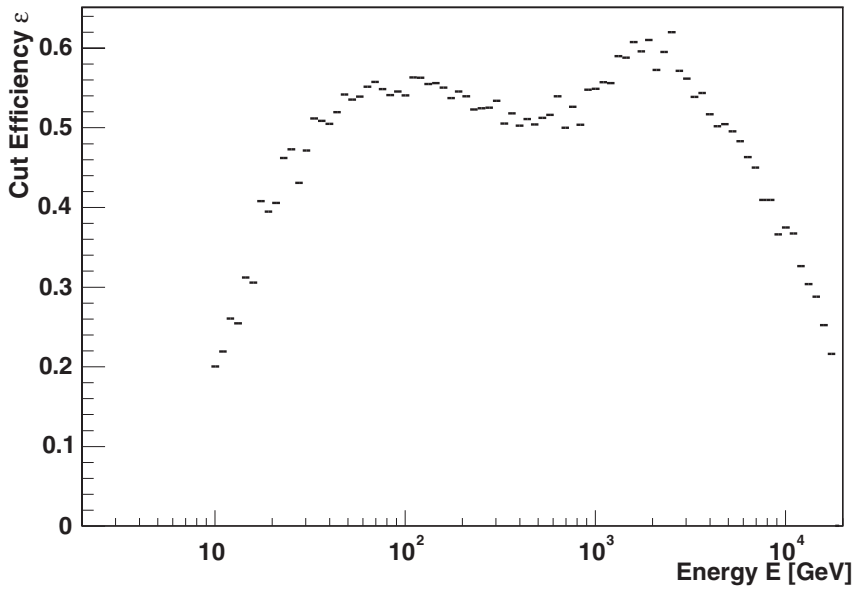

FIGURE 5.19: *Typical overall cut efficiency for γ events (γ survival probability) as a function of energy for loose cuts as used in flux and light curve calculations. All event selection cuts such as the hadronness h,* DIST*, and* LEAKAGE *cuts are included.*

γ-ray showers for which the energy reconstruction does not work very well. Additionally, a lower DIST cut can be applied.

Flux and light curve determination. The computation of differential energy spectra and light curves follows this basic structure:

1. Find DIST, *hadronness* and ALPHA cut values as a function of SIZE. The cuts are determined by requesting a minimum γ efficiency. Alternatively manual cuts in these variables can be specified.

2. Calculate the effective collection areas from MC γ events. This is accomplished by filling (a) all MC γ events and (b) the MC γ events that survive all γ selection cuts into histograms with fine energy bins (125 bins between 2 GeV and 200 TeV). The collection areas in energy bins used for the flux calculation are determined by weighting the "fine" collection areas with the expected spectral slope. Therefore, it is not necessary to tune the spectral slope of the MC sample.

3. Loop over the data set to determine the time range of the data. The binning for the light curve is created automatically taking into account the requested timescale for the light curve bins. Alternatively a manual binning can be supplied.

4. Read the data sample, apply all analysis cuts and fill the surviving events into histograms with a binning in estimated energy and the zenith angle (or time). Calculate effective observation times. Exactly the same cuts as in step (2) are applied.

5. Read OFF data sample (if requested) for background estimation, apply all analysis cuts and fill the surviving events into histograms with a binning in estimated energy and the zenith angle or in energy and time. Calculate effective observation times. Exactly the same cuts as in step (2) are applied.

6. For each bin of estimated energy and zenith angle (or time) compute the number of excess events either using the ALPHA or the θ^2 cut method. Compute the significance of the excesses.

7. Calculate absolute fluxes as a function of estimated energy and zenith angle (differential energy spectrum).

8. Calculate absolute fluxes as a function of estimated energy and time (light curves).

9. Transform the results computed in units of estimated energy into units of measured (true) energy.

The flux implementation offers the option of calculating

(a) more than one differential energy spectrum at a time. This is particularly interesting if the data set spans over a large zenith angle range, as the shower properties and the energy threshold change with the zenith angle. Ideally, absolute fluxes should obviously be independent of the zenith angles.

(b) more than one light curve at a time. This is useful when dealing with high γ statistics data samples. Then light curves in different energy ranges can be determined, as e.g. done in sect. 7.8.3. The energy ranges for the light curves can be fixed individually.

The spectra are determined in bins of estimated energy. The estimated energy of a γ-ray event is inferred from image parameters as discussed in sect. 5.4.4. Due to the finite energy resolution and the bias of the energy estimation, distributions in estimated energy have to be transformed into distributions in measured (true) energy. This is accomplished in the unfolding step (cf. sect. 5.6.6).

Error propagation. The error on the absolute differential fluxes is propagated from the error on the number of excess events, the effective collection area and the effective observation time in the respective energy bin. In case of light curves, the error on the effective collection area is regarded as a systematic error, as the collection areas for the bins of time are correlated. These correlations are particularly strong in the case of small bins of time.

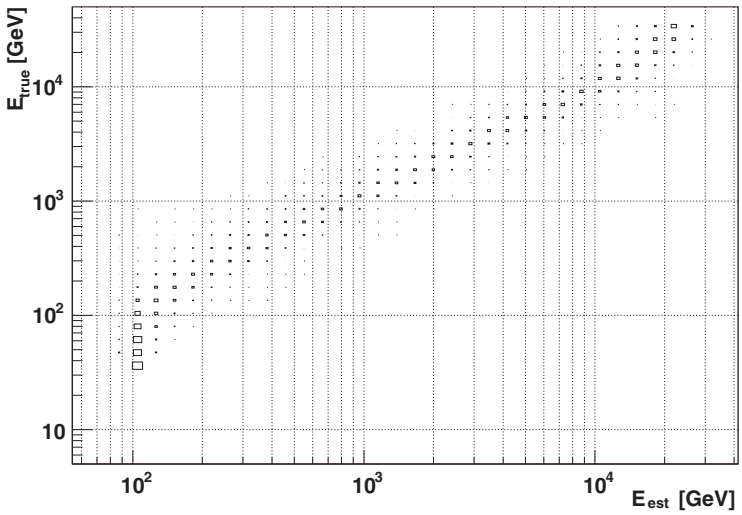

FIGURE 5.20: *The migration matrix describes the migration of events from bins of true energy to bins of estimated energy. It is determined during the flux calculation from an independent MC control sample. During the unfolding procedure, the matrix is used when converting distributions in estimated energy into distributions in true energy. Note the degeneracy towards low energies in the 100 GeV region.*

5.6.4 Monte Carlo tests

The flux determination code has been tested using MC γs. To this end, a differential energy spectrum of a data sample with a simulated spectral slope of $\alpha_{\text{sim}} = 2.6$ has been determined. The slope could be reproduced as $\alpha = 2.60 \pm 0.05$ (fig. 5.21) over an energy range of 40 GeV–4 TeV, which corresponds to the input energy range.

An additional and more realistic test consisted of mixing hadronic background with an amount of MC γs equivalent to that expected from the Crab nebula. The spectrum could be reproduced with a slope of $\alpha = 2.54 \pm 0.10$. In fig. 5.22 we show the respective spectrum along with a fit as obtained from the measured Crab nebula spectrum.

5.6.5 Light curves

Usually the evolution of the integral flux in bins of time is called a light curve. Conceptually, its determination is similar to that of the fluxes. Instead of determining the number of excess events $N_{\text{Excess}}(E,\theta)$ in bins of energy and zenith angle, the number of excess events in bins of time and energy has to be found: $N_{\text{Excess}}(E,t)$. Both approaches are equivalent, as the zenith angle $\theta(t)$ is a function of time. In the case of small time bins, the zenith angle can be assumed to be constant in each time bin; this is not possible for large bins of time, as they are needed for light curves spanning over many days. Often time bins covering whole observation nights or even longer periods are required, and, in such cases, θ has to be properly averaged.

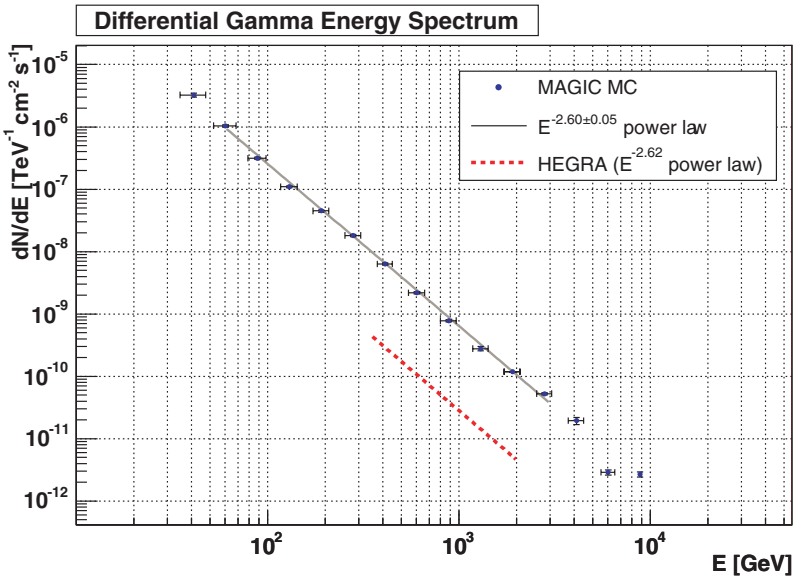

FIGURE 5.21: *Test of the flux algorithm with a power law distributed pure MC γ sample with a simulated spectral slope of $\alpha_{sim} = 2.6$. As no meaningful observation time is available in that test, it was arbitrarily chosen. The spectrum could be reconstructed with a slope of $\alpha = 2.60 \pm 0.05$. Note that the horizontal error bars denote the energy resolution in the respective bin. A power law fit obtained from the measured Crab nebula spectrum has been included for comparison, taken from [Aha00c].*

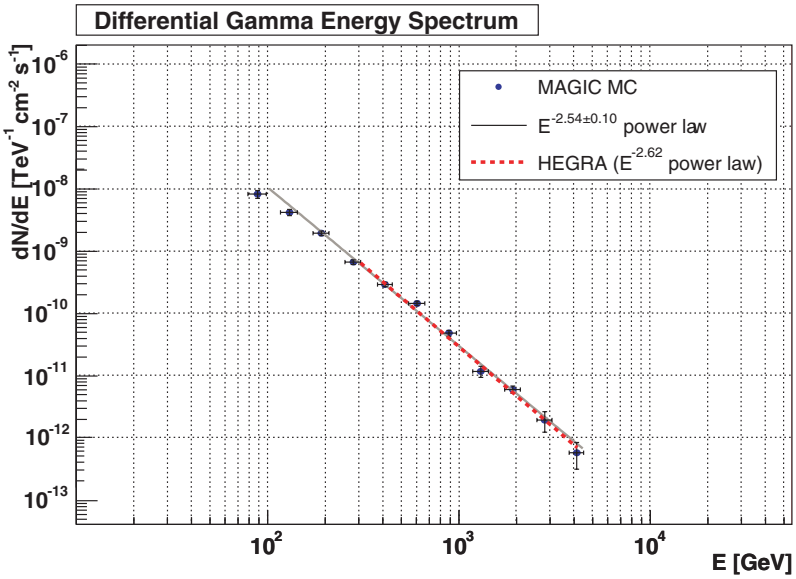

FIGURE 5.22: *Test of the flux algorithm with MC γ and real* OFF *(hadronic) data. The energies of a power law distributed MC γ sample with a simulated spectral slope of $\alpha = -2.6$ were smeared with the MAGIC energy resolution and the sample was mixed with real hadronic background. The amount of γs was chosen so as to resemble a Crab nebula-like source. The spectrum could be reproduced with a slope of $\alpha = 2.54 \pm 0.10$. Note that the horizontal error bars denote the energy resolution in the respective bin. When representing wide–range bins with data points, the correct energy is determined by the method proposed by [Laf95]. A power law fit obtained from the measured Crab nebula spectrum has been included for comparison, taken from [Aha00c].*

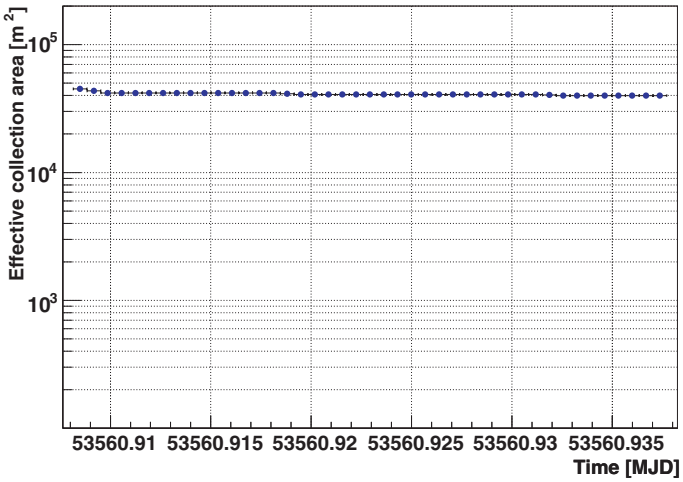

FIGURE 5.23: *Effective collection areas are calculated for each time bin i by determining the average zenith angle θ_i.*

Fig. 5.23 shows the effective collection area in individual 2-minute bins of time. According to expectations, it stays roughly constant for the given example of a low zenith angle observation. Typical control plots for light curve determination are shown in fig. 5.24. Generally in IACT astronomy, a signal of at least 5σ is required in order to claim a significant detection. However, once a γ excess in the data has convincingly been ascertained, the significance of the excess in each individual bin of the light curve needs only to be on the $1.5\sigma - 2\sigma$ level. Equally important is the observation of a Gaussian distribution of the background levels of the individual bins. Explicit long-term and short-term light curves and control plots are shown in sect. 7.6 and sect. 7.8.

5.6.6 Unfolding of the differential energy spectra

Due to the finite resolution and the given bias of the energy estimator discussed in sect. 5.4.4, the reconstructed energy is only an estimate of the true energy of a given event. Therefore, mathematically speaking, any measured distribution in energy is a convolution of a distribution in true energy with a migration matrix M_{ij} (fig. 5.20) that describes the migration of events from bins of true energy to bins of estimated energy

$$N(E^i_{\text{est}}) = \sum_k M_{ij} \cdot N(E^j_{\text{true}}). \tag{5.13}$$

In the case of MAGIC, at the low energy end of distribution in estimated energy, the events suffer from a bad resolution of the energy estimator and a bias towards higher energies—at the trigger threshold mostly such events are likely to trigger whose energy tends to be overestimated. At the high energy end, due to low statistics and the exponential behavior of the energy spectra, even small migrations will considerably alter the differential flux.

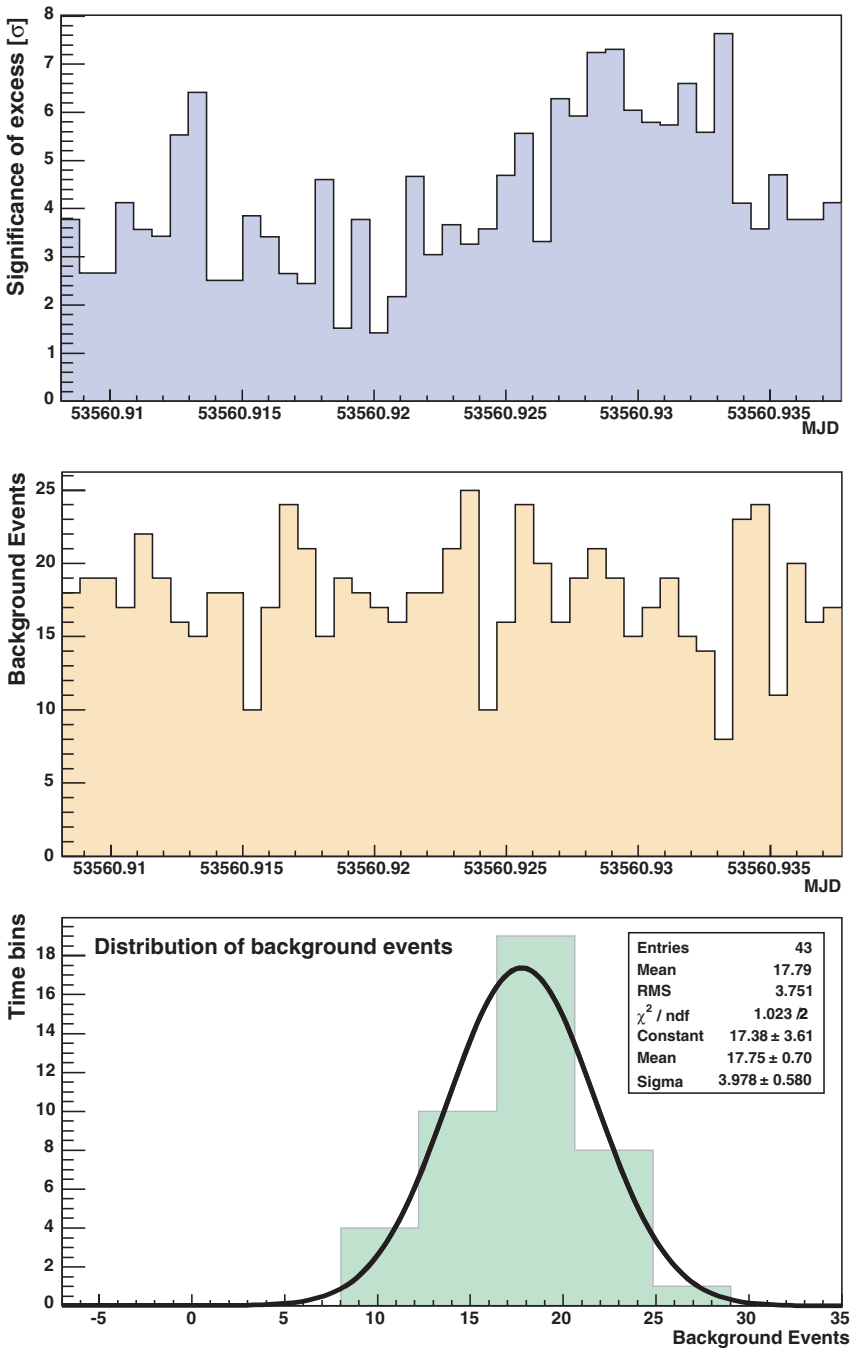

FIGURE 5.24: *Control plots for light curve determination. Upper panel: Significance of the excess in each individual time bin. Middle panel: Background found for the individual time bins. Lower panel: Distribution of background events.*

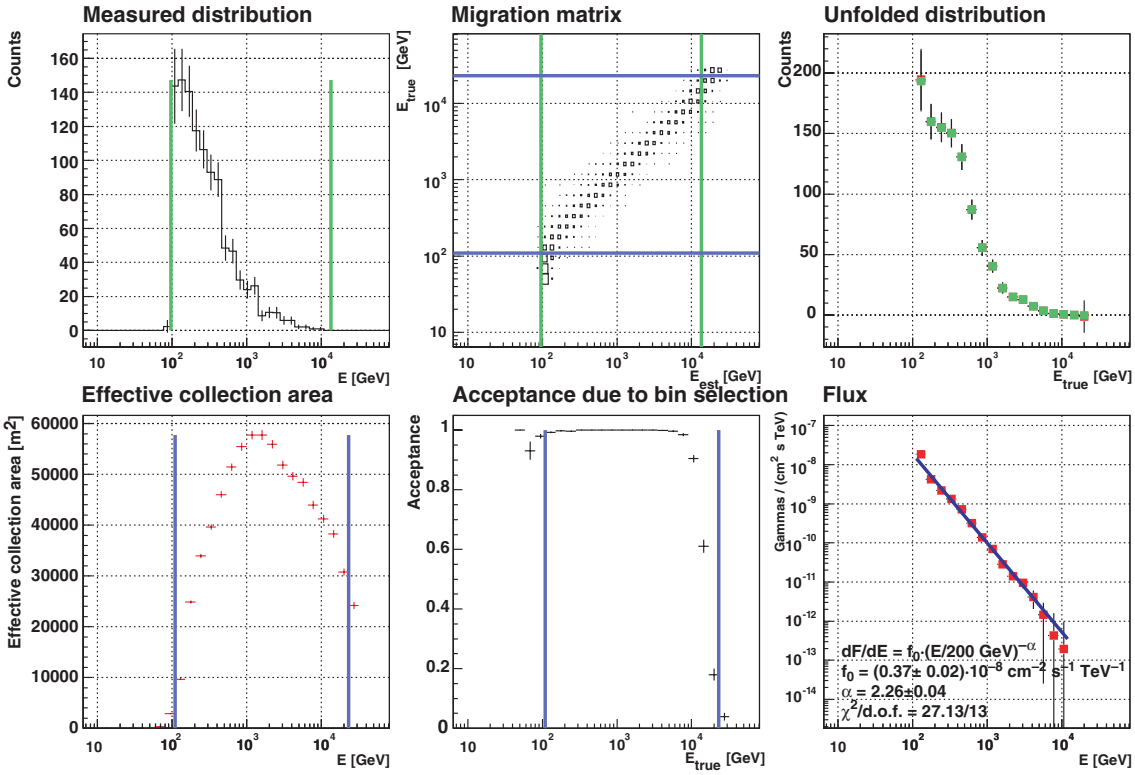

FIGURE 5.25: *Exemplary control plots of the energy unfolding: The upper row of plots shows the measured distribution $N(E_{est})$, the migration matrix M_{ij}, and the corresponding unfolded distribution $N(E_{true})$. Lower plots: Both measured and unfolded distributions may be restricted to a certain energy range (green and blue bars), by inspecting the effective collection area $A_{eff}(E_{true})$ for the unfolded distribution and the acceptance due to the range selection. The resulting spectrum is shown in the lower right panel.*

The task of the unfolding step is to invert the relation (5.13) in order to recover the distribution $N(E_{\mathrm{true}})$ from the measured distribution $N(E_{\mathrm{est}})$. The unfolding methods implemented for MAGIC are discussed in [Ber89, Any91, Sch94, Miz05]. Control plots for the unfolding step are shown in fig. 5.25.

The spectrum in bins of true energy is determined as discussed in sect. 5.6.3, using the effective collection areas $A_{\mathrm{eff}}(E_{\mathrm{true}})$ given in bins of true energy.

5.7 Wrap–up: The analysis chain

A flow diagram of the analysis chain including the flux determination is given in fig. 5.26. The observational and MC data pass universal signal extractors, calibrations, image cleanings and image parameterizations. Independent MC γ samples are used to train the γ/hadron separation and the energy estimation. All events in the data samples used in a particular analysis are tagged with hadronness values and estimated energies. The flux

and light curve calculation code applies the same cuts to all data samples and computes collection areas, observation times and γ excesses in energy bins, which become the input for flux and light curve calculations.

5.8 Systematic errors

Apart from statistical errors, the reconstructed γ-ray flux is also afflicted with systematic errors, most of which are difficult to assess. The most important systematic effects are:

1. **Photon losses in the telescope optical system.** The assumed mirror reflectivity of 85% and the PSF of the optical system (assumed as 14 mm unless stated otherwise) can differ from the in situ conditions. While the mirrors are affected by aging, the PSF depends critically on the accuracy of the active mirror control system, which refocuses the mirror segments regularly during data taking (estimated uncertainty: 5%). Furthermore, the effects of dust on the protective plexiglass window at the PMT camera entrance and light losses at the PMT light concentrators may add 3% and 5% to the uncertainties, respectively. Photon losses were estimated in part by the analysis of muon ring images [Goe05b].

2. **Detector system.** The systematic error of the light–to–photoelectron conversion has been estimated to be 5%–10% [Lor05]. This quantity is difficult to measure and is dominated by the uncertainty of the light collection efficiency of the first PMT dynode. The hardware flatfielding (equalization of PMT gains) induces uncertainties of about 2%. The total systematic error of the absolute light calibration system is estimated to be 8% [Gau05]. Trigger inefficiencies and defective PMTs account for about 10% uncertainty.

3. **Atmospheric conditions and atmospheric model.** The MC simulations use the U.S. standard atmosphere [Bil05] and do not include atmospheric and weather data concurrently recorded with the VHE observations. In general, atmospheric parameters like humidity, high clouds, and calima[3] may lead to an underestimation of the measured flux. The subsequent systematic effect on the flux level is estimated to be 15%—in agreement with comparisons of models with measurements on the Canary Islands [Ber00].

4. **Analysis chain.** Possible differences of simulated and real γ-rays may lead to systematic errors on the computation of effective collection areas. This error may be as big as 10% and is energy–dependent. In addition, different analysis parameters (e.g. different signal extraction methods, image cleaning parameters, unfolding

[3] fine dust or sand blown over the Atlantic Ocean from the Sahara Desert to the Canary Islands.

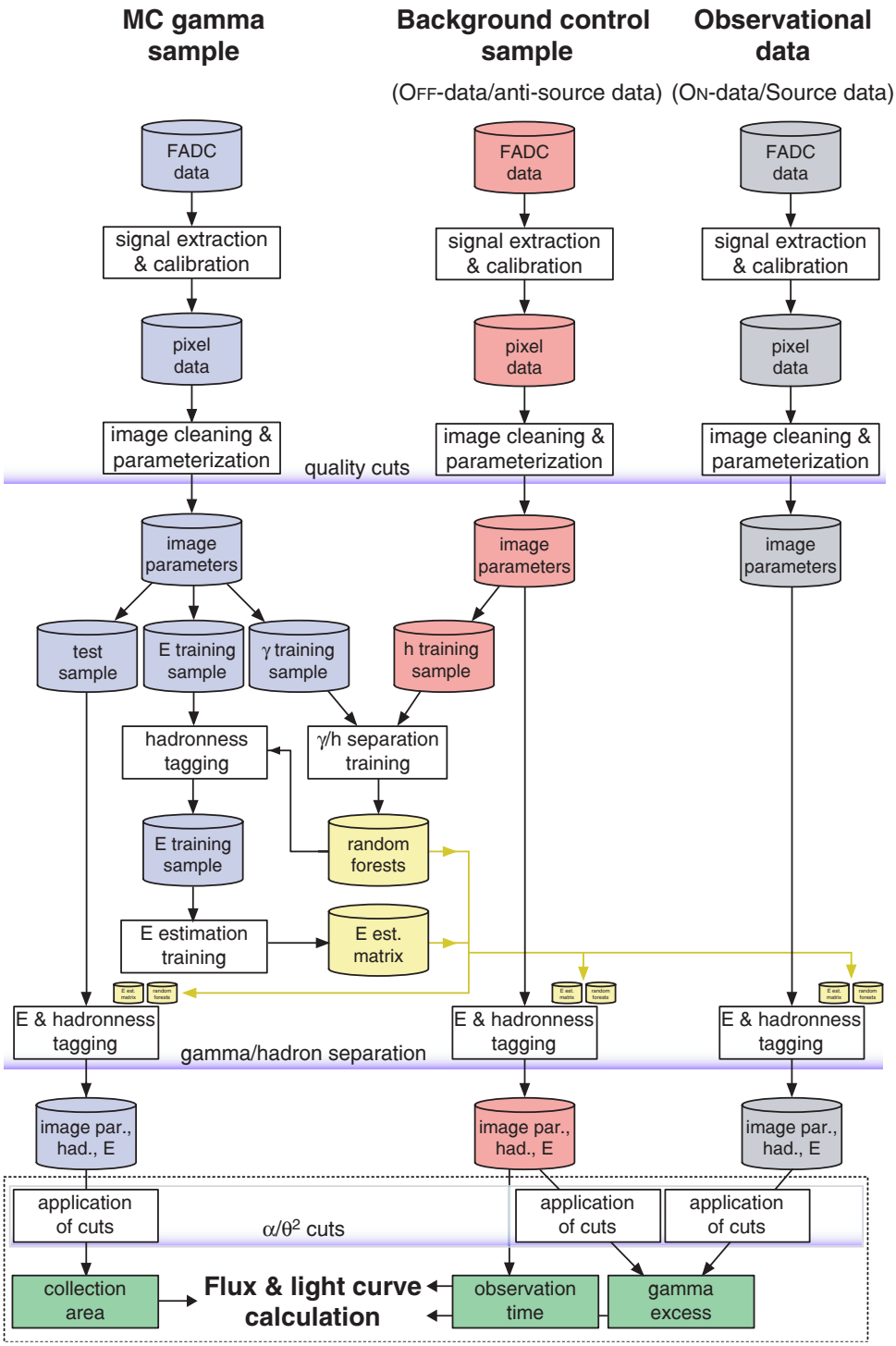

FIGURE 5.26: *The MAGIC analysis chain relies on the use of MC data that resemble gammas, observational data from the direction of the observed source and a background control sample. Sect. 4.7 elaborates on the data-taking modes used to obtain these data samples.*

parameters) may introduce systematic errors, although variations of the analysis parameters showed only minimal changes in the results ($\approx 2\%$).

The overall systematic error on the flux level is estimated to be $\approx 35\%$ for a spectrum with a slope of ≈ 2.5. It has to be stressed, however, that most of the relevant effects lead to an underestimation of the measured γ-ray rate or to an overestimation of the γ-ray efficiency, i.e. to an overall underestimation of the flux. The influence of systematic errors on the spectral slope (i.e. energy-dependent or SIZE-dependent systematic effects) is assumed to be 0.2 based on the experience from previous and other Cherenkov telescopes.

Chapter 6

Analysis of Crab nebula data

During and shortly after the telescope commissioning, the Crab nebula was observed with the MAGIC telescope for testing and calibration purposes. Here the results obtained from these observations are presented.[1] This analysis was the first one applied to an extended MAGIC data set of almost 15 hours worth of low zenith angle Crab nebula data. In the context of this thesis, it is used as reference analysis for the other analyses presented. With its steady and high flux of γ-rays, the Crab nebula is a good means to study the telescope performance.

6.1 The Crab nebula

The Crab nebula was the first source detected at VHE γ-ray energies employing the IACT technique [Wee89] and exhibits a steady and strong emission in this energy range. Therefore it is often referred to as the standard "candle" of VHE γ-ray astronomy. It has also been observed extensively over a very wide range of wavelengths, covering the radio, optical and X-ray bands, as well as high energy regions up to tens of TeV. The spectrum is dominated by synchrotron radiation up to $\approx 10^8$ eV and by inverse Compton photons scattered off the accelerated relativistic electrons. A recent review of the VHE observational status is given in [Aha04a].

The Crab nebula is the remnant of a supernova explosion that occurred in 1054 AD. It is well documented by Chinese, Korean and Native American astronomers [May39, Col99]. To date, the remaining compact central object is a neutron star with a rotation period of 33 ms and a spin–down luminosity of 10^{38} erg s^{-1}. Pulsed γ emission has been observed by the EGRET detector up to a few ten GeV, where the detection is limited both by statistics

[1] This chapter is based on the analysis presented on the 29th International Cosmic Ray Conference [Wag05b]

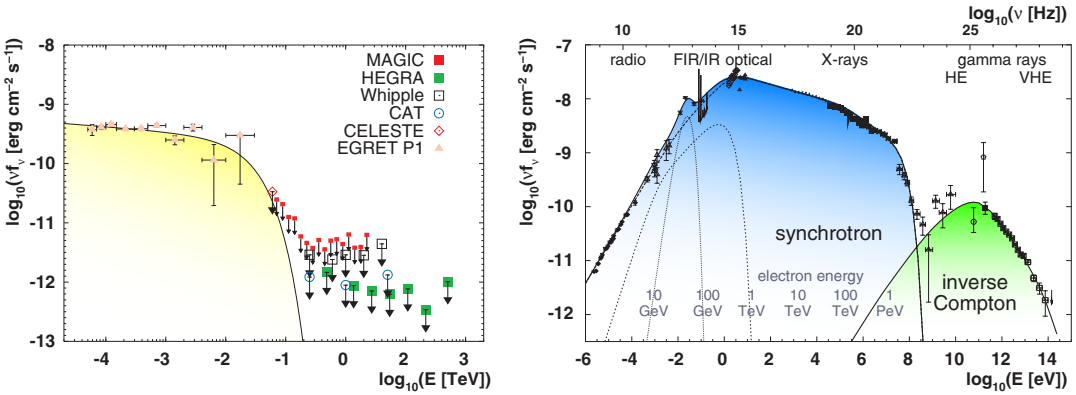

FIGURE 6.1: *Left figure: Pulsed emission spectrum of the Crab nebula. The solid line is power law fit with a cutoff at 25 GeV so as to match the EGRET data and the CELESTE upper limit. Observational data as compiled by [Aha04a], except for the MAGIC* 2σ *upper limits [Ott06a]. Right figure: Overall emission spectrum of the Crab nebula. Observational data as compiled by [Aha04a] along with a model prediction that takes into account synchrotron, far–IR and CMB photon fields and IC scattering on the pulsar electrons using a mean magnetic field of* 161 μG. *The numbers given in blue denote the energies of the relativistic electrons.*

and detector energy resolution. The measured spectrum along with upper limits obtained by VHE detectors is shown in the left panel of fig. 6.1. The existence of a cutoff is expected by most theoretical models for pulsed emission, which propose the origin of γ-rays close to the polar cap or the magnetosphere (outer gap) of the pulsar.

The pulsar emits a wind of accelerated electrons, positrons and ions with a luminosity close to the spin–down luminosity. It terminates in a standing reverse shock approx. 4×10^{17} cm away from the pulsar. The observed steady γ-ray emission from the nebula is dominated by non–thermal processes, covering a huge energy range: From radio frequencies up to a few MeV the spectrum is dominated by synchrotron emission, which originates from electrons and positrons of $E \gtrapprox 10^{15}$ eV and is produced close to its theoretical limit [Aha00a]. These $e^{\pm}$ are also responsible for the production of VHE photons by IC scattering of the ambient photons in the nebula. These mainly comprise the synchrotron photons, IR emission from dust, and 2.7K CMB radiation. The overall SED can be described by a relatively smooth double peak structure with three breaks, connected by four power law type spectra. Model calculations [Aha04a] that take into account electron injection and the mentioned seed photon fields (stellar light was found to be negligible) for the IC process are in good agreement with the observational data, which in the VHE domain extend at least up to 80 TeV (fig. 6.1, right panel) and constrain the magnetic field in the γ emission region to a level of 160 μG. The VHE γ-ray data show evidence for the predicted gradual softening of the energy spectrum towards high energies (> 10 TeV), i.e. evidence for a decreasing acceleration beyond an electron energy of 1 PeV. Recently a cutoff of the γ-ray spectrum at (14.3 ± 2.1) TeV has also been reported [Aha06d].

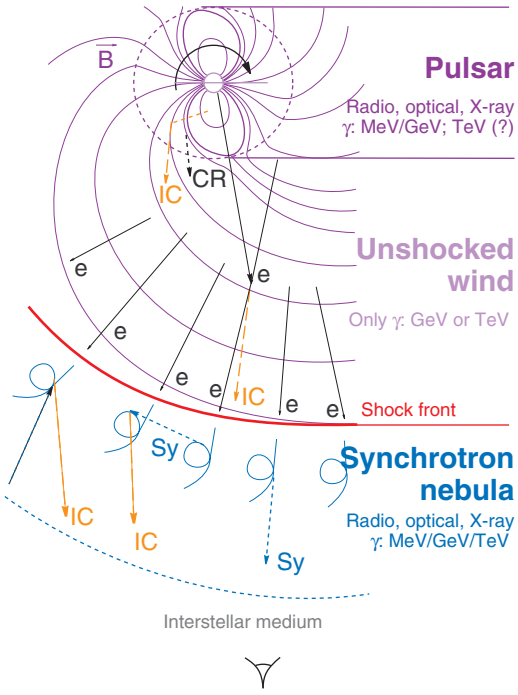

FIGURE 6.2: *Radiation from a pulsar-wind nebula complex is thought to arise from three regions: Pulsar—pulsed γ-ray emission. Unshocked wind—inverse Compton scattering of external photon fields. Synchrotron nebula—synchrotron and IC emission (taken from [Aha03a]).*

The nebula remains an interesting source, since the predicted inverse Compton peak at energies close to 100 GeV [Jag92, Hil98] and the upper energy limit for pulsed emission have not yet been observed. In particular, the limit on the maximum pulsed emission γ energy will be the decisive factor in validating pulsar models.

6.2 Data sample and run selection

A total of 13 hours ON-source data, consisting of 2.8M events taken in September and October 2004 and 4.5M events taken in January 2005 were included in this analysis (tab. 6.1). The analysis is restricted to a sample of low zenith angle observations ($\theta < 30°$). Quality checks were performed in order to reject runs with unstable trigger rates due to variable atmospheric conditions or hardware instabilities. The subsequent analysis follows the description given in sect. 5 unless stated otherwise.

Calibration, flatfielding and event reconstruction. The camera was flatfielded and the gains of the PMTs were calibrated on a run-by-run basis employing the MAGIC standard calibration procedure (cf. sect. 5). After calibration, a cleaning algorithm was applied to the shower images to remove the contribution of the night sky light background, using a cut in the absolute number of photoelectrons per PMT pixel of 7 ph.el. for core pixels

Date	Zenith angle	Events	t_{obs}
2004/09/13	22° –30°	347 k	1.7 ks
2004/09/14	21° –30°	206 k	1.0 ks
2004/09/21	15° –30°	247 k	3.3 ks
2004/09/22	14° –30°	512 k	2.5 ks
2004/10/10	6° –15°	511 k	2.5 ks
2004/10/11	6° –17°	650 k	3.0 ks
2004/10/22	12° –19°	293 k	1.3 ks
2004	6° –30°	2766 k	5.50 h
2005/01/02	28° –31°	90 k	0.4 ks
2005/01/03	2° –31°	1129 k	7.9 ks
2005/01/04	6° –22°	1490 k	7.6 ks
2005/01/13	6° – 8°	153 k	0.9 ks
2005/01/15	6° –20°	1356 k	6.9 ks
2005/01/16	8° –14°	197 k	1.7 ks
2005	2° –31°	4415 k	7.05 h

TABLE 6.1: *Data sample used for the present analysis. Listed are* ON *data, i.e. pointings of the telescope in the direction of the Crab nebula. A smaller amount of* OFF *data, pointing the telescope at a region with similar night sky background light, was used as control sample (not listed here).*

and 5 ph.el. for boundary pixels, respectively. Finally, the images were parameterized in terms of Hillas parameters [Hil98].

Rejection of the hadronic background. For γ/hadron separation, the Random Forest (RF) method was used. MC simulated γs and real hadronic background data were used as training samples. The trained random forests were used to tag each event with a hadronness value (h), which is related to the event's probability to be of hadronic origin. An appropriate cut in h yields a sample retaining most of the γ–candidates while suppressing a large fraction of the hadronic background, i.e. only γ-like hadronic showers remained. Finally, a cut in ALPHA, the angle between the shower major axis and the line connecting the shower center of gravity with the source location in the field of view, further suppresses background (overall cut efficiency/γ survival probability: $\approx 60\%$). The cuts in h and ALPHA are chosen as a function of energy, because at lower energies the discrimination power between γs and hadrons degrades, because γ and hadron images look more and more similar. In addition, the ALPHA distributions broaden, since the shower images contain fewer PMT pixels and thus the reconstruction quality of the shower direction worsens.

Energy estimation. The recorded light content of γ-showers below a few TeV and with an impact parameter < 120 m is, in first order, proportional to the initial energy. In order to estimate the energy of each event, random forests were trained for fine energy bins using log(SIZE), DIST, WIDTH, LENGTH, log(SIZE/(LENGTH $\times$ WIDTH)), CONC,

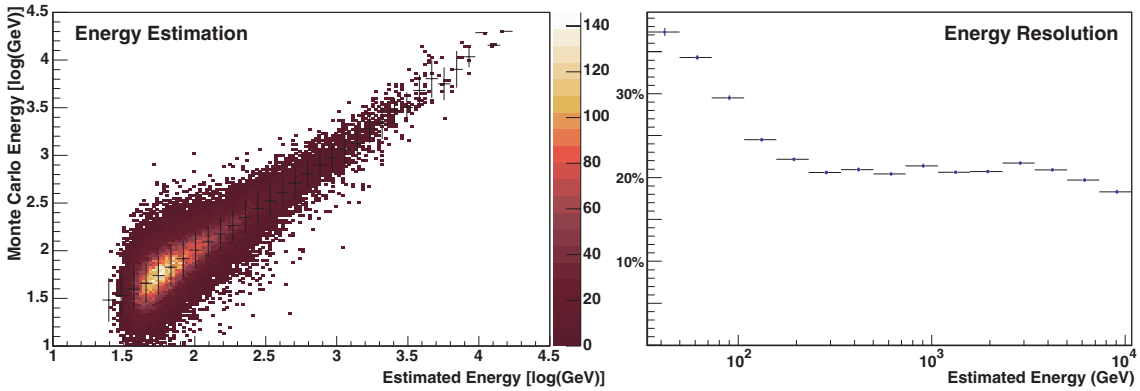

FIGURE 6.3: *Left panel: Estimated energy vs. true energy, for MC simulated γ events above 30* GeV. *Right panel: Energy resolution as a function of (estimated) energy.*

LEAKAGE, and the zenith angle θ. After training, these RFs provide an estimated energy on event-by-event basis (fig. 6.3).

6.3 Signal extraction and γ excess determination

Alpha distribution and sky map. In fig. 6.4 we show two ALPHA distributions for the data subsample of 2004 October 10. For SIZEs of 360 ph.el. and above, a signal of $20.4\sigma/\sqrt{h}$ matches very well the expected sensitivity of the MAGIC telescope for a Crab–like source and is well compatible with the latest MAGIC measurements of the Crab nebula [Ott06b]. When cutting at higher SIZEs, as e.g. 2000 ph.el. and higher, a very clean γ-ray sample is obtained.

Fig. 6.5 shows a γ excess sky map of the corresponding sky region created using the DISP-method (cf. sect. 5.4.5). The maximum of the excess is found at $(\mathrm{RA},\,\mathrm{dec}) = (5^{\mathrm{h}}34^{\mathrm{m}}21\overset{\mathrm{s}}{.}9 \pm 2\overset{\mathrm{s}}{.}4, 22°2'22\overset{''}{.}8 \pm 24\overset{''}{.}8)$. The quoted errors only include the uncertainty of the positional reconstruction, while the tracking inaccuracy is $\approx 1.5'$. The position of the Crab pulsar, $(\mathrm{RA},\,\mathrm{dec}) = (5^{\mathrm{h}}34^{\mathrm{m}}32\overset{\mathrm{s}}{.}0, 22°0'52\overset{''}{.}1)$ [Han99], is still compatible with the position of the maximum excess.

6.4 Flux stability and differential energy spectrum

As the Crab nebula is expected to be a steady source of VHE γ-rays, we expect no variations in its light curve. The integral flux of the Crab nebula above 200 GeV was determined for the individual days of this analysis (fig. 6.6). The average flux found is

$$F_{E>200\,\mathrm{GeV}} = (2.16 \pm 0.07) \times 10^{-10}\ \mathrm{cm}^{-2}\ \mathrm{s}^{-1}.$$

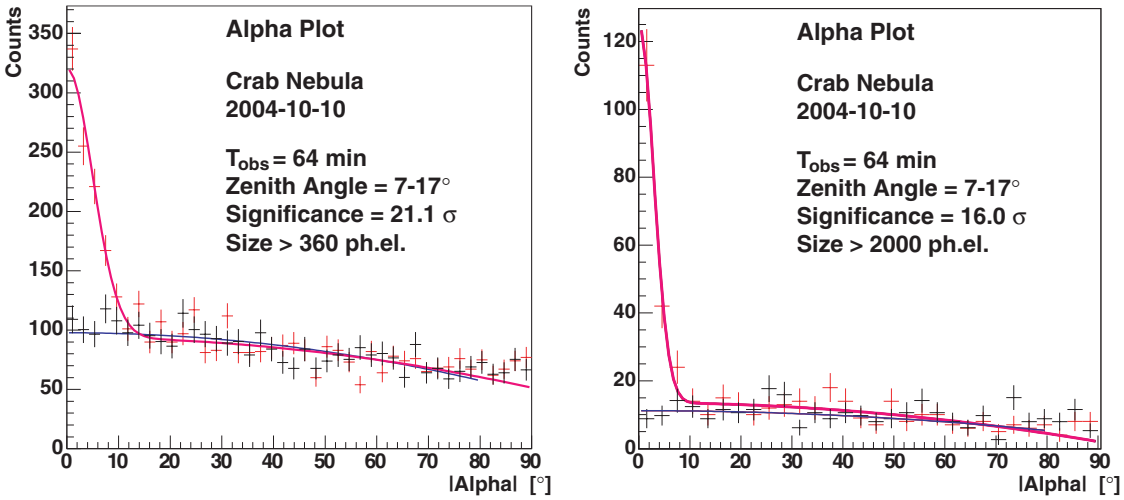

FIGURE 6.4: ALPHA *distributions. Left panel: For* SIZE $\geq$ 360 ph.el. *(*$\gtrapprox$ 200 GeV*), Right panel: for* SIZE $\geq$ 2000 ph.el. *(*$\gtrapprox$ 1 TeV*). Note that the latter* γ *sample is nearly background-free.*

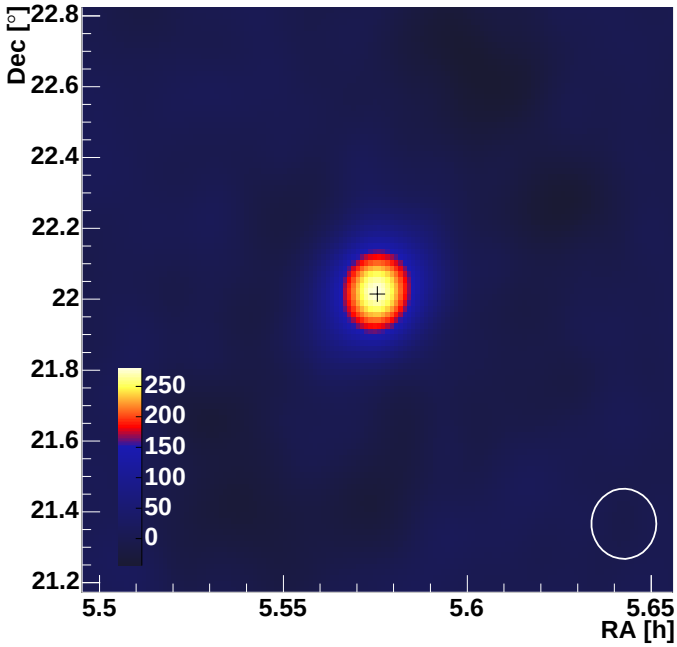

FIGURE 6.5: *Smoothed* DISP*–sky map for the Crab nebula for* 200 ph.el. $<$ SIZE $<$ 500 ph.el. *The black cross indicates the nominal source position. The units represented by the color–code are* 10^{-5} *events* sr^{-1} *(an area with about* 0.1° *radius). The white circle represents the MAGIC PSF for* γ*-rays.*

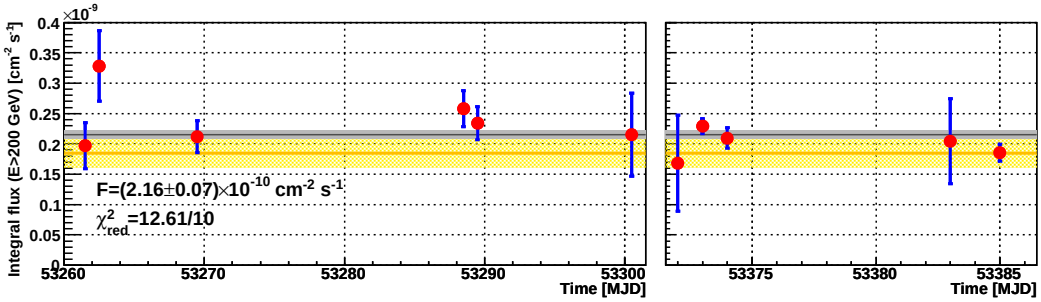

FIGURE 6.6: *Light curve for $E > 200$ GeV, i.e. the temporal evolution of the integral flux, for all days considered in this analysis. The black line was obtained by fitting a constant flux ansatz to the data. The gray band corresponds to the statistical error. The fit assuming a constant flux gave a $\chi^2_{red} = 1.26$. For comparison, the extrapolated flux from HEGRA measurements [Luc03] and its statistical error is shown as dashed yellow line and band.*

A fit with a constant flux ansatz resulted in a reduced χ^2 of 12.61/10, indicating that indeed a steady flux was measured. We compare our measurements to the reported integral flux of $F_{E>350\,\mathrm{GeV}} = (8.1 \pm 0.1_{\mathrm{stat}} \pm 0.2_{\mathrm{syst}}) \times 10^{-11}\ \mathrm{cm}^{-2}\ \mathrm{s}^{-1}$ by HEGRA [Luc03], which has been extrapolated to 200 GeV for that purpose using $F_{E>200\,\mathrm{GeV}} = F_{E>350\,\mathrm{GeV}} \times (200\,\mathrm{GeV}/350\,\mathrm{GeV})^{(-\alpha+1)}$ with the power-law slope of the Crab nebula energy spectrum α (see below). Within systematic errors (not shown in fig. 6.6), the HEGRA and MAGIC results agree well.

For calculating true energies from estimated energies, a "spillover correction" was applied:[2] $c_i = N_\gamma^{(E_{\mathrm{true}} \in B_i)} / N_\gamma^{(E_{\mathrm{estimated}} \in B_i)}$ for each bin B_i of estimated energy [Kra01a]. When multiplied with the number of excess events, it yields the number of events belonging to the respective bin of true energy.

For the final flux calculation, the data have to be corrected for various losses, such as for the different detector inefficiencies, dead–time effects, atmospheric transmission corrections etc. We estimate the systematic uncertainty in the flux to be ≈35% while the systematic uncertainty to the power law slope is ≈ 0.2. Fig. 6.7 shows the differential spectra obtained for the two data sets analyzed. As these agree nicely within statistics, a pure power law fit was performed for the combined spectrum in the region where no curvature of the spectrum is expected, between 450 GeV and 6.5 TeV. It yields

$$\frac{\mathrm{d}F}{\mathrm{d}E} = (10.4 \pm 0.9) \cdot 10^{-10} \times \left(\frac{E}{250\,\mathrm{GeV}} \right)^{-2.58 \pm 0.04} \mathrm{TeV}^{-1}\ \mathrm{cm}^{-2}\ \mathrm{s}^{-1}$$

At energies below a few 100 GeV the Crab nebula spectrum is expected to deviate from the aforementioned pure power law behavior due to the impact of the inverse Compton peak, which currently is modeled to lie at a few 10 GeV [Jag92]. In agreement with

[2] At the time at which this analysis was performed, the unfolding routines described in sect. 5.6.6 were not yet implemented.

expectations, the measured data points below 300 GeV lie below the extrapolated power law, and a curved fit from 95 GeV onwards results in

$$\frac{\mathrm{d}F}{\mathrm{d}E} = (7.8 \pm 0.4) \cdot 10^{-10} \times \left(\frac{E}{250\,\mathrm{GeV}} \right)^{(-2.35\pm0.09)-(0.09\pm0.07)\log_{10}\left(\frac{E}{250\,\mathrm{GeV}}\right)} \mathrm{TeV}^{-1}\,\mathrm{cm}^{-2}\,\mathrm{s}^{-1}$$

with spectral indices of $\alpha_{\text{Log-P}}(200\,\mathrm{GeV}) = 2.34$ and $\alpha_{\text{Log-P}}(1TeV) = 2.47$, respectively (cf. sect. 7.7.1 for a description of the curvature fit used). Fig. 6.8 compares the spectral energy distribution for the Crab nebula with other experimental data. The EGRET data points show the high energy end of the synchrotron peak and the onset of the IC peak. In the VHE region, data by other IACT, namely Whipple, CANGAROO and in particular HEGRA, cover energies from 0.5 up to 80 TeV with high accuracy. In addition, data points from the TIBET air shower array[3] and the solar tower experiment CELESTE are shown. Note that large error bars of the CELESTE data arise among other issues from the very basic gamma/hadron separation in this type of experiment and the subsequent high ON and OFF event numbers, which yield the γ excess.

6.5 Conclusions

The Crab nebula was observed in 2004 and early 2005 to test the gross performance of the telescope. The analysis presented here between 95 and 7500 GeV confirmed expectations. γ-ray emission was found with a high significance of $20.4\sigma/\sqrt{\mathrm{h}}$. In the spectral overlap region, the measured spectrum is consistent with previous observations by other experiments, which were restricted to higher energies. Moreover, the two data sets used in this chapter, which were analyzed independently, are in good agreement and could be combined.

We calculated an energy resolution of $\approx 20\%$ at energies for $E \gtrapprox 100\,\mathrm{GeV}$. Although run–in data were used for this analysis, a good flux stability was observed. Although the analysis concerning the lower energy points is still preliminary, in part due to the small data sample analyzed, this study represents the first attempt to open the energy region of down to 100 GeV to the imaging air Cherenkov telescopes.

Comparison with leptonic models for the Crab nebula γ emission. In leptonic models, the observed synchrotron photon flux allows to infer the underlying electron spectrum, when assuming a magnetic field strength in the in region where the synchrotron emission takes place. When doing so, and by correctly taking into account other sources of ambient photons available for the IC process, the expected IC γ-ray spectrum at VHE can be predicted. [Hil98] find a magnetic field strength of $B = 160\,\mu\mathrm{G}$ in the nebula. The resulting expected IC spectrum is shown in the left panel of fig. 6.9 along with the expected spectra

[3] `http://www.icrr.u-tokyo.ac.jp/em/`

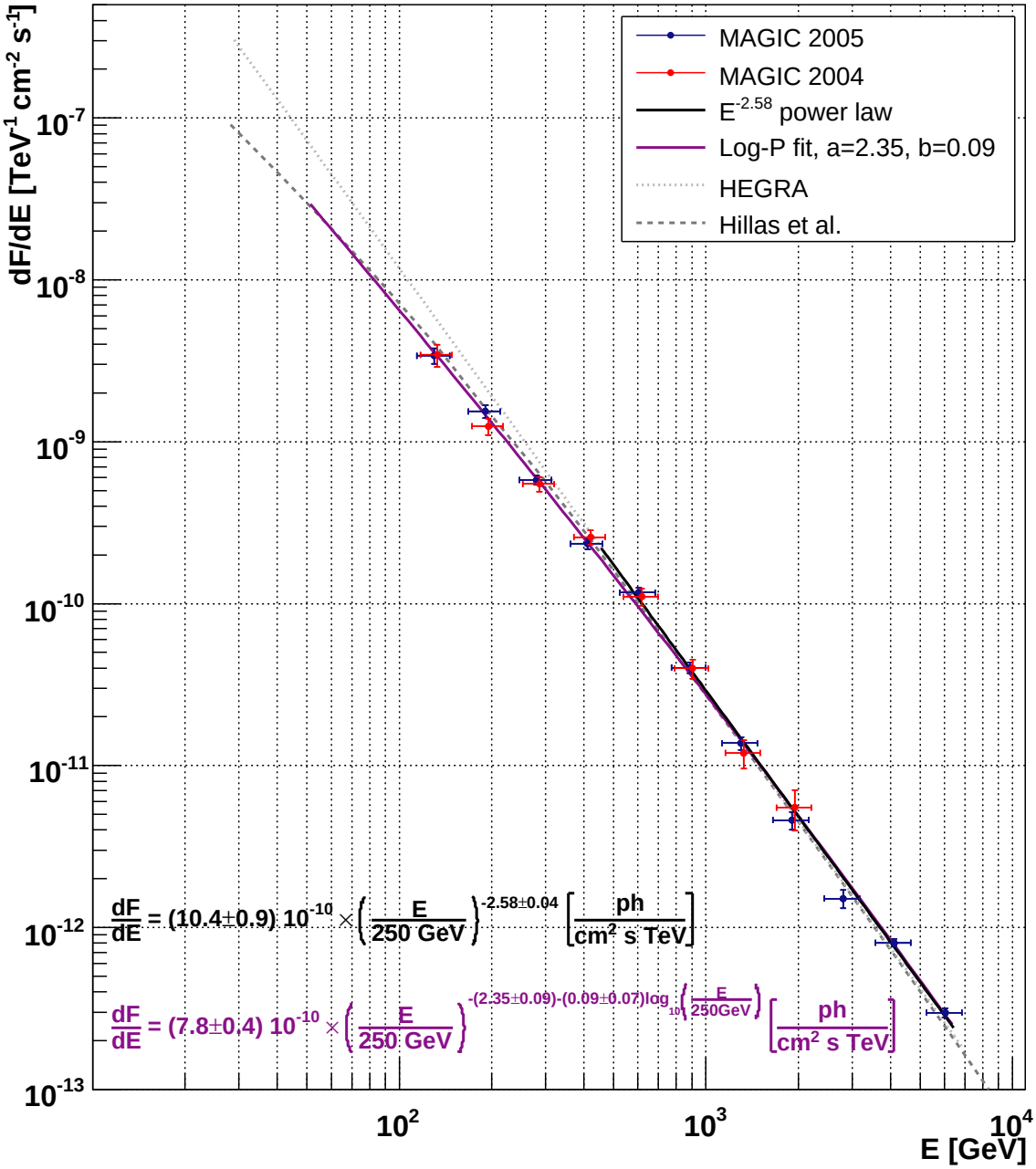

FIGURE 6.7: *Measured differential Crab nebula spectra for the 2004 (red markers) and 2005 (blue markers) data sets. The horizontal error bars represent the statistical energy resolution for the respective energy bins. A power law fit to the combined data between 450 GeV and 6.5 TeV yields a differential flux of* $\mathrm{d}F/\mathrm{d}E = (10.4 \pm 0.9) \times 10^{-10} \, (E/250\,\mathrm{GeV})^{(-2.58 \pm 0.04)}$ $\mathrm{TeV}^{-1}\,\mathrm{cm}^{-2}\,\mathrm{s}^{-1}$. *Additionally, a curvature fit was performed (for details on the fit function, see sect. 7.7.1), yielding slopes* $\alpha_{\textit{Log-P}}(200\,\mathrm{GeV}) = 2.34$ *and* $\alpha_{\textit{Log-P}}(1\,\mathrm{TeV}) = 2.47$. *For comparison, the extrapolation of the pure power law parameterization found for HEGRA data above 500 GeV [Aha04a] as well as a curved parameterization for the Whipple data [Hil98] are also shown.*

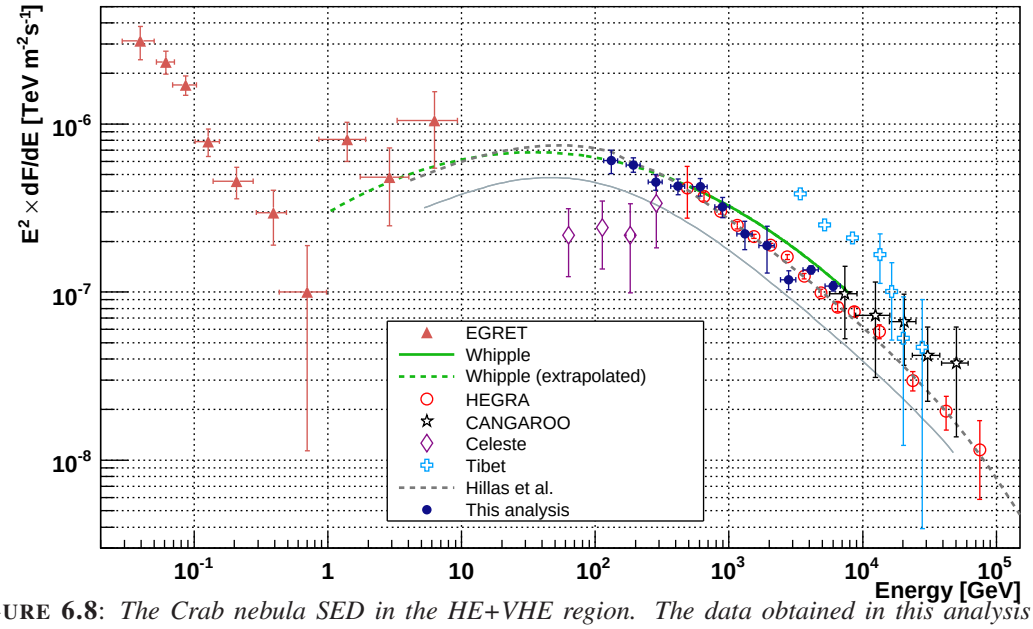

FIGURE 6.8: *The Crab nebula SED in the HE+VHE region. The data obtained in this analysis have been combined to form one spectrum, which is compared to measurements by HEGRA [Aha04a], Whipple (curved fit to the data down to 500 GeV, extrapolation below) [Hil98], CANGAROO [Tan98], the TIBET air shower array [Ame99], the solar tower experiment CELESTE [Nus03] and the model by [Hil98].*

for $B = 100\,\mu$G and $B = 400\,\mu$G. In [Aha04a] the magnetic field strength is deduced by a χ^2 minimization of the emission model. The best–fit value found is $B = 161.6\,\mu$G. Based on the spectral form of the found IC peak, we show predictions for different B values in the right panel of fig. 6.9. (For small variations of B the flux scales with $(B/B_0)^{-2}$). For comparison, fig. 6.9 also includes the spectrum found in this analysis. The current best–fit value found in [Aha04a] is well compatible with the MAGIC measurements.

Combined IACT observations—a proof of principle. When observing a given VHE γ-ray source with two IACT installations located at very different latitudes, it is possible to enlarge substantially the range over which its differential energy spectrum can be measured. This comes about by the fact that for large zenith angle observations the energy threshold for observations scales with the empirical dependency of $\approx \cos^{-2.7}(\theta)$, while at the same time the sensitivity at higher energy increases. The Crab nebula spectrum presented here was the first data with which the feasibility of such observations could be shown by combining it with a Crab nebula spectrum obtained by H.E.S.S. at large zenith angles (fig. 6.10). By combining the measured spectra of a standard candle like the Crab nebula, also possibilities for the cross–calibration of different IACT installations are given. As currently IACT cannot be directly calibrated (cf. sect. 4.6), this is an important issue when comparing the results of the individual installations. Prospects and first results of such combined observations, which might eventually be performed by a global network of Cherenkov telescopes (GNCT), are discussed in [Hor05, Maz05].

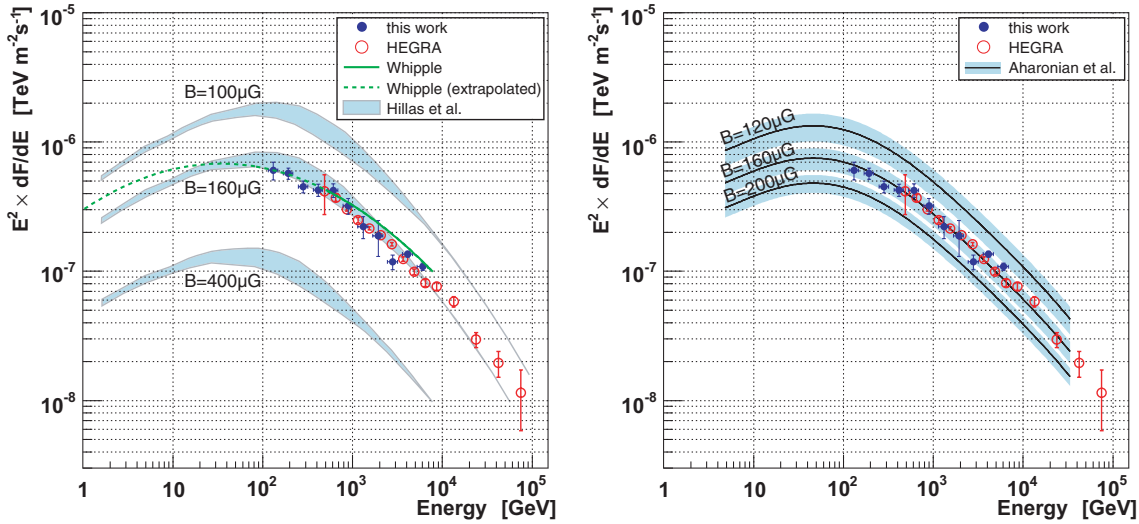

FIGURE 6.9: *Left: SSC model calculations by [Hil98] employing different magnetic field strengths compared to a parameterization of Whipple, HEGRA and MAGIC data. Right: SSC model calculations by [Aha04a] employing different magnetic field strengths compared to HEGRA and MAGIC data.*

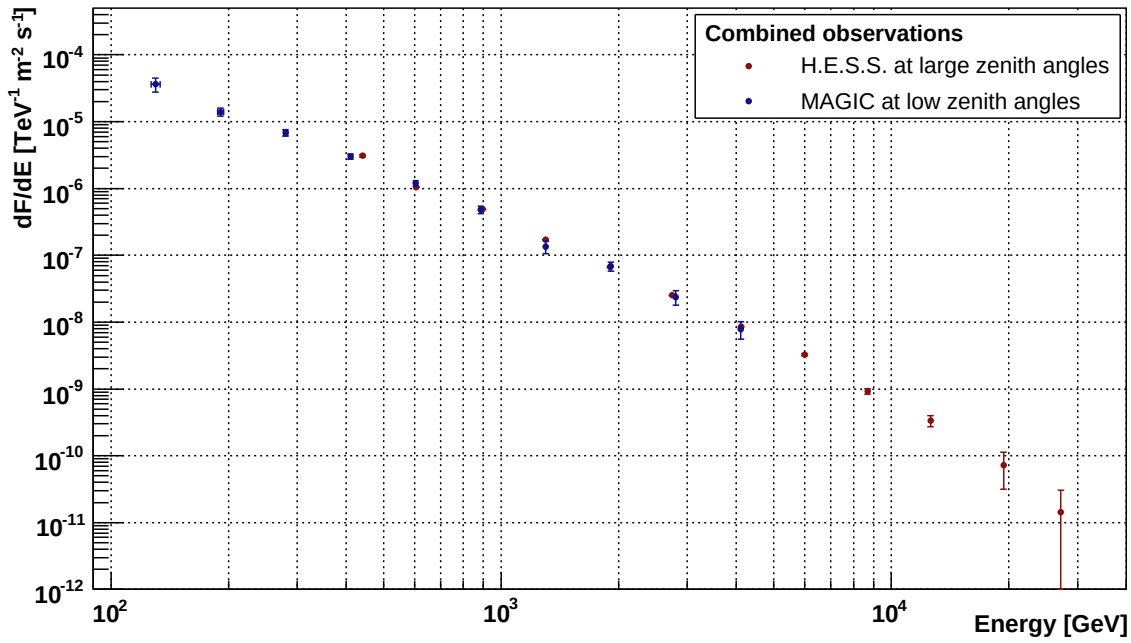

FIGURE 6.10: *Combined spectrum of the Crab nebula as observed with MAGIC and H.E.S.S. (the latter taken from [Hor05]).*

Chapter 7

Long–term observations of the AGN Markarian 501

The AGN Markarian (Mkn) 501 is one of the best–studied objects in VHE γ-rays, as it was the second extragalactic object detected in the VHE γ-ray range [Qui96]. Only one year after its detection Mkn 501 exhibited an unprecedented high flux level at X-ray and γ-ray energies during its famous flare in 1997, making it the brightest object of the VHE γ-ray sky for a couple of months.

7.1 Introduction

Mkn 501 first appeared in a catalog of 1515 strong UV sources. In 1972, a radio counterpart could be identified [Col72], which shortly after was classified as a BL Lac object and measured to have a redshift of $z = 0.034$ [Ulr75], which makes Mkn 501 the second closest BL Lac object after Mkn 421. An X-ray identification [Sch78] could be used to classify Mkn 501 further as an HBL object [Muf84]. Along with 1ES 2344+514, PKS 0548–322, H 2356–309 and 1H 1426 it is regarded as an "*X-ray selected*" or extreme BL Lac object (XBL, [Cos01]), pointing to the fact that its synchrotron spectrum extends well into the X-ray range. The BL Lac catalog by [Nie06] lists Mkn 501 as HBL with a peak synchrotron frequency of $7 \cdot 10^{16}$ Hz, equivalent to ≈ 0.3 keV. This measurement presumably reflects the quiescent state of Mkn 501, cf. fig. 7.47.

Mkn 501 is the second established blazar in VHE γ-rays [Qui96, Bra97] after Mkn 421. In 1997, it went into a state of high activity and strong variability with flux doubling times of $\Delta t \lessapprox 0.5$d [Qui99]. It showed an integral flux of up to 10 times that of the Crab nebula above 1 TeV [Aha99c] such that an energy spectrum up to 16 TeV could be determined from data of a single night [Aha99b], which followed a power law with evidence for an

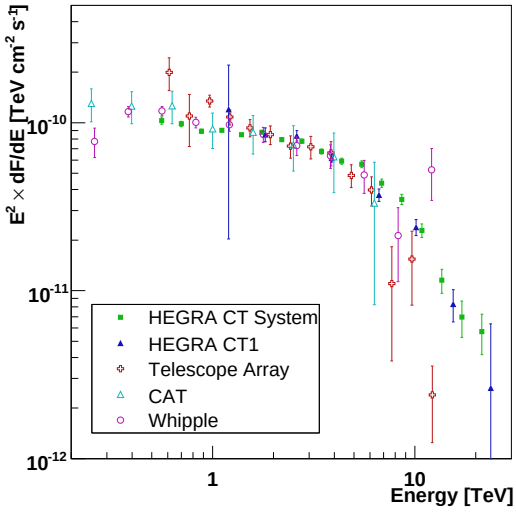

FIGURE 7.1: *SEDs of Mkn 501 measured by different groups during the 1997 flare—HEGRA CT1 [Kra01a], HEGRA CT System [Aha99b], CAT [Bar98a], Telescope Array [Hay98], and Whipple [Sam98]*

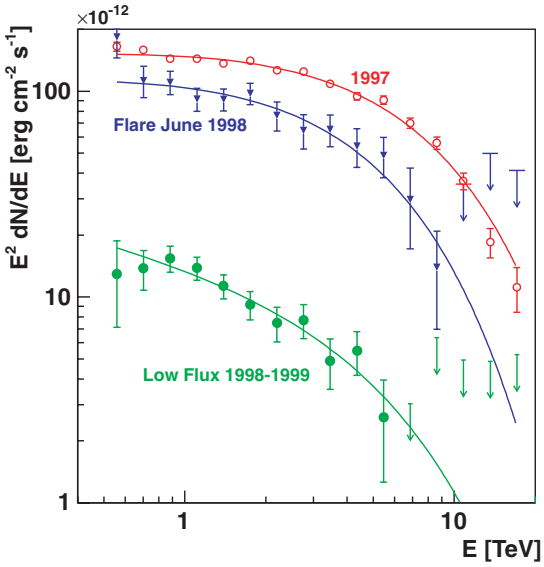

FIGURE 7.2: *SEDs measured by the HEGRA CT System during 1997, the 1998 flare, and the 1998/9 low–flux period. The solid lines show fits of the form* $\mathrm{d}F/\mathrm{d}E \propto E^{-\alpha}\exp\left(-E/E_0\right)$. *Figure taken from [Aha01c].*

exponential cutoff (fig. 7.1). The increased activity level could also be observed in the X-ray energy range [Pia98], where measurements showed a shift of the synchrotron peak energy towards substantially higher energies, $\gtrapprox 100\,\mathrm{keV}$, as compared to the previous measurements in the quiescent state.

During the following years (1998 and 1999), the mean flux was more than an order of magnitude lower [Aha01c] than in 1997 (fig. 7.2). While during the big flare of 1997 no noticeable change of the spectral shape was observed [Qui99, Aha99c], the low state spectrum of 1998–1999 was significantly softer. On the nights of 1998 June 27 and 28, a flare surpassing two times the Crab nebula flux was observed. Mkn 501 was found at very low flux levels with no apparent outbursts in 2000, while a correlated X-ray/VHE γ-ray flare is reported for 2004 June 11 [Gli06] on a flux level of ≈ 1 Crab. The long–term X-ray light curve as measured with the ASM instrument is given in fig. 7.3.

7.2 Aims of the observation

As Mkn 501 is now a well–studied object in particular in the VHE domain, new observations with MAGIC should be well justified by the prospect of scientific results that were not attainable by earlier IACT telescopes. Therefore we discuss here aspects of its observation particularly related to MAGIC's unprecedented low energy threshold and its very high sensitivity.

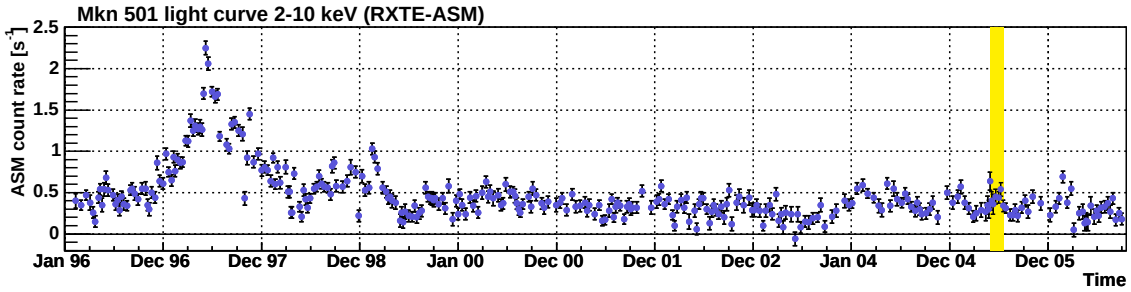

FIGURE 7.3: *Long–term observation (1996-2006) of Mkn 501 in the 2–10 keV energy band as measured with ASM on board of the RXTE satellite (for a description of the instrument, see sect. 7.6. Data available at [XTE06]). The big flare of 1997 is clearly visible. The period during which the MAGIC observations presented in this thesis were performed is marked.*

The significant detection of sources in a non–flaring state was a tedious task for the previous generation of IACTs: the HEGRA CT1 telescope could claim a signal on a 5.2σ significance level of Mkn 501 comprising 351 γ-ray excess events only after 147 hours of observations [Bra97], and the CT system found a 5.2σ signal of 1ES1959+650 after 108 hours. In contrast to that, a detection of 1ES1959+650 with the MAGIC telescope on the 8.8σ level required only 7.0 hours [Ton06]. Preparatory studies for the Mkn 501 observations with MAGIC estimated that about one hour of observation should result in a significant detection on the 5σ level.

Spectrum determination with an unprecedented low energy limit. Due to its low energy threshold of below 100 GeV, MAGIC substantially decreases the minimum observable energy for Mkn 501 as compared to previous measurements. This is particularly interesting because in SSC models the peak of the inverse Compton (IC) photon distribution is expected to scale with the synchrotron peak. The synchrotron peak energy for Mkn 501 in turn is known to undergo substantial changes during flares. First attempts to identify the IC peak during the 1997 flare are reported by the CAT collaboration. The indication of the maximum of the measured curved spectral shape was found at $(520-890)$ GeV, just above their telescope's threshold, scaling with intensity [Dja99]. After reconstructing the intrinsic flare spectrum, the maximum peak energy is found at (1.5 ± 0.1) TeV to (3.2 ± 0.2) TeV, depending on the EBL model used [Guy00]. Observations at low energies will be useful to constrain further the SSC model parameters for Mkn 501, because the IC peak is a necessary and characteristic feature in SSC models.

Observation with substantially higher sensitivity. In general, the advantage of the "third generation" IACT installations like MAGIC is their dramatically increased sensitivity as compared to their precursor experiments. MAGIC allows for significant detections of Mkn 501 not only during flares, but also during its low flux state, for which up to now only poor data exist. The data set analyzed here allows for the determination of differential spectra on a night-to-night basis. Thus comparisons of different flux states

are possible with high significance; namely a better quantification of the hardening of the spectra, and the possible displacement of the IC peak in the data and in turn in the SSC model.

Quantification of flux variabilities and characterization of flares. The measured photon flux from Mkn 501 is sufficiently large to obtain a significant detection on the $> 5\sigma$ level signal in timescales of ≈ 1 hour, even more so during flares. (For fluxes equivalent to the 1997 intensity level one expects a 5σ signal in less than one minute). This allows (1) the determination of spectra on a per–day basis and (2) the measurement of time–resolved spectral changes from far shorter observation times during measurements with enhanced flux level.

Determination of high–resolution light curves. With a detection significance of $> 5\sigma/\sqrt{\mathrm{h}}$ (this is equal to a flux of $\approx 15\%$ that of the Crab nebula) light curves with significances of the individual data points of $> 2.5\sigma$ allow 4 data points per hour; when working with 2σ data points, 6 data points per hour can be achieved. (Mind that a demonstration of a γ signal usually allows lower significance levels to be accepted for the single light curve data points, as long as the background is well controlled). This already would allow for time resolutions of the order of 10 minutes at flux levels representing an assumed baseline flux of Mkn 501. For flaring states exceeding the flux level of the Crab nebula, the determination of light curves with unprecedented resolutions of 5 or even 1 minute is feasible. This makes the MAGIC telescope a unique tool for recording fast and significant changes of the observed flux level.

X-ray flares of Mkn 501 and implications for γ-ray flares. For VHE γ-ray blazars, a correlation between X-ray flux level and VHE γ-ray flux level is expected in SSC models, although exceptions have been reported [Kra04]. The detailed acceleration mechanism behind the VHE photoproduction is still debated, while it is widely accepted that the observed X-rays are dominantly synchrotron radiation from highly relativistic electrons in the jet. Leptonic models can quite naturally explain X-ray—VHE correlations; orphan flares in the VHE domain however are difficult to explain in such models. Hadronic models attribute the VHE emission to synchrotron radiation of relativistic protons ($E \geq 10^{18}$ eV) in the jet, though other hadronic processes might also contribute. Leptonic models are pushed to the limit by the observed rapid variability, but are not yet ruled out. At the same time hadronic models face difficulties to explain the rapid variability.

Note that in pure SSC models the scaling between the VHE γ-ray and X-ray emission follows a square root law, i.e. $I_{\mathrm{sy}} \propto \sqrt{I_{\mathrm{VHE}}}$. Thus characteristic doubling or halving times in the VHE domain should be shorter than those in the X-ray domain.

Flaring of Mkn 501 has been observed both in X-rays and VHE γ-rays [Qui96, Bra97, Cat97b, Hay98, Kat99, Sam00, Pet00]. In VHE γ-rays significant variability on timescales of 2 hours (fig. 7.4) has been reported by various groups [Qui99, Hay98,

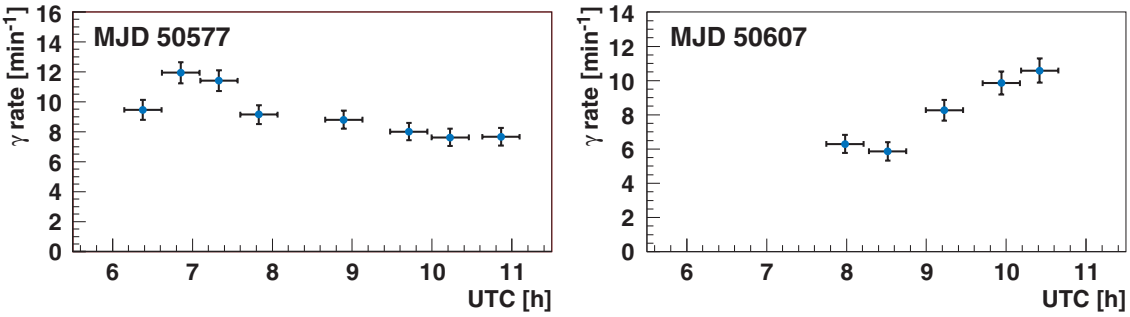

FIGURE 7.4: *Sub–hour γ-ray variability of Mkn 501 as observed by Whipple on 1997 May 9 (left figure) and 1997 June 8 (right figure) [Qui99].*

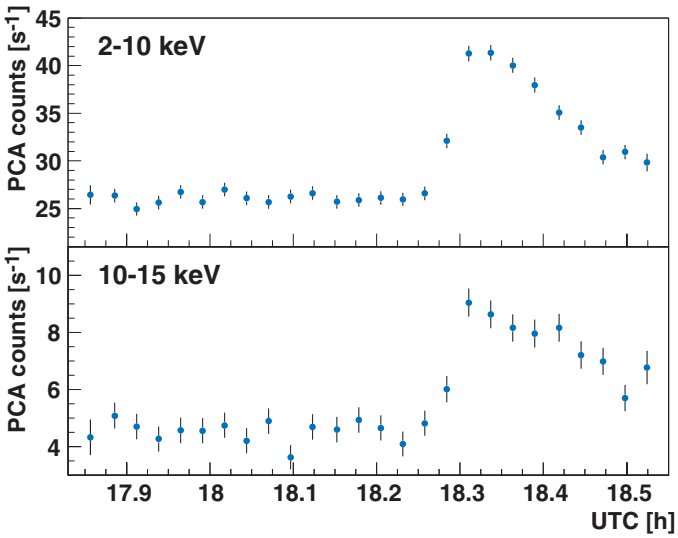

FIGURE 7.5: *1998 May 25 sub–hour X-ray flare of Mkn 501 as reported by [Cat00]. The plot shows measurements in two energy bands performed with the Proportional Counter Array instrument [Jah96] on board of RXTE (adapted from [Cat00]).*

Aha99c, Dja99]. Typical X-ray flux variations from 30% to 300% were observed on a timescale of days during the 1997 flare [Pia98] and in 1998 [Sam00].

The fastest variations in X-rays were observed on timescales of 12 hours [Gio90] and < 200 s and < 600 s for rise and decay time of one identified fast flare [Cat00] (fig. 7.5) with the Proportional Counter Array instrument [Jah96] on board of the Rossi X-ray Timing Explorer (RXTE) satellite [Bra93]. The latter, if real, would lead to substantial constraints on the properties of the flaring region [Cui04]. Following this claim, a systematic analysis of $(2-10)$ keV RXTE X-ray archival data has been performed by [Xue05]. The claimed flare could not be unambiguously confirmed, as the authors found another $\lesssim 200$ s flare exactly one satellite orbit (1.6 hours) later. Additionally, they found accompanying electron flares. Both findings could indicate that the flares might be instrumental artifacts. The study, however, revealed a third ≈ 800 s flare with a peak amplitude of 30 % above the baseline. Substructures as short as $20-30$ seconds were also reported (fig. 7.6), and the flare might even be composed of two subflares. Additional findings were: (1) the con-

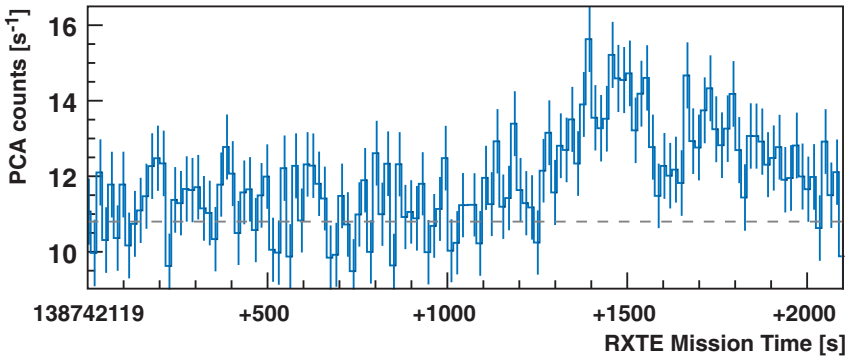

FIGURE 7.6: *Sub–hour X-ray flare from Mkn 501 as reported by [Xue05]. The flare, peaking 30% above the baseline, lasted for 800 s and shows substructures as short as 20-30 s (adapted from [Xue05]).*

firmation of a spectral hardening during the buildup of long (months to $>$ 1 year) flares (hardness–intensity correlation) and (2) the presence of intermediate (days to weeks) X-ray flares. This implies no apparent quiescent state of the object; unlike Mkn 421, the flux of Mkn 501 has never completely vanished since its discovery 10 years ago. The amplitudes found for intermediate flares were found to be $4-5$ times above the steady state. No conclusions on spectral evolution were possible as the data quality was not good enough for such a study.

The flaring hierarchy suggested for Mkn 501 implies a scale–invariant nature of flaring processes [Cui04] and that there might not be any fundamental difference among long, intermediate and rapid flares, as they could all be caused by the same mechanism. Although not thoroughly understood, the flares in blazars might be related to internal shocks in the jet [Ree78, Spa01] or to major ejection events of new components of relativistic plasma into the jet [Boe97b, Mas97]. Different flare durations then might be caused by a hierarchy of inhomogeneities in the jet, energized so as to produce flares by the shocks. If the jets are magnetically dominated, the flares might be associated with magnetic reconnection events [Lyu03]. Proton synchrotron models naturally require magnetically dominated jets to produce VHE emission [Mue03, Aha00a].

7.3 Lorentz invariance

Rapid flaring of distant objects might help to clarify an interesting fundamental physics question. Many quantum gravity scenarios predict an observable time dispersion for high energy radiation originating at very large distances ($\gg$ Mpc) from Earth [Ame98, Gar98, Gam99]. This is due to an effective energy dependence of the speed of light, which comes about by the propagation through a gravitational medium containing quantum fluctuations on a scale comparable to the Planck length $L_{\mathrm{Planck}} \approx 10^{-33}$ cm, with a timescale of the order of $1/E_{\mathrm{Planck}} = 1/10^{19}$ GeV. Different approaches to quantum gravity lead to a

similar quantification of the first order effects[1] of such an expected time delay [Ame98]:

$$\Delta t \simeq \xi \frac{E}{E_{\mathrm{qg}}} \frac{D}{\mathrm{c}} \tag{7.1}$$

with the sign of the deformation $\xi = \pm 1$, the traversed distance D, the energy of the observed radiation E and the energy scale for quantum gravitational effects E_{qg}. Generally, E_{qg} is assumed to be of the order of E_{Planck}, but the value might be considerably smaller and VHE energy observations may help to set constraints on E_{qg} and, in turn, to set limits on Lorentz invariance violations.

Limits on E_{qg}. Naturally rapidly changing features of VHE γ-ray emitters, such as gamma-ray bursts (GRB) and fast flaring AGNs at large distances, are the most promising handles for probing the quantum gravity scale. While formula (7.1) clearly favors high energy differences, cascading effects of $\mathrm{e}^+\mathrm{e}^-$ pairs created by EBL absorption in presence of intergalactic magnetic fields [Pla95] might pose an energy limit above which arrival time delays cannot unambiguously be attributed to quantum–gravity effects. Conversely, the non–observation of time delays may also be interpreted as a limit on the magnitude of intergalactic magnetic fields.

The obvious candidates, GRBs, however, have not yet been successfully observed with VHE γ-ray detectors [Alb06d]. Additionally, the redshift determination for GRBs is not trivial. A lower limit on E_{qg} from an ensemble of 35 GRBs with known redshifts using X-ray data[2] is given by [Ell06] as $E_{\mathrm{qg}} \geq 0.9 \cdot 10^{16}$ GeV. The analysis of single GRBs (GRB 930131 and GRB 021206) was used to infer limits of $E_{\mathrm{qg}} \geq 8.3 \cdot 10^{16}$ GeV [Sch99] and $E_{\mathrm{qg}} \geq 1.8 \cdot 10^{17}$ GeV [Bog04], respectively. The redshifts of these two GRBs, however, were not measured but only indirectly inferred by exploiting spectral GRB characteristics, which does not make these two limits very robust.

An attractive alternative for constraining E_{qg} are rapid flares as observed from BL Lac objects. A prime candidate is Mkn 421, for which flux doubling times of $O(15\,\mathrm{min})$ have been reported [Gai96, Sch02b]. Using Whipple observational data of the 1996 May 15 flare of Mkn 421, [Bil99] have inferred a lower limit of $E_{\mathrm{qg}} \gtrsim 6 \cdot 10^{16}$ GeV by the non–observation of high energy events outside a 280 second time bin.

An approach that exploits much faster phenomena, namely the periodicity of the Crab pulsar at the expense of a much smaller distance from Earth, was used to place a lower limit of $E_{\mathrm{qg}} > 1.8 \cdot 10^{15}$ GeV on the quantum gravity scale [Kaa99].

[1] If the time delay were due to second order effects $\lambda = 2$, a suppression by a factor $(E/E_{\mathrm{qg}})^{\lambda}$ would currently exclude any experimental handle on it. Recent findings [Jac03, Ell04b] constrain the order of the effects to $\lambda < 1.74$ *for electrons* and suggest a linear modification of the dispersion relation for photons.

[2] BATSE (a detector on board of CGRO), HETE, and SWIFT observations in the $25 - 55$ MeV and $115 - 320$ keV range

Object	Distance	ΔE	Δt	E_{qg}	Ref.
GRB 930131	$z \gtrapprox 0.055^{*}$	70 keV – 200 MeV	25 ms	$> 8.3 \times 10^{16}$ GeV	[Sch99]
Mkn 421	$z = 0.030$	1 TeV – 2 TeV	280 s	$> 6 \times 10^{16}$ GeV	[Bil99]
Crab nebula	2.2 kpc	70 MeV – 100 MeV	0.35 ms	$> 1.8 \times 10^{15}$ GeV	[Kaa99]
GRB 021206	$z = 0.3^{**}$	3 MeV – 17 MeV	11.2 ms	$> 1.8 \times 10^{17}$ GeV	[Bog04]

TABLE 7.1: *Limits on the quantum gravity energy scales inferred from time difference measurements of individual objects in literature. * distance inferred by assuming a minimum peak luminosity. ** distance inferred from GRB spectral parameters and its duration.*

Tab. 7.1 summarizes the limits obtained so far from the observation of individual astrophysical objects.

Limits on E_{qg} for electrons. Synchrotron radiation observed from the Crab nebula severely constrains the leading order of the dispersion relation of the *electron* $(E/E_{\mathrm{qg}})^{\lambda}$ to $\lambda < 1.74$ [Jac03, Ell04b]. However, these measurements do not constrain the modification of the dispersion relation of the *photon*. In fact, certain models [Ell04b] even suggest a linear modification of the photon dispersion relation, but not for the electron [Ell04a].

Limits on E_{qg} from VHE photon observations. [Ste01b, Ste03] argue that a broken Lorentz invariance leads to a modification of the threshold energy for the intergalactic absorption process $\gamma\gamma \rightarrow \mathrm{e}^{-}\mathrm{e}^{+}$ (cf. sect. 1.2.2), implying $M_{\mathrm{qg}} \geq E_{\gamma}^{3}/8m_{\mathrm{e}}^{2}$. The observation of EBL absorption effects up to $E_{\gamma} > 20$ TeV is interpreted as a constraint on the quantum gravity scale $M_{\mathrm{qg}} \geq 0.3 M_{\mathrm{Planck}}$.

Limits on E_{qg} from time differences in VHE γ-ray light curves of different energies. Rapidly changing flux levels recorded in the form of high–resolution light curves in different photon energy bands offer themselves for imposing limits on the quantum gravity energy scale. Sect. 7.8.3 discusses in more detail the approach chosen in this thesis to constrain the quantum gravity energy scale.

7.4 Data sample

The data analyzed here were originally taken in the framework of a proposal for observations of established VHE blazars in quiescent state; the lowest flux state so far observed for Mkn 501 was 20% that of the Crab nebula[3] in 1998/9 (fig. 7.7). The MAGIC observations were scheduled over a period of about six weeks, for about one hour per day so as to be able to infer diurnal spectra. The observations were carried out in ON/OFF mode, i.e. apart from observations in the direction of Mkn 501, a region with the same declination as

[3] As the energy range of this analysis and in the cited references are not directly comparable, we convert the fluxes in "Crab units", "c.u.". The spectral index of the Mkn 501 low flux state and the Crab nebula are not grossly different, therefore providing Crab units is appropriate for comparisons.

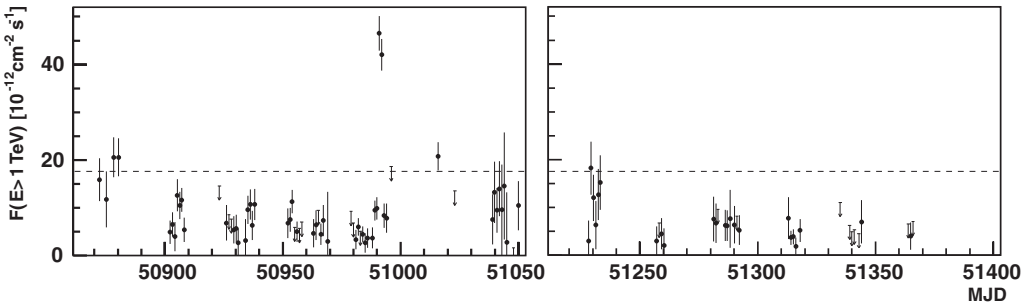

FIGURE 7.7: *Light curve for the observations of Mkn 501 in 1998/9 with the HEGRA telescope system at energies of 1 TeV and above. The mean emission level was found at 33% of the Crab nebula flux, while the lowest flux levels observed were found at 20% of the Crab nebula flux. The dashed line indicates the steady emission level of the Crab nebula (adapted from [Aha01c]).*

that of Mkn 501, from which no γ-rays were expected, was selected to obtain background control data. The data analysis followed the scheme outlined in sect. 5.

Quality checks and run selection. Mkn 501 was observed during 24 nights in June and July 2005. Part of the data was taken in the presence of (moderate) moonshine. The obtained data were scanned for bad atmospheric conditions, technical problems with the telescope and deviating or fluctuating event rates. After quality cuts, and a cut restricting the zenith angle to $\theta_{\max} = 30°$, 29.7 hours of data remained.

In addition, 4.5 hours of OFF-data were taken at two sky positions close to the position of Mkn 501 (OFF position 1: RA $= 17^{\mathrm{h}}30^{\mathrm{m}}$, dec $= 39°53'00''$; OFF position 2: RA $= 17^{\mathrm{h}}09^{\mathrm{m}}16^{\mathrm{s}}$, dec $= 39°45'36''$).

7.5 Event reconstruction and excess determination

The data analysis was carried out as discussed in sect. 5. The events were cleaned using an absolute image cleaning with thresholds of 7 ph.el. for core pixels and 5 ph.el. for boundary pixels, respectively. After the calculation of Hillas parameters, random forests using MC γs and hadrons taken from the Mkn 501 OFF data sample were used to train the γ/hadron separation. Tab. 7.2 summarizes the γ signal found on diurnal basis. A total number of about 14,000 γ-rays of energies of 150 GeV and above were found. About one third of these γ-rays were registered on the two nights of 2005 July 01 and 2005 July 10. The detection significance is well above 5σ for almost every observation night, peaking at significances of about 40σ and more for the observation nights with high flux level. The average diurnal flux levels range from 0.25 Crab units (c.u.) to levels of 3 c.u. and 2.7 c.u. for 2005 July 01 and 2005 July 10, respectively.

A number of ALPHA plots are exemplarily shown in fig. 7.8. For all these plots, a clear signal is seen over a background that well matches the control sample composed of the

Observation night designation	start [UTC]	t_{up} [hours]	t_{eff} [hours]	ZA range [deg]	Rate [Hz]	N_γ	Signif. [σ]	F [10^{-10} cm^{-2} s^{-1}]
2005/05/29	28.05.2005 23:28:29	0.84	0.71	19.8 – 28.9	225	176	7.2	0.75 ± 0.11
2005/06/01	31.05.2005 23:08:35	1.93	1.41	12.0 – 30.0	227	588	12.7	0.99 ± 0.13
2005/06/04	03.06.2005 23:15:53	0.56	0.56	20.7 – 26.9	223	231	9.6	0.96 ± 0.21
2005/06/06	05.06.2005 23:00:16	1.76	0.94	11.9 – 28.3	221	396	10.8	1.02 ± 0.17
2005/06/10	09.06.2005 23:22:02	0.47	0.47	16.8 – 21.5	232	146	7.1	1.14 ± 0.24
2005/06/11	10.06.2005 23:01:37	0.90	0.85	15.4 – 24.4	222	299	7.8	0.69 ± 0.17
2005/06/12$^\bullet$	11.06.2005 22:27:41	0.53	0.53	24.1 – 30.0	212	143	7.3	0.68 ± 0.20
2005/06/13$^\bullet$	12.06.2005 22:20:57	1.74	1.53	13.2 – 30.0	211	523	12.2	0.76 ± 0.12
2005/06/14$^\bullet$	13.06.2005 22:17:13	2.63	2.01	11.0 – 30.0	167	776	12.7	0.77 ± 0.11
2005/06/15$^\bullet$	14.06.2005 22:12:11	3.73	3.42	11.0 – 30.0	123	1652	26.9	1.48 ± 0.09
2005/06/17$^\bullet$	16.06.2005 23:00:33	3.67	3.07	11.0 – 30.0	134	870	15.6	0.70 ± 0.07
2005/06/18$^\bullet$	18.06.2005 02:11:35	0.41	0.24	25.4 – 30.0	124	46	5.7	0.57 ± 0.22
2005/06/28	27.06.2005 22:19:56	0.87	0.80	12.5 – 20.0	220	285	8.6	0.76 ± 0.18
2005/07/01	30.06.2005 21:43:23	1.09	1.09	13.8 – 24.4	173	2305	49.9	7.61 ± 0.27
2005/07/04	03.07.2005 21:43:52	0.68	0.66	15.5 – 22.2	235	485	15.8	2.23 ± 0.23
2005/07/05	04.07.2005 21:44:52	0.82	0.39	13.7 – 21.3	173	114	7.2	1.06 ± 0.25
2005/07/07	06.07.2005 21:58:58	0.54	0.54	13.1 – 17.6	218	360	12.5	1.50 ± 0.23
2005/07/09	08.07.2005 22:03:33	0.98	0.98	11.0 – 15.7	220	557	13.8	1.36 ± 0.18
2005/07/10$^\bullet$	09.07.2005 21:44:46	0.76	0.76	12.0 – 18.0	222	1406	38.3	6.60 ± 0.30
2005/07/12$^\bullet$	11.07.2005 21:52:13	1.63	1.39	11.0 – 15.6	177	754	14.7	1.20 ± 0.15
2005/07/13$^\bullet$	12.07.2005 22:11:02	0.78	0.77	11.0 – 12.7	147	857	28.2	4.04 ± 0.24
2005/07/14$^\bullet$	13.07.2005 21:55:15	1.07	0.34	11.0 – 14.1	132	241	14.1	2.20 ± 0.29
2005/07/15$^\bullet$	14.07.2005 22:02:21	0.20	0.16	11.8 – 12.8	187	31	4.4	0.61 ± 0.32
2005/07/16$^\bullet$	15.07.2005 23:43:48	1.06	1.00	18.8 – 30.0	127	403	12.6	0.67 ± 0.10
Total observation time:		**29.65**	**24.62**					
2005/05/29	30.05.2005 00:12:50	0.92	0.65	17.0 – 26.7	221			
2005/06/10	09.06.2005 23:52:19	0.58	0.58	13.8 – 18.9	227			
2005/06/29	28.06.2005 22:01:32	1.41	0.28	11.9 – 25.3	221			
2005/07/02	01.07.2005 22:14:34	0.52	0.39	15.8 – 20.9	216			
2005/07/06	05.07.2005 21:46:49	0.72	0.53	15.5 – 23.0	215			
2005/07/08	07.07.2005 22:08:07	0.30	0.30	15.2 – 18.0	217			
Total observation time:		**4.45**	**2.73**					

TABLE 7.2: *Analysis results for individual nights. t_{up} denotes the nominal observation time, t_{eff} the effective observation time after cuts (including zenith angle and data quality cuts), F the integral flux above $E =$ 200 GeV, N_γ is the total number of γ-ray candidates. The symbol $^\bullet$ indicates observations performed during (moderate) moonshine. The observation nights are designated by the date of the following day.*

OFF data sets. The ALPHA plots include events with a SIZE of 200 ph.el. and above ($\gtrapprox$ 250 GeV), with a dynamic (SIZE dependent) hadronness cut applied. It should be mentioned that the cuts used were not particularly optimized for significance.

Low energy events. The sensitivity of the current MAGIC standard analysis allows for the detection of lowest energy signals ($\lessapprox$ 100 GeV) only from strong sources with fluxes of the order of the Crab nebula. Therefore the Mkn 501 data set during days with high flux levels lends itself to the observation of low energy events. Fig. 7.9 shows ALPHA plots in the low energy region for the observations on 2005 July 1. Although the analysis applied in this thesis is not particularly optimized for this energy range, a significance of 4.8σ is found for $E_{\rm est} < 100$ GeV. The ALPHA distribution shows the typical broadening expected for this energy region, in which the ALPHA determination deteriorates due to

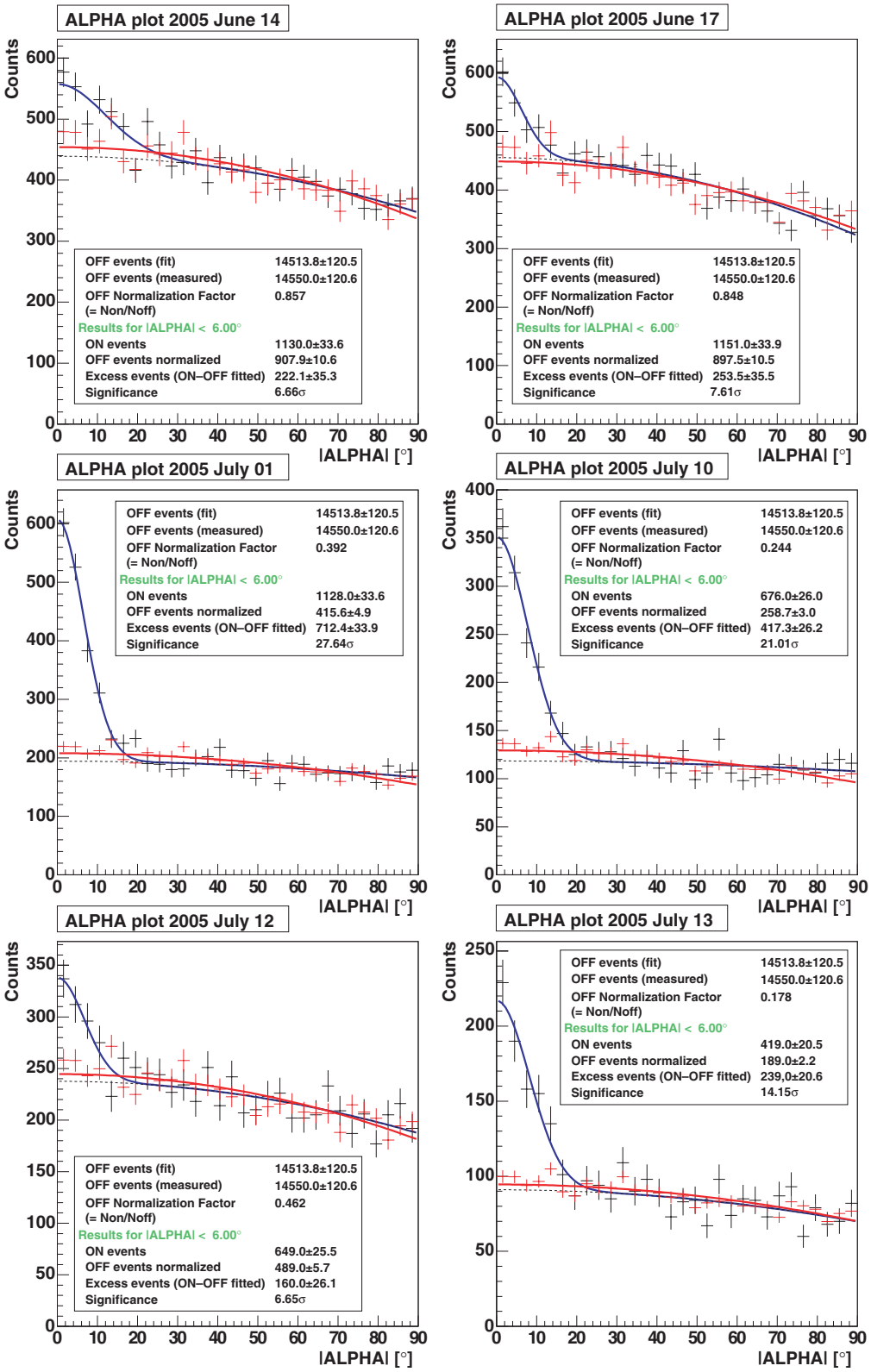

FIGURE 7.8: ALPHA *plots for Mkn 501 observations of 2005 June 14, 17, July 1, 10, 12, and 13 for 200* ph.el. *and above.*

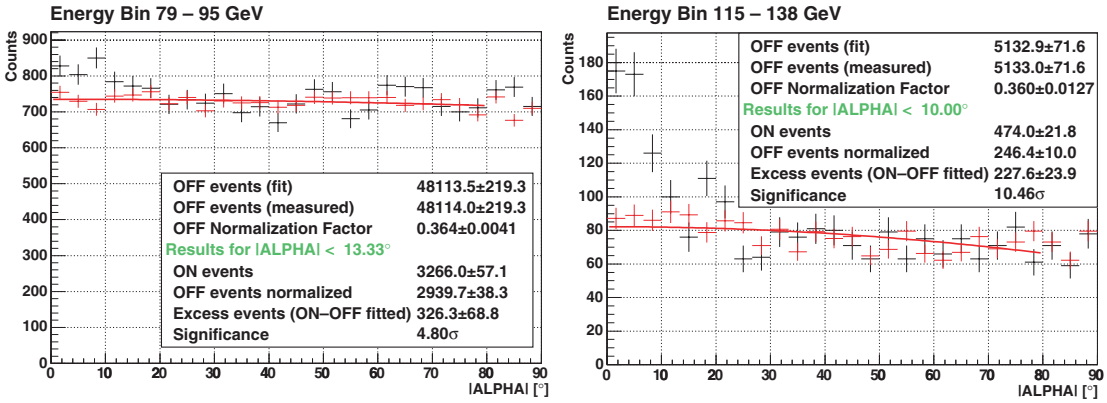

FIGURE 7.9: *Low energy* ALPHA *plots for Mkn 501 observations. Exemplarily, we show two low energy* ALPHA *plots for 2005 July 1. Due to the high flux level on that day, a high number of* γ*-rays is to be expected. Left panel: In the* $80-95$ GeV *energy region an almost significant signal on the* 4.8σ *level is seen, with the typical broad* ALPHA *distribution expected at low energies. Right panel: At energies above 100 GeV a high–significance* γ *signal is observed. Note that the quoted energies are estimated energies (for the bias of the energy estimation, see sect. 5.4.4).*

the small shower images. Above 100 GeV, very clear and highly significant signals are seen, as is exemplarily shown for the $115-138$ GeV bin.

Source position. To confirm the source position for the γ excess found, a DISP analysis was performed on the data sets of 2005 July 1 and 2005 July 10. Using a control sample comprising data from July 02 and July 08 for background subtraction, a sky map (fig. 7.10) was produced. When performing a fit with a Gaussian function to the distribution of incoming directions, the excess position is found at $(\mathrm{RA},\,\mathrm{dec}) = (16.^{\mathrm{h}}900 \pm 0.^{\mathrm{h}}015, 39.^{\circ}77 \pm 0.^{\circ}12)$ These uncertainties only stem from the center–of–excess determination and do not include the tracking uncertainty of 1.5 arcmin. The expected source position of Mkn 501, $(\mathrm{RA},\,\mathrm{dec}) = (16.^{\mathrm{h}}897, 39.^{\circ}76)$ [Ma98], therefore, is well matched within uncertainties.

7.6 Studies of the overall light curve

As the online analysis results for the observation night of 2005 July 1 showed flux levels of four times the Crab nebula flux, IAU circular #8562 [Goe05a] was issued shortly after the observations to alert the astrophysics community and to stimulate possible observations at other wavelengths. The varying flux level in the data is shown in a light curve (fig. 7.11) containing integral flux points for each observation night. The VHE light curve as measured by MAGIC shows a base flux level of $F = 0.7 \cdot 10^{-10}\ \mathrm{cm}^{-2}\ \mathrm{s}^{-1}$ ($E > 200$ GeV), equivalent to about 30% of the Crab nebula flux. Atop the baseline, flux level fluxes seven, six and four times higher were observed in the nights of 2005 July 1,

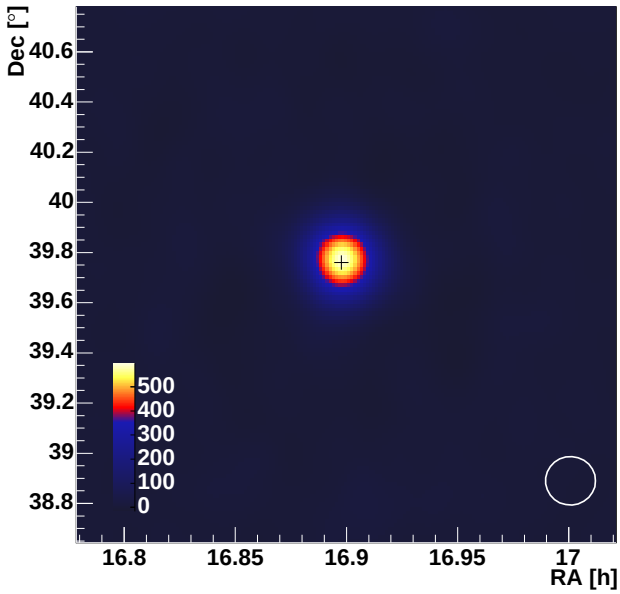

FIGURE 7.10: *Smoothed sky map around the position of Mkn 501 produced with the* DISP *analysis: The plots shows the arrival directions of γ-ray candidates above 300 ph.el., that were selected by imposing a hadronness cut of $h < 0.1$. The units represented by the color–code are 10^{-5} events sr^{-1}, i.e. events within a circular area with $r = 0.1^\circ$. The white circle indicates the γ-ray PSF (angular resolution) of MAGIC of $\sigma = 0.1^\circ$.*

10, and 13, respectively.[4] The base flux levels observed in the past are reported as 8% of the Crab nebula flux above 300 GeV in 1995 [Qui96] and about one third of it in 1997 [Bra97] and 1998/9 [Aha01c]. Interestingly, the flux level returned to moderately elevated levels on the days following these three days. Therefore, rapid changes of the flux level—"flares"—were to be expected in the data set. The study of such flares is interesting in view of the up-to-now observed timescales for flares of Mkn 501, which are of the order of days. A closer study of the different flux levels, their spectral properties and of the flare properties is presented in the next sections.

X-ray light curve and VHE γ-ray/X-ray correlation. The All Sky Monitor (ASM, [Lev96]) on board of the Rossi X-ray Timing Explorer (RXTE, [Bra93]) satellite consists of three scanning shadow cameras. Position-sensitive proportional counters register the image of slit masks, which are used to infer directional and intensity information in the $(2-10)$ keV range. RXTE has been operational since 1996. The ASM scans $\approx 80\%$ of the sky every 1.5 h and provides count–rates. The middle panel of fig. 7.11 shows the ASM light curve for Mkn 501. To obtain concurrent data points, individual ASM observations ("dwells") have been averaged for periods ± 0.3 days around the respective diurnal MAGIC observation windows. Fig. 7.12 relates the ASM energy band to the MAGIC energy range and the SSC emission of Mkn 501.

[4]Note that the observation nights by convention are always referred to by the date of the following day (tab. 7.2); i.e. the flare of 2005 July 1 in fact took place around 22:35 UTC on 2005 June 30.

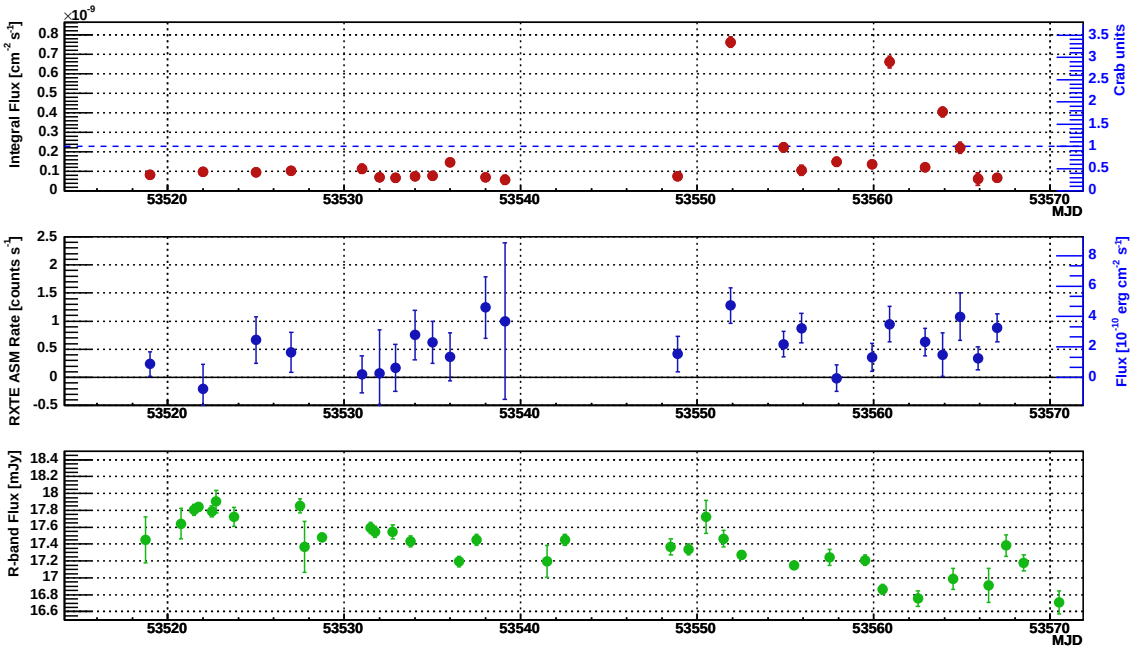

FIGURE 7.11: *Upper panel: Light curve for the observations of Mkn 501 with MAGIC (integral flux between 200 and 2000 GeV). Middle panel: X-ray light curve (2–10 keV band) as observed by the ASM instrument [Lev96] on board of the RXTE satellite [Bra93] (Data available at [Lev04]). Lower panel: Optical light curve as measured with the KVA 35cm monitoring telescope in La Palma. Data courtesy K. Nilsson [Nil06].*

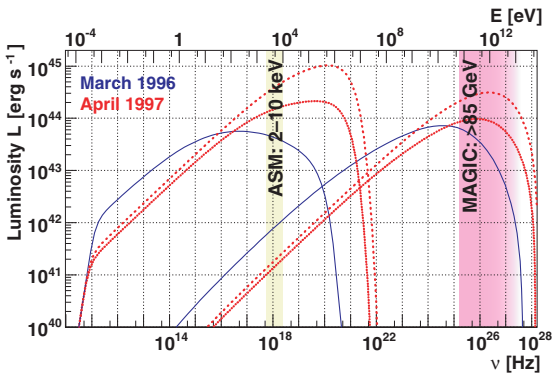

FIGURE 7.12: *ASM energy band (yellow region) together with the MAGIC energy range (red region) and SSC emission models for Mkn 501. The curves correspond to the SSC models for Mkn 501 as given in [Kat99]. Simultaneous changes of the synchrotron and IC emission should lead to correlations of ASM and VHE observations.*

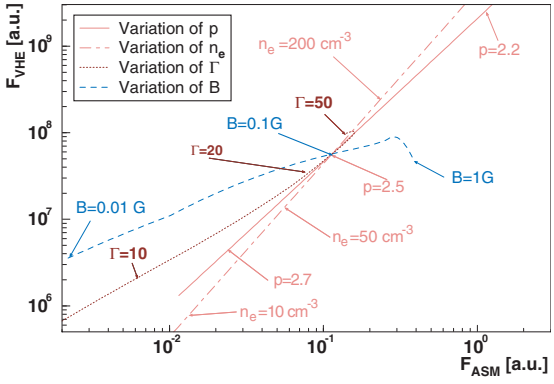

FIGURE 7.13: *Correlation between ASM and VHE γ-ray fluxes in an analytical SSC approximation. For each curve, one of the SSC model parameters Γ, B, n_e and the slope of the electron spectrum p was varied while the others were kept constant ($\Gamma = 20$, $B = 0.1$ G, $n_e = 100\,\mathrm{cm}^{-3}$, and $p = 2.5$). Taken from [Pet00].*

VHE γ-ray/X-ray correlation in the SSC model. As discussed in sect. 2.1.1, leptonic SSC models predict a correlation between synchrotron radiation and VHE γ-rays created in IC reactions. In the case of HBLs, to which Mkn 501 belongs, the synchrotron peak is expected to lie well within the X-ray domain. Therefore, significant variability of the VHE flux ought to be accompanied by a similar flux behavior in X-rays. A systematic study of possible correlations is given in [Kat05]. Here we follow estimates based on an SSC model [Pet00], which provides analytical expressions for the luminosities in the two energy ranges:

$$L_{\mathrm{sy}}^{\mathrm{normalized}} \propto \frac{B n_{\mathrm{e}}}{p-1}\left(\frac{\gamma_{\mathrm{min}}}{\gamma_{\mathrm{b}}}\right)^{p-1} \propto n_{\mathrm{e}} \tag{7.2}$$

$$L_{\mathrm{SSC}}(E) \propto \int_{\varepsilon_{\mathrm{min}}}^{\varepsilon_{\mathrm{max}}} \mathrm{d}\varepsilon \frac{L_{\mathrm{sy}}(\varepsilon)}{\varepsilon}\sqrt{\frac{E}{\varepsilon}} n_{\mathrm{e}}\left(\sqrt{\frac{3E}{4\varepsilon}}\right)\Theta(3/4-\sqrt{E\varepsilon}) \propto n_{\mathrm{e}}^2 \tag{7.3}$$

with the density of the injected electrons n_{e}, their spectral index p, their Lorentz factor at the spectral break γ_{b}, and the Heaviside function Θ. The essential point is that the synchrotron flux depends linearly, the SSC flux quadratically on the electron density, thus $F_{\mathrm{SSC}} \propto F_{\mathrm{sy}}^2$. This dependence may be altered due to an increasing $\gamma\gamma$ absorption opacity intrinsic to the source. This effect is not included in the analytical estimate, but approximated [Pet00] by using a weaker-than-quadratic relation $F_{\mathrm{SSC}} \propto F_{\mathrm{sy}}^{1.6}$. For variations of the bulk Lorentz factor Γ, the X-ray and VHE γ-ray fluxes should in good approximation show a linear correlation (fig. 7.13). Variations of the B field lead to more complex variations and ultimately to an anticorrelation for $B \gtrapprox 0.3$ G.

To quantize the correlation between X-ray flux and VHE γ-ray flux, the linear correlation coefficient (also called *Pearson's r*)

$$r = \frac{\sum_i (F_i^{\gamma} - \overline{F^{\gamma}})(F_i^{\mathrm{X}} - \overline{F^{\mathrm{X}}})}{\sqrt{\sum_i (F_i^{\gamma} - \overline{F^{\gamma}})^2}\sqrt{\sum_i (F_i^{\mathrm{X}} - \overline{F^{\mathrm{X}}})^2}} \tag{7.4}$$

with corresponding γ-ray and X-ray flux pairs F_i^{γ} and F_i^{X} and their average values $\overline{F^{\gamma}}$ and $\overline{F^{\mathrm{X}}}$ is computed. r takes a value of 1 in case of a perfect linear correlation and -1 in case of a perfect anti-correlation. The probability for either case can be computed by the significance of the deviation of r from 0. ($r = 0$ indicates that VHE γ-ray flux and X-ray flux are uncorrelated). The (asymmetric) errors on r are determined using *Fisher's z–transformation*

$$z = \frac{1}{2}\ln\left(\frac{1+r}{1-r}\right), \tag{7.5}$$

exploiting the fact that z is approximately normally distributed [Pre02, sect. 14.5]. The left panel of fig. 7.14 shows the found correlations between X-ray and VHE γ-ray data. Although the measured X-ray flux level is elevated (during quiescent episodes of Mkn 501, the average level is about 0.33 counts/s), the correlation coefficient $r = 0.39^{+0.17}_{-0.20}$ does

not indicate a too strong correlation of X-ray and VHE γ-ray radiation and is within 1.9 standard deviations different from zero. The data points before MJD 53545 do not show large variability in VHE γ-rays, while baseline fluctuations in the X-ray count–rate could make it difficult to find a correlation. When including only nights after MJD 53545, one obtains a stronger correlation, $r = 0.54^{+0.19}_{-0.28}$, with, however, a comparable significance for $r \neq 0$ of 1.8σ.

According to SSC model expectations, a linear, a quadratic, and a weaker–than–quadratic ($y = ax^{1.6} + b$) fit have been performed. The linear fit can either be forced to go through the origin, or an offset can be allowed for, motivated by a possible detection threshold of the ASM instrument. The correlation for the data points after MJD 53545 can be described by all three fits. As it is unsatisfactory to exclude the data points before MJD 53545 arbitrarily, another approach was tried by restricting the correlation test to data with X-ray count rates exceeding 0.33 s^{-1}. This choice is motivated by the average "quiescent" ASM count rate of Mkn 501. This rate might be due to an instrumental bias or to a source baseline flux of Mkn 501 or diffuse X-ray emission. The respective correlation coefficients are $r = 0.36^{+0.20}_{-0.24}$ (1.5σ away from zero) when all data points are included and $r = 0.57^{+0.19}_{-0.29}$ (1.8σ away from zero) when only data points for MJD$>$ 53545 are included (right panel of fig. 7.14). The hardly improving correlation coefficients point to the fact that the measured ASM rates lie close to the instrumental threshold. This, in connection with the fact that for Mkn 501 clearer correlations were observed in the past, particularly in strong flares, may well mean that the correlation between the γ-ray data and higher-energy ($E > 10$ keV) X-ray data would be stronger. Other, physics-related reasons that could weaken a correlation are the contribution of external photon fields to the IC process or hadronic processes that significantly contribute to the VHE γ production. As the data are better described by the quadratic and $x^{1.6}$ fits as compared to the linear fits, one could argue that this observation points to changes in the electron injection spectrum rather than to variations in the bulk Lorentz factor Γ. This behavior has also been reported for the 1997 flare of Mkn 501 [Kra00], although much more evident than in this analysis. Following [Pet00], strong magnetic fields of $B \gtrapprox 0.3$ G are excluded by the observation of a weak X-ray/VHE γ correlation.

Note that a recent systematic assessment of the long–term variability of Mkn 501 [Gli06] found a heterogeneous behavior of the X-ray/VHE γ-ray correlations: Both positive linear and quadratic correlations were observed. Even though in our analysis no unambiguous trend towards a linear or quadratic behavior can be inferred, the hint of correlation in general supports the hypothesis that a leptonic γ-ray production mechanism is at work. For a recent assessment of TeV/X-ray correlations in the framework of homogeneous SSC models see also [Kat05].

Optical light curve. The KVA 35 cm monitoring telescope (cf. sect. 4.8) was used to measure the optical emission of Mkn 501 in the *R*–band simultaneously with the VHE

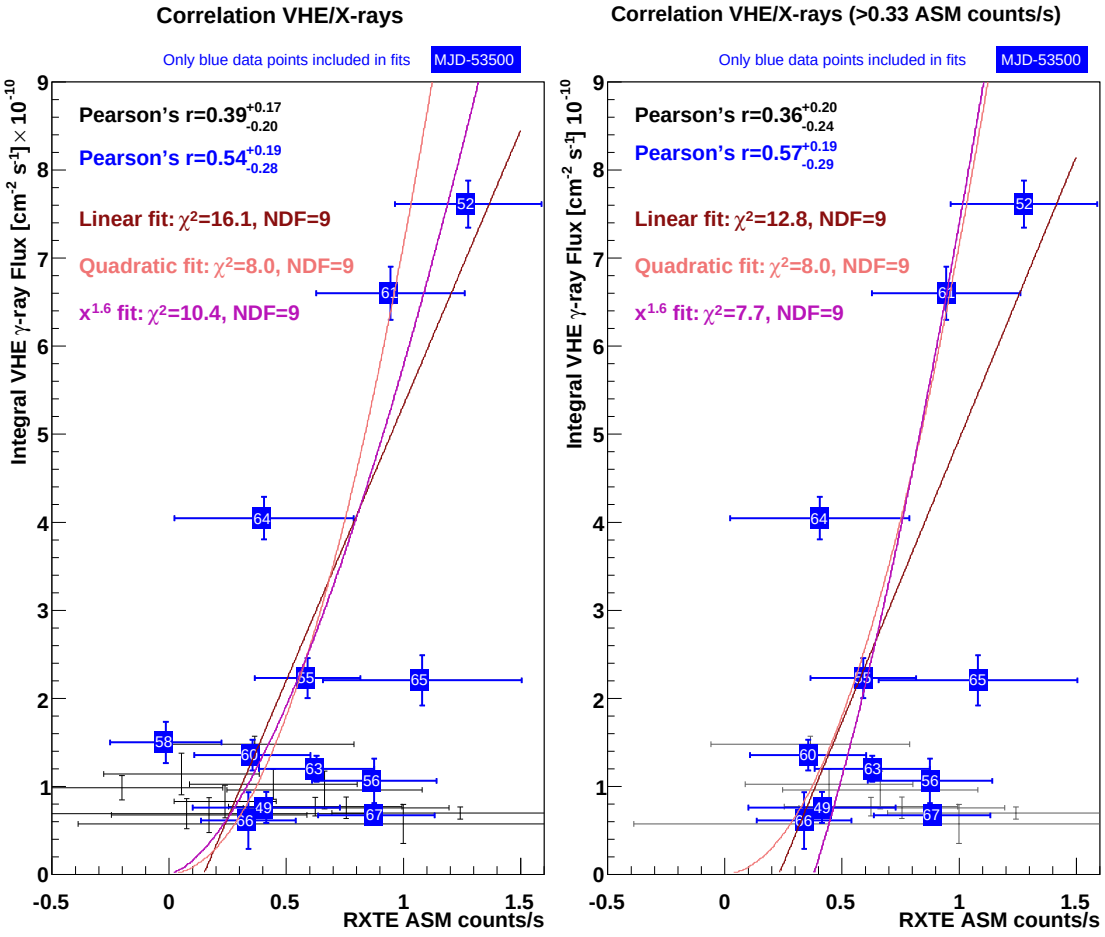

FIGURE 7.14: *Correlation of the integral VHE γ flux above 200 GeV and the X-ray flux in the* $(2-10)$ keV *energy band (ASM data available at [Lev04]). Correlation coefficients were determined for all 24 observation nights under study (black data points) and for nights after 2005 June 30 (MJD 53545; blue symbols). The respective correlation coefficients are given in the plots. Left panel: A linear fit yields a slope of* $m = (6.25 \pm 1.07) \times 10^{-10}\,\mathrm{cm}^{-2}/\mathit{counts}$. *An ASM baseline represented by an offset of 0.15 counts* s^{-1} *was allowed for. A quadratic fit through the origin yields* $a = 7.12 \pm 2.15$ *with* $F = 10^{-10} a \cdot (\mathit{counts}/\mathrm{s})^2$ *in units of ph* $\mathrm{cm}^{-2}\,\mathrm{s}^{-1}$. *A below–quadratic fit* $F = 10^{-10} a \cdot (\mathit{counts}/\mathrm{s})^{1.6}$ *in units of* $\mathrm{cm}^{-2}\,\mathrm{s}^{-1}$ *yields* $a = 5.76 \pm 1.31$. *Free parameters accounting for an ASM baseline were offered to the latter two fits, but were determined to be close to 0 with errors of 0.13 and 0.068, respectively. For the motivation of the chosen fit functions see text. Right panel: To account for a possible sensitivity limit of ASM, as an alternative approach only data points with an X-ray count rate* $> 0.33\ \mathrm{s}^{-1}$ *were considered. The correlation coefficients show comparable correlations. The data are still best described by a quadratic fit.*

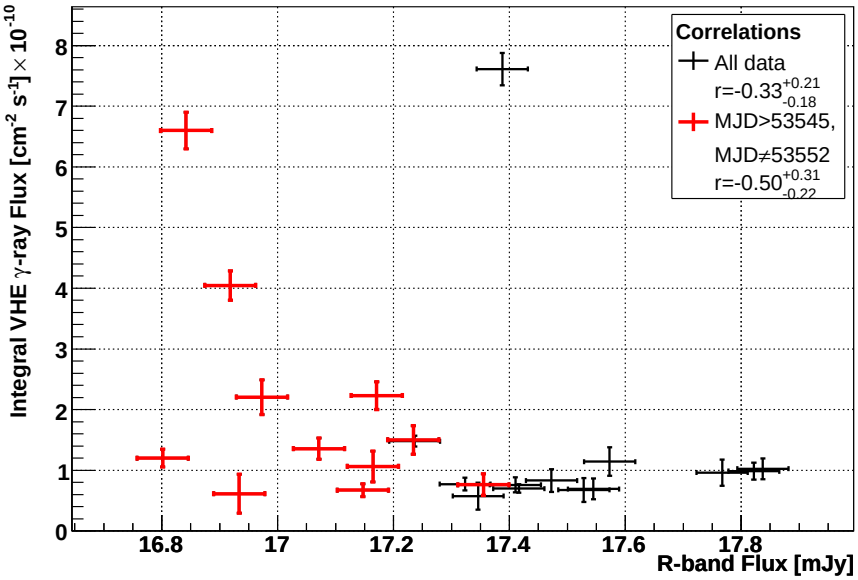

FIGURE 7.15: *Correlation of integral VHE γ flux above 200 GeV and optical flux in the R band as measured with the KVA 35cm monitoring telescope. The found correlation coefficient $r = -0.33^{+0.21}_{-0.18}$ indicates a weak anti-correlation. Note that the highest VHE γ-ray flux point exhibits a substantially higher optical flux than the next two highest VHE γ-ray flux points. Optical data courtesy K. Nilsson [Nil06].*

γ-ray measurements. Previous works [Cat97a] have shown correlated VHE γ-ray and optical variability during multiwavelength observations for Mkn 501. The optical vs. the VHE γ-ray flux (fig. 7.15) shows a weak anti–correlation ($r = -0.33^{+0.21}_{-0.18}$), which becomes more linear ($r = -0.50^{+0.31}_{-0.22}$) when data points before 2005 June 30 and the observation night of 2005 July 01 are excluded. Both values are compatible with a non–correlation with $\approx 12\%$ probability. Note that the excluded data points before 2005 June 30 have a comparatively large scatter in the optical flux while VHE flux fluctuations are rather modest. Also the emission models for Mkn 501 in 1997 in fig. 7.12 show only a weak dependency of the optical flux on the X-ray/VHE flux and, if also the model for 1996 is taken into account, even an anti-correlation might be expected.

Diurnal VHE light curves—Determination of flux levels. Fig. 7.16 shows diurnal light curves for all observation nights included in this analysis. A bin width of 2 minutes has been chosen, so that most of the data points, even on days with comparatively low flux level, feature significances of $\geq 2\sigma$. The overall γ-ray signal is significant on each but one of the days analyzed (tab. 7.2). The light curve of each observation night was fitted using a constant flux ansatz. While for most of the nights, the fits yield reduced χ^2 values close to 1, the observation nights of July 01 and July 10, 2005 show a rather bad χ^2, indicating intra-night variability. For most of the spectral studies in sect. 7.7, the observation nights were grouped according to the respective flux levels found (tab. 7.3) as to increase statistics. The two nights of July 01 and July 10, 2005 will be subjected to further studies in sect. 7.8. A day-to-day variability analysis is shown in sect. 7.8.5.

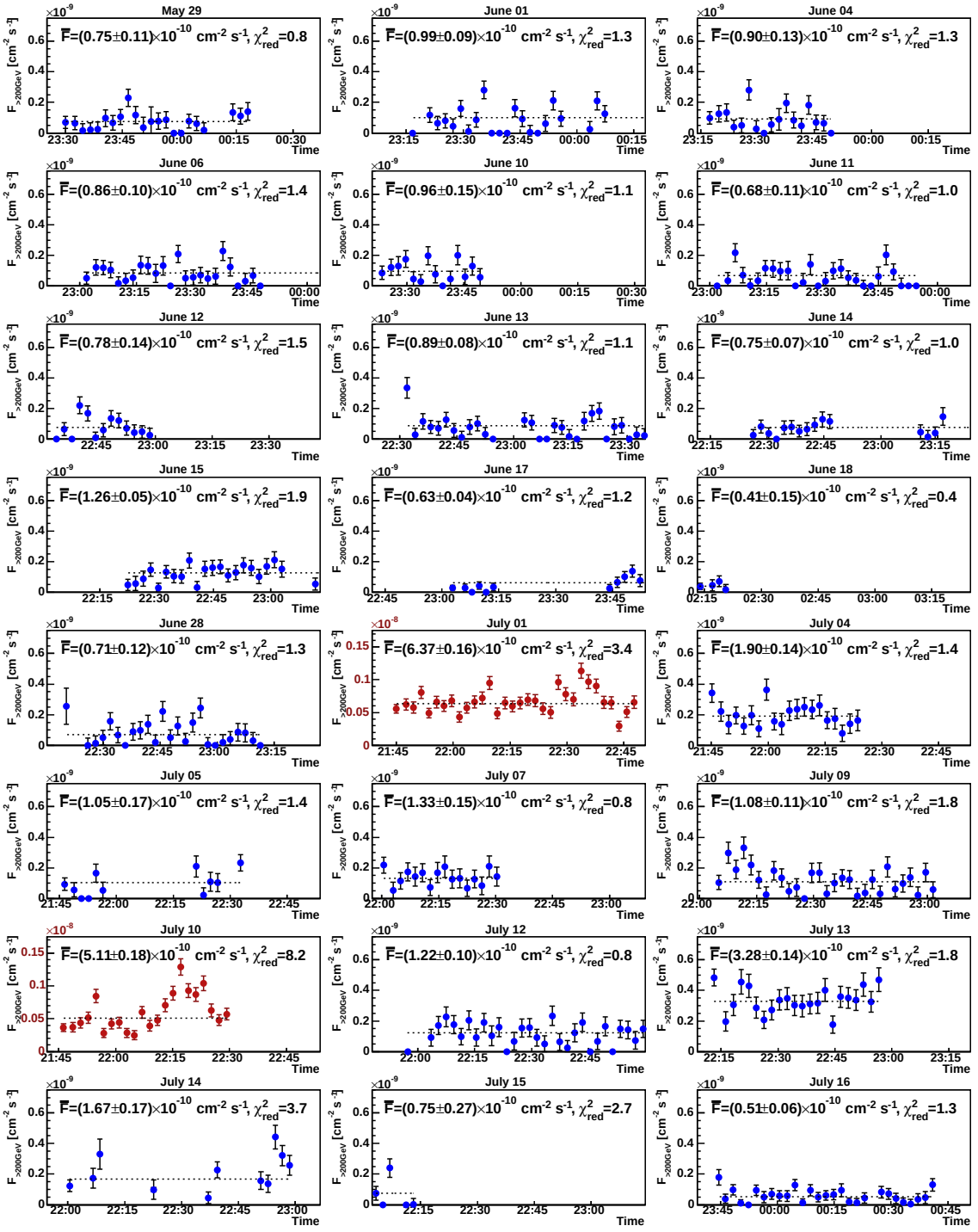

FIGURE 7.16: *Diurnal light curve (integral flux above 200 GeV). The vertical axes have an identical range (except for the two high–flux days), the horizontal axes have equal units so as to allow direct comparison of the plots. To each light curve a constant function has been fitted in order to indicate the average flux level present on the respective day.*

Baseline	Enhanced	Medium	High
$F < 0.09$	$0.09 \leq F < 0.16$	$0.16 \leq F < 0.45$	$F > 0.45$
2005/06/11	2005/05/29	2005/07/04	2005/07/01
2005/06/12	2005/06/01	2005/07/13	2005/07/10
2005/06/13	2005/06/04	2005/07/14	
2005/06/14	2005/06/06		
2005/06/17	2005/06/10		
2005/06/18	2005/06/15		
2005/06/28	2005/07/05		
2005/07/15	2005/07/07		
2005/07/16	2005/07/09		
	2005/07/12		

TABLE 7.3: *Grouping of Mkn 501 data. According to the flux level found, the observation nights were categorized as showing a baseline, enhanced, medium and high flux. F is the integrated flux between 200 GeV and 2000 GeV in units of* 10^{-9} cm^{-2} s^{-1}.

7.7 Spectrum determination

To determine differential energy spectra for the Mkn 501 observations, we group the observation nights according to their flux levels. We then study a possible correlation of the diurnal flux level and the respective spectral slopes. As the observed energy range is sensitive to the position of the inverse Compton peak, studies of the measured and EBL de-absorbed (intrinsic) spectra are performed. Since the intrinsic spectra turn out to be rather flat between 200 GeV and ≈ 4 TeV, the inferred errors on the peak position tend to be rather large. This is why the spectra before de-absorption are also studied.

7.7.1 Flux–level dependent spectra

The observation nights were grouped according to the flux level found on the individual nights according to tab. 7.3. For each flux level a differential energy spectrum was calculated. The results are shown in the usual representation for differential fluxes (fig. 7.17) as well as in a $E^2 \times \mathrm{d}F/\mathrm{d}E$ representation (fig. 7.18).

Within the SSC model the location of the IC peak is expected in the VHE region. Thus pure power law fits, as usually applied for characterizing spectral distributions in the VHE γ-ray domain, might not be appropriate. Therefore, each of the spectra was fitted both with a pure power law ansatz as well as with a function which accounts for a possible curvature in the spectrum. For the latter, functions like broken power laws or power laws with exponential cutoffs,

$$\frac{\mathrm{d}F(E)}{\mathrm{d}E} \sim E^{-\alpha} \exp\left(-\frac{E}{E_{\mathrm{cutoff}}}\right), \tag{7.6}$$

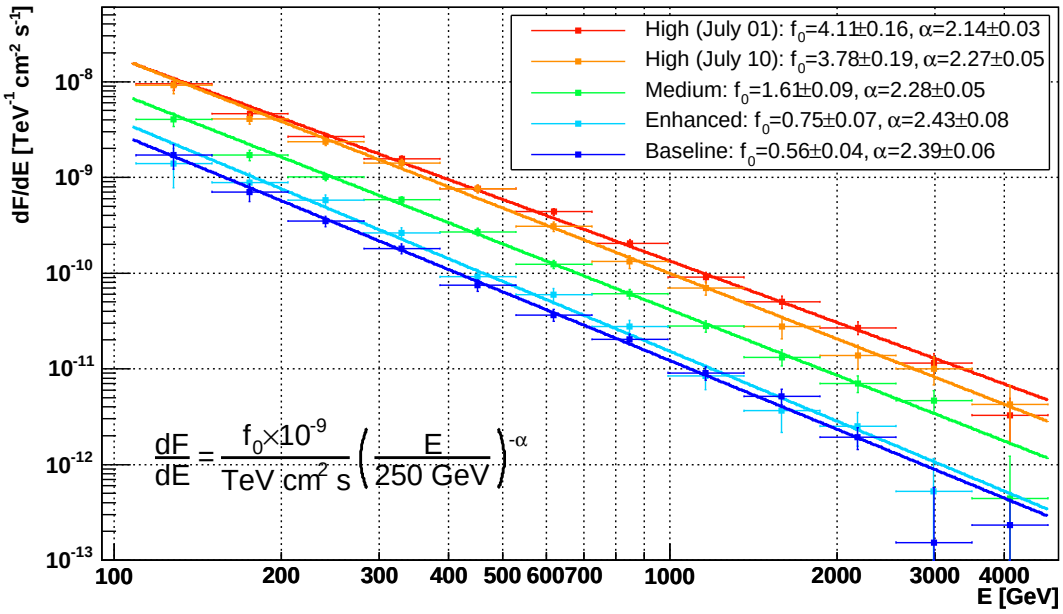

FIGURE 7.17: *Differential energy spectra for different flux levels according to the classification given in tab. 7.3. Pure power-law functions were fitted to to the spectra between 105 GeV and 4.8 TeV.*

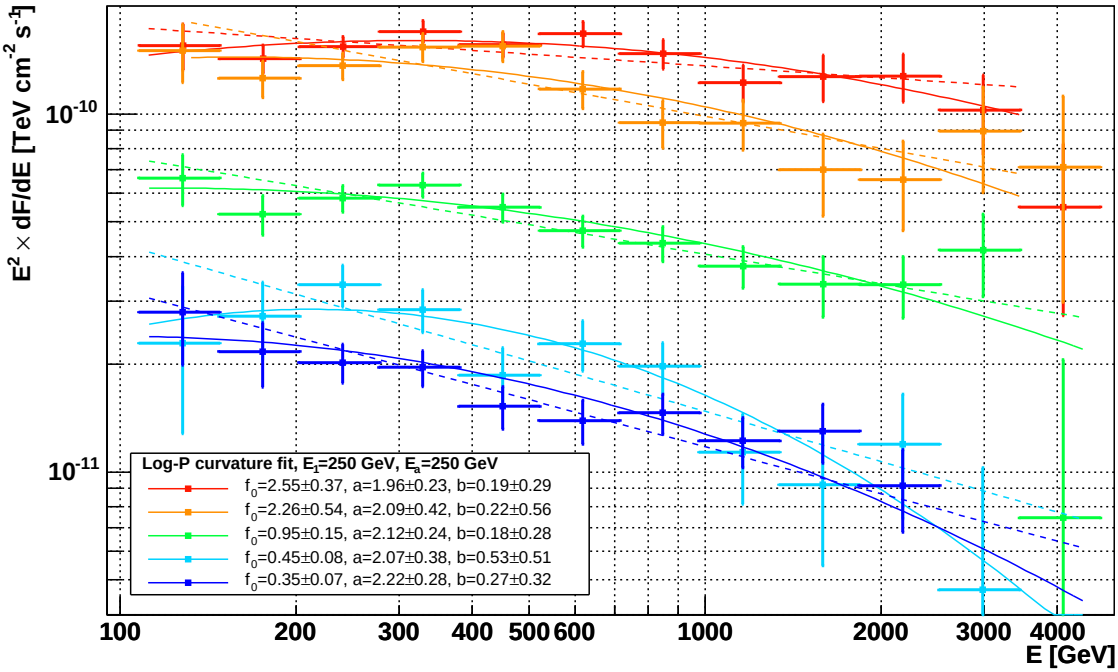

FIGURE 7.18: *Spectral energy densities for different flux levels according to the classification given in tab. 7.3. The solid curves represent curvature (Log-P) fits of the form* (7.7)*; the corresponding fit parameters are given in the caption. The dashed curves are the pure power-law fits of fig. 7.17.*

Pure power-law fit ($E_0 = 250$ GeV, normalization f_0 in units of 10^{-9} cm^{-2} s^{-1})

Data sample	f_0	α
High (2005/07/01)	4.11 ± 0.16	2.14 ± 0.03
High (2005/07/10)	3.78 ± 0.19	2.27 ± 0.05
Medium	1.61 ± 0.09	2.28 ± 0.05
Enhanced	0.75 ± 0.07	2.43 ± 0.08
Baseline	0.56 ± 0.04	2.39 ± 0.06

Curved log-parabolic fit ($E_1 = 250$ GeV, $E_a = 250$ GeV, normalization f_0 in units of 10^{-9} cm^{-2} s^{-1})

Data sample	f_0	a	b	$\alpha_{\text{Log-P}}(200\text{ GeV})$	$\alpha_{\text{Log-P}}(1\text{ TeV})$
High (2005/07/01)	2.55 ± 0.37	1.96 ± 0.23	0.19 ± 0.29	1.92	2.19
High (2005/07/10)	2.26 ± 0.54	2.09 ± 0.42	0.22 ± 0.56	2.04	2.35
Medium	0.95 ± 0.15	2.12 ± 0.24	0.18 ± 0.28	2.08	2.34
Enhanced	0.45 ± 0.08	2.07 ± 0.38	0.53 ± 0.51	1.97	2.72
Baseline	0.35 ± 0.07	2.22 ± 0.28	0.27 ± 0.32	2.16	2.55

TABLE 7.4: *Spectral properties for different flux levels. The spectra given in figs. 7.17 and 7.18 were fitted using a pure power law* $\mathrm{d}F/\mathrm{d}E = f_0 \cdot (E/E_0)^{-\alpha}$ *with* $E_0 = 250$ GeV *as well as with a curved log-parabolic function* (7.7)*, which was then used to determine the equivalent slope* $\alpha_{\text{Log-P}}(E)$ *at* $E = 200$ GeV *and* $E = 1$ TeV*, respectively, along eq.* (7.8)*.*

offer themselves. [Mas04] shows that a *log parabolic* (Log-P) model,

$$\frac{\mathrm{d}F(E)}{\mathrm{d}E} \sim \left(\frac{E}{E_1}\right)^{-\left(a+b\log\left(\frac{E}{E_a}\right)\right)}, \tag{7.7}$$

is physically well suited to describe curved spectral energy distributions in the transition region close to the IC peak, as long as the peak is not too asymmetric. a is the photon index at the reference energy E_a; b is related to the curvature radius at the parabola vertex. An energy–dependent photon index can be defined by

$$\alpha_{\text{Log-P}}(E) = a + 2b\log\left(\frac{E}{E_a}\right), \tag{7.8}$$

The maximum of the Log-P function is given by

$$E_{\text{peak}} = E_a \cdot 10^{\frac{2-a}{2b}}. \tag{7.9}$$

We have used the Log-P model to test the obtained spectra for curvature. As expected, a spectral hardening is observed with increasing flux. The resulting spectral slopes and flux normalizations for pure power law fits and log-parabolic fits are given in tab. 7.4.

7.7.2 Correlation between spectral hardness and flux level

The observed spectral hardening is a hint for a possible correlation of the flux level and the spectral slope. Therefore, for all days for which reliable spectra could be produced, the integral flux for $E \geq 200$ GeV is plotted versus the corresponding spectral index α obtained from a pure power law fit between 200 GeV and 900 GeV in fig. 7.19. A clear

correlation is visible, which can be described by a linear function for the slope $\alpha = \alpha_0 + m \cdot F$ with $\alpha_0 = (2.60 \pm 0.06)$ and $m = (-6.8 \pm 1.3) \cdot 10^8$ cm^2 s. The correlation coefficient (cf. sect. 7.6) $r = -0.47^{+0.24}_{-0.19}$ is within 1.8 standard deviations different from zero. In the context of SSC models, MAGIC observes the high energy edge of the IC peak. Thus, spectral hardening correlated with an increasing VHE γ-ray flux level can be interpreted as the observation of a moving IC peak towards higher energies as illustrated in fig. 7.20.

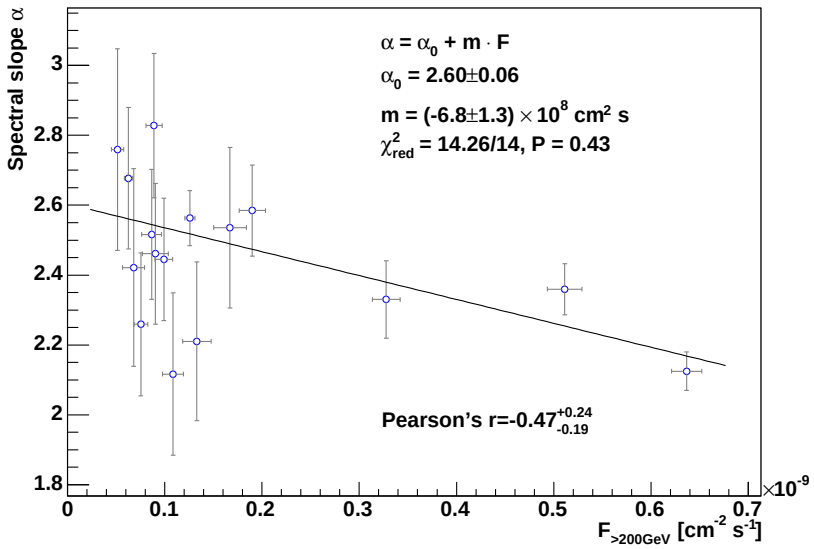

FIGURE 7.19: *Correlation of flux level and slope. The figure shows the integral flux at energies of* $E \geq 200$ GeV *and the spectral index as obtained from a power law fit to the corresponding differential energy spectrum between 200 GeV and 900 GeV. The correlation shows a clear hardening of the spectra with increasing flux level and is well described by a linear function for the slope* $\alpha = (2.60 \pm 0.06) - (6.8 \pm 1.3) \cdot 10^8$ cm^2 s $\cdot F$.

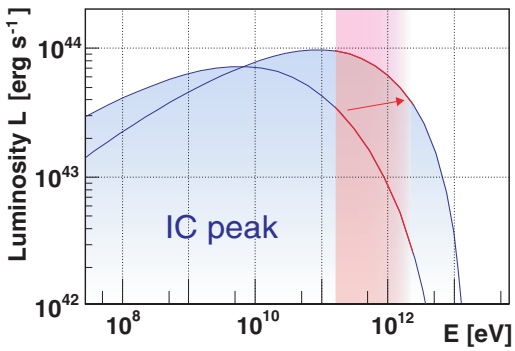

FIGURE 7.20: *Interpretation of the observed flux—spectral slope correlation as a moving IC peak towards higher energies with increasing integrated VHE* γ*-ray flux.*

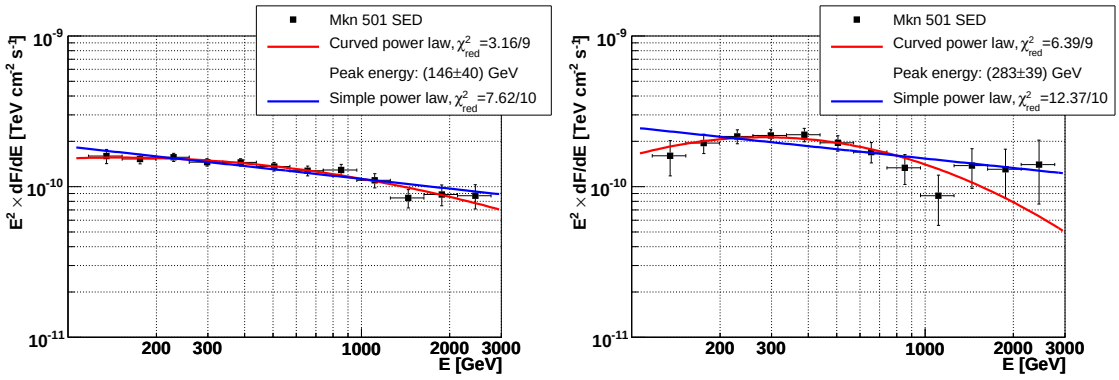

FIGURE 7.21: *Combined SED for 2005 July 1 and 2005 July 10. Left panel: runs with integrated flux* $< 0.08 \cdot 10^{-8}$ cm^{-2} s^{-1}. *Right panel: runs with integrated flux* $\geq 0.08 \cdot 10^{-8}$ cm^{-2} s^{-1}.

7.7.3 Inverse Compton peak

According to model predictions, the IC peak of the intrinsic energy distribution of Mkn 501 lies around $5-10$ TeV [Jag02]. These predictions depend strongly on the EBL model used. Observationally, a peak structure was found in Mkn 501 spectra (without EBL de-absorption!) during the 1997 flares in the 200 GeV $-$ 1 TeV region [Dja99]. The peak position should be strongly dependent on the VHE γ-ray flux level in case the peak moves to higher energies with increasing flux level. To test for possible indications of the IC peak, the curvature of the observed spectra of the two flare days are examined for a possible turnover at low energies, as the IC peak is expected to be shifted to higher energies during flares.

The data sets of 2005 July 01 and 2005 July 10 were divided into a "low flux" range (integrated flux $F_{E\geq 200\,\mathrm{GeV}} < 0.08 \cdot 10^{-8}$ cm^{-2} s^{-1}) and a "high flux" range (integrated flux $F_{E\geq 200\,\mathrm{GeV}} \geq 0.08 \cdot 10^{-8}$ cm^{-2} s^{-1}). The respective data sets for both days then were combined, their SEDs are shown in fig. 7.21. Although a fit including a curvature nicely guides the eye, the probabilities for a pure power law fit and for a Log-P model fit are comparable. When using (7.9) to compute the peak energy, one obtains $E_{\mathrm{peak}} = (146 \pm 40)$ GeV for the "low flux" sample and $E_{\mathrm{peak}} = (283 \pm 39)$ GeV for the "high flux" sample. When examining the "high flux" data sets for the two flare days individually (fig. 7.22), peak energies of $E_{\mathrm{peak}} = (257 \pm 66)$ GeV and $E_{\mathrm{peak}} = (321 \pm 43)$ GeV are found. Due to the flatness of the spectra in the energy range observed, the errors on the peak positions are comparatively large. To find a possible correlation of peak energy and the integrated flux level, those two data sets and the corresponding two "low flux" data sets (fig. 7.23) are compared in fig. 7.24. When extrapolating the linear fit applied to the data points ($\chi^2 = 1.09/2$, $P = 0.58$), at flux levels of the large flare of 1997 [Aha97], the corresponding structure should have been seen around $\approx (400-500)$ GeV. In conclusion, the spectra hint at the existence of a peak structure that is moving with the flux level (in accordance with the observations of changing spectral slopes).

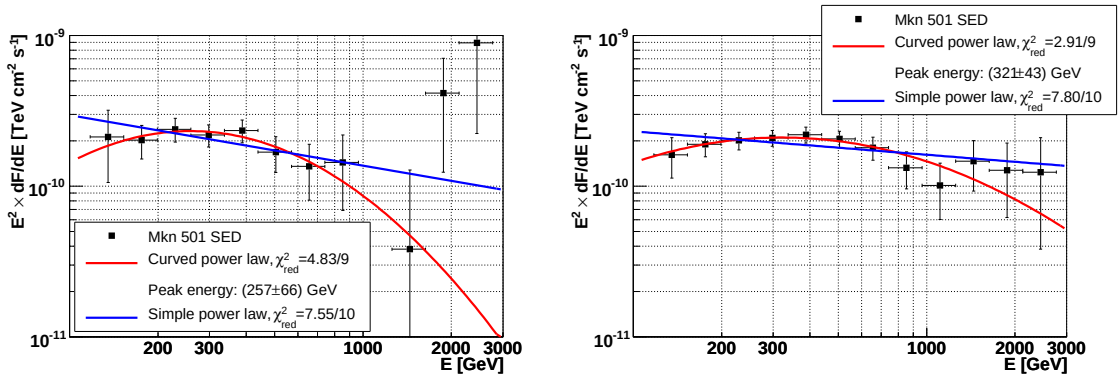

FIGURE 7.22: *SEDs for runs with integrated flux* $\geq 0.08 \cdot 10^{-8}$ cm^{-2} s^{-1}. *Left panel: for 2005 July 1. Right panel: for 2005 July 10.*

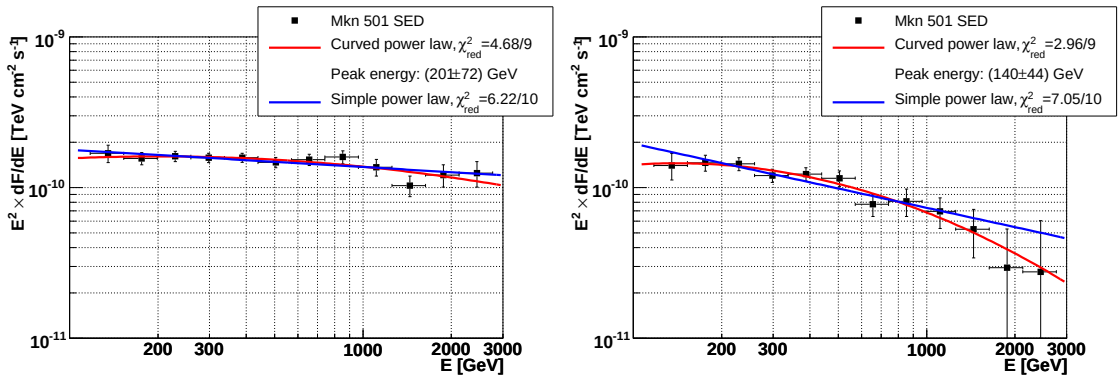

FIGURE 7.23: *SEDs for runs with integrated flux* $< 0.08 \cdot 10^{-8}$ cm^{-2} s^{-1}. *Left panel: for 2005 July 1. Right panel: for 2005 July 10.*

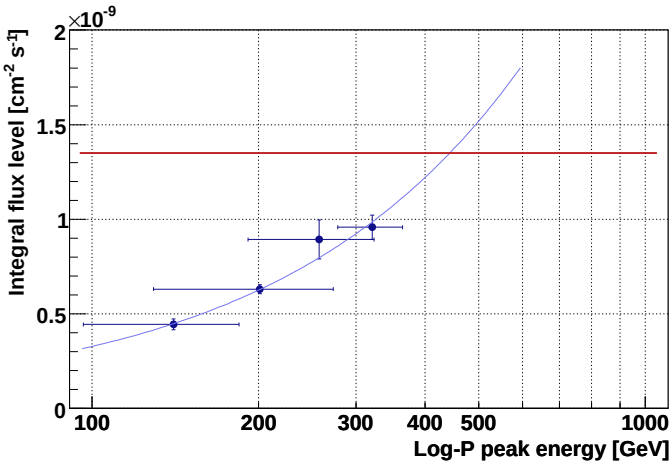

FIGURE 7.24: *Correlation of peak energy and integrated flux level. The red line indicates the flux level corresponding to* ≈ 10 *Crab units as observed during the 1997 flare of Mkn 501.*

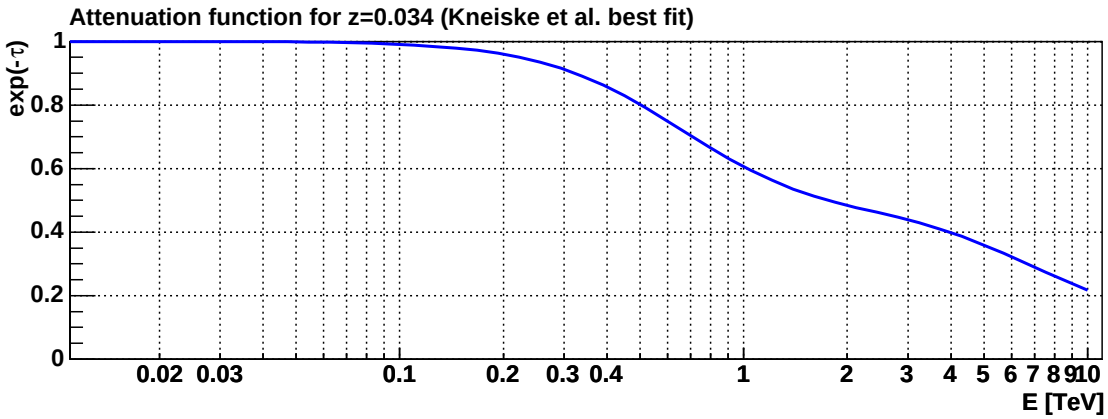

FIGURE 7.25: *Attenuation function describing the EBL absorption effects for a redshift of* $z = 0.034$.

7.7.4 Intrinsic energy spectra

As discussed in sect. 1.2.2, γ-rays emitted by astrophysical objects at large distances suffer from absorption by the extragalactic background light. This effect has to be taken into account when reconstructing the source intrinsic energy spectra of AGNs. In the particular case of Mkn 501, the attenuation function (1.6) as obtained from the "best–fit" EBL model given by [Kne04] for a redshift of $z = 0.034$ is shown in fig. 7.25. The effect of the EBL de-absorption is given in fig. 7.26, which shows the reconstructed intrinsic energy spectra of Mkn 501 at high, medium and enhanced flux levels according to tab. 7.3. As the reconstructed spectra are very flat and do not extend far beyond 4 TeV, the parabolic fits (tab. 7.5) are rather poor and have large errors, in particular on the peak energy E_{peak}. Still, a trend towards an increasing peak energy with increasing flux level is seen.

Data sample	f_0	a	b	$E_{\mathrm{peak}}[\,\mathrm{TeV}]$
High (July 1)	0.83 ± 0.11	1.82 ± 0.10	0.19 ± 0.20	1.4 ± 0.7
High (July 10)	0.65 ± 0.10	1.94 ± 0.18	0.10 ± 0.35	1.0 ± 1.3
Medium	0.27 ± 0.04	1.97 ± 0.12	0.06 ± 0.24	0.9 ± 1.2
Enhanced	0.22 ± 0.02	2.13 ± 0.16	0.38 ± 0.45	0.3 ± 0.1

TABLE 7.5: *Fit parameters for intrinsic Mkn 501 energy spectra as shown in fig. 7.26. The spectra were fitted using the log-P model, eq.* (7.7)*. The fits resulted in a flux normalization at the reference energy of 350 GeV,* f_0*, given in units of* 10^{-9} TeV^{-1} cm^{-2} s^{-1}*, the photon index a at the reference energy, and a curvature term b. The reconstructed peak energy* E_{peak}*, computed using eq.* (7.9)*, is also given.*

The intrinsic energy spectra are further discussed in sect. 7.10, where they are put in perspective with the broad band SED of Mkn 501 and spectra measured by other instruments.

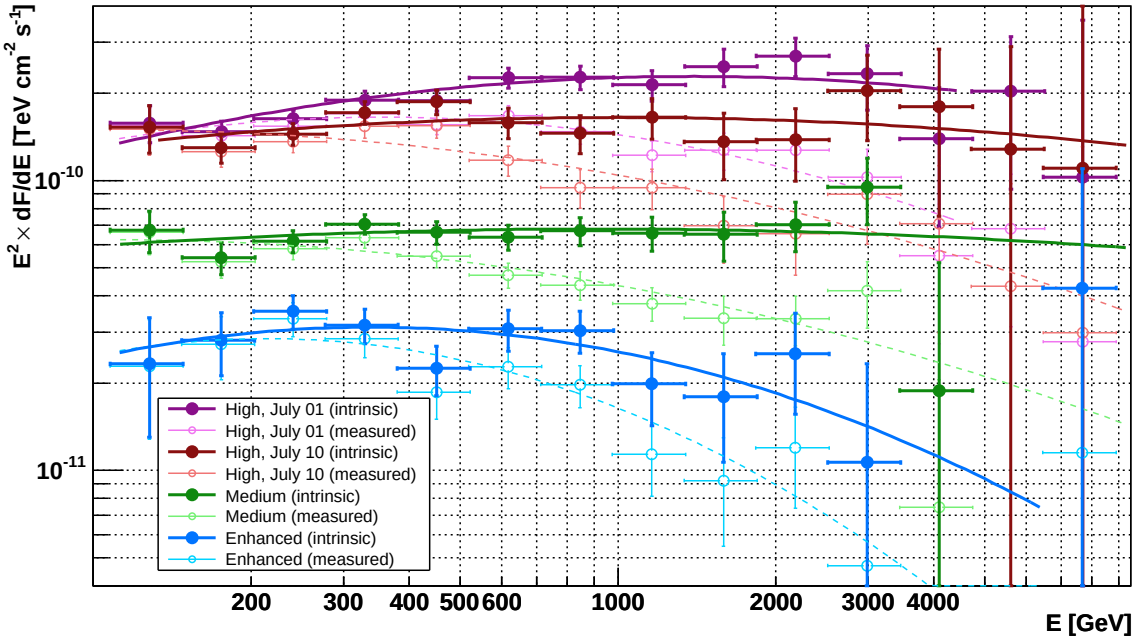

FIGURE 7.26: *Observed (hollow symbols) and intrinsic (filled symbols) energy spectra of Mkn 501. The intrinsic spectra were reconstructed by taking into account the attenuation suffered by extragalactic background light. The dashed curves are Log-P curvature fits to the observed spectra, cf. fig. 7.18. The solid curves are Log-P fits to the intrinsic energy spectra; the correspondig fit parameters are given in tab. 7.5.*

7.8 Flare analysis

For the three observation nights of 2005 July 1, 10, and 13, the overall light curve (fig. 7.11) for Mkn 501 shows a flux level significantly higher than the baseline flux of $2.5 \cdot 10^{-10}$ cm^{-2} s^{-1} for energies of 200 GeV and above.

On two of the three nights mentioned, substantial intra–night variations of the flux level are apparent. The corresponding light curves with a time resolution of 2 minutes are shown in fig. 7.27. Flux level variations of a factor exceeding three can be seen. The reduced χ^2s for fitting a constant level, in particular for the night of July 10, underline the variability. When restricting the fits to a region in which no significant variability is apparent (this is 21:45 to 22:25 for 2005 July 1 and 21:45 to 22:12 for 2005 July 10, respectively), the χ^2 values decrease considerably. The baseline fluxes found from these restricted fits, $F = (6.43 \pm 0.21) \times 10^{-10}$ cm^{-2} s^{-1} for 2005 July 1 and $F = (4.19 \pm 0.22) \times 10^{-10}$ cm^{-2} s^{-1} for 2005 July 10, are used for computing the significance *of the flares* later on.

Apart from dividing the events into bins of constant duration, they have been analyzed on a run-by-run basis (lower panels of fig. 7.27) so as to ensure that no binning effects or effects due to run stops or starts fake variability. Control plots, which show the excess events and the background events as a function of time, do not reveal any noticeable

problems: In the distribution of the individual fluxes (fig. 7.28) a clear deviation from a Gaussian distribution can be seen for both nights studied, while there is no noticeable excess in the background control region (fig. 7.29).

This phenomenon, a highly variable flux on short timescales $\tau < 1$ d, is a characteristic feature of blazars. By determining the rise and fall times of flares one can draw conclusions on the extension of the emitting region of the VHE radiation due to causality arguments. Furthermore, limits on quantum gravity effects can be posed by looking at possible time differences of characteristic features of the light curve in distinct energy bins.

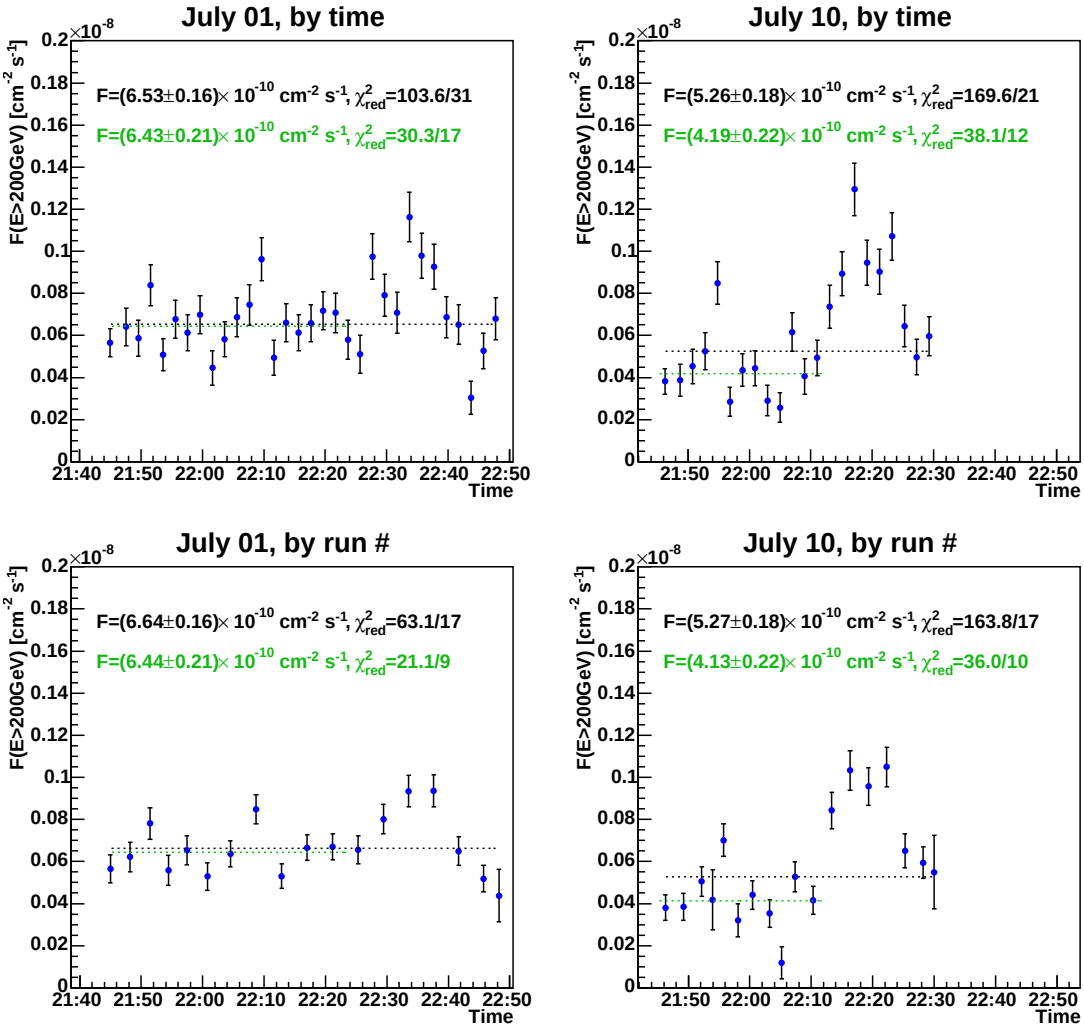

FIGURE 7.27: *Light curves for 2005 July 1 and 2005 July 10. The light curves have been fitted by a constant function over the whole data range (black captions and dashed lines.) and in a region in which no strong variability was observed (green captions and dashed lines) Upper panel: binned by run time. The probability for the constant fit over the whole range vs. for the "stable" first part of the light curve is* 2.25×10^{-11} *vs.* 2.4% *for July 1 and* 0 *vs.* 0.0146% *for July 10, respectively. Lower panel: Binned by run number as to make sure no artifacts from the start of new runs spoil the light curves. The integral light curves (*200 GeV *and above) have been produced using a lower* SIZE *cut of 250* ph.el.

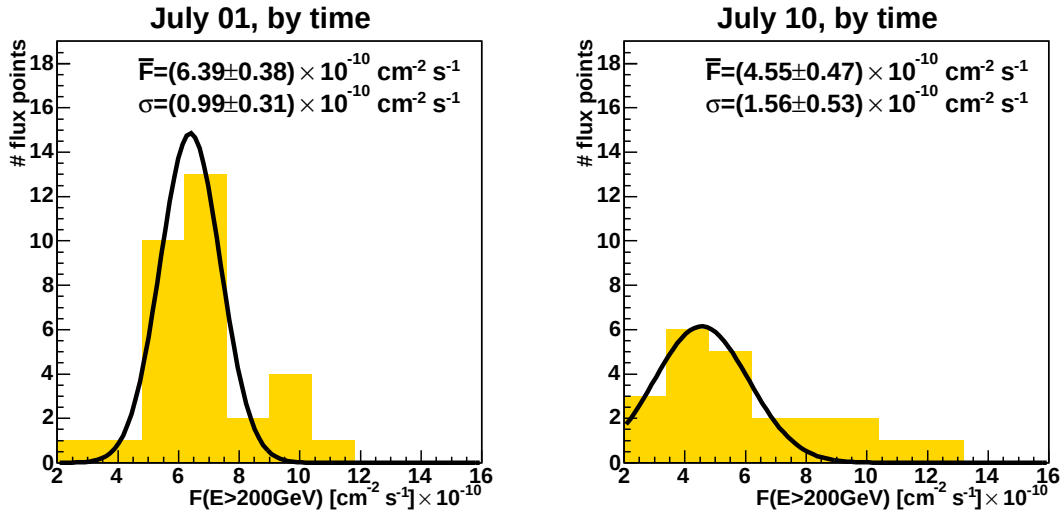

FIGURE 7.28: *Distributions of flux values for 2005 July 1 and 2005 July 10. For both nights, bins in excess of the expected Gaussian distribution in case of no flares are observed.*

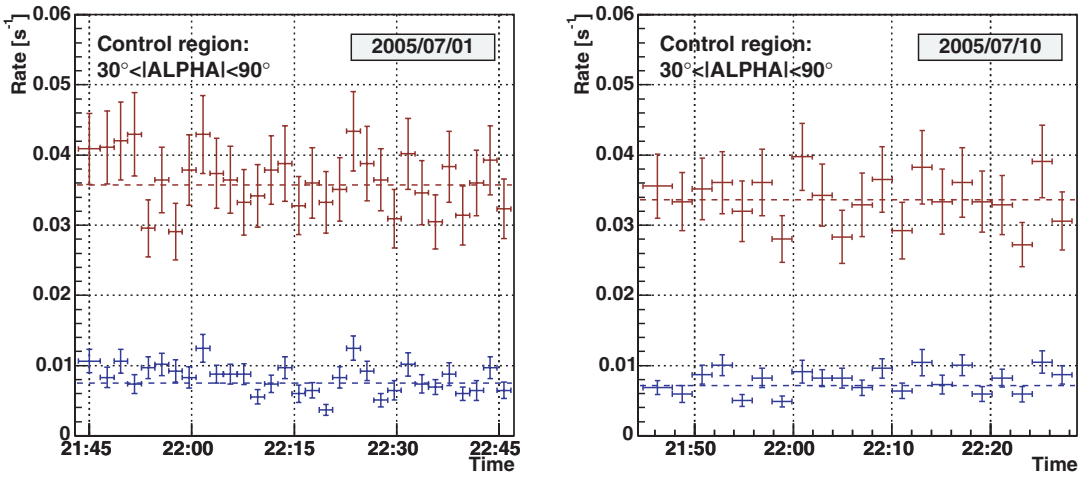

FIGURE 7.29: *Distributions of excess events in the* $30° < |\,\text{ALPHA}\,| < 90°$ *region of the* ALPHA *plots for 2005 July 1 and 2005 July 10, respectively. In this region no* γ *events from the source direction are expected. The number of events is normalized with the effective observation time. The red symbols represent* ≥ 150 GeV *energy bins, the blue symbols* ≥ 300 GeV *energy bins.*

As can be seen from fig. 7.30, almost all data points shown have a significance of at least 3σ and there is no data point less significant than 2σ. The interpretation of this finding is that there are *significant variations* present in the data sets, not necessarily sub-hour flares though. Fig. 7.31 shows for the individual bins of time the significances for an excess above or a deficit below the constant flux baselines mentioned before. The plots can be interpreted in two ways: Conservatively, we could require each of the time bins belonging to a putative flare to exceed a significance of 3σ. More pragmatically, we could quadratically sum up the individual significances, and quote one significance for

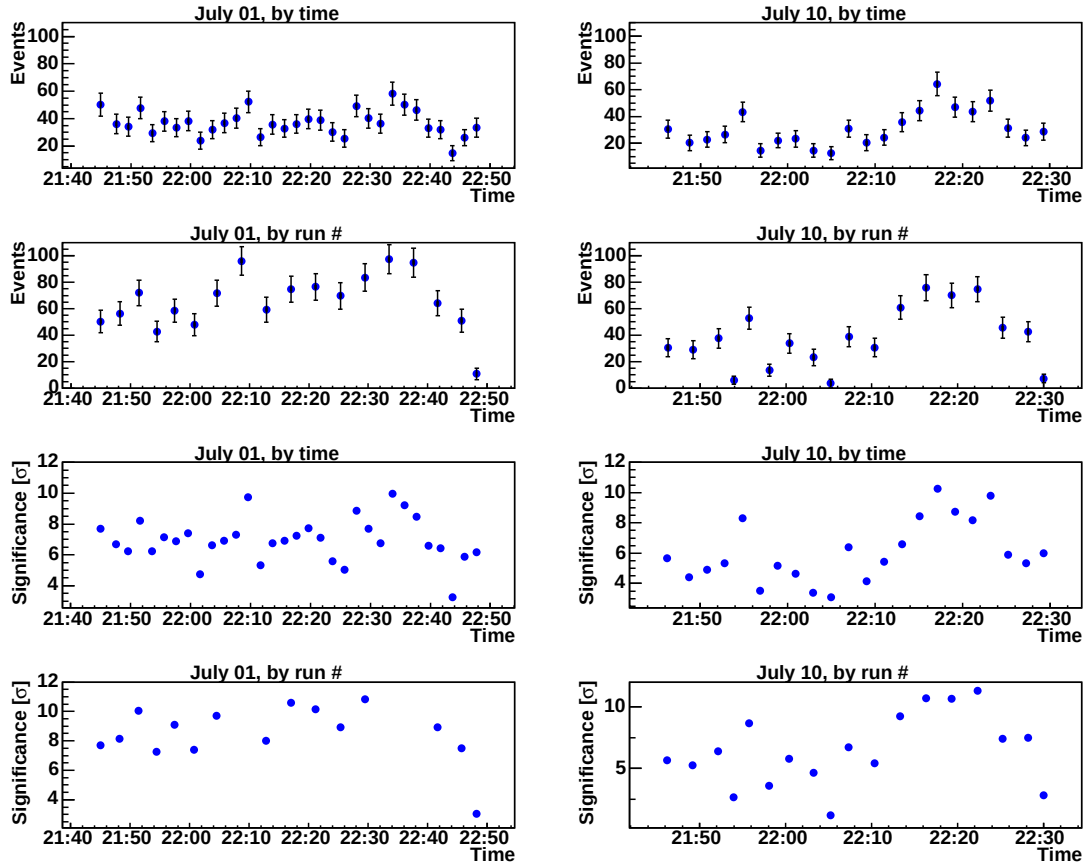

FIGURE 7.30: *The distributions of excess events and significances for 2005 July 01 and 2005 July 10 serve as control plots for fig. 7.27. As expected, the upper plots resemble the derived fluxes, because effective collection area and effective observation time do not vary much from time bin to time bin. The lower panels show the significances for the individual bins, nearly all of which are well above* 3σ.

the flare. Either way, on July 10 we would recognize a rather extended "flare complex" starting around 22:10 UTC (peak significance: 4.7σ, overall significance: 8.2σ) plus an additional flare at 21:55 UTC (2.76σ peak significance). For 2005 July 1, the 22:34 UTC bin reaches 2.8σ (peak significance), the flare complex of all three bins at that time yields 3.7σ. Note that for the 2005 July 1 light curve the baseline flux is rather badly determined.

Short–term correlations. To claim or disprove short–term ($t \ll 1$ h) correlations between VHE γ-ray and X-ray light curves, a dense sampling of the X-ray flux is necessary. Fig. 7.32 shows the timing of single X-ray observations performed by the ASM instrument. For both nights under study, the X-ray observations were not frequent enough to claim or disprove short–term correlation or an orphan flare case for such short flares. Note that, although highly interesting, no conclusions are possible at this point on the validity of correlations expected within SSC models as discussed in sect. 7.6, which could hint at possible flare mechanisms.

Note that the ASM data, meant as monitoring data, have rather large statistical and sys-

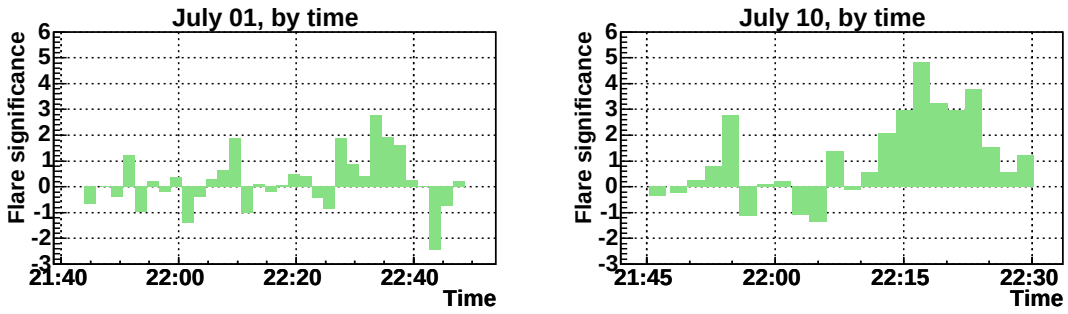

FIGURE 7.31: *Significances for the deviation of each given time bin from the flux baselines of* $F = (6.43 \pm 0.21) \times 10^{-10}\,\mathrm{cm}^{-2}\,\mathrm{s}^{-1}$ *for 2005 July 1 and* $F = (4.19 \pm 0.22) \times 10^{-10}\,\mathrm{cm}^{-2}\,\mathrm{s}^{-1}$ *for 2005 July 10. The significances are calculated according to [Li83], interpreting the baseline flux level as background over which a flare signal is found.*

tematical day-by-day errors. Also the ASM statistics are so poor that rapid flaring cannot be followed and the data have to be averaged over larger periods of time for meaningful results (as done in the inter-day correlation study in sect. 7.6). The RXTE satellite is equipped with other instruments like the Proportional Counter Array that performs pointed observations at higher precision.

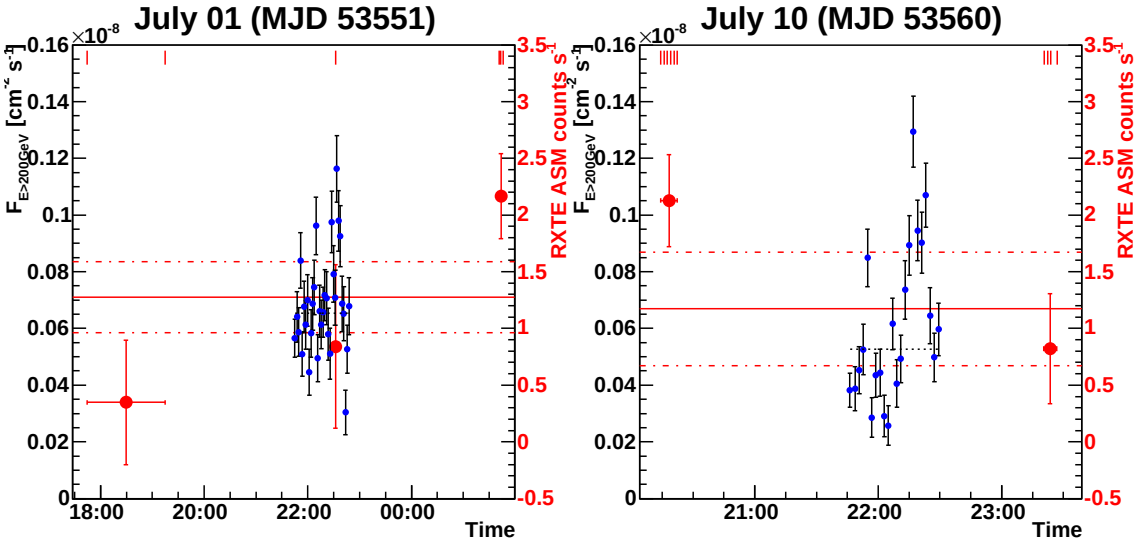

FIGURE 7.32: *Contemporaneous X-ray pointings with MAGIC data taking for 2005 July 1 and 2005 July 10. The left axis is valid for the integral VHE* γ*-ray flux data points. The small red indicators in the upper part of the plots give the exact timings of the individual ASM pointings. The right axis shows the X-ray flux level in units of ASM counts. The red lines represent the averaged ASM count–rate over 6 hours around the MAGIC measurements, while the red data points are averaged ASM data.*

7.8.1 Spectral changes during high flux levels

As shown by the data, the photon index of the Mkn 501 spectrum changes substantially with the observed diurnal flux level. As it would be interesting to study if such spectral changes also occur on the short timescale dictated by the intra-day flares, the runs taken on July 10 were split into three groups (cf. inset in fig. 7.33). From these, runs with a flux level well below the average flux were used to determine a "baseline" spectrum, while the four runs with elevated flux level were combined to calculate a "flare" spectrum. The two spectra are shown in fig. 7.33. For robustness, they were fitted with pure power laws between 95 GeV and 2.5 TeV. While the baseline spectrum has a slope of $\alpha = 2.6 \pm 0.1$, the flare spectrum is significantly harder with $\alpha = 2.1 \pm 0.1$. The sufficiently small ($P \approx 10^{-9}$) probability that the flare spectrum can be fit with the baseline slope justifies a claim that there is a significant variation of the spectral slope on a timescale smaller than 0.5 hours.

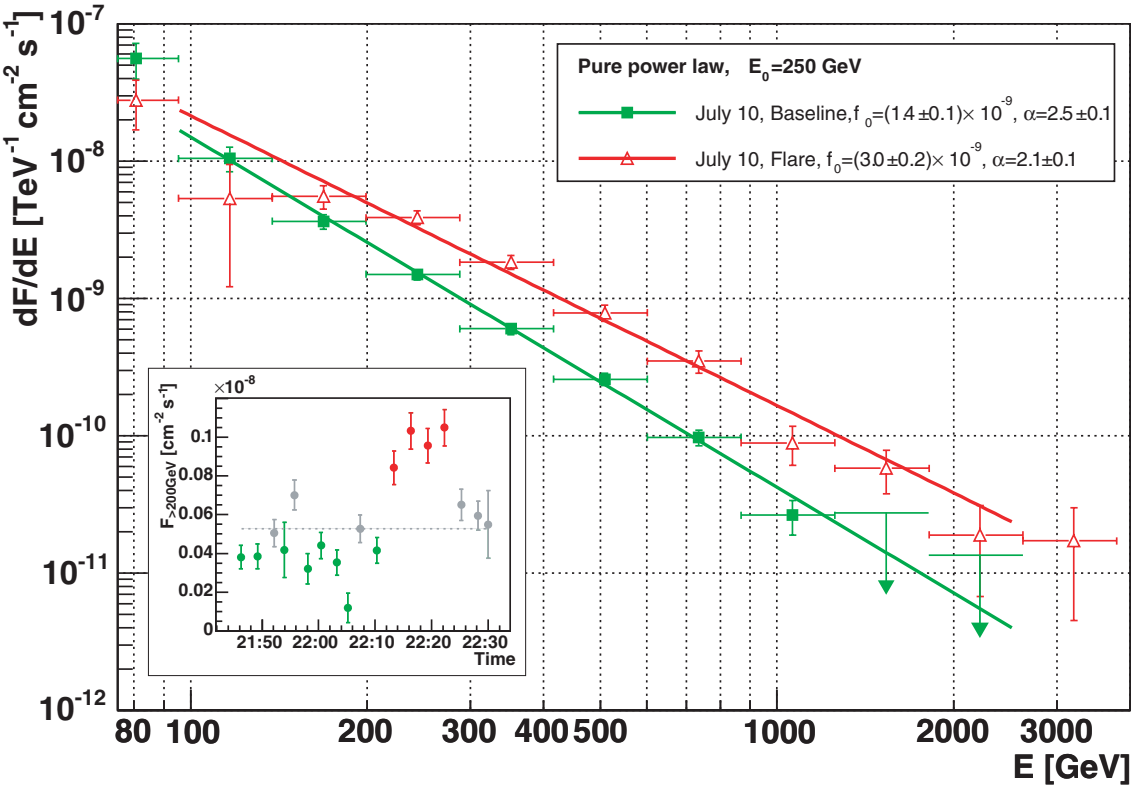

FIGURE 7.33: *Spectral changes during a flare on 2005 July 10. The plot shows pure power law fits of the form* $F = f_0 \cdot (E/250\,\mathrm{GeV})^{-\alpha}\,[\mathrm{TeV}^{-1}\,\mathrm{cm}^{-2}\,\mathrm{s}^{-1}]$ *to two (unfolded) spectra, which have been determined separately for the baseline and the flares between 95 GeV and 1.8 TeV. The inset shows the July 10 light curve on a run-by-run basis. The reduced* χ^2 *values are 4.99/6 (54.4% probability) for the fit to the baseline spectrum and 17.64/6 for the fit to the flare spectrum, the latter corresponds to a probability of 0.71% (the low probability is to be expected as the spectra exhibit a slight curvature). In order to judge the significance in the change of the slopes, a power law with a fixed slope of* $\alpha = 2.5$ *(the value obtained from the baseline spectrum fit) was fitted to the flare spectrum, yielding a reduced* χ^2 *of 45.45/7 (probability* $\approx 1.1 \cdot 10^{-7}$*).*

7.8.2 Rise and fall times

The study of flare rise and fall times is interesting as it can constrain the size R of the emission region. Employing causality arguments, one finds $R \lesssim c t_{\text{flare}} \delta/(1+z)$ (with the Doppler factor δ and the redshift of the source z), which puts the flare times into perspective with the length scales present in AGNs (cf. tab. 2.1).

To fit the flares, we employed a flare model based on the one used by [Sch02b, Sch07]:

$$F = F_{\text{baseline}} + \frac{a}{2^{\frac{t-t_0}{\tau_{\text{fall}}}} + 2^{-\frac{t-t_0}{\tau_{\text{rise}}}}} \tag{7.10}$$

with free parameters F_{baseline}, the rise and fall time constants τ_{rise}, τ_{fall}, the flare maximum time t_0 and a flare amplitude a. The base 2 is chosen such that τ_{rise} and τ_{fall} can be interpreted as doubling and halving times, respectively. The exponential increase of the flux can be shown to be a property of shock acceleration models. The average energy gain in first order Fermi acceleration is given as [Gal02]

$$\left\langle \frac{E+\Delta E}{E} \right\rangle \approx 1 + \frac{4}{3}\beta$$

with the shock velocity β, yielding a final energy of

$$E_{\text{f}} = E_{\text{i}} \left(1 + \frac{4}{3}\beta\right)^n$$

after $n \propto t_{\text{acc}}$ acceleration cycles and an initial energy E_{i}. When the acceleration time t_{acc} is the same for electrons of all relevant energies for the VHE γ-ray production, this results in an exponential increase of the observed flux [Sch07]. The exponential decrease is attributed to synchrotron and IC cooling processes.

The model is based on the assumption of rapid flares atop a constant (or slowly varying) background. Here, we take into account a slow change of the background by using a linear parameterization. Furthermore, the model assumes exponential rise and fall times with a smooth connection at the flare peak. Fits of this model to the flares are shown in fig. 7.34 for 2005 July 1 and in fig. 7.35 for July 10. For the latter day, three flare candidates are apparent. A more conservative approach was taken though by combining two of the three candidates to one longer flare. The resulting rise and fall times are summarized in tab. 7.6.

It is also possible to perform a combined fit in case more than one flare is present. Especially for overlapping flares this is appropriate. A fit then is performed using a linear combination ansatz

$$F = F_{\text{baseline}} + \frac{a_1}{2^{\frac{t-t_0}{\tau_{\text{fall}}}} + 2^{-\frac{t-t_0}{\tau_{\text{rise}}}}} + \frac{a_2}{2^{\frac{t-t_0}{\tau_{\text{fall}}}} + 2^{-\frac{t-t_0}{\tau_{\text{rise}}}}} + \ldots \tag{7.11}$$

To reduce the number of free parameters, we assume here that the flares are caused by the same flaring mechanism, therefore all flares have the same rise times τ_{rise} and fall times

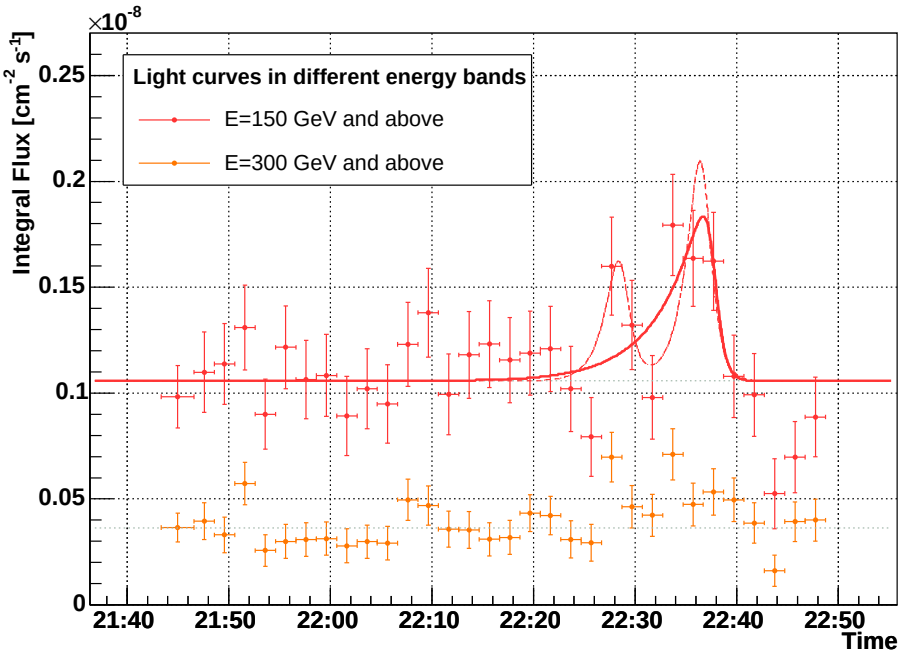

FIGURE 7.34: *Flare fits for the observation night of 2005 July 1. The fit allows the determination of rise and fall times. Shown are light curves for $E > 150$ GeV and $E > 300$ GeV. The resulting rise and fall times are summarized in tab. 7.6. The dashed lines show a combined fit to the individual flares, see text for the fit results.*

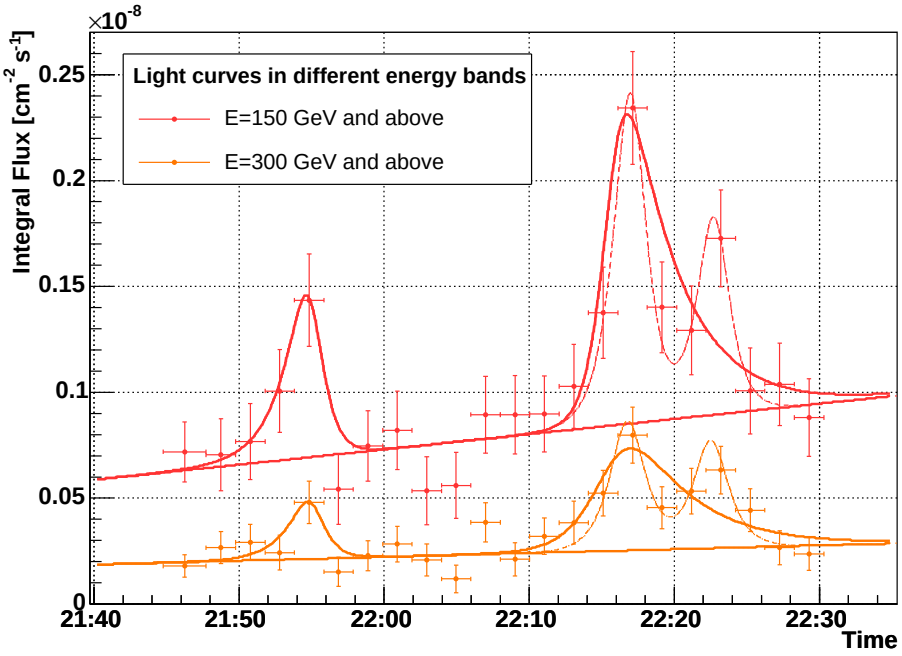

FIGURE 7.35: *Flare fits for the observation night of July 10, 2005. The fit allows the determination of rise and fall times. Shown are light curves for $E > 150$ GeV and $E > 300$ GeV. For this study, two flares were assumed, conservatively combining the two flare candidates after 22:10 UTC to one flare. The resulting rise and fall times are summarized in tab. 7.6. The dashed lines show a combined fit to the individual flares, see text for the fit results.*

Obs. night	E_{min}	Time (UTC)	t_0	τ_{rise}[s]	τ_{fall}[s]	χ^2/ndf	Fit prob.	Fig.
2005/07/01	150 GeV	22:28–22:38	22:37:44	139 ± 62.4	43.9 ± 21.8	36.1/28	14.1%	7.34
2005/07/10	150 GeV	21:48–22:00	21:55:02	68.4 ± 50.8	$32.5 \pm 16.4^*$	69.4/18	$5.7 \cdot 10^{-8}$	7.35
2005/07/10	300 GeV	21:48–22:00	21:55:05	61.6 ± 87.0	$32.5 \pm 16.5^*$	60.4/18	$1.7 \cdot 10^{-6}$	7.35
2005/07/10	150 GeV	22:06–22:28	22:15:44	35.7 ± 28.4	153 ± 50.8	28.4/18	5.7%	7.35
2005/07/10	300 GeV	22:06–22:28	22:15:48	64.0 ± 43.7	182 ± 69.9	24.9/18	12.7%	7.35

TABLE 7.6: *Doubling times for the observed flares on 2005 July 1 and 10. *) at the limit of the allowed parameter range.*

τ_{fall}. A combined fit for two flares was performed for the nights of 2005 July 01 (fig. 7.34). A two–flare fit results in $\tau_{\mathrm{rise}} = 57.9\,\mathrm{s} \pm 23.5\,\mathrm{s}$ and $\tau_{\mathrm{fall}} = 32.5\,\mathrm{s} \pm 68.1\,\mathrm{s}$ with flare peak times $t_0^{(1)}$ =22:28:40 and $t_0^{(2)}$ =22:36:43 and a χ^2_{red} = 33.7/26. It has to be noted that the undershoot before the first peak and the flat second peak are rather badly described by the flare model used. For 2005 July 10 (fig. 7.35), a combination of two double–exponential functions to the double–peak structure starting at 22:10 (again assuming identical rise and fall times for the two fits) yields $\tau_{\mathrm{rise}} = 44.7\,\mathrm{s} \pm 14.6\,\mathrm{s}$ and $\tau_{\mathrm{fall}} = 38.2\,\mathrm{s} \pm 13.3\,\mathrm{s}$ with a χ^2_{red} = 7.8/12. The flare peaks are found at $t_0^{(1)}$ = 22:17:03 and $t_0^{(2)}$ = 22:22:48 for the $E > 150$ GeV light curve. Similar time constants and peak times are found for the $E > 300$ GeV light curve.

Conservative doubling times. Doubling times can also be calculated in a robust and model-independent manner just by using the flare edges as indicated in fig. 7.36. No particular flare model is fitted to the data, only the existence of a rising or falling edge, viz. a significant change of the flux level, is required. The time in which this change occurs is normalized to the respective doubling or halving of the flux. For the shown time intervals, the most conservative approach was chosen by using the outer limits of the given binning. The average doubling time obtained employing this procedure is $\tau_{\mathrm{dbl}} = 5.6 \pm 1.1$ min.

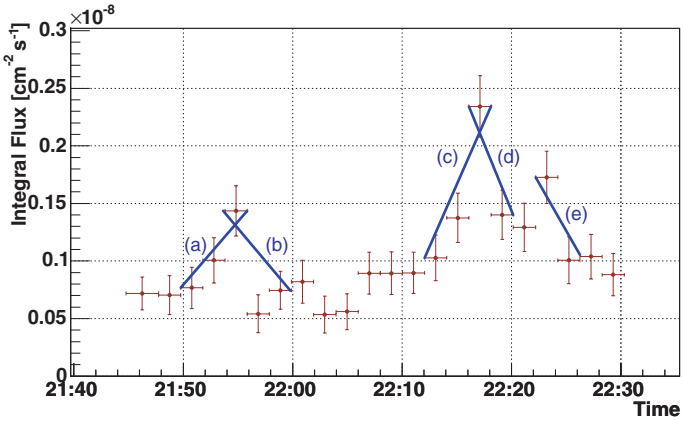

FIGURE 7.36: *Doubling times as calculated from the 2005 July 10 light curve for 150 GeV and above: For the shown time intervals, the doubling times obtained are (a)* (6.5 ± 1.4) min, *(b)* (6.3 ± 1.4) min, *(c)* (5.4 ± 1.0) min, *(d)* (4.9 ± 0.8) min, *and (e)* (4.7 ± 1.0) min.

Interpretation. Both the few nights with substantial flares and the complexity of the light curve make unambiguous interpretations difficult. Within errors, the $E > 150$ GeV light curve of 2005 July 1 can be described quite well with the flare model used here. Still, the light curve structure, especially when also regarding the $E > 300$ GeV light curve, hints at a probably more complex structure—that of a composite flare with faster rise times than the one fitted. The flares of 2005 July 10 are more pronounced, although here the structure of the light curve is also compatible with two or three flares. As for the flare fits, generally flare rise and fall times of $\tau \lessapprox 120$ s can be reported. Rise and fall doubling times are comparable; a significant difference in rise and fall times cannot be claimed. When determining doubling times without employing the fit model, doubling times of $\tau \lessapprox 5$ minutes are observed.

Causality constraint. To comply with causality, changes in the flux emission level cannot occur faster than the light travel time equivalent to the radius of the emission region. This fact translates into the relation $R \lesssim c t_{\mathrm{flare}} \delta / (1+z)$ with the Doppler boosting factor δ. When selecting the rising edge and falling edge of the combined fit to the big flare on 2005 July 10, for doubling times of $(153 \pm 51\ \mathrm{s})$ and $(33 \pm 17\ \mathrm{s})$ one finds $R\delta^{-1} \leq 6.1 \times 10^{12}$ cm and $R\delta^{-1} \leq 1.5 \times 10^{12}$ cm. The relation can be used to exclude regions in the (R, δ) plane.

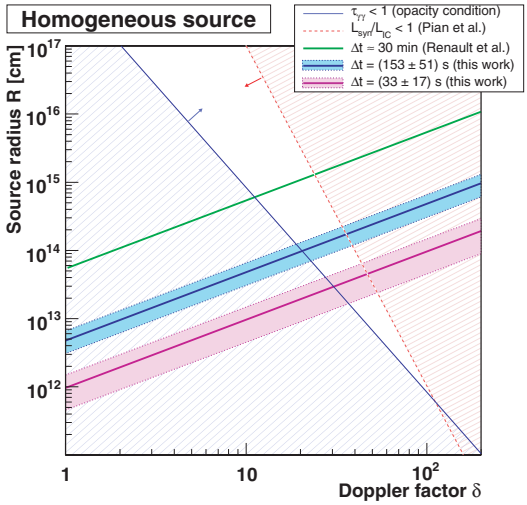

FIGURE 7.37: *Permitted values in the (R, δ) plane for the assumption of a homogeneous source: The green line shows an upper limit on R posed by the observation of $\Delta t = 30$ min variability of the Mkn 501 flux by [Ren00]. The dark blue and violet lines give the limits obtained in this work; exemplarily, a long doubling time and a doubling time in the 30 s range was chosen. The blue line indicates the lower limit on δ given by the requirement for the $\gamma\gamma$ opacity to be lower than unity [Pia98]. The red dashed line indicates a limit inferred by the Mkn 501 synchrotron/IC peak luminosity ratio [Pia98].*

We compare our results to previous observations of short VHE γ-ray flux variability in Mkn 501 [Ren00] in fig. 7.37. An additional constraint comes from requirement of VHE γ transparency of the emission region [Mat93, Tav98]. The $\gamma\gamma$ opacity is required to be smaller than $\tau_{\gamma\gamma} < 1$. The combination of the limits given here and opacity limits still

leaves room in the $\delta \lessapprox 80$ domain, although they readily limit the emission region to $R \lessapprox 10^{13}$ cm. It should be stressed that the underlying model requires a homogeneous emission region, an assumption that could be strengthened by the observation of strong short–term correlation between X-ray and VHE γ-ray emissions. Observations by [Pia98] hint at a possible revision of the homogeneity assumption (see also fig. 7.37). Clearly, dense simultaneous multiwavelength observations of fast flares would help to clarify the situation.

A conclusion that can be drawn from the observed weak day-by-day correlation (cf. sect. 7.6) and these findings is that a homogeneous SSC model can probably describe the long–term variations on characteristic timescales of ≈ 1 day, but has substantial difficulties in describing the observed minute–scale variations.

7.8.3 Lorentz invariance tests

The July 10 flare shows a clear time structure, which is visible throughout different photon energies. When assuming that this time structure is indicative for a synchronous production at the origin, its observation in different energy ranges can be employed for the search for quantum gravity effects. We also assume that delays by cascading effects from interactions of the γ-rays with the EBL are negligible in the studied energy range. Here we seek to determine the relative timing of characteristic flux features at different distinct energy ranges. The non–observation of significant time differences can then be used to infer a limit on the quantum gravity energy scale, assuming the photons at different energies were created simultaneously. The method used to determine the timing of the flux features is based on the empiric flare model (7.10). Fig. 7.38 shows the integral flux on that night in two distinct energy bands of $(150-250)$ GeV and $(600-1200)$ GeV. The data have been divided into bins of 2 minutes, very much as discussed in the previous sections. This time we assume three flares at 21:54, 22:17, and 22:23 UTC, respectively; note that for our purposes the fit of the common features of the light curves is essential, therefore even if the structure around 22:00 UTC should be due to one flare only, fitting three peaks is an acceptable procedure. In order to reduce the number of fit parameters, we further assume that the three flares have equal shapes and hence are produced by a common mechanism.

We chose to fit a linear function $f_{\text{baseline}}(t) = f_0 + m \cdot t$ as well as three double–exponential functions

$$f_{i,(a_i,t_i)}(t) = \frac{a_i}{\left(2^{\frac{t-t_i}{\tau}} + 2^{-\frac{t-t_i}{\tau}}\right)} \tag{7.12}$$

The three flares are found to feature very similar rise and fall times. Therefore an universal constant τ is determined by the combined fit of the three flares and assumed to be identical

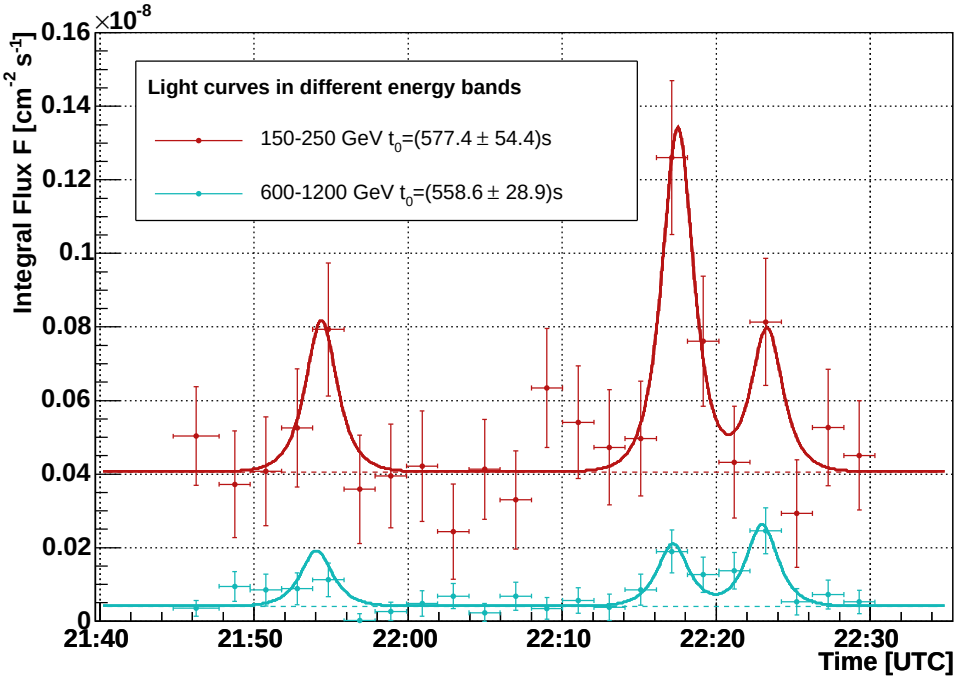

FIGURE 7.38: *Simultaneous fit to the three flares of 2005 July 10, performed for two γ-ray light curves with different energy ranges. See text for details.*

MJD	Bin width [s]	Integral flux [10^{-10} cm^{-2} s^{-1}]	
		150–250 GeV	600–1200 GeV
53560.9071	178.0	5.03 ± 1.34	0.35 ± 0.22
53560.9089	121.6	3.72 ± 1.45	0.95 ± 0.40
53560.9103	121.6	4.08 ± 1.48	0.85 ± 0.44
53560.9117	121.6	5.26 ± 1.60	0.89 ± 0.43
53560.9131	121.6	7.93 ± 1.81	1.13 ± 0.46
53560.9145	121.6	3.59 ± 1.47	0.02 ± 0.19
53560.9159	121.6	3.95 ± 1.41	0.27 ± 0.25
53560.9173	121.6	4.22 ± 1.50	0.48 ± 0.34
53560.9187	121.6	2.44 ± 1.29	0.68 ± 0.34
53560.9201	121.6	4.13 ± 1.35	0.23 ± 0.25
53560.9215	121.6	3.30 ± 1.34	0.68 ± 0.38
53560.9229	121.6	6.34 ± 1.62	0.35 ± 0.30
53560.9243	121.6	5.41 ± 1.53	0.56 ± 0.34
53560.9257	121.6	4.73 ± 1.56	0.38 ± 0.36
53560.9272	121.6	4.97 ± 1.56	0.86 ± 0.42
53560.9286	121.6	12.60 ± 2.09	1.90 ± 0.58
53560.9300	121.6	7.61 ± 1.76	1.26 ± 0.48
53560.9314	121.6	4.32 ± 1.52	1.37 ± 0.50
53560.9328	121.6	8.14 ± 1.73	2.46 ± 0.63
53560.9342	121.6	2.93 ± 1.46	0.53 ± 0.36
53560.9356	121.6	5.27 ± 1.58	0.73 ± 0.39
53560.9370	121.6	4.51 ± 1.49	0.52 ± 0.32

TABLE 7.7: *Integral flux levels for the night of July 10. For technical reasons, the width of the first bin is larger than that of the remaining bins. This is fully taken into account in the analysis.*

for rise and fall time of the flares. This universal form assumed for all three flares leaves only the amplitude a_i and the flare time t_i as free parameters for the individual flares.

First, the low energy light curve is fitted with $f = f_{\text{baseline}} + f_1 + f_2 + f_3$ to determine (1) the fit rise and fall times and (2) the relative timing of the peak positions of the three flares. This first fit results in $\tau = 37.8\,\text{s} \pm 13.1\,\text{s}$ and an error of the position of the first flare of $\Delta t_1 = 54.4\,\text{s}$. The relative timings of the two successive flares are found to be $\Delta t_{12} = (1.39 \cdot 10^3 \pm 82.3)\,\text{s}$ and $\Delta t_{23} = (3.47 \cdot 10^2 \pm 68.4)\,\text{s}$, respectively.

For the fits that shall determine possible timing differences between the two light curves, the relative flare peak times between the three flares and the flare rise time are now fixed as discussed above, thereby increasing the number of free parameters by three. The fits then return the peak time of the first flare (as measured from the first event recorded) and the error on the flare position as:

- $t_{\text{peak}} = 577.4\,\text{s} \pm 54.4\,\text{s}$, with a χ^2_{red} of $7.9/16$ for the $150\,\text{GeV} \leq E < 250\,\text{GeV}$ light curve,
- $t_{\text{peak}} = 558.6\,\text{s} \pm 28.9\,\text{s}$ with a χ^2_{red} of $11.6/16$ for the $600\,\text{GeV} \leq E < 1200\,\text{GeV}$ light curve,

Within errors, the times of the flare maxima agree well, indicating that the flares arrived synchronously in the given four energy ranges.

Accessing the quantum gravity energy scale. Objects at cosmological distances offer the possibility to search for in vacuo dispersion $\delta v \approx E/E_{\text{qg}}$, caused by a quantum–gravitational medium that responds differently to the propagation of photons of different energies. It was suggested [Ame98] that a deformed dispersion relation for photons, $\text{c}^2 \overrightarrow{p}^2 = E^2(1 + f(E/E_{\text{qg}}))$ would lead to energy–dependent velocities $\text{c} + \gamma v$ for massless particles. For small energies $E \ll E_{\text{qg}}$, a series expansion would correspond to energy–dependent velocities

$$\frac{v}{\text{c}} = 1 - \xi \frac{E}{E_{\text{qg}}} - O\left(\frac{E^2}{E_{\text{qg}}^2}\right) \tag{7.13}$$

ξ is regarded as the sign of the deformation which would be fixed by the given dynamical framework [Ame00]. In first order in E/E_{qg}, this would lead to observed arrival times displaced by

$$\Delta t \simeq \xi \frac{\Delta E}{E_{\text{qg}}} \frac{D}{\text{c}} \qquad (z \ll 1), \tag{7.14}$$

for photons with an energy difference ΔE from a γ-ray source at distance D; in particular this applies to characteristic features of blazar light curves at different energies ΔE and a possible time offset Δt of these features.

Luminosity distance. Cosmological distance measurements are only possible by determining the redshift of characteristic lines emitted, e.g. in case of AGNs emitted by the host galaxy. The redshift of Mkn 501 has been measured as $z = 0.03366 \pm 0.00007$ [Ulr75, Vau91]. The luminosity distance D_{L} traveled by photons from Mkn 501 to Earth in case of a flat universe ($\Omega_{\mathrm{k}} = 0$) relates to the Hubble distance D_{H} by

$$D_{\mathrm{L}} = (1+z) D_{\mathrm{H}} \int_0^z \frac{\mathrm{d}z'}{E(z')} \tag{7.15}$$

with $E(z) = \sqrt{\Omega_{\mathrm{m}}(1+z)^3 + \Omega_{\Lambda}}$ and the Hubble distance $D_{\mathrm{H}} = \mathrm{c}/H_0$ [Pee93]. Using the latest cosmological parameters ($H_0 = 71.1$ km s^{-1} Mpc^{-1}, $\Omega_{\mathrm{m}} = 0.26$, [PDG06, sect. 21.4]), one obtains a luminosity distance of $D_{\mathrm{L}} = 145.9$ Mpc, equal to $D_{\mathrm{L}} = 1.5 \cdot 10^{16}$ light seconds [Wri03] for Mkn 501.

Lower bound on E_{qg}/ξ. From our data, we obtained uncertainties on the flare positions of $\Delta t = 54.4$ s and $\Delta t = 28.9$ s for the two considered energy ranges. We now obtain an upper limit on the arrival time difference for the two energy ranges by error propagation. The mean energy for any of the energy ranges is computed as $\overline{E} = \int E' \cdot E'^{-\alpha} \mathrm{d}E' / \int E'^{-\alpha} \mathrm{d}E'$ with $\alpha = 2.59$, resulting in $\overline{E} = 189$ GeV and $\overline{E} = 813$ GeV, respectively. The spectral index used is the one found in sect. 7.8.1 for the July 10 baseline flux state. The resulting energy difference is $\Delta E = 624$ GeV, for which we obtain a corresponding uncertainty on the arrival time of 61.6 s. The limit on the quantum gravity energy scale is therefore given as

$$\frac{E_{\mathrm{qg}}}{\xi} \geq \Delta E \frac{D_{\mathrm{L}}}{\Delta t} = 1.5 \times 10^{16} \cdot \frac{\Delta E_{\,\mathrm{GeV}}}{\Delta t_{\,\mathrm{s}}} \,\mathrm{GeV} = 1.5 \times 10^{17} \,\mathrm{GeV} \tag{7.16}$$

When inserting today's cosmology into the calculations performed by [Bil99], who used $h_0 = 0.85$, their original lower limit on E_{qg}/ξ increases by 16%, and is now $E_{\mathrm{qg}}/\xi = 4.6 \times 10^{16}$ GeV ($h_0 = 0.73$). Calculations back in 1999 suggested $|\xi| \sim 3/2$ (from D–brane theory) up to $\xi \approx 4$ (from loop gravity), therefore the lower limit on $E_{\mathrm{qg}}/\xi \geq 4 \times 10^{16}$ GeV given by [Bil99] had been converted into $E_{\mathrm{qg}} \geq 6 \times 10^{16}$ GeV .

Remark regarding the simultaneity assumption. Note that even if the assumption of synchronous creation of the photons in the different energy bins should be replaced by a weaker assumption, namely that high energy photons are created with a slight delay w.r.t. low energy photons, the inferred lower limit still holds. When reversing the assumption, one could use a lower limit on E_{qg} inferred by independent methods, e.g. the one given by [Ell06] based on a GRB ensemble, to constrain possible source-intrinsic delays.

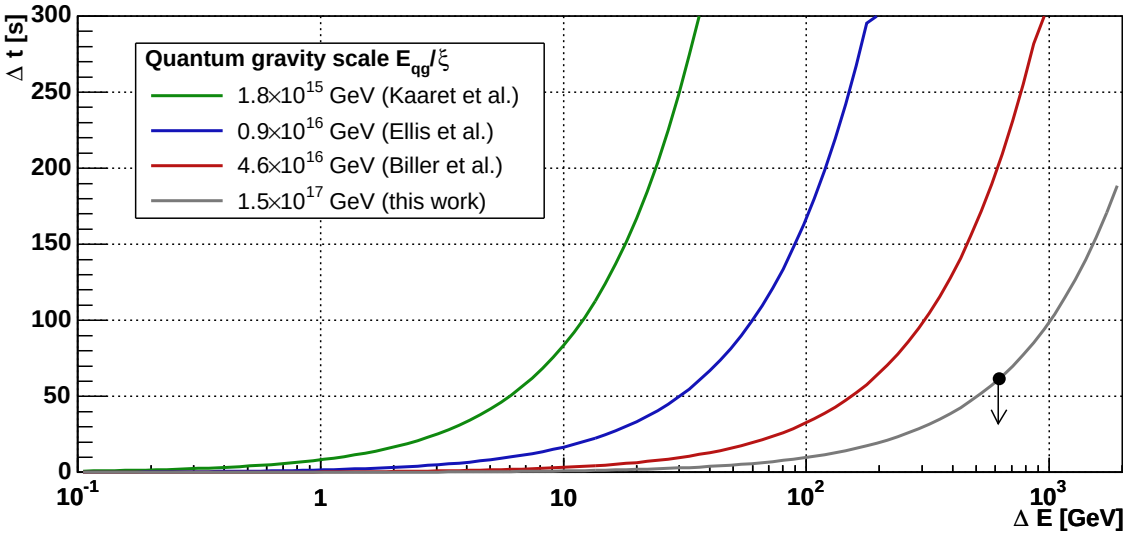

FIGURE 7.39: *Limits on the quantum gravity energy scale. Our result is obtained for an energy difference of 623.6 GeV. The limit is compared to those inferred from Crab pulsar analyses [Kaa99], GRB analyses [Ell06] and the analysis of an Mkn 421 flare [Bil99].*

7.8.4 Flare modeling

To study the temporal behavior of the flares, we compute hardness ratios from light curves for different energy ranges:

$$h_{E>150\,\mathrm{GeV}}(t) = \frac{F_{E>150\,\mathrm{GeV}}(t)}{F_{E>250\,\mathrm{GeV}}(t)}, \qquad h_{E>250\,\mathrm{GeV}}(t) = \frac{F_{E>250\,\mathrm{GeV}}(t)}{F_{E>400\,\mathrm{GeV}}(t)}$$

Fig. 7.41 tracks the time evolution of the flare candidates under study in the (F,h) plane. Three of the four flares consistently show characteristic loop patterns, while the last flare on July 10 does not. For the latter, either the variability is a convolution of statistical fluctuations and the falloff of the preceding flare or the flare is "real", but its evolution is substantially jeopardized by the preceding flare. The inspection of (F,h) patterns might constitute a helpful tool to crosscheck the flare nature of found flux variabilities. The method was first put forward for studies of the synchrotron peak [Kir98], but can also be used in the VHE regime [Geo01], assuming an internal shock model and an SSC mechanism. Characteristic hysteresis patterns are explained with the interplay of the synchrotron cooling timescale, the particle acceleration timescale and the intrinsic variability timescale. While clockwise (↻) loops come about when synchrotron cooling controls the spectral slope (information about injection propagates from high to low energies), for anticlockwise (↺) loops cooling and acceleration times are equal. Here, information about injection propagates from low to high energies. Similar (clockwise) patterns have been observed for diurnal variations of Mkn 421 [Hor03] at energies of 1 TeV and above.

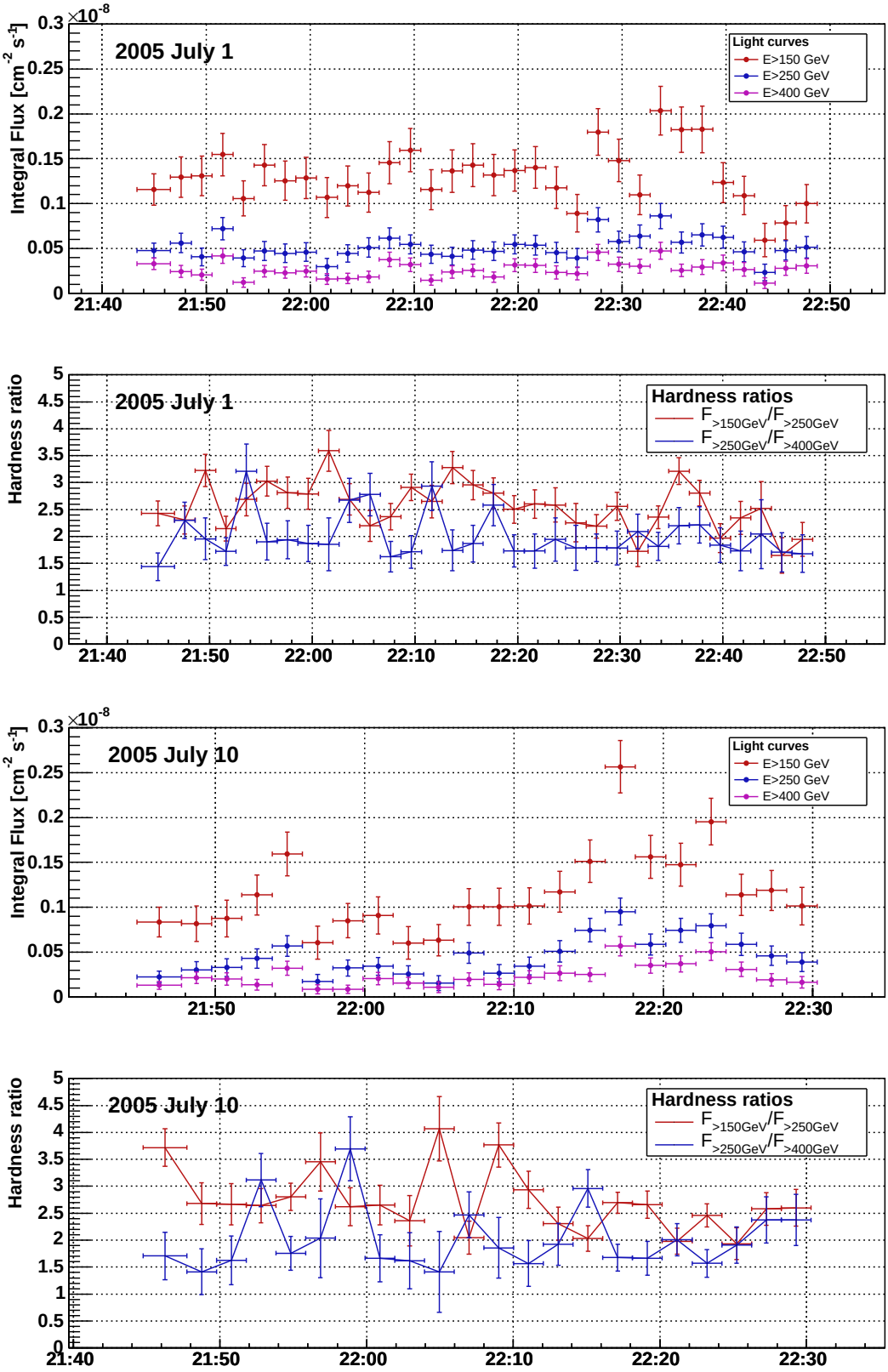

FIGURE 7.40: *Light curves for three energy ranges for the observation night of 2005 July 1 and 2005 July 10 and the resulting hardness ratios, i.e. the flux ratios, of the fluxes in the 150 GeV and above and 250 GeV and above (red) and the 250 GeV and above and the 400 GeV and above (blue) range, respectively.*

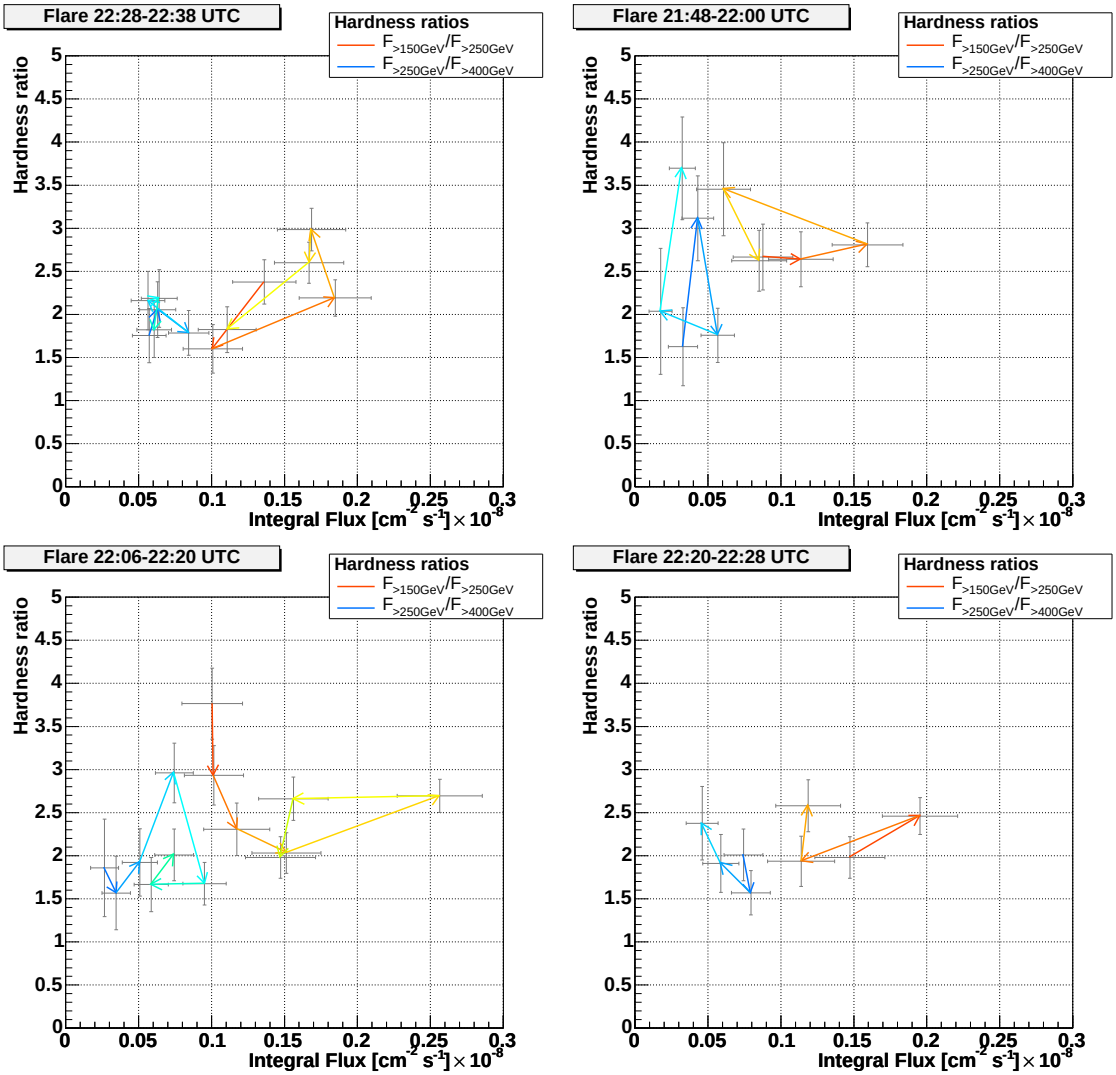

FIGURE 7.41: *Evolution of the flare candidates under study in the (F,h) plane for 2005 July 1 (upper left panel) and July 10 (three remaining panels). Blue-green and red-yellow curves represent different hardness ratios as indicated in the captions.*

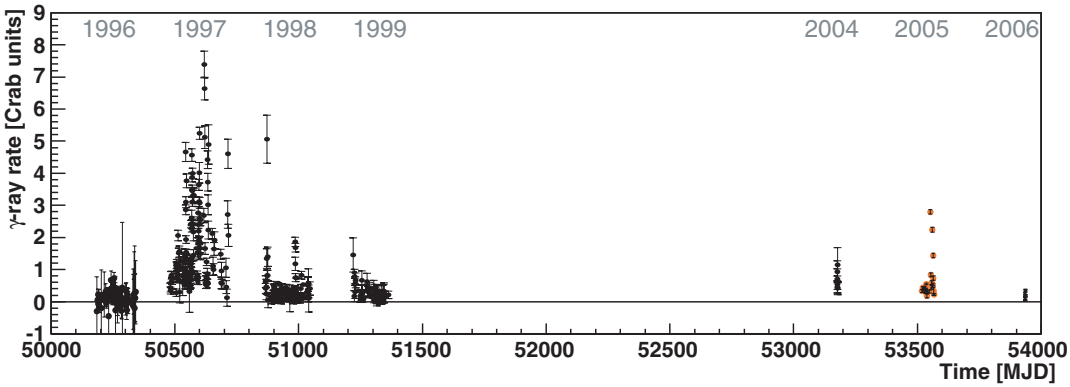

FIGURE 7.42: *Overall Mkn 501 VHE γ-ray light curve from 1996 April 11 to 2006 July 21. 1996 data from [Kra06], 1997–2004 data taken from [Gli06], 2005 data (orange markers) this work, preliminary 2006 data as measured with MAGIC [Hay06]. Note that the data have different energy thresholds and are therefore presented in Crab nebula units.*

7.8.5 Variability timescales

Mkn 501 VHE γ all-time light curve. In fig. 7.42 archival VHE γ-ray data from 1996 to 2006 are augmented with the observations presented in this thesis. They show that a flux well compatible with what could be called a baseline flux was observed at most times during our observations. The lowest flux observed in 2005 was below 0.25 c.u., but still above the lowest flux observed so far from Mkn 501 (fig. 7.7).[5] The current VHE γ-ray world data set shows a low state flux of ≈ 0.08 c.u. in 1996 [Qui96] and of $\approx 0.2 - 0.25$ c.u. derived from diurnal averages in 1998/9, and the 2005 data. A preliminary analysis of very recent data obtained with MAGIC in July 2006 [Hay06] shows an even lower flux of ≈ 0.15 c.u.

It remains to be seen how all these "low flux states" can be interpreted: Either they all comprise a modulated baseline flux (with long–baseline variations by a factor $\lessapprox 2-3$, or a slowly changing component atop real steady-state emission. Note that in contrast to Mkn 421, the X-ray flux of Mkn 501 was found never to vanish completely [Xue05], implying the presence of steady state emission. It would be interesting to establish a steady state emission also for the VHE γ-ray emission.

Day-to-day flux variability during these observations. Due to the sampling of the 2005 data (observations of around 60 minutes every 24 hours), firm conclusions on the variability evolution on the 1 h $< t \lessapprox$ 1 day scale cannot be drawn, although it can be stated that the flux levels on the flare nights of 2005 July 1 and 2005 July 10 are not preceded or succeeded by comparably high flux levels. For fitting the day–scale variability, an expo-

[5] This comparison does not hold strictly, as previous measurements did not extend to energies as low as the MAGIC observations do. Still, as the spectral slope of the Crab nebula and of Mkn 501 in its quiescent state are rather comparable, such comparisons hold to the level of qualitative discussions needed here.

nential behavior was assumed. In the following we characterize the day–scale flares by three approaches:

- in a fit–independent way, quoting the flux level change and the time period over which it occurs,
- by fitting the flare model discussed in sect. 7.8.2, and
- by fitting pure exponential functions of the form $F_0 + 2^{-((t-t_0)/\tau'_{\rm fall})}$ to the falling edges.

Even though the diurnal light curve for MJD $53515-53540$ (see fig. 7.11) is not particularly compatible with a constant ($\chi^2_{\rm red} = 58/11$), it was used to infer the baseline for the exponential fits as $F_0 = (9.01 \pm 0.37) \cdot 10^{-11}$ cm^{-2} s^{-1}.

Generally it can be said that the exponential fits did not converge and so they are assumed to be an inadequate description of the flux evolution. The flare model fits converge, although with unrealistically large χ^2 values. Clearly, the fact that our fits only provide a very poor description of the data suggests a more complex flux evolution (as expected!). Nevertheless we quote the fit results as they give a general idea of the flare characteristics. The performed fits are shown in fig. 7.43.

2005 July 01— We note an increase in flux by a factor of 7 from 2005 June 28 to 2005 July 1 (in 36 hours) and a falloff from 2005 July 1 to 2005 July 4 by a factor of ≈ 3.5 (in 36 hours). When describing the falling edge with an exponential function of the form $2^{-(t/\tau)}$, a time constant of $\tau'_{\rm fall} = (1.23 \pm 0.02)$ days can be inferred. The flare model fit yields faster time constants: $\tau_{\rm rise} = (0.40 \pm 0.10)$ days and $\tau_{\rm fall} = (0.79 \pm 0.05)$ days.

2005 July 10— A similar evolution is found with a marginally steeper flux increase of a factor 4.5 within 24 hours and a falloff of about the same factor within 48 hours. Rise and fall time constants were determined as $\tau_{\rm rise} = (0.25 \pm 0.03)$ days and $\tau_{\rm fall} = (0.35 \pm 0.05)$ days, respectively. The pure exponential fit yields $\tau'_{\rm fall} = (0.84 \pm 0.07)$ days.

2005 July 13— The evolution of the flux from July 12 on is more evenly sampled: Here we find an increase by a factor of ≈ 2.9 within 24 hours, a flux level of about that of the Crab nebula on July 13, and a gradual falloff to 20% of the Crab nebula within 36 hours. The flare model describes the rising edge with $\tau_{\rm rise} = (0.25 \pm 0.05)$ days and the falling edge with $\tau_{\rm fall} = (0.35 \pm 0.04)$ days. The exponential fit to the falling edge yields $\tau'_{\rm fall} = (0.50 \pm 0.02)$ days.

2005 June 15— To study the results of the flare model fit to a small flux variation, the flux around June 15 was inspected. The data suggest a flux doubling and halving within 24 and 48 hours, respectively. Here the flare model yields $\tau_{\rm rise} = (0.25 \pm 0.16)$ days

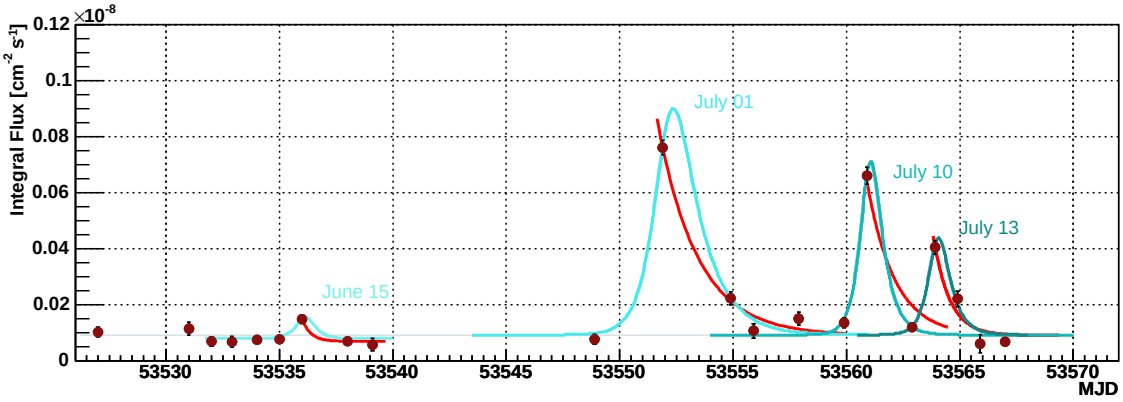

FIGURE 7.43: *Fits to the diurnal Mkn 501 VHE γ-ray light curve. The three flares of 2005 July 1, 10, and 13 and the smaller variation on June 15 are fitted with the flare model discussed in this work (blue) and for comparison with exponential functions (red). See text for details.*

and the falling edge with $\tau_{\text{fall}} = (0.25 \pm 0.13)$ days, while the exponential fit results in $\tau'_{\text{fall}} = (0.26 \pm 0.01)$.

Disregarding for a moment the rather poor description of the data by the fits, very qualitative conclusions are:

- The order of the flare rise and fall times found for all four flares under study are compatible.
- The flare fall times seem to be larger than the rise times by a factor of $1.4 - 2$.
- A finer granularity of the flux evolution cannot be claimed due to the sparse sampling and the low statistics of the data. Still, much faster variations were found on a timescale of minutes in this work and on a timescale of $\Delta t \approx 0.5$ days in earlier works for Mkn 501 [Qui99].

Variability timescales and scale invariance. As already discussed in sect. 7.2, X-ray flares of Mkn 501 have been observed on a wide range of timescales, spanning from variability on scales of months and longer, days to weeks, to rapid flares $<$ 1 hour [Xue05]. This behavior can seemingly also be reported for the VHE regime, in which long–term variations [Gli06] to variations on a scale of $\Delta t \sim 0.5$d [Qui99] and even in this thesis down to scales of few minutes along with $\Delta t \gtrsim 1$d, are observed. The wide range on which variability is apparent, spanning over more than four orders of magnitude, calls for physical explanations. For X-rays observed from Mkn 501 and Mkn 421, a scale invariance of X-ray flaring behavior is discussed by [Cui04, Xue05], which can be interpreted as an observational manifestation of a hierarchy of inhomogeneities in the jet. In this context the vastly different timescales observed simply reflect the sizes of the inhomogeneities in the acceleration regions or, alternatively, inhomogeneities in the flow of injected material

from the black hole–accretion disk system. Clearly, a proof of scale invariance would set strong constraints on the origin of the observed variability.

The 23-day quasi–periodicity. During the 1997 flare, the light curve of Mkn 501 exhibited an interesting 23-day quasi–periodicity on the 3.4σ level, hitherto unobserved in BL Lac objects [Kra01a, Kra01b]. One interpretation of the observed periodicity is given by [Bed97] with a hot spot in the accretion disk that rotates around the central black hole and that produces X-rays. The resulting VHE γ-rays are created in the jet by IC scattering. An alternative interpretation assumes Mkn 501 to be a binary black hole system [Rie00], motivated by the fact that BL Lac objects are hosted by giant elliptical galaxies, thought to be created in spiral galaxy mergers. For more detailed discussion on interpretations, see [Kra01a]. Subsequent analyses [Oso01, Oso02] show that quasi–periodicities can also be found for other blazars.

Flux volatility and diurnal flux RMS. The emerging picture of blazar variability is quite complex: Probably a non–trivial interplay of matter falling in from the accretion disk, inhomogeneities in the jet environment and a granularity in the shock regions is responsible for the observed variability and its timescale. Therefore, one aim of long–term observations of blazars is to assess the variability properties on a statistical basis. Here we study the diurnal volatility of the observed flux from Mkn 501. Fig. 7.44 shows the overall integral light curve for energies of 200 GeV and above. The diurnal measurements have been averaged and the RMS of the individual flux measurements has been computed as a measure for the diurnal flux volatility. Apparently, the RMS increases with the flux level, indicating higher variations during high flux states. For a more quantitative assessment, fig. 7.45 shows the RMS values normalized with the respective diurnal average flux level. Interestingly, the normalized RMS is roughly constant, although the distribution of the individual normalized RMS values does not behave according to a Poissonian distribution (fig. 7.46). There is no apparent correlation between normalized RMS and average flux level.

7.8.6 Model constraints for Mkn 501

In this section we try to infer conditions of the acceleration regions responsible for the very fast flux variations observed on timescales of minutes.

Variability timescales and the central black hole. Before looking at constraints for the emission region, the size scales in the vicinity of the central black hole need to be considered. The black hole mass for Mkn 501 was estimated to be $\approx 10^9 M_\odot$ (see sect. 11.2 for more details on the methods). From this result we can calculate its gravitational radius $r_\mathrm{G} \equiv \mathrm{G}M/\mathrm{c}^2 = 1.5 \cdot 10^{14}$ cm ≈ 100 AU. The last stable orbit, i.e. the closest orbit at which particles can orbit the hole without being dragged inward or outward, is located

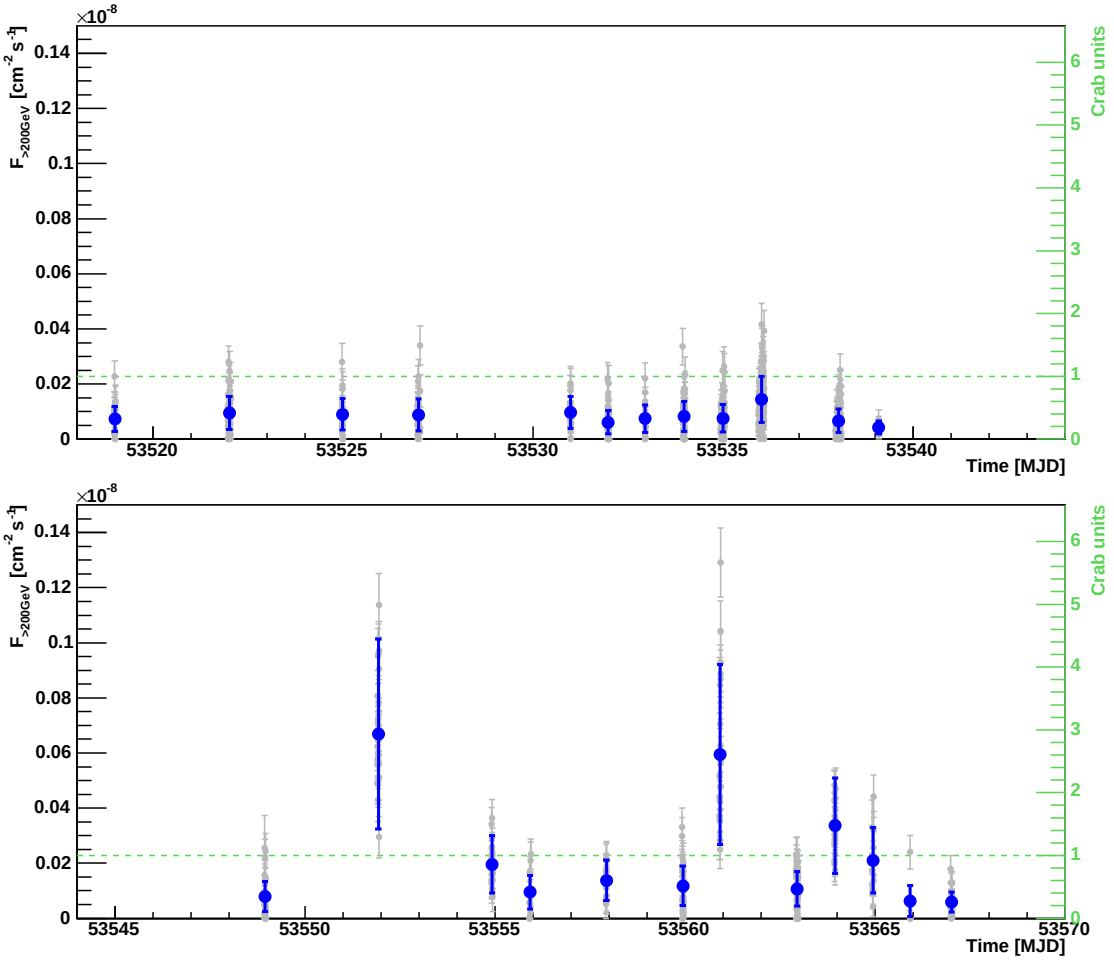

FIGURE 7.44: *Overall light curve for 200 GeV and above for Mkn 501. The gray data points show the diurnal data binned in 2-minute bins. The average daily flux and the RMS of the individual flux measurements on that day are superimposed (represented by the blue bars).*

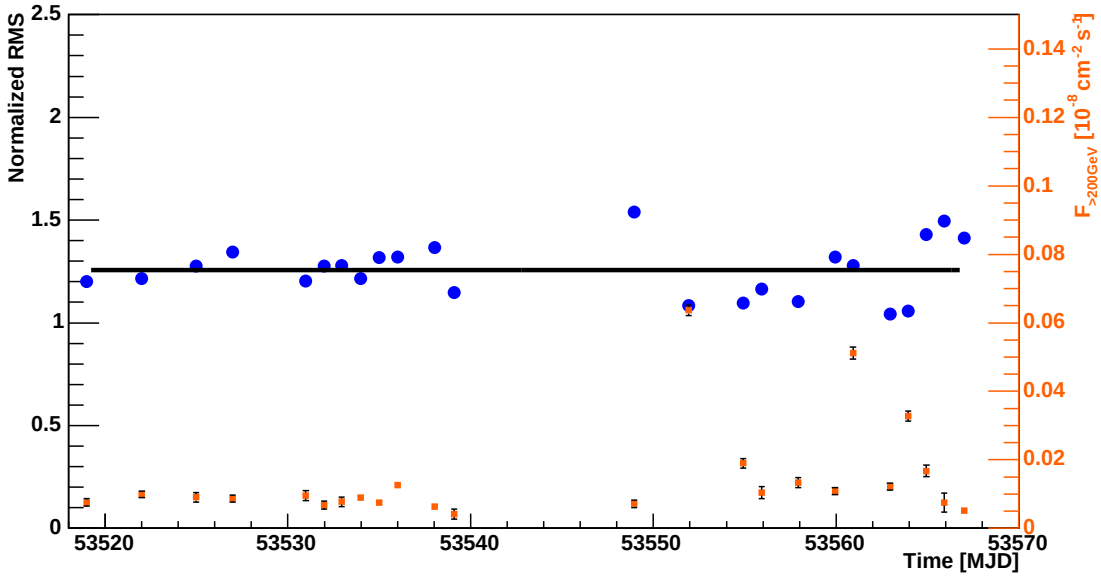

FIGURE 7.45: *RMS of the diurnal flux distributions normalized with the respective average flux level. The normalized RMS stays roughly constant, independent of the flux level. For better assessment of the plot, the diurnal light curve is superimposed.*

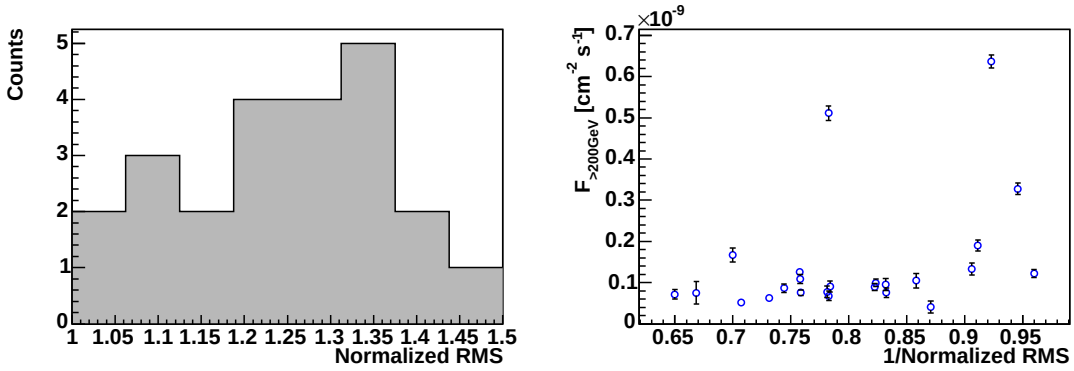

FIGURE 7.46: *Left panel: Distribution of the normalized RMS values. Right panel: Average diurnal flux versus the inverted normalized RMS. As indicated in fig. 7.45, no correlation is apparent.*

at $6r_G$ for a Schwarzschild black hole. The corresponding orbital period for the case of Mkn 501 is $T = 8.4$ days. Simulations suggest that the jet production region close to the SMBH (the "nozzle") is around $7r_G$ to $8r_G$ in size [Mei01]. For Kerr black holes with normalized angular momentum $j = 0.9$ ($j = J/J_{max}$; $J_{max} = GM^2/c$) the last stable orbit is located at $2.8r_G$, and the nozzle is expected to have a size around r_G.

Model constraints due to the observed flaring. Variability timescales may strongly constrain the physical properties of the flaring region. In the following we assume that the Doppler factor δ is not grossly exceeding $O(10)$.

- When assuming a homogeneous acceleration region, as e.g. one zone SSC models do, the size of the emission region is constrained due to causality by $R \lesssim ct_{flare}\delta/(1+z)$ with the duration of the flare t_{flare}, the Doppler factor in the emission regions $\delta \equiv 10\delta_1$ and the redshift $z = 0.034$ for Mkn 501.

  Day–scale variability in this context is equivalent to an upper limit on the emission region size of $R \lesssim 260 \times t_{days} \times 10^{14}\delta_1$ cm. This is a factor $\gtrsim 50$ larger than r_G and is unlikely to constrain the emitting region. For shorter timescales, like the observed 800 s in X-ray flares [Xue05], $R \lesssim 2.4 \times 10^{14}\delta_1$ cm is already comparable to the gravitational radius r_G of the black hole assumed to be harbored by Mkn 501. When turning to the shortest variability timescales observed, $\Delta t \approx 0.5$minutes, the constraints on the emission region reach down to $R \lesssim 0.18 \times t_{minutes} \times 10^{14}\delta_1$ cm, equivalent to $R \lesssim 0.12 \times t_{minutes} \times r_G$.

- Both the flares on timescales $\Delta t \gtrsim 1$ day and the sub-hour flares exhibit high amplitudes of multiple times the baseline intensity. [Xue05] conclude from this that the size of the flaring region might be comparable to the lateral extension of the jet (approximately the region in which a high B field is expected). If the variability originates from accretion flows, one would obtain an upper limit on the inner boundary of the flows.

- The observed flare rise time can be related to the electron acceleration time $\tau_{rise} \leq \tau_{acc}/\delta$, which in turn can be related to the energy of the accelerated electrons E_e by $\tau_{rise} = E_e/\dot{P}_{acc}$ with $\dot{P}_{acc} = \xi c E_e/r_L$ [Bed06]. ξ is the acceleration efficiency, $r_L = E_e/q_e B$ the electron Larmor radius and B the magnetic field. When assuming that the electron energy is of the order of the observed γ-ray energy, $E_e \approx E_\gamma$, one finds

$$\xi B \geq E_\gamma/(q_e c \tau_{rise}\delta). \tag{7.17}$$

- When assuming that the observed flare fall time τ_{fall} is due to synchrotron cooling, one can relate it to the total emitted radiation using $\tau_{fall} \cdot \delta \approx \tau_{sy} = E_e/\dot{P}_{sy}$ with

$$\dot{P}_{sy}(\gamma_e) = 4/3\pi\sigma_T c U_B \gamma_e^2 \tag{7.18}$$

[Ryb79]. $\sigma_T = 8\pi r_0^2/3$ is the Thomson cross–section and $U_B = B^2/8\pi$ is the magnetic energy density. Assuming that acceleration and cooling region are co-spatial, we can solve for $B \approx 125(E\tau_{\rm fall}\delta)^{-1}$ and further combine (7.17) and (7.18) to constrain the acceleration efficiency to $\xi \approx 9\cdot 10^{-3} E^{1.5}\tau_{\rm fall}/(\tau_{\rm rise}\delta^{0.5})$ [Bed06] with E in units of TeV, rise and fall times in units of seconds and the magnetic field strength in units of Gauss.

When inserting the values found in this work for sub–hour flares, $\tau_{\rm rise} \approx \tau_{\rm fall} \approx 60$ s and $E \approx 300$ GeV, one obtains $B \approx 2.6/\delta^{0.5}$ G and $\xi > 1.5\cdot 10^{-3}/\delta^{0.5}$.

7.9 SSC modeling

For the period in which the MAGIC observations were conducted, no simultaneous wide–range measurements by X-ray satellites took place. Therefore we search the BeppoSAX archives for X-ray data in the $(0.2-100)$ keV energy range for measurements performed during VHE γ-ray emission levels similar to those observed with MAGIC. To this end we utilize $1-2$ TeV HEGRA data (fig. 7.47). Measurements at VHE γ-ray levels of approx. 4.5 c.u., 1.4 c.u., and 0.25 c.u. are selected and shown along with VHE γ-ray data obtained in this analysis in fig. 7.48. In addition, contemporaneous optical and RXTE–ASM X-ray data as well as other archival data are shown in the wide–range spectral energy distribution.

Note that by using two time–averaged spectra as obtained in this work (denoted by *flare* and *baseline* in the following), we do not try to model the very fast flares found in the data, but only the flux states on a diurnal basis. A one–zone homogeneous SSC model provided by [Kra04] has been used to describe the data. The input parameters of this model are the radius of the spherically assumed emission region R, the Doppler factor δ and the magnetic field strength B in the acceleration region and the density ρ of the electrons responsible for the γ emission. Further parameters are the minimum and maximum electron energy $E_{\rm min}$ and $E_{\rm max}$, two power law slopes $n_1(E_{\rm min} < E_{\rm e} \leq E_{\rm break})$ and $n_2(E_{\rm break} < E_{\rm e} \leq E_{\rm max})$ for the electron spectrum, and the break energy $E_{\rm break}$ at which these two slopes are connected.

A starting point for the modeling is the assumption that the maximum observed energies in the VHE region are due to the saturation of the electron acceleration by synchrotron energy losses and that they are given by:

$$E^{\rm max}_{\gamma,{\rm flare}} \approx 10 E^{\rm max}_{\gamma,{\rm baseline}}. \tag{7.19}$$

The acceleration rate of electrons is given by $\dot{E}_{\rm acc} = a\xi B$ with the acceleration efficiency ξ and the magnetic field B. When comparing it with the synchrotron energy loss rate,

$\dot{E}_{\rm sy} = bB^2E^2$, one obtains from the relation of gains and losses $E_{\rm max} = \sqrt{a\xi bB}$. If the production of γ-rays by these electrons occurs in the Klein–Nishina limit, one expects

$$E^{\rm max}_{\gamma,{\rm flare}}\delta_{\rm flare} \approx 10E^{\rm max}_{\gamma,{\rm baseline}}\delta_{\rm baseline} \tag{7.20}$$

which finally yields the relation

$$\xi_{\rm flare}\delta^2_{\rm flare}/B_{\rm flare} \approx 100\xi_{\rm baseline}\delta^2_{\rm baseline}/B_{\rm baseline} \tag{7.21}$$

A flare thus can be modeled either by (1) increasing the acceleration efficiency ξ by ≈ 100 and keeping all other parameters constant. Note that such a change should affect e.g. the magnetic field B and thus is unlikely to be the only parameter to change. (2) increasing the Doppler factor δ by ≈ 10, which will however create a very strong flare. (3) decreasing B by ≈ 0.01. This results in the acceleration of electrons to higher energies without creating a synchrotron flare, since the energy losses of electrons with higher energies (by a factor of 10) are compensated by the drop in the magnetic field by a factor of 100—so in fact this would result in lower emission by a factor of 100. In summary, the combination of a slight decrease of B and an increase of δ should account for a typical spectral change expected during blazar flares. Therefore here we first try to accomplish an increase of $\Delta(\delta/\sqrt{B}) \approx 10$, and then change the electron spectrum (slopes, cutoff, density) as to match the observed flux levels in the synchrotron and IC regions.

The parameters we used are specified in fig. 7.48. The size of the homogeneous emission region ($R = 0.8 \cdot 10^{14}$ m) is much larger than that allowed by the causality constraints (at comparable Doppler factors of $\delta \approx 20$) for the short flares found in sect. 7.8.2 of $R \lessapprox 10^{11}$ m. The differences between the flare and the baseline state here are described by an increase of the Doppler factor from $\delta_{\rm baseline} = 15$ to $\delta_{\rm flare} = 21$ and a decrease of $B_{\rm baseline} = 0.095$ G to $B_{\rm flare} = 0.075$ G. At the same time, the break energy and the high energy cutoff of the electron spectrum are increased (cf. fig. 7.48). The slopes below and above the break energy are $n_1 = -2.1$, $n_2^{\rm baseline} = -3.1$, and $n_2^{\rm flare} = -2.9$, respectively. In view of the wealth of data available for Mkn 501 the model parameters found here are just a simplistic approach to describe the observations; also note that the model used here is not meant to characterize the spectrum in the radio-to-optical region accurately. Intrinsic absorption requires a much larger emitting volume for radio as compared to X-rays and γ-rays. The observed optical emission might be partially due to contributions from the accretion disk or a larger emitting volume. Other works [Kra02] find it difficult to accommodate the flaring states in simple one–zone models and show that time–dependent SSC codes and the utilization of two electron components are substantially better at describing the observations.

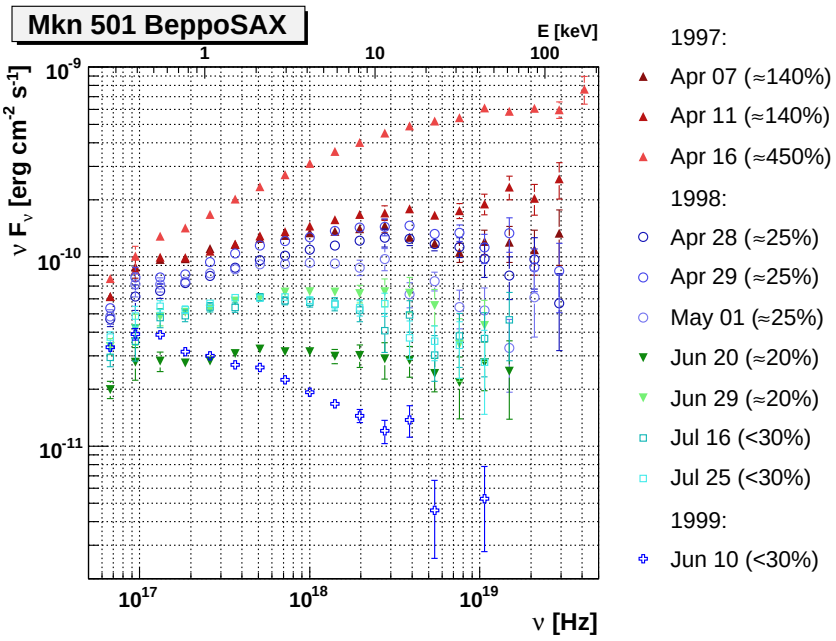

FIGURE 7.47: *BeppoSAX observations of Mkn 501 in 1997–1999 (available from [ASD06]). The measurements are compared with the approximate VHE γ-ray emission level in Crab units (values in brackets) during the X-ray observations as given by [Aha99c, Aha01c]. Appropriate BeppoSAX data sets are then selected and plotted along with the VHE γ-ray spectra obtained during this work, see fig. 7.48.*

7.10 Interpretation and conclusions

- A significant signal of Mkn 501 could be detected for most observation days: It could be shown that a significant signal for sources with a flux level of $\lessapprox 30\%$ that of the Crab nebula can be detected within 20 minutes of MAGIC observations. Therefore we conclude that instruments like MAGIC are well suited for long–term observation programs and the study of "quiescent state" physics of BL Lacs.

- A significant signal could be attained down to the $100 - 150$ GeV region. During times with high flux level, a marginal signal down to 80 GeV was detected.

- The correlations of VHE γ-ray and X-ray observations on day-by-day basis hint at an SSC origin of the VHE γ-rays. A larger than linear correlation explains flux variability with changes in the electron injection spectrum (rather than with variations of the bulk Lorentz factor Γ). Nonetheless, it is difficult to accommodate the same correlation for all days, probably due to the poor sensitivity of the ASM instrument during the observation of low fluxes. The observation of a correlation, however, supports the SSC model and discards high magnetic fields of $B \gtrapprox 0.3$ G.

- In the total observation period of about 60 days, high flux states could be detected: On two days, flux levels three times higher than that of the Crab nebula were observed, with a significant flux variability on the timescale of well below 10 minutes.

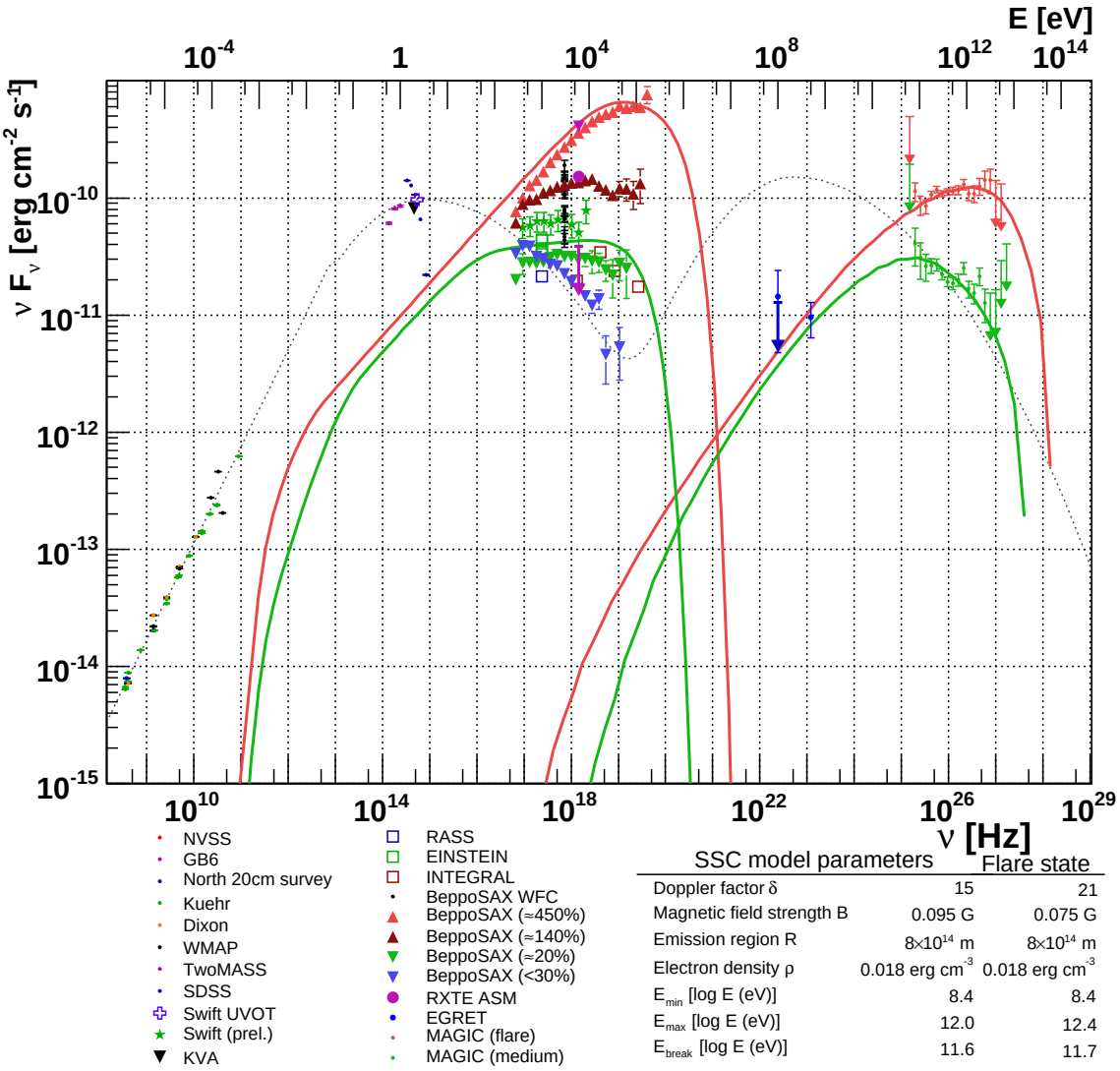

SSC model parameters	Flare state	
Doppler factor δ	15	21
Magnetic field strength B	0.095 G	0.075 G
Emission region R	$8{\times}10^{14}$ m	$8{\times}10^{14}$ m
Electron density ρ	0.018 erg cm^{-3}	0.018 erg cm^{-3}
E_{min} [log E (eV)]	8.4	8.4
E_{max} [log E (eV)]	12.0	12.4
E_{break} [log E (eV)]	11.6	11.7

FIGURE 7.48: *Overall SED for Mkn 501. Radio to sub-millimeter data: NRAO VLA sky survey [Con98], Green Bank 4.85 GHz northern sky survey [Gre96], North 20cm survey [Whi92], 5 GHz survey [Kue81], Dixon master list [Dix70], WMAP radio data [Tru03]. Optical: 2MASS [Jar03], Sloan digital sky survey photometric catalog and Swift UVOT; KVA; X-ray: RASS [Vog99], EINSTEIN, BeppoSAX [Gio02]. The BeppoSAX data set are taken from fig. 7.47 and were obtained during periods in which 4.5 c.u., 1.4 c.u.,* $\approx$ *0.2 c.u., and* $<$ *0.3 c.u. VHE fluxes were measured. RXTE–ASM: The purple circle represents the mean flux, the triangle the highest flux measured and the upper limit the lowest count–rate found during the MAGIC measurements. HE/VHE* γ*-ray: EGRET data points [Kat99] and upper limits (blue arrow, [Fic94]), Swift XRT. MAGIC medium and flare flux as obtained during this work, EBL de-absorbed. Unreferenced data taken from [ASD06]. The red and green curves represent one-zone SSC models using the SSC code given in [Kra04]. Model parameters are given in the caption and the text. In contrast to the homogeneous one–zone model used here, the dotted gray model given by [Gio02] is able also to predict radio–to–optical emission, but does not use input data above* $\nu = 10^{17}$ Hz*. Note that only RXTE–ASM and KVA data were obtained during the MAGIC observations.*

- Spectral hardening is well correlated with the flux level, which hints at a moving IC peak towards higher energies with increasing flux level. Correlations down to timescales of some 10 minutes were found for the high flux day of July 10.

- No unambiguous signal of an IC peak was found, but the measured spectra show clear curvature in the $100-500$ GeV region. A mathematical description for curved spectra yields peak energies for the observed spectra between 150 and 320 GeV. These peak energies depend on the flux level of the data sample studied, and increase with increasing flux level as expected from the observed variations of the synchrotron peak energy. In the EBL de-absorbed spectra, peak positions between $E = (0.3 \pm 0.1)$ TeV and $E = (1.4 \pm 0.7)$ TeV could be determined depending on the flux level.

- A baseline flux state of $\approx 20\%$ that of the Crab nebula is found in the energy region of 200 GeV and above. Studies of the variability timescales show that the flux increases in 48 hours or less towards high flux levels and falls off in $24-48$ hours or less to the baseline level.

- On intra-day timescales, significant flux doubling and halving times $\Delta t \lessapprox 2$min were observed.

- The found inter-day flux states were modeled using a homogeneous one–zone SSC model. The model yields a size of the emission region which is by far larger than the size for a homogeneous emission region allowed by the observed minute-scale flares. This observation shows that a homogeneous one–zone SSC model is clearly too simple to describe all observed variability timescales.

- The high time resolution with which light curves were produced could be used to infer a substantially improved lower limit on the quantum–gravity energy scale of $E_{\mathrm{qg}} > 1.5 \times 10^{17}$ GeV as obtained by observing fast blazar flares.

- The diurnal flux variations (RMS) normalized on the average diurnal integral flux was found to stay roughly constant throughout the observations.

- Clearly, regular monitoring in the VHE γ-ray range is suited for triggering multiwavelength time–of–opportunity campaigns in the case of high flux levels. Extended high resolution multiwavelength observations could help to confirm or disprove the SSC origin of fast flares by testing for the existence of short–term correlations.

Chapter 8

The BL Lac object 1ES 2344+514 during a low emission phase

The BL Lac object 1ES 2344+514 was detected in the Einstein Slew Survey [Elv92] in the energy range of $(0.2-4)$ keV. The source was identified as a BL Lac object by [Per96], who also determined a redshift of $z = 0.044$ from absorption line measurements, while no evident emission lines were found. This makes 1ES 2344+514 the fourth closest known BL Lac object detected so far (after Mkn 421, Mkn 501, and EXO 0423.4–0840).

Morphology. The object is seen as an unresolved point source at all wavelengths. Its central black hole mass was estimated to be $10^{8.80\pm0.16} M_{\odot}$ using stellar velocity dispersion measurements [Bar03]. In the optical a point source surrounded by an elliptical host galaxy with a (half-width at half-maximum) radius of $r = (7.12 \pm 0.02)$ kpc has been observed [Urr00].

Optical and FIR emission. The observed optical and far-infrared (FIR) emission of 1ES 2344+514 lies well above the level expected from pure synchrotron emission in the jet [Jar03, Urr00]. HST measurements in 1996 showed a R–band brightness of the galactic nucleus of $16\overset{\mathrm{m}}{.}83 \mp 0\overset{\mathrm{m}}{.}05$ [Urr00]. During monitoring in 1998, variations between $16\overset{\mathrm{m}}{.}47$ [Nil99] and $17\overset{\mathrm{m}}{.}00$ [Fal99] were observed. Short timescale variability was found to be weak with intra-day changes of $\Delta R = 0\overset{\mathrm{m}}{.}1$ [Xie02].

X-ray variability. One of the very first observations of the BeppoSAX satellite [Gio00] from 1996 December 3 to 1996 December 11 revealed a high variability of 1ES 2344+514 on the timescale of few hours in the $(0.1-10)$ keV band. The synchrotron peak was located in the hard X-ray band at or above 10 keV. Follow–up observations on 1998 June 26 found the object in a very low flux state, with the peak synchrotron emission shifted to lower frequencies by a factor of 20 and the corresponding integral flux decreased by a factor of 4.5. From these observations it was concluded that one electron population is

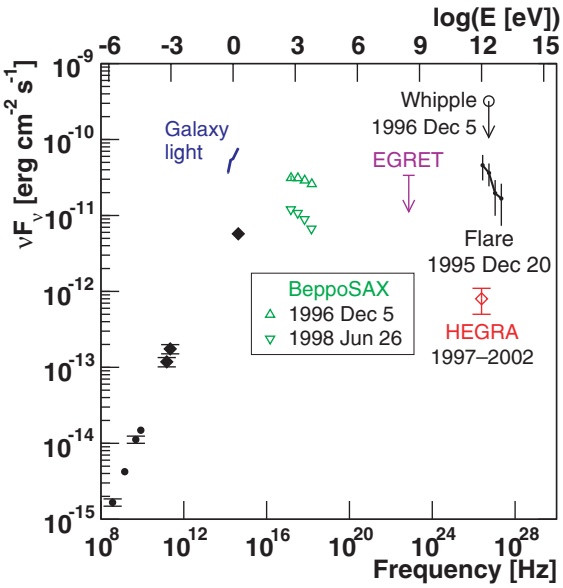

FIGURE 8.1: *Spectral energy distribution of 1ES 2344+514. The data included come from the Texas radio survey, Green Bank, VLA, galaxy photometry at millimeter wavelength, 2MASS, HST, BeppoSAX, Whipple and HEGRA. Taken from [Sch05c], see also for references.*

responsible for the steady low energy synchrotron emission while an additional population is responsible for producing higher energy X-rays with a high time variability.

Status of VHE γ-ray observations. This source was included in the first searches for VHE emission from nearby BL Lac objects based on BL Lac identifications [Per96], an approach which also led to the discovery of Mkn 421 and Mkn 501. In fact 1ES 2344+514 was selected as a candidate VHE γ-ray emitter due to the similarity in its spectral properties to Mkn 501, in particular because of its high synchrotron peak frequency. It also is regarded as an X-ray selected BL Lac object. The source was observed by the Whipple collaboration during the 1995/6 observing season with an exposure of 20.5 hours, yielding a signal on the 5.8σ level [Cat98]. The integral photon flux for energies of ≥ 350 GeV could be determined to be $F_{E\geq 350\,\mathrm{GeV}} = (1.7 \pm 0.5_{\mathrm{stat}}) \times 10^{-11}\,\mathrm{cm}^{-2}\,\mathrm{s}^{-1}$. Variability studies showed that slightly over one third of the excess measured was recorded during the night of 1995 December 20, where a photon flux of $F_{E>350\,\mathrm{GeV}} = (5.8 \pm 0.5_{\mathrm{stat}}) \times 10^{-11}\,\mathrm{cm}^{-2}\,\mathrm{s}^{-1}$ was observed. This is equal to $\approx 64\%$ the Crab nebula flux and constitutes a significance of 6.0σ. When removing the night of 1995 December 20 from the data sample, the flux level of the remaining data set drops to $F_{E>350\,\mathrm{GeV}} = (1.1 \pm 0.4_{\mathrm{stat}}) \times 10^{-11}\,\mathrm{cm}^{-2}\,\mathrm{s}^{-1}$ and with a significance of 4.0σ its excess becomes marginal.

In 2005, the Whipple collaboration reported a differential γ-ray energy spectrum between 0.8 and 12.6 TeV for the flare night [Sch05c], which can be described by a power law:

$$\frac{\mathrm{d}F}{\mathrm{d}E} = (5.1 \pm 1.0_{\mathrm{stat}} \pm 1.2_{\mathrm{syst}}) \cdot 10^{-7} \left(\frac{E}{\mathrm{TeV}}\right)^{-2.54 \pm 0.17_{\mathrm{stat}} \pm 0.07_{\mathrm{syst}}} \mathrm{TeV}^{-1}\,\mathrm{m}^{-2}\,\mathrm{s}^{-1}$$

Date	Group	Exposure [h]	Sign.	Integral Flux [10^{-7} m^{-2} s^{-1}]	E_{thresh} [TeV]	Reference
Oct 1995–Jan 1996	Whipple	20.5	5.8σ	1.7 ± 0.5	0.35	[Cat98]
1995 Dec 20	Whipple	1.85	5.3σ	6.6 ± 1.9	0.35	[Cat98]
Oct 1995–Jan 1996*	Whipple	18.65	4.0σ	1.1 ± 0.4	0.35	[Cat98]
Sep 1996–Jan 1997	Whipple	24.9	0.4σ	< 0.82 (99.9% C.L.)	0.35	[Cat98]
1997 Dec	HEGRA	15.8	n/a	< 0.29 (99% C.L.)	1.0	[Aha00b]
1997–2002	HEGRA	72.5	4.4σ	0.08 ± 0.03	0.8	[Aha04b]
1998	HEGRA	23.8	3.3σ	< 0.09 (99% C.L.)	1.0	[Kon99a]
1999–2000	Whipple	14.9	3.7σ	1.2 ± 0.3	0.43	[Bad01]
2000–2001	Whipple	9.1	1.8σ	0.9 ± 0.5	0.39	[Bad01]

TABLE 8.1: *Summary of VHE γ-ray measurements of 1ES 2344+514. *) Whipple observations in the 1995/6 season excluding the flare night of 1995 December 20.*

In the following season however, no significant signal could be found after 27.9 hours of observations, which led to an upper photon flux limit of $F_{E>350\,\text{GeV}} < 0.82 \times 10^{-11}$ cm^{-2} s^{-1}. Part of the observations were carried out simultaneously to the BeppoSAX measurements mentioned above; the non–detection in the VHE range might hint at a synchrotron peak energy $E_{\text{sy}} \gtrsim 10$ keV during the 1995 VHE γ-ray flare. The VHE γ-ray emission of 1ES 2344+514 was confirmed on a significance level of 4.4σ by the HEGRA collaboration [Aha04b], which found a quiescent flux level approximately 50 times lower than during the 1995 flare. A major part of the HEGRA observations were conducted as regular monitoring observations of 1 hour per night over a period of about 4 months in fall 1998 [Kon99a]. When combining the HEGRA observations from 1998 to 2002, the total excess is found to be on the 5.0σ significance level [Tlu03] with an integral flux $F_{E>970\,\text{GeV}} = (0.81 \pm 0.23) \cdot 10^{-12}$ cm^{-2} s^{-1}. The current VHE γ-ray observational status is summarized in tab. 8.1, the corresponding spectral energy distribution for 1ES 2344+514 is given in fig. 8.1.

8.1 Observations with the MAGIC telescope

1ES 2344+514 was observed with the MAGIC telescope in September and October 2005 under fairly low zenith angles of $\theta > 23°$. A provisional analysis showed a clear 5.5σ signal at ≥ 500 ph.el. and triggered additional observations in December 2005, which led to a total effective observation time of 27.57 hours. In the long–term ASM light curve (fig. 8.2), which only barely shows enhanced flux levels, the corresponding MAGIC observation periods are marked. The source was observed in wobble mode, therefore no additional OFF data runs were needed. The observation nights are summarized in tab. 8.2.

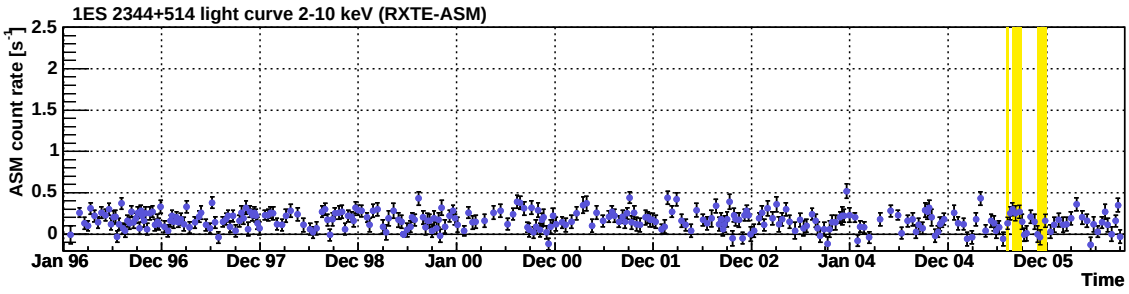

FIGURE 8.2: *Long–term ASM observations (1996–2006) of 1ES 2344+514 in the (2–10) keV energy band (data available at [XTE06]). The period during which the MAGIC observations presented in this thesis were performed are marked in yellow. Unfortunately during the VHE flare on 1995 December 20, ASM did not provide simultaneous X-ray data.*

MJD	Observation start (UTC)	Zenith angle[a] $\theta_{min} - \theta_{max}$ (deg)	Avg. ZA $\langle\theta\rangle$ (deg)	Event[b] rate (Hz)	Events (10^6)	Nominal time[c] (h)	Eff. time[d] (h)
Observation Period 32							
53585	03.08.2005 03:01:46	23.0 – 26.6	23.9	212	1.14	1.62	1.49
53587	05.08.2005 02:45:15	23.0 – 27.0	24.1	221	1.26	1.83	1.59
53589	07.08.2005 02:34:19	23.0 – 27.8	24.7	179	0.83	1.85	1.28
53591	09.08.2005 02:26:58	23.0 – 27.2	24.2	210	1.29	1.78	1.70
53593	11.08.2005 02:08:04	23.0 – 29.0	24.6	210	0.78	1.88	1.03
53595	13.08.2005 01:48:28	23.0 – 29.7	25.2	210	1.38	1.85	1.83
53597	15.08.2005 01:33:40	23.0 – 31.2	25.7	205	1.34	1.89	1.81
Observation Period 33							
53610•	28.08.2005 01:16:06	23.0 – 34.0	26.2	148	1.64	4.06	2.69
53612•	30.08.2005 03:39:12	27.0 – 34.0	30.0	141	0.82	1.89	0.94
53613•	31.08.2005 03:45:09	27.5 – 34.0	30.8	117	0.63	1.83	0.85
53616	03.09.2005 01:36:09	23.0 – 27.7	24.2	120	0.77	1.91	1.79
53619	06.09.2005 01:18:33	23.0 – 26.8	24.0	160	1.04	1.94	1.82
53625	12.09.2005 00:32:44	23.0 – 27.0	24.5	177	1.06	2.25	1.65
53639	26.09.2005 22:45:48	23.0 – 31.0	25.8	147	0.65	1.81	1.23
53642	29.09.2005 22:32:39	23.0 – 31.2	25.8	181	1.02	1.85	1.57
Observation Period 36							
53700	26.11.2005 20:58:56	23.2 – 26.8	24.8	161	0.44	0.78	0.76
53710	06.12.2005 21:01:41	25.8 – 34.0	29.4	142	0.68	2.37	0.96
Observation Period 37							
53722	18.12.2005 19:34:23	23.4 – 29.5	26.0	168	0.73	1.26	1.20
53725	21.12.2005 21:06:32	33.0 – 34.0	33.3	121	0.17	0.40	0.14
53726	22.12.2005 19:46:23	24.8 – 34.0	28.8	183	1.00	1.92	1.11
53727	23.12.2005 19:42:19	25.2 – 34.0	28.9	181	0.97	1.73	1.13
53728	24.12.2005 19:44:13	25.3 – 34.0	29.0	178	0.97	1.74	1.12
53730	26.12.2005 19:46:29	26.1 – 33.7	30.0	189	0.91	1.63	0.91
53733	29.12.2005 20:06:10	29.9 – 31.7	30.3	182	0.36	1.12	0.09
53734	30.12.2005 19:50:44	28.6 – 32.9	30.7	170	0.65	1.27	0.62
53735	31.12.2005 19:50:23	28.5 – 34.0	31.4	149	0.44	1.17	0.43
53736	01.01.2006 20:08:27	31.7 – 34.0	32.5	172	0.33	0.91	0.19

TABLE 8.2: *Summary of 1ES 2344+514 observations used in this work. The observations are grouped by observation periods which commence with each full moon. [a]The maximum zenith angle for this analysis has been set to $\theta_{max} = 34°$. [b]Raw event rate before cuts. [c]The nominal observation time is the time before any cuts (including zenith angle cuts). [d]The effective observation time is determined after the zenith angle cut and is dead–time corrected. •Data taken during moonshine.*

8.2 Event reconstruction and excess determination

This analysis encompasses data taken in August, September and December 2005. The analysis follows the scheme outlined in sect. 5.

The data were selected applying quality cuts, which required good atmospheric conditions, stable hardware conditions (decided upon by inspection of the run book) and stable event rates. Data with zenith angles higher than 34° were discarded, so as to provide a low analysis energy threshold of ≈ 140 GeV. The admixture of high zenith angle data complicates, due to a rapidly increasing energy threshold, the analysis of low energy events. After quality cuts, 27.57 hours worth of data remained. After the MAGIC standard calibration, the Cherenkov signals were extracted using the digital filter method. For the image cleaning, a minimum number of 7 ph.el. and 5 ph.el. for core and boundary pixels, respectively, were required.

For gamma/hadron separation, random forests were trained using MC γs and hadronic background. For the latter, real data events randomly selected from the background region were used.

For determining the excess, the DISP method was used; a parameterization for DISP was obtained from MC events. The corresponding θ^2 plot is shown in fig. 8.3. It indicates an excess of 528 γ events on the 10.95σ level. Note that due to the fact that the data were taken in wobble mode, the amount of ON and OFF data is almost equal and results in a normalization factor of 0.96. In this analysis, three background regions of the same size chosen symmetrically with the source position around the camera center were used for a simultaneous determination of the background, which is the reason for the comparatively smaller error bars of the OFF data as compared to the ON data.

Sky map. Fig. 8.4 shows a sky map produced by imposing a hadronness cut of $h < 0.1$ for events with SIZE > 300 ph.el. The source position could be determined from this map as $(\mathrm{RA}, \mathrm{dec}) = (23^{\mathrm{h}}46.^{\mathrm{m}}8 \pm 0.^{\mathrm{m}}42, 51^{\circ}42.'6 \pm 1.'2)$. The quoted uncertainties only come from the analysis and have to be added to the $1.5'$ positional inaccuracy of the drive system. The source position of 1ES 2344+514, $(\mathrm{RA}, \mathrm{dec}) = (23^{\mathrm{h}}46.^{\mathrm{m}}86, 51^{\circ}42.'3)$ [NED06], is well matched within uncertainties with the found excess location.

8.3 Light curve studies

The overall light curve for the observations is shown in fig. 8.5. Observation nights with effective observation times < 15 minutes are not included. The integrated flux for γ-rays with $E \geq 350$ GeV is found to be $F_{E \geq 350\,\mathrm{GeV}} = (5.79 \pm 0.83) \times 10^{-12}\,\mathrm{cm}^{-2}\,\mathrm{s}^{-1}$. The light curve indicates no major changes of the flux level and no significant flares. To judge

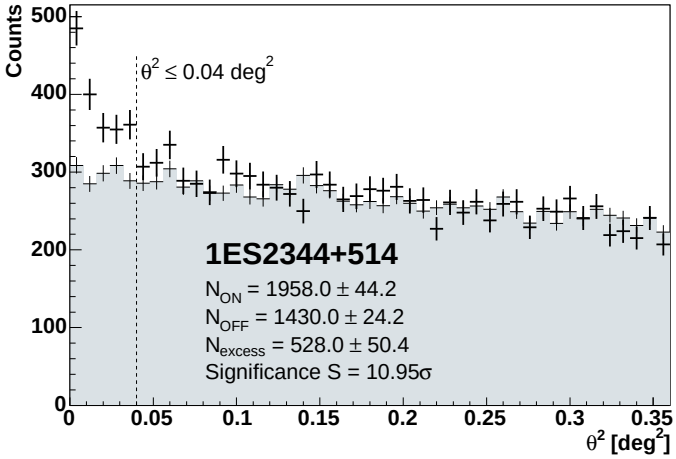

FIGURE 8.3: *θ^2 plot for the 1ES 2344+514 observations. A cut at $\theta^2 < 0.04\,\mathrm{deg}^2$ selects 528 γ-ray events on a significance level of 10.95σ. The plot has been prepared for* SIZE > 300 ph.el. *($\gtrapprox 180$ GeV) and a hadronness cut of $h = 0.1$.*

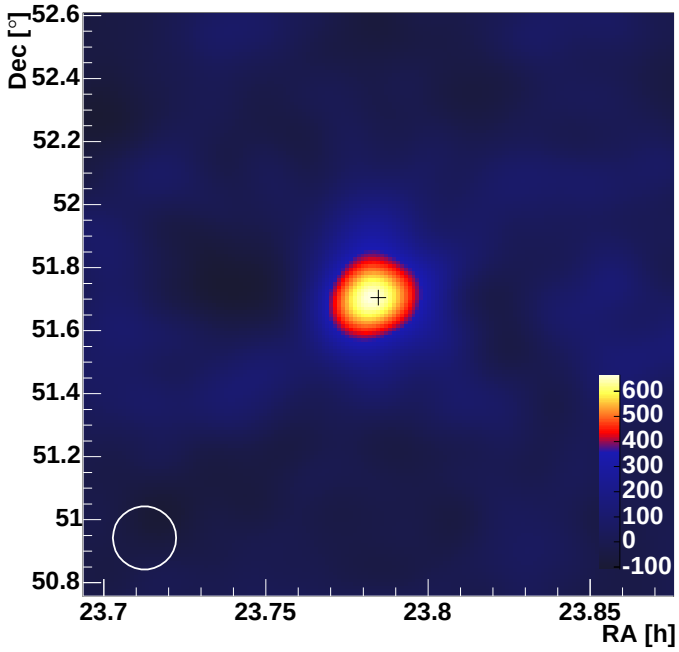

FIGURE 8.4: *Map of the sky region around the position of 1ES 2344+514 produced with the* DISP *analysis: The figure shows the arrival directions of γ-ray candidates above 300 ph.el. ($\gtrapprox 180$ GeV) that were selected by imposing a hadronness cut of $h < 0.1$. The units represented by the color–code are 10^{-5} events sr^{-1}, i.e. events within a circular area with $r = 0.1°$. The black cross marks the expected source position; the white circle indicates the γ-ray PSF (angular resolution) of the MAGIC telescope of 0.1°. The map has been smoothed with the PSF as described in sect. 5.4.5.*

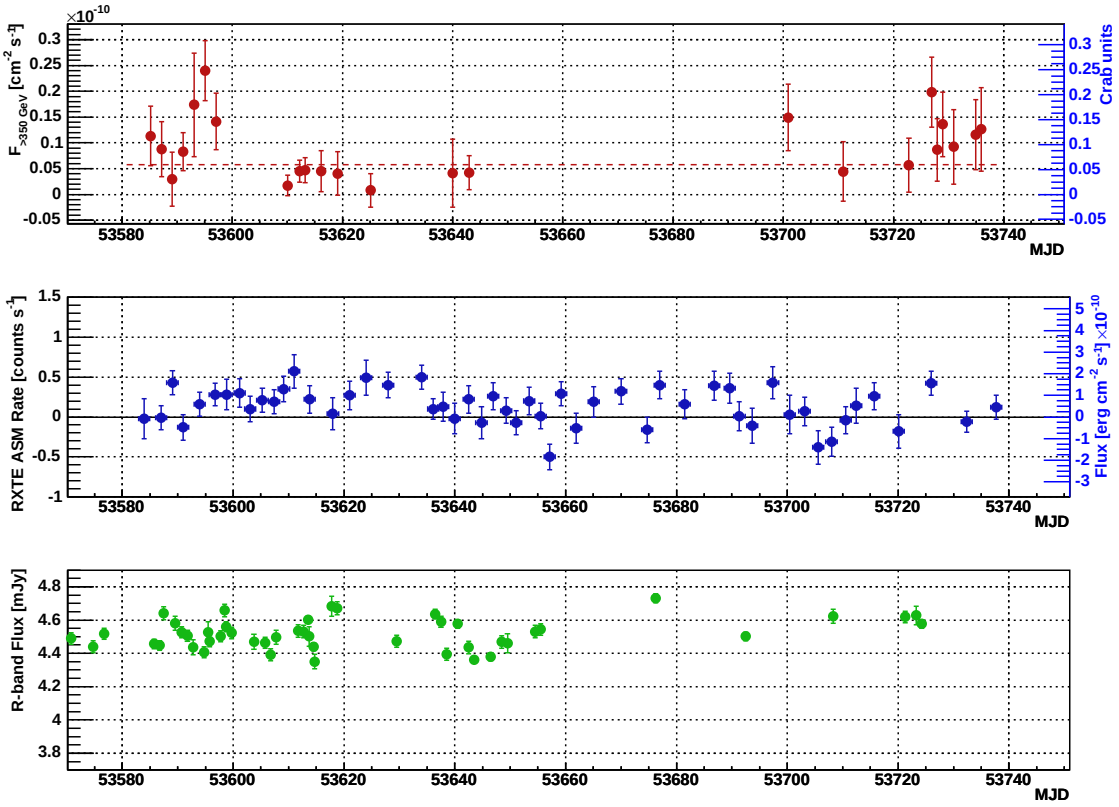

FIGURE 8.5: *Light curves for 1ES 2344+514. Upper panel: The red symbols represent the diurnal VHE light curve for γ-rays with energies of $E \geq 350$ GeV as obtained with MAGIC. Middle panel:* $(2-10)$ keV *X-ray light curve as measured with the ASM instrument on board of RXTE (data available at [XTE06]). Lower panel: Optical light curve as measured with the KVA 35cm monitoring telescope in La Palma and the 1.03 m Tuorla telescope, Tuorla Observatory, Finland. The contribution of the host galaxy is determined to be 3.7 mJy. Optical data courtesy K. Nilsson [Nil06].*

upon possible variations, constant fits have been applied to parts of the data set: The levels found for the integral flux at 350 GeV and above (in units of 10^{-12} cm^{-2} s^{-1}), the reduced χ^2 values for fits with constant functions, and the fit probabilities P are:

- 5.79 ± 0.83 for the complete data set, $\chi^2_{\rm red} = 33.0/23$, $P = 8.1\%$
- 11.0 ± 2.01 for MJD $53580-53600$, $\chi^2_{\rm red} = 8.79/6$, $P = 18.5\%$. This is equivalent to an increase of $+87\%$ w.r.t. to the global flux level
- 3.41 ± 1.01 for MJD $53605-53627$, $\chi^2_{\rm red} = 2.02/7$. This is equivalent to a decrease of -41% w.r.t. to the global flux level
- 10.6 ± 2.13 for MJD $53700-53736$, $\chi^2_{\rm red} = 4.7/8$. This is equivalent to an increase of $+83\%$ w.r.t. to the global flux level

The period MJD $53580-53600$ was subjected to a closer inspection, as it shows a possible variability pattern. In fig. 8.6 two light curves for that period are given, one for

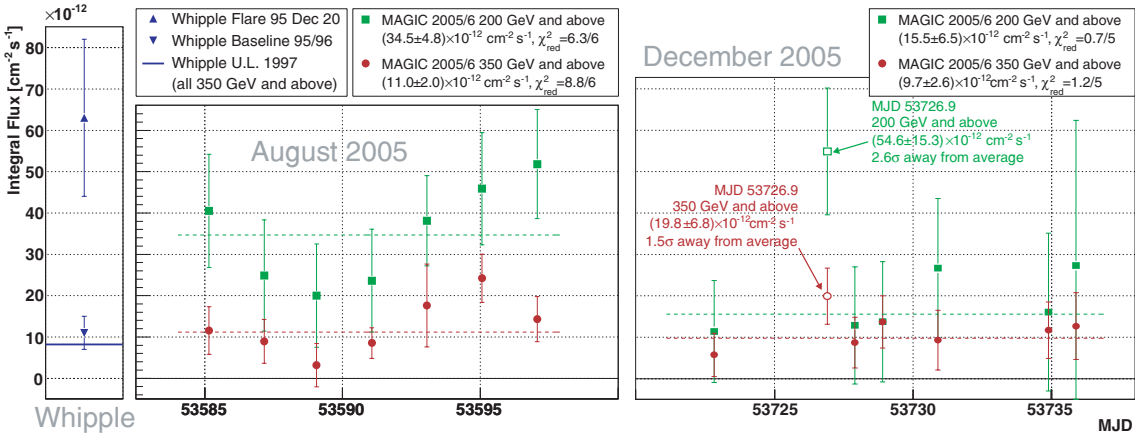

FIGURE 8.6: *Middle panel: Light curves for MJD 53585–53597 for the energy ranges $E \geq 200$ GeV and $E \geq 350$ GeV. The data points are fit with a constant flux ansatz with a probability of 39% ($E \geq 200$ GeV) and 19% ($E \geq 350$ GeV), respectively. Right panel: Light curves for MJD 53723–53736 for the energy ranges $E \geq 200$ GeV and $E \geq 350$ GeV. The data points, excluding MJD 53726.9, are fit with a constant flux ansatz. The MJD 57326.9 data point deviates from the average flux level by 1.5σ ($E \geq 350$ GeV) and 2.6σ ($E \geq 200$ GeV), respectively. Left panel: Whipple measurements at 350 GeV and above for comparison.*

$E \geq 200$ GeV and a zoom of fig. 8.5, for $E \geq 350$ GeV. Although there are hints for variability, the data are statistically compatible with a constant flux.

The same study was performed for MJD $53723 - 53736$. Here, the data point covering the measurements from MJD 53726.82 to MJD 53726.90 deviates from the average flux level found for the surrounding data points. To quantify this behavior, the average flux excluding the MJD 53726 data point was calculated. In the $E \geq 350$ GeV light curve, the flux on MJD 53726 deviates by 1.5σ from the average integral flux in the surrounding observation nights; in the $E \geq 200$ GeV light curve by 2.6σ. The single-trial chance probability for such a deviation is 0.93%; Thus the probability for observing such an excess in the 24 observation nights is 22.3%. Further investigations did not reveal any significant variations during this observation night. Therefore flux variability on a timescale smaller than 24 hours can neither be claimed nor ruled out from these observations.

X-ray light curve. The only simulataneous X-ray data for the MAGIC measurements are available from the ASM detector on board of the RXTE satellite [Lev96] and are given as count–rates which are proportional to the $(2 - 10)$ keV flux. In order to estimate whether the ASM instrument is sensitive enough to register the X-ray emission from 1ES 2344+514, we calculate from BeppoSAX measurements [Gio00] the expected ASM count–rates. The maximum and minimum BeppoSAX fluxes of $F_{\rm max} = 3.8 \cdot 10^{-11}$ erg cm^{-2} s^{-1} and $F_{\rm min} = 8.4 \cdot 10^{-12}$ erg cm^{-2} s^{-1} translate into ASM count–rates of 0.120 s^{-1} and 0.026 s^{-1}, respectively. The conversion from ASM count–rates is given by the integral Crab flux of $2.39 \cdot 10^{-8}$ erg cm^{-2} s^{-1} (2 – 10 keV) [Sew78, Rev03] and the corresponding ASM count–rate of 75.38 s^{-1} [Lev04]. Therefore the here measured ASM count–rates have to be attributed primarily to ASM detector noise.

Optical light curve. The optical brightness in the *R*-band was measured by the KVA 35 cm monitoring telescope (cf. sect. 4.8) and the 1.03 m optical telescope at Tuorla Observatory, Finland. On average an apparent brightness of $\approx 14\overset{\mathrm{m}}{.}5$ was found. This is significantly brighter than the reported measurements during 1996 ($16\overset{\mathrm{m}}{.}83 \mp 0\overset{\mathrm{m}}{.}05$, Hubble space telescope [Urr00]) and 1998 (variations between $16\overset{\mathrm{m}}{.}47$ and $17\overset{\mathrm{m}}{.}00$, [Nil99, Fal99]). In contrast to these measurements, no subtraction of the host galaxy was performed for the 2005 measurements. A more comparable number therefore is the measurement of $15\overset{\mathrm{m}}{.}5$ as reported by [Per96]. After correcting for the contribution of the host galaxy to the measured optical brightness (3.7 mJy [Nil06]), variations around the average brightness of $\approx 15\%$ are seen, which are significant given the small errors ($\lessapprox 5\%$) of the data points. Corresponding 15% variations in the VHE region, however, are below the sensitivity of MAGIC on the given timescale.

Correlation between VHE γ-rays and X-rays, VHE γ-rays and optical data. The inspection of the light curves (fig. 8.7) does not reveal any obvious correlations of VHE γ-ray data with X-ray data and optical data.

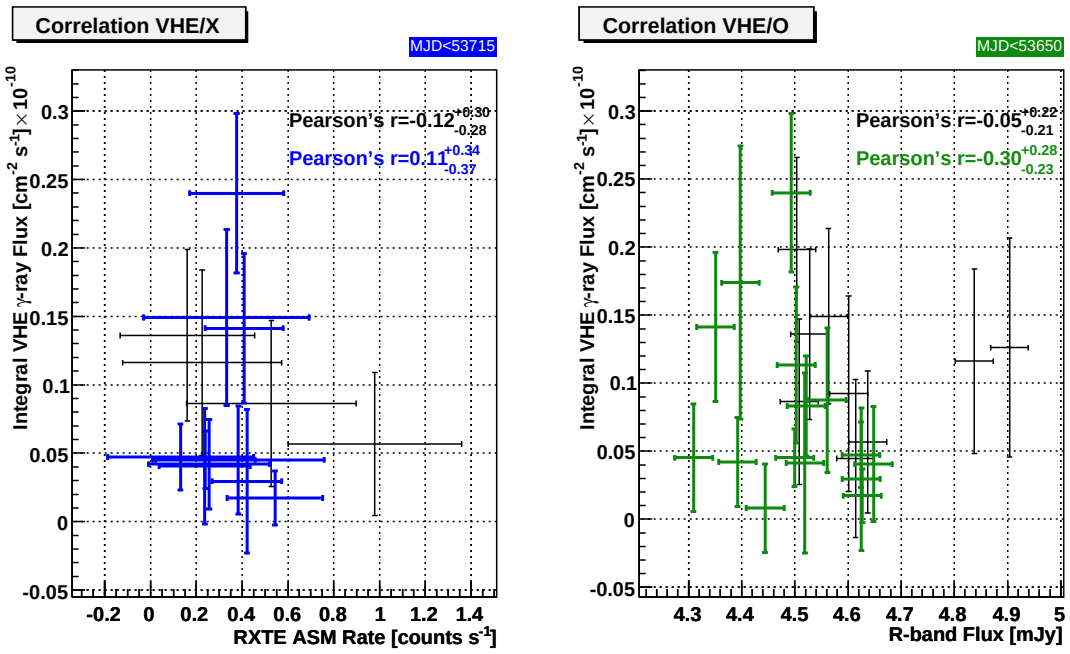

FIGURE 8.7: *Left panel: Correlation of X-ray data (obtained from [Lev04]) and VHE γ-ray measurements. Right panel: Correlation of optical [Nil06] and VHE measurements. For MJD>53715 the available X-ray data and for MJD>53650 the optical measurements were too sparse to average them meaningfully around the VHE data points. Only the data points for which a sufficient sampling of X-ray or optical data was given are marked in color. The figures include correlation coefficients as discussed in sect. 7.6 for the selected (colored symbols and legends) and for all data points (black symbols and legends).*

For the evaluation of correlations of VHE γ-ray flux and X-ray flux/optical flux only those periods should be considered in which a dense enough sampling in X-ray and optical data is given. In fig. 8.7, the corresponding data points are marked accordingly. Sufficient sampling is given for X-rays for MJD$<$53715 and for optical data for MJD$<$53650.

The X-ray data come from the ASM detector on board of the RXTE satellite [Lev96] and are given as count–rates that are proportional to the $(2-10)$ keV flux. Note that the expected ASM X-ray count–rates are well below the here observed rates. The $(2-10)$ keV flux from 1ES 2344+514, even during outbursts, is not expected to be measurable with ASM. There is also no obvious correlation of the VHE γ-ray and the optical flux. This is compatible with the nature of 1ES 2344+514 as an HBL object with its synchrotron peak far in the X-ray domain. For only modest flux variations in the VHE γ-ray domain, in an SSC model one would therefore not expect correlated variations in the optical domain.

Comparison with previous observations. In fig. 8.8 we compile a light curve from all reported VHE γ-ray measurements and upper limits for 1ES 2344+514. Except for the 1995 December 20 flare and the MAGIC data, these measurements all are on the sensitivity level of the respective instruments with which they were obtained. Therefore none of these data points exceeds a significance of 4.3σ. For the plot all reported observations with significances below 2σ were converted to upper flux limits.

In 1995/6 Whipple discovered 1ES 2344+514 at a flux level of (0.11 ± 0.05) Crab units (c.u.),[1] except for the December 1995 flare, during which (0.63 ± 0.15) c.u. were obtained [Cat98]. Follow-up observations by Whipple and HEGRA in 1996–8 yielded upper limits of 0.08 c.u. and 0.12 c.u., respectively. In 1998 and 2002, the object was observed for almost 60 h by HEGRA, resulting, when combined, in a flux of (0.053 ± 0.015) c.u. on the 5σ significance level [Tlu03]. From observations in 2002, the Whipple group could infer a low flux level of $\lessapprox 0.03$ c.u. with a marginal significance of 3.1σ [Bad01].

While the Whipple and HEGRA measurements allowed to infer a low emission state of $\leq 12\%$ of the Crab nebula flux only after long observation times, the MAGIC observations obtained in this work are the first time–resolved measurements at low emission levels. We find the flux of 1ES 2344+514 to be (0.11 ± 0.02) c.u. in August 2005 (observation period 32) and December 2005 (observation period 36&37). From the end of August to the end of September 2005 (period 33), a flux level of (0.04 ± 0.01) c.u. is found. While all these measurements are well in line with the 1997–2002 observations of 1ES 2344+514, in particular the low level observed in September 2005 is comparable with the lowest flux levels found so far for this object in 1998 and 2000.

[1] As the spectral indices of 1ES 2344+514 and the Crab nebula differ, one has to specify for which threshold energy the c.u. are given. Throughout this chapter, c.u. are given for the integral flux for $E \geq 350$ GeV. Therefore, where necessary, integral fluxes were extrapolated down to the 350 GeV threshold assuming a power law spectrum as inferred in sect. 8.4. This in particular applies to the HEGRA measurements.

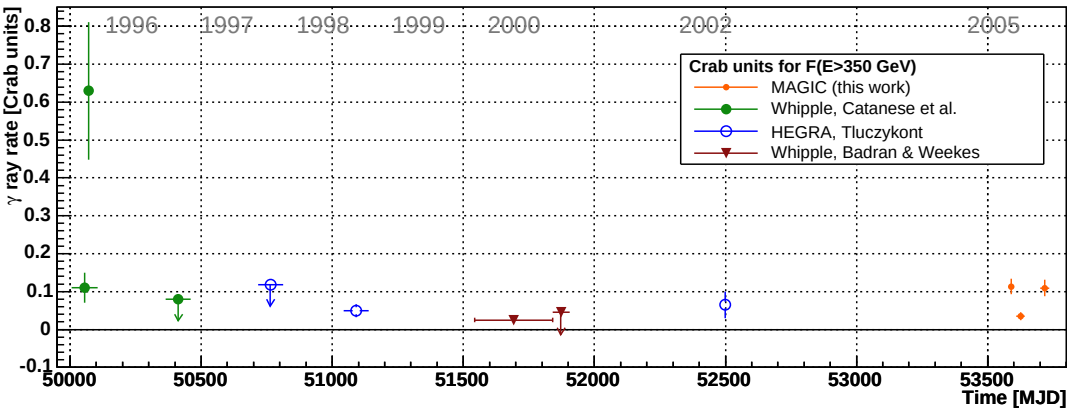

FIGURE 8.8: *Long–term VHE γ-ray light curve of 1ES 2344+514. Data have been compiled from Whipple observations [Cat98, Bad01], HEGRA observations [Tlu03], and this work. The measurements were converted into units of the integral Crab nebula flux for $E \geq 350$ GeV, extrapolating by using the spectral slope found in this analysis, as they were conducted with different energy thresholds. All reported observations with significances below 2σ were converted to upper flux limits.*

Low–level VHE γ-ray emission. It is interesting to ask whether the low flux level of ≈ 0.04 c.u. as seen by MAGIC can be attributed to a *baseline emission*. Up to now, such a baseline emission for blazars has only been observed in X-rays in Mkn 501 [Xue05], see also the discussion in sect. 7.8.5. Due to its similarity to Mkn 501, 1ES 2344+514 is a promising candidate for VHE γ-ray baseline emission studies.

The 1ES 2344+514 light curve for $E \geq 350$ GeV as given in fig. 8.8 suggests a flux level of $F \leq 0.04$ c.u. to be a viable baseline emission level. A proper definition of a blazar baseline VHE γ-ray emission must, however, contain additional phenomenological ingredients. Apart from an absolute flux level limit to discern the baseline emission from flare activity, temporal characteristics have to enter the definition, namely a constant flux level needs to be observed over an extended period. If allowing for variability, a maximum allowed variability scale must not be exceeded. In previous observations of 1ES 2344+514 it was not possible to infer temporal characteristics of its VHE γ-ray emission, owing to the inferior sensitivity of the available instruments.

The MAGIC measurements show that there is flux variability of a factor ≈ 2.5 present during the total observation time of 151 days. The time scale on which a flux close to the up to now minimum flux of (0.025 ± 0.007) c.u. (although at marginal significances) [Bad01] and (0.053 ± 0.015) c.u. [Tlu03] was observed is of the order of 20 days. During periods with emission levels of ≈ 0.1 c.u., the present analysis shows a non-significant variability pattern (MJD $53585 - 53597$). In addition, one data point off the surrounding average flux level (MJD 53726.9) by 2.6σ was found. Therefore our measurements show that probably there is no steady–state emission over extended periods of > 20 days, but a low level emission (≈ 0.10 c.u.) with marginal modest variations and intermittent small-

scale flares. As previous observations could by far not achieve a time resolution of the order of single days, our measurements and those from 1997–2002 are presumably well in line with the requirements for a low emission state. Only additional extended observations of 1ES 2344+514 will reveal further temporal characteristics of its low emission state. In this context it would be interesting to demonstrate even lower fluxes than the here measured emission levels or even a vanishing flux.

8.4 Spectrum determination

As no major changes in the flux level of 1ES 2344+514 were observed, a differential energy spectrum was calculated using the complete data set. The spectrum shown in fig. 8.9 can be fit by a pure power law of the form

$$\frac{\mathrm{d}F}{\mathrm{d}E} = (1.18 \pm 0.13) \times 10^{-11} \left(\frac{E}{500\ \mathrm{GeV}} \right)^{-2.95 \pm 0.12} \ \mathrm{TeV}^{-1}\ \mathrm{cm}^{-2}\ \mathrm{s}^{-1}$$

between 140 GeV and 5.0 TeV, which describes the data acceptably well with a probability of 13%. As the recorded data extend up to energies of some TeV, an energy domain at which non–negligible absorption by the EBL is expected, a power law fit with cutoff was also performed. For this, first the slope of the spectrum in the energy range of 100 GeV to 550 GeV was determined and than fixed such that only the normalization and the cutoff energy were left as free parameters. The fit yields

$$\frac{\mathrm{d}F}{\mathrm{d}E} = (1.55 \pm 0.19) \times 10^{-11} \left(\frac{E}{500\ \mathrm{GeV}} \right)^{-2.76} \exp\left(\frac{-E}{(2.5 \pm 2.2)\ \mathrm{TeV}} \right) \ \mathrm{TeV}^{-1}\ \mathrm{cm}^{-2}\ \mathrm{s}^{-1}$$

with a comparable probability of 20%, but a large error on the cutoff energy. Note that according to expectations, a cutoff due to the EBL absorption is not expected below $\approx$ 5 TeV (cf. sect. 1.2.2). Therefore, for any claim of a possible cutoff, one would wish for better statistics in the $5 - 8.3$ TeV energy bin.

The integral flux, when calculated for energies above 970 GeV, $F_{E>970\,\mathrm{GeV}} = (0.82 \pm 0.09) \times 10^{-12}\ \mathrm{cm}^{-2}\ \mathrm{s}^{-1}$ is in very good agreement with the flux found by HEGRA from observations from 1998 to 2002, $F_{E>970\,\mathrm{GeV}} = (0.81 \pm 0.23) \cdot 10^{-12}\ \mathrm{cm}^{-2}\ \mathrm{s}^{-1}$ [Tlu03]. This hints at the possibility that during our measurements a similar (low) emission level was found as observed by HEGRA.

Spectra for individual observation periods. To check for possible spectral changes during the observation, individual spectra were determined for August 2005 (period 32), September 2005 (period 33), and December 2005 (periods 36 and 37). Pure power law fits were performed in the energy ranges in which the spectra allowed reliable fitting (fig. 8.10). Results are summarized in tab. 8.3. While no significant changes in the spectral index were found, the flux normalization varies by a factor of 1.5 around the average value, which is consistent with the integral flux levels reported earlier.

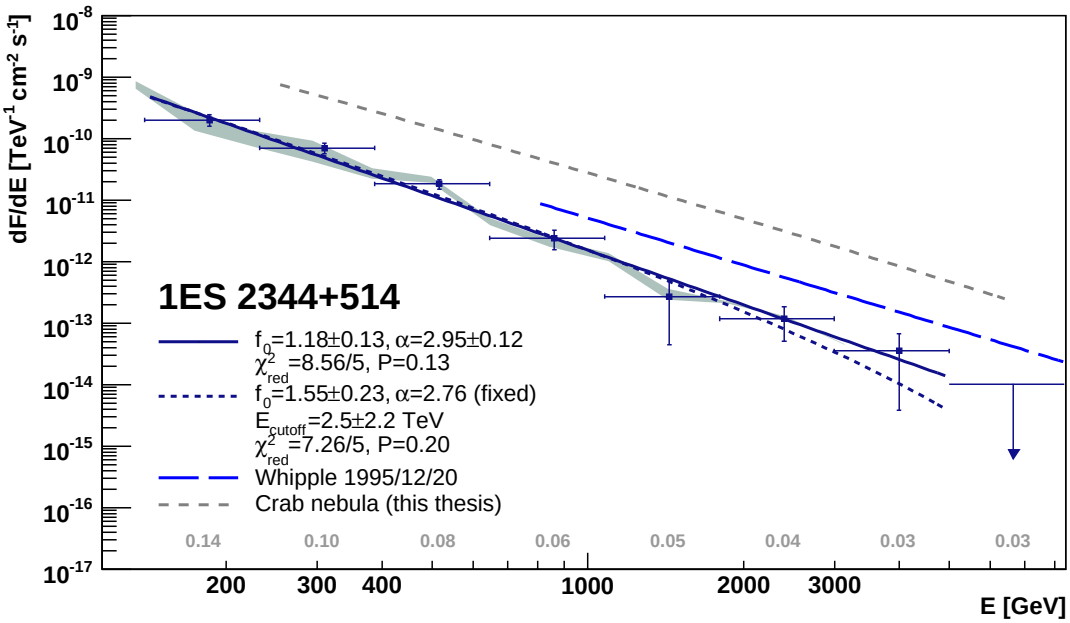

FIGURE 8.9: *Differential energy spectrum of 1ES 2344+514. The spectrum was fitted with a pure power law between* 140 GeV *and* 5.0 TeV*; the normalization* f_0 *at* $E = 500$ GeV *is given in units of* 10^{-11} TeV^{-1} cm^{-2} s^{-1}. *Additionally, a power law with cutoff was fitted (with a slope of* α*=2.76 fixed in the region below 450 GeV). See text for details. For comparison, the spectrum of the Crab Nebula and the spectrum of 1ES 2344+514 as determined for the 1995 December 20 flare [Sch05c] is also given; the numbers on the bottom of the plot give the differential flux of the 1ES 2344+514 data points in "Crab units".*

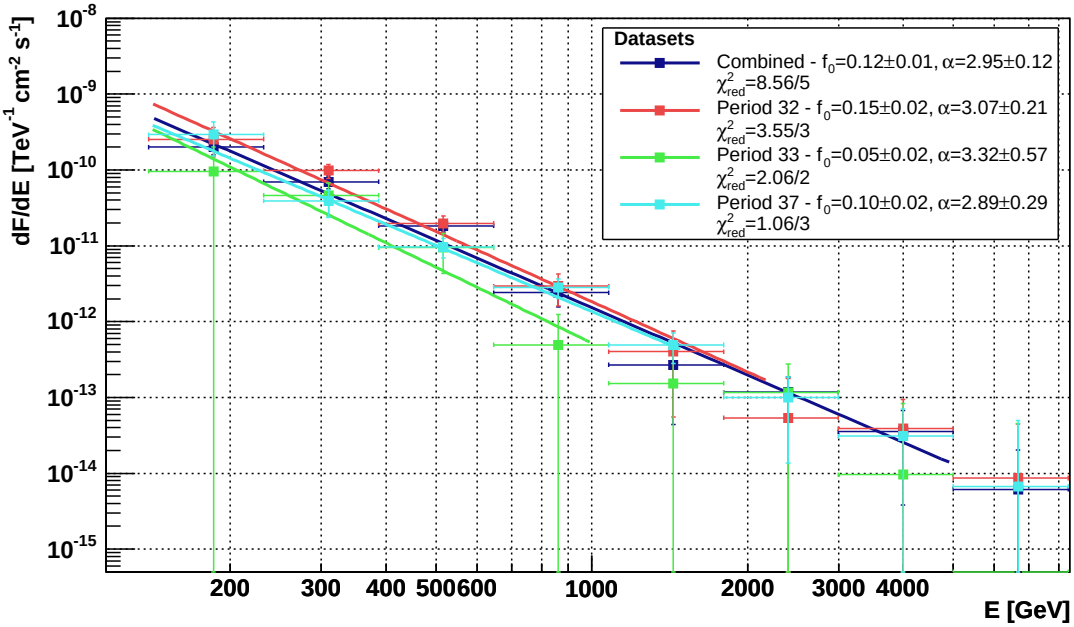

FIGURE 8.10: *Measured spectra for individual observation periods and the combined data set with pure power law fits of the form* $F = f_0 \cdot 10^{-11} \cdot (E/500\,\text{GeV})^{-\alpha}$ TeV^{-1} cm^{-2} s^{-1}. *The measurements are summarized in tab. 8.3.*

Observation period	Effective observation time	Fit range [GeV]	Flux normalization f_0 [10^{-11} TeV^{-1} cm^{-2} s^{-1}]	Spectral index α
Combined	27.57 h	140–5000	0.12 ± 0.01	2.96 ± 0.12
32	6.37 h	140–2200	0.15 ± 0.02	3.07 ± 0.21
33	12.54 h	140–1000	0.05 ± 0.02	3.32 ± 0.57
36+37	8.66 h	140–1500	0.10 ± 0.02	2.89 ± 0.29

TABLE 8.3: *Parameters of differential energy spectra for individual observation periods. f_0 denotes the flux normalization at 500 GeV. Within errors, the spectral indices are compatible.*

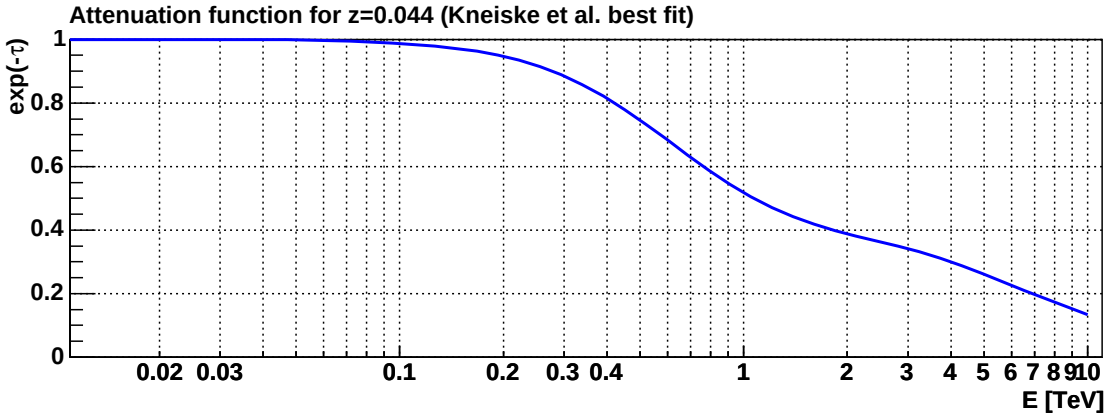

FIGURE 8.11: *Attenuation function* (1.6) *due to the EBL absorption for a redshift of $z = 0.044$. When dividing the measured spectrum by this function, the intrinsic source spectrum is obtained. Calculated using the best-fit model given in [Kne04].*

EBL de-absorption and the intrinsic spectrum. To determine the intrinsic spectrum of 1ES 2344+514, absorption effects by the EBL have to be taken into account. Therefore the attenuation function $\exp(-\tau)$ has been determined for the redshift of 1ES 2344+514 of $z = 0.044$ (fig. 8.11) using the best–fit EBL model given in [Kne04]. By multiplying the resulting attenuation function with the measured spectra using eq. (1.7), the intrinsic source spectrum can be reconstructed. Fig. 8.12 shows both the measured and the de-absorbed spectrum of 1ES 2344+514. The reconstructed intrinsic differential energy spectrum can be described by a power law of the form

$$\frac{\mathrm{d}F}{\mathrm{d}E} = (2.09 \pm 1.15) \times 10^{-11} \left(\frac{E}{500\ \mathrm{GeV}} \right)^{-2.66 \pm 0.48} \ \mathrm{TeV}^{-1}\ \mathrm{cm}^{-2}\ \mathrm{s}^{-1}$$

in the energy range between 140 GeV and 5.0 TeV. As the reconstructed intrinsic spectrum flattens towards its low energy end, a curved (Log-P) fit as discussed in sect. 7.7.1 has been performed. This fit allows the determination of the peak energy of the spectrum, which here is found at $E_{\mathrm{peak}} = (202 \pm 174)$ GeV. Note that the fit is a rather bad description of the data points; one can however interpret the flattening as a hint for a peak in the spectral energy distribution well below 400 GeV.

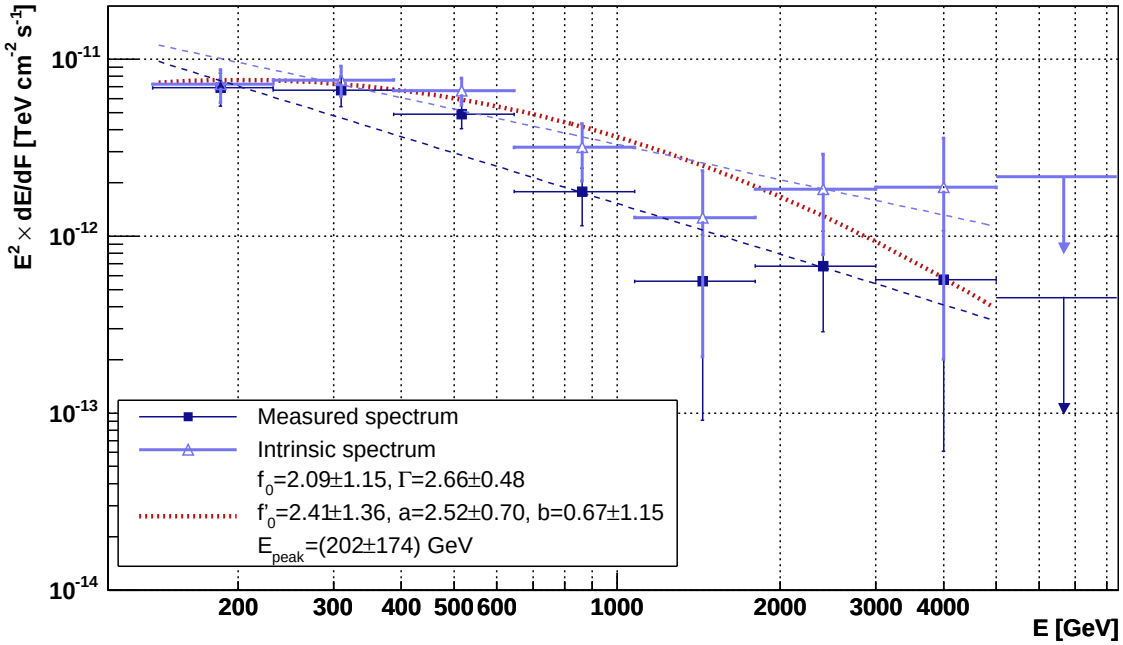

FIGURE 8.12: *Differential energy spectra of 1ES 2344+514 before ("measured") and after ("intrinsic") EBL de-absorption. The de-absorption was carried out using the attenuation function given in fig. 8.11. The spectra were fitted with pure power laws between 140 GeV and 5.0 TeV; the normalization f_0 at $E_0 = 500$ GeV is given in units of 10^{-11} TeV^{-1} cm^{-2} s^{-1}. The red–dotted curve represents a Log-P fit (cf. sect. 7.7.1) performed to infer the peak energy using eq. (7.9). Also its normalization f'_0 at $E_1 = 500$ GeV is given in units of 10^{-11} TeV^{-1} cm^{-2} s^{-1}; $E_a = 500$ GeV.*

8.5 Spectral energy distribution of 1ES 2344+514

The spectral energy distribution for 1ES 2344+514 is shown in fig. 8.13. Apart from the VHE γ-ray observations by MAGIC, Whipple, HEGRA and an upper limit of EGRET, X-ray measurements performed by EINSTEIN, ROSAT, and BeppoSAX are the most relevant measurements for modeling the SED. As the published HEGRA and Whipple data points were not corrected for EBL absorption effects, we also plot the *measured* MAGIC energy spectrum. The EBL effects are accordingly accounted for inside the SSC model instead. The figure also includes optical measurements and radio measurements, although the latter cannot be described by the used one–zone SSC model provided by [Kra04]. The model input parameters and the application of the model have been described in sect. 7.9. Two BeppoSAX data sets are shown: one was obtained simultaneously with Whipple observations on 1996 December 5. The second set was taken during a quiescent period of 1ES 2344+514, and thus might represent a low X-ray emission state of the object, although not necessarily exactly correspond to the MAGIC measurements. It should be stressed that most of the data points shown in the SED were not measured simultaneously, which makes SED modeling very difficult. The modeling of the low emission state and the flare state was done along the guidelines outlined in sect. 7.9. The size of the emission region R was chosen such that it can account for day-scale variability along with

the Doppler factors δ chosen, $R \leq \delta_1 \times t_d \times 2.48 \times 10^{14}$m with $\delta_1 = 10 \cdot \delta$ and t_d in units of days. The input parameters used here are specified in fig. 8.13. The models shown are to describe the flare state of 1995 and the MAGIC observations in 2005. As for both 1995 and 2005 VHE observations no simultaneous X-ray data were available, the form of the high-emission level synchrotron peak was modeled using the 1996 December 5 BeppoSAX data; the model for 1995 December 20 was then inferred by further increasing the Doppler factor. The models differ in the following model input parameters:

1. the Doppler factor is increased from $\delta_{\text{low}} = 8.4$ to $\delta_{\text{flare}} = 15.2$ (The Doppler factor for the 1996 December 5 model was $\delta_{1996/12/05} = 13.2$),
2. the magnetic field strength is decreased from $B_{\text{low}} = 0.095$ G to $B_{\text{flare}} = 0.070$ G,
3. the electron density is increased from $\rho_{\text{low}} = 0.016\,\text{erg}\,\text{cm}^{-3}$ vs. $\rho_{\text{flare}} = 0.025\,\text{erg}\,\text{cm}^{-3}$,
4. further the form of the electron spectrum is changed by increasing minimum, maximum, and break energy.

The slopes of the electron spectrum were kept constant at $n_1 = -2.2$ and $n_2 = -3.2$.

8.6 Interpretation and conclusions

- A significant signal of 1ES 2344+514 was detected for a total effective observation time of 27.57 hours. The total data sample permitted the determination of a differential energy spectrum up to energies of 5 TeV. It is the first VHE γ-ray spectrum derived for this object in a low flux state and impressively shows MAGIC's ability to observe objects at low flux levels of 5% of the Crab nebula flux and below in reasonable observation times of around 25 hours.
- The obtained spectrum agrees well with the integral flux determined from the 4.4σ evidence published by the HEGRA collaboration. According to expectations, the measured spectrum is softer than the flare spectrum observed on 1995 December 20 reported by the Whipple collaboration.
- The obtained light curve shows evidence for variations of the flux level of a factor ≈ 2.5 on the timescale of ≈ 150 days. No significant variation of the spectral index was observed, however. One flare candidate on a timescale of 24 hours was observed with a significance of 2.6σ. For the first time, a temporal characterization of a VHE γ-ray emitter at its low flux level could be performed. Moreover, the low flux level found during part of the observations, along with previous measurements

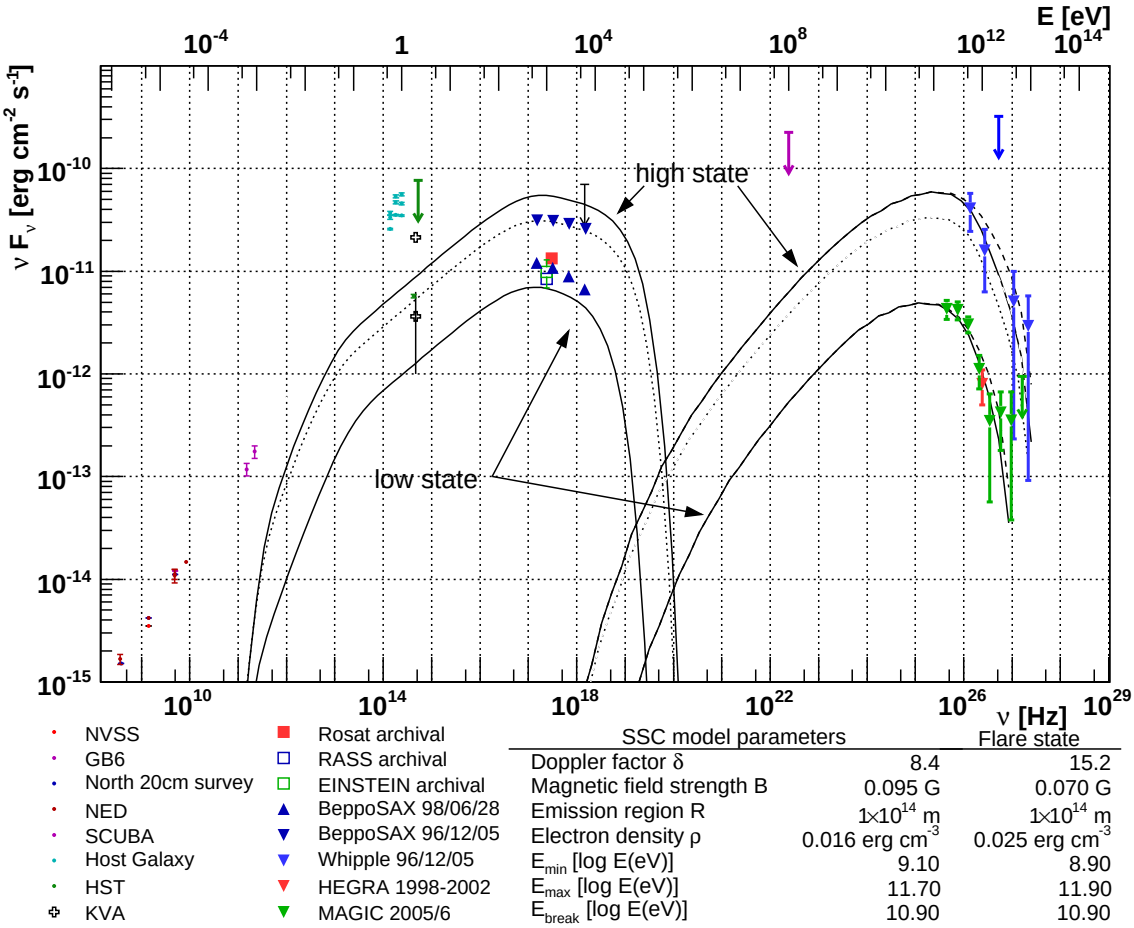

SSC model parameters		Flare state
Doppler factor δ	8.4	15.2
Magnetic field strength B	0.095 G	0.070 G
Emission region R	1×10^{14} m	1×10^{14} m
Electron density ρ	0.016 erg cm^{-3}	0.025 erg cm^{-3}
E_{min} [log E(eV)]	9.10	8.90
E_{max} [log E(eV)]	11.70	11.90
E_{break} [log E(eV)]	10.90	10.90

FIGURE 8.13: *Overall SED for 1ES 2344+514. Radio to sub-millimeter data: NRAO VLA sky survey [Con98], Green Bank 4.85 GHz northern sky survey [Gre96], North 20cm survey [Whi92], NED archival data [NED06], SCUBA. Optical: KVA monitoring data [Nil06] without and with 3.7 mJy host galaxy contribution subtracted. The latter data point has a rather large error due to the subtraction uncertainties. Further optical measurements: HST host galaxy, HST galaxy core, HST galaxy core upper limit (green arrow) [Sch06]. X-ray: Rosat, RASS [Vog99], EINSTEIN, BeppoSAX [Sch06], RXTE–ASM upper limit (thin black arrow) from data taken simultaneously with the MAGIC VHE data. The two BeppoSAX data sets represent a low emission state and data taken contemporaneously with the Whipple upper limit of 1996 December 5 (blue arrow). Measured γ-ray spectra and upper limits: EGRET upper limit (purple arrow) [Har99], HEGRA [Aha04b], Whipple [Sch05c] spectrum of 1995 December 20 (blue triangles) and upper limit of 1996 December 5 (blue arrow). Further archival data taken from [ASD06]. The SEDs were modeled using the homogeneous SSC model code provided in [Kra04]. The dotted curve was modeled to match the 1996 December 5 BeppoSAX data; The solid curves were then modeled to represent the 1995 Whipple and 2005 MAGIC flux states, respectively. The corresponding model input parameters are given in the caption. The SSC model includes EBL absorption effects [Mac96], the EBL de-absorbed spectra are given by the dashed curves. Note that only KVA and ASM data are contemporaneous with the MAGIC data.*

by Whipple and HEGRA, can be attributed to the lowest VHE γ-ray emission level of ≈ 0.04 c.u. found so far for 1ES 2344+514.

- The spectral energy distributions both for the low flux state MAGIC observations and for the flare observation of Whipple from 1995 December 20 can be accommodated in a homogeneous one–zone SSC model with an emission region size compatible with the flux variability timescale suggested by the data.

Chapter 9

First observations of VHE γ-ray emission from the blazar PG 1553+113

9.1 Introduction

The BL Lac object PG 1553+113 was first identified with a $15\overset{\text{m}}{.}5$ blue stellar object in the Palomar–Green survey of UV excess stellar objects [Gre86]. It was the first BL Lac object discovered in an optical survey. PG 1553+113 has been observed in a broad range of wavelengths, also during multiwavelength campaigns [Ost06a]. Based on its spectral characteristics [Mil83, Fal90], its optical variability ($\Delta m = 1.8$, [Mil88]) and the broad-band spectral energy distribution up to X-rays (detections by BeppoSAX [Don05] and XMM Newton [Per05]) the object was classified as a high–frequency peaked BL Lac [Gio95] or more recently as an "intermediate BL Lac" [Lau99, Nie06] with the synchrotron peak in the SED at $\nu^{\text{sy}}_{\text{peak}} = 3 \cdot 10^{16}$ Hz. Recent multiwavelength observations claim an XBL nature even more extreme than that of Mkn 501 [Ost06b].

Redshift determination. BL Lac objects generally exhibit only weak spectral lines, which makes redshift determinations difficult. In several measurement campaigns no emission or absorption lines could be found in the spectrum of PG 1553+113. It has to be stressed that the frequently cited initial determination of $z = 0.36$ [Mil83] was found to be based on a misidentified emission line and could not be reproduced [Fal90, Fal94]. Therefore indirect methods were employed to pose limits on its redshift: No host galaxy of PG 1553+113 could be resolved in the HST survey of 110 BL Lac objects [Sca00]. Thus, according to [Aha06c, Sba05], a lower limit of $z > 0.25$ can be assumed, because $\approx 80\%$ of the probed objects have known redshifts, of which 39 with $z < 0.25$ and 28 with $0.25 < z < 0.6$ have their host galaxies resolved. A lower limit on the redshift of PG 1553+113 is given with $z > 0.09$ by Very Large Telescope optical spectroscopy [Sba06].

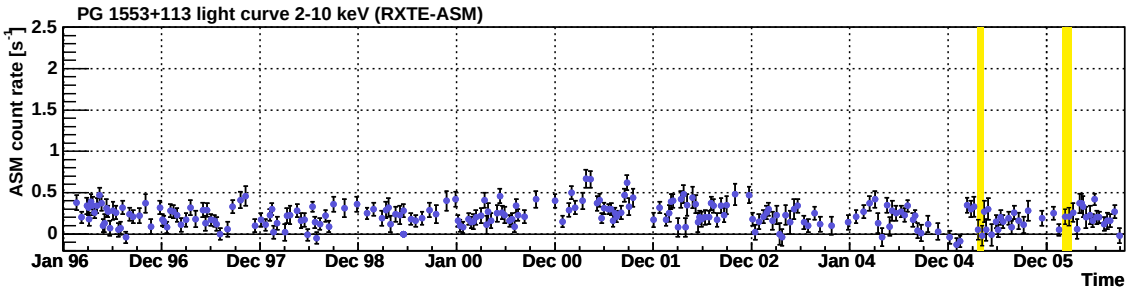

FIGURE 9.1: *Long–term RXTE ASM observation (1996-2006) of PG 1553+113 in the 2–10 keV energy band. MAGIC observations are marked in yellow. Data available at [XTE06].*

Multiwavelength properties. A dedicated multiwavelength study was carried out on PG 1553+113 during the three weeks from 2003 April 22 to 2003 May 12 [Ost06a], triggered by an optical flare ($13\overset{\text{m}}{.}4$ in the *R* band). Observations included radio, optical, and X-ray measurements. While in $(0.1-10)$ keV X-rays a significant flare with a doubling time of 10 days was observed with RXTE's Proportional Counter Array [Jah96], no significant changes in the optical brightness of the object were found ($13\overset{\text{m}}{.}55-13\overset{\text{m}}{.}66$ in the *R* band). The X-ray flux level was found to increase from 0.5×10^{-11} erg cm^{-2} s^{-1} to 1.2×10^{-11} erg cm^{-2} s^{-1} at the peak of the flare. The previously found unusually weak radio flux of PG 1553+113 [Fal90] was confirmed.

In [Ost06b] follow-up observations of PG 1553+113 in May 2003 are reported: Here, an optical flare of $\approx 0\overset{\text{m}}{.}15$ was observed succeeding a distinct X-ray flare. Both flares took about 10 days to reach maximum brightness, which hints at a possible common origin.

Generally in SSC models optical variability is expected to lead X-ray variability in case the X-rays stem from IC processes; possible delayed radio or optical flares are conceivable if the X-rays are due to synchrotron emission. Such delayed emission, however, was observed shortly after the end of the multiwavelength campaign, as well as during the May 2003 observations. Therefore, these observations are interpreted as supportive of a SSC model at work and a synchrotron origin of the X-ray emission. The corresponding SED analysis puts PG 1553+113 in the group of extreme HBLs.

VHE observational status. Tab. 9.1 summarizes the observations of PG 1553+113 in VHE γ-rays. Until recently, only upper limits were reported by the Whipple and Milagro collaborations [Cal03, Wil05]. In 2006, H.E.S.S. [Aha06c] and MAGIC [Alb06a] detected the object with significances of $> 4.0\sigma$ and 8.8σ, respectively. The MAGIC analysis of this source is presented in this chapter. H.E.S.S. could determine the differential energy spectrum to be very soft with a photon index of $\alpha = 4.0\pm0.6$ and reported an observed integral flux above 200 GeV of $(4.8\pm1.3\pm1.0)\cdot10^{-12}$ cm^{-2} s^{-1}.

Source selection. In spite of an unknown but possibly large redshift, PG 1553+113 is among the prime candidates for VHE γ-ray emitting BL Lacs due to its flux in the radio and X-ray domains, cf. sect. 2.4. Therefore, observations with the MAGIC telescope

Date	Group	Exposure [h]	Sign.	Integral Flux [10^{-12} cm^{-2} s^{-1}]	E_{thresh} GeV	Reference
2002	Whipple	2.82	0.8σ	< 16.2 (97% U.L.)	390	[Cal03]
2000–2003	Milagro	906	n/a	< 583 (95% U.L.)	100	[Wil05]
2005	H.E.S.S.	7.6	4.0σ	$4.8 \pm 1.3 \pm 1.0$	200	[Aha06c]
2005 & 2006	MAGIC	22.3	8.8σ	10 ± 4.0	85	[Alb06a], this analysis

TABLE 9.1: *Summary of VHE γ-ray measurements of PG 1553+113. While the upper limit given in [Cal03] was determined from Whipple IACT observations, the limit given by [Wil05] was posed using date from the Milagro water Cherenkov detector.*

were approved for April and May 2005. A detected marginal signal led to follow–up observations in 2006. The MAGIC measurements were accompanied by dedicated optical observations using the collaborating 35cm KVA optical telescope.

9.2 Observations

PG 1553+113 was observed with the MAGIC telescope for 11.1 hours in April and May 2005 and for 19 hours from January to April 2006.[1] Simultaneous observations were performed in the optical by the KVA 35 cm monitoring telescope (cf. sect. 4.8). X-ray data by RXTE–ASM [Lev96] were also available for the entire observation time.

The 2005 data have been divided into two samples due to the poorer PSF during the April 2005 observations. Therefore, the April 2005 data have been analyzed using MC simulations with an increased PSF (20 mm) as compared to the May 2005 data and the 2006 data (14 mm). Tab. 9.2 shows the ON data sample used for this analysis. In addition, OFF data were taken on sky positions with similar (extragalactic) background light conditions and following the same zenith angle distribution as the ON data (tab. 9.3). These data were used to determine the background content in the ON region.

9.3 Run selection

Data checks. To exploit the low energy threshold at low zenith angles, the measurements above $\theta = 30^\circ$ were removed from the analysis. Additionally, data taken during non–optimal weather or telescope conditions and those affected by hardware problems were rejected. The mean zenith angle for the analysis is 22° and the threshold energy 120 GeV.

Signal extraction, calibration and image reconstruction. The data set was calibrated employing the standard MARS calibration, using a spline extractor for the 2005 data set

[1] The analysis discussed here has also been submitted to the Astrophysical Journal Letters [Alb06a].

Observation start (UTC)	Zenith angle[a] $\theta_{min} - \theta_{max}$ (deg)	Avg. ZA $\langle\theta\rangle$ (deg)	Event[b] rate (Hz)	Events (10^6)	Nominal time[c] (h)	Eff. time[d] (h)
17.04.2005 03:03:56	17.6 – 22.3	18.8	194	0.52	1.38	0.75
18.04.2005 03:35:50	17.9 – 22.0	19.7	191	0.36	0.74	0.52
03.05.2005 01:31:47	17.6 – 22.9	19.4	248	1.52	1.92	1.71
09.05.2005 00:47:42	12.6 – 30.0	20.5	258	0.91	1.02	0.98
10.05.2005 00:36:08	17.6 – 25.6	20.1	213	1.71	2.38	2.22
13.05.2005 00:08:56	17.6 – 28.3	20.9	223	1.87	2.52	2.33
2005				**6.89**	**9.96**	**8.51**
02.02.2006 06:07:49	28.3 – 30.0	29.1	167	0.35	0.55	0.15
03.02.2006 06:06:01	28.7 – 30.0	29.3	183	0.33	0.48	0.12
04.02.2006 04:33:58	26.8 – 30.0	28.4	177	1.22	2.19	0.28
06.02.2006 05:42:38	25.7 – 30.0	27.8	187	0.65	0.97	0.39
27.02.2006 03:49:40	18.3 – 30.0	23.2	178	1.35	2.47	1.37
03.03.2006 04:43:04	17.7 – 29.5	21.9	189	0.89	1.58	1.31
04.03.2006 05:09:08	23.4 – 24.2	23.8	183	0.45	0.07	0.07
05.03.2006 04:34:25	17.6 – 29.6	22.1	188	1.00	1.65	1.49
08.03.2006 03:44:10	17.6 – 30.0	21.9	189	1.60	2.45	1.80
09.03.2006 04:24:28	21.2 – 28.5	24.6	187	0.50	0.82	0.75
24.03.2006 03:25:00	25.6 – 28.6	27.1	165	0.17	0.35	0.29
25.03.2006 03:20:15	19.0 – 28.8	23.3	177	0.69	1.18	1.08
28.03.2006 03:09:57	17.6 – 28.5	21.5	181	1.02	1.60	1.57
30.03.2006 03:05:09	17.6 – 27.9	21.0	165	0.89	1.61	1.50
02.04.2006 02:53:58	17.6 – 27.8	20.6	125	0.65	1.90	1.45
03.04.2006 02:51:51	17.6 – 27.5	21.0	123	0.69	1.60	1.56
2006				**12.45**	**21.47**	**15.18**

TABLE 9.2: *Summary of observations of PG 1553+113. [a]The maximum zenith angle for these observations has been set to $\theta_{max} = 30^\circ$. [b]Raw event rate before cuts. [c]The nominal observation time is the time before any cuts (including zenith angle cuts). [d]The effective observation time is determined after the zenith angle cut and is dead–time corrected.*

Observation start (UTC)	Zenith angle[a] $\theta_{min} - \theta_{max}$ (deg)	Avg. ZA $\langle\theta\rangle$ (deg)	Event[b] rate (Hz)	Events (10^6)	Nominal time[c] (h)	Eff. time[d] (h)
03.05.2005 23:18:25	13.9 – 20.9	15.9	178	0.78	1.90	1.23
05.05.2005 21:24:28	17.0 – 27.5	21.6	217	0.98	1.31	1.26
07.05.2005 00:50:35	17.6 – 23.2	19.5	189	1.46	2.18	2.14
13.05.2005 23:07:11	13.9 – 17.1	15.0	206	0.49	1.02	0.66
2005				**3.71**	**6.41**	**5.29**
05.02.2006 04:42:22	24.4 – 30.0	27.1	217	1.46	1.94	0.52
04.03.2006 04:38:25	17.6 – 27.4	20.3	235	0.98	1.69	1.15
07.03.2006 04:18:58	17.6 – 28.8	21.1	220	1.41	1.84	1.78
26.03.2006 03:18:09	17.5 – 26.3	20.1	182	1.26	1.96	1.92
29.03.2006 03:06:48	17.6 – 26.2	20.7	213	1.99	2.68	2.59
01.04.2006 02:54:34	17.6 – 26.2	21.0	109	0.45	1.29	1.14
2006				**7.55**	**11.40**	**9.10**

TABLE 9.3: *Summary of* OFF *observations for PG 1553+113. [a]The maximum zenith angle for these observations has been set to $\theta_{max} = 30^\circ$. [b]Raw event rate before cuts. [c]The nominal observation time is the time before any cuts (including zenith angle cuts). [d]The effective observation time is determined after the zenith angle cut and is dead–time corrected.*

and the default digital filter extractor for the 2006 data set. This choice was motivated by the fact that the FADC pulses arrived very early in the readout window in 2005. Under such conditions the spline extractor is more efficient than the digital filter. The images were cleaned using an absolute image cleaning, with levels of 7 and 5 photoelectrons for core and boundary pixels, respectively.

Analysis. The analysis was performed as outlined in sect. 5. Two training samples, for γs and hadrons respectively, are needed for training random forests. The γ training sample was created using MC simulations with a PSF of 14 mm added at the camera simulation level. For the April 2005 data 20 mm were used. The zenith angle range used was the same as used later on in the analysis, i.e. $18^\circ \leq \theta \leq 30^\circ$. The upper ZA cut $\theta \leq 30^\circ$ was applied in order to profit from the low energy threshold only given for low ZA.

The hadron training sample was created by using a total number of $5 \cdot 10^4$ events randomly chosen from the OFF data included in the analysis. The small contamination of γ events in the hadron sample is too small to pose a problem during the training; even in hadronic OFF data, small contributions of lepton-initiated showers are expected. The use of real hadronic OFF data has the advantage that this sample has the same conditions (weather conditions, telescope performance) as the hadronic background to be suppressed.

During training, so-called "spark" cuts,[2] a cut in SIZE > 100 ph.el., a core pixel cut of 4 pixels and a LEAKAGE < 0.1 cut have been applied. These cuts are required to ensure that only genuine air shower events are included in the training.

The parameters included in the training were: log SIZE, LENGTH, WIDTH, DIST, CONC2, and ASYM. For producing sky maps, alternative RFs were trained omitting the DIST parameter and using the DISP parameter instead.

9.4 Excess determination and position reconstruction

For both of the observational periods, a very clear gamma signal is seen in the image parameter ALPHA. When defining the signal region as $|\,\text{ALPHA}| < 12^\circ$, an excess of 1032 events over 8730 background events yields a total significance of 8.8σ for the combined data sample (fig. 9.2). The background was estimated by fitting a second order polynomial (without linear term) to the ALPHA distribution of the normalized OFF data. The individual results for 2005 and 2006 are given in tab. 9.4. Employing the DISP analysis, a sky map was produced. Fig. 9.3 shows the position of the found γ-ray excess, which is centered at $(\text{RA, dec}) = (15^\text{h}55^\text{m}.8 \pm 0.04, 11^\circ 12^\text{m}.6 \pm 0.78)$. The uncertainties do not include the inaccuracy of the drive system (1.5 arcmin). Within errors, the excess matches well the position of PG 1553+113 (given in [Bea02]).

[2] Rare discharges in the PMT that triggered the readout and look like small, very roundish events

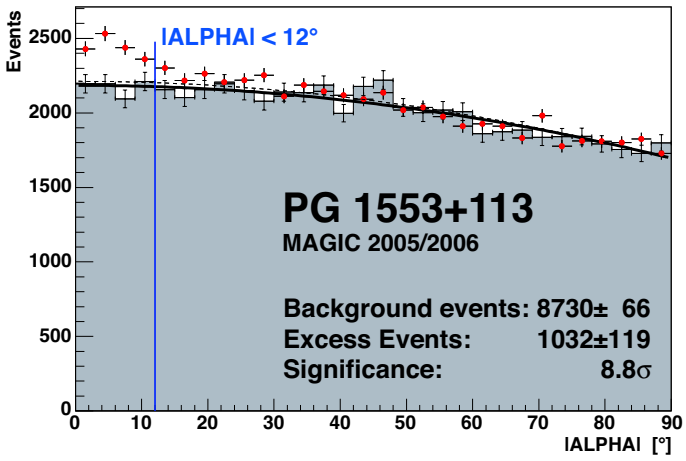

FIGURE 9.2: ALPHA *plot for PG 1553+113. For* $|\,\text{ALPHA}| < 12^\circ$ *an excess at the* 8.8σ *level is obtained.*

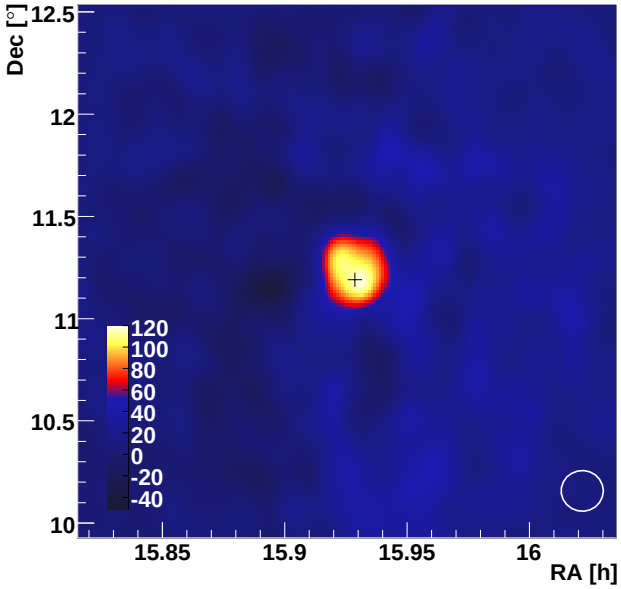

FIGURE 9.3: *Smoothed sky map for the expected position of PG 1553+113 obtained applying a* DISP *analysis to the data. The sky map was created using events between* $300-800$ GeV *with a hadronness cut of* $h < 0.15$*. The comparatively high energy range was chosen as the directional image parameter* DISP *is usually not well defined for very low energies. The units represented by the color–code are* 10^{-5} *events* sr^{-1}*, i.e. events within a circular area with* $r = 0.1^\circ$*. The white circle indicates the* γ*-ray PSF (angular resolution) of MAGIC of* $\sigma = 0.1^\circ$*.*

Year	N_{on}	N_{OFF}	N_{Excess}	Significance	$F_{E>200\,\text{GeV}}$	Spectral index α
2005	3944	3501 ± 26.3	443 ± 68	6.7σ	2.0 ± 0.6	4.31 ± 0.45
2006	5815	5227 ± 39.2	588 ± 86	7.0σ	0.6 ± 0.2	3.95 ± 0.23
2005+2006	9761	8730 ± 66	1032 ± 119	8.8σ	1.0 ± 0.4	4.21 ± 0.25

TABLE 9.4: *MAGIC observation results for PG 1553. Fluxes are given in units of* 10^{-11} $\text{cm}^{-2}\,\text{sec}^{-1}$*. As the* OFF *samples for the 2005 and 2006 analysis are not independent, the significances for the two analyses cannot be added (quadratically).*

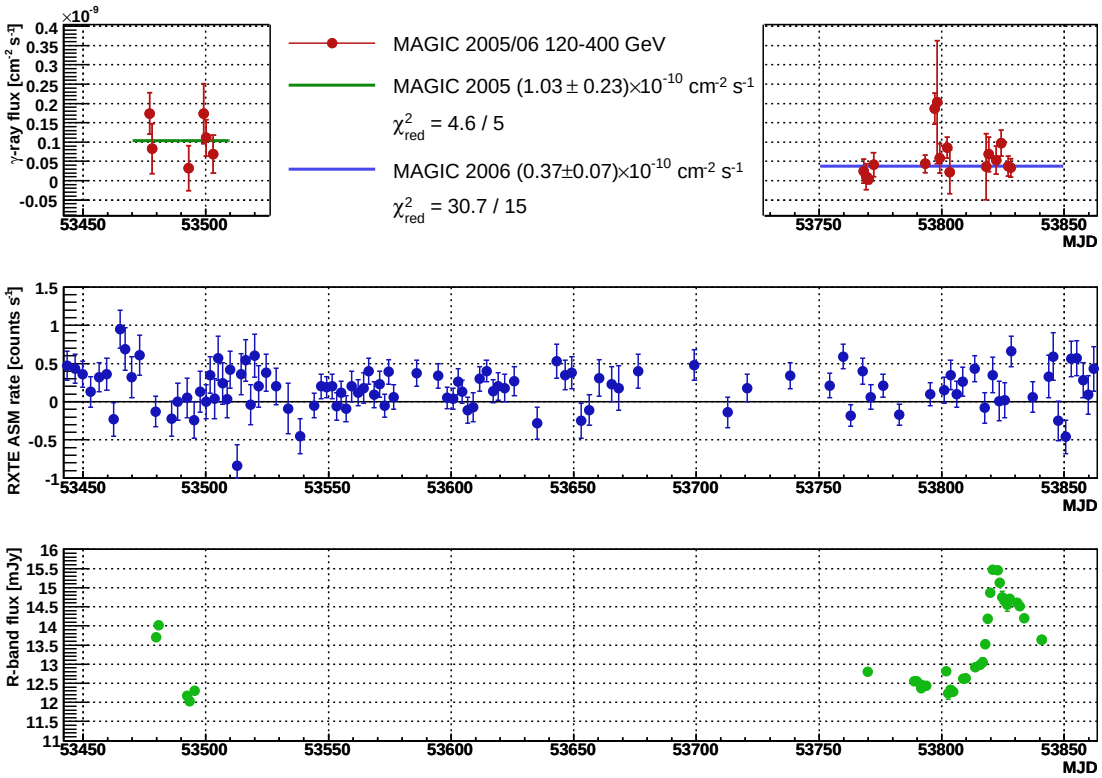

FIGURE 9.4: *Light curve for the PG 1553 observations. The upper panel shows integral gamma ray flux data points obtained in the (120−400) GeV energy range with MAGIC. The upper energy limit was not set to infinity so as not to contaminate the data points due to the extremely steeply falling energy spectrum of the source. The data point at MJD 53798 has a very large error, as the effective observation time was very short. It was included for comparison with the MJD 53797 data point, as that observation shows a* 3.75σ *deviation from the average flux in 2006. The middle panel shows X-ray measurements [XTE06] obtained with the ASM instrument [Lev96] on board of the RXTE satellite [Bra93]. The lower panel presents optical measurements in the R-band performed with the optical 35cm KVA telescope [Nil06].*

9.5 Light curve

The VHE γ-ray light curve for PG 1553+113 together with the ASM X-ray light curve in the $(2-10)$ keV range and the optical R–band light curve is shown in fig. 9.4. The measurements in 2005 are compatible ($\chi^2_{\mathrm{red}} = 0.92$) with a constant integral flux of $(10.0 \pm 0.23) \cdot 10^{-11}\,\mathrm{cm}^{-2}\,\mathrm{s}^{-1}$ in the $120\,\mathrm{GeV} - 400\,\mathrm{GeV}$ range. The upper cut was chosen because of the steep spectrum, cf. sect. 9.6. For 2006, a flux level of $(3.7 \pm 0.8) \cdot 10^{-11}\,\mathrm{cm}^{-2}\,\mathrm{s}^{-1}$ is determined, with a χ^2_{red} of 2.04. Therefore a significant decrease of the flux by a factor of $\gtrapprox 3$ can be reported.

The X-ray data do not show significant variability and are consistent with a mean count–rate of (0.15 ± 0.03) counts s^{-1}.

The optical brightness, however, varies between $13\overset{\mathrm{m}}{.}2$ and $13\overset{\mathrm{m}}{.}5$ (typical errors are of the order of 5%). When comparing this brightness to the magnitude that triggered the

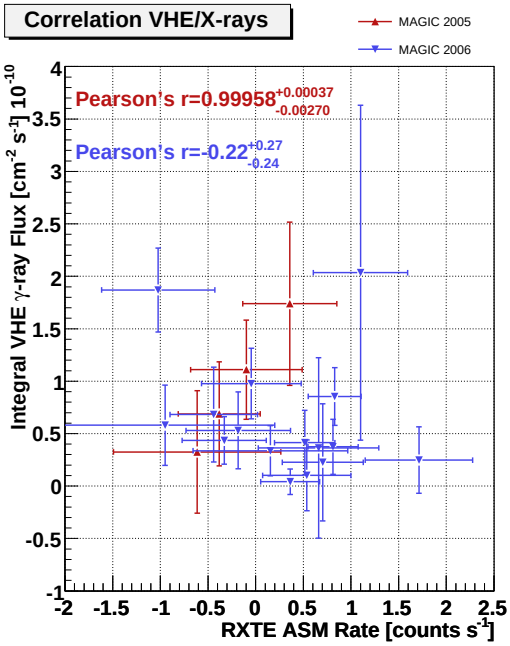

FIGURE 9.5: *Correlation of the MAGIC VHE γ-ray measurements and X-ray measurements in the 2–10 keV range as performed by ASM [Lev04]. Blue data points represent measurements in 2006, while red data points show measurements performed in 2005. The figure also shows the found correlation coefficients (cf. sect. 7.6).*

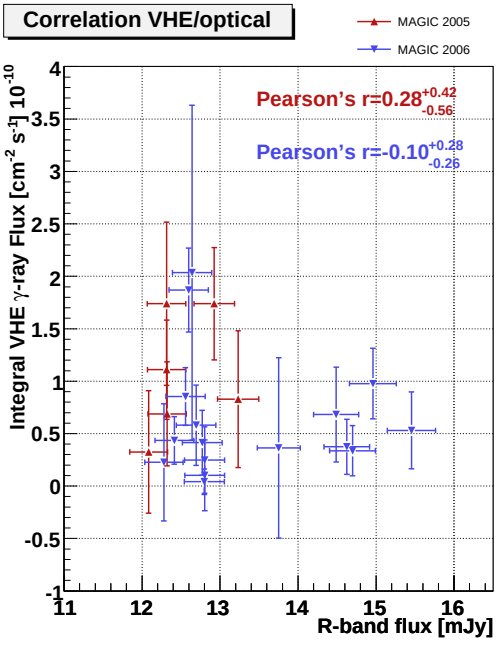

FIGURE 9.6: *Correlation of the VHE and contemporaneous optical measurements conducted with the 35cm KVA telescope in the R–band. Blue data points represent measurements in 2006, while red data points show measurements performed in 2005. The figure also shows the found correlation coefficients (cf. sect. 7.6).*

multiwavelength campaign in 2003, $13\overset{\text{m}}{.}4$, an high intensity level of PG 1553+113 in the optical can be assumed for the 2005 and 2006 data under study here. The *R*–band flux shows a strong, well–defined flare starting at MJD 53810, which reached its maximum brightness around MJD 53822 and leveled off with a less steep slope towards the end of the observations. As the host galaxy cannot be resolved in the optical, this variability ought to be attributed to the AGN itself.

When putting the observed optical flare in perspective with the multiwavelength observations back in 2003 [Ost06b] however, more complex scenarios that can explain isolated optical and X-ray flares might have to be conceived. Interestingly, the only significant (3.75σ) deviation of an individual VHE γ data point during our observations was recorded on MJD 53797 with $F = (1.86 \pm 0.40) \times 10^{-10}$ cm^{-2} s^{-1}, few days prior to the onset of the optical flare.

Correlations of VHE γ emission with X-ray data. In fig. 9.5 the VHE data points are correlated with $(2-10)$ keV X-ray data obtained from the ASM instrument (cf. sect. 7.6 for a short description). To obtain concurrent data points with the VHE light curve, individual ASM observations ("dwells") have been averaged for periods ± 0.3 days around the respective diurnal MAGIC observation window. For the 2006 data set, no correlation

is seen. The 2005 data, however, seem to show a linear correlation ($r = 0.99958^{+0.00037}_{-0.00270}$, small errors partially due to the large error bars), which has to be subjected to further study.

Correlations of VHE γ emission with optical data. The most striking feature of the multiwavelength light curves shown in fig. 9.4 is an increase in the R–band optical flux by 25% during the 2006 observations, interpreted as significant short–term variability. Before the optical flare (on MJD 53791), the KVA telescope measured a high linear polarization of $(8.3 \pm 0.2)\%$, suggesting that the observed optical flux indeed synchrotron radiation. No correlations to the VHE γ-ray flux were found (fig. 9.6), however. Still, a possible connection between the high optical emission level and the γ-ray detection cannot be excluded. The optical flare without X-ray or γ-ray counterpart may still be explained by external-inverse-Compton (EIC) models, which predict a time lag of the X-rays and γ-rays with respect to the optical emission. Since the MAGIC observations of PG 1553+113 had to be terminated at 2006 April 1 due to a scheduled shutdown of the telescope, it was not possible to pursue this presumption.

9.6 Spectrum determination

For determining the energy spectrum of PG 1553+113, the May 2005 and 2006 data sets were combined. The April 2005 data set had to be omitted as the PSF of the telescope optics in that period was inferior to the data taken later. Not only would data with different PSFs be difficult to combine on the level of the flux calculation, but a high PSF would also jeopardize the recognition of low energy events, which are to be expected to be dominant for very far away sources due to EBL absorption effects.

Distributions of excess events for 2005 and 2006 were determined individually and combined at the unfolding level. The resulting differential energy spectrum is shown in fig. 9.7. It can be described well with a pure power law of the form

$$\frac{\mathrm{d}F}{\mathrm{d}E} = (0.18 \pm 0.03) \cdot 10^{-9} \times \left(\frac{E}{200\,\mathrm{GeV}}\right)^{-4.21 \pm 0.25} \mathrm{TeV}^{-1}\,\mathrm{cm}^{-2}\,\mathrm{s}^{-1}$$

The spectrum is in agreement with the H.E.S.S. measurements [Aha06c] starting at $E \gtrapprox 200$ GeV and yields the softest photon index observed so far in the VHE γ-ray domain.

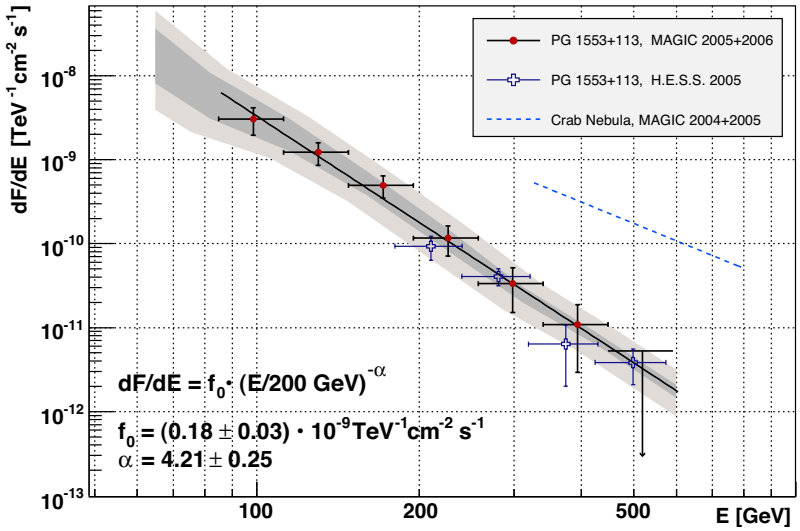

FIGURE 9.7: *Combined differential energy spectrum of PG 1553+113 for the 2005/6 observations. The figure contains statistical (vertical error bars) and systematic (shaded band) errors. The systematic errors have been inferred by varying certain analysis parameters such as the image cleaning levels (dark shaded band). The total 35% systematic uncertainty on the flux level is indicated by the light-brown shaded band. For comparison, the H.E.S.S. measurements [Aha06c, Ben06] and a fit to the MAGIC Crab nebula spectrum (cf. sect. 6 and [Wag05b]) are included.*

9.7 A determination of an upper redshift limit for PG 1553+113

Due to the absence of apparent spectral lines in the optical spectrum of PG 1553+113, no redshift has so far been determined for this object yet. By assuming a redshift and an EBL model, an intrinsic spectrum can be inferred using eq. (1.7). Here the "best–fit" model given in [Kne04] has been used. Fig. 9.8 shows the de-absorbed spectra for assumed redshifts $z = 0.4 - 0.8$. In the spectral energy density representation ($E^2 \times \mathrm{d}E/\mathrm{d}F$), the resulting intrinsic spectra show a turnover at ≈ 200 GeV with increasing slopes in the energy region of $200 - 600$ GeV. The spectra are fitted with simple power laws in this energy region. The corresponding spectral slopes are also listed in fig. 9.8.

When plotting the power law indices of these slopes versus the assumed redshift, one can obtain a lower limit on the redshift of PG 1553+113 by requiring $\Gamma > 1.5$ [Mal01] as done in fig. 9.9.

In one–zone SSC models harder spectra cannot easily be explained, as they would require extreme jet parameters like $\delta \approx 100$ and at the same time very small magnetic field strengths of $B \leq 0.01$ G [Aha01b]. For such environments, however, the radiation efficiency can be shown to be extremely small. Also shock–acceleration models yield slopes for the accelerated particles of $s = 1.5$, with a subsequent γ photon index of $\Gamma = 1.5$ or larger both for proton–γ and electron–γ (IC) interactions (see discussion in [Aha06b];

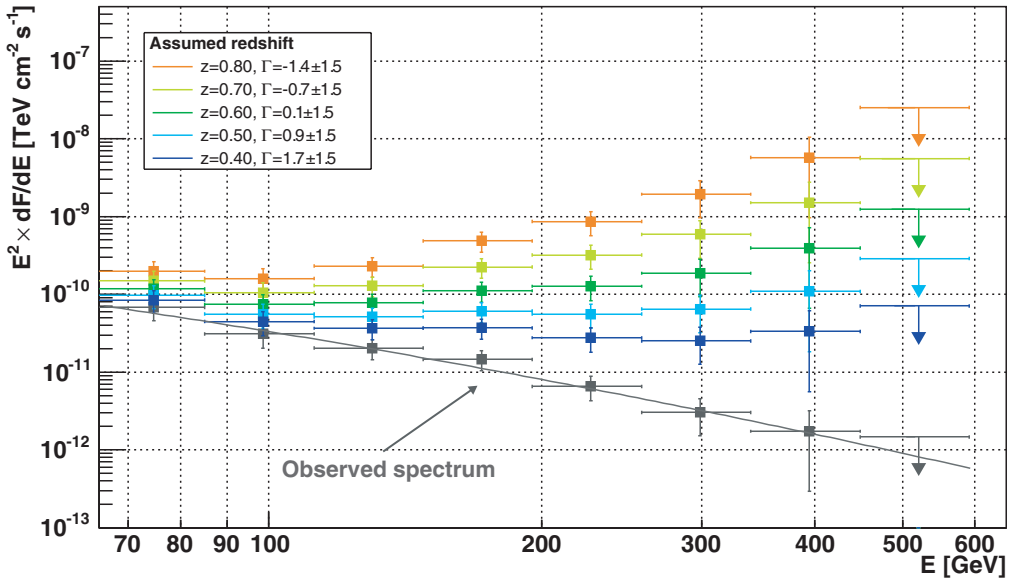

FIGURE 9.8: *EBL de-absorbed SEDs for assumed redshifts between $z = 0.4$ and $z = 0.8$. Power laws have been fit to the de-absorbed spectra in the range 200 GeV to 600 GeV, resulting in the indicated spectral slopes Γ. The gray data points represent the measured spectrum, the gray curve shows the $\alpha = 4.21$ power-law fit to it.*

but see [Kat06b, Kat06a] for models that would explain harder spectra). De-absorbing the close and well–studied objects Mkn 421 and Mkn 501 confirms this theoretical view with inferred photon indices of $\Gamma \approx 1.5 - 2.8$.

The 2σ limit derived here is $z < 0.78$, in accordance with the limit given in [Aha06c], $z < 0.74$. More elaborate methods [Maz06], making additional assumptions on the form of the intrinsic spectrum, yield $z \leq 0.42$ for a one–peak intrinsic spectrum and claim a multiple–peak structure of the intrinsic spectrum when $z > 0.42$. In sect. 11.3.3 an alternative redshift limit for PG 1553+113 is established by imposing a limit on the source-intrinsic VHE γ-ray luminosity.

9.8 Interpretation and conclusions

PG 1553+113 is among the most promising objects of the VHE γ emission candidate blazars presented in sect. 2.4.2. With no apparent emission lines in the spectrum of the host galaxy, only lower limits on its distance could by claimed up to now, the most recent one being $z > 0.09$.

The detection of PG 1553+113 as a VHE γ-ray emitter is claimed here on a significance level of 8.8σ. The flux level observed and the spectral form is well compatible with the

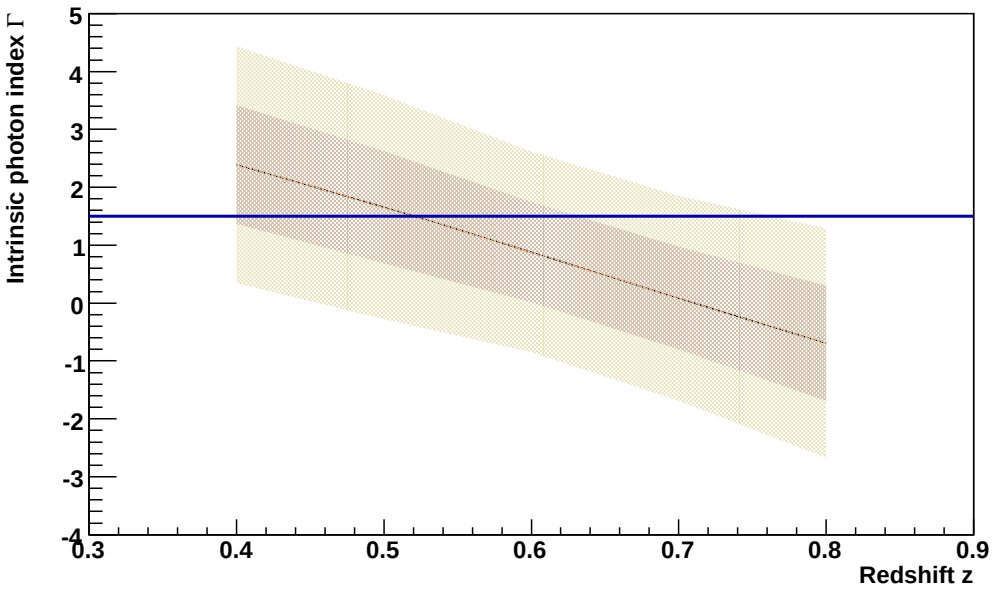

FIGURE 9.9: *Redshift limit determination: The putative spectral index* Γ *after EBL de-absorption for different redshifts (solid, black curve). The contours mark the* 1σ *(orange) and* 2σ *(yellow) errors on the determined spectral index. The assumption of a minimum slope of* $\Gamma = 1.5$ *(blue line) leads to an upper limit on the redshift of PG 1553+113.*

findings of the H.E.S.S. collaboration, which observed the object almost simultaneously with MAGIC. The spectrum obtained in this thesis extends to substantially lower energies than that reported by H.E.S.S. Modest changes in the flux level of about a factor of $2-3$ were found between the 2005 and 2006 observations.

No X-ray variability was found during the observations. A significant optical flare was recorded during the 2006 observations, but no correlation to the VHE or X-ray emission is apparent. A detection of a VHE baseline flux level cannot yet be claimed. Although there was no short–term flux variability observed in the presence of an optical outburst in 2006, more observations of PG 1553+113 would be necessary to check on this aspect.

A combination of the spectral data points obtained at VHE with non–contemporaneous data at other wavelengths is shown in fig. 9.10 along with the one-zone homogeneous SSC model provided by [Kra04]. For this purpose a redshift of $z = 0.3$ was assumed.

The inferred very soft spectrum of PG 1553+113 is the steepest observed so far in the VHE γ-ray regime. It is well compatible with H.E.S.S. measurements at $E \gtrapprox 200$ GeV, making PG 1553+113 a confirmed source.

Such a steep spectrum is a novel finding in VHE γ-ray astronomy and underlines the importance of low energy threshold instruments: At energies of 500 GeV a flux equivalent to only $\lessapprox 2\%$ of the Crab nebula was recorded, while the < 150 GeV flux is of the order

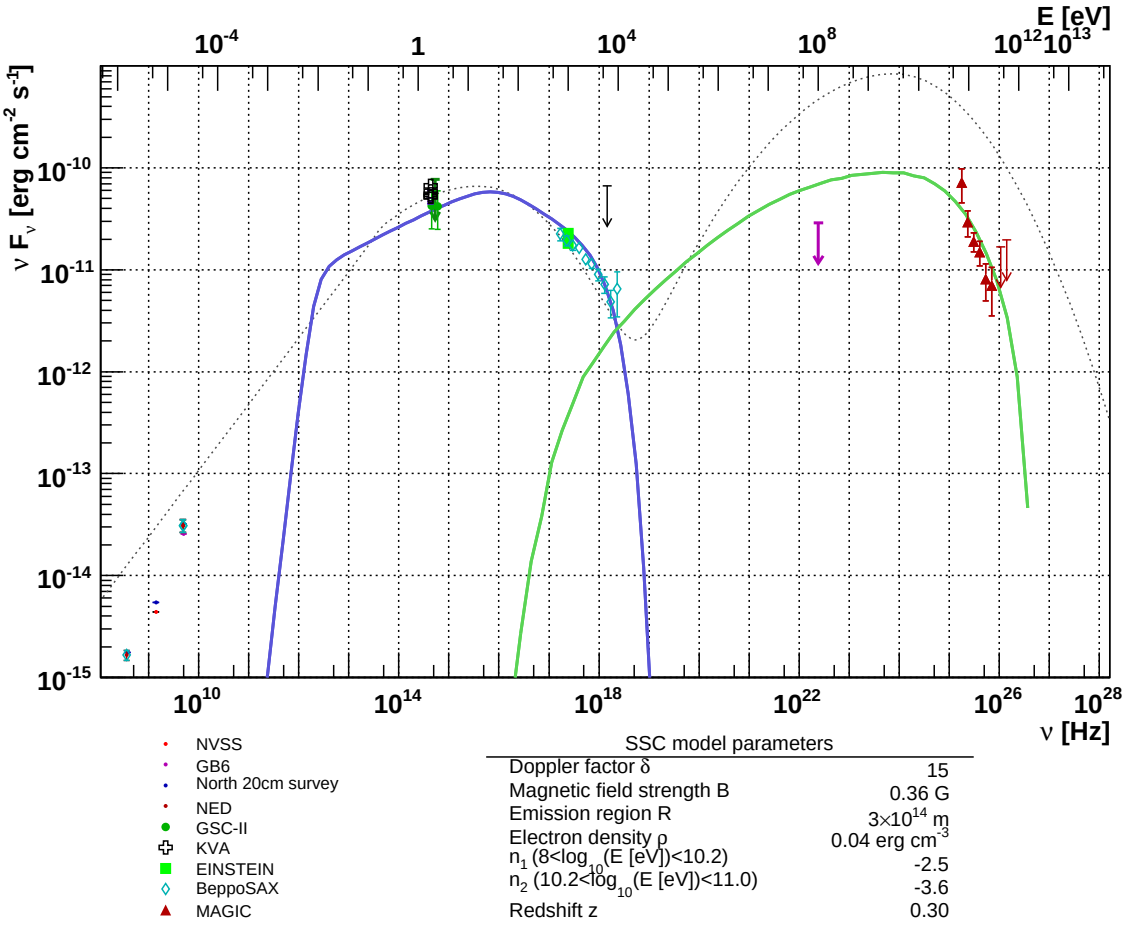

FIGURE 9.10: *Overall SED for PG 1553+113. Radio to sub-millimeter data: NRAO VLA sky survey [Con98], Green Bank 4.85 GHz northern sky survey [Gre96], North 20cm survey [Whi92], NED archival data [NED06]. Optical: Guide star catalog II [Rus90], KVA monitoring data [Nil06]. X-ray: EINSTEIN, BeppoSAX [Gio02]; RXTE–ASM upper limit (black arrow). γ-ray: EGRET upper limit (purple arrow) [Fic94], H.E.S.S. [Aha06c]. The gray dotted curve is the best–fit model available given by [Gio02], which, however, included only up to X-ray data points as input. The solid, colored curves were obtained using the homogeneous one–zone SSC model given in [Kra04]. The corresponding model parameters are given in the caption. Blue curve: Synchrotron emission. Green curve: Intrinsic SSC emission. The γ-ray data have been EBL de-absorbed using the model given in [Kne04] assuming a redshift of $z = 0.3$. Only the ASM and the KVA data are contemporaneous with the MAGIC data.*

of the Crab nebula flux in that energy range.

If the soft spectrum is due to EBL absorption effects, it makes PG 1553+113 a promising candidate for a very distant VHE γ-ray source. In this framework, an upper redshift limit can be derived from the measured spectral photon index. This is possible when assuming that γ-ray production models are at work, for which the intrinsic photon index cannot be smaller than $\Gamma < 1.5$ (SSC models and variants, but also hadronic models). By using a conservative EBL model [Kne04], an upper redshift limit of $z < 0.78$ was be inferred. Therefore, PG 1553+113 is an extreme object probably in either sense: in its large distance or in the softness of its spectrum.

The detection of a similar object in the allowed redshift range would very strongly constrain EBL models.

Note that it is well conceivable, too, that PG 1553+113 is located at relatively moderate redshifts of $z \approx 0.15$, although this might be at odds with the fact that no distance could be measured yet. Then the intrinsic spectrum would be comparatively soft with a photon index of $\Gamma \approx 3.2$, well in line with other recently detected objects with such soft spectra, like PKS 2005 and Mkn 180 (cf. sect. 11.3.2).

If PG 1553+113 is indeed is very far away ($z \gtrsim 0.2$), the resulting hard intrinsic spectrum is comparable to those of most of the previously observed blazars, but might have an unprecedentedly high luminosity at VHE γ-ray energies of $L_{500\,\mathrm{GeV}} \gtrsim 10^{44}$ erg sr^{-1} s^{-1}. For a discussion of the distance dependence of the intrinsic photon index of PG 1553+113, see sect. 11.3. The implications of the observations of PG 1553+113 stress the urge of a redshift determination for this BL Lac object.

Chapter 10

Detection of VHE γ-rays from BL Lacertae

BL Lacertae (1ES 2200+420), the prototype and eponym of the BL Lac objects, was observed in detail in the optical [Qia04], UV [Kaw91] and X-ray [Rav02] regimes. Compared to the already detected VHE γ-ray BL Lac objects (tab. 2.3), it exhibits a substantially lower synchrotron peak frequency ($\nu_{\text{peak}} = 1.9 \cdot 10^{14}$ Hz, equivalent to photon energies around 1 eV), which classifies it as an LBL object [Fos98, Nie06]. The object was first observed in the high energy γ-ray domain above 100 MeV by EGRET during two major outbursts: In 1995 it was detected on a 4.4σ significance level with a flux of $F_{E\geq 100\,\text{MeV}} = 4 \times 10^{-7}\,\text{cm}^{-2}\,\text{s}^{-1}$ [Cat97b] and subsequently in 1997 on a 10σ significance level with a flux of $F_{E\geq 100\,\text{MeV}} = 1.7 \times 10^{-6}\,\text{cm}^{-2}\,\text{s}^{-1}$, the latter well correlated with an optical flare [Blo97a]. Note that for LBLs the synchrotron bump peaks in the optical/UV region, therefore such optical flares could be the counterpart to X-ray flares observed from HBLs like e.g. Mkn 501. BL Lacertae was the target of an extensive multiwavelength campaign in the second half of 2000 [Boe03], encompassing radio, optical, X-ray and VHE γ-ray observations. It was found in two distinct emission states, one of which exhibited a synchrotron peak cutoff at $\gtrapprox 10$ keV. With these results, the SED could be modeled [Boe04] using both leptonic SSC and synchrotron proton blazar models and thus predictions for the VHE emission could be inferred.

In the VHE region accessible to Cherenkov telescopes, so far only upper limits are published, except for a yet unconfirmed detection [Nes01] on the 7.2σ level at energies of $E \geq 1$ TeV in 1998. An integral flux of $F_{E\geq 1\,\text{TeV}} = (2.1 \pm 0.4) \times 10^{-11}\,\text{cm}^{-2}\,\text{s}^{-1}$ was inferred from this observation. More extensive measurements carried out at the same time with the HEGRA CT1 telescope, however, led to an upper limit of $0.2 \times 10^{-11}\,\text{cm}^{-2}\,\text{s}^{-1}$ for an identical energy threshold [Tlu03]. Further upper limits in the VHE range are $F_{E\geq 1.1\,\text{TeV}} < 4.10 \times 10^{-12}\,\text{cm}^{-2}\,\text{s}^{-1}$ from a marginal signal on the 3σ level, [Aha04b]; $F_{E\geq 1\,\text{TeV}} < 3.0 \times 10^{-12}\,\text{cm}^{-2}\,\text{s}^{-1}$ [Kra03]; $F_{E\geq 350\,\text{GeV}} < 7.1 \times 10^{-12}\,\text{cm}^{-2}\,\text{s}^{-1}$ [Hor04a].

Observation start (UTC)	Zenith angle $\theta_{min} - \theta_{max}$ (deg)	Avg. ZA $\langle\theta\rangle$ (deg)	Event[b] rate (Hz)	Events (10^6)	Nominal time[c] (h)	Eff. time[d] (h)
02.08.2005 02:05:45	13.5 – 18.0	14.7	220	1.02	1.46	1.29
04.08.2005 01:47:10	13.5 – 18.4	14.9	224	1.28	1.70	1.59
08.08.2005 01:28:46	13.5 – 16.0	14.3	210	0.88	1.29	1.15
10.08.2005 01:15:01	13.5 – 16.3	14.4	221	1.02	1.45	1.28
03.09.2005 00:09:39	13.5 – 18.6	15.4	114	0.38	1.26	0.92
04.09.2005 23:46:18	13.5 – 18.5	15.3	165	0.55	1.58	0.93
10.09.2005 23:37:03	13.5 – 14.5	13.8	153	0.37	0.67	0.67
25.09.2005 23:36:45	16.0 – 17.1	16.5	153	0.09	0.21	0.16
28.09.2005 22:35:39	13.5 – 28.5	17.7	164	1.04	2.05	1.75
05.10.2005 23:07:03	17.1 – 25.0	20.8	155	0.49	0.92	0.88
25.10.2005 21:43:30	16.5 – 24.1	20.1	214	0.67	0.89	0.86
28.10.2005 19:49:11	16.1 – 24.8	20.8	213	0.53	2.62	0.69
29.10.2005 21:05:37	14.4 – 22.9	19.0	195	0.45	1.09	0.64
31.10.2005 20:48:34	13.9 – 24.6	18.3	216	1.09	1.45	1.40
19.11.2005 19:40:02	14.2 – 18.8	16.2	228	0.59	0.71	0.71
20.11.2005 20:36:11	21.3 – 28.9	25.0	220	0.57	0.80	0.72
24.11.2005 19:40:39	16.0 – 28.9	22.2	122	0.55	1.44	1.26
26.11.2005 19:43:24	17.2 – 28.4	22.7	164	0.65	1.18	1.10
02.12.2005 19:38:20	19.7 – 28.8	24.1	191	0.61	0.91	0.88
Total:				**12.83**	**23.46**	**18.88**

TABLE 10.1: *Summary of BL Lacertae observations used in this work. [b]Raw event rate before cuts. [c]The nominal observation time is the time before any cuts (including zenith angle cuts). [d]The effective observation time is determined after the zenith angle cut and is dead–time corrected.*

10.1 Observations

Based on SSC model predictions (cf. sect. 2.4.2) BL Lacertae was observed with the MAGIC telescope for over 20 hours. Tab. 10.1 summarizes the measurements. The effective observation time before quality cuts is 18.88 hours; after quality cuts (bad weather, unstable event rates) 16.94 hours were retained. As background control sample, the data given in tab. 10.2 were used. Note that of the 19.4 hours only 3.18 hours are dedicated BL Lacertae OFF data, i.e. were taken at a sky position close to the position of BL Lacertae and with identical declination. Therefore compatible OFF data with similar observation conditions, in particular similar night sky background conditions, were identified in the MAGIC data sample as to increase the volume of OFF events as compared to that of the ON events taken. This was done because a poor OFF/ON ratio would artificially deteriorate the significance of a weak signal (the OFF statistics enter the calculation of the significance, eq. (5.5)).

10.2 Event reconstruction and excess determination

The data analysis was performed as described in sect. 5: The FADC signal was extracted using the digital filter algorithm and then calibrated using the standard MARS calibration.

Observation start (UTC)	Zenith angle[a] $\theta_{min} - \theta_{max}$ (deg)	Avg. ZA $\langle\theta\rangle$ (deg)	Event[b] rate (Hz)	Events (10^6)	Nominal time[c] (h)	Eff. time[d] (h)
12.08.2005* 00:55:28	13.5 – 20.0	15.5	228	1.17	1.43	1.56
03.09.2005* 00:26:40	13.5 – 13.9	13.6	115	0.14	0.33	0.27
05.09.2005 00:20:39	13.5 – 13.8	13.6	160	0.20	0.35	0.30
11.09.2005* 00:22:09	13.7 – 14.6	14.1	150	0.13	0.24	0.20
01.10.2005* 23:41:53	17.5 – 22.4	19.9	180	0.37	0.57	0.62
29.10.2005 04:03:37	9.0 – 20.3	13.3	166	1.15	2.06	1.27
04.11.2005 02:39:08	10.4 – 21.5	15.7	146	0.56	1.26	0.91
07.11.2005 21:52:44	9.0 – 12.1	10.7	147	0.57	1.48	0.39
20.11.2005 22:17:00	9.6 – 21.4	15.4	207	0.66	0.97	0.89
26.11.2005 03:18:02	9.0 – 30.0	17.1	160	1.53	2.82	2.04
02.12.2005 03:44:06	27.1 – 30.0	28.0	141	1.01	1.88	1.06
04.12.2005 00:39:15	23.4 – 26.0	24.2	167	0.49	0.77	0.81
04.12.2005* 20:14:47	24.2 – 30.0	27.0	181	0.52	0.94	0.53
31.12.2005 01:10:59	27.1 – 29.6	27.8	181	0.85	1.34	1.30
01.01.2006 23:04:50	9.0 – 17.7	13.0	137	0.55	1.95	0.59
02.01.2006 22:07:39	23.4 – 24.8	23.9	184	0.37	0.52	0.56
03.01.2006 23:15:19	9.0 – 14.0	11.1	149	0.80	1.70	0.75
18.01.2006 21:30:22	17.4 – 23.6	20.5	120	0.21	0.43	0.48
22.01.2006 22:50:56	9.0 – 30.0	19.6	164	1.38	2.64	1.51
31.01.2006 21:22:18	9.0 – 14.6	11.7	129	0.35	0.74	0.51
05.02.2006 04:42:22	24.4 – 30.0	27.1	217	1.46	1.94	0.52
20.02.2006 22:08:55	9.0 – 18.8	13.6	198	1.08	1.53	0.89
21.02.2006 22:14:30	9.0 – 18.6	13.5	218	1.05	1.33	0.87
20.03.2006 20:49:03	23.2 – 30.0	26.5	175	0.54	0.87	0.52
Total:				**17.14**	**30.1**	**19.4**

TABLE 10.2: *Summary of* OFF *observations for BL Lacertae.* [a]*The zenith angle range for these observations has been set to* $13.5^\circ \leq \theta \leq 30^\circ$ *according to the zenith angle range of the* ON *data.* [b]*Raw event rate before cuts.* [c]*The nominal observation time is the time before any cuts (including zenith angle cuts).* [d]*The effective observation time is determined after the zenith angle cut and is dead–time corrected.* [*]*Dedicated BL Lacertae* OFF *observations.*

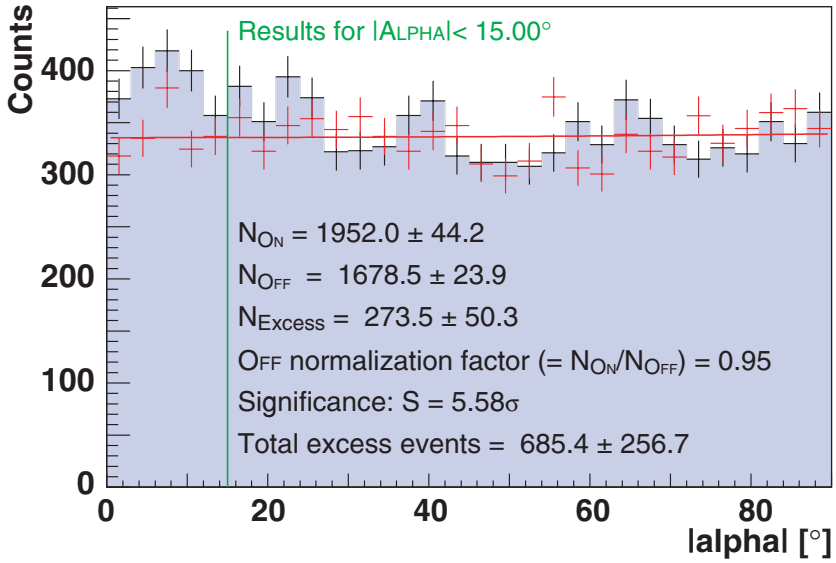

FIGURE 10.1: ALPHA *plot for BL Lacertae for* SIZE $>$ 400 ph.el. ($\gtrapprox$ 230 GeV) *and a hadronness cut of* $h < 0.15$. *The background has been estimated by a second order polynomial fit (without linear term) to the* OFF *data.*

The events were cleaned using an absolute image cleaning with thresholds of 7 ph.el. for core pixels and 5 ph.el. for boundary pixels, respectively. After the calculation of Hillas parameters, random forests using MC γs and hadrons taken from the OFF data sample were used to train the γ/hadron separation.

The resulting ALPHA plot for SIZE $>$ 400 ph.el. ($\gtrapprox$ 230 GeV) and a hadronness cut of $h < 0.15$ is shown in fig. 10.1. Since the excess for $|\,\text{ALPHA}| < 15°$ is exceeding 5σ, the form of the ALPHA peak has to be further studied. It should however be noted that the claimed signal is marginal. A sky map (fig. 10.2) also shows a marginal excess at the celestial position of BL Lacertae, but due to the low significance (large errors) of the detection, no conclusions are possible about any structure. MAGIC is going to take further data on this source in the 2006 observational season to confirm or reject the claim of VHE emission.

10.3 Light curve

A light curve was determined for energies of 400 GeV and above. Data points below a significance of 1.2σ were rejected and converted into upper limits using the method discussed in [Rol05]. The light curve is shown in fig. 10.3, the number of determined ON and background events as well as the corresponding significances are given in tab. 10.3. The flux levels found vary between 11% and 30% that of the Crab nebula in the corresponding energy region.

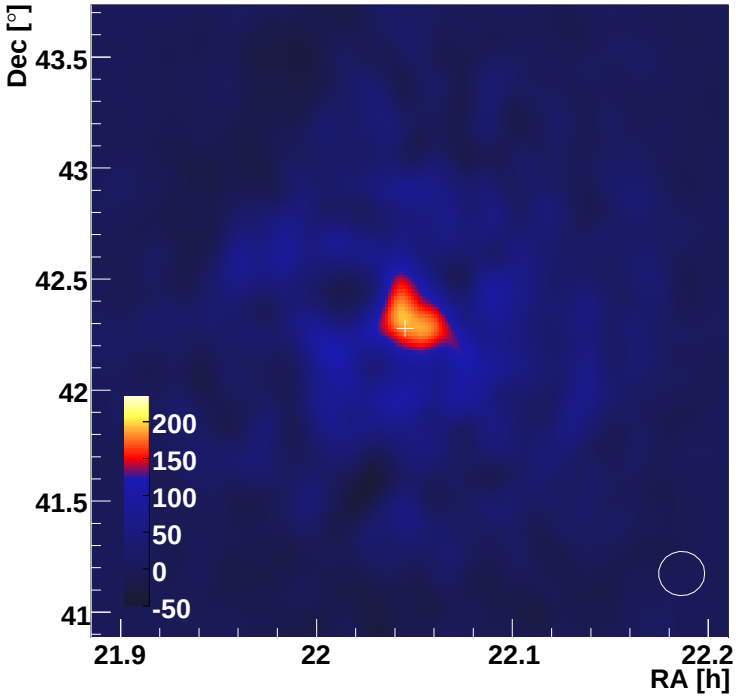

FIGURE 10.2: *Smoothed sky map of the BL Lacertae position for* 150 ph.el. $<$ SIZE $<$ 400 ph.el. *(*115 GeV $\lessapprox E \lessapprox$ 230 GeV*) and a hadronness cut of 0.2. This low energy range was chosen because of the steep energy spectrum, in spite of that fact that at low energies directional Hillas parameters are badly determined. The white cross indicates the nominal source position [Ma98]. The units represented by the color–code are* 10^{-5} *events* sr^{-1}*, i.e. events within a circular area with* $r = 0.1°$*. The white circle indicates the* γ*-ray PSF (angular resolution) of MAGIC of* $\sigma = 0.1°$*.*

MJD	ON events	OFF events	Excess events	Significance
53583 – 53594	192 ± 13.9	154.3 ± 9.9	37.3 ± 17.0	2.25σ
53600 – 53625	68 ± 8.2	54.3 ± 5.0	13.7 ± 9.7	1.46σ
53638 – 53643	90 ± 9.5	96.7 ± 7.2	UL: 21.66	n/a
53643 – 53669	107 ± 10.3	110 ± 7.9	UL: 28.26	n/a
53669 – 53676	94 ± 9.7	120 ± 8.4	UL: 12.58	n/a
53676 – 53696	100 ± 10.0	67.3 ± 5.7	32.7 ± 11.5	2.97σ

TABLE 10.3: *Light curve data for BL Lacertae (400 GeV and above,* $|$ ALPHA$| < 10°$*). "UL" denotes an upper limit.*

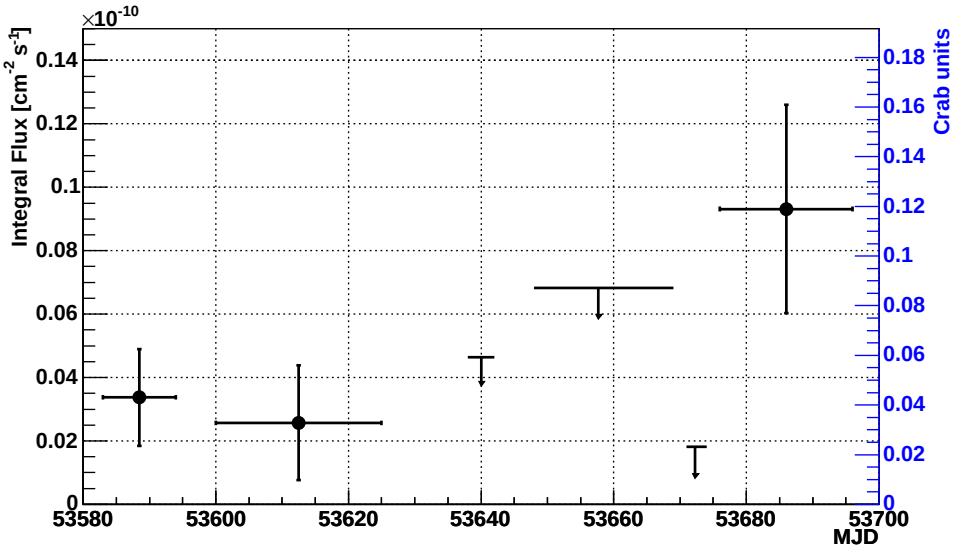

FIGURE 10.3: *Light curve for BL Lacertae above 400 GeV, upper limits calculated using [Rol05]*

10.4 Differential energy spectrum

For a 5σ excess signal it is impossible to determine a spectrum with high precision. Only a coarse estimate over typically one decade in energy is possible.

A tentative differential energy spectrum determined for BL Lacertae is shown in fig. 10.4. A fit with a pure power law yields a soft spectral index of $\alpha = 3.7 \pm 0.5$. This finding is compatible with the light curve, as the integrated flux for energies of 400 GeV and above as inferred from the spectrum is given as $F = (0.18 \pm 0.10) \times 10^{-11}$ cm^{-2} s^{-1}. For energies of 1 TeV and above, one obtains a flux of $F = (0.015 \pm 0.0085) \times 10^{-11}$ cm^{-2} s^{-1}, which agrees well with the previous upper limits in this energy range and is equal to 2.1% of the Crab nebula flux.

10.5 Conclusions

A first analysis of the BL Lacertae data taken with the MAGIC telescope in 2005 yielded a γ signal on the 5.6σ significance level. Establishing BL Lacertae as a VHE source is desirable as it belongs to the class of LBLs, i.e. its synchrotron peak is located at much lower energies than those of the established BL Lac objects, all of which are HBLs. According to SSC models (cf. sect. 2.1.1) LBLs exhibit a higher luminosity in the energy range of their synchrotron emission at the expense of the VHE γ-ray luminosity. Still, BL Lacertae is a promising candidate object due to the SSC predictions given in sect. 2.4.2.

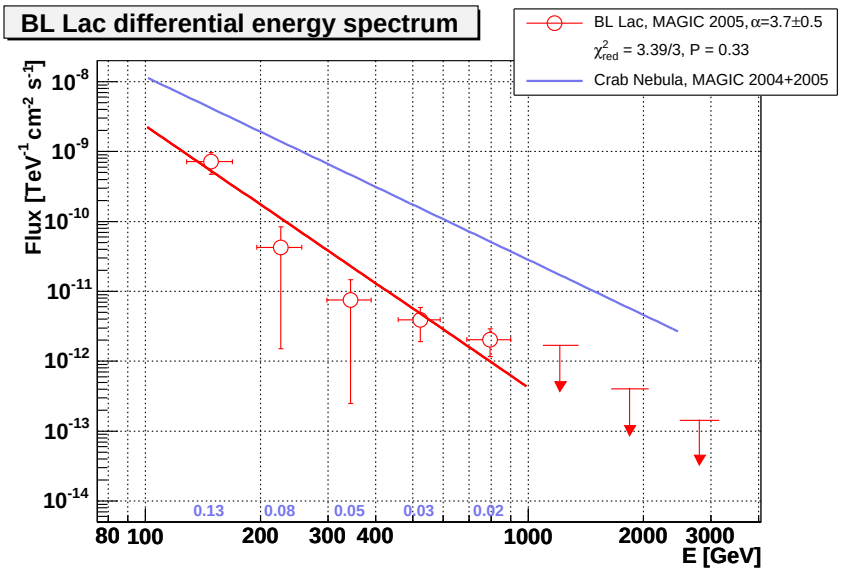

FIGURE 10.4: *Tentative differential energy spectrum for BL Lacertae. In addition, a power law fit to the Crab nebula spectrum is shown for comparison. The numbers below the BL Lacertae data points indicate the fraction of the Crab nebula flux observed.*

Model	Luminosity [erg s^{-1}]	Magn. field B[G]	Emission region R[cm]	Doppler factor δ	Flux prediction [cm^{-2} s^{-1}]
Leptonic, July 26–27	3×10^{40}	1.4	2.5×10^{15}	16	1.2×10^{-12}
Leptonic, November 1	4×10^{40}	1.4	2.5×10^{15}	18	8.6×10^{-12}
Hadronic, July 26–27	6×10^{44}	40	1.1×10^{15}	7	$(2.9-4.0)\times10^{-11}$
Hadronic, November 1	7×10^{44}	40	1.5×10^{15}	9	$(4.7-6.7)\times10^{-11}$

TABLE 10.4: *SED model fit parameters and VHE γ-ray flux predictions for BL Lacertae as given by [Boe04]. The VHE γ-ray predictions are given as integrated fluxes above 100* GeV.

Spectral energy distribution of BL Lacertae. The observational data of the multiwavelength campaign in 2000 [Boe03] have been used to model the SED of BL Lacertae in [Boe04]. The leptonic model used [Boe02] is a one-zone time-dependent relativistic jet model that includes SSC contributions, EIC contributions and contributions from reprocessed photons from the broad-line region. The hadronic model employed is described in [Mue03], with identical shapes of the electron and proton injection spectra. Measurements of the observed superluminal motion yielded $\Gamma \gtrsim 8$, which motivates the expectation of a Doppler boosting factor of the same order. A limit on the emission region is reported as $R \lesssim 1.6\times10^{14}\cdot\delta$ cm. The spectral fits for both models are shown in fig. 10.5 (SSC models) and fig. 10.6 (hadronic models). The corresponding fit parameters and model predictions are given in tab. 10.4. We added the power law fit to our tentative differential energy spectrum to the figures.

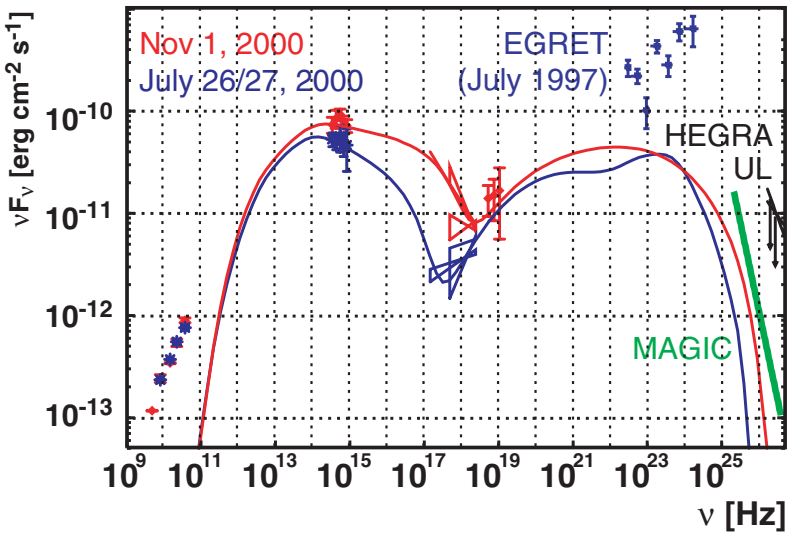

FIGURE 10.5: *Modeled spectral energy distribution for BL Lacertae. Measurements from 2001 November 1 and 200 July 26/27, along with SSC model predictions by [Boe04]. The MAGIC 2005 spectrum found here has been superimposed. HEGRA-UL denotes the HEGRA upper limit give in [Aha04b]. Note that the data are not contemporaneous with the MAGIC VHE γ-ray data.*

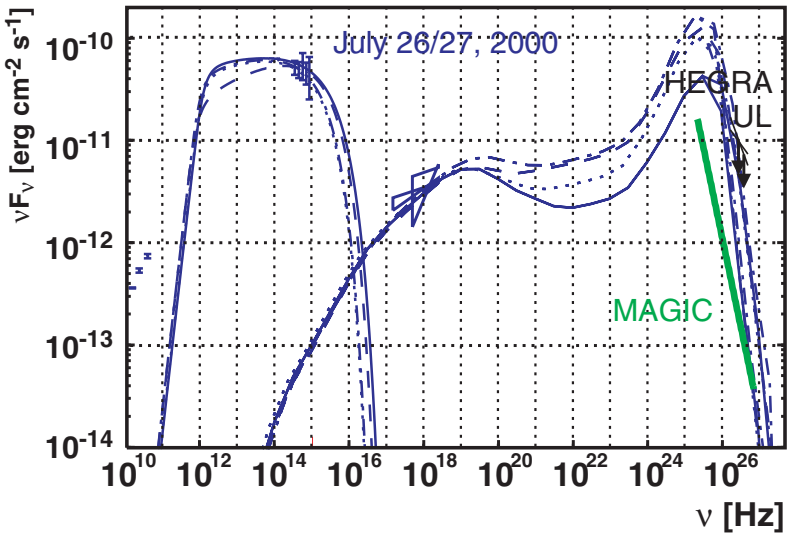

FIGURE 10.6: *Modeled spectral energy distribution for BL Lacertae. Hadronic synchrotron proton blazar model fits to 2000 July 26/27 data as calculated by [Boe04]. The MAGIC 2005 spectrum found here has been superimposed. HEGRA-UL denotes the HEGRA upper limit give in [Aha04b]. Note that the data are not contemporaneous with the MAGIC VHE γ-ray data.*

Chapter 11

A synoptic study of VHE γ-ray blazars detected to date

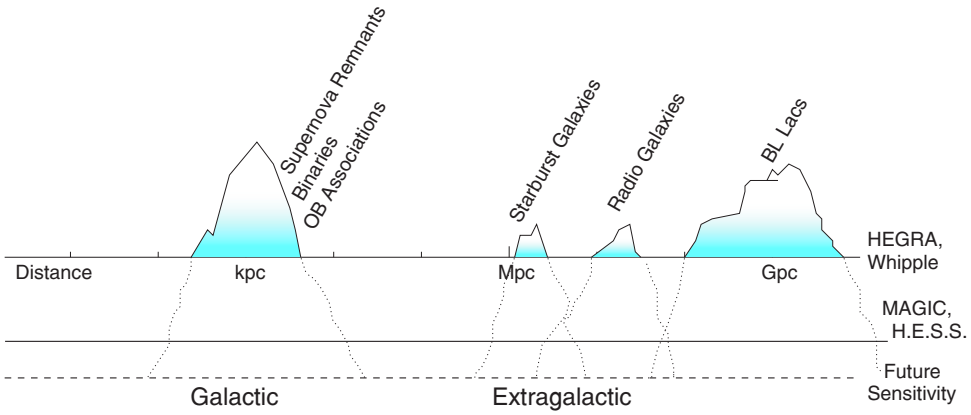

FIGURE 11.1: *A picture that is currently emerging: Previous instruments like Whipple and HEGRA barely saw the "tips of the icebergs" [Hor04b] of the VHE γ-ray universe. Increased sensitivity and lowered energy thresholds allow us to view deeper into the universe.*

In order to assess both the acceleration mechanisms in blazars and the EBL absorption effects, a large sample of VHE γ-ray emitting objects is desirable. Ideally it should encompass a wide range in redshift for EBL studies and at the same time comprise groups of sources at comparable distances in order to study intrinsic properties of the individual sources without possible systematic uncertainties caused by the EBL de-absorption.

The preconditions for such studies have recently improved since new instruments like H.E.S.S. and MAGIC became operational: In 2002, only a few nearby sources were regarded as established VHE γ-ray emitters and provided barely enough data to perform comparative studies. To date, the VHE γ-ray blazar sample comprises 13 HBL objects plus BL Lacertae, the latter not yet considered an established VHE γ-ray source. In addition, the redshift range of the known sources was enlarged; at the same time, objects at

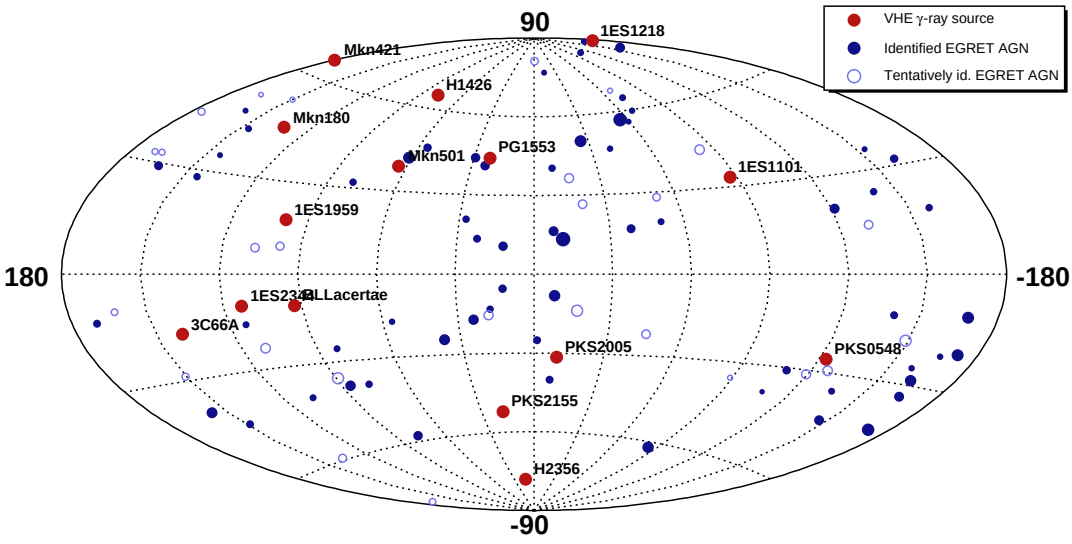

FIGURE 11.2: *Currently known VHE γ-ray blazars along with the identified and tentatively identified AGNs in the 3rd EGRET catalog of γ-ray sources [Har99]. The sources are shown in galactic coordinates. Note that only a few of the VHE γ-ray sources have been detected by EGRET.*

very similar distances have been found, for which possible systematic redshift–dependent effects due to the EBL absorption should be similar.

In this section, we want to assess common features of the currently known VHE γ-ray blazar sample (cf. tab. 2.3), which in fig. 11.2 is shown along with the AGNs identified in the 3rd EGRET catalog. First the detected objects are brought into context with the blazar searches conducted by IACT experiments and the expected EBL attenuation. We then will study the black hole mass distribution of these objects and infer the intrinsic emission properties of all objects for which VHE γ-ray spectra could be determined. Finally we will seek correlations of these observed VHE γ-ray and X-ray emission properties with the black hole mass estimations and correlations among them.

11.1 Population studies: The γ-ray horizon

Apart from the study of the intrinsic properties of BL Lac objects, a synoptic overview of the observed objects can be performed. In fig. 11.3 we plot the known VHE γ-ray emitters along with the energy thresholds of a collection of unobserved VHE γ-ray emission candidate sources. Mind that many of the non-observations can be assumed to be of instrumental origin; it further has to be noted that only for Mkn 501 and Mkn 421 indications of exponential high energy cutoffs have been observed thanks to high γ statistics. The figures also show the Fazio–Stecker–relation (FSR) for different EBL models as given by [Kne04]. The models differ in the IR density, dust properties and the star forma-

tion rate in the early universe. The FSR relation yields the viewing distance at which the optical depth for the process

$$\gamma_{\mathrm{VHE}} + \gamma_{\mathrm{EBL}} \longrightarrow \mathrm{e}^{+} + \mathrm{e}^{-} \tag{11.1}$$

(discussed in sect. 1.2.2) reaches unity, i.e. at which the universe becomes opaque to VHE γ-rays. Thus the FSR defines the *cosmological gamma–ray horizon*. The determination of the γ-ray horizon using BL Lacs is promising since they are the only extragalactic sources known to emit at GeV to TeV γ-ray energies at cosmological distances.

It is seen that with a decreasing instrumental energy threshold, the universe "opens up", providing access to a larger source population. Therefore, the threshold-energy vs. redshift planes in fig. 11.3 can be divided into a region in which VHE γ sources are likely to be detected and a region in which detections are not expected due to the EBL attenuation. While HEGRA observations were restricted by the FSR to a maximum redshift of $z \lesssim 0.1$, MAGIC has the potential to push this limit higher by a factor of 10 in redshift.

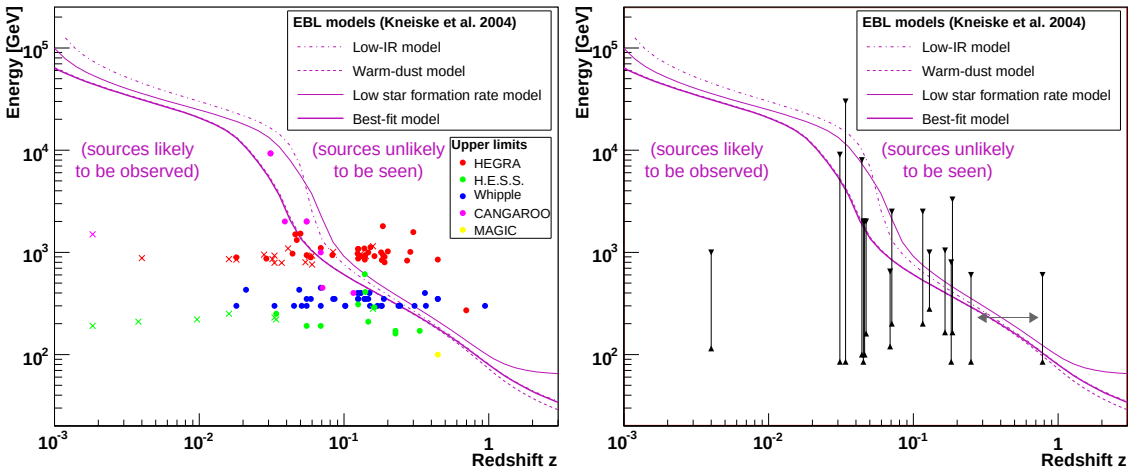

FIGURE 11.3: *Left figure: Upper limits on AGN VHE γ-ray emission searches. The colored markers represent the energy thresholds of the non-observations; Dots represent BL Lac type objects, crosses represent other AGN object types (starburst galaxies, radio galaxies, etc.). Right figure: Detected sources. The data points show the energy range of the measured γ-rays. The most distant ("double") data point is meant to represent PG 1553+113 due to its unknown redshift. Data from searches by Whipple [Ker95, Hor04a], HEGRA [Aha04b], H.E.S.S. [Aha05c], CANGAROO [Nis02] and MAGIC. The superimposed lines represent Fazio–Stecker relations (attenuation by a factor e^{-1}) for different EBL models discussed in [Kne04]. The thick solid line represents their "best fit" model and is used henceforth if not stated otherwise.*

11.2 Black hole masses in AGNs

It is well established that all galaxies with a massive bulge component host supermassive black holes (SMBH) in their centers [Beg03]. Recently, the existence of SMBH could be

proven for our own galaxy and our neighboring galaxy M31 [Sch02a, Ben05]. According to the AGN paradigm presented earlier, the central engines of AGNs are thought to be powered by SMBH [Lyn69]. While direct evidence for this concept is still elusive at present, there are a couple of indirect methods to infer the masses of the central black holes: $M_\bullet$ is determined using the $M_\bullet - \sigma$ relation found from stellar and gas kinematics and maser emission [Fer00, Geb00]. An alternative method determines $M_\bullet$ from the orbital radius and the Doppler velocity of the broad line region, which is thought to be bound to the gravitational potential of the black hole [Bla82]. Due to the lack of emission lines, however, this reverberation mapping technique cannot be applied to blazars. A more empirical relation of $M_\bullet$ and the galaxy bulge luminosity [McL02] can also be used to determine the black hole mass. Limits on the expected black hole masses can be derived from the Eddington luminosity limit

$$L \leq L_{\mathrm{Eddington}} = \frac{4\pi \mathrm{Gc\ m_p}}{\sigma_\mathrm{T}} \approx 1.3 \times 10^{38} \frac{M_\bullet}{M_\odot}\ \mathrm{erg\ s^{-1}} \tag{11.2}$$

with the proton mass $\mathrm{m_p}$ and the Thomson cross–section σ_T as $M_\bullet \geq 8 \times 10^5 (L/10^{44}\ \mathrm{erg\ s^{-1}}) M_\odot$ with the solar mass $M_\odot$.

Here we estimate the black hole masses of VHE γ-ray emitting BL Lacs employing the tight correlation of the black hole masses of nearby galaxies and the stellar velocity dispersion σ. The relation

$$M_\bullet = (1.34 \pm 0.20) \cdot 10^8 \times \left(\frac{\sigma}{200\ \mathrm{km\ s^{-1}}} \right)^{4.02 \pm 0.32} \tag{11.3}$$

was derived by [Tre02] using a high–quality sample of black hole mass measurements. This approach assumes that AGN host galaxies are similar to non–active galaxies as far as the $M_\bullet - \sigma$ relation is concerned. The velocity dispersions are collected from literature or are inferred from the fundamental plane [Djo87], a relation of the effective galaxy radius R_e, the velocity dispersion σ, and the average surface brightness in the R-band $\langle \mu_\mathrm{e} \rangle_R$ [Bet01], thought to be valid for elliptical galaxies, in particular AGNs and radio galaxies. The black hole masses for the VHE γ-ray BL Lac sample studied here are given in tab. 11.1. (For few of the BL Lac objects under study here, no central black hole mass estimations exist: PKS 2155, PG 1553, 1ES 1101). Note that the determination of $M_\bullet$ suffers from rather large systematic uncertainties due to the different methods used.[1]

Recent estimations of the black hole masses for 452 AGNs find them distributed over a large range of $(10^6 - 7 \cdot 10^9) M_\odot$ with no evidence for dependencies on the radio loudness of the objects [Woo02a, Woo02b]. As fig. 11.4 shows, the VHE γ-ray emitting BL Lacs detected up to now at different redshifts are in first order flatly distributed in their black

[1] Further note that bulge luminosity measurements, which are also available for some of the blazars discussed here [Fal02, Fal03], were not used due to their comparatively larger scatter. For a comparative study anyway using values inferred by different methods is not advisable due to possible different systematics.

Object	σ[km s^{-1}]	log($M_\bullet/M_\odot$) [Bar03]	σ[km s^{-1}]	log($M_\bullet/M_\odot$) [Fal02]	σ[km s^{-1}]	log($M_\bullet/M_\odot$) [Wu02]	log($M_\bullet/M_\odot$) (average)
BL Lac	—	—	—	—	245 ± 16	8.48 ± 0.15	8.48
Mkn 421	219 ± 11	8.29 ± 0.18	236 ± 10	8.42 ± 0.15	324 ± 18	8.97 ± 0.12	8.56
Mkn 501	372 ± 18	9.21 ± 0.11	291 ± 13	8.78 ± 0.11	—	—	9.00
1ES 2344	294 ± 24	8.80 ± 0.15	—	—	389 ± 20	9.29 ± 0.12	9.04
Mkn 180	209 ± 11	8.20 ± 0.19	244 ± 10	8.47 ± 0.14	251 ± 16	8.52 ± 0.15	8.40
1ES 1959	—	—	195 ± 15	8.08 ± 0.23	219 ± 15	8.28 ± 0.19	8.18
PKS 0548	202 ± 24	8.14 ± 0.24	—	—	—	—	8.14
PKS 2005	—	—	—	—	257 ± 16	8.57 ± 0.14	
1H 1426	—	—	—	—	269 ± 16	8.65 ± 0.13	
1H 2356	—	—	—	—	195 ± 14	8.08 ± 0.23	
1ES 1218	—	—	—	—	191 ± 14	8.04 ± 0.24	

TABLE 11.1: *Mass estimation (in units of the solar mass, $M_\odot$) for the central black holes of known VHE γ-ray emitting blazars employing the stellar velocity dispersion method and the $M_\bullet - \sigma$ relation given by [Tre02]. σ values taken from [Wu02] were indirectly inferred using the fundamental plane of radio galaxies [Bet01]. If more than one value is given in the literature, the average black hole mass is used. Due to the probably different systematic errors of the different data sets, the largest error was used henceforth as error for the average $M_\bullet$ value.*

hole masses between $10^8 - 10^{9.5} M_\odot$. Note that although AGNs harbor black holes with masses $M_\bullet > 10^6 M_\odot$, up to now only BL Lacs with heavy black holes, $M_\bullet \gtrapprox 10^8 M_\odot$, have been discovered in VHE γ-rays. This is in agreement with a recent study of the black hole mass distribution of 66 BL Lac objects [Woo05], which reports a $M_\bullet$ range of $(10^7 - 4 \cdot 10^9) M_\odot$ and could not find any correlation of $M_\bullet$ with radio or X-ray luminosity. We will later show the distribution of the VHE γ-ray emitting objects in luminosity and will see that there is no selection effect in luminosity at work. The black hole masses of VHE γ-ray emitting BL Lacs are compared to those of 375 AGNs collected from [Woo02a] in fig. 11.5. There are several selection effects seen in this figure: (1) Seyfert galaxies are spiral galaxies and therefore are expected to harbor comparatively light-weight black holes. (2) Distant Seyfert galaxies ($z \gtrapprox 1.0$) might just not be luminous enough to obtain black hole mass estimations.

11.3 Intrinsic VHE γ-ray emission parameters

Through VHE observations, we can determine observables that characterize the VHE jet emission and thus the jet properties. The differential energy spectra measured in the VHE energy range suffer EBL absorption as discussed in sect. 1.2.2. To recover the intrinsic spectra, they are reconstructed along eq. (1.7), employing the EBL "best fit" model given in [Kne04]. In fig. 11.6 measured spectra of all known VHE γ-ray emitting BL Lacs are presented together with their inferred intrinsic spectra, which for simplicity have been assumed to be pure power laws.

For the sources Mkn 421, Mkn 501, 1ES 2344, and 1ES 1959, clearly distinct flux states

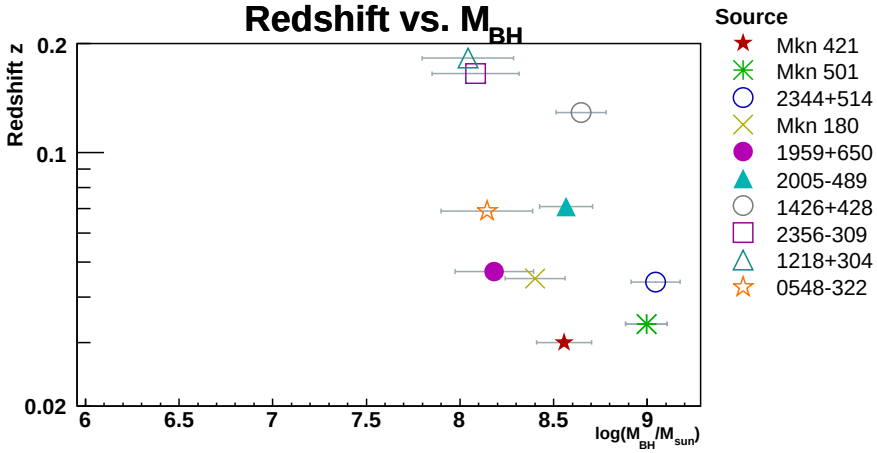

FIGURE 11.4: *Redshift vs. black hole mass distribution for the known VHE γ-ray emitting AGNs. As expected, there is no dependence on redshift.*

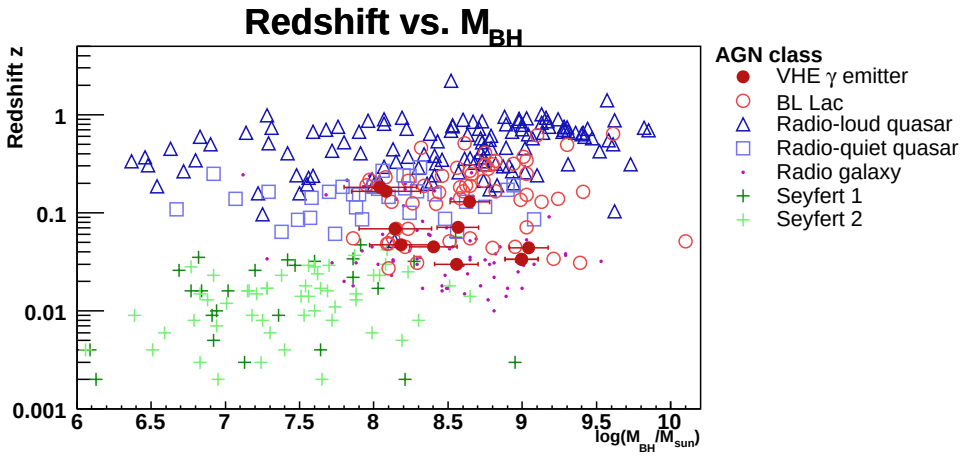

FIGURE 11.5: *The redshift vs. black hole mass distribution for 375 AGNs as collected by [Woo02a] and the known VHE γ-ray emitting AGNs. Note that Seyfert galaxies are spiral galaxies and thus have less massive central black holes than elliptical galaxies (such as radio galaxies and blazars).*

were found at different times. Accordingly, for each of those sources two spectra, one "low state" and one "flare" spectrum, are considered. Low–state spectra are characterized by the absence of intense ($\gtrapprox 0.2$ c.u.) flux levels and short–term variability, while flare spectra were obtained during outbursts of the respective sources (e.g. the 1995 flare of 1ES 2344, the 2002 flare of 1ES 1959 and the 1997 flare of Mkn 501). For Mkn 501, additionally the two extreme flux states found in this thesis are included. Note that for none of those sources, even for those with only one flux state, can a true "baseline" flux state be claimed yet. Note also that PG 1553+113, with its unknown redshift, is plotted for three different assumed redshifts just for illustration and its inferred "intrinsic spectrum" is not used in the following discussion.

Two observables are extracted: One of them is the luminosity at 500 GeV, $L_{500\,\mathrm{GeV}} = d_L^2 \cdot F(500\,\mathrm{GeV})$ with the luminosity distance d_L (cf. sect. 7.8.3). The luminosity characterizes the emitted energy per time and steradian and thus is independent of the observer's distance. The luminosity is extracted at 500 GeV, as this is an energy at which the γ-ray flux has been measured for all sources under study, so that no extrapolations are required. Additionally, the intrinsic photon index Γ in the region around 500 GeV is determined by fitting the intrinsic spectra with pure power laws over a restricted spectral range.

The photon indices of the reconstructed intrinsic spectra vary from $\Gamma = 1.0 - 3.3$. As discussed in sect. 9.7, spectra with $\Gamma < 1.5$ are difficult to explain in current acceleration models (only if the IC peak is close to 500 GeV, $\Gamma < 1.5$ is expected; such high IC peaks are, however, rather unlikely). This goes in line with indications that the EBL absorption effects are smaller than modeled [Aha06b]. For this study, the main emphasis is put on comparing the included objects, thus a common EBL model for all sources has been used; a lower EBL level would soften the intrinsic spectra, i.e. increase the value of Γ.

For PG 1553+113, intrinsic spectra for three different (exemplary) redshifts have been reconstructed, as the distance of this object has not yet been determined (cf. sect. 9.1 & 9.7). One clearly sees the effect of the EBL de-absorption for high redshifts. While for an assumed $z = 0.1$ and $z = 0.3$ the reconstructed spectrum hardens as compared to the measured spectrum, the reconstructed spectrum for $z = 0.7$ shows quite an unphysical spectral slope (and improbably high intrinsic fluxes at energies of some hundred GeV) which most probably points to a wrong EBL absorption model.

11.3.1 Correlation of X-ray and VHE γ-ray luminosity

In SSC models, the X-ray and the VHE emissions are closely connected owing to their common origin. Therefore, in fig. 11.7, we plot the VHE γ-ray luminosity at 500 GeV versus the X-ray luminosity at 1 keV as given in [Cos02] for non–flare states. According to expectations, a trend towards a correlation is visible. A clear, strong correlation is not expected because of different magnetic fields in the individual objects. Note that, while

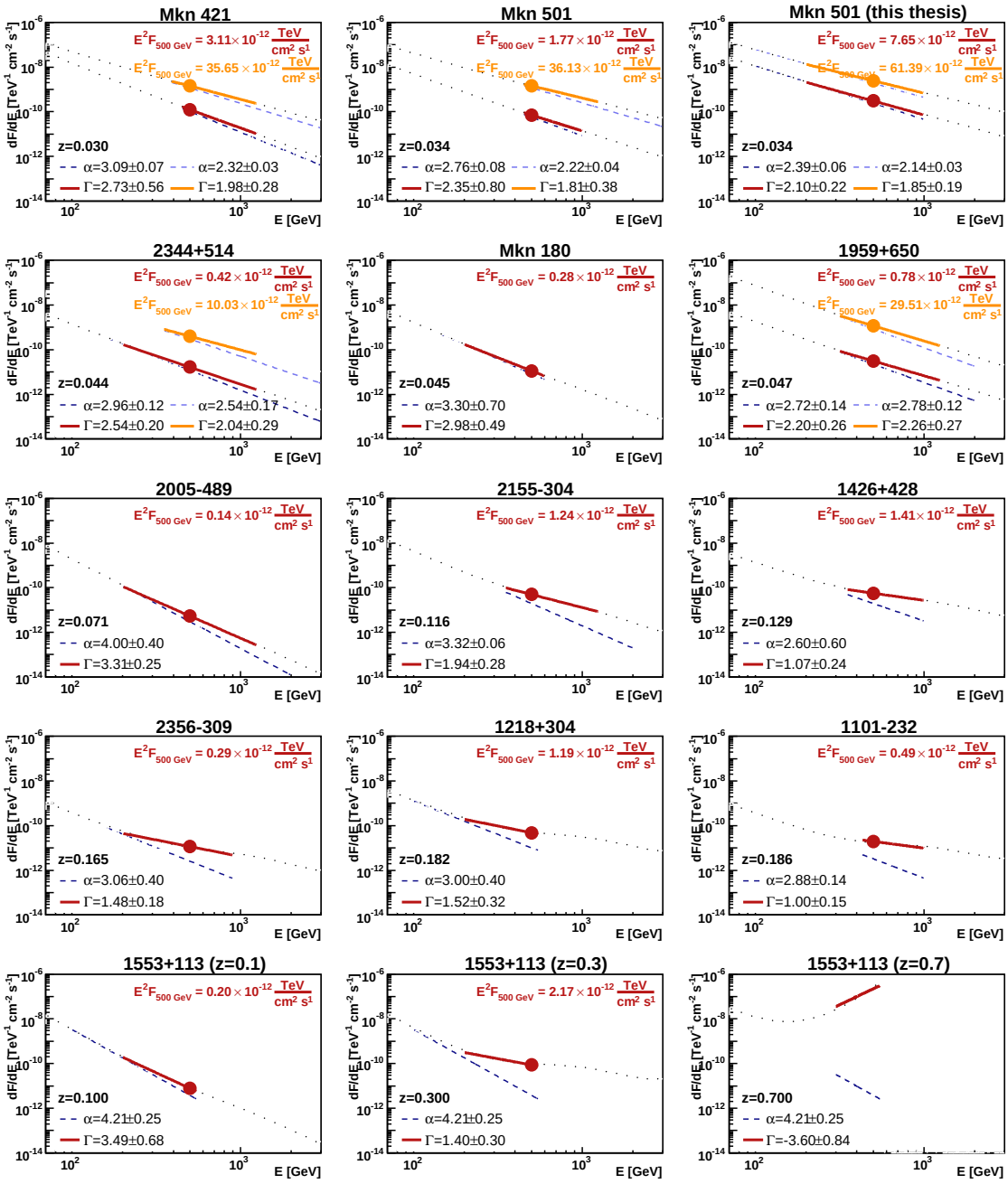

FIGURE 11.6: *Spectra of VHE γ-ray emitting blazars. The dashed blue lines represent measured spectra. The intrinsic spectra are inferred by using the "best fit" EBL model given in [Kne04] (dotted gray lines) and are fit with a simple power law represented by solid red lines. If flare states have been reported, they are included and represented by orange lines. For correlation studies, the differential flux at 500 GeV is extracted. References: Mkn 421 [Aha99a, Kre02], Mkn 501 [Aha01c, Aha99c] and this thesis, 1ES 2344 [Sch05c] and this thesis, 1ES 1959 [Alb06f, Dan05], PKS 2155 [Aha05f], 1H 1426 [Hor01, Aha02a], PKS 2005 [Aha05e], 1ES 1218 [Alb06b], 1ES 2356 & 1ES 1101 [Aha06b], PG 1553 this thesis, Mkn 180 [Alb06c]. The last plot is shown for reference and is not further used.*

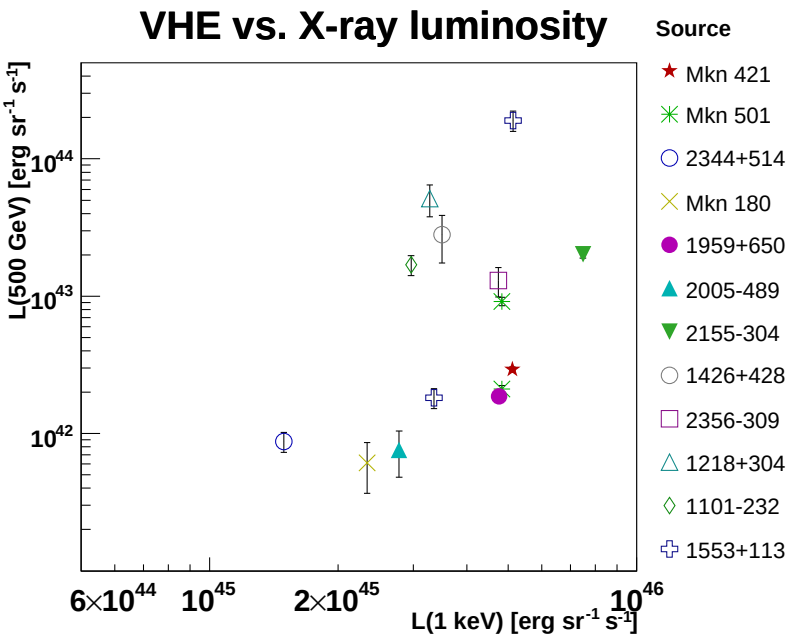

FIGURE 11.7: *VHE γ-ray luminosity at 500 GeV vs. X-ray luminosity at 1 keV (the latter taken from [Cos02]) for known VHE γ-ray emitters. The plot includes only assumed low flux states. The two data points for PG 1553 (open crosses) are for assumed redshifts of $z = 0.1$ ($L = 1.8 \cdot 10^{42}$ erg sr^{-1} s^{-1}) and $z = 0.3$ ($L = 1.9 \cdot 10^{44}$ erg sr^{-1} s^{-1}), respectively. It should be noted that the 500 GeV data points have an additional systematic error of typically 35%. The systematic error of the X-ray luminosities is unfortunately unknown.*

the VHE γ-ray luminosities span over almost three decades, the X-ray luminosities do so over one decade only. One might also interpret fig. 11.7 such that the luminosity at 1 keV is nearly independent of that at 500 GeV: Thermal contributions to the 1 keV radiation could be a possible explanation.

11.3.2 Correlations of intrinsic VHE γ-ray emission parameters with the black hole properties or redshift

Microquasars show observational and morphological properties of AGNs [Mir92], in particular they harbor stellar mass black holes and accretion disk systems. Also from microquasar observations, it is thought that simple scale laws govern black hole physics [Mir04]. This implies that one might expect that the properties of the VHE γ-ray emission found in blazars might also be connected to the properties of the central engines of these objects, like the SMBH mass and its spin. Of these, only on black hole masses do estimators exist to date. Moreover, the environment in which the SMBH is embedded might be equally important, like the accretion power and other accretion disk properties. To find possible correlations of the properties of the VHE γ-ray emission and fundamental AGN properties, we plot the intrinsic photon index and the 500 GeV luminosity versus

$M_\bullet$, the black hole mass. Apart from correlations with the black hole mass, we will test for possible correlations with the distance of the individual sources. They are not expected, but may point to certain selection effects in the data sample.

A first study of source properties which correlates the black hole masses of the then-established five VHE sources with emission parameters in the X-ray and VHE regime is discussed in [Kra04]. No correlations were found, except for an indication of a connection between the X-ray flare duty cycle and the central black hole mass. Note that a correlation with the black hole mass is expected, since scaling laws govern the physics around black holes, in particular the length scales and time scales of flows [Mir99], e.g. the orbital period of the last stable orbit around the BH.

Fig. 11.8 shows the correlations between black hole masses and redshifts respectively and the (1) intrinsic photon index and (2) the VHE γ-ray luminosity. As was to be expected, a selection effect is responsible for the fact that only sources with hard intrinsic spectra are visible at large distances ($z \gtrsim 0.1$), because soft spectra suffer EBL absorption and thus easily fall below the current sensitivity limits. An alternative explanation for the prevalent hard spectra at large distances is an overcorrection of the EBL attenuation effects by the EBL model used. In this context it should be noted that conspicuously, very hard ($\Gamma \ll 2.0$) spectra have up to now been only reconstructed for distant ($z \gtrapprox 0.1$) sources. None of the nearby sources, for which no strong modifications of the measured spectra by the EBL attenuation are expected, show photon indices much below $\Gamma \approx 2.0$. Therefore, although theory allows spectral indices down to $\Gamma = 1.5$ (see the discussion in sect. 9.7 and references therein), an overestimation of the EBL might well be responsible for the observed hard photon indices at high redshifts.

While there is no obvious correlation between $M_\bullet$ and the VHE γ-ray luminosity, it might be that the current data populate only a certain area in the $M_\bullet$—Γ plane. Owing to the large uncertainties of the $M_\bullet$ determination and the still poor statistics, the future will have to show if such trends are real. Perhaps also other parameters, such as the SMBH spin or the accretion rate, are more sensitive to the VHE γ-ray emission properties. Currently there is no easy way to access the SMBH spin, however; the accretion rate might be indirectly accessible through the (radio) jet power.

Before instruments like MAGIC and H.E.S.S. became operational, the average photon index observed in BL Lac objects was $\Gamma = 2.1$, which raised the hope that AGNs would in general exhibit rather hard spectra in the VHE range. Taking into account the whole current AGN sample, this average has not changed much, although obviously a new population of objects with intrinsically softer spectra (Mkn 180, PKS 2005) could be tapped. The AGN BL Lacertae seems to exhibit a rather soft spectrum, too. Additionally, the number of objects with observed soft spectra increased substantially. The tendency towards hard intrinsic spectra for distance sources could be (1) a selection effect or (2) an indication that the EBL absorption for the distant sources is estimated too high (which is

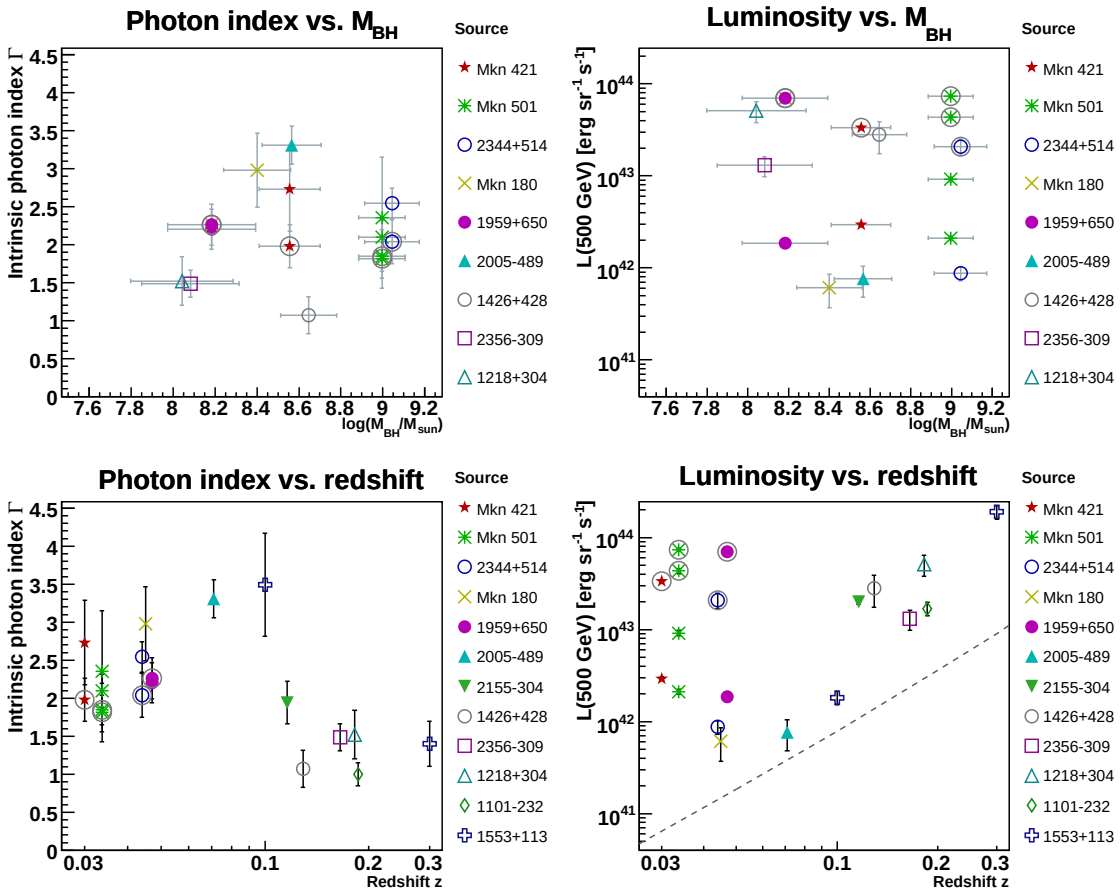

FIGURE 11.8: *Correlations of black hole mass and redshift with intrinsic photon index and VHE γ-ray luminosity. For Mkn 421, Mkn 501, 1ES 2344 and 1ES 1959 flare flux levels are also included, which are marked by additional gray circles. The two data points for PG 1553 (open crosses) are for assumed redshifts of $z = 0.1$ and $z = 0.3$, respectively. The dashed line in the lower right plot marks the sensitivity limit of current IACT (selection effect), not including EBL attenuation effects. Such a selection effect also exists in the photon index vs. redshift plane, leaving the upper right corner of the plane empty.*

in accordance with the latest findings detailed in [Aha06b]).

11.3.3 500 GeV luminosity for PG 1553+113 at different distances

The luminosity vs. redshift plot offers a possibility to pose limits on the yet unknown distance of PG 1553+113. With increasing distance, the luminosity of PG 1553+113 has to increase in order to sustain the flux level measured at Earth. The effect is stronger than quadratic ($L \geq d^2 \cdot F$) due to $\gamma\gamma$ absorption caused by the EBL. In fig. 11.9 we show the source luminosity (1) when only considering the distance effect and (2) when also taking into account the EBL absorption effect. Due to the exponential behavior of the EBL attenuation, the latter effect is by far the more dominant. To account for it, we used the best-fit model given in [Kne04]. We assume here that PG 1553+113 is an "off the

shelf" blazar, i.e. with no extraordinarily high luminosity. This assumption is difficult to quantify, but when translating it into the limit that the luminosity of PG 1553+113 is not more than 30 times higher than the highest luminosities observed, this implies a 2σ limit of $z < 0.43$. Among the extreme BL Lac objects Mkn 501, 1ES 2344, and 1H 1426, we find $L_{\rm max}(500\,{\rm GeV}) \lessapprox 10^{43.9}$ erg sr^{-1} s^{-1} for Mkn 501 in the flare state. Further studies are needed to quantify which blazar luminosities should be considered unphysical. An extreme luminosity of $L(500\,{\rm GeV}) = 10^{46.9}$ erg sr^{-1} s^{-1}—this is $\approx$ 1000-times more luminous than any observed blazar at present—, yields a limit of $z < 0.57$. When conservatively using the "low IR" model given in [Kne04], which assumes the least possible infrared star formation rate as allowed by galaxy counts, these two limits transform into $z < 0.48$ and $z < 0.68$, respectively.

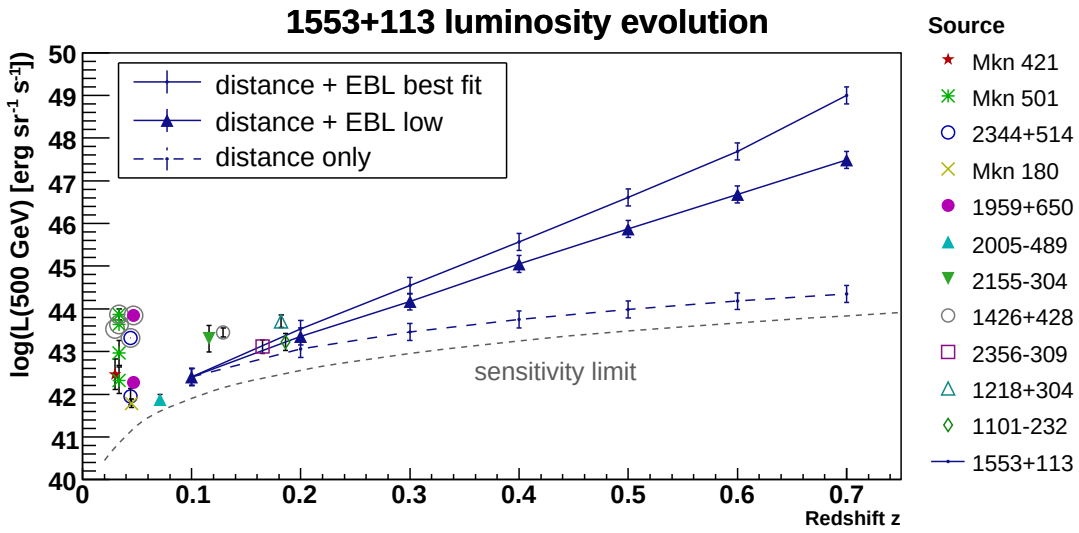

FIGURE 11.9: *Luminosity evolution for PG 1553+113 at different distances. Together with the luminosities of the other known VHE γ-ray emitting blazars, the luminosity of PG 1553+113 as a function of its assumed distance is shown. The upper curves include both the distance and the EBL attenuation effect, the latter calculated using the "best-fit" and the "low IR" model given in [Kne04]. The lower curve illustrates how weak the distance–only effect is. The gray dashed line indicates the current IACT sensitivity limit, also neglecting EBL attenuation effects.*

Note that these limits do not only depend on a good knowledge of the EBL attenuation over a wide range in redshift, but also on an assumable reasonable maximum VHE blazar luminosity. In this context it should be mentioned that the observed luminosity is strongly dependent on the jet Doppler factor. In any case, the study presented here shows that either a strikingly high luminosity or a very high Doppler factor is needed to explain the observations should PG 1553+113 be more distant that $z \gtrapprox 0.35$. It might also be that the blazar populations at large distances show significantly different properties than the close-by objects at $z < 0.2$, or that such very extreme objects are so rare that a sufficiently large volume had to be probed to find one of them.

11.3.4 Correlation between the intrinsic photon index and the VHE γ-ray luminosity

Fig. 11.10 relates the intrinsic photon indices to the VHE γ-ray luminosities. Both the objects with different observed flux states and the objects found in only one state contribute to a trend towards a correlation already studied in sect. 7.7.2 and 7.8.1 for Mkn 501: The higher the VHE γ-ray luminosity, the harder the spectrum. Within SSC models this would be compatible with a moving IC peak towards higher energies and an IC peak energy $\lessapprox 500\,\mathrm{GeV}$. Globally, i.e. for all objects under study here with a known redshift, the $\Gamma - L(500\,\mathrm{GeV})$ correlation reads as $\Gamma = \Gamma_0 + m \cdot \log_{10} L$ with $\Gamma_0 = 34.5 \pm 4.5$ and $m = -0.76 \pm 0.10$. The fit which led to this correlation has a reduced $\chi^2_{\mathrm{red}} = 48.6/14$. The corresponding linear correlation coefficient $r = -0.72^{+0.16}_{-0.11}$ is within 3.3 standard deviations different from zero (excluding the PG 1553 data due to the unknown distance and hence luminosity of this object). When particularly considering only those blazars for which quiescent and flare states are known, it is seen that their evolution in the $\Gamma - L(500\,\mathrm{GeV})$ is well matched by the found correlation. In addition, the Mkn 501 states found in the literature are very well compatible with the states obtained in this work. Fig. 11.11 shows the corresponding $\Delta\Gamma - \Delta L$ points for these four blazars. Mkn 501 and 1ES 2344 show a similar change in spectral slope and a luminosity increase of $\Delta L \approx 20$. The luminosity increase of Mkn 421 observed up to now is much lower with $\Delta L \approx 10$.

11.3.5 Variability timescales and X-ray duty cycles

To assess connections of timing properties and the black hole masses, the X-ray duty cycles are determined from ASM data (fig. 11.12). Following a method described in [Kra04] the $(2-10)$ keV X-ray light curve is plotted and the fraction of time during which the ASM flux significantly exceeds 50% of the time average flux is determined for all BL Lacs under study (note that 1ES 1218 was not monitored by ASM). Objects which are classified as extreme BL Lacs show substantially more activity than the other objects. Extreme BL Lacs have their synchrotron peak in the hard X-ray regime and include Mkn 501, 1ES 2344, 1H 1426, H 2356–309 and PKS 0548–322 [Cos01].

As a timing property of the VHE emission, we collect the minimum variability timescales from literature. The two quantities are plotted against the black hole mass and the VHE γ-ray luminosity in fig. 11.13.

- **Duty cycle vs. luminosity.** Supporting the claim that variability is a defining property of BL Lac type objects, a flat distribution of the duty cycle in luminosity is found. Note the special role that Mkn 421 plays with its substantially higher duty cycle as compared to the other objects.

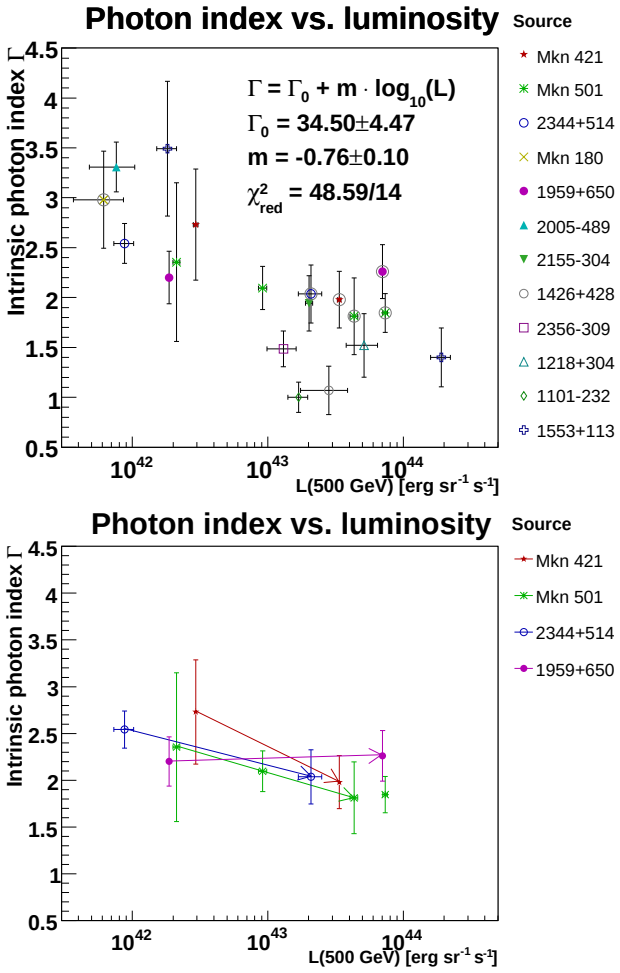

FIGURE 11.10: *Upper figure: Intrinsic photon index vs. luminosity. Additional flare states of sources are marked by gray circles. The results of a linear fit of the form* $\Gamma = \Gamma_0 + m \log_{10} L$ *are given in the figure. The two data points for PG 1553 (open crosses), not included in this fit, are for assumed redshifts of* $z = 0.1$ *(low luminosity) and* $z = 0.3$ *(high luminosity), respectively. Lower figure: As before, but only for the four blazars for which low and high VHE* γ *flux states have been observed.*

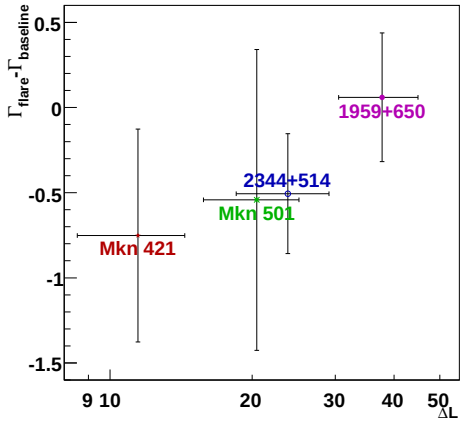

FIGURE 11.11: *Evolution of intrinsic photon index and luminosity from low to high VHE* γ *flux states: Difference of intrinsic photon index versus luminosity ratio* $\Delta L = L_{flare}/L_{baseline}$.

- **Variability timescales vs.** $M_\bullet$ The observed VHE variability timescales do not seem to scale with the black hole mass: The doubling times for Mkn 501 inferred in this work (cf. sect. 7.8.2) clearly do not support such scaling, and may simply mean that (1) the flaring mechanism is working in a much smaller region than the black hole radius and more importantly (2) the black hole and its properties (accretion power, rotation speed) as such do not influence the flaring process too much, but the embedding environment and the jet environment also play an important role. Note that, in spite of the expected scaling behavior of the flow properties around black holes with their masses, two AGNs hosting the more massive black holes, Mkn 501 and Mkn 421, seem to exhibit the shortest variability timescales in the VHE range. This, however, may be a selection effect caused (1) by the proximity of those two AGNs, (2) by instrumentation, since short time variability can only be measured for high fluxes and strong sources.
- **Variability timescales vs. luminosity.** As for possible correlations with the luminosity, one has to bear in mind that dim objects may not allow short variability in the VHE domain to be inferred due to insufficient sensitivity. Therefore, the VHE variability timescale plots show lower limits, which make strong claims impossible.

11.4 Concluding comments on the correlation studies

The studies performed for the full sample of 12 known VHE γ-ray emitting blazars yield the following results:

- Only AGN that host black holes with $M_\bullet \gtrapprox 10^8 M_\odot$ show VHE γ emission.
- While the VHE luminosity of VHE γ blazars spans over almost three decades, the corresponding X-ray luminosity only spans over one decade.
- There are no obvious correlations of the VHE γ emission properties with the black hole masses of the blazars. This is also true for the flare duty cycles and the flare timescales. These observations stress that the black hole mass itself might not be as influential to the VHE γ-ray emission as e.g. the environment in the acceleration region.
- There is a 3.3σ indication that the VHE γ luminosity L is correlated with the spectral hardness. This correlation can be formulated as a decrease of $\Delta\Gamma \approx 0.7$ per decade of luminosity.
- This behavior is also found for individual sources that were observed in different emission states: There are strong indications that in variable sources the observed spectra become harder with increasing luminosity.

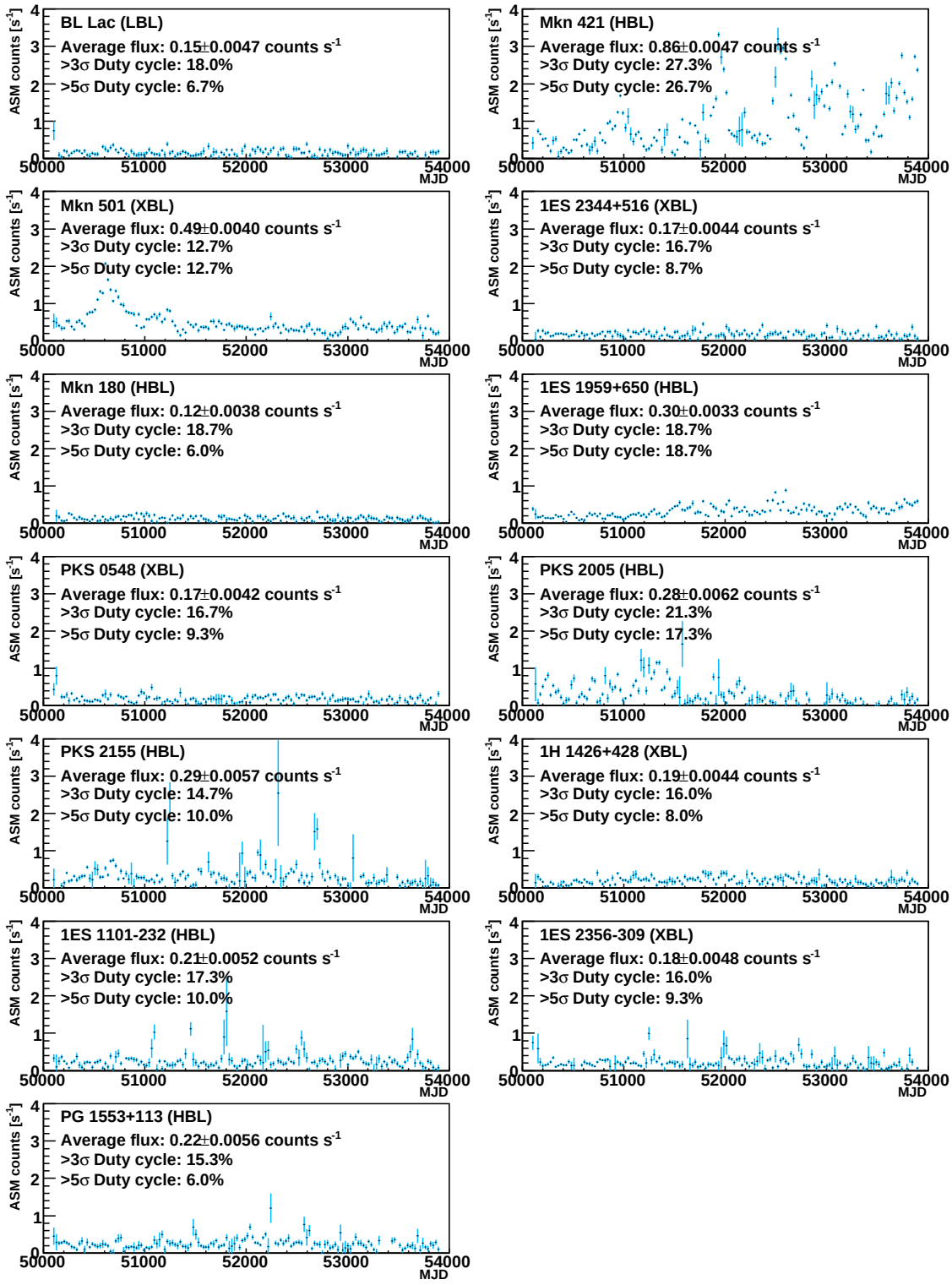

FIGURE 11.12: *X-ray flare duty cycles of VHE γ-ray emitting AGNs. ASM X-ray light curves [Lev04] in the (2–10) keV range. The flare duty cycle (the fraction of time in which the respective object significantly exceeds its average X-ray flux by 50% and more) is computed. For convenience the axis ranges are fixed for all plots. HBL: High–frequency peaked BL Lac object, synchrotron peak in the UV/X-ray range; XBL: Extreme BL Lac object, synchrotron spectrum extends well into the X-ray range.*

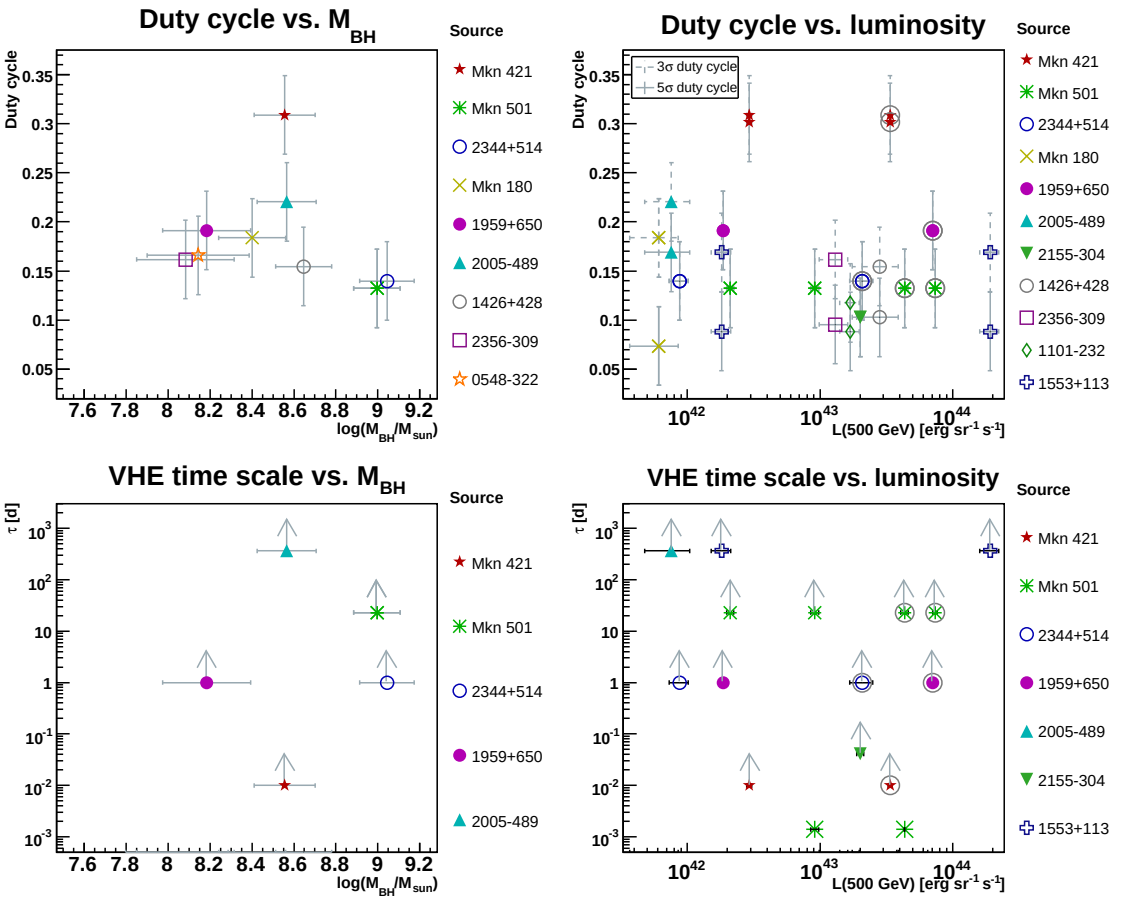

FIGURE 11.13: *Correlations of temporal properties with the black hole mass and the luminosity. For the VHE γ variability timescale, lower limits are given as found in the literature, plus Mkn 501 data points representing the doubling times of $\tau \lessapprox 5$ min as found in this work. For Mkn 421, Mkn 501, 1ES 2344 and 1ES 1959 flare flux levels are also included, which are marked by additional gray circles. The two data points for PG 1553 represent assumed redshifts of $z = 0.1$ (lower luminosity) and $z = 0.3$ (higher luminosity), respectively.*

- A hint at a marginal correlation between the intrinsic spectral hardness and the source distance is likely due to an EBL overprediction by the current EBL models.

- The found luminosity distribution of the VHE γ blazar sample can be used to constrain the yet unknown distance of PG 1553+113 when assuming that the properties of this blazar are not too different from the most extreme objects in the blazar sample. Conversely, a large distance of PG 1553+113 implies an unusually high luminosity or an unusually high jet Doppler factor.

11.5 Implications of the synoptic studies

After about two years of searching for extragalactic VHE sources with MAGIC and three years with H.E.S.S. it can be said that, with these instruments, the era of blazar astronomy has been entered—astronomy being understood as the study of generic properties of a given class of objects. With the current sample of VHE blazars and the given sensitivity of the instruments, VHE blazar astronomy starts to become less biased: Not only blazars with hard spectra or in flaring state are observed, but also quiescent emission states in the VHE range have been observed and studied in detail. These observations will allow a substantially enhanced time–dependent modeling of VHE γ-ray emission. When more sources will be discovered in the future, it will become easier to disentangle EBL absorption effects and intrinsic absorption effects from the measured source spectra. The benefit of such synoptic studies can already be illustrated by comparisons of objects at approximately identical redshifts. Also clues for neutrino astrophysics are already possible today with such synoptic studies.

AGNs with similar redshift. Today's enlarged sample of VHE blazars starts containing groups of objects at very similar distances, e.g. 1ES 1218 and 1ES 1101, or the triplet 1ES 2344, Mkn 180, and 1ES 1959 (fig. 11.14). Such groups offer themselves for direct comparison between the respective individual objects, as systematic deviations of the EBL absorption models should be small. Here we particularly consider the triplet 1ES 2344, Mkn 180, and 1ES 1959. Judging from the predicted SEDs (fig. 11.15) from SSC modeling, Mkn 180 and 1ES 1959 should show similar VHE fluxes, or more specifically, similar spectral behavior. Nonetheless, the intrinsic photon indices (cf. fig. 11.6) and the inferred luminosities in the VHE range of those two objects differ substantially, although their black hole masses are quite compatible with each other. That might hint at different production mechanisms prevalent in these two blazars. While 1ES 2344 cannot quite be included in this comparison, as its black hole mass is comparatively larger, its luminosity in the low state is well comparable with that of 1ES 1959 (the data used here ought to represent its low state, too [Alb06f]) and with that of Mkn 180 (the data used

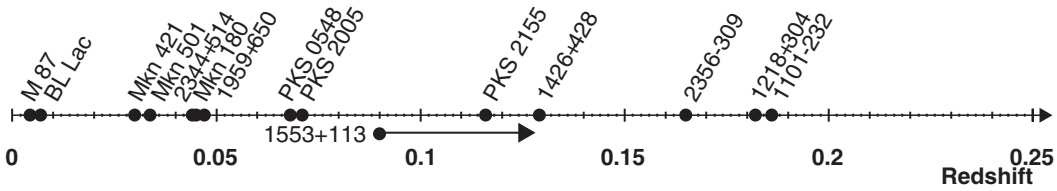

FIGURE 11.14: *Redshifts of the known VHE γ-ray blazars. For PG 1553, the lower redshift limit of $z = 0.09$ [Sba06] is indicated.*

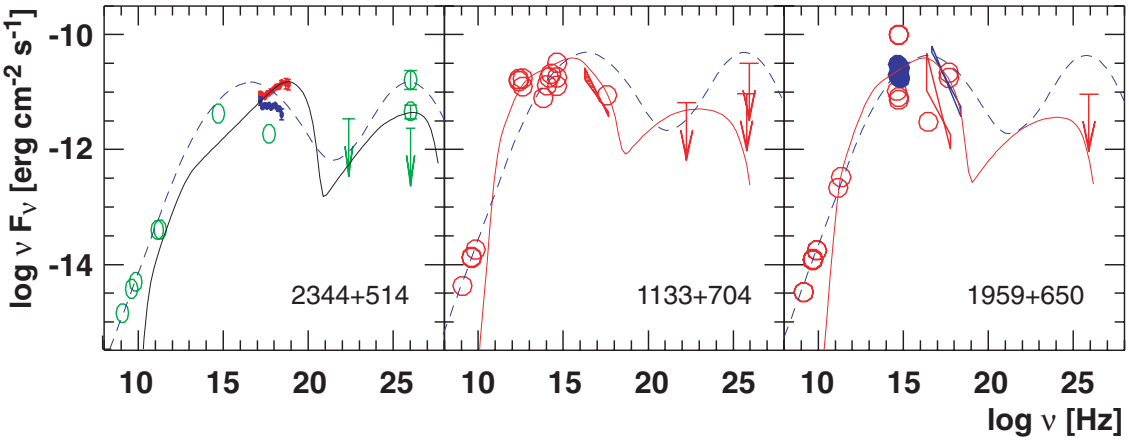

FIGURE 11.15: *Modeled SEDs for 1ES 2344, Mkn 180, and 1ES 1959, three VHE γ-ray emitting blazars at a comparable redshift. The black hole mass of 1ES 2344 is considerably larger than that of the other two objects. When comparing 1ES 1959 and Mkn 180, quite different intrinsic VHE γ-ray spectra are apparent (Data points and spectral fits taken from [Cos02]).*

were taken during an optical outburst; as no other data are available on that object yet, it is difficult to judge whether a baseline VHE flux or a flare was seen).

Prospects for VHE ν point source searches. There are two relevant reasons for a combined "multi-messenger" blazar astronomy, which make neutrino detectability studies using γ-ray observational data important:

1. It is well conceivable that the observed flare characteristics can be explained by a combination of leptonic and hadronic acceleration mechanisms. One can surmise that a hadronic mechanism is responsible for a baseline VHE γ-ray emission, while flares are produced by additional lepton acceleration. Neutrinos play a decisive role for testing such scenarios.

2. Any test and quantification of mixtures of hadronic and leptonic acceleration is much facilitated by multi–messenger observations, as neutrino detectors would unambiguously pin down the hadronic admixture.

Hadronic γ-ray production by pp or pγ collisions via π^0 decay (cf. sect. 1.2.1) is accompanied by simultaneous VHE electron, positron, and neutrino emissions through $\pi^{\pm} \rightarrow \mu^{\pm}\nu_{\mu}$ and $\nu^{\pm} \rightarrow e^{\pm}\nu_{\mu}\nu_{e}$. Theory [Dar96, Dar97] predicts that the VHE ν emission exhibits similar fluxes, light curves and energy spectra as VHE γ-ray quantities. One expects a similar power law index of the incident protons and the produced neutrinos.[2] [Mue03] find a dominance of ν emission from LBLs as compared to HBLs, arguing that higher proton synchrotron losses in HBLs lead to lower meson production rates there. From charged kaon production high energy neutrinos, $E_{\nu} \gtrsim 10^9$ GeV, would be expected. Calculations show [Dar97] that a γ-ray flare with $F \approx 10^{-9}$ cm^{-2} s^{-1} at energies above 1 TeV with a photon index of $\Gamma = 2$ lasting for one day would yield three ν events in a km^2 detector.

With large–scale ν telescopes like the IceCube detector [Ach05] currently being constructed, findings on the "average blazar" might be of interest for the expected ν fluxes from point–like ν sources. First searches for such an evidence were performed by the AMANDA collaboration [Ack05]. The observation of two neutrino events from the direction of 1ES 1959 during its 2002 flare [Ber05] stimulated calculations that assessed the neutrino flux in presence of the γ-ray flux observed from that flare [Hal05]. Major findings were that only the pp production mechanism for pions is in reach of the current neutrino detectors, and that mild bulk Lorentz factors ($\Gamma_{\mathrm{bulk}} \approx 1$) are required for detectable neutrino fluxes, as the pp pion production threshold is given by

$$E_{\mathrm{p}}^{\mathrm{thr}} = \Gamma_{\mathrm{bulk}} \frac{\left(2m_{\mathrm{p}} + m_{\pi}\right)^2 - 2m_{\mathrm{p}}^2}{2m_{\mathrm{p}}} \approx \Gamma_{\mathrm{bulk}} \cdot 1.23 \text{ GeV}.$$

A clear dependence of the neutrino flux on the spectral index of the γ-rays was also predicted. In view of the effective detection area of neutrino telescopes (fig. 11.16) and their energy thresholds ($E_{\mathrm{thr}}^{\nu} \approx 60$ GeV for AMANDA and $E_{\mathrm{thr}}^{\nu} \approx 100$ GeV for IceCube), the average intrinsic blazar VHE photon index found during quiescent and flare states, as well as the blazar duty cycle are relevant for reliable ν flux predictions from these objects. Blazars, together with GRBs, are the most promising extragalactic ν point source candidates.

[2] γ-rays produced by subsequent IC cooling of the produced $e^{\pm}$ are expected to exhibit a γ-ray spectrum with $\Gamma = -(n+1)/2 \approx 1.5 - 2$ and to be delayed by $\Delta t \sim \sqrt{E}^{-1}$.

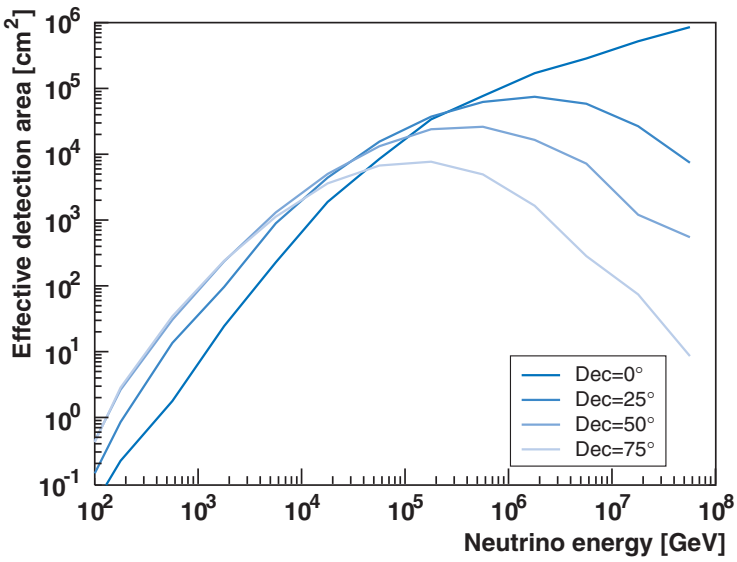

FIGURE 11.16: *Effective detection area as a function of neutrino energy at different declinations for AMANDA-II (taken from [Ack05]).*

Chapter 12

Concluding remarks

This thesis has shown how the merits of the new generation of Imaging Air Cherenkov Telescopes, in particular a substantially lowered energy threshold and an increased sensitivity, add to the knowledge of blazars and contribute to the understanding of AGN physics.

All four blazars discussed in this thesis were observed in VHE γ-rays at high significance levels. For each of these sources, a differential energy spectrum down to ≈ 100 GeV could be reconstructed, which is particularly interesting in case of the previously detected high–frequency peaked BL Lac objects Mkn 501 and 1ES 2344+514. For these, the IC peak energy is expected to lie well within the energy range covered by today's Cherenkov telescopes. The determination of the IC peak constitutes valuable input for the modeling of the VHE γ-ray emission in the framework of leptonic acceleration models.

The discovery of PG 1553+113 and BL Lacerate can also mainly be attributed to the low energy threshold of MAGIC. Due to the fact that these sources were found to have rather soft γ-ray spectra, their detection was possible only with an instrument sensitive to the rather large ($\approx 10\%$ Crab) fluxes in this energy range. This thesis adds two more sources to the group of blazars with soft γ-ray spectra, to which also the only recently discovered objects PKS 2005–489 and Mkn 180 belong. The implications of the special status of PG 1553+113 with its unprecedented soft γ-ray spectrum and its yet undetermined redshift were discussed in this thesis. BL Lacertae is the first source belonging to the class of low–frequency peaked BL Lac objects that has been discovered at VHE γ-rays. The existence of VHE emission from these objects was predicted, but up to now no LBL had been found to emit VHE γ-rays.

In the past, most of the VHE γ-ray emitting AGNs were discovered during a phase of high activity, rendering our current observational record biased towards high emission states. In contrast to that, the increased sensitivity of MAGIC allows to study also low emission states of AGNs, as first demonstrated for 1ES 1959+650 [Ton06, Alb06f] and in

this thesis for 1ES 2344+514. While the characteristics of blazar low level γ-ray emission at VHE are mostly elusive, in this thesis a first time–resolved analysis of the emission of 1ES 2344+514 could be conducted.

For blazars in outburst, the high sensitivity of the MAGIC telescope facilitates timing studies of the VHE γ-ray emission with a time resolution down to time scales of minutes. This could be demonstrated for the first time for the blazar Mkn 501 during two observation nights in July 2005, where a time resolution of two minutes was used to study short–term flares. The found doubling times of the order of minutes and below severely constrain the size of the corresponding emission regions to values which almost are not compatible any longer with the commonly used homogeneous one–zone SSC models. This poses new challenges for explaining the origin of these flares.

The flares were also used to infer a limit on the energy scale for quantum gravity effects of $E_{\mathrm{qg}} \geq 1.5 \cdot 10^{17}$ GeV. The method is based on the cosmological distance of Mkn 501 and on the ability to create light curves with sufficient statistics in distinct energy bands. It is competitive to alternative approaches, which e.g. make use of the more distant gamma-ray bursts at the expense of lower energy differences (in the X-ray range). The limit given in this thesis is among the best limits found so far and well compatible with other limits found with different approaches.

This thesis has also shown the necessity of coordinated multiwavelength observations: Only for Mkn 501 and only on diurnal basis could the available X-ray all-sky monitor data be used in connection with the MAGIC γ-ray data. Dedicated simultaneous measurements with higher sensitivity in the keV energy domain (using pointed detectors) would ease much a detailed modeling of the non–thermal emission of extragalactic sources. In particular during strong flares, so-called time-of-opportunity campaigns will be essential to understand the mechanism responsible for the short-term variability observed. Also the study of low emission states will profit from simultaneous X-ray and VHE γ-ray observations.

Before the new generation Cherenkov telescopes (in particular H.E.S.S. and MAGIC) became operational, only six firmly detected extragalactic VHE γ-ray sources were known; not for all of them differential energy spectra had been inferred. To date, there are 13 high–frequency peaked BL Lac objects known to emit VHE γ-rays. In addition, the radio galaxy M87 and BL Lacertae, the latter belonging to the group of low–frequency peaked BL Lac objects, were discovered. The substantially enlarged sample of HBL objects calls for a synoptic study of these sources, which to our best knowledge was performed for the first time in this thesis. We addressed both the properties of the VHE γ-ray emission itself (luminosity, spectral hardness, temporal properties) and those of the accompanying X-ray emission and of the black hole in the centers of the host galaxies.

Among the 11 high–frequency peaked BL Lac objects under study, we found a weak

correlation between the X-ray and the VHE γ-ray emission. Further on, a correlation of the source luminosity and the spectral hardness is observed, both among the individual sources and for the four sources that were found at different flux states (Mkn 421, Mkn 501, 1ES 2344+514, and 1ES 1959+650). Currently no dependencies of the VHE emission properties on the black hole mass of the host galaxy can be reported; it is likely that also other properties of the black hole—accretion disk system are important in this context, like the accretion rate and the black hole spin. These properties can, however, not yet directly be measured.

As far as correlations of luminosity and spectral hardness with the source distance are concerned, it is likely that the current models for the extragalactic background light overpredict the corresponding VHE γ-ray attenuation. In clarifying the situation, very distant ($z \gtrapprox 0.2$) sources will play a decisive role; PG 1553+113 with its yet undetermined distance might be a good candidate for such a source, as soon as a measurement of its redshift succeeds. Note that in this thesis indirect methods were used to limit the distance of PG 1553+113. From assumptions on the EBL background, a distance limit for PG 1553+113 corresponding to $z < 0.78$ was posed. It was also shown that luminosity arguments can be used to limit the distance of this source to at maximum $z < 0.68$.

The near future of VHE γ-ray blazar astronomy. Since 2003, on average two new blazars have been detected per year, with more discoveries to come. When comparing this rate to the ten years it took to find the first six blazars at VHE γ-ray energies from 1992–2002, one can with good reason hope to accumulate many more sources in the near future, which will refine synoptic HBL studies and reveal further properties of this class of objects. In addition, with the observation of BL Lacerate as the first LBL object, also BL Lacs with substantially lower synchrotron peak energies have now been found to emit VHE γ-rays. This will certainly help to study possible blazar sequence scenarios and their underlying physics in the near future.

A second 17 m diameter MAGIC telescope, which becomes operational at the end of 2007, the upcoming VERITAS array of four Cherenkov telescopes, and the construction of a 28 m diameter central telescope for the H.E.S.S. phase II facilitate a further lowering of the detection threshold and a further increase of the instrumental sensitivity. In addition, monitoring efforts targeted at few strong and violent blazars like Mkn 421 and Mkn 501 in the individual collaborations will very soon provide long–term data on these objects.

But not only these individual instrumental upgrades guarantee advances in AGN physics; also a strong networking effort, leading to a "Global Network of Cherenkov Telescopes", will help to further elucidate the acceleration processes leading to VHE γ-ray emission in AGNs. A first aspect, namely simultaneous observations from different geographical latitudes and the possibility for a cross–calibration of Cherenkov telescopes were touched upon in this thesis. Even more, also the so-called multi-messenger approach gains im-

portance once hadronic acceleration is to be unambiguously proven or the quantification of the mixture of leptonic and hadronic acceleration is to be assessed. To this end, the collaboration of VHE γ-ray detectors and neutrino detectors like IceCube offers itself.

The final closure of the energy gap between EGRET ($E \lessapprox 5$ GeV) and the IACT installations ($E \gtrapprox 40$ GeV) will take place with the launch of the GLAST satellite in the second half of 2007. Already today, and in particular once a good spectral coverage of the typical AGN spectrum with high sensitivity instruments is achieved, so-called multiwavelength campaigns, i.e. simultaneous observations at various wavelengths, will become crucial. The main task will be the transition from the current, rather simple leptonic or protonic emission models to models which can accurately describe the temporal evolution of the emission, including the short–term variability as observed in Mkn 501 in this thesis.

Bibliography

[Ach05] A. Achterberg et al. The IceCube Collaboration: contributions to the 29th International Cosmic Ray Conference (ICRC 2005). In *Proceedings of the 29th International Cosmic Ray Conference*, Aug, 2005. arXiv:astro-ph/0509330. Cited on page 246.

[Ack05] M. Ackermann et al. Search for extraterrestrial point sources of high energy neutrinos with AMANDA–II using data collected in 2000–2002. *Physical Review D* **71 7**, 077102 (2005). Cited on page 246, 247.

[Aha97] F. Aharonian et al. Measurement of the flux, spectrum, and variability of TeV γ–rays from Mkn 501 during a state of high activity. *Astronomy & Astrophysics* **327**, L5–L8 (1997). Cited on page 154.

[Aha99a] F. A. Aharonian et al. Observations of Mkn 421 during 1997 and 1998 in the energy range above 500 GeV with the HEGRA stereoscopic Cherenkov telescope system. *Astronomy & Astrophysics* **350**, 757–764 (1999). arXiv:astro-ph/9905032. Cited on page 234.

[Aha99b] F. A. Aharonian et al. The time averaged TeV energy spectrum of Mkn 501 of the extraordinary 1997 outburst as measured with the stereoscopic Cherenkov telescope system of HEGRA. *Astronomy & Astrophysics* **349**, 11–28 (1999). Cited on page 33, 131, 132.

[Aha99c] F.A. Aharonian et al. The temporal characteristics of the TeV gamma–radiation from Mkn 501 in 1997. I. Data from the stereoscopic imaging atmospheric Cherenkov telescope system of HEGRA. *Astronomy & Astrophysics* **342**, 69–86 (1999). arXiv:astro-ph/9808296. Cited on page 131, 132, 135, 183, 234.

[Aha00a] F. A. Aharonian. TeV gamma rays from BL Lac objects due to synchrotron radiation of extremely high energy protons. *New Astronomy* **5**, 377–395 (2000). arXiv:astro-ph/0003159. Cited on page 28, 120, 136.

[Aha00b] F. A. Aharonian et al. HEGRA search for TeV emission from BL Lacertae objects. *Astronomy & Astrophysics* **353**, 847–852 (2000). arXiv:astro-ph/9903455. Cited on page 189.

[Aha00c] F. A. Aharonian et al. The energy spectrum of TeV gamma-rays from the Crab nebula as measured by the HEGRA system of imaging air Cerenkov telescopes. *Astrophysical Journal* **539**, 317–324 (2000). Cited on page 112.

[Aha01a] F. Aharonian et al. Reanalysis of the high energy cutoff of the 1997 Mkn 501 TeV energy spectrum. *Astronomy & Astrophysics* **366**, 62–67 (2001). Cited on page 13.

[Aha01b] F. A. Aharonian. TeV blazars and cosmic infrared background radiation. In *Proceedings of the 27th International Cosmic Ray Conference*, page 250, Hamburg, 2001. arXiv:astro-ph/0112314. Cited on page 11, 214.

[Aha01c] F. A. Aharonian et al. The TeV Energy Spectrum of Markarian 501 Measured with the Stereoscopic Telescope System of HEGRA during 1998 and 1999. *Astrophysical Journal* **546**, 898–902 (2001). Cited on page 33, 132, 139, 143, 183, 234.

[Aha02a] F. Aharonian. TeV gamma rays from the blazar H 1426+428 and the diffuse extragalactic background radiation. *Astronomy & Astrophysics* **384**, L23–L26 (2002). Cited on page 36, 234.

[Aha02b] F. A. Aharonian, A. A. Belyanin, E. V. Derishev, V. V. Kocharovsky, and Vl. V. Kocharovsky. Constraints on the extremely high–energy cosmic ray accelerators from classical electrodynamics. *Physical Reviev D* **66 2**, 023005 (2002). arXiv:astro-ph/0202229. Cited on page 29.

[Aha02c] F. A. Aharonian et al. Variations of the TeV energy spectrum at different flux levels of Mkn 421 observed with the HEGRA system of Cherenkov telescopes. *Astronomy & Astrophysics* **393**, 89–99 (2002). Cited on page 33.

[Aha03a] F. A. Aharonian and S. V. Bogovalov. Exploring physics of rotation powered pulsars with sub-10 GeV imaging atmospheric Cherenkov telescopes. *New Astronomy* **8**, 85–103 (2003). arXiv:astro-ph/0208036. Cited on page 121.

[Aha03b] F. A. Aharonian et al. Detection of TeV gamma–rays from the BL Lac 1ES 1959+650 in its low states and during a major outburst in 2002. *Astronomy & Astrophysics* **406**, L9–L13 (2003). Cited on page 33, 36.

[Aha04a] F. Aharonian et al. The Crab Nebula and Pulsar between 500 GeV and 80 TeV: Observations with the HEGRA Stereoscopic Air Cerenkov Telescopes. *Astrophysical Journal* **614**, 897–913 (2004). arXiv:astro-ph/0407118. Cited on page 119, 120, 127, 128, 129.

[Aha04b] F. A. Aharonian et al. Observations of 54 Active Galactic Nuclei with the HEGRA system of Cherenkov telescopes. *Astronomy & Astrophysics* **421**, 529–537 (2004). arXiv:astro-ph/0401301. Cited on page 36, 40, 189, 203, 219, 226, 229.

[Aha05a] F. Aharonian et al. A search for very high energy γ–ray emission from the starburst galaxy NGC 253 with HESS. *Astronomy & Astrophysics* **442**, 177–183 (2005). arXiv:astro-ph/0507370. Cited on page 16.

[Aha05b] F. Aharonian et al. Discovery of Very High Energy Gamma Rays Associated with an X–ray Binary. *Science* **309**, 746–749 (2005). arXiv:astro-ph/0508298. Cited on page 18.

[Aha05c] F. Aharonian et al. Observations of selected AGN with HESS. *Astronomy & Astrophysics* **441**, 465–472 (2005). arXiv:astro-ph/0507207. Cited on page 229.

[Aha05d] F. Aharonian et al. The unidentified TeV source (TeV J2032+4130) and surrounding field: Final HEGRA IACT-System results. *Astronomy and Astrophysics* **431**, 197–202 (2005). Cited on page 17.

[Aha05e] F. A. Aharonian et al. Discovery of VHE gamma rays from PKS 2005–489. *Astronomy & Astrophysics* **436**, L17–L20 (2005). Cited on page 36, 40, 234.

[Aha05f] F. A. Aharonian et al. H.E.S.S. observations of PKS 2155-304. *Astronomy & Astrophysics* **430**, 865–875 (2005). arXiv:astro-ph/0411582. Cited on page 36, 234.

[Aha06a] F. Aharonian et al. Observations of 14 young open star clusters with the HEGRA system of Cherenkov telescopes. *Astronomy & Astrophysics* **454**, 775–779 (2006). Cited on page 18.

[Aha06b] F. A. Aharonian et al. A low level of extragalactic background light as revealed by γ-rays from blazars. *Nature* **440**, 1018–1021 (2006). arXiv:astro-ph/0508073. Cited on page 10, 11, 12, 36, 41, 214, 233, 234, 237.

[Aha06c] F. A. Aharonian et al. Evidence for VHE γ-ray emission from the distant BL Lac PG 1553+113. *Astronomy & Astrophysics* **448**, L19–L23 (2006). arXiv:astro-ph/0601545. Cited on page 12, 36, 205, 206, 207, 213, 214, 215, 217.

[Aha06d] F. A. Aharonian et al. Observations of the Crab Nebula with H.E.S.S. *Astronomy & Astrophysics* **457**, 899–915 (2006). Cited on page 120.

[Alb06a] J. Albert et al. Detection of VHE radiation from the BL Lac PG 1553+113 with the MAGIC telescope. *Astrophysical Journal Letters* (2006). Submitted to Astrophysical Journal Letters, arXiv:astro-ph/0606161. Cited on page 12, 36, 206, 207.

[Alb06b] J. Albert et al. Discovery of Very High Energy Gamma Rays from 1ES 1218+30.4. *Astrophysical Journal Letters* **642**, L119–L122 (2006). arXiv:astro-ph/0603529. Cited on page 36, 41, 234.

[Alb06c] J. Albert et al. Discovery of VHE-emission from Mkn 180 with MAGIC during an optical outburst. *Astrophysical Journal Letters* **648**, L105–L108 (2006). arXiv:astro-ph/0606630. Cited on page 36, 41, 234.

[Alb06d] J. Albert et al. Flux Upper Limit on Gamma–Ray Emission by GRB 050713a from MAGIC Telescope Observations. *Astrophysical Journal Letters* **641**, L9–L12 (2006). arXiv:astro-ph/0602231. Cited on page 16, 137.

[Alb06e] J. Albert et al. Observation of Gamma Rays from the Galactic Center with the MAGIC Telescope. *Astrophysical Journal Letters* **638**, L101–L104 (2006). arXiv:astro-ph/0512469. Cited on page 55.

[Alb06f] J. Albert et al. Observation of Very High Energy Gamma–Ray Emission from the Active Galactic Nucleus 1ES 1959+650 Using the MAGIC Telescope. *Astrophysical Journal* **639**, 761–765 (2006). arXiv:astro-ph/0508543. Cited on page 36, 234, 244, 249.

[Alb06g] J. Albert et al. Observations of Mkn 421 with the MAGIC telescope. *Astrophysical Journal* (2006). Submitted to Astrophysical Journal, arXiv:astro-ph/0603478. Cited on page 13.

[Alb06h] J. Albert et al. Variable Very High Energy Gamma–Ray Emission from the Microquasar LS I +61 303. *Science* **312**, 1771–1773 (2006). arXiv:astro-ph/0605549. Cited on page 18.

[Alc00a] J. Alcaraz et al. Cosmic protons. *Physics Letters* **B490**, 27–35 (2000). Cited on page 83.

[Alc00b] J. Alcaraz et al. Helium in near earth orbit. *Physics Letters* **B494**, 392 (2000). Cited on page 83.

[Ame98] G. Amelino-Camelina, J. Ellis, N. E. Mavromatos, D. V. Nanopoulos, and S. Sarkar. Tests of quantum gravity from observations of gamma–ray bursts. *Nature* **393**, 763–765 (1998). Cited on page 19, 136, 137, 169.

[Ame99] M. Amenomori et al. Observation of Multi-TeV Gamma Rays from the Crab Nebula using the Tibet Air Shower Array. *Astrophysical Journal Letters* **525**, L93–L96 (1999). arXiv:astro-ph/9909172. Cited on page 128.

[Ame00] G. Amelino-Camelina. Are We at the Dawn of Quantum-Gravity Phenomenology? *Lecture Notes in Physics* **541**, 1–49 (2000). arXiv:gr-qc/9910089. Cited on page 169.

[Ant93] R. Antonucci. Unified models for active galactic nuclei and quasars. *Annual Review of Astronomy and Astrophysics* **31**, 473–521 (1993). Cited on page 23.

[Ant05] S. Antón and I. W. A. Browne. The recognition of blazars and the blazar spectral sequence. *Monthly Notices of the Royal Astronomical Society* **356**, 225–231 (2005). arXiv:astro-ph/0409643. Cited on page 28, 29.

[Any91] V. B. Anykeyev, A. A. Spiridonov, and V. P. Zhigunov. Comparative investigation of unfolding methods. *Nuclear Instruments and Methods in Physics Research A* **303**, 350–369 (1991). Cited on page 115.

[ASD06] ASI Science Data Center, http://www.asdc.asi.it/. Cited on page 183, 184, 203.

[Bad01] H. M. Badran and T. C. Weekes. TeV gamma-ray observations from the blazar, 1ES2344+514 with the Whipple Cherenkov Imaging Telescope. In *Proceedings of the 27th International Cosmic Ray Conference*, pages 2653–2656, August, 2001. Cited on page 189, 196, 197.

[Bai04] C. Baixeras et al. Commissioning and first tests of the MAGIC telescope. *Nuclear Instruments and Methods in Physics Research A* **518**, 188–192 (2004). Cited on page 57.

[Bar98a] A. Barrau. *Astrophysique gamma de tres haute energie: etude du noyau activ de galaxie Mrk 501 et implications cosmologiques*. Ph. D. thesis, Universite de Grenoble, 1998. Cited on page 132.

[Bar98b] J. Barrio et al. The MAGIC Telescope—Design study for the construction of a 17 m Čerenkov telescope for Gamma–Astronomy above 10 GeV. *MPI-PhE 98-05* (1998). `http://wwwmagic.mppmu.mpg.de/publications/proposals/`. Cited on page 51, 53, 58.

[Bar03] A. J. Barth, L. C. Ho, and W. L. W. Sargent. The Black Hole Masses and Host Galaxies of BL Lacertae Objects. *Astrophysical Journal* **583**, 134–144 (2003). `arXiv:astro-ph/0209562`. Cited on page 187, 231.

[Bar05] H. Bartko et al. Tests of a prototype multiplexed fiber-optic ultra-fast FADC data acquisition system for the MAGIC telescope. *Nuclear Instruments and Methods in Physics Research A* **548**, 464–486 (2005). `arXiv:astro-ph/0505204`. Cited on page 89.

[Bas05] D. Bastieri, C. Bigongiari, E. Bisesi, et al. Using the photons from the Crab Nebula seen by GLAST to calibrate MAGIC and the imaging air Cherenkov telescopes. *Astroparticle Physics* **23**, 572–576 (2005). Cited on page 81.

[Bea02] A. J. Beasley, D. Gordon, A. B. Peck, et al. The VLBA Calibrator Survey-VCS1. *Astrophysical Journal Supplement* **141**, 13–21 (2002). `arXiv:astro-ph/0201414`. Cited on page 209.

[Bed93] W. Bednarek. On the gamma–ray emission from 3C 279. *Astrophysical Journal Letters* **402**, L29–L32 (1993). Cited on page 28.

[Bed97] W. Bednarek and R. J. Protheroe. Modulation of AGN gamma–rays by interaction with X-rays from an accretion disc hotspot. *Monthly Notices of the Royal Astronomical Society* **290**, 139–144 (1997). `arXiv:astro-ph/9612211`. Cited on page 34, 177.

[Bed06] W. Bednarek, private communication. July, 2006. Cited on page 180, 181.

[Beg03] M. C. Begelman. Evidence for Black Holes. *Science* **300**, 1898–1904 (2003). Cited on page 229.

[Bei05] M. Beilicke et al. Observation of the Giant Radio Galaxy M87 at TeV Energies with H.E.S.S. In *22nd Texas Symposium on Relativistic Astrophysics*, 2005. `arXiv:astro-ph/0504395`. Cited on page 36.

[Ben05] R. Bender et al. HST STIS Spectroscopy of the Triple Nucleus of M31: Two Nested Disks in Keplerian Rotation around a Supermassive Black Hole. *Astrophysical Journal* **631**, 280–300 (2005). `arXiv:astro-ph/0509839`. Cited on page 230.

[Ben06] W. Benbow, private communication. May, 2006. Cited on page 214.

[Ber89] M. Bertero. *Linear inverse and ill-posed problems*, volume 75, pages 1–120. Academic Press, New York, 1989. Cited on page 115.

[Ber00] K. Bernlöhr. Impact of atmospheric parameters on the atmospheric Cherenkov technique. *Astroparticle Physics* **12**, 255–268 (2000). `arXiv:astro-ph/9908093`. Cited on page 116.

[Ber05] E. Bernardini. Multi–messenger studies with AMANDA/IceCube: Observations and strategies. In B. Degrange, editor, *Proceedings Towards A Network Of Cherenkov Detectors VII*, pages 307–315, May, 2005. Cited on page 29, 246.

[Bet01] D. Bettoni, R. Falomo, G. Fasano, F. Govoni, M. Salvo, and R. Scarpa. The fundamental plane of radio galaxies. *Astronomy & Astrophysics* **380**, 471–477 (2001). `arXiv:astro-ph/0110420`. Cited on page 230, 231.

[Bha00] P. Bhattacharjee. Origin and propagation of extremely high energy cosmic rays. *Physics Reports* **327**, 109–247 (2000). arXiv:astro-ph/9811011. Cited on page 6.

[Bie03] P. L. Biermann et al. Single and binary black holes and their active environment. In *Proceedings of the 7eme Colloquium Cosmologie, High Energy Astrophysics from and for Space*, June, 2003. arXiv:astro-ph/0211503. Cited on page 22.

[Big04] C. Bigongiari et al. The MAGIC telescope reflecting surface. *Nuclear Instruments and Methods in Physics Research A* **518**, 193–194 (2004). Cited on page 59.

[Bil99] S. D. Biller et al. Limits to Quantum Gravity Effects on Energy Dependence of the Speed of Light from Observations of TeV Flares in Active Galaxies. *Physical Review Letters* **83**, 2108–2111 (1999). arXiv:gr-qc/9810044. Cited on page 19, 137, 138, 170, 171.

[Bil05] D. K. Bilitza. U.S. Standard Atmosphere 1976, http://modelweb.gsfc.nasa.gov/atmos/. Cited on page 116.

[Bla48] P. M. S. Blackett. A possible contribution to the night sky from the Cerenkov radiation emitted by cosmic rays. In *The Emission Spectra of the Night Sky and Aurorae*, page 34, 1948. Cited on page 49, 52.

[Bla82] R. D. Blandford and C. F. McKee. Reverberation mapping of the emission line regions of Seyfert galaxies and quasars. *Astrophysical Journal* **255**, 419–439 (1982). Cited on page 230.

[Bla87] R. Blandford and D. Eichler. Particle Acceleration at Astrophysical Shocks—a Theory of Cosmic-Ray Origin. *Physics Reports* **154**, 1 (1987). Cited on page 8.

[Bla05] O. Blanch and M. Martinez. Exploring the gamma ray horizon with the next generation of gamma ray telescopes. Part 1: Theoretical predictions. *Astroparticle Physics* **23**, 588–597 (2005). arXiv:astro-ph/0107582. Cited on page 12.

[Blo96] S. D. Bloom and A. P. Marscher. An Analysis of the Synchrotron Self-Compton Model for the Multi–Wave Band Spectra of Blazars. *Astrophysical Journal* **461**, 657 (1996). Cited on page 26.

[Blo97a] S. D. Bloom et al. Observations of a Correlated Gamma–Ray and Optical Flare for BL Lacertae. *Astrophysical Journal* **490**, L145 (1997). arXiv:astro-ph/9709264. Cited on page 219.

[Blo97b] S. D. Bloom, R. C. Hartman, H. Teraesranta, M. Tornikoski, and E. Valtaoja. Possible New Identifications for EGRET Sources. *Astrophysical Journal Letters* **488**, L23 (1997). arXiv:astro-ph/9709279. Cited on page 10.

[Boc04] R. K. Bock et al. Methods for multidimensional event classification: a case study using images from a Cherenkov gamma–ray telescope. *Nuclear Instruments and Methods in Physics Research A* **516**, 511–528 (2004). Cited on page 96.

[Boe97a] M. Böttcher. *Zeitabhängiger Strahlungstransport in Jets von aktiven galaktischen Kernen*. Ph. D. Thesis, Universität Bonn, 1997. Cited on page 22.

[Boe97b] M. Böttcher et al. γ–ray emission and spectral evolution of pair plasmas in AGN jets. I. General theory and a prediction for the GeV–TeV emission from ultrarelativistic jets. *Astronomy & Astrophysics* **324**, 395–409 (1997). Cited on page 136.

[Boe02] M. Böttcher and J. Chiang. X-Ray Spectral Variability Signatures of Flares in BL Lacertae Objects. *Astrophysical Journal* **581**, 127–142 (2002). arXiv:astro-ph/0208238. Cited on page 225.

[Boe03] M. Böttcher, A. P. Marscher, M. Ravasio, et al. Coordinated Multiwavelength Observations of BL Lacertae in 2000. *Astrophysical Journal* **596**, 847–859 (2003). arXiv:astro-ph/0307022. Cited on page 219, 225.

[Boe04] M. Böttcher and A. Reimer. Modeling the Multiwavelength Spectra and Variability of BL Lacertae in 2000. *Astrophysical Journal* **609**, 576–588 (2004). arXiv:astro-ph/0403627. Cited on page 219, 225, 226.

[Bog04] S. E. Boggs, C. B. Wunderer, K. Hurley, and W. Coburn. Testing Lorentz Invariance with GRB 021206. *Astrophysical Journal Letters* **611**, L77–L80 (2004). arXiv:astro-ph/0310307. Cited on page 137, 138.

[Bra93] H. V. Bradt, R. E. Rothschild, and J. H. Swank. X-ray timing explorer mission. *Astronomy & Astrophysics Supplement* **97**, 355–360 (1993). Cited on page 135, 143, 144, 211.

[Bra97] S. Bradbury et al. Detection of γ-rays above 1.5 TeV from Mkn 501. *Astronomy & Astrophysics* **320**, L5–L8 (1997). arXiv:astro-ph/9612058. Cited on page 36, 131, 133, 134, 143.

[Bre01] L. Breiman. Random forests. *Machine Learning* **45**, 5 (2001). Cited on page 96.

[Bre04] L. Breiman and A. Cutler. Random forests, http://www.stat.berkeley.edu/users/breiman/RandomForests/. Cited on page 96.

[Bri00] M. S. Briggs. BATSE Gamma-Ray Burst Skymaps, http://www.batse.msfc.nasa.gov/batse/grb/skymap/. Cited on page 17.

[Buc99] J. H. Buckley. Observations of blazars with the Whipple Observatory gamma-ray telescope. *Astroparticle Physics* **11**, 119–129 (1999). Cited on page 26.

[Buc06] J. H. Buckley, private communication. Jul, 2006. Cited on page 26.

[But03] Y. M. Butt et al. Chandra/Very Large Array Follow–Up of TeV J2032+4131, the Only Unidentified TeV Gamma–Ray Source. *Astrophysical Journal* **597**, 494–512 (2003). arXiv:astro-ph/0302342. Cited on page 17.

[Cac04] A. Caccianga and M. J. M. Marchã. The CLASS blazar survey: testing the blazar sequence. *Monthly Notices of the Royal Astronomical Society* **348**, 937–954 (2004). arXiv:astro-ph/0311384. Cited on page 28.

[Cal03] I. de la Calle Perez et al. Search for High–Energy Gamma Rays from an X–Ray–selected Blazar Sample. *Astrophysical Journal* **599**, 909–917 (2003). arXiv:astro-ph/0309063. Cited on page 206, 207.

[Cat97a] M. Catanese. Multiwavelength Observations of a Flare from Markarian 501. *Astrophysical Journal Letters* **487**, L143–L146 (1997). arXiv:astro-ph/9707179. Cited on page 33, 148.

[Cat97b] M. Catanese et al. Detection of Gamma Rays with E $>$ 100 MeV from BL Lacertae. *Astrophysical Journal* **480**, 562 (1997). Cited on page 134, 219.

[Cat98] M. Catanese et al. Discovery of Gamma–Ray Emission above 350 GeV from the BL Lacertae Object 1ES 2344+514. *Astrophysical Journal* **501**, 616 (1998). arXiv:astro-ph/9712325. Cited on page 33, 36, 188, 189, 196, 197.

[Cat00] M. Catanese and R. M. Sambruna. A Rapid X-ray Flare from Markarian 501. *Astrophysical Journal* **534**, L39–L42 (2000). arXiv:astro-ph/0003153. Cited on page 135.

[Cel01] A. Celotti, G. Ghisellini, and M. Chiaberge. Large-scale jets in active galactic nuclei: multiwavelength mapping. *Monthly Notices of the Royal Astronomical Society* **321**, L1–L5 (2001). arXiv:astro-ph/0008021. Cited on page 32.

[Cha99] P. M. Chadwick et al. Very High Energy Gamma Rays from PKS 2155-304. *Astrophysical Journal* **513**, 161–167 (1999). Cited on page 36.

[Che34] P. A. Cherenkov. Visible light from clear liquids under the action of gamma radiation. *C. R. (Doklady) Akad. Sci. URSS* **2**, 451–454 (1934). Cited on page 49.

[Che86] K. S. Cheng, C. Ho, and M. Ruderman. Energetic Radiation from Rapidly Spinning Pulsars. II. Vela and Crab. *Astrophysical Journal* **300**, 522 (1986). Cited on page 17.

[Chi92] J. Chiang and R. W. Romani. Gamma radiation from pulsar magnetospheric gaps. *Astrophysical Journal* **400**, 629–637 (1992). Cited on page 17.

[Cip06] S. Ciprini, E. Lindfors, K. Nilsson, and L. Ostorero. Optical Monitoring of PKS 2155-304 during August-September 2004 with the KVA Telescope. In H. R. Miller, K. Marshall, J. R. Webb, and M. F. Aller, editors, *Astronomical Society of the Pacific Conference Series*, May, 2006. `arXiv:astro-ph/0509023`. Cited on page 86.

[Clo06] D. Clowe, M. Bradač, A. H. Gonzalez, M. Markevitch, S. W. Randall, C. Jones, and D. Zaritsky. A direct empirical proof of the existence of dark matter. *Astrophysical Journal Letters* **648**, L109–L113 (2006). `arXiv:astro-ph/0608407`. Cited on page 19.

[Col72] G. Colla et al. The B2 Catalogue of radio sources—second part. *Astronomy & Astrophysics Supplement* **7**, 1 (1972). Cited on page 131.

[Col98] D. Colladay and V. A. Kostelecký. Lorentz-violating extension of the standard model. *Physical Review D* **58**, 116002 (1998). `arXiv:hep-ph/9809521`. Cited on page 19.

[Col99] W. P. Claspy G. W. Collins II and J. C. Martin. A Reinterpretation of Historical References to the Supernova of A.D. 1054. *Publications of the Astronomial Society of the Pacific* **111**, 871–880 (1999). Cited on page 119.

[Con98] J. J. Condon, W. D. Cotton, E. W. Greisen, E. W., Q. F. Yin, R. A. Perley, G. B. Taylor, and J. J. Broderick. The NRAO VLA Sky Survey. *Astronomical Journal* **115**, 1693–1716 (1998). Cited on page 184, 203, 217.

[Cop99] P. S. Coppi and F. A. Aharonian. Simultaneous X-Ray and Gamma-Ray Observations of TeV Blazars: Testing Synchro-Compton Emission Models and Probing the Infrared Extragalactic Background. *Astrophysical Journal* **521**, L33–L36 (1999). `arXiv:astro-ph/9903159`. Cited on page 35.

[Cor03] J. Cortina et al. Camera Control and Central Control of the MAGIC Telescope. In *Proceedings of the 28th International Cosmic Ray Conference*, pages 2931–2934, July, 2003. Cited on page 59.

[Cor05] J. Cortina et al. Technical Performance of the MAGIC telescope. In *Proceedings of the 29th International Cosmic Ray Conference*, volume 5, pages 359–362, Aug, 2005. `arXiv:astro-ph/0508274`. Cited on page 57.

[Cos01] L. Costamante, G. Ghisellini, P. Giommi, et al. Extreme synchrotron BL Lac objects. Stretching the blazar sequence. *Astronomy & Astrophysics* **371**, 512–526 (2001). Cited on page 131, 239.

[Cos02] L. Costamante and G. Ghisellini. TeV candidate BL Lac objects. *Astronomy & Astrophysics* **384**, 56–71 (2002). `arXiv:astro-ph/0112201`. Cited on page 32, 37, 38, 39, 41, 233, 235, 245.

[Cui04] W. Cui. X-Ray Flaring Activity of Markarian 421. *Astrophysical Journal* **605**, 662–669 (2004). `arXiv:astro-ph/0401222`. Cited on page 135, 136, 176.

[Dan05] M. K. Daniel et al. Spectrum of Very High Energy Gamma–Rays from the blazar 1ES 1959+650 during Flaring Activity in 2002. *Astrophysical Journal* **621**, 181–187 (2005). `arXiv:astro-ph/0503085`. Cited on page 29, 234.

[Dar96] A. Dar and N. J. Shaviv. The extragalactic neutrino background radiations from blazars and cosmic rays. *Astroparticle Physics* **4**, 343–349 (1996). `arXiv:astro-ph/9504083`. Cited on page 246.

[Dar97] A. Dar and A. Laor. Hadronic Production of TeV Gamma–Ray Flares from Blazars. *Astrophysical Journal Letters* **478**, L5+ (1997). `arXiv:astro-ph/9610252`. Cited on page 28, 246.

[Dar98] A. Dar. Can Fireball Models Explain Gamma–Ray Bursts? *Astrophysical Journal Letters* **500**, L93 (1998). arXiv:astro-ph/9709231. Cited on page 16.

[Dau97] A. Daum et al. First results on the performance of the HEGRA IACT array. *Astroparticle Physics* **8**, 1–2 (1997). Cited on page xxviii, 58.

[Der94] C. D. Dermer and R. Schlickeiser. On the location of the acceleration and emission sites in gamma-ray blazars. *Astrophysical Journal Supplement* **90**, 945–948 (1994). Cited on page 24.

[Dix70] R. S. Dixon. A Master List of Radio Sources. *Astrophysical Journal Supplement* **20**, 1–503 (1970). Cited on page 184.

[Dja99] A. Djannati-Ataï et al. Very High Energy Gamma–ray spectral properties of Mkn 501 from CAT Čerenkov telescope observations in 1997. *Astronomy & Astrophysics* **350**, 17–24 (1999). arXiv:astro-ph/9906060. Cited on page 33, 133, 135, 154.

[Dja02] A. Djannati-Ataï et al. Detection of the BL Lac object 1ES 1426+428 in the Very High Energy gamma–ray band by the CAT Telescope from 1998-2000. *Astronomy & Astrophysics* **391**, L25–L28 (2002). arXiv:astro-ph/0207618. Cited on page 36.

[Djo87] S. Djorgovski and M. Davis. Fundamental properties of elliptical galaxies. *Astrophysical Journal* **313**, 59–68 (1987). Cited on page 230.

[Dol06] H. Dole, G. Lagache, J.-L. Puget, et al. The cosmic infrared background resolved by Spitzer. Contributions of mid-infrared galaxies to the far-infrared background. *Astronomy & Astrophysics* **451**, 417–429 (2006). arXiv:astro-ph/0603208. Cited on page 11.

[Dom05a] E. Domingo-Santamaría et al. The DISP analysis method for point-like or extended gamma source searches/studies with the MAGIC telescope. In *Proceedings of the 29th International Cosmic Ray Conference*, volume 5, pages 363–366, Aug, 2005. arXiv:astro-ph/0508274. Cited on page 102.

[Dom05b] E. Domingo-Santamaría and D. F. Torres. High energy γ–ray emission from the starburst nucleus of NGC 253. *Astronomy & Astrophysics* **444**, 403–415 (2005). arXiv:astro-ph/0506240. Cited on page 16.

[Don95] L. Dondi and G. Ghisellini. Gamma–ray–loud blazars and beaming. *Monthly Notices of the Royal Astronomical Society* **273**, 583–595 (1995). Cited on page 31.

[Don01] D. Donato, G. Ghisellini, G. Tagliaferri, and G. Fossati. Hard X-ray properties of blazars. *Astronomy & Astrophysics* **375**, 739–751 (2001). arXiv:astro-ph/0105203. Cited on page 26.

[Don03] A.-C. Donea and R. J. Protheroe. Radiation fields of disk, BLR and torus in quasars and blazars: implications for γ–ray absorption. *Astroparticle Physics* **18**, 377–393 (2003). arXiv:astro-ph/0202068. Cited on page 10.

[Don05] D. Donato, R. M. Sambruna, and M. Gliozzi. Six years of BeppoSAX observations of blazars: A spectral catalog. *Astronomy & Astrophysics* **433**, 1163–1169 (2005). arXiv:physics/0412114. Cited on page 205.

[Dop99] M. A. Dopita. What Physics Drives the Unified Model? In Y. Terzian, E. Khachikian, and D. Weedman, editors, *IAU Symposium 194: Activity in Galaxies and Related Phenomena*, pages 199–207, 1999. Cited on page 23.

[Dwe98] E. Dwek et al. The COBE Diffuse Infrared Background Experiment Search for the Cosmic Infrared Background. IV. Cosmological Implications. *Astrophysical Journal* **508**, 106–122 (1998). arXiv:astro-ph/9806129. Cited on page 10.

[Ell04a] J. Ellis, N. E. Mavromatos, and D. V. Nanopoulos. Synchrotron radiation and quantum gravity. *Nature* **428**, 386 (2004). arXiv:astro-ph/0309144. Cited on page 138.

[Ell04b] J. R. Ellis, N. E. Mavromatos, and A. S. Sakharov. Synchrotron radiation from the Crab Nebula discriminates between models of space-time foam. *Astroparticle Physics* **20**, 669–682 (2004). arXiv:astro-ph/0308403. Cited on page 137, 138.

[Ell06] J. Ellis, N. E. Mavromatos, D. V. Nanopoulos, A. S. Sakharov, and E. K. G. Sarkisyan. Robust limits on Lorentz violation from gamma-ray bursts. *Astroparticle Physics* **25**, 402–411 (2006). arXiv:astro-ph/0510172. Cited on page 19, 137, 170, 171.

[Elt64] L. Elterman. Parameters for attenuation in the atmospheric windows for fifteen wavelengths. *Applied Optics* **3**, 745–750 (1964). Cited on page 83.

[Elt66] L. Elterman. *Handbook of Geophysics and Space Environments*. McGraw–Hill, 1966. Cited on page 83.

[Elv92] M. Elvis, D. Plummer, J. Schachter, and G. Fabbiano. The Einstein Slew Survey. *Astrophysical Journal Supplement* **80**, 257–303 (1992). Cited on page 187.

[Fal90] R. Falomo and A. Treves. PG 1553+11—A bright optically selected BL Lacertae object. *Publications of the Astronomial Society of the Pacific* **102**, 1120–1125 (1990). Cited on page 205, 206.

[Fal94] R. Falomo, R. Scarpa, and M. Bersanelli. Optical spectrophotometry of blazars. *Astrophysical Journal Supplement* **93**, 125–143 (1994). Cited on page 205.

[Fal99] R. Falomo and J. K. Kotilainen. Optical imaging of the host galaxies of X–ray selected BL Lacertae objects. *Astronomy & Astrophysics* **352**, 85–102 (1999). arXiv:astro-ph/9910106. Cited on page 187, 195.

[Fal02] R. Falomo, J. K. Kotilainen, and A. Treves. The Black Hole Mass of BL Lacertae Objects from the Stellar Velocity Dispersion of the Host Galaxy. *Astrophysical Journal Letters* **569**, L35–L38 (2002). arXiv:astro-ph/0203199. Cited on page 230, 231.

[Fal03] R. Falomo, N. Carangelo, and A. Treves. Host galaxies and black hole masses of low- and high-luminosity radio-loud active nuclei. *Monthly Notices of the Royal Astronomical Society* **343**, 505–511 (2003). arXiv:astro-ph/0304190. Cited on page 230.

[Feg97] D. J. Fegan. Gamma/hadron separation at TeV energies. *Journal of Physics G* **23**, 1013–1060 (1997). Cited on page 96.

[Fer49] E. Fermi. On the Origin of the Cosmic Radiation. *Physical Review* **75**, 1169–1174 (1949). Cited on page 8.

[Fer00] L. Ferrarese and D. Merritt. A Fundamental Relation between Supermassive Black Holes and Their Host Galaxies. *Astrophysical Journal Letters* **539**, L9–L12 (2000). arXiv:astro-ph/0006053. Cited on page 230.

[Fic94] C. E. Fichtel, D. L. Bertsch, J. Chiang, et al. The first energetic gamma–ray experiment telescope (EGRET) source catalog. *Astrophysical Journal Supplement* **94**, 551–581 (1994). Cited on page 184, 217.

[Fom94] V. P. Fomin et al. New methods of atmospheric Cherenkov imaging for gamma–ray astronomy. I. The false source method. *Astroparticle Physics* **2**, 137–150 (1994). Cited on page 85, 100.

[Fos98] G. Fossati et al. A unifying view of the spectral energy distributions of blazars. *Monthly Notices of the Royal Astronomical Society* **299**, 433–448 (1998). arXiv:astro-ph/9804103. Cited on page 27, 29, 32, 38, 39, 41, 219.

[Fri88] W. Fricke et al. Fifth fundamental catalogue (FK5). Part 1: The basic fundamental stars. *Veröffentlichungen des Astronomischen Rechen-Instituts Heidelberg* **32**, 1–106 (1988). Cited on page xxviii, 72.

[Gai90] T. K. Gaisser. *Cosmic Rays And Particle Physics*. Cambridge University Press, 1990. Cited on page 47.

[Gai96] J. A. Gaidos et al. Very Rapid and Energetic Bursts of TeV Photons from the Active Galaxy Markarian 421. *Nature* **383**, 319 (1996). Cited on page 33, 137.

[Gal02] Y. A. Gallant. Particle Acceleration at Relativistic Shocks. *LNP Volume 589: Relativistic Flows in Astrophysics* **589**, 24 (2002). arXiv:astro-ph/0201243. Cited on page 163.

[Gam99] R. Gambini and G. Pullin. Nonstandard optics from quantum space-time. *Physical Review D* **59**, 124021 (1999). arXiv:gr-qc/9809038. Cited on page 136.

[Gar98] L. J. Garay. Spacetime Foam as a Quantum Thermal Bath. *Physical Review Letters* **80**, 2508–2511 (1998). arXiv:gr-qc/9801024. Cited on page 136.

[Gar06] M. Garczarczyk. Ph. D. Thesis in preparation, Universität Rostock, 2006. Cited on page 16, 59.

[Gau05] M. Gaug et al. Calibration of the MAGIC telescope. In *Proceedings of the 29th International Cosmic Ray Conference*, Aug, 2005. arXiv:astro-ph/0508274. Cited on page 90, 116.

[GCN06] GCN: The Gamma ray bursts Coordinates Network, http://gcn.gsfc.nasa.gov/. Cited on page 16, 65.

[Geb00] K. Gebhardt et al. A Relationship between Nuclear Black Hole Mass and Galaxy Velocity Dispersion. *Astrophysical Journal Letters* **539**, L13–L16 (2000). arXiv:astro-ph/0006289. Cited on page 230.

[Geo01] M. Georganopoulos, J. G. Kirk, and A. Mastichiadis. The Beaming Pattern and Spectrum of Radiation from Inverse Compton Scattering in Blazars. *Astrophysical Journal* **561**, 111–117 (2001). arXiv:astro-ph/0107152. Cited on page 171.

[Geo05] M. Georganopoulos, D. Kazanas, E. E. Perlman, and F. W. Stecker. Bulk Comptonization of the Cosmic Microwave Background by Extragalactic Jets as a Probe of Their Matter Content. *Astrophysical Journal* **625**, 656–666 (2005). arXiv:astro-ph/0502201. Cited on page 30.

[Ghi89] G. Ghisellini and L. Maraschi. Bulk acceleration in relativistic jets and the spectral properties of blazars. *Astrophysical Journal* **340**, 181–189 (1989). Cited on page 24.

[Ghi98] G. Ghisellini et al. A theoretical unifying scheme for gamma–ray bright blazars. *Monthly Notices of the Royal Astronomical Society* **301**, 451–468 (1998). arXiv:astro-ph/9807317. Cited on page 27, 29.

[Ghi02] G. Ghisellini, A. Celotti, and L. Costamante. Low power BL Lacertae objects and the blazar sequence. Clues on the particle acceleration process. *Astronomy & Astrophysics* **386**, 833–842 (2002). Cited on page 29, 32, 38.

[Gie06] B. Giebels. Extragalactic γ-ray astrophysics with HESS. Talk given at *2nd Workshop On TeV Particle Astrophysics*, Madison, (2006). Cited on page 36, 41.

[Gin21] C. Gini. Measurement of inequality of income. *Economic Journal* **31**, 22–43 (1921). Cited on page 96.

[Gio90] P. Giommi et al. A study of BL Lacertae-type objects with Exosat. I—Flux correlations, luminosity variability, and spectral variability. *Astrophysical Journal* **356**, 432–455 (1990). Cited on page 135.

[Gio95] P. Giommi, S. G. Ansari, and A. Micol. Radio to X-ray energy distribution of BL Lacertae objects. *Astronomy & Astrophysics Supplement* **109**, 267–291 (1995). Cited on page 205.

[Gio00] P. Giommi, P. Padovani, and E. Perlman. Detection of exceptional X-ray spectral variability in the TeV BL Lac 1ES 2344+514. *Monthly Notices of the Royal Astronomical Society* **317**, 743–749 (2000). arXiv:astro-ph/9907377. Cited on page 187, 194.

[Gio02] P. Giommi et al. A Catalog of 157 X-ray Spectra and 84 Spectral Energy Distributions of Blazars Observed with BeppoSAX. In P. Giommi, E. Massaro, and G. Palumbo, editors, *Blazar Astrophysics with BeppoSAX and Other Observatories*, page 63, 2002. `arXiv:astro-ph/0209596`. Cited on page 184, 217.

[Gli06] M. Gliozzi, R. M. Sambruna, I. Jung, H. Krawczynski, D. Horan, and F. Tavecchio. Long-Term X-Ray and TeV variability of Mrk 501. *Astrophysical Journal* **646**, 61–75 (2006). `arXiv:astro-ph/0603693`. Cited on page 33, 132, 146, 174, 176.

[Goe05a] F. Goebel. Markarian 501. *IAU circular* **8562**, 2 (2005). Cited on page 142.

[Goe05b] F. Goebel et al. Absolute energy scale calibration of the magic telescope using muon images. In *Proceedings of the 29th International Cosmic Ray Conference*, volume 5, pages 179–182, Pune, 2005. `arXiv:astro-ph/0508274`. Cited on page 91, 116.

[Gou66] R. J. Gould and G. Schréder. Opacity of the Universe to High–Energy Photons. *Physical Review Letters* **16**, 252–254 (1966). Cited on page 10.

[Gre60] K. Greisen. Cosmic Ray Showers. *Annual Review of Nuclear and Particle Science* **10**, 63–108 (1960). Cited on page 46.

[Gre66] K. Greisen. End to the Cosmic-Ray Spectrum? *Physical Review Letters* **16**, 748–750 (1966). Cited on page 7.

[Gre86] R. F. Green, M. Schmidt, and J. Liebert. The Palomar–Green catalog of ultraviolet-excess stellar objects. *Astrophysical Journal Supplement* **61**, 305–352 (1986). Cited on page xxix, 205.

[Gre95] I. A. Grenier. Spatial distribution of the unidentified EGRET sources off the galactic plane. *Advances in Space Research* **15**, 73 (1995). Cited on page 18.

[Gre96] P. C. Gregory, W. K. Scott, K. Douglas, and J. J. Condon. The GB6 Catalog of Radio Sources. *Astrophysical Journal Supplement* **103**, 427 (1996). Cited on page 184, 203, 217.

[Guy00] J. Guy, C. Renault, F. A. Aharonian, M. Rivoal, and J.-P. Tavernet. Constraints on the cosmic infra-red background based on BeppoSAX and CAT spectra of Markarian 501. *Astronomy & Astrophysics* **359**, 419–428 (2000). `arXiv:astro-ph/0004355`. Cited on page 133.

[Hal05] F. Halzen and D. Hooper. High energy neutrinos from the TeV Blazar 1ES 1959+650. *Astroparticle Physics* **23**, 537–542 (2005). `arXiv:astro-ph/0502449`. Cited on page 246.

[Han99] J. L. Han and W. W. Tian. Pulsars identified from the NRAO VLA Sky Survey. *Astronomy & Astrophysics Supplement* **136**, 571–577 (1999). Cited on page 123.

[Har92] R. C. Hartman et al. Detection of high–energy gamma radiation from quasar 3C 279 by the EGRET telescope on the Compton Gamma Ray Observatory. *Astrophysical Journal Letters* **385**, L1–L4 (1992). Cited on page 36.

[Har99] R. C. Hartman, D. L. Bertsch, S. D. Bloom, et al. The Third EGRET Catalog of High–Energy Gamma–Ray Sources. *Astrophysical Journal Supplement* **123**, 79–202 (1999). Cited on page 10, 13, 15, 203, 228.

[Hau01] G. H. Hauser and E. Dwek. The Cosmic Infrared Background: Measurements and Implications. *Annual Review of Astronomy and Astrophysics* **39**, 249–307 (2001). `arXiv:astro-ph/0105539`. Cited on page 10.

[Hay98] N. Hayashida et al. Observations of TeV Gamma Ray Flares from Markarian 501 with the Telescope Array Prototype. *Astrophysical Journal Letters* **504**, L71 (1998). Cited on page 132, 134, 135.

[Hay00] N. Hayashida. Updated AGASA event list above 4×10^{19} eV, `arXiv:astro-ph/0008102`. Cited on page 7.

[Hay06] M. Hayashida, private communication. August, 2006. Cited on page 174.

[Hec98] D. Heck et al. CORSIKA: A Monte Carlo Code to Simulate Extensive Air Showers, `http://www-ik.fzk.de/corsika/`. Cited on page xxvii, 83.

[Hen06] T. Hengstebeck. Ph. D. Thesis in preparation, Humboldt-Universität zu Berlin, 2006. Cited on page 96, 99.

[Hes12] V. F. Hess. Über Beobachtungen der durchdringenden Strahlung bei sieben Freiballonfahrten. *Physikalische Zeitschrift* **13**, 1084–1091 (1912). Cited on page 5.

[Hil61] D. A. Hill and N. A. Porter. Photography of Čerenkov light from Extensive Air Showers in the Atmosphere. *Nature* **191**, 690 (1961). Cited on page 49.

[Hil85] A. M. Hillas. Cerenkov light images of EAS produced by primary gamma rays and by nuclei. In F. C. Jones, editor, *Proceedings of the 19th International Cosmic Ray Conference*, volume 3, pages 445–448, August, 1985. Cited on page 93.

[Hil98] A. M. Hillas et al. The Spectrum of TeV Gamma Rays from the Crab Nebula. *Astrophysical Journal* **503**, 744–759 (1998). Cited on page 121, 122, 126, 127, 128, 129.

[Hol03] J. Holder et al. Detection of TeV Gamma Rays from the BL Lacertae Object 1ES 1959+650 with the Whipple 10 Meter Telescope. *Astrophysical Journal* **583**, L9–L12 (2003). `arXiv:astro-ph/0212170`. Cited on page 36.

[Hor01] D. Horan et al. Observations of 1H 1426+428 with the Whipple 10 m imaging atmospheric Cherenkov telescope. In *Proceedings of the 27th International Cosmic Ray Conference*, page 2622, August, 2001. Cited on page 234.

[Hor02] D. Horan et al. Detection of the BL Lacertae Object H1426+428 at TeV Gamma–Ray Energies. *Astrophysical Journal* **571**, 753–762 (2002). `arXiv:astro-ph/0202185`. Cited on page 36.

[Hor03] D. Horns. Multi-wavelength Observations of the TeV Blazars Mkn 421, 1ES1959+650, and H1426+428 with the HEGRA Cherenkov Telescopes and the RXTE X-ray Satellite. In L. O. Takalo and E. Valtaoja, editors, *ASP Conference Series 299: High Energy Blazar Astronomy*, July, 2003. `arXiv:astro-ph/0209454`. Cited on page 171.

[Hor04a] D. Horan et al. Constraints on the Very High Energy Emission from BL Lacertae Objects. *Astrophysical Journal* **603**, 51–61 (2004). `arXiv:astro-ph/0311397`. Cited on page 219, 229.

[Hor04b] D. Horan and T. C. Weekes. Extragalactic sources of TeV gamma rays: a summary. *New Astronomy Review* **48**, 527–535 (2004). `arXiv:astro-ph/0310391`. Cited on page 227.

[Hor05] D. Horns, F. Goebel, D. Mazin, R. M. Wagner, and S. Wagner. Concept of a Global Network of Cherenkov Telescopes (GNCT) and first joint observations of H.E.S.S and MAGIC. In B. Degrange, editor, *Proceedings Towards A Network Of Cherenkov Detectors VII*, pages 141–146, May, 2005. Cited on page 128, 129.

[Ito02] C. Itoh et al. Detection of diffuse TeV gamma–ray emission from the neaby starburst galaxy NGC 253. *Astronomy & Astrophysics* **396**, L1–L4 (2002). `arXiv:astro-ph/0211530`. Cited on page 16.

[Jac03] T. Jacobson, S. Liberati, and D. Mattingly. A strong astrophysical constraint on the violation of special relativity by quantum gravity. *Nature* **424**, 1019–1021 (2003). `arXiv:astro-ph/0212190`. Cited on page 137, 138.

[Jac06] T. Jacobson, S. Liberati, and D. Mattingly. Lorentz violation at high energy: Concepts, phenomena, and astrophysical constraints. *Annals of Physics* **321**, 150–196 (2006). `arXiv:astro-ph/0505267`. Cited on page 19.

[Jag92] O. C. de Jager and A. K. Harding. The expected high–energy to ultra–high–energy gamma–ray spectrum of the Crab Nebula. *Astrophysical Journal* **396**, 161–172 (1992). Cited on page 121, 125.

[Jag02] O. C. de Jager and F. W. Stecker. Extragalactic Gamma-Ray Absorption and the Intrinsic Spectrum of Markarian 501 during the 1997 Flare. *Astrophysical Journal* **566**, 738–743 (2002). arXiv:astro-ph/0107103. Cited on page 154.

[Jah96] K. Jahoda et al. In-orbit performance and calibration of the Rossi X-ray Timing Explorer (RXTE) Proportional Counter Array (PCA). In O. H. Siegmund and M. A. Gummin, editors, *Proc. SPIE Vol. 2808, p. 59-70, EUV, X-Ray, and Gamma–Ray Instrumentation for Astronomy VII*, October, 1996. Cited on page 135, 206.

[Jak06] P. Jakobsson et al. A mean redshift of 2.8 for Swift gamma–ray bursts. *Astronomy & Astrophysics* **447**, 897–903 (2006). arXiv:astro-ph/0509888. Cited on page 16.

[Jar03] T. H. Jarrett et al. The 2MASS Large Galaxy Atlas. *Astronomical Journal* **125**, 525–554 (2003). Cited on page xxvii, 184, 187.

[Jel63] J. V. Jelley and N. A. Porter. Čerenkov Radiation from the Night Sky, and its Application to γ-Ray Astronomy. *Quarterly Journal of the Royal Astronomical Society* **4**, 275 (1963). Cited on page 49.

[Jes05] S. Jester, D. E. Harris, H. L. Marshall, K. K. Meisenheimer, R. Perley, and H.-J. Roeser. New HST and Chandra results on the jet in 3C273. *Bulletin of the American Astronomical Society* **37**, 475 (2005). Cited on page 25.

[Jes06] S. Jester, D. E. Harris, H. L. Marshall, and K. Meisenheimer. New Chandra observations of the jet in 3C 273. I. Softer X-ray than radio spectra and the X-ray emission mechanism. *Astrophysical Journal* **648**, 900–909 (2006). arXiv:astro-ph/0605529. Cited on page 25.

[Kaa99] P. Kaaret. Pulsar Radiation and Quantum Gravity. *Astronomy & Astrophysics* **345**, L32–L34 (1999). arXiv:astro-ph/9903464. Cited on page 137, 138, 171.

[Kan96] G. Kanbach et al. Characteristics of galactic gamma–ray sources in the second EGRET catalog. *Astronomy & Astrophysics Supplement* **120**, C461 (1996). Cited on page 18.

[Kas05] A. Kashlinsky. Cosmic infrared background and early galaxy evolution. *Physics Reports* **409**, 361–438 (2005). arXiv:astro-ph/0412235. Cited on page 10.

[Kat99] J. Kataoka et al. High–Energy Emission from the TeV Blazar Markarian 501 during Multiwavelength Observations in 1996. *Astrophysical Journal* **514**, 138–147 (1999). arXiv:astro-ph/9811014. Cited on page 134, 144, 184.

[Kat05] K. Katarzyński, G. Ghisellini, F. Tavecchio, L. Maraschi, G. Fossati, and A. Mastichiadis. Correlation between the TeV and X-ray emission in high–energy peaked BL Lac objects. *Astronomy & Astrophysics* **433**, 479–496 (2005). arXiv:astro-ph/0412405. Cited on page 145, 146.

[Kat06a] K. Katarzyński, G. Ghisellini, A. Mastichiadis, F. Tavecchio, and L. Maraschi. Stochastic particle acceleration and synchrotron self-Compton radiation in TeV blazars. *Astronomy & Astrophysics* **453**, 47–56 (2006). arXiv:astro-ph/0603362. Cited on page 215.

[Kat06b] K. Katarzyński, G. Ghisellini, F. Tavecchio, J. Gracia, and L. Maraschi. Hard TeV spectra of blazars and the constraints to the infrared intergalactic background. *Monthly Notices of the Royal Astronomical Society* **368**, L52–L56 (2006). arXiv:astro-ph/0603030. Cited on page 215.

[Kaw91] N. Kawai et al. Multifrequency observations of BL Lacertae in 1988. *Astrophysical Journal* **382** **382**, 508–514 (1991). Cited on page 219.

[Kem99] A. K. Kembhavi and J. V. Narlikar. *Quasars and Active Galactic Nuclei*. Cambridge University Press, 1999. Cited on page 21, 23.

[Ker95] A. D. Kerrick et al. Upper Limits on TeV Gamma–Ray Emission from Active Galactic Nuclei. *Astrophysical Journal* **452**, 588 (1995). Cited on page 36, 229.

[Kin02] M. Kino, F. Takahara, and M. Kusunose. Energetics of TeV Blazars and physical constraints on their emission regions. *Astrophysical Journal* **564**, 97–107 (2002). arXiv:astro-ph/0107436. Cited on page 30, 31.

[Kir94] J. G. Kirk. Particle Acceleration. In A. O. Benz and T. J.-L. Courvoisier, editors, *Saas-Fee Advanced Course 24: Plasma Astrophysics*, page 225, 1994. http://www.mpi-hd.mpg.de/personalhomes/kirk/publications/. Cited on page 8.

[Kir98] J. G. Kirk, F. M. Rieger, and A. Mastichiadis. Particle acceleration and synchrotron emission in blazar jets. *Astronomy & Astrophysics* **333**, 452–458 (1998). arXiv:astro-ph/9801265. Cited on page 171.

[Kir99] J. G. Kirk and A. Mastichiadis. Variability patterns of synchrotron and inverse Compton emission in blazars. *Astroparticle Physics* **11**, 45–48 (1999). Cited on page 24.

[Kne02] T. M. Kneiske, K. Mannheim, and D. H. Hartmann. Implications of cosmological gamma–ray absorption. I. Evolution of the metagalactic radiation field. *Astronomy & Astrophysics* **386**, 1–11 (2002). arXiv:astro-ph/0202104. Cited on page 10, 11, 13.

[Kne04] T. M. Kneiske, T. Bretz, K. Mannheim, and D. H. Hartmann. Implications of cosmological gamma–ray absorption. II. Modification of gamma–ray spectra. *Astronomy & Astrophysics* **413**, 807–815 (2004). arXiv:astro-ph/0309141. Cited on page 11, 40, 156, 200, 214, 217, 218, 228, 229, 231, 234, 237, 238.

[Kon99a] A. Konopelko. TeV Gamma–Ray Observations of the BL Lac Object 1ES 2344+514 with the HEGRA system of IACTs. In *Proceedings of the 26th International Cosmic Ray Conference*, number 3, page 426, Aug, 1999. Cited on page 189.

[Kon99b] A. K. Konopelko et al. Evidence for Intergalactic Absorption in the TeV Gamma–Ray Spectrum of Markarian 501. *Astrophysical Journal Letters* **518**, L13–L15 (1999). arXiv:astro-ph/9904057. Cited on page 14.

[Kra99] D. Kranich et al. TeV gamma–ray observations of the Crab and Mkn 501 during moonshine and twilight. *Astroparticle Physics* **12**, 65–74 (1999). arXiv:astro-ph/9901330. Cited on page 53.

[Kra00] H. Krawczynski, P. S. Coppi, T. Maccarone, and F. A. Aharonian. X–ray/TeV–gamma–ray observations of several strong flares of Mkn 501 during 1997 and implications. *Astronomy & Astrophysics* **353**, 97–107 (2000). arXiv:astro-ph/9911224. Cited on page 146.

[Kra01a] D. Kranich. *Temporal and spectral characteristics of the active galactic nucleus Mkn 501 during a phase of high activity in the TeV range*. Ph. D. thesis, Technische Universität München, 2001. http://wwwmagic.mppmu.mpg.de/publications/theses/. Cited on page 125, 132, 177.

[Kra01b] D. Kranich, O. de Jager, M. Kestel, and E. Lorenz. QPO analysis of the TeV and X–ray lightcurve of Mkn 501 in 1997—final results. In *Proceedings of the 27th International Cosmic Ray Conference*, pages 2630–2633, August, 2001. Cited on page 177.

[Kra01c] H. Krawczynski et al. Simultaneous X-Ray and TeV Gamma–Ray Observation of the TeV Blazar Markarian 421 during 2000 February and May. *Astrophysical Journal* **559**, 187–195 (2001). arXiv:astro-ph/0105331. Cited on page 26.

[Kra02] H. Krawczinski, P. S. Coppi, and F. Aharonian. Time-dependent modelling of the Markarian 501 X-ray and TeV gamma–ray data taken during 1997 March and April. *Monthly Notices of the Royal Astronomical Society* **336**, 721–735 (2002). arXiv:astro-ph/0204229. Cited on page 32, 34, 182.

[Kra03] D. Kranich. TeV Observations of BL Lac Objects. In L. O. Takalo and E. Valtaoja, editors, *ASP Conference Series 299: High Energy Blazar Astronomy*, July, 2003. Cited on page 219.

[Kra04] H. Krawczynski, S. B. Hughes, D. Horan, et al. Multiwavelength Observations of Strong Flares from the TeV Blazar 1ES 1959+650. *Astrophysical Journal* **601**, 151–164 (2004). `arXiv:astro-ph/0310158`. Cited on page 30, 32, 134, 181, 184, 201, 203, 216, 217, 236, 239.

[Kra06] D. Kranich, private communication. July, 2006. Cited on page 174.

[Kre02] F. Krennrich et al. Discovery of Spectral Variability of Markarian 421 at TeV Energies. *Astrophysical Journal Letters* **575**, L9–L13 (2002). `arXiv:astro-ph/0207184`. Cited on page 33, 234.

[Kud99] T. Kudoh, S. Aoki, S. Koide, and K. Shibata. Are blazar jets magnetically driven outflows? *Astronomische Nachrichten* **320**, 311 (1999). Cited on page 24.

[Kue81] H. Kuehr, A. Witzel, I. I. K. Pauliny-Toth, and U. Nauber. A catalogue of extragalactic radio sources having flux densities greater than 1 Jy at 5 GHz. *Astronomy & Astrophysics Supplement* **45**, 367–430 (1981). Cited on page 184.

[Laf95] G. D. Lafferty and T. R. Wyatt. Where to stick your data points: The treatment of measurements within wide bins. *Nuclear Instruments and Methods in Physics Research A* **355**, 541–547 (1995). Cited on page 112.

[Lag05] G. Lagache, J.-L. Puget, and H. Dole. Dusty Infrared Galaxies: Sources of the Cosmic Infrared Background. *Annual Review of Astronomy and Astrophysics* **43**, 727–768 (2005). `arXiv:astro-ph/0507298`. Cited on page 10.

[Lan04a] H. Landt, P. Padovani, E. S. Perlman, and P. Giommi. A physical classification scheme for blazars. *Monthly Notices of the Royal Astronomical Society* **351**, 83–100 (2004). `arXiv:astro-ph/0402494`. Cited on page 24.

[Lan04b] M. J. Lang. Evidence for TeV gamma ray emission from TeV J2032+4130 in Whipple archival data. *Astronomy & Astrophysics* **423**, 415–419 (2004). `arXiv:astro-ph/0405513`. Cited on page 17.

[Lau99] S. A. Laurent-Muehleisen et al. The RGB Sample of Intermediate BL Lacertae Objects. *Astrophysical Journal* **525**, 127–143 (1999). `arXiv:astro-ph/9905133`. Cited on page 205.

[Les01] R. W. Lessard et al. A new analysis method for reconstructing the arrival direction of TeV gamma rays using a single imaging atmospheric Cherenkov telescope. *Astroparticle Physics* **15**, 1–18 (2001). `arXiv:astro-ph/0005468`. Cited on page 102.

[Lev96] A. M. Levine, H. V. Brandt, W. Cui, et al. First Results from the All-Sky Monitor on the Rossi X-Ray Timing Explorer. *Astrophysical Journal Letters* **469**, L33 (1996). `arXiv:astro-ph/9608109`. Cited on page 143, 144, 194, 196, 207, 211.

[Lev04] A. Levine. Rossi X-Ray Timing Explorer Project—Home Page for the All-Sky Monitor (ASM) team, `http://xte.mit.edu/`. Cited on page 144, 147, 194, 195, 212, 242.

[Li83] T.-P. Li and Y.-Q. Ma. Analysis methods for results in gamma–ray astronomy. *Astrophysical Journal* **272**, 317–324 (1983). Cited on page 103, 161.

[Lom06] G. Lombardi, V. Zitelli, S. Ortolani, and M. Pedani. El Roque de Los Muchachos Site Characteristics. I. Temperature Analysis. *Publications of the Astronomial Society of the Pacific* **118**, 1198–1204 (2006). Cited on page 58.

[Lon92] M. S. Longair. *High Energy Astrophysics*. Cambridge University Press, 1992. Cited on page 7, 9, 25, 43.

[Lon03] K. S. Long et al. Chandra CCD Imagery of the Northeast and Northwest Limbs of SN 1006. *Astrophysical Journal* **586**, 1162–1178 (2003). Cited on page 35.

[Lor05] E. Lorenz, private communication. Sep, 2005. Cited on page 116.

[Luc03] F. Lucarelli et al. Observations of the Crab Nebula with the HEGRA system of IACTs in convergent mode using a topological trigger. *Astroparticle Physics* **19**, 339–350 (2003). arXiv:astro-ph/0209447. Cited on page 125.

[Lyn69] D. Lynden-Bell. Galactic Nuclei as Collapsed Old Quasars. *Nature* **223**, 690 (1969). Cited on page 21, 230.

[Lyu03] M. Lyutikov. Role of reconnection in AGN jets. *New Astronomy Review* **47**, 513–515 (2003). arXiv:astro-ph/0211338. Cited on page 136.

[Ma98] C. Ma, E. F. Arias, T. M. Eubanks, et al. The International Celestial Reference Frame as Realized by Very Long Baseline Interferometry. *Astronomical Journal* **116**, 516–546 (1998). Cited on page 142, 223.

[Mac96] D. MacMinn and J. Primack. Probing the era of Galaxy Formation via TeV Gamma–Ray Absorption by the Near Infrared Extragalactic Background. *Space Science Reviews* **75**, 413–422 (1996). arXiv:astro-ph/9504032. Cited on page 203.

[Mad06] G. M. Madejski and M. Sikora. High Energy Observations of Blazars: the Future. In H. R. Miller, K. Marshall, J. R. Webb, and M. F. Aller, editors, *Astronomical Society of the Pacific Conference Series*, May, 2006. Cited on page 8.

[Maj05] P. Majumdar et al. Monte Carlo simulation for the MAGIC telescope. In *Proceedings of the 29th International Cosmic Ray Conference*, volume 5, pages 203–206, Aug, 2005. arXiv:astro-ph/0508274. Cited on page 83, 97.

[Mal01] M. A. Malkov and L. O'C Drury. Nonlinear theory of diffusive acceleration of particles by shock waves. *Reports of Progress in Physics* **64**, 429–481 (2001). Cited on page 214.

[Man92] K. Mannheim and P. L. Biermann. Gamma–ray flaring of 3C 279—A proton–initiated cascade in the jet? *Astronomy and Astrophysics Letters* **253**, L21–L24 (1992). Cited on page 28.

[Man93] K. Mannheim. The proton blazar. *Astronomy & Astrophysics* **269**, 67–76 (1993). arXiv:astro-ph/9302006. Cited on page 28.

[Man98] K. Mannheim. Possible Production of High–Energy Gamma Rays from Proton Acceleration in the Extragalactic Radio Source Markarian 501. *Science* **279**, 684 (1998). arXiv:astro-ph/9803241. Cited on page 28.

[Man05] P. Mantsch. The Pierre Auger Observatory—Progress and first results. In *Proceedings of the 29th International Cosmic Ray Conference*, volume 10, pages 115–124, Aug, 2005. http://icrc2005.tifr.res.in/. Cited on page 7.

[Mar85] A. P. Marscher and W. K. Gear. Models for high-frequency radio outbursts in extragalactic sources, with application to the early 1983 millimeter-to-infrared flare of 3C 273. *Astrophysical Journal* **298**, 114–127 (1985). Cited on page 26.

[Mar92] L. Maraschi, G. Ghisellini, and A. Celotti. A jet model for the gamma–ray emitting blazar 3C 279. *Astrophysical Journal Letters* **397**, L5–L9 (1992). Cited on page 26.

[Mar99] L. Maraschi et al. Simultaneous X-Ray and TeV Observations of a Rapid Flare from Markarian 421. *Astrophysical Journal Letters* **526**, L81–L84 (1999). Cited on page 26.

[Mar02] A. P. Marscher, S. G. Jorstad, J.-L. Gómez, M. F. Aller, H. Teräsranta, M. L. Lister, and A. M. Stirling. Observational evidence for the accretion-disk origin for a radio jet in an active galaxy. *Nature* **417**, 625–627 (2002). Cited on page 24.

[Mas97] A. Mastichiadis and J. G. Kirk. Variability in the synchrotron self-Compton model of blazar emission. *Astronomy & Astrophysics* **320**, 19–25 (1997). arXiv:astro-ph/9610058. Cited on page 34, 35, 136.

[Mas02] A. Mastichiadis and J. G. Kirk. Models of Variability in Blazar Jets. *Publications of the Astronomical Society of Australia* **19**, 138–142 (2002). Cited on page 34.

[Mas04] E. Massaro et al. Log-parabolic spectra and particle acceleration in the BL Lac object Mkn 421: Spectral analysis of the complete BeppoSAX wide band X-ray data set. *Astronomy & Astrophysics* **413**, 489–503 (2004). arXiv:astro-ph/0312260. Cited on page 152.

[Mat93] J. R. Mattox et al. The EGRET detection of quasar 1633+382. *Astrophysical Journal* **410**, 609–614 (1993). Cited on page 31, 166.

[Mat05] D. Mattingly. Modern Tests of Lorentz Invariance. *Living Reviews in Relativity* **8**, 5 (2005). http://relativity.livingreviews.org/Articles/lrr-2005-5/. Cited on page 19.

[May39] N. U. Mayall. The Crab Nebula, a Probable Supernova. *Astronomical Society of the Pacific Leaflets* **3**, 145 (1939). Cited on page 119.

[Maz05] D. Mazin, F. Goebel, D. Horns, G. Rowell, R. M. Wagner, and S. Wagner. Concept of a Global Network of Cherenkov telescopes and first joint observations of H.E.S.S. and MAGIC. In *Proceedings of the 29th International Cosmic Ray Conference*, volume 4, pages 331–334, Aug, 2005. arXiv:astro-ph/0508273. Cited on page 128.

[Maz06] D. Mazin. Observations of Extragalactic Sources with the MAGIC Telescope—TeV Blazars and Extragalactic Background Light. In J. M. Paredes, O. Reimer, and D. F. Torres, editors, *The Multi-messenger Approach to Unidentified Gamma–ray Sources*, July, 2006. Cited on page 12, 215.

[McI74] B. McInnes and M. F. Walker. Astronomical Site Testing in the Canary Islands. *Publications of the Astronomial Society of the Pacific* **86**, 529 (1974). Cited on page 58.

[McL02] R. J. McLure and J. S. Dunlop. On the black hole-bulge mass relation in active and inactive galaxies. *Monthly Notices of the Royal Astronomical Society* **331**, 795–804 (2002). arXiv:astro-ph/0108417. Cited on page 230.

[Mei01] D. L. Meier, S. Koide, and Y. Uchida. Magnetohydrodynamic Production of Relativistic Jets. *Science* **291**, 84–92 (2001). Cited on page 24, 25, 180.

[Mer96] M. Merck et al. Study of the spectral characteristics of unidentified galactic EGRET sources. Are they pulsar-like? *Astronomy & Astrophysics Supplement* **120**, C465 (1996). Cited on page 18.

[Mes02] P. Mészáros. Theories of Gamma–Ray Bursts. *Annual Review of Astronomy and Astrophysics* **40**, 137–169 (2002). arXiv:astro-ph/0111170. Cited on page xxviii, 16.

[Mil83] H. R. Miller and R. F. Green. Optical/UV Observations of the BL Lac Object, PG 1553+11. *Bulletin of the American Astronomical Society* **15**, 957 (1983). Cited on page 205.

[Mil88] H. R. Miller et al. The ultraviolet/optical variability of PG 1553+11. In E. J. Rolfe, editor, *A Decade of UV Astronomy with the IUE Satellite, Volume 2*, pages 303–304, June, 1988. Cited on page 205.

[Mir92] I. F. Mirabel et al. A double-sided radio jet from the compact Galactic Centre annihilator 1E140.7–2942. *Nature* **358**, 215–217 (1992). Cited on page 18, 235.

[Mir94a] I. F. Mirabel and L. F. Rodriguez. A Superluminal Source in the Galaxy. *Nature* **371**, 46 (1994). Cited on page 18.

[Mir94b] R. Mirzoyan and E. Lorenz. Measurement of the Night Sky Light Background at La Palma. *MPI–PhE/94–35* (1994). http://wwwmagic.mppmu.mpg.de/publications/articles/. Cited on page 52.

[Mir97] R. Mirzoyan and E. Lorenz. On the calibration accuracy of light sensors in atmospheric cherenkov, fluorescence and neutrino experiments. In *Proceedings of the 25th International Cosmic Ray Conference*, volume 7, pages 265–268, 1997. Cited on page 91.

[Mir99] I. F. Mirabel and L. F. Rodríguez. Sources of Relativistic Jets in the Galaxy. *Annual Review of Astronomy and Astrophysics* **37**, 409–443 (1999). arXiv:astro-ph/9902062. Cited on page 18, 236.

[Mir03] R. Mirzoyan et al. The Active Mirror Control of the MAGIC Telescope. In *Proceedings of the 28th International Cosmic Ray Conference*, pages 2935–2938, July, 2003. Cited on page 59.

[Mir04] I. F. Mirabel. Microquasar-AGN-GRB Connections. In V. Schoenfelder, G. Lichti, and C. Winkler, editors, *ESA SP-552: 5th INTEGRAL Workshop on the INTEGRAL Universe*, October, 2004. arXiv:astro-ph/0405433. Cited on page 235.

[Miz05] S. Mizobuchi, E. Aliu, D. Mazin, M. Teshima, R. M. Wagner, W. Wittek, and H. Yoshii. Reconstruction methods of energy spectra for high redshift sources with the MAGIC telescope. In *Proceedings of the 29th International Cosmic Ray Conference*, volume 5, pages 323–326, Aug, 2005. arXiv:astro-ph/0508274. Cited on page 115.

[Mor06] D. C. Morris, J. Reeves, V. Pal'shin, et al. GRB 050713A: High Energy Observations of the GRB Prompt and Afterglow Emission. *Astrophysical Journal* (2006). Accepted for publication, arXiv:astro-ph/0602490. Cited on page 16.

[Mue01] A. Mücke and R. J. Protheroe. A proton synchrotron blazar model for flaring in Markarian 501. *Astroparticle Physics* **15**, 121–136 (2001). arXiv:astro-ph/0004052. Cited on page 28.

[Mue03] A. Mücke et al. BL Lac objects in the synchrotron proton blazar model. *Astroparticle Physics* **18**, 593–613 (2003). arXiv:astro-ph/0206164. Cited on page 28, 136, 225, 246.

[Muf84] S. L. Mufson et al. Coordinated multifrequency observations of the BL Lacertae objects Mrk 180 and Mrk 501. *Astrophysical Journal* **285**, 571–579 (1984). Cited on page 131.

[Mye06] J. D. Myers. Swift grb information, http://swift.gsfc.nasa.gov/docs/swift/archive/grbtable/. Cited on page 17.

[NED06] NASA/IPAC Extragalactic Database, http://nedwww.ipac.caltech.edu/. Cited on page 191, 203, 217.

[Nes01] Y. I. Neshpor et al. BL Lac: A New Ultrahigh–Energy Gamma–Ray Source. *Astronomy Reports* **45**, 249–254 (2001). arXiv:astro-ph/0111448. Cited on page 219.

[Nie06] E. Nieppola et al. Spectral energy distributions of a large sample of BL Lacertae objects. *Astronomy & Astrophysics* **445**, 441–450 (2006). arXiv:astro-ph/0509045. Cited on page 27, 131, 205, 219.

[Nil99] K. Nilsson et al. Two-dimensional Photometric Decomposition of the TeV BL Lacertae Objects Markarian 421, Markarian 501, and 1ES 2344+514. *Publications of the Astronomial Society of the Pacific* **111**, 1223–1232 (1999). Cited on page 187, 195.

[Nil06] K. Nilsson, private communication. April, 2006. Cited on page 144, 148, 193, 195, 203, 211, 217.

[Nis52] J. Nishimura and K. Kamata. On the Theory of Cascade Showers, I. *Progress of Theoretical Physics* **7**, 182–192 (1952). http://ptp.ipap.jp/link?PTP/7/185. Cited on page 46.

[Nis99] T. Nishiyama. Detection of a new TeV gamma–ray source of BL Lac object 1ES 1959+650. In *Proceedings of the 26th International Cosmic Ray Conference*, number 3, page 370, Aug, 1999. Cited on page 36.

[Nis02] K. Nishijima. Very High Energy Gamma-ray Observations of AGN with CANGAROO. *Publications of the Astronomical Society of Australia* **19**, 26–28 (2002). Cited on page 229.

[Nol03] P. L. Nolan, W. F. Tompkins, I. A. Grenier, and P. F. Michelson. Variability of EGRET Gamma–Ray Sources. *Astrophysical Journal* **597**, 615–627 (2003). arXiv:astro-ph/0307188. Cited on page 18.

[Nus03] E. Nuss. CELESTE Observations of the Crab Nebula and Mkn 421 in 1999-2000 and 2000-2001. In *Proceedings of the 28th International Cosmic Ray Conference*, volume 5, pages 2607–2610, July, 2003. Cited on page 128.

[Nyq28] H. Nyquist. Certain topics in telegraph transmission theory. *Transactions of the AIEE* **47**, 617–644 (1928). Cited on page 61.

[Ong98] R. A. Ong. Very high–energy gamma–ray astronomy. *Physics Reports* **305**, 93–202 (1998). Cited on page 8.

[Ose01] S. Oser et al. High–Energy Gamma-Ray Observations of the Crab Nebula and Pulsar with the Solar Tower Atmospheric Cerenkov Effect Experiment. *Astrophysical Journal* **547**, 949–958 (2001). Cited on page 51.

[Oso01] S. Osone and M. Teshima. Long periodicity of Blaser with RXTE ASM. In *Proceedings of the 27th International Cosmic Ray Conference*, pages 2695–2699, August, 2001. Cited on page 177.

[Oso02] S. Osone and M. Teshima. Long periodicity of Blazar with RXTE ASM, TA and HEGRA. In R. Enomoto, M. Mori, and S. Yanagita, editors, *The Universe Viewed in Gamma-Rays*, Tsukuba, 2002. arXiv:astro-ph/0211640. Cited on page 177.

[Ost06a] M. A. Osterman, H. R. Miller, et al. Analysis of Simultaneous Observations of the BL Lac Object PG 1553+11 in the Radio, Optical, and X-ray Regimes. In H. R. Miller, K. Marshall, J. R. Webb, and M. F. Aller, editors, *Astronomical Society of the Pacific Conference Series*, May, 2006. Cited on page 205, 206.

[Ost06b] M. A. Osterman, H. R. Miller, et al. Multiwavelength Observations of the Extreme X-Ray Selected BL Lac Object PG 1553+11 (1ES 1553+113). *Astronomical Journal* **132**, 873–882 (2006). arXiv:astro-ph/0605076. Cited on page 205, 206, 212.

[Ott06a] N. Otte, private communication. June, 2006. Cited on page 120.

[Ott06b] N. Otte and P. Majumdar. The Crab nebula in VHE gamma-rays from 60 GeV to 9 TeV, http://wwwmagic.mppmu.mpg.de/documents/. MAGIC internal note TDAS06–08. Cited on page 123.

[Pac99] W. S. Paciesas et al. The Fourth BATSE Gamma–Ray Burst Catalog (Revised). *Astrophysical Journal Supplement* **122**, 465–495 (1999). arXiv:astro-ph/9903205. Cited on page 17.

[Pad03] P. Padovani, E. S. Perlman, H. Landt, P. Giommi, and M. Perri. What Types of Jets Does Nature Make? A New Population of Radio Quasars. *Astrophysical Journal* **588**, 128–142 (2003). arXiv:astro-ph/0301227. Cited on page 28.

[Pan04a] D. Paneque. *The MAGIC telescope: Development of new technologies and first observations*. Ph. D. Thesis, Technische Universität München, 2004. http://wwwmagic.mppmu.mpg.de/publications/theses/. Cited on page 53.

[Pan04b] D. Paneque et al. A method to enhance the sensitivity of photomultipliers for Air Cherenkov Telescopes by applying a lacquer that scatters light. *Nuclear Instruments and Methods in Physics Research A* **518**, 619–621 (2004). Cited on page 59.

[Par00a] J. M. Paredes, J. Martí, M. M. Ribó, and M. Massi. Discovery of a High–Energy Gamma–Ray–Emitting Persistent Microquasar. *Science* **288**, 2340–2342 (2000). arXiv:astro-ph/0102235. Cited on page 18.

[Par00b] J. van Paradijs, C. Kouveliotou, and R. A. M. J. Wijers. Gamma-Ray Burst Afterglows. *Annual Review of Astronomy and Astrophysics* **38**, 379–425 (2000). Cited on page 16, 65.

[Pau99] S. Paul, W. Weise, N. Kaiser, N. Beisert, S. Fritsch, B. Kirchlechner, M. Kuckein, R. Kuhn, and R. Wagner. *Teilchen und Kerne*. Fachschaft MPI, Technische Universität München, 1999. Cited on page 5, 50.

[PDG06] W.-M. Yao et al. Review Of Particle Physics. *Journal of Physics G* **33**, 1–1232 (2006). `http://pdg.lbl.gov/`. Cited on page 7, 11, 45, 46, 50, 170.

[Pee93] P. J. E. Peebles. *Principles of Physical Cosmology*. Princeton Theories in Physics. Princeton University Press, 1993. Cited on page 170.

[Per96] E. S. Perlman et al. The Einstein Slew Survey Sample of BL Lacertae Objects. *Astrophysical Journal Supplement* **104**, 251 (1996). Cited on page 187, 188, 195.

[Per01] E. S. Perlman et al. Surveys and the Blazar Parameter Space. In P. Padovani and C. M. Urry, editors, *ASP Conference Series 227: Blazar Demographics and Physics*, pages 200–207, 2001. `arXiv:astro-ph/0012185`. Cited on page 28.

[Per05] E. S. Perlman et al. Intrinsic Curvature in the X-Ray Spectra of BL Lacertae Objects. *Astrophysical Journal* **625**, 727–740 (2005). `arXiv:astro-ph/0502298`. Cited on page 205.

[Pet96] D. Petry et al. Detection of VHE γ–rays from Mkn 421 with the HEGRA Cherenkov Telescopes. *Astronomy & Astrophysics* **311**, L13–L16 (1996). `arXiv:astro-ph/9606159`. Cited on page 36.

[Pet00] D. Petry et al. Multiwavelength Observations of Markarian 501 during the 1997 High State. *Astrophysical Journal* **536**, 742–755 (2000). `arXiv:astro-ph/0002255`. Cited on page 134, 144, 145, 146.

[Pia98] E. Pian et al. BeppoSAX Observations of Unprecedented Synchrotron Activity in the BL Lacertae Object Markarian 501. *Astrophysical Journal Letters* **492**, L17 (1998). `arXiv:astro-ph/9710331`. Cited on page 32, 132, 135, 166, 167.

[Pin03] G. Piner. Blazars (VLBA & GLAST). In J. D. Romney and M. J. Reid, editors, *Future Directions in High Resolution Astronomy: A Celebration of the 10th Anniversary of the VLBA*, page 12, Socorro, NM, 2003. Cited on page 33.

[Pin04] B. G. Piner and P. G. Edwards. The Parsec-Scale Structure and Jet Motions of the TeV Blazars 1ES 1959+650, PKS 2155-304, and 1ES 2344+514. *Astrophysical Journal* **600**, 115–126 (2004). `arXiv:astro-ph/0309547`. Cited on page 33.

[Pla95] R. Plaga. Detecting Intergalactic Magnetic Fields Using Time Delays in Pulses of Gamma-Rays. *Nature* **374**, 430 (1995). Cited on page 137.

[Poh00] M. Pohl and R. Schlickeiser. On the conversion of blast wave energy into radiation in active galactic nuclei and gamma–ray bursts. *Astronomy & Astrophysics* **354**, 395–410 (2000). `arXiv:astro-ph/9911452`. Cited on page 28.

[Pra04] F. Prada, A. Klypin, J. Flix, M. Martínez, and E. Simonneau. Dark Matter Annihilation in the Milky Way Galaxy: Effects of Baryonic Compression. *Physical Review Letters* **93 24**, 241301 (2004). Cited on page 19.

[Pre02] W. H. Press and S. A. Teukolsky. *Numerical Recipes in C++: The Art of Scientific Computing*. Cambridge University Press, 2002. Cited on page 145.

[Pri01] J. R. Primack et al. Probing Galaxy Formation with High–Energy Gamma Rays. In F. A. Aharonian and H. J. Völk, editors, *American Institute of Physics Conference Series*, volume 558, page 463, 2001. `arXiv:astro-ph/0011475`. Cited on page 11.

[Pun92] M. Punch et al. Detection of TeV photons from the active galaxy Markarian 421. *Nature* **358**, 477 (1992). Cited on page 33, 36.

[Qia04] S.-J. Qian, X.-Z. Zhang, and T. P. Krichbaum. BL Lacertae: Hard Optical Spectrum and GeV γ-ray Emission. *Chinese Journal of Astronomy and Astrophysics* **4**, 231–246 (2004). Cited on page 219.

[Qui96] J. Quinn et al. Detection of Gamma Rays with E $>$ 300 GeV from Markarian 501. *Astrophysical Journal* **456**, L83 (1996). Cited on page 33, 36, 131, 134, 143, 174.

[Qui99] J. Quinn et al. The Flux Variability of Markarian 501 in Very High Energy Gamma Rays. *Astrophysical Journal* **518**, 693–698 (1999). `arXiv:astro-ph/9903088`. Cited on page 131, 132, 135, 176.

[Rao88] M. V. S. Rao and S. Sinha. The origin of the hump in the Cerenkov lateral distribution in gamma–ray showers and a possible means of separating them from proton showers. *Journal of Physics G* **14**, 811–827 (1988). Cited on page 50, 51.

[Rav02] M. Ravasio et al. BL Lacertae: Complex spectral variability and rapid synchrotron flare detected with BeppoSAX. *Astronomy & Astrophysics* **383**, 763–772 (2002). `arXiv:astro-ph/0201307`. Cited on page 219.

[Ree78] M. J. Rees. The M87 jet—Internal shocks in a plasma beam. *Annual Review of Astronomy and Astrophysics* **184**, 61P–65P (1978). Cited on page 34, 136.

[Ree84] M. J. Rees. Black Hole Models for Active Galactic Nuclei. *Annual Review of Astronomy and Astrophysics* **22**, 471–506 (1984). Cited on page 21.

[Ree92] M. J. Rees and P. Meszaros. Relativistic fireballs—Energy conversion and time-scales. *Monthly Notices of the Royal Astronomical Society* **258**, 41P–43P (1992). Cited on page 16.

[Ren00] C. Renault, N. Renaud, and G. Henri. Intensity correlation between observations at different wavelengths for Mkn 501 in 1997. *Nuclear Physics B Proceedings Supplements* **80**, C126 (2000). Cited on page 166.

[Ren01] C. Renault, A. Barrau, G. Lagache, and J.-L. Puget. New constraints on the cosmic mid-infrared background using TeV gamma-ray astronomy. *Astronomy & Astrophysics* **371**, 771–778 (2001). `arXiv:astro-ph/0012094`. Cited on page 11.

[Rev03] M. Revnivtsev, M. Gilfanov, R. Sunyaev, K. Jahoda, and C. Markwardt. The spectrum of the cosmic X-ray background observed by RTXE/PCA. *Astronomy & Astrophysics* **411**, 329–334 (2003). `arXiv:astro-ph/0306569`. Cited on page 194.

[Rie00] F. M. Rieger and K. Mannheim. Implications of a possible 23 day periodicity for binary black hole models in Mkn 501. *Astronomy & Astrophysics* **359**, 948–952 (2000). `arXiv:astro-ph/0005478`. Cited on page 177.

[Rie05] F. M. Rieger and P. Duffy. Particle Acceleration in Astrophysical Shear Flows. *Chinese Journal of Astronony and Astrophysics* **5**, 195–200 (2005). `arXiv:astro-ph/0501153`. Cited on page 28.

[Roa73] F. E. Roach and J. L. Gordon. *The Light of the Night Sky*. D. Reidel Publishing Company, 1973. Cited on page 52.

[Rob96] I. Robson. *Active Galactic Nuclei*. John Wiley, 1996. Cited on page 21.

[Roe88] S. Röser and U. Bastian. A new star catalogue of SAO type. *Astronomy & Astrophysics Supplement* **74**, 449–451 (1988). Cited on page xxix, 72.

[Rol05] W. A. Rolke, A. M. López, and J. Conrad. Limits and confidence intervals in the presence of nuisance parameters. *Nuclear Instruments and Methods in Physics Research A* **551**, 493–503 (2005). `arXiv:physics/0403059`. Cited on page 222, 224.

[Ros41] B. Rossi and K. Greisen. Cosmic Ray Theory. *Reviews of Modern Physics* **13**, 240–309 (1941). Cited on page 45.

[Ros95] J. Rose. Calibration of next generation Cerenkov telescopes using muon ring images. In M. Cresti, editor, *Proc. Towards a major atmospheric Cherenkov detector IV*, pages 241–247, Padova, 1995. Cited on page 91.

[Rud75] M. A. Ruderman and P. G. Sutherland. Theory of pulsars—Polar caps, sparks, and coherent microwave radiation. *Astrophysical Journal* **196**, 51–72 (1975). Cited on page 17.

[Ruj02] A. de Rújula. GRBs in the cannonball model: an overview. In P. Durouchoux, Y. Fuchs, and J. Rodriguez, editors, *New Views on Microquasars*, page 177, 2002. arXiv:astro-ph/0207033. Cited on page 16.

[Rus90] J. L. Russell, B. M. Lasker, B. J. McLean, C. R. Sturch, and H. Jenkner. The Guide Star Catalog. II—Photometric and astrometric models and solutions. *Astronomical Journal* **99**, 2059–2081 (1990). Cited on page 217.

[Ryb79] G. B. Rybicki and A. P. Lightman. *Radiative Processes in Astrophysics*. Wiley, 1979. Cited on page 181.

[Sam98] F. W. Samuelson et al. The TeV Spectrum of Markarian 501. *Astrophysical Journal Letters* **501**, L17 (1998). Cited on page 132.

[Sam00] R. M. Sambruna et al. Correlated Intense X-Ray and TeV Activity of Markarian 501 in 1998 June. *Astrophysical Journal* **538**, 127–133 (2000). arXiv:astro-ph/0002215. Cited on page 134, 135.

[Sba05] B. Sbarufatti, A. Treves, and R. Falomo. Imaging Redshifts of BL Lacertae Objects. *Astrophysical Journal* **635**, 173–179 (2005). arXiv:astro-ph/0508200. Cited on page 205.

[Sba06] B. Sbarufatti, A. Treves, R. Falomo, J. Heidt, J. Kotilainen, and R. Scarpa. ESO–VLT optical spectroscopy of BL Lac objects: II. New redshifts, featureless objects and classification assessments. *Astronomical Journal* **132**, 1–19 (2006). arXiv:astro-ph/0601506. Cited on page 205, 245.

[Sca00] R. Scarpa et al. The Hubble Space Telescope Survey of BL Lacertae Objects. I. Surface Brightness Profiles, Magnitudes, and Radii of Host Galaxies. *Astrophysical Journal* **532**, 740–815 (2000). arXiv:astro-ph/9911147. Cited on page 205.

[Sch78] D. A. Schwartz et al. Identification of 4U 1651+39 with the BL Lacertae object Markarian 501 with the modulation collimator on HEAO 1. *Astrophysical Journal Letters* **224**, L103–L105 (1978). Cited on page 131.

[Sch94] M. Schmelling. The method of reduced cross-entropy A general approach to unfold probability distributions. *Nuclear Instruments and Methods in Physics Research A* **340**, 400–412 (1994). Cited on page 115.

[Sch99] B. E. Schaefer. Severe Limits on Variations of the Speed of Light with Frequency. *Physical Review Letters* **82**, 4964–4966 (1999). arXiv:astro-ph/9810479. Cited on page 137, 138.

[Sch01] V. Schönfelder, editor. *The Universe in Gamma Rays*. Springer, 2001. Cited on page 13.

[Sch02a] R. Schödel, T. Ott, R. Genzel, et al. A star in a 15.2-year orbit around the supermassive black hole at the centre of the Milky Way. *Nature* **419**, 694–696 (2002). Cited on page 230.

[Sch02b] T. Schweizer. *Analysis of The Large Gamma Ray Flares of Mkn 421 as observed with HEGRA CT1 on the island La Palma in 2001*. Ph. D. Thesis, IFAE Barcelona, 2002. http://wwwmagic.mppmu.mpg.de/publications/theses/. Cited on page 33, 137, 163.

[Sch02c] T. Schweizer, E. Lorenz, M. Martinez, A. Ostankov, and D. Paneque. The optical calibration of the MAGIC telescope camera. *IEEE Transactions on Nuclear Science* **49**, 2497–2503 (2002). Cited on page 62.

[Sch05a] F. Schmidt. CORSIKA Shower Images, `http://www.ast.leeds.ac.uk/ fs/`. Cited on page 48.

[Sch05b] M. Schroedter. Upper Limits on the Extragalactic Background Light from the Very High Energy Gamma-Ray Spectra of Blazars. *Astrophysical Journal* **628**, 617–628 (2005). `arXiv:astro-ph/0504397`. Cited on page 11.

[Sch05c] M. Schroedter et al. A Very High Energy Gamma–Ray Spectrum of 1ES 2344+514. *Astrophysical Journal* **634**, 947–954 (2005). `arXiv:astro-ph/0508499`. Cited on page 188, 199, 203, 234.

[Sch06] M. Schroedter, private communication. May, 2006. Cited on page 203.

[Sch07] T. Schweizer and E. Lorenz. Study of short flare times of the VHE γ–emission of Mkn 421 during the high state of 2001. (2007). Paper in preparation. Cited on page 163.

[Sew78] F. D. Seward. A trip to the Crab Nebula. *Journal of the British Interplanetary Society* **31**, 83–92 (1978). Cited on page 194.

[Sha49] C. E. Shannon. Communication in the presence of noise. *Proceedings of the Institute of Radio Engineers* **37**, 10–21 (1949). Cited on page 61.

[Sik00] M. Sikora and G. Madejski. On Pair Content and Variability of Subparsec Jets in Quasars. *Astrophysical Journal* **534**, 109–113 (2000). `arXiv:astro-ph/9912335`. Cited on page 30.

[Sik01a] M. Sikora, M. Błażejowski, M. C. Begelman, and R. Moderski. Modeling the Production of Flares in Gamma-Ray Quasars. *Astrophysical Journal* **554**, 1–11 (2001). `arXiv:astro-ph/0102091`. Cited on page 33.

[Sik01b] M. Sikora and G. Madejski. Blazars. In F. A. Aharonian and H. J. Völk, editors, *American Institute of Physics Conference Series*, volume 558, page 275, 2001. `arXiv:astro-ph/0101382`. Cited on page 26.

[Sik05] M. Sikora, G. M. Madejski, J.-P. Lasota, and M. C. Begelman. Are Quasar Jets Matter or Poynting Flux Dominated? In T. Bulik, B. Rudak, and G. Madejski, editors, *AIP Conference Proceedings 801: Astrophysical Sources of High Energy Particles and Radiation*, November, 2005. `arXiv:astro-ph/0509685`. Cited on page 24.

[Sil88] A. Sillanpaa, S. Haarala, and T. Korhonen. Optical monitoring of quasars and BL Lac objects. *Astronomy & Astrophysics Supplement* **72**, 347–354 (1988). Cited on page 86.

[Sil91] A. Sillanpaa, S. Mikkola, and L. Valtaoja. Optical monitoring of quasars and BL Lacertae objects. II. *Astronomy & Astrophysics Supplement* **88**, 225–231 (1991). Cited on page 86.

[Sla03] Slalib web page, `http://star-www.rl.ac.uk/star/docs/sun67.htx/node1.html`. Cited on page 67, 68, 69.

[Spa01] M. Spada, G. Ghisellini, D. Lazzati, and A. Celotti. Internal shocks in the jets of radio-loud quasars. *Monthly Notices of the Royal Astronomical Society* **325**, 1559–1570 (2001). `arXiv:astro-ph/0103424`. Cited on page 34, 136.

[Spe06] D. N. Spergel et al. `arXiv:astro-ph/0603449`. Submitted to Astrophysical Journal. Cited on page 19.

[Spr05] R. W. Springer et al. Measurements of UHECR Spectrum with the HiRes detector. In *Proceedings of the 29th International Cosmic Ray Conference*, volume 7, pages 391–394, Aug, 2005. `http://icrc2005.tifr.res.in/`. Cited on page 7.

[Ste71] F. W. Stecker. *Cosmic Gamma Rays*. Mono Book Corporation, Baltimore, 1971. Cited on page 9.

[Ste92] F. W. Stecker, O. C. de Jager, and M. H. Salamon. TeV gamma rays from 3C 279—A possible probe of origin and intergalactic infrared radiation fields. *Astrophysical Journal Letters* **390**, L49–L52 (1992). Cited on page 10.

[Ste96] F. W. Stecker and O. C. de Jager. Absorption of High Energy Gamma-Ray by Low Energy Intergalactic Photons. *Space Science Reviews* **75**, 401–412 (1996). arXiv:astro-ph/9501065. Cited on page 11.

[Ste01a] F. W. Stecker. TeV Gamma–Ray Absorption and the Intergalactic Infrared Background. In M. Harwit and M. G. Hauser, editors, *IAU Symposium 204: The Extragalactic Infrared Background and Its Cosmological Implications*, January, 2001. arXiv:astro-ph/0010015. Cited on page 12.

[Ste01b] F. W. Stecker and S. L. Glashow. New tests of Lorentz invariance following from observations of the highest energy cosmic/γ-rays. *Astroparticle Physics* **16**, 97–99 (2001). arXiv:astro-ph/0102226. Cited on page 138.

[Ste03] F. W. Stecker. Constraints on Lorentz invariance violating quantum gravity and large extra dimensions models using high energy γ-ray observations. *Astroparticle Physics* **20**, 85–90 (2003). arXiv:astro-ph/0308214. Cited on page 138.

[Tak98] M. Takeda et al. Extension of the Cosmic-Ray Energy Spectrum beyond the Predicted Greisen-Zatsepin-Kuz'min Cutoff. *Physical Review Letters* **81**, 1163–1166 (1998). arXiv:astro-ph/9807193. Cited on page 7.

[Tak99] M. Takeda et al. Small-Scale Anisotropy of Cosmic Rays above 10^{19} eV Observed with the Akeno Giant Air Shower Array. *Astrophysical Journal* **522**, 225–237 (1999). arXiv:astro-ph/9902239. Cited on page 6.

[Tak00] T. Takahashi et al. Complex Spectral Variability from Intensive Multiwavelength Monitoring of Markarian 421 in 1998. *Astrophysical Journal Letters* **542**, L105–L109 (2000). arXiv:astro-ph/0008505. Cited on page 26, 30.

[Tan98] T. Tanimori et al. Detection of Gamma Rays of up to 50 TeV from the Crab Nebula. *Astrophysical Journal Letters* **492**, L33 (1998). Cited on page 128.

[Tav98] F. Tavecchio, L. Maraschi, and G. Ghisellini. Constraints on the Physical Parameters of TeV Blazars. *Astrophysical Journal* **509**, 608–619 (1998). Cited on page 31, 32, 166.

[Tav00] F. Tavecchio, L. Maraschi, R. M. Sambruna, and C. M. Urry. The X-Ray Jet of PKS 0637-752: Inverse Compton Radiation from the Cosmic Microwave Background? *Astrophysical Journal Letters* **544**, L23–L26 (2000). arXiv:astro-ph/0007441. Cited on page 27, 33.

[Tav01] F. Tavecchio et al. Theoretical Implications from the Spectral Evolution of Markarian 501 Observed with BeppoSAX. *Astrophysical Journal* **554**, 725–733 (2001). Cited on page 30.

[Tlu03] M. Tluczykont. *Beobachtung und Nachweis von Aktiven Galaktischen Kernen und Suche nach Galaktischen Objekten im TeV-Energiebereich mit den HEGRA-Cherenkov-Teleskopen sowie Modellierung eines Photonspektrums durch den Zerfall neutraler Pionen aus schockbeschleunigten Hadronen*. Ph. D. Thesis, Universität Hamburg, 2003. http://www.physnet.uni-hamburg.de/. Cited on page 33, 189, 196, 197, 198, 219.

[Ton06] N. Tonello. *Study of the VHE gamma–ray emission from the Active Galactic Nucleus 1ES1959+650*. Ph. D. Thesis, Technische Universität München, 2006. http://wwwmagic.mppmu.mpg.de/publications/theses/. Cited on page 133, 249.

[Tor04] D. F. Torres, E. Domingo-Santamaría, and G. E. Romero. High–Energy Gamma Rays from Stellar Associations. *Astrophysical Journal Letters* **601**, L75–L78 (2004). arXiv:astro-ph/0312128. Cited on page 18.

[Tre02] S. Tremaine et al. The Slope of the Black Hole Mass versus Velocity Dispersion Correlation. *Astrophysical Journal* **574**, 740–753 (2002). arXiv:astro-ph/0203468. Cited on page 230, 231.

[Tru03] S. A. Trushkin. Radio spectra of the WMAP catalog sources. *Bulletin of the Special Astrophysical Observatory* **55**, 90–132 (2003). arXiv:astro-ph/0307205. Cited on page 184.

[Tsv98] Z. I. Tsvetanov et al. M87: A Misaligned BL Lacertae Object? *Astrophysical Journal Letters* **493**, L83 (1998). Cited on page 34, 36.

[Uch06] Y. Uchiyama, C. M. Urry, C. C. Cheung, S. Jester, J. van Duyne, P. Coppi, R. M. Sambruna, T. Takahashi, F. Tavecchio, and L. Maraschi. Shedding New Light on the 3C 273 Jet with the Spitzer Space Telescope. *Astrophysical Journal* **648**, 910–921 (2006). arXiv:astro-ph/0605530. Cited on page 25.

[Ulr75] M. Ulrich et al. Nonthermal continuum radiation in three elliptical galaxies. *Astrophysical Journal* **198**, 261–266 (1975). Cited on page 131, 170.

[Urr95] C. M. Urry and P. Padovani. Unified Schemes for Radio-Loud Active Galactic Nuclei. *Publications of the Astronomial Society of the Pacific* **107**, 803 (1995). arXiv:astro-ph/9506063. Cited on page 21, 23.

[Urr00] C. M. Urry et al. The Hubble Space Telescope Survey of BL Lacertae Objects. II. Host Galaxies. *Astrophysical Journal* **532**, 816–829 (2000). arXiv:astro-ph/9911109. Cited on page 187, 195.

[Vas00] V. V. Vassiliev. Extragalactic background light absorption signal in the TeV gamma–ray spectra of blazars. *Astroparticle Physics* **12**, 217–238 (2000). arXiv:astro-ph/9908088. Cited on page 12.

[Vau91] G. de Vaucouleurs, A. de Vaucouleurs, H. G. Corvin Jr., R. J. Buta, G. Paturel, and P. Fouque. *Third Reference Catalogue of Bright Galaxies*. Springer-Verlag Berlin Heidelberg New York, 1991. Cited on page 170.

[Ver94] R. C. Vermeulen and M. H. Cohen. Superluminal motion statistics and cosmology. *Astrophysical Journal* **430**, 467–494 (1994). Cited on page 34.

[Vie00] J. R. Vieira. Milky Way outline catalog, http://www.skymap.com/milkyway cat.htm, (2000). Cited on page 15.

[Vog99] W. Voges et al. The ROSAT all-sky survey bright source catalogue. *Astronomy & Astrophysics* **349**, 389–405 (1999). arXiv:astro-ph/9909315. Cited on page 184, 203.

[Wag03a] R. M. Wagner and T. Bretz. The MAGIC Analysis and Reconstruction Software. In *Proceedings of the 28th International Cosmic Ray Conference*, volume 7, pages 2947–2950, July, 2003. Cited on page 87.

[Wag03b] R. M. Wagner, T. Bretz, and D. Dorner. The Tracking System of the MAGIC Telescope. In *Proceedings of the 28th International Cosmic Ray Conference*, volume 7, pages 2943–2946, July, 2003. Cited on page 62.

[Wag05a] R. M. Wagner, T. Bretz, and D. Dorner. A scalable drive system concept for future projects. In B. Degrange, editor, *Proceedings Towards A Network Of Cherenkov Detectors VII*, pages 599–603, May, 2005. Cited on page 63.

[Wag05b] R. M. Wagner et al. Observations of the Crab nebula with the MAGIC telescope. In *Proceedings of the 29th International Cosmic Ray Conference*, volume 4, pages 163–166, Aug, 2005. arXiv:astro-ph/0508244. Cited on page 119, 214.

[Wal97] P. T. Wallace. Pointing and tracking software for the Gemini 8-m Telescopes. In A. L. Ardeberg, editor, *Proc. SPIE Vol. 2871, Optical Telescopes of Today and Tomorrow*, March, 1997. Cited on page 69.

[Wal00] P. M. Wallace et al. A Systematic Search for Short–Term Variability of EGRET Sources. *Astrophysical Journal* **540**, 184–191 (2000). arXiv:astro-ph/0004252. Cited on page 18.

[Wal01] P.T. Wallace. TPOINT—A Telescope Pointing Analysis System, http://www.tpsoft.demon.co.uk/. Cited on page 69.

[Wat05] A. A. Watson. Observations of ultra-high energy cosmic rays. Talk given at *9th International Conference on Topics in Astroparticle and Underground Physics*, Zaragoza, (2005). Cited on page 7.

[Wee88] T. C. Weekes. Very high energy gamma–ray astronomy. *Physics Reports* **160**, 1 (1988). Cited on page 8.

[Wee89] T. C. Weekes et al. Observation of TeV gamma rays from the Crab nebula using the atmospheric Cerenkov imaging technique. *Astrophysical Journal* **342**, 379–395 (1989). Cited on page 13, 93, 119.

[Wer93] K. Werner. Strings, pomerons and the VENUS model of hadronic interactions at ultrarelativistic energies. *Physics Reports* **232**, 87–299 (1993). Cited on page 83.

[Whi92] R. L. White and R. H. Becker. A new catalog of 30,239 1.4 GHz sources. *Astrophysical Journal Supplement* **79**, 331–467 (1992). Cited on page 184, 203, 217.

[Wie94] B. Wiebel. Chemical Composition in High Energy Cosmic Rays. (1994). Technical Report, Bergische Universität–Gesamthochschule Wuppertal, Germany, WUB 94–08. Cited on page 46.

[Wil05] D. Williams et al. Studies of Nearby Blazars with Milagro. In F. A. Aharonian, H. J. Völk, and D. Horns, editors, *AIP Conference Proceedings 745: High Energy Gamma–Ray Astronomy*, volume 745, February, 2005. Cited on page 206, 207.

[Wit00] W. Wittek. Rotation of the sky image in a camera of telescopes with Alt–Az mount, http://wwwmagic.mppmu.mpg.de/documents/. MAGIC internal note TDAS00–11. Cited on page 68.

[Woo02a] J.-H. Woo and C. M. Urry. Active Galactic Nucleus Black Hole Masses and Bolometric Luminosities. *Astrophysical Journal* **579**, 530–544 (2002). arXiv:astro-ph/0207249. Cited on page 230, 231, 232.

[Woo02b] J.-H. Woo and C. M. Urry. The Independence of Active Galactic Nucleus Black Hole Mass and Radio Loudness. *Astrophysical Journal Letters* **581**, L5–L7 (2002). Cited on page 230.

[Woo05] J.-H. Woo, C. M. Urry, R. P. van der Marel, P. Lira, and J. Maza. Black Hole Masses and Host Galaxy Evolution of Radio-Loud Active Galactic Nuclei. *Astrophysical Journal* **631**, 762–772 (2005). arXiv:astro-ph/0506316. Cited on page 231.

[Wri03] E. L. Wright. Cosmology calculator, http://www.astro.ucla.edu/wright/CosmoCalc.html. Cited on page 170.

[Wu02] X.-B. Wu, F. K. Liu, and T. Z. Zhang. Supermassive black hole masses of AGNs with elliptical hosts. *Astronomy & Astrophysics* **389**, 742–751 (2002). arXiv:astro-ph/0203158. Cited on page 231.

[Xie02] G. Z. Xie et al. Photometric monitoring of 12 BL Lacertae objects. *Monthly Notices of the Royal Astronomical Society* **329**, 689–699 (2002). Cited on page 187.

[XTE06] RXTE weather webpage, http://heasarc.gsfc.nasa.gov/xteweather/. Cited on page 133, 190, 193, 206, 211.

[Xue05] Y. Xue and W. Cui. X-Ray Flares from Markarian 501. *Astrophysical Journal* **622**, 160–167 (2005). arXiv:astro-ph/0412226. Cited on page 33, 135, 136, 174, 176, 180, 197.

[Yos05] S. Yoshida. Cosmic Ray Measurements above 1 EeV. In *Proceedings of the 29th International Cosmic Ray Conference*, volume 10, pages 297–302, Aug, 2005. http://icrc2005.tifr.res.in/. Cited on page 7.

[Zat66] G. T. Zatsepin and V. A. Kuz'min. Upper Limit of the Spectrum of Cosmic Rays. *Journal of Experimental and Theoretical Physics Letters* **4**, 78 (1966). Cited on page 7.

[Zim05] J. Zimmermann. *Statistical Learning in High Energy and Astrophysics*. Ph. D. Thesis, Universität München, München, 2005. http://edoc.ub.uni-muenchen.de/archive/00004353/. Cited on page 95.

[Zwi33] F. Zwicky. Die Rotverschiebung von extragalaktischen Nebeln. *Helvetica Physica Acta* **6**, 110–127 (1933). Cited on page 18.

Acknowledgments

Foremost I would like to thank Prof. Dr. S. Bethke, Prof. Dr. M. Teshima and Dr. R. Mirzoyan for having given me the opportunity to carry out this work in an extremely vital, fascinating and competitive field of physics and at the same time at an excellent place for scientific research. I also benefitted much from the opportunity to present my work at several international conferences and schools.

Further sincere thanks go to Dr. E. Lorenz, the "father" of the MAGIC telescope, who supervised this thesis, for many fruitful and inspiring discussions, for his commitment and his valuable help.

I enjoyed a very collaborative atmosphere in the MPI MAGIC group: Thanks to everybody for the wonderful time. The same goes for all members of the MAGIC collaboration, of course. I particularly acknowledge the many and fruitful discussions with P. Majumdar, N. Otte, D. Mazin, N. Tonello, A. Moralejo, D. Paneque, H. Bartko, F. Goebel, W. Wittek, and R. Bock. A special thanks to N. Otte for additionally sharing all the academic and non–academic gossip. Thanks to N. Nowak for all the astronomy–related discussions and enlightenments.

Many thanks to E. Lorenz, R. Mirzoyan, P. Majumdar, W. Wittek, F. Goebel, M. Meyer, and H. Meyer for their valuable comments which led to many improvements of the manuscript. I am much indebted to N. Wilcke for proof-reading the text. The communication with M. Schroedter, J. Buckley, G. Kanbach, M. Tluczykont, D. Horns, J. Kataoka, W. Bednarek, K. Nilsson, and E. Lindfors is acknowledged.

This research profitted considerably from using NASA's Astrophysics Data System and the NASA/IPAC Extragalactic Database.

Representative for the numerous people that develop useful computing tools vital also for scientific work, the efforts of the Free Software Foundation and of L. Torvalds and D. Knuth are acknowledged. The work of the LEO team, the creators and maintainers of the incredibly helpful online dictionary at `http://dict.leo.org/`, is acknowledged.

Finally I want to thank my girl-friend Nina Nowak for her patience throughout the last years, for the great many discussions on physics (and ROOT!) even at off-work times, and for her motivation and support, and of course—last but not least—my parents for every possible support.